frontiers | Research Topics

Advances in characterizing and monitoring land cover/use and associated ecosystem changes using remote sensing data

Edited by
George Xian, Sanath Sathyachandran Kumar, Seth Munson and Xiaoyang Zhang

Published in
Frontiers in Environmental Science
Frontiers in Ecology and Evolution
Frontiers in Earth Science

ISSN 1664-8714
ISBN 978-2-8325-4268-2
DOI 10.3389/978-2-8325-4268-2

About Frontiers

Frontiers is more than just an open access publisher of scholarly articles: it is a pioneering approach to the world of academia, radically improving the way scholarly research is managed. The grand vision of Frontiers is a world where all people have an equal opportunity to seek, share and generate knowledge. Frontiers provides immediate and permanent online open access to all its publications, but this alone is not enough to realize our grand goals.

Frontiers journal series

The Frontiers journal series is a multi-tier and interdisciplinary set of open-access, online journals, promising a paradigm shift from the current review, selection and dissemination processes in academic publishing. All Frontiers journals are driven by researchers for researchers; therefore, they constitute a service to the scholarly community. At the same time, the *Frontiers journal series* operates on a revolutionary invention, the tiered publishing system, initially addressing specific communities of scholars, and gradually climbing up to broader public understanding, thus serving the interests of the lay society, too.

Dedication to quality

Each Frontiers article is a landmark of the highest quality, thanks to genuinely collaborative interactions between authors and review editors, who include some of the world's best academicians. Research must be certified by peers before entering a stream of knowledge that may eventually reach the public - and shape society; therefore, Frontiers only applies the most rigorous and unbiased reviews. Frontiers revolutionizes research publishing by freely delivering the most outstanding research, evaluated with no bias from both the academic and social point of view. By applying the most advanced information technologies, Frontiers is catapulting scholarly publishing into a new generation.

What are Frontiers Research Topics?

Frontiers Research Topics are very popular trademarks of the *Frontiers journals series*: they are collections of at least ten articles, all centered on a particular subject. With their unique mix of varied contributions from Original Research to Review Articles, Frontiers Research Topics unify the most influential researchers, the latest key findings and historical advances in a hot research area.

Find out more on how to host your own Frontiers Research Topic or contribute to one as an author by contacting the Frontiers editorial office: frontiersin.org/about/contact

Advances in characterizing and monitoring land cover/use and associated ecosystem changes using remote sensing data

Topic editors

George Xian — United States Geological Survey (USGS), United States Department of the Interior, United States

Sanath Sathyachandran Kumar — Earth Resources Observation and Science Center, United States Geological Survey (USGS), United States

Seth Munson — U.S. Geological Survey, Southwest Biological Science Center, United States

Xiaoyang Zhang — South Dakota State University, United States

Citation

Xian, G., Kumar, S. S., Munson, S., Zhang, X., eds. (2024). *Advances in characterizing and monitoring land cover/use and associated ecosystem changes using remote sensing data*. Lausanne: Frontiers Media SA. doi: 10.3389/978-2-8325-4268-2

Table of contents

frontiers | Frontiers in Ecology and Evolution

TYPE Original Research
PUBLISHED 02 March 2023
DOI 10.3389/fevo.2023.1093454

OPEN ACCESS

EDITED BY
George Xian,
United States Geological Survey (USGS),
United States

REVIEWED BY
Qiqi Zhu,
China University of Geosciences Wuhan,
China
Hanxi Wang,
Harbin Normal University,
China

*CORRESPONDENCE
Lihua Wang
✉ wanglihua1@nbu.edu.cn

SPECIALTY SECTION
This article was submitted to Environmental Informatics and Remote Sensing,
a section of the journal
Frontiers in Ecology and Evolution

RECEIVED 09 November 2022
ACCEPTED 10 February 2023
PUBLISHED 02 March 2023

CITATION
Ma H, Wang L, Sun W, Yang S, Gao Y, Fan L, Yang G and Wang Y (2023) A new rice identification algorithm under complex terrain combining multi-characteristic parameters and homogeneous objects based on time series dual-polarization synthetic aperture radar. *Front. Ecol. Evol.* 11:1093454.
doi: 10.3389/fevo.2023.1093454

A new rice identification algorithm under complex terrain combining multi-characteristic parameters and homogeneous objects based on time series dual-polarization synthetic aperture radar

Hao Ma[1], Lihua Wang[1,2,3]*, Weiwei Sun[1], Songling Yang[1], Yanghua Gao[3], Li Fan[3], Gang Yang[1] and Yumiao Wang[1]

[1]Department of Geography and Spatial Information Techniques, Zhejiang Collaborative Innovation Center-Land and Marine Spatial Utilization and Governance Research, Ningbo University, Ningbo, China, [2]Donghai Academy, Ningbo University, Ningbo, China, [3]Chongqing Institute of Meteorological Sciences, Chongqing, China

Accurate mapping of rice-growing areas is essential to ascertain the spatial distribution of rice fields, and ensure food security. It is a challenging task to timely and accurate identify rice under the complex terrain due to its diversified land cover, small- or middle-sized rice fields with fragmented distribution. In this paper, the time series VV and VH backscatter coefficient datasets were first constructed based on 411 sentinel-1 synthetic aperture radar (SAR) images in Chongqing city with complex terrain. Then, the rice multi-characteristic parameters, including SAR backscatter features, composite features, rice phenological parameters, texture features and topographic features, were generated. On this basis, the homogeneous image objects were produced. Furthermore, a rice identification algorithm combining multi-characteristic parameters and homogeneous objects based on time series dual-polarization SAR (MPHO-DPSAR) was established. The research demonstrated that the MPHO-DPSAR algorithm can achieve accurate mapping of small and medium-sized and fragmented rice fields in regions under complex terrain according to the accuracy evaluation at three levels and the comparison with other three classical rice identification methods. The suitability and limitations of proposed MPHO-DPSAR algorithm were also discussed from the aspects of SAR data temporal and spatial resolution, rice phenology, and surface landscape complexity.

KEYWORDS

rice, multi-characteristic parameters, homogeneous objects, time series, dual-polarization, synthetic aperture radar

1. Introduction

Rice is one of the most important food crops for mankind and the staple food for nearly half of the world's population, especially in East Asian countries with large populations and limited arable land *per capita* (Corcione et al., 2016; Xie and Chen, 2019; Han et al., 2022). Sufficient food supply is the foundation of human survival, social stability and economic development (Zheng et al., 2016). Meantime, rice is an important source of agricultural

carbon emissions, which releases carbon in the form of greenhouse gases such as CO_2, CH_4, and N_2O during its growth (Chen and Pan, 2022; Lin et al., 2022). The development of low-carbon agriculture is an important measure to achieve the goal of comprehensive energy conservation and emission reduction (Lin et al., 2022). Therefore, monitoring the rice planting area is the basis for the government to accelerate the construction of a modern, low-carbon rice industry system, and to promote the continuous increase of farmers' income and the sustainable development of the rice industry. Timely and accurate mapping of paddy fields is of great significance for assisting in formulating food policies, ensuring food supply, promoting carbon emission reduction and developing smart agriculture.

Compared with the traditional rice identification methods based on field investigation, the application of optical remote sensing technology in agricultural monitoring is becoming increasingly mature (Yin et al., 2019; Zhu et al., 2022). Optical spectral reflectance, vegetation indices and rice phenological parameters can be used to map rice fields. The optical spectral reflectance of rice fluctuates with the rice nutrient conditions and canopy structure change (He et al., 2021). The spectral indices constructed based on spectral reflectance data can highlight the physical and chemical parameters and growth conditions of rice. Among them, vegetation indices are indicators that reflect rice growth status and canopy coverage, such as the Normalized Difference Vegetation Index (NDVI; Belgiu and Csillik, 2018; Belgiu et al., 2021), and Enhanced Vegetation Index (EVI; Cao et al., 2020). Rice phenological parameters can reflect the growth rhythm of rice that is different from other crops (Zhang and Lin, 2019; Ni et al., 2021). Previous researches have released global land cover datasets based on spectral reflectance and spectral indices using MODIS, Envisat and Sentinel-2 data. Representative datasets are MCD12Q1 (Sulla-Menashe et al., 2019), GlobCover (Arino et al., 2008) and FROM-GLC (Gong et al., 2012), all contain farmland distribution information. However, the spatial resolution of the MCD12Q1 and GlobCover datasets is only 500 m and 300 m, respectively. And none of the three datasets distinguish specific crop types. In addition, the MCD12Q1, GlobCover and FROM-GLC datasets were updated to 2019, 2009, and 2017, respectively. Eventually, optical remote sensing is easily affected by weather conditions, cannot obtain information on objects occluded by clouds and cloud shadows, and cannot ensure that satellite data is obtained in the best phenological stage for rice identification, which makes it difficult to reconstruct the optical remote sensing time series curve, and affects the accuracy of rice identification.

In contrast to optical remote sensing, synthetic aperture radar (SAR) has proven to be an attractive alternative for rice monitoring and mapping due to the independence of SAR signals from the cloud and solar radiation (Torbick et al., 2017; Pan et al., 2021). Many studies have used single-temporal SAR backscatter characteristics to monitor rice (Gao et al., 2019), whereas single-temporal SAR data usually results in low identification accuracy due to missing key phenological stage information (Lopez-Sanchez et al., 2012; Li et al., 2014). Compared with single-temporal SAR data, multi-temporal or time-series SAR data can capture phenological information about rice in the whole growth cycle, thereby contributing to improving rice identification accuracy (Yang et al., 2017, 2018; Csorba et al., 2019; Chandra Paul et al., 2020; Pang et al., 2021; Zhan et al., 2021). At present, most studies on rice identification using SAR have focused on the flat terrain areas where rice fields are concentrated and large-sized, such as the Mekong Delta (Bouvet and Le Toan, 2011; Clauss et al., 2018), Bangladesh (Panigrahy et al., 2012), Vijayawada in India (Mandal et al., 2020), and Northeast China and the Middle and Lower Yangtze Valley Plain (Zhan et al., 2021). However, in the mountainous and hilly areas represented by Chongqing, timely and accurate paddy rice identification based on remote sensing faces many difficulties and challenges for the following reasons: (1) Chongqing city is located in the transition zone between the rice growing area in southwest China and the rice growing area in the middle and lower reaches of the Yangtze River (Lisan, 1993), and the terrain is mainly mountainous and hilly. Therefore, the fields in Chongqing are small and scattered. In most cases, a pixel contains multiple land types, forming a mixed pixel. (2) Mountain topography and great altitude differences lead to large differences in water and heat conditions in various regions, inconsistent rice planting times, and inconsistent rice phenology. Therefore, the best time to identify rice varies from region to region. (3) Chongqing is located in the subtropical monsoon humid climate zone. Under the combined effect of climate, topography and water vapor from the Yangtze River, the annual average foggy days in Chongqing are as high as 104 days. Therefore, it is difficult to obtain high-quality optical remote sensing images. Due to these challenges, few researchers have conducted satellite-based rice monitoring in Chongqing.

In addition, given the inherent speckle noise of SAR images, the mixed pixels and pixel heterogeneity at the edge of rice fields, the recognition accuracy of rice still needs to be further improved. Previous studies showed that spatial domain filtering can reduce the influence of speckle noise in SAR data, and time series smoothing methods [Gaussian fitting (Bazzi et al., 2019), Savitzky–Golay filtering (Krishnan and Seelamantula, 2013), double logistic regression (Zheng et al., 2016), etc] can be used to reconstruct time series SAR data (Zeng et al., 2020). Both are beneficial to improving rice identification accuracy. Moreover, compared with the pixel-based method, the object-based classification method can avoid a large number of broken patches in the classification results and can obtain more accurate mapping results in the application of crop classification (Peña-Barragán et al., 2011; Belgiu and Csillik, 2018). Therefore, this paper focuses on solving the difficulties of high-precision rice identification in Chongqing due to factors such as cloudy and foggy weather (annual average of 104 days of cloudy and foggy weather), fragmented and small- and middle-sized rice fields, large fluctuations in terrain, significant differences in precipitation and temperature within the region, and large changes in rice phenological information.

The main research objectives of this study are to: (1) reconstruct the Sentinel-1 SAR time-series backscatter data, and suppress inherent speckle noise in SAR data, (2) calculate multi-characteristic parameters and analyze the separability of rice and other land cover types in each feature image, (3) propose a rice identification algorithm combining multi-characteristic parameters and homogeneous objects based on time series dual-polarization SAR (MPHO-DPSAR), (4) generate an annual map of rice fields in Chongqing in 2020.

2. Materials and methods

2.1. Study area and data

2.1.1. Study area

Chongqing is located in the southwest of China, in the upper reaches of the Yangtze River, between 105°11′E ~ 110°11′E and 28°10'N ~ 32°13'N, and has an area of 82,400 km^2. The elevation span is large (73.1–2796.8 m) and the terrain is strongly undulating. So, the landforms are various, mainly mountains, hills, tablelands, and flatlands. Specifically, in Chongqing, 38.61% of the areas are below 500 m, 25.41% are between 500 and 800 m, 20.42% are between 800 and 1,200 m, and 15.56% are over 1,200 m (Figure 1).

In terms of climate, Chongqing has a humid subtropical monsoon climate, with an annual average sunshine duration of 1,000–1,400 h, which is one of the areas with the least annual sunshine in China. The annual average temperature, annual precipitation, and annual sunshine duration vary greatly within the study area (Table 1). Affected by the topography and climate, the annual average foggy day in Chongqing is 104 days a year, so it is known as the "Fog City."

The main crops in Chongqing are rice, corn, and wheat, of which the distribution area of rice is 655,000 hm^2, accounting for 32.9% of the planting area of all grain crops (Chongqing Statistics Bureau, 2020). In recent decades, many cultivated lands have been converted into construction land due to urbanization or returned to forest or grasslands due to ecological restoration, resulting in a rapid decline in the rice field area. From 2000 to 2020, the rice fields area in Chongqing dropped from 780,000 hm^2 to 660,000 hm^2 (Chongqing Statistics Bureau, 2020). The crop phenology data measured by the Chongqing Institute of Meteorological Sciences showed that the rice is single-season rice. The sowing and transplanting stage of rice is from March to mid-May, the growth stage is from mid-May to mid-August. Specifically, the growth stage includes five specific stages: the tillering stage, jointing stage, booting stage, heading stage and milk-ripe stage. The mature harvest stage is from mid-August to late September. As for corn, the sowing stage is from mid-March to late May, the growth stage is from June to early August, and the harvest is from late August to early September. For wheat, the sowing stage is in November and the harvest stage is in April of the following year.

2.1.2. Data and pre-processing

2.1.2.1. Sentinel-1 synthetic aperture radar image data

Sentinel-1A SAR is a C-band radar imaging system developed by the European Commission (EC) and the European Space Agency (ESA) and launched in 2014. The Sentinel-1A SAR has four imaging modes and can produce dual-polarization data. A total of 411 scenes Level-1 Ground range detected image of Interferometric Wide Swath (IW) SAR with dual-polarization (VV and VH) in 2020, covering Chongqing were applied, a spatial resolution of 10 m and a temporal resolution of 12 days. The temporal resolution of overlapping regions of adjacent images is less than 12 days (Figure 1).

2.1.2.2. Sentinel-1 synthetic aperture radar image preprocessing

Sentinel-1 SAR image data preprocessing included four main steps. (1) The SAR image pixel values were converted into the backscatter coefficient δ_0 by radiometric calibration. (2) Correction of SAR image distortion caused by terrain changes and sensor tilt was performed through range Doppler terrain correction. (3) A 3 × 3 mean filter was used to smooth the SAR image to reduce noise and improve the quality of the SAR image. (4) Backscatters to dB (Eq. 1) is a logarithmic transformation of the backscatter coefficient, so that the SAR image histogram approximates a Gaussian distribution, and the number of data storage bits becomes smaller, which is also conducive to data analysis and visualization.

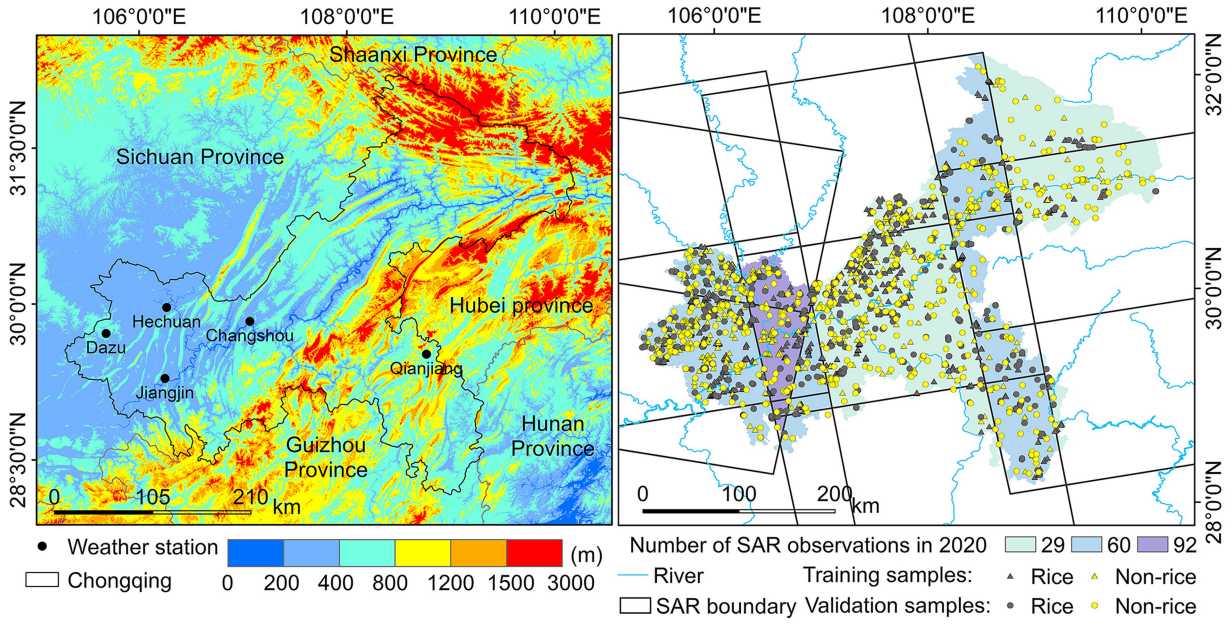

FIGURE 1
Topography of the study area, spatial range of SAR observations and spatial distribution of sample points.

TABLE 1 The annual average temperature, annual precipitation, and annual average sunshine duration in Chongqing in 2020.

Weather station	Altitude (m)	Annual precipitation (mm)	Annual average temperature (°C)	Annual sunshine duration (h)
Jiangjin	261.4	1319.6	18.9	1070.0
Hechuan	364.5	1085.2	18.0	1055.9
Changshou	377.6	1280.3	18.1	962.9
Dazu	541.0	1002.9	17.1	1128.8
Qianjiang	786.9	1808.6	14.7	819.1

$$\delta = 10 * \log_{10} \delta_0 \quad (1)$$

where δ_0 is the original backscatter coefficient, δ is the backscatter coefficient after backscatters to dB.

2.1.2.3. Other auxiliary data

Other auxiliary data include DEM data, multispectral images, field survey data, Google Earth high-resolution imagery, and agricultural statistics.

The DEM data was collected by the advanced land observing satellite (ALOS) L-band SAR with a horizontal and vertical accuracy of 12.5 meters. Multispectral images from an unmanned aerial vehicle (UAV) and field survey data were acquired from July 30 to August 3, 2020. The UAV equipment is a DJI Phantom 4Pro, and the obtained multispectral images include blue, green, red, red edge, and near-infrared bands. The sample point collection device is a handheld GPS locator, with a positioning accuracy of about 1 m, and a total of 400 sample points were collected (Figure 1). Google Earth high-resolution imagery was used as an auxiliary data source for 2060 sample points selection through visual interpretation (Figure 1). Among them, the training and validation samples of rice are 600 and 500, respectively. Non-rice includes 4 sub-categories (build, forest, and grasslands, water bodies, dry land (wheat/corn)). Each sub-category has 200 training samples, a total of 800, and 140 validation samples, a total of 560. The agricultural statistics refer to the area of rice fields in all districts and counties in Chongqing in 2020, obtained from the statistical yearbook, and used for subsequent evaluation of rice identification accuracy at the district/county level.

2.2. Methods

The rice field map was generated based on the Sentinel-1 dual-polarization SAR backscatter time series and ALOS-12.5 m DEM. We first performed SG filtering on the preprocessed SAR image to construct smooth VH backscatter time-series. We first performed SG filter to reconstruct the time series Sentinel-1 image to construct a smooth VV and VH backscatter coefficient time series data set, and analyzed the unique temporal backscatter characteristics of rice. Further, the MPHO-DPSAR algorithm combining multi-feature parameters and homogeneous objects was established for mapping rice fields. The accuracy evaluation of the rice fields map was carried out on three levels, namely district/county level, object level, and rice field level. The technical route is shown in Figure 2.

2.2.1. Reconstruction of the sentinel-1 synthetic aperture radar time-series backscatter data

Although the mean filter had been applied in the SAR image to reduce speckle noise, some noises still existed in the backscatter coefficient image due to the influence of the coherent superposition of scattering from multiple targets. At the transplanting stage and early growth stage of rice, the backscatter intensity of shallow water and land areas with high water content is similar to that of rice fields, which increases the difficulty of rice identification (Nguyen et al., 2015; Son et al., 2021). In addition, rainfall will reduce the radar backscatter intensity, which will disturb the rice time-series curve of the backscatter intensity in different polarizations SAR, resulting in an inaccurate change rule of the SAR backscatter coefficient of rice growth (Yu et al., 2020). Therefore, in order to make the SAR backscatter information more accurately reflect the rice growth rhythm and minimize the influence of noise and other environmental factors, we reconstructed the Sentinel-1 SAR time-series backscatter data.

The method of combining mean value compositing and the Savitzky–Golay (SG) filtering algorithm was used for the reconstruction of the sentinel-1 SAR time-series backscatter data. We first performed a 12-day mean value compositing of the backscatter coefficient to alleviate the fluctuation. Secondly, SG filtering (Krishnan and Seelamantula, 2013, Gir et al., 2015) was used to obtain the variation trend of the SAR backscatter coefficient time series. The length of the SG filter fitting window and the polynomial fitting times were set to 3 and 3 respectively, which can ensure that the noise of the time series data was effectively suppressed, and the various characteristics of the time series backscatter coefficient can be preserved to the maximum extent. Figure 3 showed the reconstruction results of the time-series SAR VH backscatter coefficients of rice. Compared with the original VH backscatter profile, noise and outliers caused by environmental factors were weakened, and the reconstructed backscatter coefficient time series curve can more clearly reflect the intensity-changing trend with rice growth.

2.2.2. Temporal backscatter characteristics of rice and other land types

The varying backscatter signature of rice were presented throughout the whole growth cycle. The overall performance was a trend of first falling, then rising and then falling (Figure 4). Specifically, the sowing stage of rice begins in early March (DOY 61), rice fields are submerged for land preparation, field topography leveling and weeding to provide a suitable environment for rice planting. At this stage, the humidity of the rice fields gradually increases, the roughness gradually decreases. The specular reflection is the main backscatter mechanism, which makes the SAR backscatter coefficient drop rapidly from −19 dB to −24 dB (the lowest value). At the stage of rice

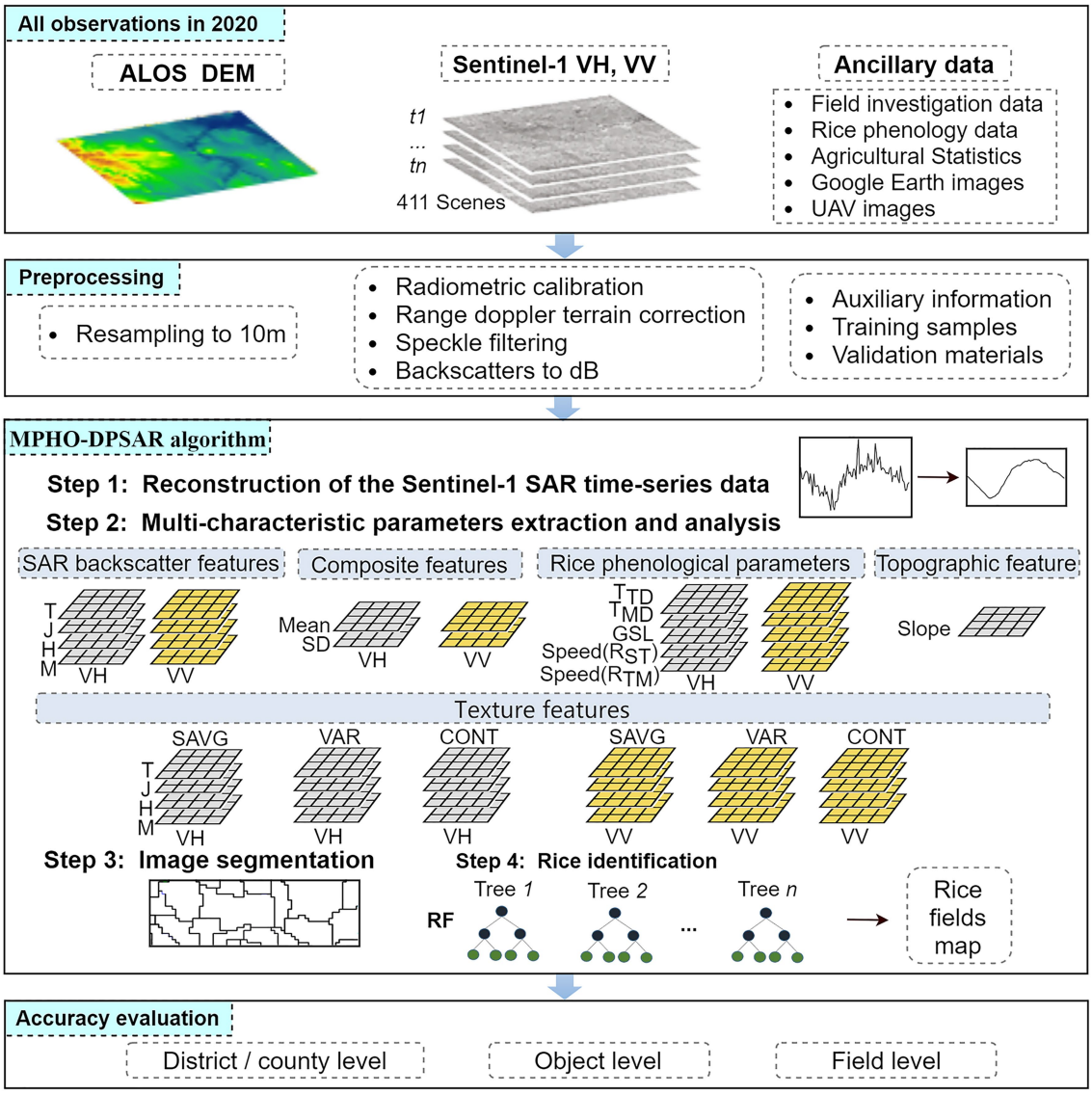

FIGURE 2
Schematic flow of MPHO-DPSAR method, T, J, H, and M denote the rice transplanting, jointing, heading, and mature stage, respectively.

transplanting in mid-to-late April (DOY 110), the rice seedlings are relatively short and their distribution is very sparse. Also, the water content of the rice fields is high, which triggers the backscatter mechanism to be dominated by specular reflection with less volume scattering and double scattering. Accordingly, the backscatter coefficient begins to gradually increase. At the stage of rice jointing period in mid-June (DOY 160), rice grows taller rapidly with the number of leaves, biomass and roughness of rice fields gradually increasing. The main backscatter mechanisms transform to volume scattering from the rice canopy, double scattering between the rice stem and the underlying surface of the rice field, and specular reflection from the water body in the rice field (Torbick et al., 2017; Son et al., 2021). The VH backscatter coefficient accordingly increased from −24 dB to about −18 dB. In late July (DOY 200), rice began to head, with higher plant height and more leaves. The leaves almost completely cover the water body of the rice fields. Double scattering is reduced and the backscatter mechanism is mainly volume scatter. The backscatter intensity of rice fields continued to increase, reaching about −17 dB. Rice matures in mid-to-late August, the backscatter intensity accordingly reaches the maximum (−15 dB). Then as the rice ears drop and the leaves turn yellow, the backscatter intensity of the rice fields correspondingly decreases. After the rice harvest, the backscatter intensity of rice fields continues to decrease. If its water content is high, the backscattering coefficient will be lower, close to that of water.

The variation characteristics of SAR backscatter coefficient curves of rice and other land cover types are different (Figure 4). Because double scattering occurs primarily in built-up areas, the backscatter coefficient was correspondingly high and remained stable at around −9 dB throughout the year. Specular reflection occurs mostly in water bodies, the backscatter coefficient was correspondingly less than −25 dB. The interaction between electromagnetic waves and forest/grasslands mainly produces volume scattering, thus the backscatter coefficient fluctuated around −15 dB. As for the corn at the stage of

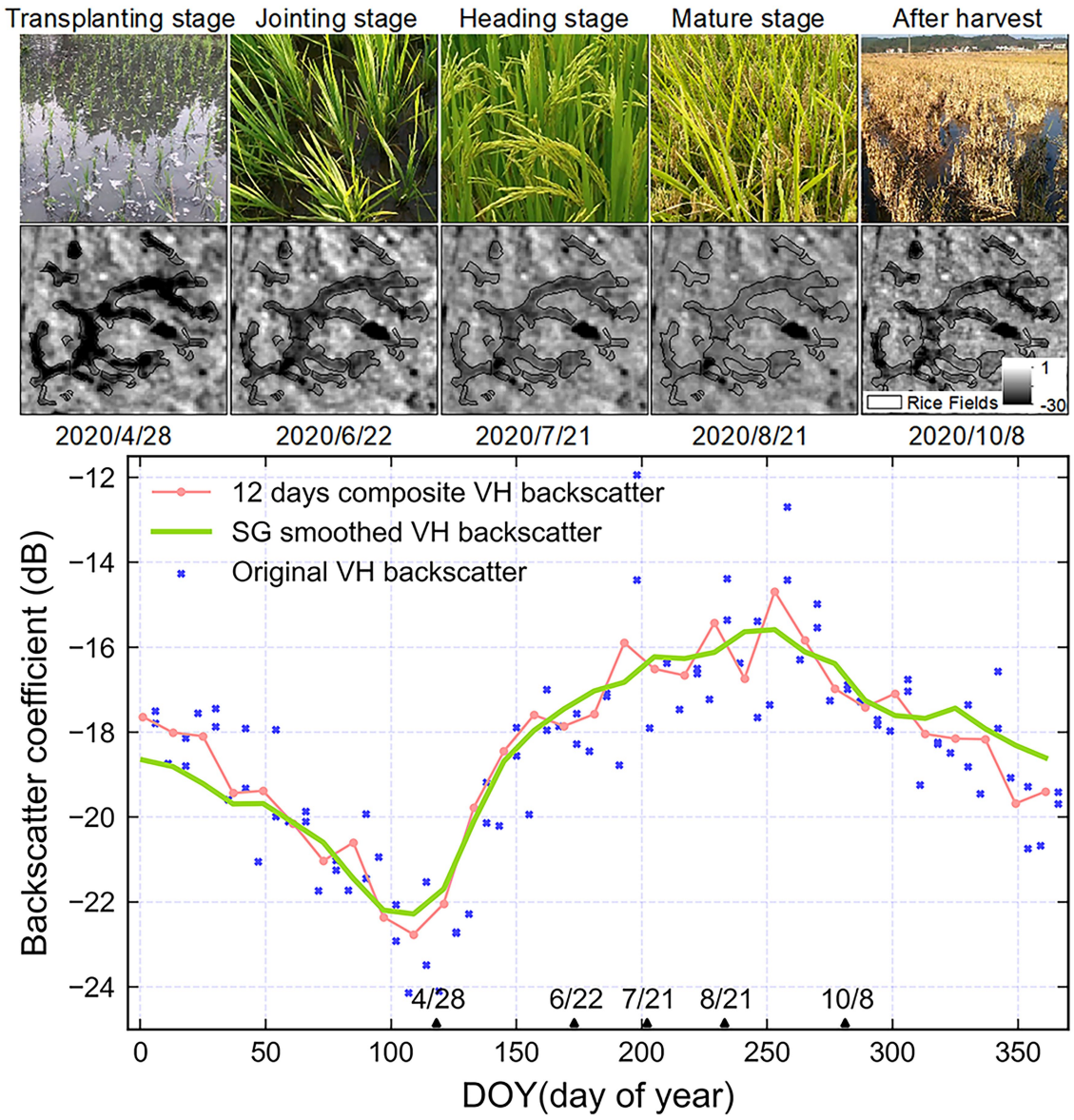

FIGURE 3
Rice fields status at key phenological stages and reconstruction of the sentinel-1 SAR time-series backscatter characteristics.

sowing and jointing (DOY70-150), its backscatter mechanism is mainly rough surface scattering and double scattering between corn stem and underlying surface. The backscatter coefficient varied slowly between −16 and -17 dB. At the stage of jointing to mature (DOY 150–200), the backscatter mechanism mainly transforms to volume scattering from corn canopy. The backscatter coefficient correspondingly increased to about -14 dB. Then the backscatter coefficient began to decrease after harvest. As for the wheat, the backscatter coefficient in its phenological period (DOY330-DOY130 in the following year) was basically between −19.5 and −16.5 dB.

In terms of the difference in temporal backscattering characteristics between rice and other land types, it gradually increased before the rice transplanting stage. From the rice transplanting stage to the mature stage, it gradually decreased. Specifically, in the middle and late August when rice entered the mature stage, the backscatter coefficients of forest/grasslands, corn and wheat were basically the same as those of rice, but the separability of rice and water was the highest.

2.2.3. Multi-characteristic parameters extraction

Considering the special phenological characteristics of rice, the complex topographic conditions and surface landscape of Chongqing, multi-characteristic parameters were extracted (Table 2), including SAR backscatter features, composite features, rice phenological parameters, texture features, and a topographic feature.

The composite features included mean composite ($Mean_{VH}$, $Mean_{VV}$) and standard deviation composite (SD_{VH}, SD_{VV}) based on all Sentinel-1 VV and VH images throughout the rice growing season.

Considering the phenological characteristics of the whole life cycle of rice, we extracted five rice phenological parameters based on the backscatter coefficients of VH and VV time series (Figure 5), respectively, which are the transplanting date (TD), rice agronomy

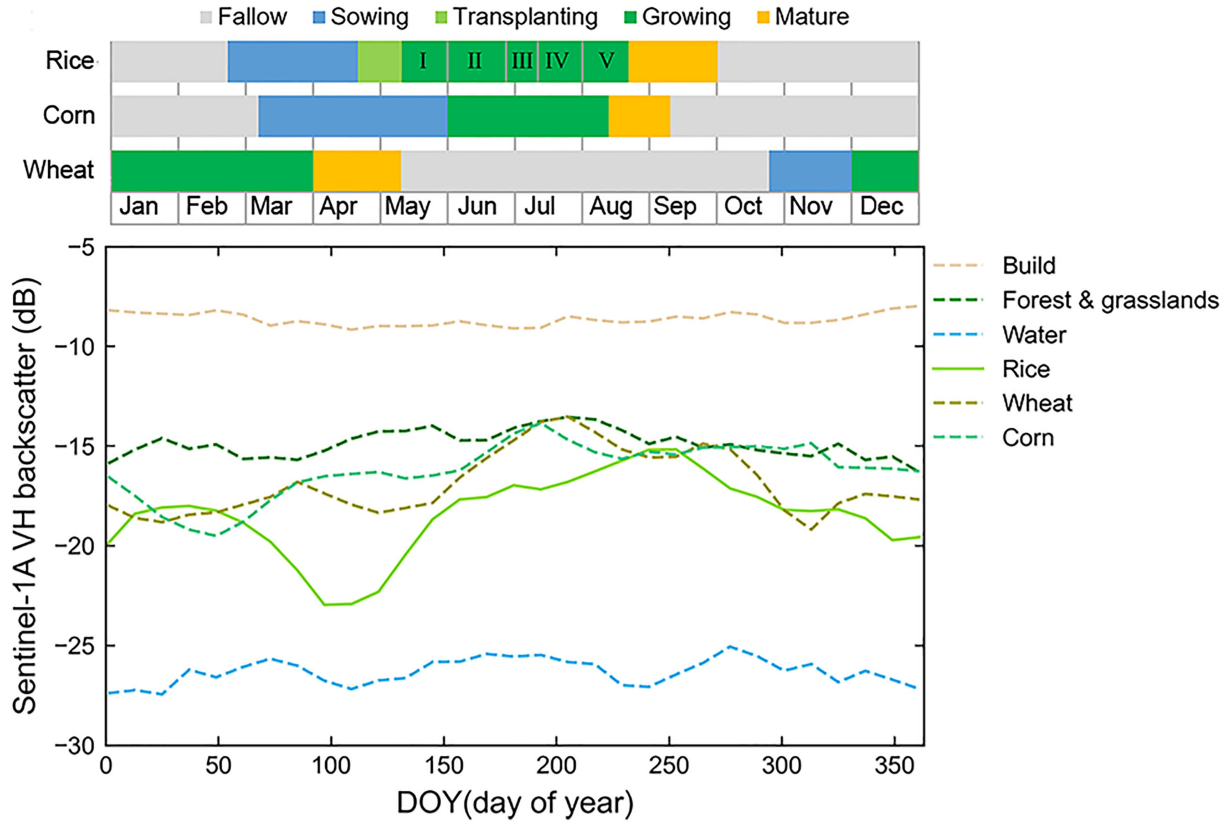

FIGURE 4
Main crop cropping calendar and temporal characteristics of VH backscatter for rice and other land types. I, II, III, IV, and V denote the tillering stage, jointing stage, booting stage, heading stage and milk-ripe stage of rice, respectively.

flooding decline speed (Speed (R_{ST})), mature date (MD), green-up speed (Speed (R_{TM})) and growing season length (GSL). The rice transplanting date (TD) was defined as 5 days after the day of year (DOY) of the SAR backscatter reaches the local annual minima. The rice agronomy flooding decline speed (Speed (R_{ST})) was defined as the ratio of the SAR backscatter changes over the number of days from rice field submerged date (SD) to TD. The rice mature date (MD) was defined as DOY when the SAR backscatter reaches the maximum. The green-up speed (Speed (R_{TM})) was defined as the ratio of the SAR backscatter changes over the number of days from rice TD to MD. The growing season length (GSL) was defined as the length from rice TD to MD (Wang et al., 2022).

SAR images have significant advantages in displaying texture features (Peña-Barragán et al., 2011; Li et al., 2022). Considering data redundancy and computational efficiency, three texture parameters (SAVG/sum average, VAR/variance and CONT/contrast) were selected for rice identification according to the feature importance calculated by the random forest algorithm (Table 3).

The complex topographical conditions lead to the rice fields being fragmented and dominated by small- and medium-sized. Therefore, topographic slope information (Slope) was also considered.

2.2.4. Homogeneous objects and identification algorithm

The multi-resolution segmentation algorithm merges pixels or objects level by level from bottom to top (Dragut et al., 2014). The algorithm can effectively fuse spectral and spatial features of pixels or objects, locally minimize the average heterogeneity and maximize the internal homogeneity of objects. Thus, it is suitable for the Chongqing area with highly complex surface landscapes.

The segmentation scale determines the object size, which directly affects the accuracy of rice identification (Figure 6). Therefore, it is necessary to determine the optimal segmentation scale. The change rate of the image local variance under different segmentation scales (Figure 6) was calculated to determine the optimal segmentation scale (Drăguţ et al., 2010). Here, the optimal segmentation scale, the local peak, was 5. In addition, the spectral weight of the backscattering coefficient (w_{color}) is set to 0.9, and the shape weight (w_{shape}) is 0.1 in the segmentation algorithm (Eq. 2). The weight of spatial shape parameter (h_{shape}) was further divided (Eq. 3) by the compactness (h_{cpt}) of 0.8, and the smoothness (h_{smooth}) of 0.2 (Drăguţ et al., 2010; Dragut et al., 2014).

$$homogeneous\ object = w_{color} * h_{color} + \left(1 - \mathrm{w}_{color}\right) * h_{shape} \quad (2)$$

$$h_{shape} = w_{cpt} * h_{cpt} + \left(1 - w_{cpt}\right) * h_{smooth} \quad (3)$$

where w_{color} is the weight of color and w_{cpt} is the weight of compactness.

TABLE 2 Multi-characteristic parameters, including five types of features in this study.

Feature types	Features		Description
	VH polarization	VV polarization	
SAR backscatter features	$\delta_{VH\text{-}transplanting}$	$\delta_{VV\text{-}transplanting}$	VH and VV backscatter coefficients at four key rice phenological stages
	$\delta_{VH\text{-}jointing}$	$\delta_{VV\text{-}jointing}$	
	$\delta_{VH\text{-}heading}$	$\delta_{VV\text{-}heading}$	
	$\delta_{VH\text{-}mature}$	$\delta_{VV\text{-}mature}$	
Composite features	$Mean_{VH}$	$Mean_{VV}$	Mean and standard deviation of all SAR backscatter coefficients during the whole rice growth
	SD_{VH}	SD_{VV}	
Rice phenological parameters	TD_{VH}	TD_{VV}	Rice phenological parameters extracted based on VH and VV time series, respectively
	Speed ($R_{ST\text{-}VH}$)	Speed ($R_{ST\text{-}VV}$)	
	MD_{VH}	MD_{VV}	
	Speed ($R_{TM\text{-}VH}$)	Speed ($R_{ST\text{-}VV}$)	
	GSL_{VH}	GSL_{VV}	
Texture features	$SAVG_{VH\text{-}transplanting}$	$SAVG_{VV\text{-}transplanting}$	Three texture features (SAVG/sum average, VAR/variance and CONT/contrast) based on VH and VV backscatter coefficients at four key rice phenological stages
	$SAVG_{VH\text{-}joining}$	$SAVG_{VV\text{-}joining}$	
	$SAVG_{VH\text{-}heading}$	$SAVG_{VV\text{-}heading}$	
	$SAVG_{VH\text{-}mature}$	$SAVG_{VV\text{-}mature}$	
	$VAR_{VH\text{-}transplanting}$	$VAR_{VV\text{-}transplanting}$	
	$VAR_{VH\text{-}joining}$	$VAR_{VV\text{-}joining}$	
	$VAR_{VH\text{-}heading}$	$VAR_{VV\text{-}heading}$	
	$VAR_{VH\text{-}mature}$	$VAR_{VV\text{-}mature}$	
	$CONT_{VH\text{-}transplanting}$	$CONT_{VV\text{-}transplanting}$	
	$CONT_{VH\text{-}joining}$	$CONT_{VV\text{-}joining}$	
	$CONT_{VH\text{-}heading}$	$CONT_{VV\text{-}heading}$	
	$CONT_{VH\text{-}mature}$	$CONT_{VV\text{-}mature}$	
Topographic feature	Slope		Topographic slope information

The SAR backscatter coefficients at four key phenological stages of rice (transplanting, jointing, heading and mature stages) under VH and VV polarization modes were represented as $\delta_{VH\text{-}transplanting}$, $\delta_{VH\text{-}jointing}$, $\delta_{VH\text{-}heading}$, $\delta_{VH\text{-}mature}$, $\delta_{VV\text{-}transplanting}$, $\delta_{VV\text{-}jointing}$, $\delta_{VV\text{-}heading}$, $\delta_{VV\text{-}mature}$, respectively.

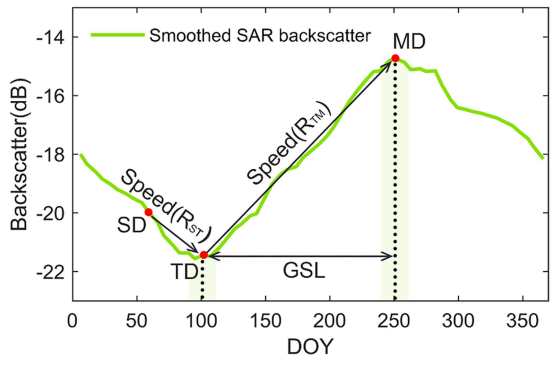

FIGURE 5
An VH backscatter profile of the rice field and schematic diagram of rice phenological parameters.

Random forest integrates many classification and regression trees (CARTs) together to form an integrated classifier through the idea of ensemble learning. It has the advantages of flexibility and high precision, which is suitable for high-dimensional data. In the paper, the bootstrap method was firstly used to randomly select a certain proportion of samples as the training sample set. Secondly, when splitting the nodes of the CART, features from the abovementioned multi-characteristic parameters were extracted, and the nodes were split according to the principle of the smallest Gini coefficient. Repeating the above operation to establish 50 CARTs, and then form a random forest classifier, the results were decided by the votes of all CARTs.

3. Results

3.1. Separability of rice and other land cover types in each feature image

The separability of rice and other land types in multi-characteristic parameters was further evaluated (Figure 7). For SAR backscatter features, the value of $\delta_{VH\text{-}transplanting}$ (−28 to −20 dB), $\delta_{VH\text{-}jointing}$ (−20 to −16 dB) are higher than that of water bodies, lower than that of other land types. The value of $\delta_{VH\text{-}heading}$ (−19 to -14 dB),

TABLE 3 Feature importance of texture features calculated by the random forest algorithm. The three texture features of highest importance were selected for this study (shown in bold).

	Transplanting stage		Jointing stage		Heading stage		Mature stage	
Texture features	Feature importance		Feature importance		Feature importance		Feature importance	
	VV	VH	VV	VH	VV	VH	VV	VH
Sum Average/SAVG	**43.32**	**41.68**	**44.75**	**37.88**	**34.94**	**36.93**	**26.37**	**32.71**
Variance/VAR	**9.38**	**5.62**	**12.53**	**8.28**	**9.88**	**6.16**	**10.80**	**9.33**
Contrast/CONT	**7.49**	**5.67**	**7.10**	**4.53**	**5.53**	**8.67**	**9.98**	**7.84**
Correlation/CORR	4.95	4.60	4.39	4.90	5.17	5.30	7.12	7.58
Information measure of Corr/IMCORR	3.76	3.20	2.64	3.82	3.27	3.51	3.70	6.29
Entropy/ENT	0.00	0.36	0.00	0.73	1.09	1.04	1.33	0.00
Sum entropy/SENT	0.66	0.87	0.98	0.00	0.50	0.91	1.05	0.35
Angular second Moment/ASM	0.21	0.48	0.18	0.20	1.15	1.17	0.48	0.00

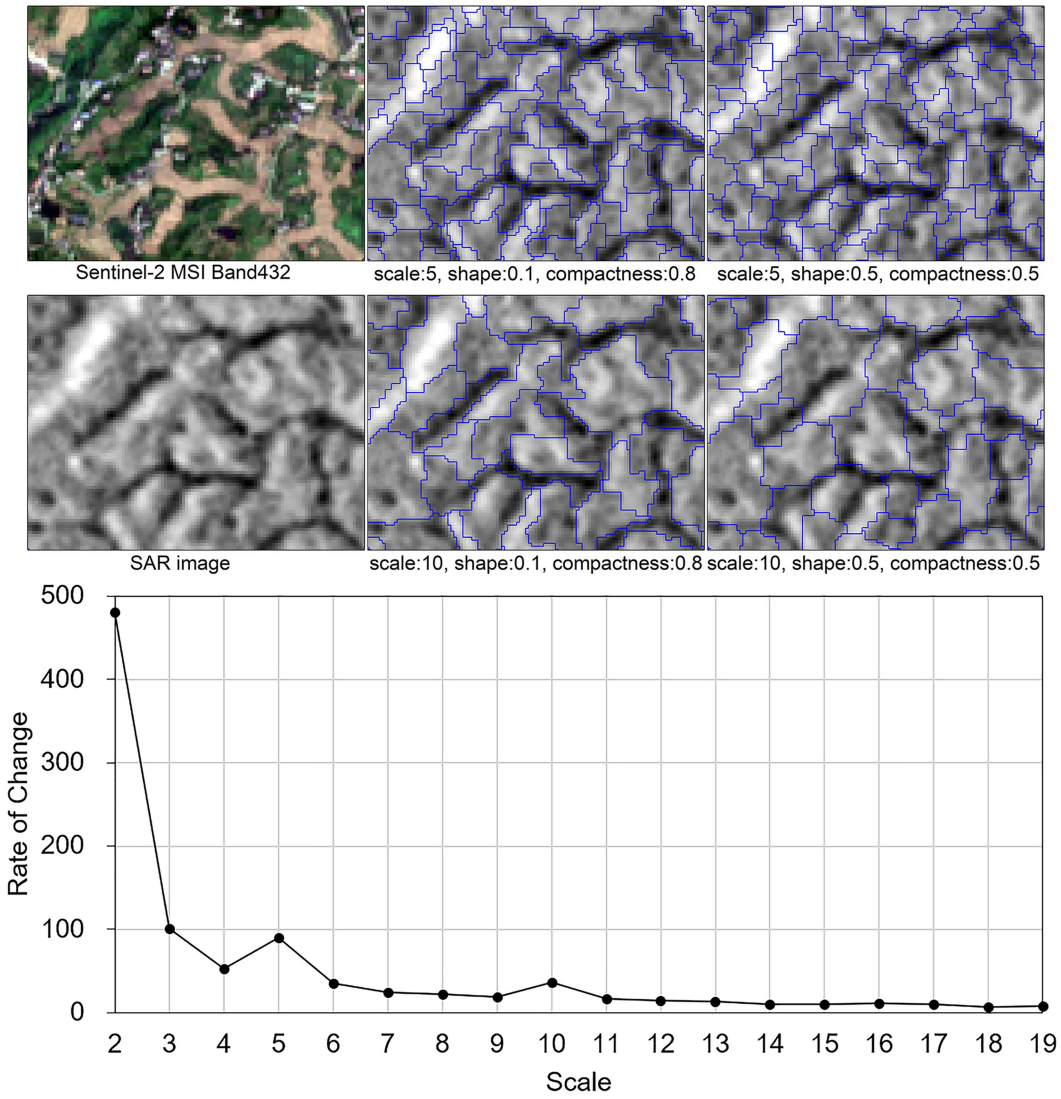

FIGURE 6
Multiresolution segmentation results with different segmentation parameters and rate of change (ROC) of the local variance.

10.3389/fevo.2023.1093454

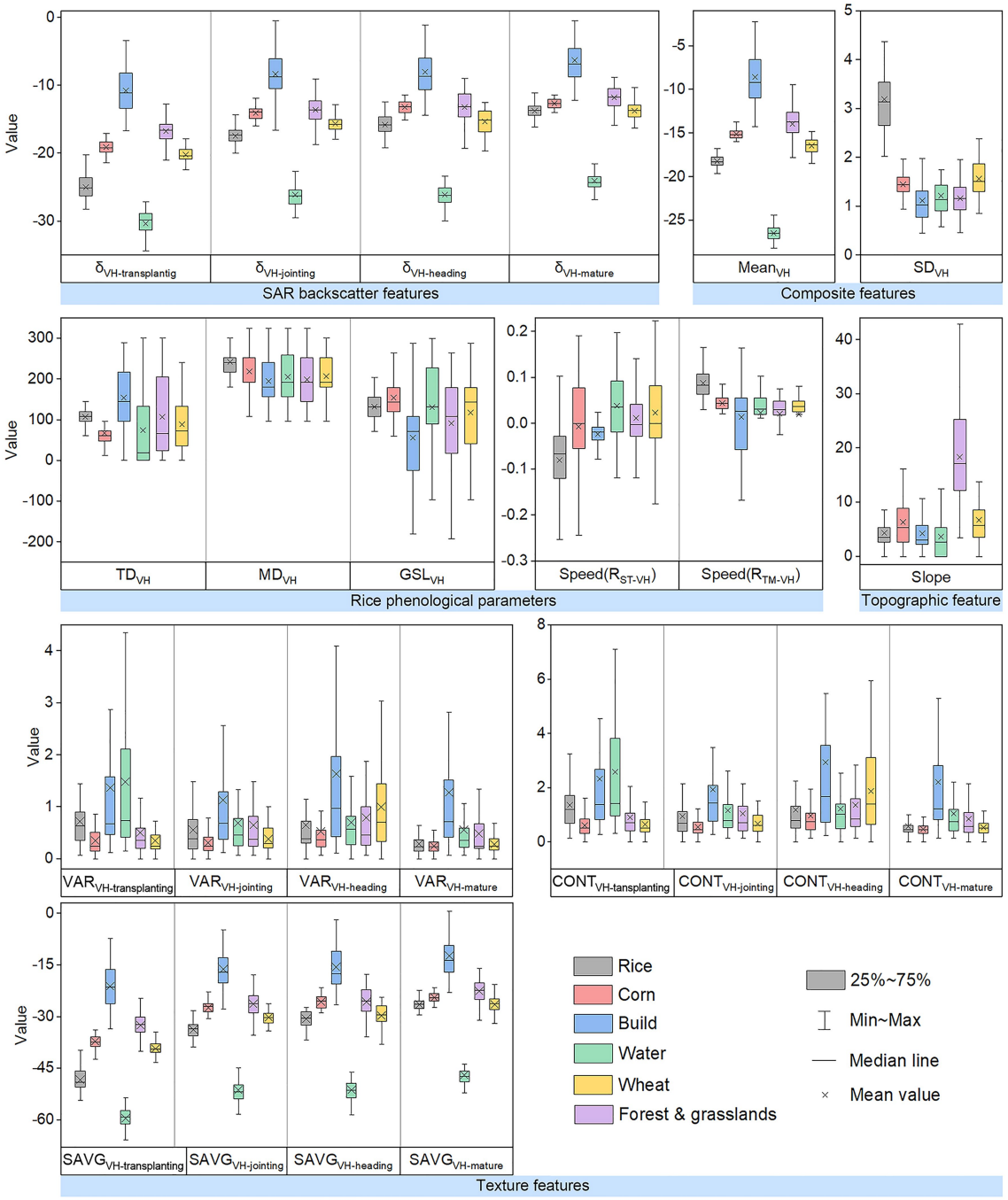

FIGURE 7
Separability of rice and other land cover types in each feature image based on VH Polarimetric Images. The $\delta_{VH\text{-}transplanting}$, $\delta_{VH\text{-}jointing}$, $\delta_{VH\text{-}heading}$, $\delta_{VH\text{-}mature}$ represent SAR backscatter coefficients at four key phenological stages of rice (transplanting, jointing, heading and mature stages), $Mean_{VH}$ and SD_{VH} represent the mean and standard deviation calculated based on all Sentinel-1 images throughout the rice growing season, $SAVG_{VH\text{-}transplanting}$, $SAVG_{VH\text{-}joining}$, $SAVG_{VH\text{-}heading}$, $SAVG_{VH\text{-}mature}$, $VAR_{VH\text{-}transplanting}$, $VAR_{VH\text{-}joining}$, $VAR_{VH\text{-}heading}$, $VAR_{VH\text{-}mature}$, $CONT_{VH\text{-}transplanting}$, $CONT_{VH\text{-}joining}$, $CONT_{VH\text{-}heading}$ and $CONT_{VH\text{-}mature}$ represent three types of texture parameters at four key phenological stages of rice, namely sum average, variance and contrast, slope represents topographic slope information.

$\delta_{VH\text{-}mature}$ (−17 to -12 dB) are lower than those of build, corn, forest, and grasslands. The VV backscatter coefficients of rice and other land types in the four key phenological stages are higher than VH backscattering coefficients. Especially in the transplanting stage, the separability of rice and corn in $\delta_{VV\text{-}transplanting}$ is higher than$\delta_{VH\text{-}transplanting}$. Therefore, the SAR backscatter coefficients at VH and VV polarizations are key indicators for identifying rice fields. However, only using SAR backscatter features cannot achieve the purpose of identifying rice well, because the SAR backscatter features of rice partially coincide with those of other land types. In particular, the recognition effect is not good in the mountainous area due to the heterogeneity of the land cover.

For composite features, the $Mean_{VH}$ of rice is concentrated between −20 and -17 dB, which is larger than water and smaller than that of build, forest, and grasslands, corn, and wheat. The SD_{VH} of rice was between 2 and 4.5, higher than other land types. Compared with the $Mean_{VH}$ and SD_{VH}, the overlap of $Mean_{VV}$ and SD_{VV} between rice and other land types is less, and the separation is higher. The composite features based on time series SAR data reflect the average level and dispersion of the backscatter coefficients of rice during the growth period, which can expand the distinguishability of rice and other land types.

For rice phenological parameters, the TD_{VH}, MD_{VH} and GSL_{VH} of rice are between 70 and 150, 190 and 300, and 80 and 200, respectively. The TD_{VV}, MD_{VV} and GSL_{VV} of rice are between 60 and 140, 210 and 310, and 110 and 210, respectively. The Speed ($R_{ST\text{-}VH}$) and Speed ($R_{ST\text{-}VV}$) of rice are lower than that of other land cover types, the Speed ($R_{TM\text{-}VH}$) and Speed ($R_{TM\text{-}VV}$) are higher than that of other land types. In addition, compared with other land types, the rice phenological parameters are more concentrated and rice is more recognizable. Therefore, rice phenological parameters can help to better eliminate some vegetation that may be misclassified, such as herbaceous vegetation that is seasonally submerged by the summer monsoon.

For texture features, the $SAVG_{VH\text{-}transplanting}$, $SAVG_{VH\text{-}joining}$, $SAVG_{VH\text{-}heading}$ and $SAVG_{VH\text{-}mature}$ of rice are between −50 dB to −36 dB, −35 dB to -27 dB, −33 dB to -25 dB, and −27 dB to -22 dB, which are higher than that of the water, lower than that of other land types. The $CONT_{VH\text{-}transplanting}$, $CONT_{VV\text{-}transplanting}$, $VAR_{VH\text{-}transplanting}$ and $VAR_{VV\text{-}transplanting}$ of rice are higher than those of corn, forest/grasslands, wheat at the transplanting stage. The $CONT_{VH\text{-}mature}$, $CONT_{VV\text{-}mature}$, $VAR_{VH\text{-}mature}$ and $VAR_{VV\text{-}mature}$ of rice are lower than those of building, water, and forest/grasslands at the mature stage. Therefore, the SAR texture features are helpful to better identify rice fields.

Terrain slope information (Slope) is important auxiliary data, which is used to cover up forests and grasslands in mountainous areas, as well as the shadows caused by high mountains on SAR images, which can improve the accuracy of the rice fields map.

3.2. Annual map of rice fields in Chongqing in 2020

The spatial distribution of rice fields extracted by the MPHO-DPSAR algorithm (Figure 8) showed that the area of rice fields in Chongqing in 2020 is 632,400 hm^2, which were mainly distributed in the hilly areas in the mid-west of Chongqing with the terrain relatively flat. There also were many rice fields distributed in the valleys in the northeast and south of Chongqing. Figures 8B–E shows the distribution of rice fields in the four sites (b–e) in Figure 8A. That is, the distribution of rice fields is mainly zonal and dispersed, which is very different from rice fields distributed in succession in plain areas. The main reason is that there are many mountains and hills in Chongqing, and paddy fields are mainly distributed in the relatively flat strip of narrow area between many small hills. Figures 8B'–E' shows the VH polarization image of Sentinel-1 during the transplanting period. The Figure 8F is a comparison chart between the mapping results of the algorithm and the mapping results of the statistics. For the rice classified area by the MPHO-DPSAR algorithm, the rice classified area is 458.92km^2 in Hechuan District, which is the largest. The rice classified area in Jiangjin, Yongchuan and Fuling is 397.00 km^2, 316.35 km^2 and 363.25 km^2, respectively, all of which are more than 300 km^2. There are less than 20km^2 rice fields in Shapingba, Jiulongpo, Chengkou, Jiangbei, Nan'an and Dadukou.

4. Discussion

4.1. Accuracy evaluation at three levels

The accuracy evaluation of the rice fields map was carried out on three levels, namely district/county level, object level, and rice field level.

At the district/county level, the linear regression between the MPHO-DPSAR derived results and agricultural statistics data was performed. The correlation coefficient of determination (R^2) is 0.97. And the regression slope is 0.94, close to 1, which presented a significant linear correlation between the two datasets, and indicated the high precision of the resultant rice fields map (Figure 9).

At the object level, the confusion matrix showed that the user's accuracy (UA), producer's accuracy (PA), F1 score, overall accuracy (OA) and Kappa coefficient were 0.96, 0.93, 0.95, 0.95 and 0.90, respectively (Table 4).

At the rice field level, the precise rice fields map based on UAV images was used to verify the accuracy of MPHO-DPSAR derived results in low-altitude regions in Hechuan District and middle-altitude regions in Zhongxian County. For rice fields in the two regions, the ratio of recognized and unrecognized rice fields of different sizes was calculated. The results showed that the proportion of recognized paddy fields continued to increase with the size of a single paddy field increased. And more than 80% of the rice fields can be accurately recognized by the MPHO-DPSAR algorithm when the size of a single rice field is larger than 600 m^2, corresponding to 6 pixels (Figure 10). This shows that the MPHO-DPSAR algorithm is suitable for identifying small and medium-sized rice fields in complex terrain.

4.2. Comparison with other rice identification methods

The study reproduced two classic rice identification methods based on remote sensing technology, which were further applied to identify rice fields in the complex terrain in Chongqing. The method I mainly utilized the "V" shaped feature in the Sentinel-1 SAR VH backscatter time series during the rice growth season (Zhan et al., 2021). The method II applied multi-temporal Landsat spectral reflectance and spectral indices to construct a decision tree to identify rice (Cao et al., 2020). In addition, this study also compared the decision tree algorithm developed by our team for rice identification in Chongqing (marked as method III), which integrated rice phenological and topographic features (Wang et al., 2022).

The performance of the four rice identification algorithms showed that the proposed MPHO-DPSAR algorithm in this paper obtained the best classification accuracy, with all the accuracy indicators highest (Table 5). As for the UA, our algorithm achieved a recognition accuracy of 0.96, which was much higher than that of the method I. The low UA of the method I indicated that a large number of non-rice fields (wet grassland and other crops) were

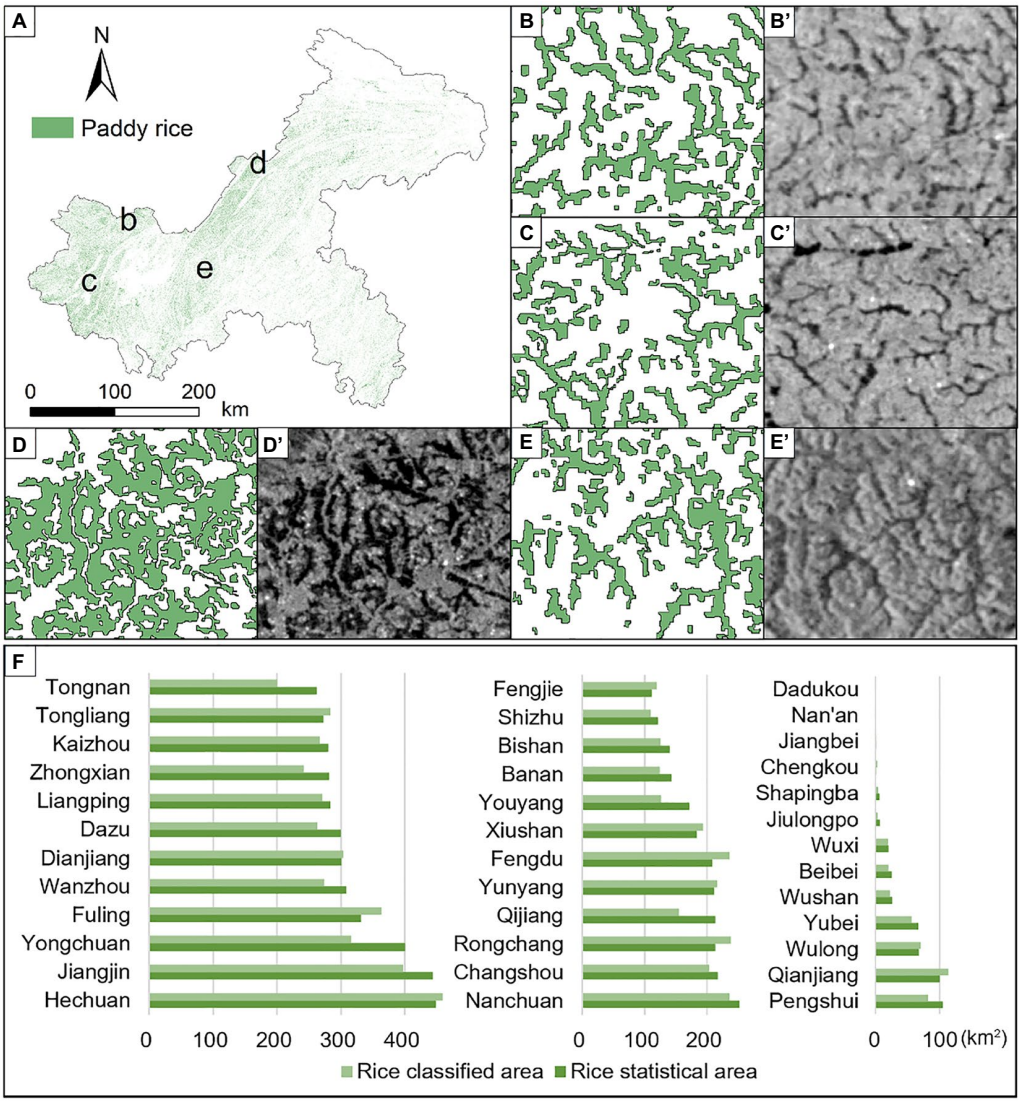

FIGURE 8
The rice fields map of Chongqing in 2020 based on the MPHO-DPSAR algorithm. Four regions, denoted as b–e in **(A)**, randomly selected for zoom-in views shown in **(B–E)**, respectively. The corresponding SAR image in transplanting stage shown in (B'–E'), respectively. The **(F)** is a comparison chart between the mapping results of the algorithm and the mapping results of the statistics.

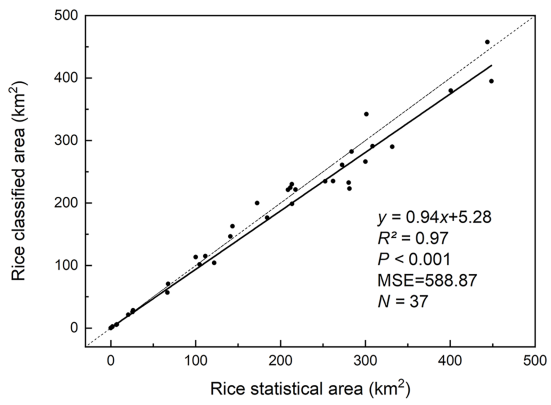

FIGURE 9
Correlation between MPHO-DPSAR derived results and the statistics of rice fields area.

TABLE 4 Accuracy assessment of rice fields map in 2020.

	Land cover types	UA	PA	F1 score	OA	Kappa
This study	Rice	0.96	0.93	0.95	0.95	0.90
	Non-rice	0.94	0.97	0.95		

identified as rice fields. Because this method only uses the Sentinel-1 VH polarization image, it does not make full use of the rich information provided by the VV polarization image, especially the method does not consider the terrain feature parameters. As for the PA, the method II obtained the accuracy of 0.69, indicating that there were serious omissions. Because this method sets a threshold value for the difference image of the EVI (Enhanced Vegetation Index) of two fixed dates to identify rice fields after masking other

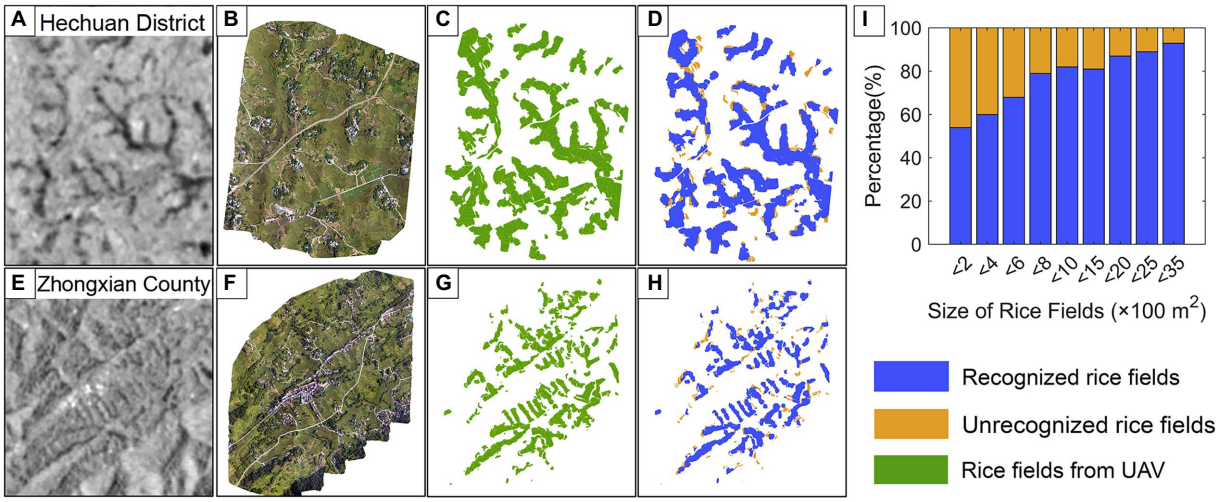

FIGURE 10
Accuracy assessment of rice fields map in two pilot regions based on UAV images. **(A,E)** Sentinel-1 VH images during rice transplanting stage. **(B,F)** UAV images in two pilot regions. **(C,G)** Real rice fields based on UAV images. **(D,H)** The recognized and unrecognized parts within each rice field for two pilot regions. **(I)** Proportions of recognized and unrecognized area with the changes of rice field sizes.

TABLE 5 The comparison of rice mapping performances of the four methods.

	Land cover types	UA	PA	F1 score	OA	Kappa
This study	Rice	0.96	0.93	0.95	0.95	0.90
Method I	Rice	0.64	0.91	0.75	0.71	0.44
Method II	Rice	0.8	0.69	0.74	0.77	0.54
Method III	Rice	0.96	0.85	0.9	0.88	0.84

land types, it does not consider the inconsistent phenology of rice in the study area. The method III achieved the same UA (0.96), but other accuracy indicators were lower than those of this study. The main reasons are the comprehensive utilization of dual-polarization SAR backscatter features, composite features, rice phenological parameters, texture features and a topographic feature in this study. While the method III only employed VH polarization-based rice phenological and topographic features, without considering VV polarization-based features and texture features.

The high identification accuracy of our proposed algorithm could be attributed to the following reasons. (1) Abundant dual-polarization Sentinel-1A SAR data has high temporal of 12 days and high spatial resolution of 10 m (ENVISAT: 35d/20-500 m, RADARSAT-1: 24d/10-100 m, PALSAR-2: 45d/25 m). Therefore, the time-series SAR backscatter coefficients could accurately reflect rice characteristics at the whole phenological period and meet the needs of small- and middle-sized rice fields identification in Chongqing. Moreover, the dual-polarization SAR data can reflect the backscatter characteristics of rice under different polarization modes, which is helpful for the rice identification. (2) Sufficient rice identifiability features were extracted. The scattering mechanism of rice, which is different from other land types, can be well reflected in the backscatter features of time series SAR. The texture features well reflect the structures of rice fields and the connection between the rice fields and surrounding objects. The rice phenological parameters highlight the unique phenological cycle and growth characteristics. The composite features based on time series SAR data display the average level and dispersion of the backscatter coefficients of rice during the rice whole growth period. The use of the slope information is beneficial to obtain a suitable terrain environment for rice cultivation, especially in areas with complex terrain. (3) There were enough high-quality ground truth samples from field survey and UAV observation for algorithm training and accuracy verification. (4) The MPHO-DPSAR algorithm can effectively integrate the spectral features and spatial features of land cover types, locally minimize the average heterogeneity and maximize the internal homogeneity of objects, which is suitable for the regions with highly complex surface landscapes.

4.3. Sources of errors in rice mapping

It is still a challenging task to produce high-precision rice mapping in large spatial areas with complex terrain. The accuracy of rice mapping is mainly affected by several factors, including the temporal and spatial resolution of SAR images, the complexity of the surface landscape, the size of rice fields, the segmentation algorithm and rice feature parameters.

The higher the spatial resolution, the higher the ability of the image to distinguish the details of the ground target. Although the Sentinel-1 SAR image with a spatial resolution of 10 m can meet the requirements of accurate rice field mapping in Chongqing. The rice fields mapping accuracy will be higher if the SAR image with a higher spatial resolution is used. The time-series SAR backscatter coefficients can reflect the variety of rice in the different growth states, which is important for elucidating the unique phenological characteristics of rice. The high temporal resolution of SAR images is beneficial to measure the complete phenological parameters characteristics of rice

growth, thus improving the rice fields mapping accuracy (Wang et al., 2022).

SAR image distortion (foreshortening, layover, and shadow) caused by complex mountainous terrain may not be completely corrected by terrain correction in the SAR preprocessing step, which will affect the accuracy of rice identification (Wang et al., 2022). The foreshortening leads to larger SAR backscatter coefficients of objects at high altitudes, while the shadow results in the backscatter coefficient smaller, which increases the difficulty of rice identification. Most of the existing studies (Son et al., 2021; Zhan et al., 2021) on rice identification using SAR images were aimed at regions with simple topography and large-sized rice fields. In contrast, the terrain of the study area in this paper is complex, and the rice fields are small- and middle-sized and fragmented. In addition, other land cover types that have similar trends to the SAR backscatter curve of rice may be misclassified. For example, the lotus pond in Tuqiao Town, Tongliang District, and the grassland that is seasonally submerged due to the impoundment and drainage of the Three Gorges Reservoir.

Under the complex terrain, the area and shape of rice are quite diversity. Therefore, the optimal segmentation scale of multi-resolution segmentation algorithm determined in this paper are relative. In general, when the segmentation scale is reduced, the homogeneity of objects will be improved, the probability of dividing different land types into single objects will be reduced, and the accuracy of rice recognition will be improved. However, too small segmentation scale will lead to great heterogeneity between objects belonging to the same category, which is not conducive to rice recognition. Therefore, it is necessary to find a balance between segmentation scale and recognition accuracy.

4.4. The applicable conditions and potential improvements

The proposed MPHO-DPSAR algorithm for rice identification integrates SAR backscatter features, composite features, rice phenological parameters, texture features and a topographic feature. Therefore, enough SAR acquisitions are required to generate a time series dataset. At present, only Sentinel-1A SAR images covering Chongqing with a time resolution of 12 days were applied due to no Sentinel-1B data available. For the region covered by both Sentinel-1A and Sentinel-1B, the temporal resolution of SAR images can reach 6 days, which can more accurately obtain the phenological information of rice, and help to improve the recognition accuracy. In addition, other SAR sensor data (e.g., GF-3, RADARSAT) can also be supplemented to generate denser time-series datasets, then to obtain rice complete phenological information.

The proposed MPHO-DPSAR algorithm can be applied to rice identification in other regions. Firstly, the four key phenological stages of rice, including transplanting, jointing, heading and mature stage, should be clarified. Rice phenology has little difference in a certain spatial range and is relatively stable in different years, so the rice phenology data can be used for many years (Dong et al., 2015). Once obtaining the rice phenological data, the corresponding multi-characteristic parameters can be extracted, and then the MPHO-DPSAR algorithm can be used for high-precision rice mapping. For regions without rice phenology data, the rice phenology can be estimated based on air temperature data (Son et al., 2021). Because temperature is an important factor affecting plant growth and crop phenology (Dong et al., 2015). A temperature-based phenology algorithm was previously proposed to identify rice and achieved an overall accuracy higher than 84% (Dong et al., 2015).

There are many clouds and fog in Chongqing, so SAR has advantages over optical remote sensing for rice recognition in Chongqing. However, in regions with less cloudy and rainy weather, compared with using a single type of remote sensing image, multi-source heterogeneous optical remote sensing image and SAR image can be integrated for rice mapping, then to achieve complementary advantages of data sources (He et al., 2021).

5. Conclusion

In this study, we reconstructed the Sentinel-1 SAR time-series backscatter data, calculated multi-characteristic parameters, including SAR backscatter features, composite features, rice phenology parameters, texture features, and topographic features, and analyzed the separability of rice and other land cover types in each feature image. On this basis, a rice identification algorithm combining multi-characteristic parameters and homogeneous objects based on time series dual-polarization SAR (MPHO-DPSAR) for high-precision rice fields mapping was proposed. We tested the performance of the algorithm in Chongqing city with complex terrain, fragmentation, small and medium-sized paddy fields, and compared its performance with three existing methods. Results show that the MPHO-DPSAR was able to provide an accurate rice fields map with an overall accuracy of 95%, which is better than the existing methods. The MPHO-DPSAR derived results were in good agreement with the statistics of rice fields area in districts and counties, the correlation coefficient of determination (R^2) was 0.97. The local verification based on UAV images shows that more than 80% of the rice fields can be accurately identified by the MPHO-DPSAR algorithm when the size of a single rice field is larger than 600 m2, corresponding to 6 pixels. In addition, MPHO-DPSAR algorithm can be applied to rice recognition based on time-series optical remote sensing and SAR data to realize the complementary advantages of multi-source heterogeneous data sources. It can also be combined with the temperature-based phenology algorithm, so that MPHO-DPSAR algorithm can be applied to regions where rice phenological data are not released. This study can provide new methods and references for satellite-based rice monitoring in other regions. In future work, we will test the potential of the MPHO-DPSAR algorithm on early season rice fields mapping.

Data availability statement

The original contributions presented in the study are included in the article/Supplementary material, further inquiries can be directed to the corresponding author.

Author contributions

HM: writing, methodology, and formal analysis. LW: project administration, reviewing, and editing. WS: conceptualization. SY, YG, and LF: investigation and project administration. GY and YW:

investigation and methodology. All authors participated in the final writing—review and editing of the manuscript.

Funding

This research was supported in part by the National Natural Science Foundation of China (Nos. 42176174, 42122009, and 42171311), in part by the National Science Foundation for Post-Doctoral Scientists of China (No. 2020 M683258), Zhejiang Provincial Natural Science Foundation of China (Nos. LY22D010002, LR19D010001), Key Projects of Major Scientific and Technological Tasks in Ningbo (No. 2021Z107), Public Projects of Ningbo City (No. 2022S101), and Chongqing Natural Science Foundation (No. CSTB2022NSCQ-MSX0588).

Acknowledgments

We sincerely thank the ESA for providing time-series Sentinel-1 Level-1 SAR products and thank all reviewers who provided detailed and valuable comments or suggestions to improve this manuscript.

Conflict of interest

The authors declare that the research was conducted in the absence of any commercial or financial relationships that could be construed as a potential conflict of interest.

Publisher's note

Supplementary material

The Supplementary material for this article can be found online at: https://www.frontiersin.org/articles/10.3389/fevo.2023.1093454/full#supplementary-material

References

Arino, O., Bicheron, P., Frédéric, A., Latham, J., Witt, R., and Weber, J.-L. (2008). GLOBCOVER: the most detailed portrait of Earth. *European Space Agency Bull.* 2008, 24–31.

Bazzi, H., Baghdadi, N., El Hajj, M., Zribi, M., Minh, D. H. T., Ndikumana, E., et al. (2019). Mapping Paddy Rice using Sentinel-1 SAR time series in Camargue, France. *Remote Sens.* 11:887. doi: 10.3390/rs11070887

Belgiu, M., Bijker, W., Csillik, O., and Stein, A. (2021). Phenology-based sample generation for supervised crop type classification. *Int. J. Appl. Earth Obs. Geoinf.* 95:102264. doi: 10.1016/j.jag.2020.102264

Belgiu, M., and Csillik, O. (2018). Sentinel-2 cropland mapping using pixel-based and object-based time-weighted dynamic time warping analysis. *Remote Sens. Environ.* 204, 509–523. doi: 10.1016/j.rse.2017.10.005

Bouvet, A., and Le Toan, T. (2011). Use of ENVISAT/ASAR wide-swath data for timely rice fields mapping in the Mekong River Delta. *Remote Sens. Environ.* 115, 1090–1101. doi: 10.1016/j.rse.2010.12.014

Cao, J., Cai, X., Tan, J., Cui, Y., Xie, H., Liu, F., et al. (2020). Mapping paddy rice using Landsat time series data in the Ganfu plain irrigation system, southern China, from 1988–2017. *Int. J. Remote Sens.* 42, 1556–1576. doi: 10.1080/01431161.2020.1841321

Chandra Paul, G., Saha, S., and Hembram, T. K. (2020). Application of phenology-based algorithm and linear regression model for estimating rice cultivated areas and yield using remote sensing data in Bansloi River basin, eastern India. *Rem. Sens. Appl.* 19:100367. doi: 10.1016/j.rsase.2020.100367

Chen, T., and Pan, J. (2022). Estimation and temporal and spatial pattern of anthropogenic CH4 emissions in China from 2009 to 2019. *Chin. Environ. Sci.* 1:914. doi: 10.19674/j.cnki.issn1000-6923.20220914.004

Chongqing Statistics Bureau. (2020). *Chongqing statistical year book 2020*. Beijing: China Statistics Press.

Clauss, K., Ottinger, M., Leinenkugel, P., and Kuenzer, C. (2018). Estimating rice production in the Mekong Delta, Vietnam, utilizing time series of Sentinel-1 SAR data. *Int. J. Appl. Earth Obs. Geoinf.* 73, 574–585. doi: 10.1016/j.jag.2018.07.022

Corcione, V., Nunziata, F., Mascolo, L., and Migliaccio, M. (2016). A study of the use of COSMO-SkyMed SAR PingPong polarimetric mode for rice growth monitoring. *Int. J. Remote Sens.* 37, 633–647. doi: 10.1080/01431161.2015.1131902

Csorba, A., Szegi, T., Fodor, H., Bukombe, B., Uwiragiye, Y., Naramabuye, F. X., et al. (2019). Characterization of rice agriculture in the Southern Province of Rwanda by means of microwave remote sensing. *Phys. Chem. Earth* 112, 58–65. doi: 10.1016/j.pce.2019.02.002

Dong, J., Xiao, X., Kou, W., Qin, Y., Zhang, G., Li, L., et al. (2015). Tracking the dynamics of paddy rice planting area in 1986–2010 through time series Landsat images and phenology-based algorithms. *Remote Sens. Environ.* 160, 99–113. doi: 10.1016/j.rse.2015.01.004

Dragut, L., Csillik, O., Eisank, C., and Tiede, D. (2014). Automated parameterization for multi-scale image segmentation on multiple layers. *ISPRS J. Photogramm. Remote Sens.* 88, 119–127. doi: 10.1016/j.isprsjprs.2013.11.018

Drŏguţ, L., Tiede, D., and Levick, S. R. (2010). ESP: a tool to estimate scale parameter for multi-resolution image segmentation of remotely sensed data. *Int. J. Geogr. Inf. Sci.* 24, 859–871. doi: 10.1080/13658810903174803

Gao, H., Wang, C., and Yang, M. (2019). Analysis and classification of crop scattering characteristics based on GF-3 polarized SAR data. *Eng. Surv. Mapp.* 28, 50–56. doi: 10.19349/j.cnki.issn 1006-7949.2019.03.010

Gir, R., Jain, L., and Rai, R. (2015). Speckle reduction of synthetic aperture radar images using median filter and savitzky-golay filter. *Int. J. Comput. Appl.* 113.

Gong, P., Wang, J., Yu, L., Zhao, Y., Zhao, Y., Liang, L., et al. (2012). Finer resolution observation and monitoring of global land cover: first mapping results with Landsat TM and ETM+ data. *Int. J. Remote Sens.* 34, 2607–2654. doi: 10.1080/01431161.2012.748992

Han, J., Zhang, Z., Luo, Y., Cao, J., Zhang, L., Zhuang, H., et al. (2022). Annual paddy rice planting area and cropping intensity datasets and their dynamics in the Asian monsoon region from 2000 to 2020. *Agric. Syst.* 200:103437. doi: 10.1016/j.agsy.2022.103437

He, Y., Dong, J., Liao, X., Sun, L., Wang, Z., You, N., et al. (2021). Examining rice distribution and cropping intensity in a mixed single- and double-cropping region in South China using all available sentinel 1/2 images. *Int. J. Appl. Earth Obs. Geoinf.* 101:102351. doi: 10.1016/j.jag.2021.102351

Krishnan, S. R., and Seelamantula, C. S. (2013). On the selection of optimum Savitzky-Golay filters. *IEEE Trans. Signal Process.* 61, 380–391. doi: 10.1109/TSP.2012.2225055

Li, K., Brisco, B., Yun, S., and Touzi, R. (2014). Polarimetric decomposition with RADARSAT-2 for rice mapping and monitoring. *Can. J. Remote. Sens.* 38, 169–179. doi: 10.5589/m12-024

Li, C., Chen, W., Wang, Y., Wang, Y., Ma, C., Li, Y., et al. (2022). Mapping winter wheat with optical and SAR images based on Google earth engine in Henan Province, China. *Remote Sens.* 14:284. doi: 10.3390/rs14020284

Lin, B., Xu, M., and Wang, X. (2022). China's agricultural carbon emission reduction policies, research status and prospects. *Chin. J. Ecol. Agric.* 30, 500–515. doi: 10.12357/cjea.20210843

Lisan, Z. (1993). *The theory and practice of agricultural regionalization in China*. Hefei: University of Science and Technology of China Press.

Lopez-Sanchez, J. M., Cloude, S. R., and Ballester-Berman, J. D. (2012). Rice phenology monitoring by means of SAR polarimetry at X-band. *IEEE Trans. Geosci. Remote Sens.* 50, 2695–2709. doi: 10.1109/TGRS.2011.2176740

Mandal, D., Kumar, V., Ratha, D., Lopez-Sanchez, J. M., Bhattacharya, A., McNairn, H., et al. (2020). Assessment of rice growth conditions in a semi-arid region of India using

the generalized radar vegetation index derived from RADARSAT-2 polarimetric SAR data. *Remote Sens. Environ.* 237:111561. doi: 10.1016/j.rse.2019.111561

Nguyen, D., Wagner, W., Naeimi, V., and Cao, S. (2015). Rice-planted area extraction by time series analysis of ENVISAT ASAR WS data using a phenology-based classification approach: a case study for red River Delta, Vietnam. *Int. Arch. Photogramm. Remote. Sens. Spat. Inf. Sci.* XL-7/W3, 77–83. doi: 10.5194/isprsarchives-XL-7-W3-77-2015

Ni, R., Tian, J., Li, X., Yin, D., Li, J., Gong, H., et al. (2021). An enhanced pixel-based phenological feature for accurate paddy rice mapping with Sentinel-2 imagery in Google earth engine. *ISPRS J. Photogramm. Remote Sens.* 178, 282–296. doi: 10.1016/j.isprsjprs.2021.06.018

Pan, B., Zheng, Y., Shen, R., Ye, T., Zhao, W., Dong, J., et al. (2021). High resolution distribution dataset of double-season Paddy Rice in China. *Remote Sens.* 13:4609. doi: 10.3390/rs13224609

Pang, J., Zhang, R., Yu, B., Liao, M., Lv, J., Xie, L., et al. (2021). Pixel-level rice planting information monitoring in Fujin City based on time-series SAR imagery. *Int. J. Appl. Earth Obs. Geoinf.* 104:102551. doi: 10.1016/j.jag.2021.102551

Panigrahy, S., Jain, V., Patnaik, C., and Parihar, J. S. (2012). Identification of Aman Rice crop in Bangladesh using temporal C-band SAR – a feasibility study. *J. Indian Soc. Remote Sens.* 40, 599–606. doi: 10.1007/s12524-011-0193-0

Peña-Barragán, J. M., Ngugi, M. K., Plant, R. E., and Six, J. (2011). Object-based crop identification using multiple vegetation indices, textural features and crop phenology. *Remote Sens. Environ.* 115, 1301–1316. doi: 10.1016/j.rse.2011.01.009

Son, N.-T., Chen, C.-F., Chen, C.-R., Toscano, P., Cheng, Y.-S., Guo, H.-Y., et al. (2021). A phenological object-based approach for rice crop classification using time-series Sentinel-1 synthetic aperture radar (SAR) data in Taiwan. *Int. J. Remote Sens.* 42, 2722–2739. doi: 10.1080/01431161.2020.1862440

Sulla-Menashe, D., Gray, J. M., Abercrombie, S. P., and Friedl, M. A. (2019). Hierarchical mapping of annual global land cover 2001 to present: the MODIS collection 6 land cover product. *Remote Sens. Environ.* 222, 183–194. doi: 10.1016/j.rse.2018.12.013

Torbick, N., Chowdhury, D., Salas, W., and Qi, J. (2017). Monitoring Rice agriculture across Myanmar using time series Sentinel-1 assisted by Landsat-8 and PALSAR-2. *Remote Sens.* 9:119. doi: 10.3390/rs9020119

Wang, L., Ma, H., Li, J., Gao, Y., Fan, L., Yang, Z., et al. (2022). An automated extraction of small- and middle-sized rice fields under complex terrain based on SAR time series: a case study of Chongqing. *Comput. Electron. Agric.* 200:107232. doi: 10.1016/j.compag.2022.107232

Xie, H., and Chen, Z. W. (2019). Prospects for agricultural sustainable intensification: A review of research. *Land* 8:157. doi: 10.3390/land8110157

Yang, H., Pan, B., Wu, W., and Tai, J. (2018). Field-based rice classification in Wuhua county through integration of multi-temporal sentinel-1A and Landsat-8 OLI data. *Int. J. Appl. Earth Obs. Geoinf.* 69, 226–236. doi: 10.1016/j.jag.2018.02.019

Yang, Z., Shao, Y., Li, K., Liu, Q., Liu, L., and Brisco, B. (2017). An improved scheme for rice phenology estimation based on time-series multispectral HJ-1A/B and polarimetric RADARSAT-2 data. *Remote Sens. Environ.* 195, 184–201. doi: 10.1016/j.rse.2017.04.016

Yin, Q., Liu, M., Cheng, J., Ke, Y., and Chen, X. (2019). Mapping Paddy Rice planting area in northeastern China using spatiotemporal data fusion and phenology-based method. *Remote Sens.* 11:1699. doi: 10.3390/rs11141699

Yu, L., Huang, Y., Liu, J., and Duan, L. (2020). Extraction of polarization characteristics of Oryza sativa growth under the rainfall fluctuation. *J. Zhejiang A&F Univ.* 37, 992–998. doi: 10.11833/j.issn.2095-0756.20190605

Zeng, L., Wardlow, B. D., Xiang, D., Hu, S., and Li, D. (2020). A review of vegetation phenological metrics extraction using time-series, multispectral satellite data. *Remote Sens. Environ.* 237:111511. doi: 10.1016/j.rse.2019.111511

Zhan, P., Zhu, W., and Li, N. (2021). An automated rice mapping method based on flooding signals in synthetic aperture radar time series. *Remote Sens. Environ.* 252:112112. doi: 10.1016/j.rse.2020.112112

Zhang, M., and Lin, H. (2019). Object-based rice mapping using time-series and phenological data. *Adv. Space Res.* 63, 190–202. doi: 10.1016/j.asr.2018.09.018

Zheng, H., Cheng, T., Yao, X., Deng, X., Tian, Y., Cao, W., et al. (2016). Detection of rice phenology through time series analysis of ground-based spectral index data. *Field Crop Res.* 198, 131–139. doi: 10.1016/j.fcr.2016.08.027

Zhu, Q., Guo, X., Deng, W., Shi, S., Guan, Q., Zhong, Y., et al. (2022). Land-use/land-cover change detection based on a Siamese global learning framework for high spatial resolution remote sensing imagery. *ISPRS J. Photogramm. Remote Sens.* 184, 63–78. doi: 10.1016/j.isprsjprs.2021.12.005

frontiers | Frontiers in Environmental Science

TYPE Original Research
PUBLISHED 10 March 2023
DOI 10.3389/fenvs.2023.1088816

OPEN ACCESS

EDITED BY
Sanath Sathyachandran Kumar,
United States Geological Survey (USGS), United States

REVIEWED BY
Xiankun Yang,
Guangzhou University, China
Gui Jin,
China University of Geosciences Wuhan, China
Wei Song,
Institute of Geographic Sciences and Natural Resources Research (CAS), China

*CORRESPONDENCE
Cheng Jin,
jincheng@njnu.edu.cn

SPECIALTY SECTION
This article was submitted to Land Use Dynamics, a section of the journal Frontiers in Environmental Science

RECEIVED 03 November 2022
ACCEPTED 27 February 2023
PUBLISHED 10 March 2023

CITATION
Zhang S, Jin C, Pan X, Wei L and Shao H (2023), Coastal land use change and evaluation of ecosystem services value enhancement under the background of Yangtze River protection: Taking Jiangyin coastal areas as an example.
Front. Environ. Sci. 11:1088816.
doi: 10.3389/fenvs.2023.1088816

Coastal land use change and evaluation of ecosystem services value enhancement under the background of Yangtze River protection: Taking Jiangyin coastal areas as an example

Shiyu Zhang[1], Cheng Jin[1,2]*, Xiaoqing Pan[1], Luyao Wei[1] and Haiyan Shao[1]

[1]School of Geography, Nanjing Normal University, Nanjing, China, [2]Jiangsu Center for Collaborative Innovation in Geographical Information Resource Development and Application, Nanjing, China

Evaluating the ecosystem service value is an important step to promote the sustainable development and the construction of ecological civilization of the Yangtze River Economic Belt, the related research is already very rich. However, they neglect the evaluation of coastal areas and lack the deeper thinking of ecological value. To improve these deficiencies, this study takes the coastal area of Jiangyin as the study area, constructs the evaluation method system of ecosystem service value based on the land use data in 2016 and 2020, explores the temporal and spatial variation characteristics of land use and ecosystem service value in the study area, and analyzes reasons for these changes. The results show that: (1) Cultivated land is the main land type in the coastal area, with an area change rate of -15.89%, forest land increases rapidly, with a growth rate of 281.62%, followed by water area with a growth rate of 55.98%, garden land decreases the most, with a decrease rate of 86.36%, followed by construction land of 62.19%. Land use mainly presents the characteristics of changes from construction land to other land, construction land and green space, and cultivated land to cultivated land, water area and forest land. (2) The net increase of ecosystem service value in the coastal area is 483 million, with a growth rate of 137.27%. Among them, the value of forest land accounts for the largest proportion, with a net increase of 264 million yuan and a growth rate of 109.54%. In terms of single function, flood regulation and storage accounts for the main ecosystem service value, reaching more than 65%, with a net increase of 394 million yuan. (3) In terms of spatial distribution, the ecosystem service value of water conservation, flood regulation and storage has a spatial distribution characteristic of being high in the east and low in the west, while the distribution of ecosystem service value of wind prevention and sand fixation is both high and low in the west. In addition, this study further explores the response mechanism of ecological value to the protection measures along the river and the transformation path of ecosystem service value, which provides a new path for the study of government-led evaluation of ecological protection effects in important coastal areas and ecologically sustainable development with regional multi-subject participation.

KEYWORDS

ecosystem services, evaluation of ecosystem services value, land use change, yangtze river protection, Jiangyin

1 Introduction

The Yangtze River is the key area of China's economic and social development, and it also has a high position in safeguarding national ecological security. Since modern times, due to the influence of unreasonable production and lifestyle, the Yangtze River Economic Belt has become one of the areas with the most prominent water environment problems in China. The area of farmland, forests, grasslands, wetlands and other ecosystems has decreased, the ecosystem pattern has changed drastically, the soil erosion in the upstream and downstream areas has been serious, the contradiction between people and land has intensified along the Yangtze River, lakes have shrunk, the ecosystem functions of forests and wetlands have gradually deteriorated. In this context, evaluating the function of coastal ecosystems and studying the effect of ecological protection has become an important step in promoting the sustainable development of the Yangtze River Economic Belt and the construction of ecological civilization. Specifically, quantifying and evaluating ecosystem functions can deepen the research on ecosystem function evaluation and scientifically evaluate the development status of different ecosystems in theory, and improve the economic benefits of natural resources and promote sustainable economic and social development in practice.

Ecosystem service value (ESV) is the direct embodiment of ecosystem functions. Ecosystem services (ES) are products and services that are directly or indirectly obtained through the structure, functions and processes of ecosystems to support life (Xie et al., 2015). In the past few decades, scholars have gradually realized that the value of ecosystem services has a great impact on the sustainable development of social economy (Kohler, 1984; Rudolf, 1997; Bockstael et al., 2000; Boyd and Banzhaf, 2007; Fisher et al., 2009). They have carried out evaluation studies on the ecosystem service value with various contents, varied perspectives, multi-dimensional scales, and multiple methods (Costanza et al., 1998; Sun, 2011; Yu and Bi, 2011; Xie, 2017). In terms of research content, on one hand, it includes the evaluation of all ecosystem services (ecosystem material products, ecosystem regulation service and culture), on the other hand, scholars focus on ecosystem regulation service, which is the main type of ecosystem services. They research water conservation (Cheng and Shi, 2004; Sheng et al., 2010), soil conservation (Pimentel et al., 1995; Xiao et al., 2000), carbon sequestration and oxygen release (Liu and Lu, 2008; Zhou et al., 2013), air purification (Wu et al., 2009), water purification (He and Kang, 2008), flood regulation and storage (Liu, 2007), wind prevention and sand fixation (Jiang et al., 2016) and other regulation services. In terms of research perspective, various ecosystems (United Nations, 2014), such as forests (O'Brien, 1998), plateaus (Xie et al., 2003), wetlands (Duan et al., 2005; Jiang et al., 2015; Zhou et al., 2021; The Encyclopedia of Earth, 2022), and the theory of ecosystem protection are focused and discussed. In terms of research scale, it involves globe (Costanza et al., 1998), nation (Ma et al., 2017), province (Bai et al., 2017; Song and Ouyang, 2020), city (Wang et al., 2017; Dong et al., 2019) county (Pema et al., 2020) and other spatial scopes (Qiu et al., 2017; Shifaw et al., 2019). Scholars evaluate the value of ecosystem services at different scales to explore their spatial distribution and driving factors, and provide new perspectives for ecological protection in different situations. The research methods are divided into two types: value evaluation and material quality evaluation (Fu and Zhang, 2014), in terms of value evaluation, Costanza et al. (Costanza et al., 1998) published research on global ecosystem services and their value in 1997, which attracted a lot of attention. Xie (Xie et al., 2003) referred to some results of global ecosystem service value evaluation by Constanza et al. and integrated questionnaire surveys to establish a service value table per unit area, which has been widely used. However, considering different research angles, scales, and the complexity of estimation, the value evaluation method has been questioned a lot, and different theoretical frameworks and evaluation methods have been formed (Ouyang et al., 1999; Sukhdev et al., 2010). In terms of material quality evaluation, it is generally assessed by combining observed data and ecological models (Fu and Zhang, 2014), and it also has different evaluation methods on large and small scales (Feng et al., 2010). Comparing the two research methods, the former calculation is more convenient and fast, suitable for comparative research under different changing conditions, while the latter calculation is more complicated but more rigorous, suitable for long-term and continuous analysis. In general, the research on ecosystem service value has already been very rich, but the lack of reliable data and the inconsistency of evaluation methods have made these researches still insufficient.

With the deepening of research, many scholars have noticed the topic of land use, which has always been a hot topic in various fields, especially in recent years, the urbanization process has given birth to the discussion of land use efficiency (Jin et al., 2018) and the relationship between land use and ecosystem services (Daily, 1997). They believe that ESV and Land Use Change (LUC) influence each other, and land is the carrier of ESV, changes in land use patterns will affect ecological processes such as the water cycle by changing the structure and function of ecosystems, leading to changes in ecosystem services. Evaluation of ecosystem services also affects land development and land use planning (Li et al., 2010; Lawler et al., 2014; Ouyang et al., 2016). Therefore, the quantitative evaluation of ecosystem services under the background of land use change has become a research hotspot. At present, there are many studies on the response of ESV to LUC (Dale, 1997; Fu et al., 2000; Su et al., 2010; Wainger et al., 2010; Sonter et al., 2017; Tolessa et al., 2017; Li et al., 2018). Based on the value equivalent method proposed by Xie, most scholars have evaluated ESV from different perspectives and scales in combination with LUC (Zhao et al., 2004; Liu et al., 2018; Lei et al., 2019; Wang and Ma, 2020), on this basis, explore the impact of LUC on ESV and the spatial dependence of service values on land use patterns. Although these studies adopt a variety of methods and draw conclusions with their own characteristics, most of them ignore the role of human activities and lack the discussion on the response mechanism of ESV to the cause of LUC.

Therefore, on the basis of the existing research on ESV evaluation and value evaluation combined with LUC, it is not

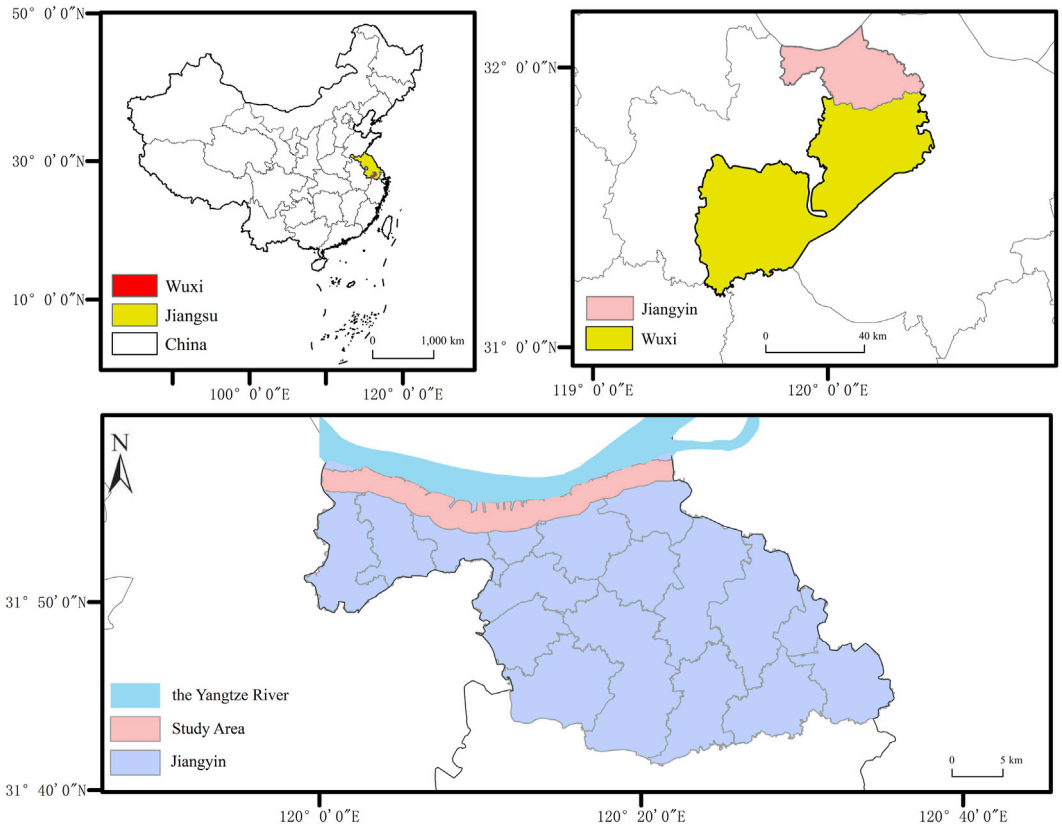

FIGURE 1
Location of Jiangyin and the study area.

difficult to see that it is still not easy to select a suitable study area, suitable research content and suitable research methods to carry out the evaluation of ESV. Specifically, when selecting study areas, many scholars blindly select large spatial areas and ignore small regional units in order to evaluate more general evaluation conclusions for direct use in subsequent research. In terms of research content, most studies directly evaluate all indicators of the ecosystem services in the study area, and make a general summary in order to win by quantity, while omitting the consideration of combining land, economy, society and other factors. In terms of research methods, the most serious problem is the use of general accounting methods and calculation parameters, ignoring regional differences, and the results obtained are basically not typical.

Based on this, in terms of the study area, this study selects the coastal area in Jiangyin, a special regional unit with prominent human-land conflicts (Zhou et al., 2011; Wang et al., 2020a). On one hand, there are few studies on the evaluation and protection of relevant ESV along large rivers; on the other hand, the small study area facilitates the analysis of specific driving factors of LUC (Zhang et al., 2013). In terms of research content, since regulation service is the most important type of ecosystem services, and the value cannot be measured uniformly (Lai et al., 2013), choosing the regulation service to build the accounting system can produce regional differences. In terms of research methods, some accounting methods are optimized, and some accounting parameters are innovated in this research to carry out accounting, so as to better understand the spatial differences of service value. On the whole, this study analyzes the land use changes in the coastal area under the land use data in 2016 and 2020, scientifically evaluates the functional and structural changes of ecosystem regulation service value, explores the reasons for the changes, and further explores the response mechanism of ecological value to government protection policies and the transformation path of ecological value, providing new ideas for the study of the government-led evaluation of ecological protection effects in important coastal areas and ecologically sustainable development with regional multi-subject participation.

2 Materials and methods

2.1 Study area

Jiangyin is located in the southeast of Jiangsu Province, it is 31 degrees 55 min north latitude and 120 degrees 17 min east longitude. Jiangyin, which is adjacent to the Yangtze River in the north, is a very important riverside city in the lower reaches of the Yangtze River (Figure 1). In recent years, due to over-exploitation of the economy, it has brought a heavy ecological burden to the Jiangyin section of the Yangtze River, and the contradiction

between human and land is very prominent. In order to ease the pressure of ecological environment, over the years, Jiangyin has attached great importance to and vigorously promoted environmental protection and ecological construction, adhered to the development policy of giving priority to environmental protection, improved the coordination of economic, social and environmental resources, made certain achievements, among them, ESV reached 61.9 billion in 2022, and became the first batch of national ecological cities.

Considering the typicality of the coastal area in Jiangyin in the following aspects, this study selects the area 2 km along the Yangtze River in Jiangyin as the study area, and the details are as follows: (1) In recent years, there have been some problems in the area 2 km along the Yangtze River in Jiangyin, such as high-intensity development along the Yangtze River, a high proportion of shoreline construction, serious water quality problems and deterioration of ecological environment. So it is the hardest hit area of ecological problems, and it is also the key area to explore ecological protection. (2) There are many types of ecosystems within 2 km along the Yangtze River in Jiangyin, and the shoreline of the Yangtze River is an important part of the ecosystem along the Yangtze River. It is a strategic resource and an important carrier to promote the high-quality development of the Yangtze River Economic Belt by relying on the golden waterway, and it is also the key object of ecological restoration and protection. The protection of the Yangtze River area can not only take into account the ecological protection of the Yangtze River, but also relate to the economic and social development of coastal urban areas, and provide the optimization ideas of ecology and development for the main urban areas, which is a measure to achieve the integration of ecological benefits and economic and social benefits. (3) Enterprises and production activities gather within 2 km along the Yangtze River in Jiangyin, and the contradiction between people and land is prominent. Analyzing the 2 km along the Yangtze River can provide more detailed suggestions for the follow-up industrial transformation and upgrading and ecological protection measures.

2.2 Data sources

The land use data used in this study comes from Jiangyin Bureau of Natural Resources and Planning, in 2016, the National Ecological Civilization Experimental Zone began to be implemented. In 2020, the third national land survey in Jiangsu Province was completed, the land use types in the province changed, in the same year, the realization and protection of the ecosystem value of the Yangtze River Basin received full attention from the government. Based on this, this study selects two periods of land use data in 2016 and 2020, which can more intuitively show the land use change and the improvement of ecosystem service value in the coastal area of Jiangyin. Statistical data such as rainfall is from the Statistical Yearbook of Jiangyin, and data such as evapotranspiration, surface runoff, and purification of air pollutants refer to relevant materials and literature, the NDVI data comes from Geospatial Data Cloud (https://www.gscloud.cn/), and the NPP data comes from MOD17A3HGF.v006 version of NASA. The specific data sources will be stated in Section 2.3.2 of this paper.

2.3 Methods

2.3.1 Regulation service function index selection

The selection of ecosystem regulation services is an important part of ESV evaluation. However, many related studies lack specific reasons for the selection, which reduces the rationality and accuracy of the research. Based on this, this study will clarify the reasons for the selection while constructing the ecosystem regulation service accounting system, in order to improve the reliability of the research and provide a theoretical basis for follow-up research. The accounting system of this study contains seven indicators including water conservation, flood regulation and storage, air purification, water purification, wind prevention and sand fixation, carbon sequestration, and oxygen release. The specific reasons are as follows:

Water ecosystem is the environment on which human beings depend for survival. Water resources include four elements: water quantity, water quality, water energy, and aquatic organisms. Based on this, water ecosystem services can be divided into four categories: water supply, water energy, aquatic organisms, and environmental benefits (Cai et al., 2003), among them, aquatic organisms highlight the importance of carbon sequestration and oxygen release, and environmental benefits highlight the importance of water conservation, flood regulation and storage, and water purification. Where water resources are abundant, these functions are very obvious. Jiangyin is close to the Yangtze River, where the pressure of flood control of lakes is high, the problems of water environment are serious, and the contradiction of water resources is intensified. In this way, research on water conservation, flood regulation and storage, water purification, carbon sequestration and oxygen release can be carried out. In addition, the importance of evaluating these functions is also reflected in other ecosystems. For example, wetland ecosystems can reduce flood peaks, delay flood processes, and reduce economic damage caused by floods, it also has important ecological value (Hans et al., 2001; Yao and Yang, 2009) to apply natural wetlands to water purification and carbon sequestration and oxygen release. The forest ecosystem can make the soil more permeable to rainwater, making the water conservation ability outstanding, and the forest photosynthesis is strong, making the carbon sequestration and oxygen release function obvious. The coastal area in Jiangyin is rich in types of wetlands and forests, so evaluating the above functions plays an important role in exploring ESV in Jiangyin (Cao et al., 2013).

In Jiangyin, there are rich and diverse ecological lands. Among them, vegetation, as an important natural resource, has an obvious function of wind prevention and sand fixation (Han et al., 2011). Although this function is generally applicable to wind erosion areas, some studies have shown that vegetation coverage and the amount of soil wind erosion are negatively correlated (Huang et al., 2001). Therefore, under the background of land use changes in Jiangyin, it is necessary to study the function of wind prevention and sand fixation. In addition, air purification is also a regulation service that cannot be ignored, especially in the context of the rapid development of urbanization in recent years, the urban air pollution problem in

TABLE 1 Ecosystem regulation service function.

Service type	Evaluation method	Calculation function	Parameter introduction	Parameter source
Water Conservation	Model method for water conservation capacity	$TQ = \sum_{i=1}^{j} (P_i - R_i - ET_i) \times A_i \times 10^{-3}$	TQ is the water conservation capacity (m^3);	64
			P_i is the rainfall (mm);	
			R_i is the surface runoff (mm);	
			ET_i is evapotranspiration (mm);	
			A_i is the area of the ecosystem of type i (km^2); i is the type i ecosystem in the study area;	
			j is the total number of ecosystem types in the study area.	
Flood Regulation and Storage	The sum of water storage capacity of vegetation and stagnant water in flood period	$C_{fm} = C_{vfm} + C_{rfm} + C_{lfm} + C_{mfm}$ $C_{vfm} = \sum_{i=1}^{n} (P_i - R_{fi}) \times A_i \times 1000$ $C_{rfm} = 0.29 \times C_t$ $C_{lfm} = e^{4.924} \times A^{1.128} \times 3.19$ $C_{mfm} = C_{sws} + C_{sr}$ $C_{sws} = S \times h \times \rho \times (F - E) \times 10^{-2}/\rho_w$ $C_{sr} = S \times H \times 10^{-2}$	C_{fm} is the flood storage capacity (m^3/a);	64
			C_{vfm} is the vegetation flood storage capacity (m^3/a);	
			C_{rfm} is the reservoir flood storage capacity (m^3/a);	
			C_{lfm} is the lake flood storage capacity (m^3/a);	
			C_{mfm} is the swamp flood storage capacity (m^3/a);	
			P_i is the rainstorm rainfall (mm);	
			R_{fi} is rainstorm runoff of the vegetation ecosystem of type i (mm);	
			A_i is the area of the vegetation ecosystem of type i (km^2); i is the vegetation ecosystem of type i in the accounting area, i = 1,2, . . . , n;	
			C_t is the total storage capacity of the reservoir (m^3);	
			C_{sws} is the swamp soil water storage capacity (m^3/a);	
			C_{sr} is the swamp surface water retention (m^3/a);	
			S is the total area of swamp (km^2); h is the water storage depth of marsh wetland soil (m);	
			ρ is the bulk density of swamp wetland soil (g/cm^3);	
			F is the saturated water content of marsh wetland soil (dimensionless);	
			E is the natural moisture content of swamp wetland before flooding (dimensionless);	
			ρ_w is the density of water (g/cm^3);	
			H is the surface stagnant water height of swamp wetland (m).	
Air Purification	Self-purification ability of ecosystem	$Q_{\alpha p} = \sum_{i=1}^{n} \sum_{j=1}^{m} Q_{ij} \times A_j$	$Q_{\alpha p}$ is the air purification capacity of the ecosystem (kg/a);	
			Q_{ij} is the purification amount of type j ecosystem to type i air pollutants per unit	

(Continued on following page)

TABLE 1 (*Continued*) Ecosystem regulation service function.

Service type	Evaluation method	Calculation function	Parameter introduction	Parameter source
			area (kg/km^2·a); i is the air pollutant category, i = 1,2, . . . , n;	
			j is the ecosystem type, j = 1,2, . . ., m;	
			A_j is the area of type j ecosystem (km^2).	
Water Purification	Purification function of ecosystem water environment	$Q_{wp} = \sum_{i=1}^{n}\sum_{j=1}^{m} P_{ij} \times A_j$	Q_{wp} is the purification amount of water pollutants (kg/a);	
			P_{ij} is the purification amount of type i pollutants by type j ecosystem per unit area (kg/km^2·a); i is the water pollutant category, i = 1,2, . . . , n; A_j is the area of the type j ecosystem (km^2);	
			j is the ecosystem type, j = 1,2, . . . , m.	
Wind Prevention and Sand Fixation	Wind erosion reduction of ecosystem	$Q_{sf} = 0.1699 \times (WF \times EF \times SCF \times K')^{1.3711} \times (1 - C^{1.3711})$ $WF = Wf \times \frac{\rho}{g} \times SW \times SD$ $K' = \frac{(AC^*AB)}{(AC^*AC)} = 1/\cos a$ SCF is the soil crust factor; C is the vegetation cover factor; $C = (NDVI - NDVI_{min})/(NDVI_{max} - NDVI_{min})$	Q_{sf} is the amount of wind prevention and sand fixation (t/a);	GEP (2023)
			WF is the climatic erosion factor (kg/m);	
			K' is the surface roughness factor;	
			EF is the soil erosion factor;	
			Wf is the multi-month average wind factor;	
			ρ is the air density; g is the acceleration of gravity;	
			SW is the monthly annual average soil moisture factor, (dimensionless);	
			SD is snow cover factor.	
Carbon Sequestration	NEP method	$Q_{CO_2} = M_{CO_2}/M_C \times NEP$ $NEP = \alpha \times NPP \times M_{C_6}/M_{C_6H_{10}O_5}$	Q_{CO_2} is the carbon sequestration of ecosystem (tCO_2/a);	GEP (2023)
			M_{CO_2}/M_C =44/12 is the coefficient of conversion of C into CO_2;	
			NEP is net ecosystem productivity (TC/a);	
			α is conversion factor	
			NPP is net primary productivity (t dry matter/a);	
			$M_{C_6}/M_{C_6H_{10}O_5}$ =72/162 is the coefficient of conversion of dry matter into C.	
Oxygen Release	NEP method	$Q_{CO_2} = M_{CO_2}/M_C \times NEP$ $Q_{op} = M_{O_2}/M_{CO_2} \times Q_{tCO_2}$	Q_{CO_2} is the carbon sequestration of ecosystem (tCO_2/a);	GEP (2023)
			M_{CO_2}/M_C =44/12 is the coefficient of conversion of C into CO_2;	
			NEP is net ecosystem productivity (TC/a);	
			Q_{op} is Oxygen release for ecosystem (t);	
			M_{O_2}/M_{CO_2} =32/44 is the coefficient of CO_2 conversion to O_2;	
			Q_{tCO_2} is Carbon sequestration for ecosystem (tCO_2/a).	

Jiangyin is still difficult (Wu et al., 2009), and the evaluation methods for the value of air purification are also very diverse. Therefore, research based on this can enrich the research content and research methods. It is worth noting that although the importance of the above-mentioned regulation services is reflected in different ecosystems, they can still be valued in other ecological lands, so the selection of these seven indicators will not affect the scientificity of subsequent research.

2.3.2 Accounting methods

The evaluation types of ecosystem regulation service functions in Jiangyin include water conservation, flood regulation and storage, air purification, water purification, wind prevention and sand fixation, carbon sequestration and oxygen release. The evaluation method, calculation formula and calculation parameters of each service type are shown in Table 1.

In Table 1, the evaluation methods of each function are different, and the sources of parameters are also diverse. Among them, (1) water conservation: we use the model method for water conservation capacity to evaluate the function quantity, and the rainfall data in the calculation function comes from "Jiangyin Statistical Yearbook 2021" (Jiangyin Statistics Bureau, 2021), the evapotranspiration data is calculated according to the Haude method, and the surface runoff data of different land types come from "Guidelines for Ecosystem Product Value Accounting (Trial)" provided by Jiangyin. (2) Flood regulation and storage: This function is characterized by the sum of water storage capacity of vegetation and stagnant water (reservoirs, lakes, swamps) in flood period. The data of rainstorm rainfall comes from "Jiangyin Statistical Yearbook 2021" (Jiangyin Statistics Bureau, 2021), and the data of rainstorm runoff of different land types come from "Guidelines for Ecosystem Product Value Accounting (Trial) ", the total storage capacity of the reservoir refers to "Jiangyin Statistical Yearbook 2021" (Jiangyin Statistics Bureau, 2021), and the bulk density and other parameters of the swamp flood storage capacity are from "Guidelines for Ecosystem Product Value Accounting (Trial)". (3) Air purification: We use the self-purification ability of ecosystem to estimate the function quantity. The types of air pollutants are SO_2, NO_X and dust. The data of the purification amount of air pollutants in different land types come from "Guidelines for Ecosystem Product Value Accounting (Trial) ". (4) Water purification: We use the purification function of ecosystem water environment as the evaluation index, the pollutant types are COD, ammonia nitrogen and total phosphorus, and the data comes from "Guidelines for Ecosystem Product Value Accounting (Trial) ". (5) Wind prevention and sand fixation: We take the wind erosion reduction of ecosystem as the evaluation index. The calculation process of parameters such as soil erosion factor and climate erosion factor refer to Appendix C.2 of "The Technical Guide on Gross Ecosystem Product (GEP)" (GEP, 2023), and NDVI data comes from Geospatial Data Cloud (https://www.gscloud.cn/). (6) Carbon sequestration and oxygen release: We all use the NEP method to estimate their function quantity, and the conversion factor comes from Appendix C.3 of "The Technical Guide on Gross Ecosystem Product (GEP)" (GEP, 2023).

The evaluation types of ecosystem regulation service value in Jiangyin include water conservation, flood regulation and storage, air purification, water purification, wind prevention and sand fixation, carbon sequestration and oxygen release. The evaluation methods, calculation formulas and calculation parameters of each service type are shown in Table 2.

In Table 2, we use the shadow project method to evaluate the value of water conservation, and use the replacement cost method to evaluate the value of other regulation services. The cost sources of each method are different. Among them, (1) Water conservation, flood regulation and storage: cost data refer to "Specifications for Assessment of Forest Ecosystem Services" (Forest Ecosystem Services, 2008). (2) Air purification: The treatment cost comes from (Shi, 2016). In addition, we calculate the value of negative ions, which is composed of indicators such as negative ion concentration (Yao et al., 2019), negative ion lifetime (Wang and Yu, 2013), negative ion production cost (Forest Ecosystem Services, 2008) and vegetation height, so as to jointly evaluate the air purification value. (3) Water purification: The treatment cost refers to the market price. (4) Wind prevention and sand fixation: the cost refers to "Specifications for Assessment of Forest Ecosystem Services" (Forest Ecosystem Services, 2008). (5) Carbon fixation: The carbon dioxide price refers to the Swedish carbon tax rate. (6) Oxygen release: The price of medical oxygen production refers to the average price of oxygen on the website of the Ministry of Health of the People's Republic of China.

3 Results analysis

3.1 Analysis of land use change

According to the data of land use in 2016 and 2020, it can be seen in Figure 2 that the land use types in the study area were mainly cultivated land, generally distributed in the west of the area; followed by the water area, which was more scattered, combined with Table 3, the sum of the area of the two areas exceeded half of the total area. In terms of area change, the area of forest land, grassland and green space increased significantly. Combined with Table 3, it can be quantitatively analyzed that the land types and land type areas in the study area underwent great changes, and the total area of each land type increased by 8.55 km^2. Among them, the forest land area increased the most, with a net increase of 3.83 km^2, and the garden land area decreased the most, with a net decrease of 2.85 km^2. In addition, the water area increased by 2.63 km^2, the cultivated land area decreased by 1.64 km^2, and the wetland area decreased by 0.03 km^2. Due to the high concentration of coastal enterprises and the long coastline, the area of grassland and green space was 0 in 2016 and increased by 3.06 km^2 and 2.54 km^2 in 2020. In terms of area change rate, the area of forest land had the largest change rate, with an increase rate of 281.62%, the change rates of garden land and water area were also relatively large, which were -86.36% and 55.98%, by contrast, the change rates of cultivated land and wetland were small (Table 3).

According to Table 4, the characteristics of land use transfer are as follows: (1) The transfer-in and transfer-out areas of other land and construction land were the largest, accounting for 24.39km^2 and 64.51 km^2 respectively, among which the main transfer-in sources of other land were construction land,

TABLE 2 Ecosystem regulation service value.

Service type	Evaluation method	Calculation function	Parameter introduction	Parameter source
Water Conservation	Shadow project	$V_{wr} = Q_{wr} \times C_{we}$	V_{wr} is the value of water conservation (yuan/a);	69
			Q_{wr} is the total water conservation in the accounting area (m^3/a);	
			C_{we} is the project cost and maintenance cost per unit capacity of the reservoir (yuan/m^3).	
Flood Regulation and Storage	Replacement cost method	$V_{fm} = C_{fm} \times C_{we}$	V_{fm} is the value of ecosystem flood regulation and storage (yuan/a);	69
			C_{fm} is the flood storage capacity of ecosystem (m^3/a);	
			C_{we} is the project cost and maintenance cost per unit capacity of the reservoir (yuan/m^3).	
Air Purification	Replacement cost method	$V_{ap} = \sum_{i=1}^{n} Q_i \times c_i$ $U_A = 5.256 \times 10^{15} \times A \times H \times K_A \times Q_A/L$	V_{ap} is the value of air purification for ecosystem (yuan/a);	69
			Q_i is the purification amount of the type i air pollutants (t/a); i is the air pollutant category, i = 1,2, . . . , n;	
			c_i is the treatment cost of type i air pollutants (yuan/t);	
			U_A is the negative ion value (yuan/a);	
			A is the area of ecosystem (hm^2);	
			H is the vegetation height (m/a);	
			K_A is the negative ion production cost (yuan/piece);	
			Q_A is the negative ion concentration (units/cubic centimeter);	
			L is negative ion lifetime (min)	
Water Purification	Replacement cost method	$V_{wp} = \sum_{i=1}^{n} Q_{wpi} \times c_i$	V_{wp} is the value of water purification for ecosystem (yuan/a);	
			Q_{wpi} is the purified amount of the type i water pollutant (ton/a); c_i is the unit treatment cost of type i water pollutants (yuan/t);	
			i is the type i water pollutant category in the study area, i = 1,2, . . . , n.	
Wind Prevention and Sand Fixation	Replacement cost method	$V_{sf} = \frac{Q_{sf}}{\rho \cdot h} \times c$	V_{sf} is the value of wind prevention and sand fixation (yuan/t);	69
			Q_{sf} is the amount of wind prevention and sand fixation (t/a);	
			ρ is the soil bulk density (t/m^3); h is the thickness of sand covered by soil desertification (m);	
			c is the unit cost of desertification control project or the unit cost of vegetation restoration (yuan/m^2).	
Carbon Sequestration	Replacement cost method	$V_{Cf} = Q_{CO_2} \times C_c$	V_{Cf} is the value of carbon sequestration for ecosystem (yuan/a);	
			Q_{CO_2} is total carbon sequestration for ecosystem (tCO_2/a);	
			C_c is the price of carbon dioxide (yuan/t).	
Oxygen Release	Replacement cost method	$V_{op} = Q_{op} \times C_o$	V_{op} is the value of oxygen release for ecosystem (yuan/a);	
			Q_{op} is the oxygen release of ecosystem (tO_2/a);	
			C_o is the price of medical oxygen production (yuan/t).	

cultivated land and garden land, and the main transfer-out sources of construction land were other land, construction land and green space. (2) The difference between the transfer-in area and the transfer-out area of construction land was the largest, and the main transfer-in sources were construction land, garden land and cultivated land. (3) The

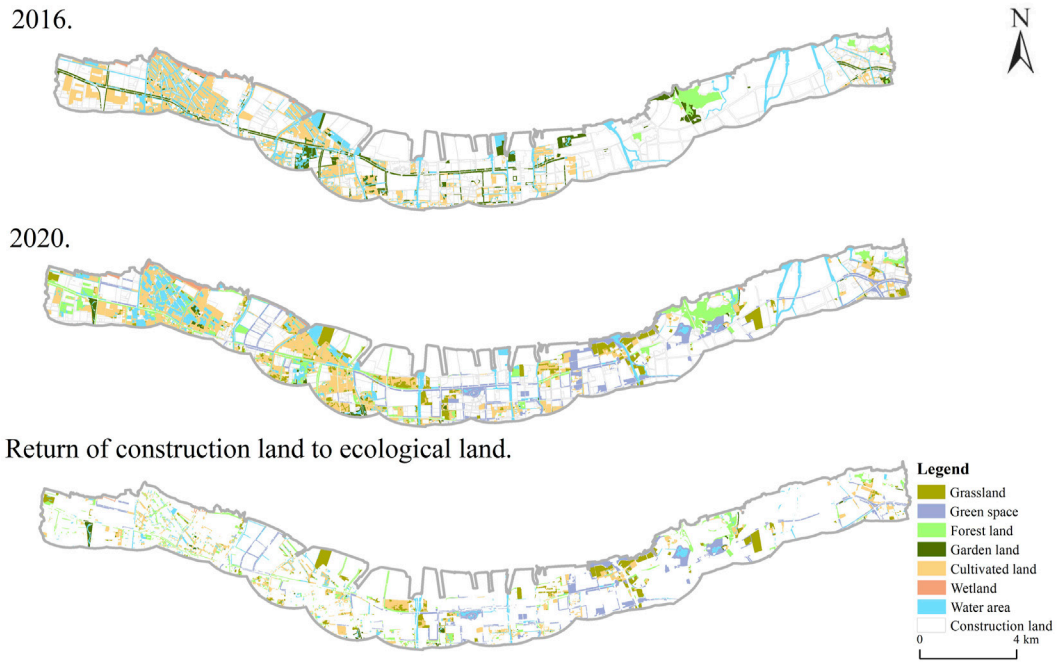

FIGURE 2
Land use situation and changes of return of construction land to ecological land in the study area of Jiangyin in 2016 and 2020.

TABLE 3 Changes of land use area of the study area in Jiangyin.

Land	2016		2020		Area change
Use type	Area/km^2	Proportion/%	Area/km^2	Proportion/%	Area change rate/%
Forest land	1.36	1.60	5.19	9.73	281.62
Grassland	0	0	3.06	5.74	0
Cultivated land	10.32	12.15	8.68	16.28	-15.89
Wetland	0.74	0.87	0.71	1.33	-4.05
Water area	4.68	5.51	7.30	13.69	55.98
Garden land	3.30	3.89	0.45	0.84	-86.36
Green space	0	0	3.54	6.64	0
Construction land	64.51	75.97	24.39	45.74	-62.19

transfer-in area and transfer-out area of forest land were 5.19 km^2 and 1.36 km^2, respectively, the main transfer-in sources of forest land were cultivated land, garden land and construction land, and the transfer-in area and transfer-out area of cultivated land were 8.57 km^2 and 10.32 km^2, respectively, the main transfer-out sources of cultivated land were cultivated land, water area and forest land (Table 4).

Combined with the obvious changes in some land types in Table 3 and Table 4, such as the large increase in the area of forest land due to the transfer of cultivated land, garden land, and construction land, the moderate transfer of cultivated land and the large transfer of construction land. To find out the reason, we can explore the contribution made by Jiangyin in balancing ecological and economic benefits from the perspective of the government. First, the increase of forest land not only benefited from the forest protection measures in response to the protection of the Yangtze River, but also benefited from ecological engineering construction. These measures have largely protected forest resources and indirectly affected ecological and social economic benefits. Second, cultivated land is the foundation of grain production, it is also an important part of "converting farmland to forests". Therefore, moderately adjusting cultivated land can take ecological benefits into consideration without affecting grain production. Third,

TABLE 4 Transfer matrix of land use types of the study area in Jiangyin from 2016 to 2020/km^2.

2016	2020								
	Grassland	Cultivated land	Forest land	Green space	Wetland	Water area	Garden land	Other land	Construction land
Grassland	0	0	0	0	0	0	0	0	0
Cultivated land	0.0679	5.2398	1.4689	0.3558	0.0058	2.2318	0.1504	0.5311	0.2676
Forest land	0.0197	0.0001	1.1242	0.0002	0	0.0011	0	0.0031	0.2071
Green space	0	0	0	0	0	0	0	0	0
Wetland	0	0	0.0306	0	0.5986	0.0875	0	0.0000	0.0245
Water area	0.1149	0.2487	0.1660	0.0867	0.0567	3.5209	0.0106	0.2490	0.2240
Garden land	0.1337	0.2898	1.2341	0.7890	0	0.2050	0.0616	0.3114	0.2715
Other land	0.0374	0.0821	0.0423	0.0313	0	0.0312	0.0114	0.2581	0.0983
Construction land	2.5247	2.7103	1.1264	4.2756	0.0469	0.9445	0.2139	29.3635	23.3015

reducing the area of construction land can optimize the land supply structure, reduce the consumption of land resources, and realize the sustainable use of land resources. On the other hand, it can optimize the industrial structure and promote industrial upgrading, turning to green path development.

3.2 Regulation service value change analysis

3.2.1 Value change of single function of ecosystem regulation service

According to the accounting methods of ecosystem regulation services provided in Table 1 and Table 2, combined with the land use area data of Jiangyin in Table 3, we can obtain the changes of function quantities and values of seven types of ecosystem regulation services in 2016 and 2020 (Table 5) and their spatial distribution characteristics (Figure 3).

In Figure 3, the spatial distribution characteristics of the value of flood regulation and storage change significantly, which is consistent with the substantial increase of its value in Table 5, and the changes of spatial characteristics of other regulation services are not significant, which is also consistent with the results in Table 5. Combined with Table 5, it can be quantitatively analyzed that in 2016 and 2020, the value of flood regulation and storage accounted for the highest proportion of the total value, and it increased the most, which was the main contributor, while the value of oxygen release accounted for the lowest proportion, it also had the smallest change. In terms of changes, the value of regulation services in the study area increased significantly, with a change of 483 million. Among them, water conservation, flood regulation and storage, water purification, wind prevention and sand fixation, and carbon sequestration all increased, with flood regulation and storage having the largest change of 394 million, followed by water conservation of 40 million.

To investigate the reason, it can be seen from Table 3 that the change in the value of regulation services comes from the change of the function quantity. On one hand, the change of the function quantity is caused by the change of the area of different land types, which is intuitively reflected in Table 1, such as water conservation, flood regulation and storage, water purification and other regulation services, the area of some land types decreased, but benefiting from the large increase in the area of forest land and water area, the function quantity increased. On the other hand, the change of function quantity is affected by multiple factors, such as air purification, wind prevention and sand fixation, carbon fixation, and oxygen release, some parameters in their accounting methods are affected by multiple factors. Among them, the vegetation coverage factor is influenced by NDVI data, which is related to vegetation coverage and other natural factors, NEP is affected by NPP, which is related to LUC, temperature and precipitation (Guo et al., 2008). Therefore, judging from the results, the change of value is not strongly correlated with the change in land type area, but it is also affected to a certain extent.

3.2.2 Structural changes of ecosystem regulation service value

According to the data of the function quantities and values of seven types of ecosystem regulation services in the study area obtained in Table 5, combined with the land use data in Table 3, the value of each land use type in 2016 and 2020 can be obtained (Table 6).

The change of land use types in the study area affects the function of ecosystem, so the values of ecosystem regulation services also change. It can be seen from Table 6 that in 2016 and 2020, the value of forest land accounts for the largest proportion of the total value, and is the largest contributor to the value of ecosystem assets, the value of grassland was 0 in 2016 and second only to forest land in 2020. In terms of changes, the composition of the ecological value of the study area underwent major changes, and the total value increased by 480 million. Among them, the total value of forest land, grassland, wetland, water area and green space all increased, forest land had the largest increase, with an increase of 264 million, and the growth rate reached 109.54%, followed by grassland, with an increase of 176 million, and cultivated land had the smallest increase of only 0.6 million,

TABLE 5 Changes of function quantity and value of regulation services in 2016&2020.

Ecosystem regulation service	2016		2020		Changes
	Function quantity	Value (billion)	Function quantity	Value (billion)	Variation (billion)
Water conservation	1480198.07	0.09	8055865.99	0.49	0.4
Flood regulation and storage	30989979.14	2.33	83272479.10	6.27	3.94
Air purification	11906182.49	0.17	11913105.20	0.11	-0.06
Water purification	3206566.93	0.22	6855225.43	0.47	0.25
Wind prevention and sand fixation	146321.14	0.61	394564.15	0.90	0.29
Carbon sequestration	8013.24	0.096	8645.25	0.104	0.008
Oxygen release	5827.97	0.0583	5763.50	0.0576	-0.0007
Total		3.58		8.41	4.83

garden land was the only land type with a decrease in value, with a net decrease of 8 million yuan and a decrease rate of -83.3%.

Combined with Table 3 and Table 5, we can see that the reason for the value change of different land types is not single. Among them, the phenomenon of value change of forest land, grassland, water area, garden land and green space is consistent with Table 3, while the reduction of cultivated land and wetland brought about the increase of their value, this phenomenon is due to the comprehensive influence of many factors. Firstly, changes of regulation services such as water conservation of cultivated land and wetland are strongly correlated with changes of the area of land types, the reduction of the two land types led to the decrease of the regulation service value. Secondly, changes of function quantities of wind prevention and sand fixation, carbon sequestration, and oxygen release are less correlated with LUC. For wind prevention and sand fixation, the vegetation coverage factor in the accounting method is represented by NDVI, and NDVI is related to vegetation coverage and other natural factors, in Table 4, the transfer of cultivated land changed the vegetation coverage, which led to the change of the function quantity. For carbon sequestration and oxygen release, NEP is affected by NPP, and NPP is affected by multiple factors, making the correlation between the value of cultivated land and wetland and land type areas weak, from the results, the value of cultivated land and wetland increased slightly.

4 Discussion

4.1 Response mechanism of ecological value to the protection measures along the river in Jiangyin

Generally speaking, protection measures based on ecological problems such as the deterioration of ecological environment and the prominent contradiction between human and land will objectively change the area and type of land use, and the change of land use will be directly reflected in the change of ecosystem service value. Many previous studies have explored this (Wang et al., 2021; Li and Li, 2022; Liu et al., 2022), but most scholars focus on the interaction between LUC and ESV, while ignoring the actual causes of land use change, which makes the logic chain of the whole research incomplete. Based on this, this study will briefly discuss the response of ecological value to the reasons behind LUC in order to complete the logic chain and provide suggestions for subsequent ecological protection.

Combining Table 3 and Table 5, in Section 3.2.1, we analyzed the root cause of the change of the value. Among them, the value of water conservation, flood regulation and storage, and water purification are affected by changes of land types. The value changes of wind prevention and sand fixation, carbon sequestration, and oxygen release are affected by many factors, and LUC is also one of the influencing factors. So we can explore the protection measures launched by Jiangyin that lead to LUC according to some changes. For example, the increase of the value of water conservation, flood regulation and storage, and water purification is due to the increase of the area of forest land and water areas, this is reflected in the measures taken by Jiangyin for forest land and water areas. In terms of forest land, under the background of the sharp contradiction between forest land protection and economic development and the relatively weak forestry foundation, Jiangyin has carried out ecological restoration measures, which has promoted a substantial increase in the area of forest land in the coastal area. In terms of water areas, under the background of serious water source and river pollution and soil erosion in recent years, Jiangyin has improved the supply capacity of water source protected areas, promoted the normal operation of protected areas through source control and interception, and reduced soil erosion, then adopted measures such as river dredging and shore appearance treatment, which reduced pollution and improved the ecological problems of water areas.

In addition to the increase of the area of forest land and water areas, changes of other land types such as grassland and green space are also important influencing factors, this is reflected in the governance of mines and shorelines in the coastal area by Jiangyin. Under the background of long-term development of the mountain body and serious damage to agricultural land and construction land, Jiangyin closed the quarry mines and carried out several mining area treatment projects, effectively controlling the mine geological environment, curbing the trend of continuous

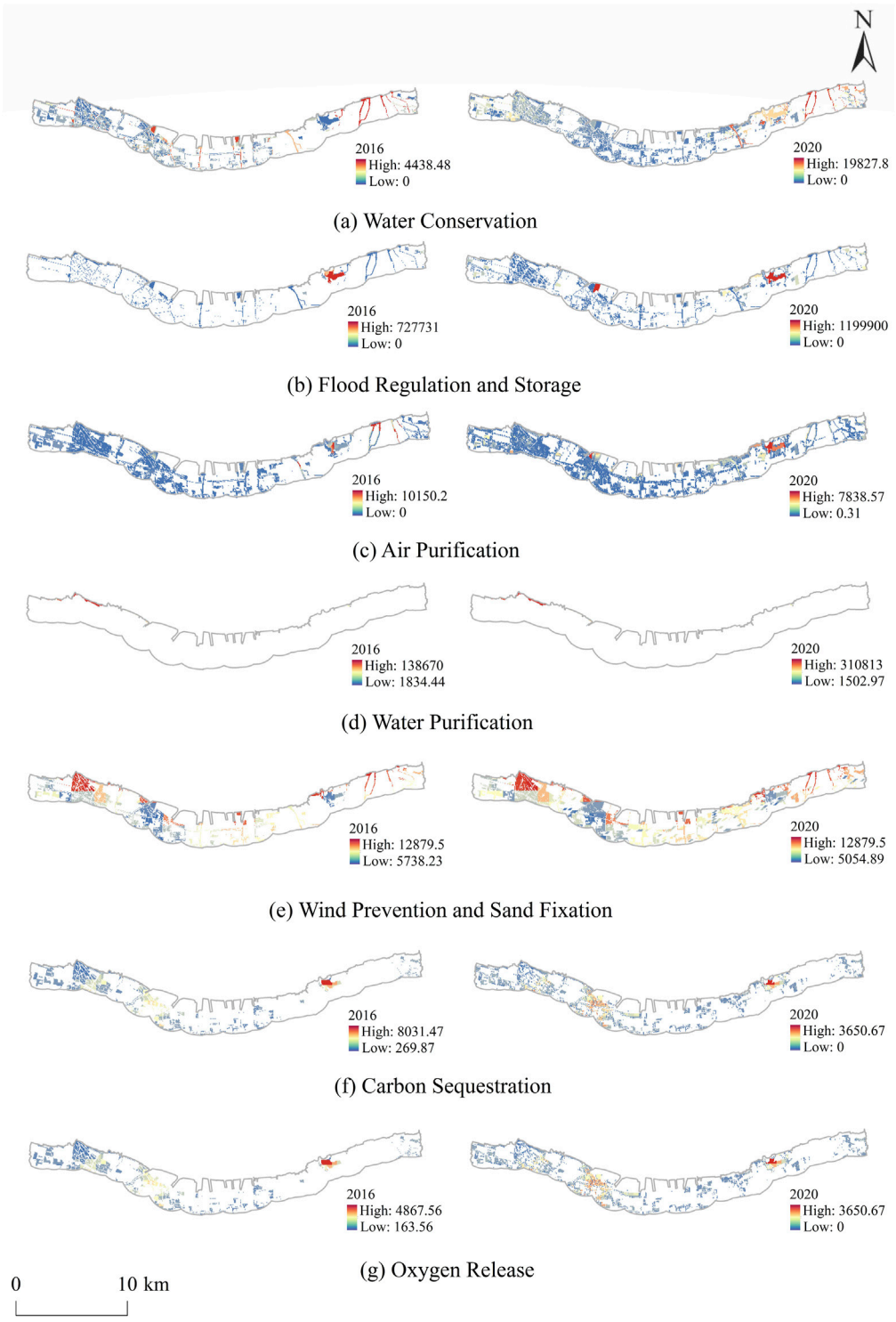

FIGURE 3
The spatial distribution of the value of regulation services in the study area in 2016 and 2020 **(A–G)**.

land damage, and increasing the area of ecological land. In terms of coordinating the development of the shoreline, Jiangyin has successively completed the closure and relocation of chemical enterprises along the river, optimized the ecological environment along the coast, reduced the development intensity of the shoreline, increased the green area of the riverside, which offers the potential to increase the ESV.

Combined with Table 3, we also find that the protection measures by Jiangyin still lacking, which is reflected in the reduction of wetlands, the reason is the lack of awareness of

TABLE 6 Changes of land use value of the study area in Jiangyin.

Period	Forest land (billion)	Grassland (billion)	Cultivated land (billion)	Wetland (billion)	Water area (billion)	Garden land (billion)	Green space (billion)	Total
2016	2.41	0.00	0.457	0.26	0.30	0.096	0.00	3.523
2020	5.05	1.76	0.463	0.51	0.54	0.016	0.02	8.359
Value change	2.64	1.76	0.006	0.25	0.24	-0.08	0.02	4.836
Change rate of value/%	109.54		1.31	96.15	80	-83.3		137.27

wetland protection and inadequate protection measures. Therefore, considering that human-induced economic and social factors play a leading role in the change of land use quantity (Verburg et al., 2004) (this process can be visualized by PSR framework (Figure 4)), combined with the change of land use along the river, we can put forward the method of setting the ecological protection red line, which is an important measure to construct the regional ecological security pattern and promote the regional economic and social development. Firstly, compulsory and strict protection can be carried out for areas with important ecological functions and fragile water ecological environments along the river (Kong et al., 2019), and demonstration projects can be developed in this area. Secondly, an integrated management and control system should be established for areas with reduced service value, daily supervision should be strengthened, and ecological compensation mechanism should be improved, on this basis, ecological re-greening should be implemented, and ecological protection projects such as returning farmland to forests should be vigorously promoted. Thirdly, the development activities of areas with increased service value should be further restricted and developed moderately. Finally, it is also an indispensable step to consider making tenure security one of the major planned outcomes of land-use planning process (Uchendu et al., 2017). In a word, scientific classification of land is conducive to regulating land resources macroscopically, reducing land use costs and promoting urban development.

In general, when studying the interaction between ecological value and LUC, it is necessary to explore the relationship between ecological value and the actual causes of LUC. This part briefly summarizes the response mechanism of ecological value to the protection measures along the river in Jiangyin, and put forward relevant ecological protection suggestions, but there are still many deficiencies in the research. On one hand, the discussion on the response mechanism is not comprehensive enough, and the discussion on the protection measures of other land types is ignored. On the other hand, due to the limitations of data acquisition and other reasons, this study only considered the government-led social and economic actions behind LUC, ignoring individual factors and natural factors. The direction of future research is to increase the discussion of other ecological land protection measures and the response mechanism of ecological value to non-government factors.

4.2 The transformation path of ecosystem service value

Before the effective transformation of ecological value, we must understand that the monetization evaluation of ecosystem service value is aimed at showing the potential value of ecosystem service scientifically, which is not the same as market manifestation (Shi and Chen, 2022). The correlation between the two is that market manifestation can transform the potential value of ecosystem services into actual economic value through different means, and there are two ways, namely, market mechanism and government regulation. Market mechanism means and government regulation means are respectively through ecological industrialization and ecological compensation and other mechanisms to make potential value appear, so that it can be transformed into realistic economic value (Shi, 2021).

The value of ecosystem services cannot be directly transformed into economic value. In addition, due to the disunity of the current value accounting system, the indicators and methods adopted by different researchers are also different, which leads to the difficulty in comparing the values of different types of ecosystems in different degrees, and the unconvincing results. In addition, the market of ecological products lacks institutional guarantee. Therefore, in order to effectively transform the ecological value, extensive data collection and collaboration and sharing among government departments, social organizations, companies and enterprises are required by different means. Specifically, ecological products are carriers and attachments of ecosystem service value, and ecological value depends on ecological products. Therefore, we can also discuss the transformation of ecosystem service value from the perspective of ecological product transformation. Many studies have explored from this perspective, some scholars propose that the government should be the guide and the market should be the main body to establish an operation transformation mechanism for ecological products from resources to assets and then to capital (Nie and Jin, 2019), some believe that both the government and the market can be the main body (Liu and Mou, 2020), and the two main bodies have different realization paths. However, these typical studies have some shortcomings. On one hand, they are based on the premise that the concept of ecological products is not yet clear, on the other hand, most of them are normative analyzes with subjective judgments, which cannot be combined with specific cases. In addition, there are also studies based on the classification of ecological products (Wang et al., 2020b; Gao et al., 2020). These scholars have different

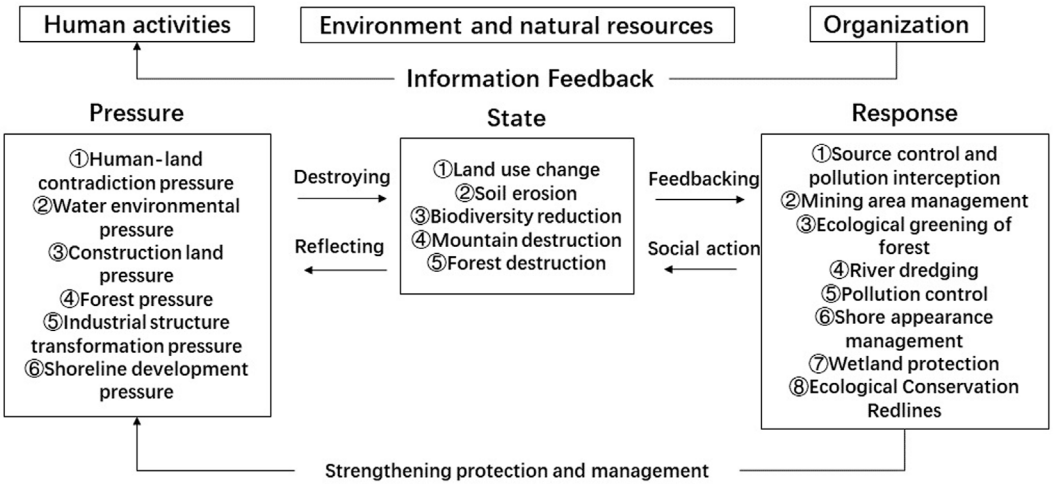

FIGURE 4
"Pressure-State-Response" framework of ecological value.

classifications of ecological products and put forward multiple models, but this type of research lacks empirical analysis, making the conclusions not typical. Based on this, according to the attribute differences of ecological products, we divide them into three categories, namely, pure public products, private products and quasi-public products. Combined with the existing research, the transformation paths of three different types of products are proposed:

Firstly, in terms of the value transformation of ecological products that are purely public products, the government, as the main body, can lead private individuals or enterprises to improve the ecological compensation mechanism and optimize market trading rules. The "Opinions on Adjusting and Perfecting the Ecological Compensation Policies" issued by Jiangyin in 2022 raised the compensation standard, curbed the "non-agriculturalization", and realized the greening of the society and the profits of farmers and fishermen, thus realizing the transformation of the value of ecological products. This measure reflected the leading role of the Jiangyin Municipal Government. In addition, Jiangyin can take the form of transfer payment and redemption to make ecological compensation and financial subsidies for ecological functional areas such as natural wetlands and ecological public welfare forests, as well as farmers and fishermen, so as to improve the ecological compensation mechanism. Jiangyin can also build and improve a series of trading mechanisms for ecological resources and ecological products, such as carbon sink trading and emission trading, to promote and optimize the construction of relevant market trading rules and systems (Figure 5).

Secondly, in terms of the value transformation of ecological products with private product attributes, private individuals or enterprises, as suppliers, can innovate and process ecological products and expand the ecological value chain with the assistance of the government, so as to transform ecological value into industrial value. Jiangyin is rich in its own characteristic ecological products, and the market plays a decisive role in the allocation of ecological resources. Therefore, Jiangyin can rely on its own regional brand products, such as Huaxi rice, Gushanshui peach, Huangtu grape, Yuecheng Cuiguan pear and other characteristic aquatic products along the river. On the basis of rural revitalization and cross-regional cooperation, through innovative processing of resource endowments and expansion of the product value chain, it can expand its own ecological advantages and promote the transformation of ecological advantages into industrial advantages, develop and utilize ecological products according to local conditions, and convert ecological value into industrial value (Figure 5).

Thirdly, the value transformation of ecological products of quasi-public products should be considered from two aspects. On one hand, the government can guide the establishment of environmental protection funds and ecological banks to promote individuals or enterprises; For another hand, under the authorization of the government, individuals or enterprises can enhance the ecological value of ecological products through various ways and convert them into ecological product income. Therefore, the Jiangyin Municipal Government should set up environmental protection fund and "Two Mountains" banks, actively guide individuals and various financial enterprises to increase their support for regional green development, and give priority to key projects for realizing ecological product value. What's more, the Jiangyin Municipal Government can entrust the ecological resources to the market entities in the form of authorization, and promote the cooperation between individuals and financial institutions and counties to set up relevant special funds, promote the centralized flow of resources, enhance the ecological value, and enrich the ways to realize the value of ecological products, so as to effectively transform the ecological value into ecological products operational income (Figure 5).

To sum up, taking the classification of ecological products as a perspective to study the transformation of ecological value can clearly reflect the collaboration among multiple subjects such as the government and enterprises under different circumstances.

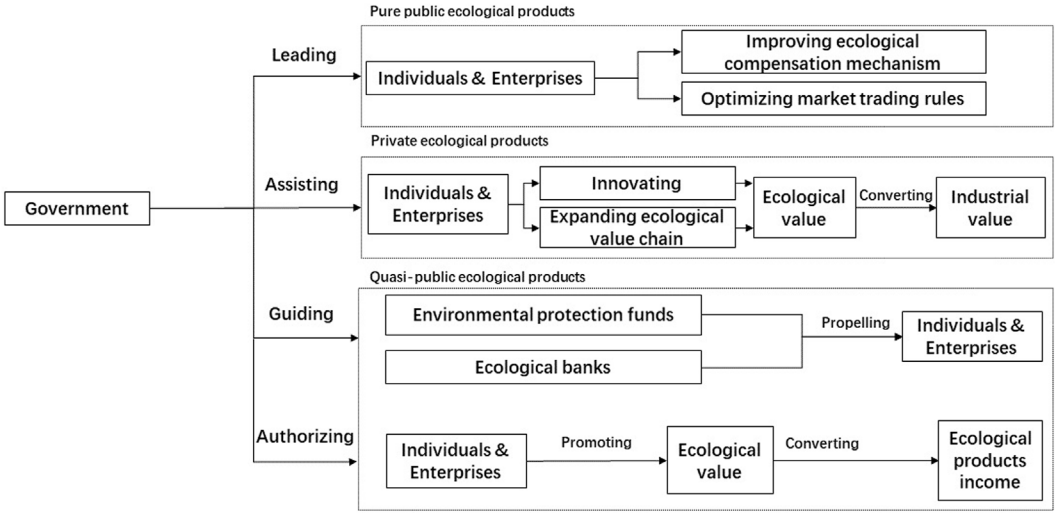

FIGURE 5
Framework of ecosystem service value transformation.

Combined with the quantitative analysis of the coastal ecosystem services in this study, it can provide a theoretical basis for the practice and innovation path of the subsequent value transformation of ecological products. However, there are still many shortcomings in this study. First, the combination of theoretical research and practical application is insufficient. Second, there are some bottlenecks in the value transformation of ecological products, for example, the accounting system for the value of ecological products is not perfect, and the market transaction mechanism for the value transformation of ecological products is not yet mature. In future research, we will comprehensively use theoretical analysis and empirical analysis, focus on the realization of the value of emerging ecological products, and deeply explore the more accurate and detailed transformation paths of different types of ecological products in different regions.

5 Conclusion

This study takes the coastal area of Jiangyin as the study area, analyzes the changes of land use data in 2016 and 2020, and the changes of ecosystem regulation service value under LUC, and draws some different conclusions from previous studies. The results showed that:

(1) In 2016 and 2020, the overall land use changes in the study area were relatively large, and the cultivated land and water area accounted for more than half of the total area. The total area of each land type increased by 8.55 km^2, with the largest increase in forest land and the largest decrease in garden land. The grassland and green space grew from scratch, with a net increase of 3.06 km^2 and 3.54 km^2 respectively; the transfer-in area of other land was the largest, and the main transfer-in sources were construction land, cultivated land and garden land, the transfer-out area of construction land was the largest, and the main transfer-out sources were other land, construction land and green space.
(2) In terms of the structural changes of ecosystem regulation service value, the total value of regulation service in the study area increased by 480 million yuan, of which forest land increased the most, by 264 million yuan, with a growth rate of 109.54%, while cultivated land increased the least, only by 0.6 million yuan. Garden land was the only land type with a decrease in value, with a net decrease of 8 million yuan and a decrease rate of -83.3%. In 2016 and 2020, the value of forest land accounted for the largest proportion of the total value, the value of grassland was 0 in 2016, and its proportion was second only to forest land in 2020, the value of other land types changed little.
(3) In terms of the value change of single function of ecosystem regulation service, the value of flood regulation and storage accounted for the highest proportion and the largest change in 2016 and 2020, the increase of the value of water conservation was second only to flood regulation and storage, both of which were mainly due to the substantial increase of forest land, the value of air purification and oxygen release decreased, and the value of other functions increased.

However, there are still many deficiencies and the content that needs to be improved in this study, the details are as follows:

(1) The selection of some parameters refers to earlier literature, which reduces the accuracy of the results. Improving the timeliness of data is one of the key points in future research. (2) The accounting methods of value are not rich enough, and the pertinence is weak. One of the key points of future research is to optimize the accounting methods. (3) The discussion on the response mechanism of protection measures is not comprehensive enough, ignoring the discussion on the protection measures of other land types, only the

government-led factors behind the land use change are considered. In future research, we will increase the discussion of other ecological land protection measures and the response mechanism of ecological value to non-government factors. (4) There are some defects in the transformation path of ecological value. In future research, we will comprehensively use theoretical analysis and empirical analysis, focus on the realization of the value of emerging ecological products, and deepen the exploration of more accurate and detailed transformation paths for different types of ecological products in different regions.

Data availability statement

The data analyzed in this study is subject to the following licenses/restrictions: The original contributions presented in the study are included in the article/Supplementary Material, further inquiries can be directed to the corresponding author. Requests to access these datasets should be directed to jincheng@njnu.edu.cn.

Author contributions

Conceptualization methodology formal analysis investigation writing—original draft preparation data curation visualization, SZ; software resources, SZ, XP, LW, and HS; validation supervision project administration, SZ and CJ; writing—review and editing, SZ, CJ, and HS; funding acquisition, CJ. All authors have read and agreed to the published version of the manuscript.

Funding

This research was financially supported by the National Natural Science Foundation of China (Grant Nos. 41871137, 42271235 and 42201212) and the Foundation of Humanity and Social Sciences of the Ministry of Education of China (Grant No. 22YJCZH185).

Conflict of interest

The authors declare that the research was conducted in the absence of any commercial or financial relationships that could be construed as a potential conflict of interest.

Publisher's note

All claims expressed in this article are solely those of the authors and do not necessarily represent those of their affiliated organizations, or those of the publisher, the editors and the reviewers. Any product that may be evaluated in this article, or claim that may be made by its manufacturer, is not guaranteed or endorsed by the publisher.

References

Bai, Y., Li, H., Wang, X. Y., Juha, M. A., Jiang, B., Wang, M., et al. (2017). Evaluating natural resource assets and gross ecosystem products using ecological accounting system: A case study in yunnan province. *J. Nat. Resour.* 7, 1100–1112. doi:10.11849/zrzyxb.20160755

Bockstael, N. E., Freeman, A. M., Kopp, R. J., Portney, P. R., and Smith, V. K. (2000). On measuring economic values for nature. *Environ. Sci. Technol.* 34, 1384–1389. doi:10.1021/es990673l

Boyd, J., and Banzhaf, S. (2007). What are ecosystem services? The need for standardized environmental accounting units. *Ecol. Econ.* 63, 616–626. doi:10.1016/j.ecolecon.2007.01.002

Cai, Q. H., Tao, T., and Deng, H. B. (2003). Discussion on freshwater ecosystem service and its evaluation index system. *Chin. J. Appl. Ecol.* 1, 135–138. doi:10.3321/j.issn:1001-9332.2003.01.030

Cao, S. K., Cao, G. C., Chen, K. L., Jie, J. A., Ma, L., and Zhang, T. (2013). Evaluation of use value of water ecosystem service functions in the Qinghai Lake. *Ecol. Econ.* 9, 163–167+180. doi:10.3969/j.issn.1671-4407.2013.09.036

Cheng, G. W., and Shi, P. L. (2004). Benefits of forest water conservation and its economical value evaluation in upper reaches of Yangtse River. *Soil Water Conserv. China* 4, 17–20. doi:10.3969/j.issn.1672-3007.2004.04.004

Costanza, R., Arge, R., Groot, R. D., Farber, S., Grasso, M., Hannon, B., et al. (1998). The value of the world's ecosystem services and natural capital. *Ecol. Econ.* 25, 3–15. doi:10.1016/S0921-8009(98)00020-2

Daily, G. C. (1997). *Nature's services: Societal dependence on natural ecosystems*. Washington D C: Island Press.

Dale, V. H. (1997). The relationship between land-use change and climate change. *Ecol. Appl.* 3, 753–769. doi:10.1890/1051-0761(1997)007[0753:TRBLUC]2.0.CO;2

Dong, T., Zhang, L., Xiao, Y., Zheng, H., Huang, B. B., and Ouyang, Z. Y. (2019). Assessment of ecological assets and gross ecosystem product value in ordos city. *Acta Ecol. Sin.* 9, 3062–3074. doi:10.5846/stxb201805291183

Duan, X. N., Wang, X. K., and Ouyang, Z. Y. (2005). Evaluation of wetland ecosystem services in Wuliangsuhai. *Resour. Sci.* 2, 110–115. doi:10.3321/j.issn:1007-7588.2005.02.018

Feng, X. M., Fu, B. J., Yang, X. J., and Lu, Y. (2010). Remote sensing of ecosystem services: An opportunity for spatially explicit assessment. *Chin. Geogr. Sci.* 20, 522–535. doi:10.1007/s11769-010-0428-y

Fisher, B., Turner, R. K., and Morling, P. (2009). Defining and classifying ecosystem services for decision making. *Ecol. Econ.* 68, 643–653. doi:10.1016/j.ecolecon.2008.09.014

Forest Ecosystem Services (2008). *Specifications for assessment of forest ecosystem services*. Beijing: Standards Press of China.

Fu, B., Chen, L., Ma, K., Zhou, H., and Wang, J. (2000). The relationships between land use and soil conditions in the hilly area of the Loess Plateau in Northern Shaanxi, China. *Catena* 1, 69–78. doi:10.1016/S0341-8162(99)00084-3

Fu, B. J., and Zhang, L. W. (2014). Land-use change and ecosystem services: Concepts, methods and progress. *Prog. Geogr.* 4, 441–446. doi:10.11820/dlkxjz.2014.04.001

Gao, X. L., Lin, Y. Q., Xu, W. H., and Ouyang, Z. Y. (2020). Research progress on the value realization of ecological products. *Acta Ecol. Sin.* 1, 24. doi:10.5846/stxb201807211563

GEP (2023). The technical guideline on gross ecosystem product (GEP). (1.0 version)

Guo, Z. X., Li, F., Liu, D. W., Song, K. S., Wang, Z. M., Yang, G., et al. (2008). Analysis of temporal-spatial characteristics and factors influencing vegetation NPP in northeast China from 2000 to 2006. *Resourses Sci.* 8, 1226–1235.

Han, Y. W., Tuo, X. S., Gao, J. X., Liu, C. C., and Gao, X. T. (2011). Assessment on the sand-fixing function and its value of the vegetation in eco-function protection areas of the lower reaches of the Heihe River. *J. Nat. Resour.* 1, 58–65. doi:10.11849/zrzyxb.2011.01.006

Hans, B., Brian, K. S., and Bent, L. (2001). Are phragmites-dominated wetlands a net source or net sink of greenhouse gases? *Aquat. Bot.* 2-4, 313–324. doi:10.1016/S0304-3770(01)00145-0

He, J. N., and Kang, W. X. (2008). Purification function and value of dongting lake wetland. *J. Central South Univ. For. Technol.* 2, 24–28+34. doi:10.3969/j.issn.1673-923X.2008.02.016

Huang, F. X., Niu, H. S., Wang, M. X., Wang, Y. S., and Ding, G. D. (2001). The relationship between vegetation cover and sand transport flux at Mu Us Sandland. *Acta Geogr. Sin.* 6, 700–710. doi:10.3321/j.issn:0375-5444.2001.06.009

Jiang, B., Zhang, L., and Ouyang, Z. Y. (2015). Ecosystem services valuation of qinghai lake. *Chin. J. Appl. Ecol.* 10, 3137–3144. doi:10.13287/j.1001-9332.20150921.019

Jiang, L., Xiao, Y., Rao, E. M., Wang, L. Y., and Ouyang, Z. Y. (2016). Effects of land use and cover change (LUCC) on ecosystem sand fixing service in Inner Mongolia. *Acta Ecol. Sin.* 12, 3734–3747. doi:10.5846/stxb201504130745

Jiangyin Statistics Bureau (2021). *Jiangyin statistical Yearbook 2021*. Beijing, China: China Statistics Press.

Jin, G., Deng, X. Z., Zhao, X. D., Guo, B. S., and Yang, J. (2018). Spatio-temporal patterns of urban land use efficiency in the Yangtze River Economic Zone during 2005-2014. *Acta Geogr. Sin.* 7, 1242–1252. doi:10.11821/dlxb201807005

Kohler, V. (1984). Many efficasy evaluation problem of the forestry. *Allgenmeine For. Jugdgeitung* 11, 52–58.

Kong, L. Q., Wang, Y. Q., Zheng, H., Xiao, Y., Xu, W. H., Zhang, L., et al. (2019). A method for evaluating ecological space and ecological conservation redlines in river basins: A case of the Yangtze River Basin. *Acta Ecol. Sin.* 3, 835–843. doi:10.5846/stxb201802060314

Lai, M., Wu, S. H., Dai, E. F., Yin, Y. H., and Zhao, D. S. (2013). The indirect value of ecosystem services in the Three-River headwaters region. *J. Nat. Resour.* 1, 38–50. doi:10.11849/zrzyxb.2013.01.005

Lawler, J. J., Lewis, D. J., Nelson, E., Plantinga, A. J., Polasky, S., Withey, J. C., et al. (2014). Projected landuse change impacts on ecosystem services in the United States. *Proc. Natl. Acad. Sci. U. S. A.* 20, 7492–7497. doi:10.1073/pnas.1405557111

Lei, J. C., Wang, S., Wang, J. M., Wu, S. Q., You, X. B., Wu, J., et al. (2019). Effects of land use change on ecosystem services value of Xunwu County. *Acta Ecol. Sin.* 9, 3089–3099. doi:10.5846/stxb201802010280

Li, T. H., Li, W. K., and Qian, Z. H. (2010). Variations in ecosystem service value in response to land use changes in Shenzhen. *Ecol. Econ.* 7, 1427–1435. doi:10.1016/j.ecolecon.2008.05.018

Li, X., and Li, J. Z. (2022). Response mechanism of ecosystem service value to urban and rural construction land expansion in the three outlets of the southern Jingjiang River. *Remote Sens. Nat. Resour.* 2, 278–288. doi:10.6046/zrzyyg.2021180

Li, Y. F., Zhan, J. Y., Liu, Y., Zhang, F., and Zhang, M. (2018). Response of ecosystem services to land use and cover change: A case study in chengdu city. *Resour. Conservation Recycl.* 132, 291. doi:10.1016/j.resconrec.2017.03.009

Liu, J. Y., and Mou, D. G. (2020). Research progress of ecological product value and its realization mechanism. *Ecol. Econ.* 10, 207–212.

Liu, L. Q., Jiang, K., Hu, Z., and Feng, W. W. (2022). Response characteristics of ecosystem services values in territorial space development of Xiong'an New Area. *Acta Ecol. Sin.* 6, 2098–2111. doi:10.5846/stxb202101080080

Liu, X. H., and Lu, X. G. (2008). Assessment of service value of wetland ecosystem carbon sequestration in the Sanjiang Plain excluded Muling-Xingkai Plain on south of Wanda Mountain. *Wetl. Sci.* 2, 212–217. doi:10.13248/j.cnki.wetlandsci.2008.02.002

Liu, X. T. (2007). Water storage and flood regulation functions of marsh wetland in the Sanjiang Plain. *Wetl. Sci.* 1, 64–68. doi:10.3969/j.issn.1672-5948.2007.01.010

Liu, Y. R., Wang, C., and Yan, L. J. (2018). Impacts of land use change on ecosystem services in the agricultural area of north China plain: A case study of shangqiu city, henan province, China. *Chin. J. Appl. Ecol.* 5, 1597–1606. doi:10.13287/j.1001-9332.201805.011

Ma, G. X., Yu, F., Wang, J. N., Zhou, X. F., Yuan, J., Mou, X. J., et al. (2017). Measuring gross ecosystem product (GEP) of 2015 for terrestrial ecosystems in China. *China Environ. Sci.* 4, 1474–1482. doi:10.3969/j.issn.1000-6923.2017.04.035

Nie, B. H., and Jin, L. F. (2019). Thinking on value realization route of ecological products in China. *Nat. Resour. Econ. China* 7, 34–37+57. doi:10.19676/j.cnki.1672-6995.0000312

O'Brien, S. T. (1998). Nature's services: Societal dependence on natural ecosystems. *Electron. Green J.* 8. doi:10.5070/G31810307

Ouyang, Z. Y., Wang, X. K., and Miao, H. (1999). A primary study on Chinese terrestrial ecosystem services and their ecological-economic values. *Acta Ecol. Sin.* 5, 607–613. doi:10.3321/j.issn:1000-0933.1999.05.004

Ouyang, Z. Y., Zheng, H., Xiao, Y., Polasky, S., Liu, J. G., Xu, W. H., et al. (2016). Improvements in ecosystem services from investments in natural capital. *Science* 6292, 1455–1459. doi:10.1126/science.aaf2295

Pema, D., Xiao, Y., Ouyang, Z. Y., and Wang, L. Y. (2020). Assessment of ecological conservation effect in Xishui county based on gross ecosystem product. *Acta Ecol. Sin.* 2, 499–509. doi:10.5846/stxb201812202767

Pimentel, D., Harvey, C., Resosudarmo, P., Sinclair, K., Kurz, D., McNair, M., et al. (1995). Environmental and economic costs of soil erosion and conservation benefits. *Science* 5201, 1117–1123. doi:10.1126/science.267.5201.1117

Qiu, S. S., Yue, W. Z., Zhang, H., and Qi, J. G. (2017). Island ecosystem services value, land-use change, and the national new area policy in zhoushan archipelago, China. *Isl. Stud. J.* 2, 177–198. doi:10.24043/isj.20

Rudolf, N. (1997). The some evaluate problem of forestry in the inside. *Allgenmeine For. Relbuns* 11, 66–72.

Sheng, L., Jin, Y., and Huang, J. F. (2010). Value estimation of conserving water and soil of ecosystem in China. *J. Nat. Resour.* 7, 1105–1113. doi:10.11849/zrzyxb.2010.07.006

Shi, H. X. (2016). *Study on ecological effect characteristics and valuing physical account from grain for green project in regions containing the upper and middle reaches of China's Yangtze and Yellow River*. Beijing, China: Chinese Academy of Forestry.

Shi, M. J., and Chen, L. N. (2022). Theoretical connotation and practical challenges of GEP accounting in China. *Chin. J. Environ. Manag.* 2, 5–10. doi:10.16868/j.cnki.1674-6252.2022.02.005

Shi, M. J. (2021). Path and mechanism for realizing value of the ecological product. *J. Environ. Econ.* 2, 1–6. doi:10.19511/j.cnki.jee.2021.02.001

Shifaw, E., Sha, J. M., Li, X. M., Bao, Z. C., and Zhou, Z. L. (2019). An insight into land-cover changes and their impacts on ecosystem services before and after the implementation of a comprehensive experimental zone plan in Pingtan island, China. *Land Use Policy* 82, 631–642. doi:10.1016/j.landusepol.2018.12.036

Song, C. S., and Ouyang, Z. Y. (2020). Gross ecosystem product accounting for ecological benefits assessment: A case study of qinghai province. *Acta Ecol. Sin.* 10, 3207–3217. doi:10.5846/stxb202004260999

Sonter, L. J., Johnson, J. A., Nicholson, C. C., Richardson, L. L., Watson, K. B., and Ricketts, T. H. (2017). Multi-Site interactions: Understanding the offsite impacts of land use change on the use and supply of ecosystem services. *Ecosyst. Serv.* 23, 158–164. doi:10.1016/j.ecoser.2016.12.012

Su, W., Gu, C., Yang, G., Chen, S., and Zhen, F. (2010). Measuring the impact of urban sprawl on natural landscape pattern of the Western Taihu Lake Watershed, China. *Landsc. Urban Plan.* 1, 61–67. doi:10.1016/j.landurbplan.2009.12.003

Sukhdev, P., Wittmer, H., Schröter-Schlaack, C., and Neshover, C. (2010). "Mainstreaming the economics of nature: A synthesis of the approach, conclusion and recommendations of teeb," in Proceedings of the 10th meeting of the Conference of Parties to the CBD, Nagoya, Japan, 18 to 29 October 2010.

Sun, J. (2011). Research advances and trends in ecosystem services and evaluation in China. *Procedia Environ. Sci.* 10, 1791–1796. doi:10.1016/j.proenv.2011.09.280

The Encyclopedia of Earth (2022). Ecosystems and human well-being: Wetlands and water. Available online: https://editors.eol.org/eoearth/wiki/Ecosystems_and_Human_Well-being:_Wetlands_and_Water_(full_report) [accessed on 12 October 2022].

Tolessa, T., Senbeta, F., and Kidane, M. (2017). The impact of land use/land cover change on ecosystem services in the Central Highlands of Ethiopia. *Ecosyst. Serv.* 23, 47–54. doi:10.1016/j.ecoser.2016.11.010

Uchendu, E. C., Anna, S., Walter, T. V., Fahria, M., Samuel, M., Danilo, A., et al. (2017). Combining land-use planning and tenure security: A tenure responsive land-use planning approach for developing countries. *J. Environ. Plan. Manag.* 9, 1622–1639. doi:10.1080/09640568.2016.1245655

United Nations (2014). *System of environmental- economic accounting 2012-experimental ecosystem accounting*. 1st ed. New York: United Nations.

Verburg, P. H., Schot, P. P., Dijst, M. J., and Veldkamp, A. (2004). Land use change modelling: Current practice and research priorities. *GeoJournal* 4, 309–324. doi:10.1007/s10708-004-4946-y

Wainger, L. A., King, D. M., Mack, R. N., Price, E. W., and Maslin, T. (2010). Can the concept of ecosystem services be practically applied to improve natural resource management decisions? *Ecol. Econ.* 5, 978–987. doi:10.1016/j.ecolecon.2009.12.011

Wang, L., Wan, X., and Wang, H. (2020). Evaluation of ecological service of forests along the yangtze River in Jiangsu province. *J. Jiangsu For. Sci. Technol.* 3, 16–21+45. doi:10.3969/j.issn.1001-7380.2020.03.004

Wang, L. Y., Xiao, Y., Ouyang, Z. Y., Wei, Q., Bo, W. J., Zhang, J., et al. (2017). Gross ecosystem product accounting in the national key ecological function area. *China Popul. Resour. Environ.* 3, 146–154. doi:10.3969/j.issn.1002-2104.2017.03.018

Wang, Q. C., Xi, Y. T., Liu, X. R., Zhou, W., and Xu, X. R. (2021). Spatial-temporal response of ecological service value to land use change: A case study of xuzhou city. *Remote Sens. Nat. Resour.* 3, 219–228. doi:10.6046/zrzyyg.2020305

Wang, W., and Yu, Z. (2013). Research progress on negative air ions in urban environment in China. *Ecol. Environ. Sci.* 4, 705–711. doi:10.3969/j.issn.1674-5906.2013.04.025

Wang, X. H., Zhu, Y. Y., Wen, Y. H., Xie, J., and Liu, G. H. (2020). The basic patterns and innovation path of realizing the value of ecological products. *Environ. Prot.* 14, 14–17. doi:10.14026/j.cnki.0253-9705.2020.14.003

Wang, Y. Q., and Ma, J. M. (2020). Effects of land use change on ecosystem services value in Guangxi section of the Pearl River-West River economic belt at the county scale. *Acta Ecol. Sin.* 21, 7826–7839. doi:10.5846/stxb201909181953

Wu, Y. X., Kang, W. X., Guo, Q. H., and Wang, W. W. (2009). Functional value of absorption and purgation to atmospheric pollutants of urban forest in Guangzhou. *Sci. Silv. Sin.* 5, 42–48. doi:10.11707/j.1001-7488.20090506

Xiao, H., Ouyang, Z. Y., Zhao, J. Z., Wang, X. K., and Han, Y. S. (2000). The spatial distribution characteristics and eco-economic value of soil conservation service of ecosystems in Hainan Island by GIS. *Acta Ecol. Sin.* 4, 552–558. doi:10.3321/j.issn:1000-0933.2000.04.004

Xie, G. D. (2017). Ecological asset evaluation: Stock, quality and value. *Environ. Prot.* 11, 18–22. doi:10.14026/j.cnki.0253-9705.2017.11.003

Xie, G. D., Lu, C. X., Leng, Y. F., Zheng, D., and Li, S. C. (2003). Ecological assets valuation of the Tibetan Plateau. *J. Nat. Resour.* 2, 189–196. doi:10.11849/zrzyxb.2003.02.010

Xie, G. D., Zhang, C. X., Zhang, L. M., Chen, W. H., and Li, S. M. (2015). Improvement of the evaluation method for ecosystem service value based on per unit area. *J. Nat. Resour.* 8, 1243–1254. doi:10.11849/zrzyxb.2015.08.001

Yao, X., and Yang, G. S. (2009). Progress on the study of water purification ability of natural wetlands. *Prog. Geogr.* 5, 825–832. doi:10.11820/dlkxjz.2009.05.022

Yao, Y. P., Yu, Z. Y., Li, Z. Q., Wang, K., Fan, G. F., and Mao, Y. D. (2019). Concentration distribution characteristics of negative oxygen ions over Zhejiang Province. *Meteorological Sci. Technol.* 6, 1006–1013. doi:10.19517/j.1671-6345.20180686

Yu, Z. Y., and Bi, H. (2011). The key problems and future direction of ecosystem services research. *Energy Procedia* 5, 64–68. doi:10.1016/j.egypro.2011.03.012

Zhang, Z., Wu, C. F., and Tan, R. (2013). Application of ecosystem service value in land use change research: Bottlenecks and prospects. *Chin. J. Appl. Ecol.* 2, 556–562. doi:10.13287/j.1001-9332.2013.0191

Zhao, B., Kreuter, U., Li, B., Ma, Z. J., Chen, J. K., and Nakagoshi, N. (2004). An ecosystem service value assessment of land-use change on Chongming Island, China. *Land Use Policy* 2, 139–148. doi:10.1016/j.landusepol.2003.10.003

Zhou, B. H., Cao, J. J., Zhu, C. P., and Jin, B. S. (2011). Valuation of wetland ecosystem services along the yangtze River in anqing, anhui province. *J. Geogr. Res-Aust.* 12, 2296–2304. doi:10.11821/yj2011120017

Zhou, W. C., Zhang, M. Y., Zhang, Z. Q., Shi, Y. H., and Cui, H. X. (2021). Valuation of ecosystem service functions of dajiuhu wetland in shennongjia moutains. *Wetl. Science&Management* 2, 38–42. doi:10.3969/j.issn.1673-3290.2021.02.09

Zhou, Z. X., Li, J., and Feng, X. M. (2013). The value of fixing carbon and releasing oxygen in the Guanzhong-Tianshui economic region using GIS. *Acta Ecol. Sin.* 9, 2907–2918. doi:10.5846/stxb201202130187

frontiers | Frontiers in Ecology and Evolution

TYPE Original Research
PUBLISHED 10 March 2023
DOI 10.3389/fevo.2023.1131210

OPEN ACCESS

EDITED BY
Xiaoyang Zhang,
South Dakota State University,
United States

REVIEWED BY
Hailong Wang,
Sun Yat-sen University, Zhuhai Campus,
China
Bin Guo,
Shandong University of Science and Technology,
China

*CORRESPONDENCE
Haichao Hao
✉ haohc@stu.ecnu.edu.cn

SPECIALTY SECTION
This article was submitted to Environmental Informatics and Remote Sensing,
a section of the journal
Frontiers in Ecology and Evolution

RECEIVED 24 December 2022
ACCEPTED 13 February 2023
PUBLISHED 10 March 2023

CITATION
Zhang J, Li Z, Duan W, Zhao H, Hao H, Xiang Y and Zhang Q (2023) Assessing restoration and degradation of natural and artificial vegetation in the arid zone of Northwest China.
Front. Ecol. Evol. 11:1131210.
doi: 10.3389/fevo.2023.1131210

Assessing restoration and degradation of natural and artificial vegetation in the arid zone of Northwest China

Jinxia Zhang[1,2], Zhi Li[3], Weili Duan[3], Hongfang Zhao[1,2], Haichao Hao[1,2]*, Yanyun Xiang[4] and Qifei Zhang[5]

[1]School of Geographic Sciences, East China Normal University, Shanghai, China, [2]Key Laboratory of Geographic Information Science, Ministry of Education, East China Normal University, Shanghai, China, [3]State Key Laboratory of Desert and Oasis Ecology, Xinjiang Institute of Ecology and Geography, Urumqi, China, [4]School of Public Administration, Shanxi University of Finance and Economics, Taiyuan, China, [5]School of Geographic Sciences, Shanxi Normal University, Taiyuan, China

Assessing vegetation restoration and degradation trends is important for regional ecological conservation and sustainable development, yet few studies have examined the characteristics of these trends in natural and artificial vegetation in arid zones. In this study, we develop an assessment framework based on two common ecological indicators, Net Primary Productivity (NPP) and Water Use Efficiency (WUE). We discuss the restoration and degradation trends of natural and artificial vegetation in China's Northwest Arid Region (NAR) and analyze the similarities and differences between the changes in the two. Our results reveal the following: (1) Both natural vegetation (Nav) NPP and artificial vegetation (Arv) NPP in the NAR are dominated by significant growth, with precipitation being the most influential factor. Arv NPP changes are greater than Nav NPP. (2) WUE and NPP have similar spatial distribution characteristics, with precipitation and temperature dominating WUE changes in the Qilian Mountains and s southern Xinjiang, respectively. In the near future, Nav WUE is expected to be dominated by improvement to degradation, while Arv WUE will continue to improve under human intervention. These two indices respond differently to the environmental factors that cause their changes. (3) Nav and Arv exhibit similar restoration and degradation trends, mainly dominated by early recovery with Nav displaying a slightly more prominent restoration trend than Arv. The NPP-WUE assessment framework will help to rapidly assess vegetation degradation and restoration at large scales, providing new perspectives for research in this field.

KEYWORDS

artificial vegetation, natural vegetation, net primary productivity, water use efficiency, restoration and degradation

1. Introduction

According to the newly published *World Atlas of Desertification*, more than 75% of the world's land is already degraded. By 2050, this proportion is predicted to exceed 90% (Ádám and Křeček, 2019). As multiple regions across the globe are suffering from the effects of drought, degradation and desertification, coping with these issues has become an international flash point that will challenge the achievement of the United Nations Sustainable Development Goals

(SDGs; Stavi and Lal, 2015; Barbier and Hochard, 2018). To alleviate environmental pressures and improve ecosystems, the Chinese government started a series of ecological construction projects in the late 20th century (Lü et al., 2012; Bryan et al., 2018). The Northwest Arid Region (NAR) is one of the most ecologically fragile regions in China. In recent years, with the development of oasis agriculture, there has been serious vegetation destruction in that zone, making it a priority area for ecological construction (Fang et al., 2001; Li et al., 2019).

Artificial vegetation (Arv) is an important component of the NAR's ecosystem. Arv is also an important complement to natural ecosystems, so China's vast Arv region plays a key role in enhancing ecosystem services and mitigating climate warming (Peng et al., 2014; Tang et al., 2018). Several studies have attempted to explore the structural differences as well as the degradation and restoration patterns between Arv and natural vegetation (Nav; Domec et al., 2015; Fu et al., 2017). Recent research suggests that Nav restoration significantly improves soil organic carbon storage and inorganic nitrogen accumulation in restored areas compared to Arv restoration; it also plays an important role in improving soil aggregate stability and erosion resistance (Hu et al., 2019; Dou et al., 2020). Over the long term, Arv planting is anticipated to cause degradation of vegetation when it exceeds the natural carrying capacity, causing the growth of Nav to saturate or even decrease (Xu, 2022). These widespread trends in vegetation restoration and subsequent degradation have caused considerable concern. However, due to the complexity of the processes involved, especially in arid areas, there is considerable uncertainty in their assessment. Vegetation restoration and degradation in arid zones remains poorly studied, which limits our understanding of the change mechanisms contributing to the phenomenon.

With the development of remote sensing techniques, ecological indicators such as the Normalized Difference Vegetation Index (NDVI) and Net Primary Productivity (NPP) are now being widely used to characterize vegetation growth trends (Wessels et al., 2012; Le et al., 2016). The most popular method is the simulation of NPP estimation based on NDVI and using the Carnegie-Ames-Stanford Approach (CASA). However, there is uncertainty in assessing desertification processes when relying solely on NPP indicators. Furthermore, desertification not only has an impact on vegetation quantity, but usually also on the photosynthetic characteristics, species composition, and water use efficiency (WUE) of vegetation (Zhao et al., 2009; Zheng et al., 2011).

Water use efficiency refers to the ratio of CO^2 assimilation rate to transpiration rate or stomatal conductance of leaves and is used to reflect the physiological condition of plants (Farquhar and Richards, 1984; Law et al., 2002). Typically, WUE changes very little, but it does change significantly under certain circumstances, such as when plants become physiologically adapted to extreme climatic conditions, when photosynthesis, transpiration and stomatal conductance of leaves change, or when changes in vegetation composition occur (Do and Kang, 2014; Huang et al., 2015). In an environment that has turned arid, pore conductance preferentially decreases photosynthesis, causing transpiration to decrease and plant WUE to increase. In contrast, WUE decreases when severe drought occurs (Taylor et al., 2010; Li et al., 2015).

Vegetation productivity, species composition, and physiological characteristics respond differently to environmental stresses during the various stages of vegetation degradation. While NPP and WUE can characterize some information about changes in vegetation production and species composition, respectively, the joint use of these two indicators to build a framework can characterize different stages of vegetation degradation more effectively than the use of individual indicators alone (Ruppert et al., 2012; Horion et al., 2016). Based on this approach, the present study uses a joint WUE and NPP framework to assess the degradation and restoration trends of natural and artificial vegetation in the arid zone of northwest China and to analyze the differences between the two trends (Figure 1). The aim in conducting this research is to provide a scientific basis for vegetation conservation and ecological environment improvement in the NAR.

2. Study area

The Northwest Arid Region (NAR) is located in the interior of western China. It covers an area of about 2.11×10^6 square kilometers and includes Xinjiang, northern Gansu, and western Inner Mongolia. The NAR has a complex and diverse landscape, with undulating terrain and a topography that is dominated by plateaus, mountains, and basins. The natural landscape constitutes a special geographical pattern with the coexistence of three major ecosystems: mountain-oasis-desert (Figure 2).

Due to the perennial influence of continental climate, the NAR has little precipitation and shows a decreasing trend from east to west. Evaporation is strong and surface water is insufficient to sustain normal vegetation growth, so plants have to rely mainly on groundwater. Temperatures vary widely from day to day, season to season, and year to year, making the NAR one of the driest areas in the world. Of the few lakes that do exist, most are located in the Xinjiang Uygur Autonomous Region. Their water is typically brackish and saline, and they have large seasonal variations in area and depth. Human settlement in the NAR is relatively sparse compared to elsewhere in China, with most of the population concentrated in the region's oasis area. Unfortunately, economic development in this arid zone has not kept pace with the rest of the country, due primarily to the constraints imposed by the harsh environmental conditions and low population.

3. Data and methods

3.1. Data

The data used in this study are shown in Table 1. MODIS (Moderate-Resolution Imaging Spectroradiometer) is a new generation of "atlas-integrated" optical remote sensing instruments. Its data products help us to understand in depth the global dynamics of land, ocean, and lower atmosphere (Justice et al., 2002). GLDAS (Global Land Data Assimilation System) can generate the best land surface states and flux fields for global implementation at high

Abbreviations: CASA, Carnegie-Ames-Stanford Approach; NAR, The Northwest Arid Region; Arv, Artificial vegetation; Nav, Natural vegetation; MODIS, Moderate-resolution Imaging Spectroradiometer; NPP , Net primary production; P, Precipitation; T, Temperature; WUE, Water use efficiency; Plt, Plant transpiration; Pho, Photosynthesis; Sto, Stomata

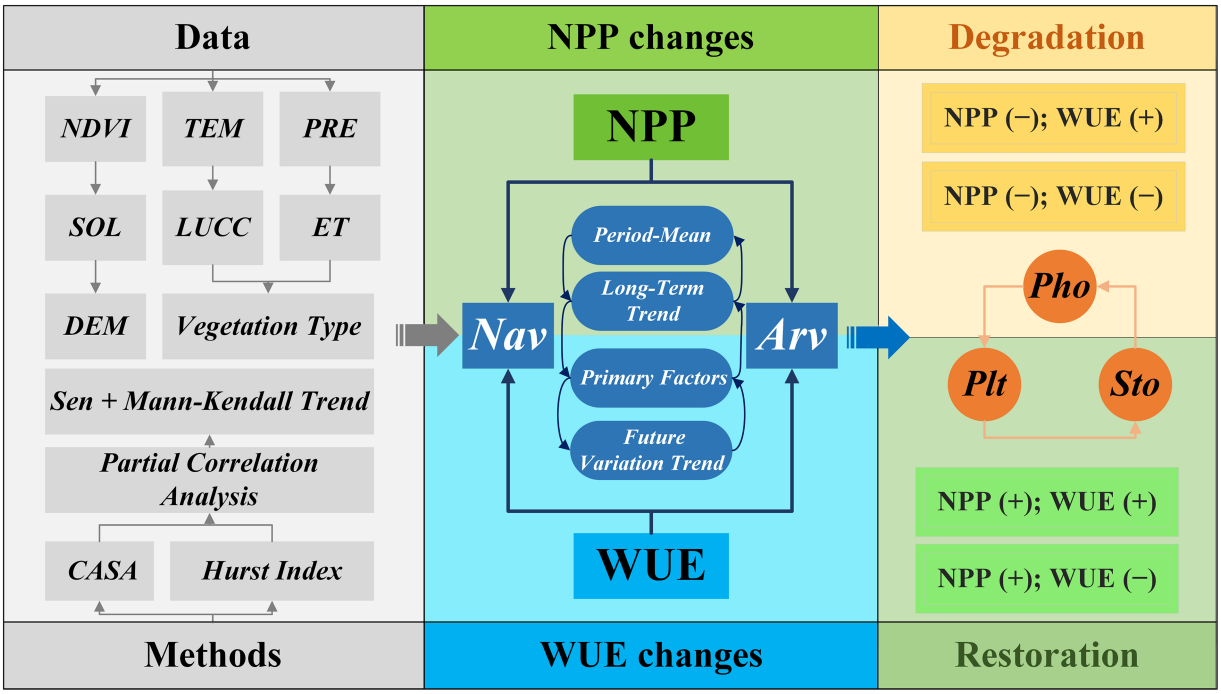

FIGURE 1
Technical roadmap for the study.

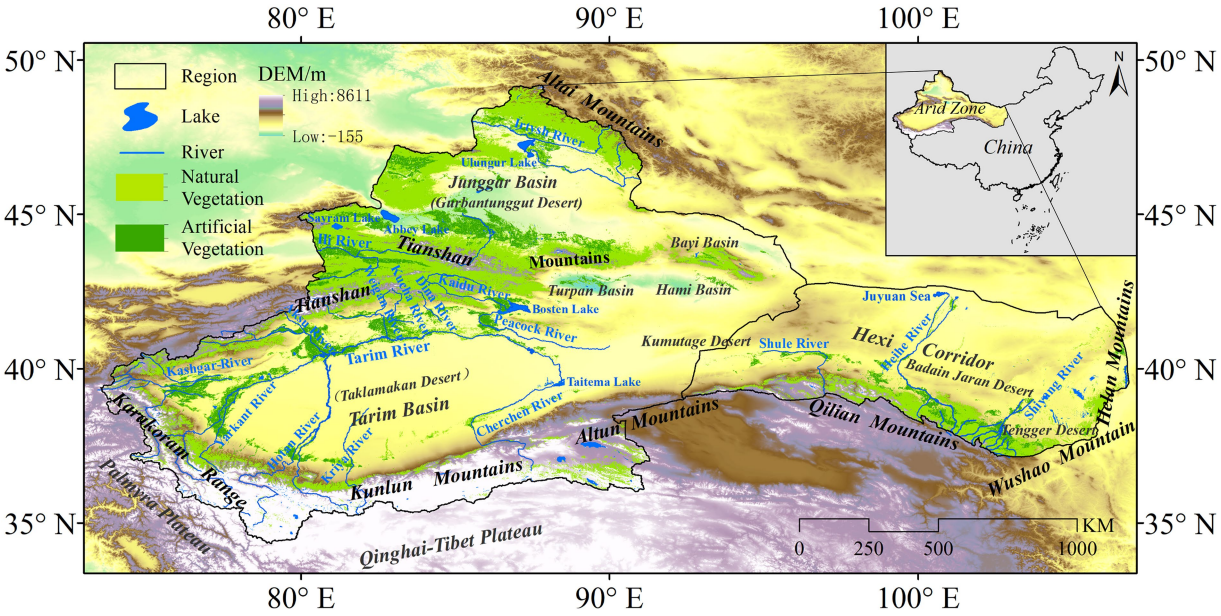

FIGURE 2
Study area. NO.: GS (2019)1822. ARV covered about 6.5% of the study area and NAV covered about 29.86%.

resolution (Rodell et al., 2004). TerraClimate is a monthly climate dataset for the global land surface that combines the WorldClim dataset with CRU Ts4.0 and JRA55 to create a high spatial resolution dataset covering a wider range of time records (Abatzoglou et al., 2018). The AVHRR evapotranspiration product uses satellite remote sensing data combined with atmospheric reanalysis products and daily ground-based meteorological data to produce a global terrestrial evapotranspiration dataset (Zhang et al., 2010). The SRTM (Shuttle Radar Topography Mission) data were jointly measured by NASA and the National Mapping Agency (NIMA) of the Department of Defense. They used the C-band in the SAR method to collect 80% of the global terrestrial topography (Farr et al., 2007). Some of the temperature and

TABLE 1 Data product type and source.

Model/ Chapter	Product	Type	Temporal resolution	Spatial resolution	Source URL	Time series
CASA	MOD13A3	NDVI	30 days	1 km	https://modis.gsfc.nasa.gov/ [Accessed on 2 August 2022]	2001–2018
	MOD17A3H	NPP	4 days	500 m	https://modis.gsfc.nasa.gov/ [Accessed on 2 August 2022]	2001–2018
	T3H(GLDAS)	Temperature	3 h	0.25°	http://ldas.gsfc.nasa.gov/ [Accessed on 13 April 2021]	2001–2018
	TerraClimate	Precipitation	monthly	1/24° ~ 4 km	https://www.ecmwf.int [Accessed on 13 April 2021]	2001–2018
	TerraClimate	SOL (Total solar radiation)	monthly	1/24° ~ 4 km	https://www.ecmwf.int [Accessed on 13 April 2021]	2001–2018
	MCD12Q1	Landcover (IGBP)	96 days	500 m	https://modis.gsfc.nasa.gov/ [Accessed on 2 August 2022]	2001–2018
Chapter	AVHRR	ET	8 days	0.05°	http://www.glass.umd.edu/download.html [Accessed on 13 April 2021]	2001–2018
	CRU-Worldclim	Temperature	monthly	1 km	http://data.tpdc.ac.cn/zh-hans/ [Accessed on 13 April 2021]	2001–2018
	CRU-Worldclim	Precipitation	monthly	1 km	http://data.tpdc.ac.cn/zh-hans/ [Accessed on 13 April 2021]	2001–2018
	SRTM	DEM	—	30 m	https://www.usgs.gov/ [Accessed on 13 April 2021]	—
	Land use type of CAS	Vegetation type	—	1 km	https://www.resdc.cn/ [Accessed on 2 August 2022]	—

precipitation data are downscaled over China using the Delta Spatial Downscaling scheme based on the global 0.5° climate dataset published by CRU and the global high-resolution climate dataset published by WorldClim (Ding and Peng, 2020).

3.2. Methods

3.2.1. WUE calculation

The water use efficiency of an ecosystem is equal to the ratio of net primary productivity (NPP) of vegetation to evapotranspiration (ET) and is calculated as:

$$\mathrm{WUE} = \frac{\mathrm{NPP}}{\mathrm{ET}} \tag{1}$$

where WUE indicates water use efficiency (g C·mm^{-1}·a^{-2}), NPP denotes the net primary productivity of vegetation (g C·m^{-2}·a^{-1}), and ET is evapotranspiration (mm·a).

3.2.2. NPP calculation

The CASA (Carnegie-Ames-Stanford Approach) model is a typical representative of light energy utilization. In this study, the NPP was simulated using the CASA model optimized by Zhu et al. (2006). Photosynthetically active radiation (APAR) and light energy utilization are the main parameters in this model. Their calculation equations are as follows:

$$\mathrm{NPP}(x,t) = \mathrm{APAR}(x,t) \times \varepsilon(x,t) \tag{2}$$

In the formula, APRP indicates the radiation on an image (x) in month t that is beneficial to plant photosynthesis, i.e., photosynthetically active radiation (MJ·m^{-2}), and ε denotes the degree of light energy utilization in an image (x) in month t, i.e., light energy utilization (gC·MJ^{-1}).

To estimate the photosynthetically active radiation absorbed by vegetation, remote sensing data can be used for the analysis. Our analysis of the determinants of light and effective radiation absorbed by vegetation shows that it is determined by the utilization of total solar radiation and photosynthetically-effective radiation. The expressions can be formulated as:

$$\mathrm{APAR}(x,t) = \mathrm{SOL}(x,t) \times \mathrm{FPAR}(x,t) \times 0.5 \tag{3}$$

where SOL(x, t) represents the total solar radiation (MJ·m^{-2}) contained in an image element (x) in month t, and FPAR(x, t) indicates the ratio of radiation absorbed by vegetation to incident radiation.

The photosynthesis of plants is influenced by factors such as temperature, precipitation, and atmospheric water-air pressure

10.3389/fevo.2023.1131210

difference, which further affects the NPP of vegetation. Therefore, in the model, these factors regulate NPP through the maximum light energy use efficiency. The formula to describe this relation can be calculated as follows:

$$\varepsilon(x,t) = T_{\varepsilon 1}(x,t) \times T_{\varepsilon 2}(x,t) \times \mathrm{W}_{\varepsilon}(x,t) \times \varepsilon_{\max} \quad (4)$$

where $T_{\varepsilon 1}(x,t)$ and $T_{\varepsilon 2}(x,t)$ indicate the stress on ε when the temperature is too high or too low; $\mathrm{W}_{\mu}(\mathrm{x,t})$ represents the effect of moisture on μ; and $\varepsilon_{\max}$ is the maximum μ (gC· MJ^{-1}) of vegetation. In this study, the value of ($\varepsilon_{\max}$) is based on the calculation results of Zhu et al. (2006).

We validated the estimation results using MOD17A3H data. As shown in Figure 3, the simulated NPP values have a good linear correlation with MODIS17A3H values ($R^2 = 0.81$). This indicates that the simulated NPP values of the improved CASA model can truly reflect the variations in NPP in the NAR. Therefore, the improved CASA model is applicable to the study of NPP estimation in the study area.

3.2.3. Hurst index

The Hurst index is often used to predict the persistence of time series. In this paper, the index is obtained based on the R/S calculation method. The calculation formula is:

$$\frac{R_{(T)}}{S_{(T)}} = C_T{}^H \quad (5)$$

$$R_{(T)} = \max_{1 \le t \le T} X_{(t,T)} - \min_{1 \le t \le T} X(t,T) \quad (6)$$

$$S_{(T)} = \left[\frac{1}{T} \sum_{t=1}^{T} \left(\mathrm{NPP}_{(t)} - \mathrm{NPP}_{(T)} \right)^2 \right]^{\frac{1}{2}} \quad (7)$$

where $X(t,T)$ represents the cumulative deviation; $\mathrm{R}_{(\mathrm{t})}$ denotes the extreme deviation; $S_{(T)}$ stands for the standard deviation; and H indicates the Hurst index, whose value is between 0 and 1. When $H = 0.5$, the future trend of the series does not have long-term correlation with the past trend; when $0 \le H < 0.5$, the series has inverse persistence, and the future trend is opposite to the past one; and when $0.5 < H \le 1$, the series has persistence, and the future trend is consistent with the past one.

3.2.4. Partial correlation analysis

In multivariate systems, partial correlation allows the study of the correlation of one element to another, while eliminating the effect of one or more confounding factors. When the number of control variables is one, the partial correlation coefficient is called the first-order partial correlation coefficient. When the number of control variables is n, the partial correlation coefficient is called the nth-order correlation coefficient. When the number of control variables is zero, the partial correlation coefficient is called the zero-order partial correlation coefficient, which is also known as the correlation coefficient. The formula for calculating the partial correlation coefficient is as follows:

$$R_{(ab \cdot c)} = \frac{R_{ab} - R_{ac} \times R_{bc}}{\sqrt{\left(1 - R^2{}_{ac}\right)\left(1 - R^2{}_{bc}\right)}} \quad (8)$$

$$R_{(ab)} = \frac{\sum_{i=1}^{n} \left[\left(a_i - \bar{a}\right)\left(b_i - \bar{b}\right) \right]}{\sqrt{\sum_{i=1}^{n} \left(a_i - \bar{a}\right)^2 \sum_{i=1}^{n} \left(b_i - \bar{b}\right)^2}} \quad (9)$$

where $R_{(ab \cdot c)}$ indicates the first-order partial correlation coefficient between ab with constant c, applicable to the analysis of the relationship between three variables; and $R_{(ab)}$ indicates the correlation coefficient between *ab*, applicable to the analysis of the relationship between two variables.

The *t*-test is generally used to test statistics, using the formula:

$$t = \frac{r_{12,34,\ldots,m}}{\sqrt{1 - r^2_{12,32,\ldots,m}}} \sqrt{n - m - 1} \quad (10)$$

where $r_{12,34,\ldots,m}$ represents the bias correlation coefficient, n indicates the number of samples, and m denotes the number of independent variables. For the present study, $p \le 0.05$ is considered statistically significant.

3.2.5. Sen+Mann-Kendall trend analysis

Theil-Sen median trend analysis (also known as Sen trend analysis or Sen's slope) is a robust nonparametric statistical approach to trend calculation. Compared to linear regression trend analysis, Sen trend analysis circumvents the effects of missing data and data distribution patterns in the time series and eliminates the interference of outliers in the time series. Its calculation formula is:

$$\beta = \mathrm{Median}\left(\frac{A_j - A_i}{j - i} \right), \forall_j > i \quad (11)$$

where A_j and A_i are the values of year *i* and *j* in A time series data; Median is the median taking function; and β is the median of the slope of all data pairs, which is the Sen slope of the time series. When $\beta > 0$, the time series has an increasing trend, whereas when $\beta < 0$, the time series has a decreasing trend.

The Mann-Kendall (MK) test is typically used in conjunction with Sen trend analysis. It is a nonparametric statistical test that is not affected by missing values and outliers, nor does it require the sample data to follow a certain distribution. Its formula can be expressed as:

$$Z = \begin{cases} \dfrac{S-1}{\sqrt{\mathrm{Var}(S)}} (S > 0) \\ 0 (S = 0) \\ \dfrac{S+1}{\sqrt{\mathrm{Var}(S)}} (S < 0) \end{cases} \quad (12)$$

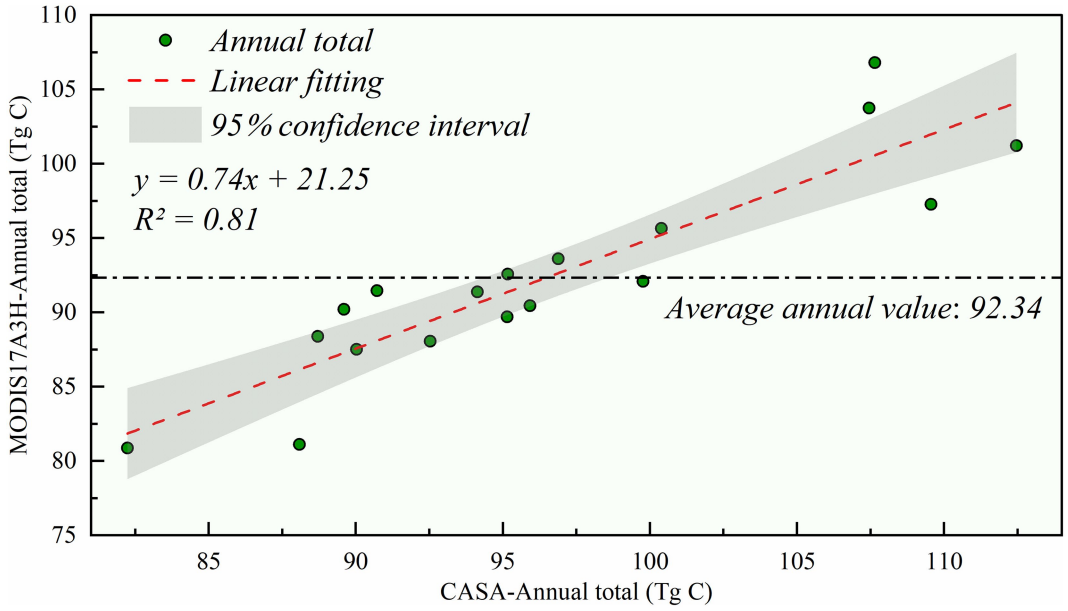

FIGURE 3
Correlation analysis between simulated annual total NPP and total annual MODIS17A3H in China's NAR, 2001–2018.

$$S = \sum_{j=1}^{n=1} \sum_{i=j+1}^{n} sign\left(A_j - A_i\right) \tag{13}$$

$$\mathrm{Var}(S) = \frac{n(n-1)(2n+5)}{18} \tag{14}$$

$$sign(\theta) = \begin{cases} 1(\theta > 0) \\ 0(\theta = 0) \\ -1(\theta < 0) \end{cases} \tag{15}$$

where A_j and A_i are A time series data; sign is the sign function; S is the test statistic; Z is the standardized test statistic; and n is the amount of data. NPP trends were classified into five categories according to the significance levels of Sen-MK trend analysis $|Z| > 1.96$ ($p < 0.05$) and $|Z| > 2.58$ ($p < 0.01$; Table 2).

3.2.6. WUE and NPP assessment of vegetation degradation and restoration

Vegetation degradation is usually accompanied by the occurrence of reduced biomass, decreased vegetation cover, increased drought-tolerant plants, and increased area of bare soil patches. NPP and WUE are used to characterize these changes. In the early degradation stage, NPP declines and plants can close stomata for physiological regulation or establish a survival advantage by increasing the area of drought-tolerant vegetation, which increases the WUE and slows the rate of NPP decline (Chen et al., 2004). In the later degradation stage, with the aggravation of further drought and anthropogenic disturbance stress, vegetation NPP decreases substantially, bare soil patches begin to appear and expand, WUE decreases, and finally a desert landscape appears (Horion et al., 2016). Based on this, we used NPP and WUE to assess land degradation and restoration, assuming that the path of vegetation restoration is the opposite of degradation (Gang et al., 2016).

3.2.7. Division of natural vegetation and artificial vegetation

Based on the spatial distribution data of 1 million vegetation types in China, downloaded from the Resource and Environmental Science and Data Center of the Chinese Academy of Sciences,[1] this study defines cultivated vegetation (including farmland, economic forests, and orchards) as artificial vegetation (Arv), while vegetation other than cultivated vegetation is defined as natural vegetation (Nav).

4. Results

4.1. NPP changes in Nav and Arv

From 2001 to 2018, the annual average NPP of vegetation in the NAR largely showed a spatial pattern of high in the north, low in the south, high in the west, and low in the east. The Ili Valley, Tianshan Mountains, Altay Mountains, and Qilian Mountains were the high value areas of Nav NPP, with values ranging from 343.09 to 711.29 g $C{\cdot}m^{-2}{\cdot}a^{-1}$. The Arv high value areas were relatively small in distribution and were located mainly in the Ili Valley and Qilian Mountains, with Arv NPP values ranging from 300 to 542.02 g $C{\cdot}m^{-2}{\cdot}a^{-1}$. The southern part of the NAR was the low value area of Nav NPP, with NPP values mainly in the range of 40 g $C{\cdot}m^{-2}{\cdot}a^{-1}$. Arv NPP low value areas were

1 https://www.resdc.cn/

TABLE 2 Criteria for grading change trends.

Trends	Sen slope (β)	MK test (Z)
Extremely significant increase	$\beta>0$	$Z>2.58$
Significant increase	$\beta>0$	$1.96<Z\leq 2.58$
No significant trend	$\forall\beta$	$-1.96\leq Z\leq 1.96$
Significant decrease	$\beta<0$	$-2.8\leq Z<-1.96$
Extremely significant decrease	$\beta<0$	$Z<-2.58$

primarily in the desert-oasis transition zone in southern Xinjiang, with NPP values mostly below 42.51 g C·m^{-2}·a^{-1} (Figure 4A).

The areas of significant increase in NPP were widely distributed, with Arv clustered around oases and Nav occurring in mountainous areas (Figure 4B). In contrast, the mountain-oasis interface and the oasis-desert transition zone were the main areas of decrease in Nav and Arv, respectively. Climate change can explain 36.38 and 25.70% of the variations in NPP of natural and natural vegetation in the NAR, respectively. Meanwhile, precipitation was the dominant climate factor affecting variations in vegetation NPP, whereas temperature played a major role only in 4.04% (Nav) and 5.89% (Nav) of the area, respectively (Figure 4C).

To better understand the future trends of vegetation NPP in the NAR, this study conducted an overlay analysis of the vegetation NPP Hurst index and interannual variation trends, which were divided into five classes (Figure 4D). Except for areas with insignificant changes, continuous improvement and improvement to degradation were distributed throughout the study area and had the largest area share. The areas of continuous degradation and degradation to improvement as well as their distributions were roughly equivalent, but the distribution of degradation to improvement was more concentrated in the northern border. In general, the development trend of the Nav improvement area in the NAR is consistent with that of Arv, mainly improvement to degradation. However, the degraded area in the future period is expected to be mainly degradation to improvement in Nav and continuous degradation in Arv (Tables 3 and 4).

4.2. WUE changes in Nav and Arv

During the study period, vegetation WUE and NPP exhibited similar spatial distributions. The mountainous regions of northern Xinjiang were the high value areas of Nav WUE, with multi-year mean WUE values generally above 1.29 g C·mm^{-1}·a^{-2}. The low value areas were mainly distributed around the Kunlun Mountains, with multi-year mean WUE values mostly below 0.40 g C·mm^{-1}·a^{-2}. The oasis center was the high value area of Arv WUE, while the low value area was mainly located at the desert edge, showing a multi-year mean WUE value below 0.35 g C·mm^{-1}·a^{-2} (Figure 5A). The long-term trend of Nav WUE change compared to Nav NPP shows some similarities. Areas of insignificant change in Nav NPP were the predominant type and the largest area (59.23%), while areas of increase and decrease in Nav WUE were 39 and 1.77%, respectively. Arv WUE and Arv NPP changed in the same direction with the largest area of growth covering 47.96%, followed by areas of insignificant change and decrease covering 47.90 and 4.14%, respectively. Overall, WUE changes were similar to NPP changes in northern and southern NAR, but there were some regions with different spatial trends. Nav WUE in northeastern NAR and northern Tarim Basin showed a more pronounced upward and downward trend than NPP, while WUE changes in the Qilian Mountains were not as pronounced as NPP changes in the eastern NAR region (Nav NPP). The trends in WUE and NPP suggest that the two indices respond differently to the environmental factors that cause them to change (Figure 5B).

Whether in reference to Nav WUE or Arv WUE, climate change explains less of the change in WUE dynamics than does NPP. Precipitation was the dominant climatic factor affecting the change in vegetation WUE in the NAR (Nav: 17.37%, Arv: 13.91%). Furthermore, the dominant role of precipitation is obvious in the Qilian Mountains. Meanwhile, temperature had less influence on vegetation WUE in the NAR (Nav. 5.89%, Arv: 2.09%), but dominated the change in WUE in southern Xinjiang (Figure 5C). Future trends in WUE are more pronounced than for NPP, but future trends in Nav WUE are consistent with those for Nav NPP. Arv WUE shows the opposite trend, with areas of improved Arv WUE dominated by sustained improvement (41.83%) and degraded areas dominated by sustained degradation (10.66%; Figure 5D).

4.3. Spatial dynamics of NPP and WUE in Nav and Arv

From the spatial dynamics of NPP-WUE, the Nav degradation phase of the NAR was dominated by late degradation, while the restoration phase was dominated by early restoration. It is worth noting that the area of early restoration was much larger than that of late degradation (Figure 6). Grasslands, shrubs, and forests showed the same trend, with late degradation and early restoration as their main contributors. Meanwhile, the percentage of early degradation and late restoration was small. Unlike other vegetation types, the restoration phase was evident in wetlands, especially the late restoration phase. Compared to Nav, Arv showed a similar trend of predominant restoration, but with a larger area of late degradation (Figure 7).

In terms of spatial distribution, the Nav restoration area was widely distributed, mainly in the central, southern, and northeastern parts of the NAR, but there was relatively concentrated distribution in the mountainous areas. Degraded areas, on the other hand, were sporadically distributed and occurred mostly in the mountain-oasis interface. The degradation phenomenon was most prominent in the Ili Valley. Meanwhile, the oasis located in the northern and southern portions of the Tianshan Mountains was the main restoration area of Arv, with degraded areas distributed in the oasis-desert transition zone in a dotted pattern. Interestingly, the oasis areas with high anthropogenic disturbance were not only the main areas of vegetation restoration, but also hot spots for serious vegetation degradation. The degradation may be related to human negligence in management and/or the cultivation area exceeding the local resource carrying capacity.

5. Discussion

5.1. Mechanism of WUE and NPP changes

The factors affecting plant WUE are somewhat complex, with the primary influences comprising the photosynthesis of leaves,

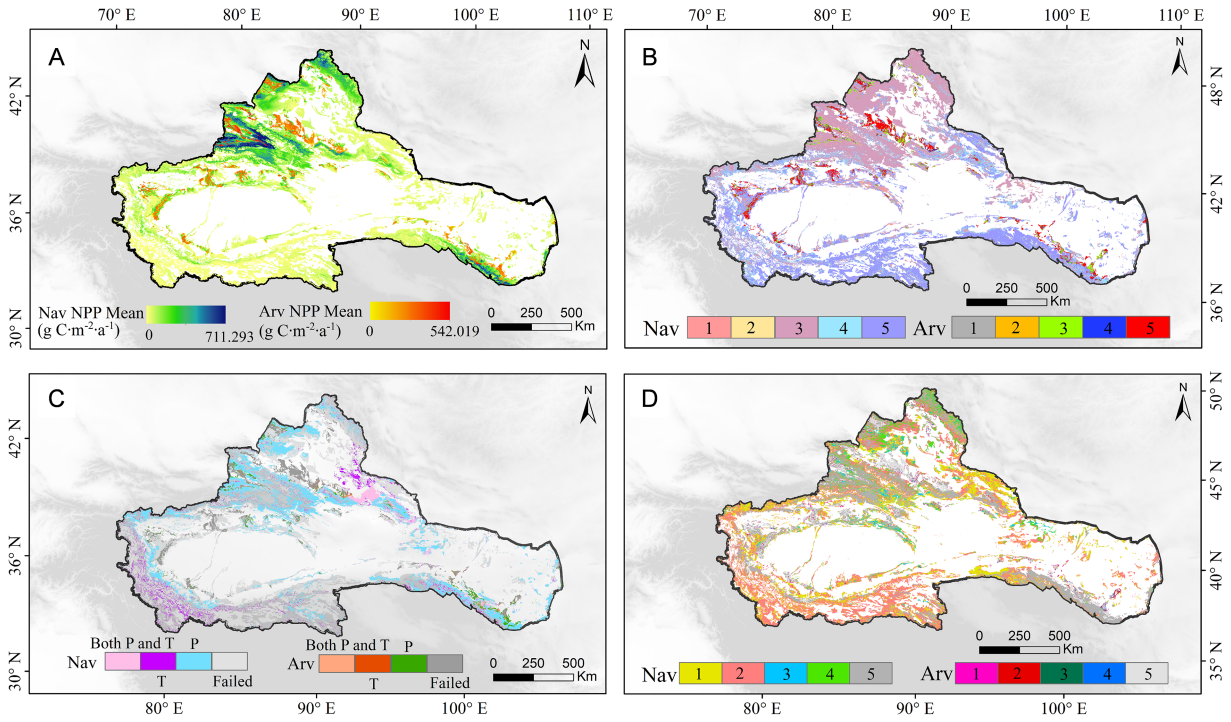

FIGURE 4
Net primary productivity (NPP) of vegetation in the NAR from 2001 to 2018: (**A**) period-mean NPP; (**B**) long-term trend of NPP (1. Extremely significant decrease, 2. Significant decrease, 3. No significant change, 4. Significant rise, 5. Extremely significant rise); (**C**) primary factors regulating interannual variations of NPP; (**D**) future variation trend of NPP (1. Sustained improvement, 2. Improvement to degradation, 3. Degradation to improvement, 4. Sustained degradation, 5. Insignificant).

TABLE 3 Assumptions of NPP and WUE trends in various stages of vegetation degradation and restoration.

Trends	Degradation and rehabilitation stage
NPP (−); WUE (+)	Early degradation stage
NPP (−); WUE (−)	Late degradation stage
NPP (+); WUE (+)	Early rehabilitation stage
NPP (+); WUE (−)	Late rehabilitation stage

transpiration, and plant stomatal conductance. These factors are also related to the direct effects of species, life type, and intrinsic plant mechanisms, as well as the indirect effects of factors such as the external plant environment (climate, soil, etc.).

Plant transpiration (Plt) and photosynthesis (Pho) form the basis for changes in WUE. Stomata (Sto) usually act as a special channel that controls the exchange of water between air and plant body. Sto also regulate the rate of plant water consumption and carbon assimilation, which in turn has an effect on plant photosynthesis and transpiration, causing additional changes in WUE. When drought occurs, stomatal *closure* preferentially decreases photosynthesis, which reduces transpiration and contributes to higher plant WUE. Leaf water potential, root system, leaf nutrients (nitrogen content, etc.), specific leaf area, plant genes, and chromosome ploidy influence vegetation WUE as well (Cernusak et al., 2011; Fang et al., 2017).

WUE also varies among habitats and species. The current results of plant WUE response to climatic environment exhibit unevenness (Li et al., 2017; Du et al., 2021). As the research progresses and more plant species are studied, the main climatic factors derived vary; in some cases, the results of the same climatic environment even show opposite conclusions. Therefore, when considering the influence of climatic environment on plant WUE, the compound effect of multiple environments should be considered (Farquhar et al., 1982; Wang et al., 2010, 2019).

Factors affecting vegetation biomass and productivity can simply be divided into two categories: biotic and abiotic factors. Biotic factors include species composition and species density, while abiotic factors are those such as light, temperature, water, CO_2, and soil (Kamali et al., 2020; Koju et al., 2020). For different ecosystems, biomass and productivity will vary due to differences in their plant species, species density, etc. Site conditions include elevation, slope, slope orientation, slope position, soil thickness and soil type, which usually act synergistically with meteorological factors to influence the growth and development of vegetation and thus biomass and productivity. Anthropogenic factors are also a non-negligible aspect and have two sides to vegetation growth (Cao et al., 2020; Yang et al., 2021). Overall, while these studies have improved our understanding of vegetation NPP changes, they also reveal that these changes are the result of a combination of multiple factors (Figure 8).

5.2. Degradation and restoration patterns in the NAR

The NAR is an ecologically fragile yet important construction area for soil and water conservation in China. Given its noted vulnerability,

TABLE 4 Table of future trends of vegetation in the NAR, 2001–2018.

	Sustained improvement	Improvement to degradation	Sustained degradation	Degradation to improvement	Insignificant
Nav	24.18%	38.27%	3.74%	5.43%	28.39%
Arv	6.79%	8.28%	2.78%	2.44%	79.71%

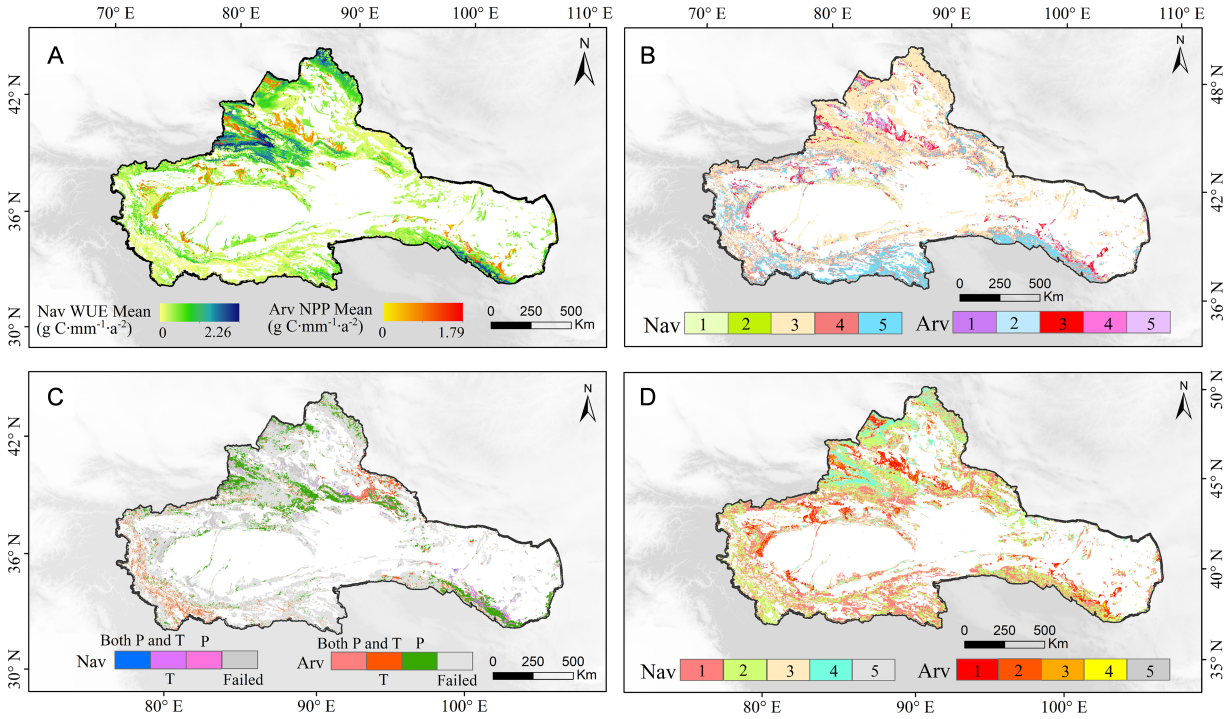

FIGURE 5
Water use efficiency of natural vegetation in China's arid northwest region from 2001 to 2018: (**A**) period-mean WUE; (**B**) long-term trend of WUE (1. Extremely significant decrease, 2. Significant decrease, 3. No significant change, 4. Significant rise, 5. Extremely significant rise); (**C**) primary factors regulating interannual variations of WUE; (**D**) future variation trend of WUE (1. Sustained improvement, 2. Improvement to degradation, 3. Degradation to improvement, 4. Sustained degradation, 5. Insignificant).

the NAR has historically received extensive research attention. From 2001 to 2018, the region was dominated by the restoration of mountains (natural vegetation) and oases (artificial vegetation), which is consistent with the results from other studies that focused on the Tianshan Mountains (Zheng et al., 2011), Altai Mountains, and oasis areas (He et al., 2021). Additionally, the vegetation restoration observed in the Qilian Mountains (Zuo et al., 2022) is in good agreement. This is also consistent with the increasing trend of WUE in the NAR (Yang et al., 2022). In contrast, vegetation degradation was found in the transition zone around the oasis (Wei et al., 2018).

Precipitation plays a key role in regulating changes in natural NPP and WUE. Accordingly, the different responses of vegetation to NPP and WUE are related to the pattern of gradually decreasing precipitation in the mountain range-oasis-desert system. Air temperature appears to be a major factor only in the western Qilian and Kunlun Mountains and the eastern part of the northern border. The increase in air temperature and precipitation well explains the restoration of vegetation in the eastern portion of Northern Xinjiang (Shen et al., 2013). Moreover, the warming trend in the super-arid region and the high intensity of anthropogenic disturbance explain the degradation trend at the edge of the oasis (Meng et al., 2020).

The restoration of artificial vegetation can be attributed to active vegetation restoration activities and advances in sustainable agricultural techniques, with arable land expansion being the main manifestation. Although there is an increasing trend in oasis cover, anthropogenic-induced water redistribution has also caused local degradation of oases in the northern region. Despite bringing positive ecological benefits for a short period, artificial vegetation saturates and fuels the expansion of artificial oases, causing the degradation of natural oases (Zhang et al., 2020). Therefore, to improve oasis stability, relevant management authorities should further control oasis size and agricultural area.

Based on the evaluation framework of NPP and WUE, this study analyzed the restoration and degradation trends of natural vegetation and artificial vegetation in the arid area of northwest China, and deepened the understanding of its change mechanism. However, there is no entry analysis of their influencing factors. In future studies, breakthroughs should be made in identifying the anthropogenic and natural factors affecting vegetation recovery and degradation and their respective weights, and in-depth studies and researches should be conducted on the attribution factors affecting vegetation recovery and degradation.

10.3389/fevo.2023.1131210

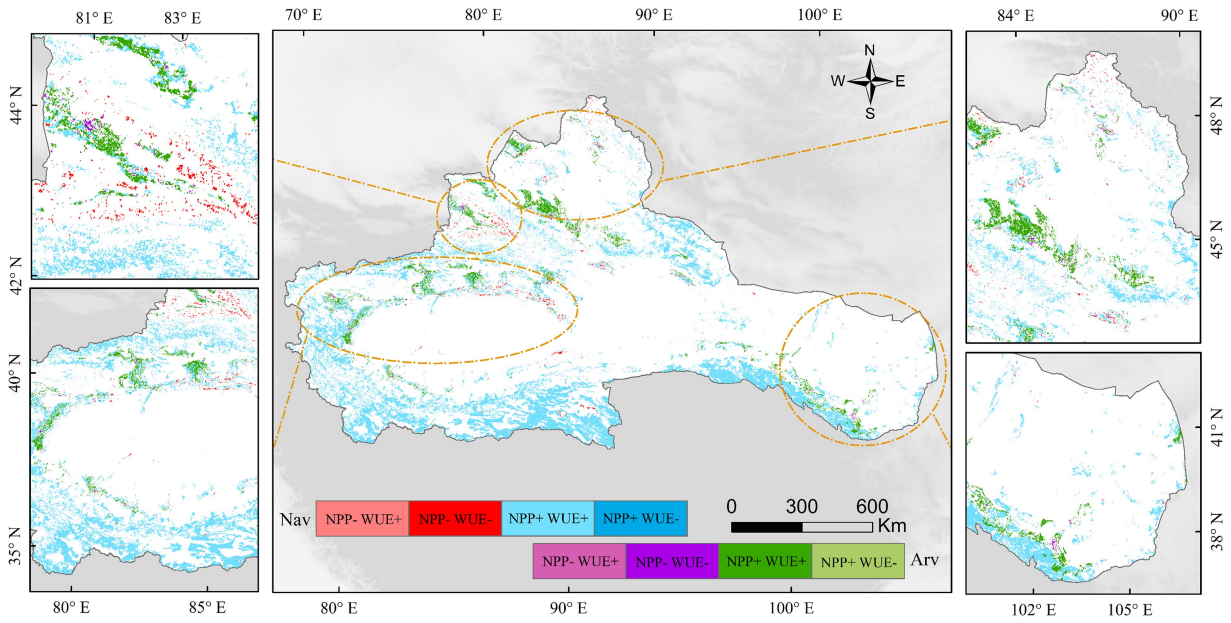

FIGURE 6
Spatial pattern of land degradation and restoration in the NAR.

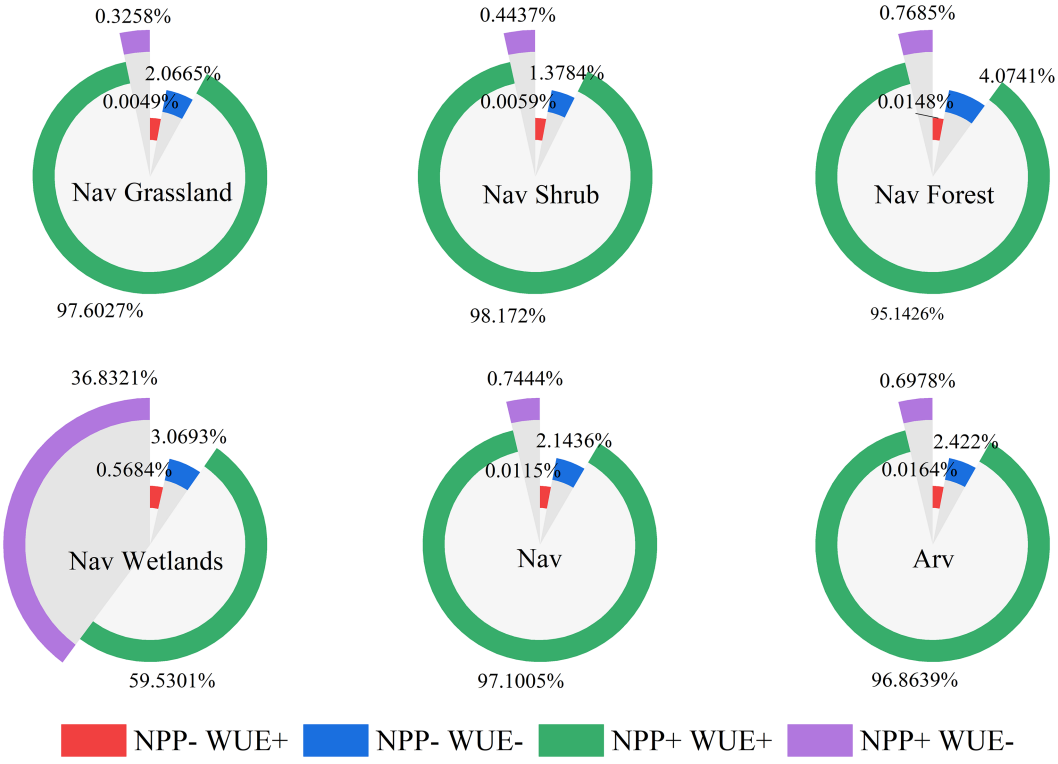

FIGURE 7
Percentage contribution of each vegetation type at different stages of degradation and restoration.

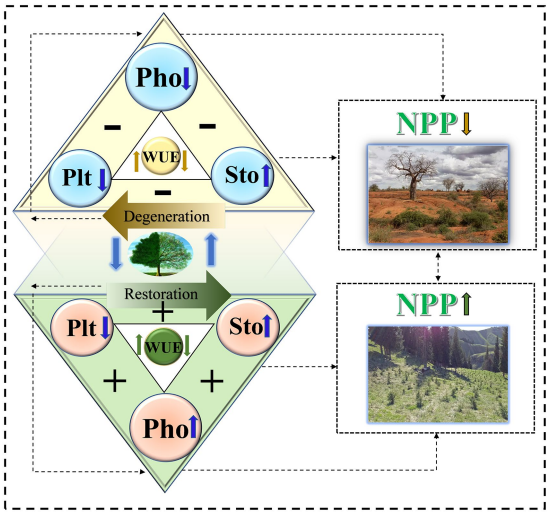

FIGURE 8
Mechanism of WUE and NPP changes.

6. Conclusion

This study evaluated the degradation and restoration trends of Nav and Arv in the arid zone of northwest China, using NPP and WUE as indicators. The research also analyzed the differences between the two. Overall, the NPP and WUE trends revealed the following:

1) Nav NPP and Arv NPP in the NAR were both dominated by significant increases, with precipitation being the main climatic factor causing their changes. Due to human activities, Arv NPP changed more than Nav NPP, and mountainous and oasis areas saw significant increases in Nav NPP and Arv NPP, respectively. Meanwhile, the relative expansion of oasis to mountains and deserts caused a decrease in Nav and Arv.
2) WUE and NPP exhibited similar spatial distributions, but climate change explained less of the dynamic changes in WUE than did NPP. Precipitation and temperature dominated the WUE changes in the Qilian Mountains and Southern Xinjiang, respectively. In the near future, Nav WUE is expected to dominate by improvement to degradation, while Arv WUE will continue to improve under human intervention.
3) Nav in the NAR is dominated by early restoration and late degradation, making the recovered area larger than the degraded area. Arv shows a similar trend, but the area of late degradation is larger than that of Nav. Early recovery and late degradation are the main trends in grassland, shrub, and forest change, while the recovery phase is more pronounced in wetlands.

Data availability statement

The original contributions presented in the study are included in the article/Supplementary material, further inquiries can be directed to the corresponding author/s.

Author contributions

All authors made significant contributions to this study. HH and ZL provided the conceptualization. JZ and HZ framed the methodology. JZ and HH wrote and prepared the original draft. JZ and WD did the review and editing. YX and QZ oversaw the project administration. ZL was responsible for funding acquisition. All authors contributed to the article and approved the submitted version.

Funding

This research was supported by National Key Research and Development Program (2019YFA0606902) and Natural Science Foundation of Xinjiang Uygur Autonomous Region (2021D01E02).

Conflict of interest

The authors declare that they have no known competing financial interests or personal relationships that could have appeared to influence the work reported in this paper.

Publisher's note

All claims expressed in this article are solely those of the authors and do not necessarily represent those of their affiliated organizations, or those of the publisher, the editors and the reviewers. Any product that may be evaluated in this article, or claim that may be made by its manufacturer, is not guaranteed or endorsed by the publisher.

Supplementary material

The Supplementary material for this article can be found online at: https://www.frontiersin.org/articles/10.3389/fevo.2023.1131210/full#supplementary-material

References

Abatzoglou, J. T., Dobrowski, S. Z., Parks, S. A., and Hegewisch, K. C. (2018). Terraclimate, a high-resolution global dataset of monthly climate and climatic water balance from 1958-2015. *Sci. Data* 5:170191. doi: 10.1038/sdata.2017.191

Ádám, K., and Křeček, J. (2019). Landscape degradation in the world and in Hungary. *Hungarian Geogr. Bull.* 68, 201–221. doi: 10.15201/hungeobull.68.3.1

Barbier, E. B., and Hochard, J. P. (2018). Land degradation and poverty. *Nat. Sustain.* 1, 623–631. doi: 10.1038/s41893-018-0155-4

Bryan, B. A., Gao, L., Ye, Y., Sun, X., Connor, J. D., Crossman, N. D., et al. (2018). China's response to a national land-system sustainability emergency. *Nature* 559, 193–204. doi: 10.1038/s41586-018-0280-2

Cao, F., Li, J., Fu, X., and Wu, G. (2020). Impacts of land conversion and management measures on net primary productivity in semi-arid grassland. *Ecosyst. Health Sustain.* 6:17. doi: 10.1080/20964129.2020.1749010

Cernusak, L. A., Winter, K., and Turner, B. L. (2011). Transpiration modulates phosphorus acquisition in tropical tree seedlings. *Tree Physiol.* 31, 878–885. doi: 10.1093/treephys/tpr077

Chen, J., Jönsson, P., Tamura, M., Gu, Z., Matsushita, B., and Eklundh, L. (2004). A simple method for reconstructing a high-quality NDVI timeseries data set based on the Savitzky–Golay filter. *Remote Sens. Environ.* 91, 332–344. doi: 10.1016/j.rse.2004.03.014

Ding, Y. X., and Peng, S. Z. (2020). Spatiotemporal trends and attribution of drought across China from 1901–2100. *Sustainability* 12:477. doi: 10.3390/su12020477

Do, N., and Kang, S. (2014). Assessing drought vulnerability using soil moisturebased water use efficiency measurements obtained from multi-sensor satellite data in Northeast Asia dryland regions. *J. Arid Environ.* 105, 22–32. doi: 10.1016/j.jaridenv.2014.02.018

Domec, J. C., King, J. S., Ward, E., Christopher Oishi, A., Palmroth, S., Radecki, A., et al. (2015). Conversion of natural forests to managed forest plantations decreases tree resistance to prolonged droughts. *For. Ecol. Manag.* 355, 58–71. doi: 10.1016/j.foreco.2015.04.012

Dou, Y., Yang, Y., An, S., and Zhu, Z. (2020). Effects of different vegetation restoration measures on soil aggregate stability and erodibility on the Loess Plateau, China. *Catena* 185:104294. doi: 10.1016/j.catena.2019.104294

Du, B., Zheng, J., Ji, H. W., Zhu, Y. H., Yuan, J., Wen, J. H., et al. (2021). Stable carbon isotope used to estimate water use efficiency can effectively indicate seasonal variation in leaf stoichiometry. *Ecol. Indic.* 121:107250. doi: 10.1016/j.ecolind.2020.107250

Fang, J., Chen, A., Peng, C., Zhao, S., and Ci, L. (2001). Changes in forest biomass carbon storage in China between 1949 and 1998. *Science* 292, 2320–2322. doi: 10.1126/science.1058629

Fang, C. H., Zhou, K. Y., Zhang, Y. W., Li, B. Z., and Han, M. Y. (2017). Effect of root pruning and nitrogen fertilization on growth of young 'fuji'apple (Malus domestica borkh.) trees. *J. Plant Nutr.* 40, 1538–1546. doi: 10.1080/01904167.2016.1240202

Farquhar, G. D., O'Leary, M. H., and Berry, J. A. (1982). On the relationship between carbon isotope discrimination and the intercellular carbon dioxide concentration in leaves. *Funct. Plant Biol.* 9, 121–137. doi: 10.1071/PP9820121

Farquhar, G. D., and Richards, R. A. (1984). Isotopic composition of plant carbon correlates with water-use efficiency of wheat genotypes. *Funct. Plant Biol.* 11, 539–552. doi: 10.1071/PP9840539

Farr, T. G., Rosen, P. A., Caro, E., Crippen, R., Duren, R., Hensley, S., et al. (2007). The shuttle radar topography mission. *Rev. Geophys.* 45, 1–33. doi: 10.1029/2005RG000183

Fu, B., Wang, S., Liu, Y., Liu, J., Liang, W., and Miao, C. (2017). Hydrogeomorphic ecosystem responses to natural and anthropogenic changes in the Loess Plateau of China. *Annu. Rev. Earth Planet. Sci.* 45, 223–243. doi: 10.1146/annurev-earth-063016-020552

Gang, C., Wang, Z., Zhou, W., Chen, Y., Li, J., Chen, J., et al. (2016). Assessing the spatiotemporal dynamic of global grassland water use efficiency in response to climate change from 2000 to 2013. *J. Agron. Crop Sci.* 202, 343–354. doi: 10.1111/jac.12137

He, P., Sun, Z., Han, Z., Dong, Y., Liu, H., Meng, X., et al. (2021). Dynamic characteristics and driving factors of vegetation greenness under changing environments in Xinjiang, China. *Environ. Sci. Pollut. Res.* 28, 42516–42532. doi: 10.1007/s11356-021-13721-z

Horion, S., Prishchepov, A., Verbesselt, J., de Beurs, K., Tagesson, T., and Fensholt, R. (2016). Revealing turning points in ecosystem functioning over the Northern Eurasian agricultural frontier. *Glob. Chang. Biol.* 22, 2801–2817. doi: 10.1111/gcb.13267

Hu, T., Hu, H., Li, F., Zhao, B., Wu, S., Zhu, G., et al. (2019). Long-term effects of post-fire restoration types on nitrogen mineralisation in a *Dahurian larch* (*Larix gmelinii*) forest in boreal China. *Sci. Total Environ.* 679, 237–247. doi: 10.1016/j.scitotenv.2019.05.008

Huang, M., Piao, S., Sun, Y., Ciais, P., Cheng, L., Mao, J., et al. (2015). Change in terrestrial ecosystem water-use efficiency over the last three decades. *Glob. Chang. Biol.* 21, 2366–2378. doi: 10.1111/gcb.12873

Justice, C. O., Townshend, J., Vermote, E. F., Masuoka, E., Wolfe, R. E., Saleous, N., et al. (2002). An overview of MODIS land data processing and product status. *Remote Sens. Environ.* 83, 3–15. doi: 10.1016/S0034-4257(02)00084-6

Kamali, A., Khosravi, M., and Hamidianpour, M. (2020). Spatial–temporal analysis of net primary production (NPP) and its relationship with climatic factors in Iran. *Environ. Monit. Assess.* 192, 718–720. doi: 10.1007/s10661-020-08667-7

Koju, U. A., Zhang, J., Maharjan, S., Bai, Y., Zhang, S., and Yao, F. (2020). Analysis of spatiotemporal dynamics of forest net primary productivity of Nepal during 2000–2015. *Int. J. Remote Sens.* 41, 4336–4364. doi: 10.1080/01431161.2020.1717667

Law, B. E., Falge, E., Gu, L., and Baldocchi, D. D. (2002). Environmental controls over carbon dioxide and water vapor exchange of terrestrial vegetation. *Agric. For. Meteorol.* 113, 97–120. doi: 10.1016/S0168-1923(02)00104-1

Le, QB, Nkonya, E, and Mirzabaev, A., 2016. Biomass productivity-based mapping of global land degradation hotspots. In, E Nkonya, A Mirzabaev and BraunJ von (eds) *Economics of land degradation and improvement—A global assessment for sustainable development*. Springer International Publishing, Cham, pp. 55–84.

Li, Y. P., Li, H. B., Li, Y. Y., and Zhang, S. Q. (2017). Improving water-use efficiency by decreasing stomatal conductance and transpiration rate to maintain higher ear photosynthetic rate in drought-resistant wheat. *Crop J.* 5, 231–239. doi: 10.1016/j.cj.2017.01.001

Li, Z., Ma, W., Liang, C., Liu, Z., Wang, W., and Wang, L. (2015). Long-term vegetation dynamics driven by climatic variations in the Inner Mongolia grassland, findings from 30-year monitoring. *Landsc. Ecol.* 30, 1701–1711. doi: 10.1007/s10980-014-0068-1

Li, Y., Piao, S., Chen, A., Ciais, P., Laurent, Z., and Li, X. (2019). Local and teleconnected temperature effects of afforestation and vegetation greening in China. *Natl. Sci. Rev.* 7, 897–912. doi: 10.1093/nsr/nwz132

Lü, Y., Fu, B., Feng, X., Zeng, Y., Liu, Y., Chang, R., et al. (2012). A policy-driven large scale ecological restoration: quantifying ecosystem services changes in the Loess Plateau of China. *PLoS One* 7:31782. doi: 10.1371/journal.pone.0031782

MENG, Y., HE, Z., LIU, B., CHEN, L., and LIU, B. (2020). Changes of spatial distribution and ecosystem service value of oasis wetlands in arid areas: taking three typical inland river basins as examples. *Resour. Sci.* 42, 2022–2034. doi: 10.18402/resci.2020.10.18

Peng, S.-S., Piao, S., Zeng, Z., Ciais, P., Zhou, L., Laurent, Z., et al. (2014). Afforestation in China cools local land surface temperature. *Proc. Natl. Acad. Sci. U. S. A.* 111, 2915–2919. doi: 10.1073/pnas.1315126111

Rodell, M., Houser, P. R., Jambor, U., Gottschalck, J., Mitchell, K., Meng, C. J., et al. (2004). The global land data assimilation system. *Bull. Amer. Meteor. Soc.* 85, 381–394. doi: 10.1175/BAMS-85-3-381

Ruppert, J. C., Holm, A., Miehe, S., Muldavin, E., Snyman, H. A., Wesche, K., et al. (2012). Meta-analysis of ANPP and rainuse efficiency confirms indicative value for degradation and supports non-linear response along precipitation gradients in drylands. *J. Veg. Sci.* 23, 1035–1050. doi: 10.1111/j.1654-1103.2012.01420.x

Shen, Y. P., Su, H. C., Wang, G. Y., Mao, W. M., Wang, S. D., Han, P., et al. (2013). The response of glaciers and snow cover to climate in Xinjiang(I):hydrological effect. *J. Glaciol. Geocryol.* 35, 513–527. doi: 10.7522/j.issn.1000-0240.2013.0061

Stavi, I., and Lal, R. (2015). Achieving zero net land degradation, challenges and opportunities. *J. Arid Environ.* 112, 44–51. doi: 10.1016/j.jaridenv.2014.01.016

Tang, X., Zhao, X., Bai, Y., Tang, Z., Wang, W., Zhao, Y., et al. (2018). Carbon pools in China's terrestrial ecosystems, new estimates based on an intensive field survey. *Proc. Natl. Acad. Sci. U. S. A.* 115, 4021–4026. doi: 10.1073/pnas.17002911

Taylor, S. H., Hulme, S. P., Rees, M., Ripley, B. S., Woodward, F. I., and Osborne, C. P. (2010). Ecophysiological traits in C3 and C4 grasses, a phylogenetically controlled screening experiment. *New Phytol.* 185, 780–791. doi: 10.1111/j.1469-8137.2009.03102.x

Wang, H., Liu, G., Li, Z., Wang, P., and Wang, Z. (2019). Comparative assessment of vegetation dynamics under the influence of climate change and human activities in five ecologically vulnerable regions of China from 2000 to 2015. *Forests* 10:317. doi: 10.3390/f10040317

Wang, Q. W., Yu, D. P., Dai, L. M., Zhou, L., Zhou, W. M., Qi, G., et al. (2010). Research progress in water use efficiency of plants under global climate change. *Chin. Acad. Sci.* 21, 3255–3265. doi: 10.13287/j.1001-9332.2010.0440

Wei, X., Wang, S., and Wang, Y. (2018). Spatial and temporal change of fractional vegetation cover in North-Western China from 2000 to 2010. *Geol. J.* 53, 427–434. doi: 10.1002/gj.3030

Wessels, K. J., Van Den Bergh, F., and Scholes, R. (2012). Limits to detectability of land degradation by trend analysis of vegetation index data. *Remote Sens. Environ.* 125, 10–22. doi: 10.1016/j.rse.2012.06.022

Xu, X. (2022). *The identification of artificial and natural modes for vegetation restoration and their degradation risk assessment—A case study in the Loess Plateau* Northwest A&F University, 1–6.

Yang, L., Feng, Q., Wen, X., Barzegar, R., Adamowski, J. F., Zhu, M., et al. (2022). Contributions of climate, elevated atmospheric CO2 concentration and land surface changes to variation in water use efficiency in Northwest China. *Catena* 213:106220. doi: 10.1016/j.catena.2022.106220

Yang, Q., Liu, G., Casazza, M., Dumontet, S., and Yang, Z. (2021). Ecosystem restoration programs challenges under climate and land use change. *Sci. Total Environ.* 807:150527. doi: 10.1016/j.scitotenv.2021.150527

Zhang, P., Deng, M., Long, A., Deng, X., Wang, H., Hai, Y., et al. (2020). Coupling analysis of social-economic water consumption and its effects on the arid environments in Xinjiang of China based on the water and ecological footprints. *Arid Land* 12, 73–89. doi: 10.1007/s40333-020-0050-5

Zhang, K., Kimball, J. S., Nemani, R. R., and Running, S. W. (2010). A continuous satellite-derived global record of land surface evapotranspiration from 1983 to 2006. *Water Resour. Res.* 46:W09522. doi: 10.1029/2009WR008800

Zhao, W., Chen, S. P., and Lin, H. G. H. (2009). Effects of long-term grazing on the morphological and functional traits of Leymus chinensis in the semiarid grassland of Inner Mongolia, China. *Ecol. Res.* 24, 99–108. doi: 10.1007/s11284-008-0486-0

Zheng, S., Lan, Z., Li, W., Shao, R., Shan, Y., Wan, H., et al. (2011). Differential responses of plant functional trait to grazing between two contrasting dominant C3 and C4 species in a typical steppe of Inner Mongolia, China. *Plant Soil* 340, 141–155. doi: 10.1007/s11104-010-0369-3

Zheng, K., Tan, L., Sun, Y., Wu, Y., Duan, Z., Xu, Y., et al. (2021). Impacts of climate change and anthropogenic activities on vegetation change, evidence from typical areas in China. *Ecol. Indic.* 126, 107648–107613. doi: 10.1016/j.ecolind.2021.107648

Zhu, W. Q., Pan, Y. Q., He, H., Yu, D., and Hu, H. (2006). Simulation of maximum light utilization of typical vegetation in China. *Chin. Sci. Bull.* 51, 700–706. doi: 10.1360/972005-555

Wen-Quan, Z. H. U., Yao-Zhong, P. A. N., and Jin-Shui, Z. H. A. N. G.Key Laboratory of Environmental Change and Natural Disaster of Ministry of Education, College of Resources Science and Technology, Beijing Normal University, Beijing 100875, China (2007). Estimation of net primary productivity of CHINESE terrestrial vegetation based on remote sensing. *Chin. J. Plant Ecol.* 31, 413–424. doi: 10.17521/cjpe.2007.0050

Zuo, Y., Li, Y., He, K., and Wen, Y. (2022). Temporal and spatial variation characteristics of vegetation coverage and quantitative analysis of its potential driving forces in the Qilian Mountains, China, 2000–2020. *Ecol. Indic.* 143:109429. doi: 10.1016/j.ecolind.2022.109429

frontiers | Frontiers in Environmental Science

TYPE Original Research
PUBLISHED 19 April 2023
DOI 10.3389/fenvs.2023.1144686

OPEN ACCESS

EDITED BY
Xiaoyang Zhang,
South Dakota State University,
United States

REVIEWED BY
Preet Lal,
Michigan State University, United States
Kyle D. Buck,
United States Environmental Protection Agency (EPA), United States

*CORRESPONDENCE
Md Sariful Islam,
shariful@vt.edu

RECEIVED 14 January 2023
ACCEPTED 03 April 2023
PUBLISHED 19 April 2023

CITATION
Islam MS, Crawford TW and Shao Y (2023), Evaluation of predicted loss of different land use and land cover (LULC) due to coastal erosion in Bangladesh. *Front. Environ. Sci.* 11:1144686. doi: 10.3389/fenvs.2023.1144686

Evaluation of predicted loss of different land use and land cover (LULC) due to coastal erosion in Bangladesh

Md Sariful Islam*, Thomas W. Crawford and Yang Shao

Department of Geography, Virginia Polytechnic Institute and State University, Blacksburg, VA, United States

Coastal erosion is one of the most significant environmental threats to coastal communities globally. In Bangladesh, coastal erosion is a regularly occurring and major destructive process, impacting both human and ecological systems at sea level. The Lower Meghna estuary, located in southern Bangladesh, is among the most vulnerable landscapes in the world to the impacts of coastal erosion. Erosion causes population displacement, loss of productive land area, loss of infrastructure and communication systems, and, most importantly, household livelihoods. With an aim to assess the impacts of historical and predicted shoreline change on different land use and land cover, this study estimated historical shoreline movement, predicted shoreline positions based on historical data, and quantified and assessed past land use and land cover change. Multi-temporal Landsat images from 1988–2021 were used to quantify historical shoreline movement and past land use and land cover. A time-series classification of historical land use and land cover (LULC) were produced to both quantify LULC change and to evaluate the utility of the future shoreline predictions for calculating amounts of lost or newly added land resources by LULC type. Our results suggest that the agricultural land is the most dominant land cover/use (76.04% of the total land loss) lost over the studied period. Our results concluded that the best performed model for predicting land loss was the 10-year time depth and 20-year time horizon model. The 10-year time depth and 20-year time horizon model was also most accurate for agricultural, forested, and inland waterbody land use/covers loss prediction. We strongly believe that our results will build a foundation for future research studying the dynamics of coastal and deltaic environments.

KEYWORDS

coastal erosion, land loss, land use and land cover, Lower Meghna river, Bangladesh

1 Introduction

Coastal erosion is one of the most prominent problems in coastal areas globally and the world's mega-deltas are heavily impacted (Woodroffe et al., 2006). Human life and natural environements are threatened by coastal erosion. Due to erosion, coastal lands are being swallowed by the seawater and people are forced to move inland. A recent global study found that the earth surface lost about 28,000 km^2 land during 1984–2015, which is twice the surface land area gained (Mentaschi et al., 2018). Coastal erosion is caused by many different physical (e.g., strong wave action, upstream discharge, river bathymetry) and anthropogenic

factors (e.g., global warming, sea level rise). Soil properties such as texture and structure govern pore size distribution have an influence on soil's erodibility. Studies suggest that soil moisture has substantial influence on water runoff and soil erosion (Wei et al., 2007; Lal et al., 2023). Due to coastal erosion, people living in the coast lose their valuable lands and properties. Climate change driven coastal erosion is posing extra risk for the coastal ecosystems. Increased frequency and severity of the events including storm, rainfall and flood, increased freshwater input to the marine systems and lengthening open water periods are influencing coastal erosion process in addition to the rising sea level (Sanò et al., 2011; Radosavljevic et al., 2016). Mean sea level rose 11–16 cm during 20th century (Hay et al., 2015; Dangendorf et al., 2017), possibly exacerbating coastal erosion globally. Land subsidence is another factor that is influencing coastal erosion risk. For instance, a study on land subsidence and its effects on coastal erosion in the Nam Dinh Coast of Vietnum found that the combined effects of land subsidence and relative sea level rise (SLR) were responsible for 66% of the observed rate of erosion (Nguyen and Takewaka, 2020). Resulting inundation from rising seas will heavily impact low-lying areas, impacting at least 100 million persons globally who live within 1 m of mean sea level (Zhang et al., 2004). This is a tremendous threat for the people living in the coastal communites.

Coastal communities in Bangladesh are vulnerable to different natural hazards and disasters due to close proximity to the sea and sea level. Most parts of coastal areas in Bangladesh are within few meters of the sea level. Extreme erosion is one of the biggest problems threatening the livelihoods of coastal populations, especially the poor. Coastal Bangladesh is highly vulnerable to coastal erosion; land erosion and accretion rates are among the highest in the world (Brammer, 2014; Ahmed et al., 2018; Crawford et al., 2021). It is a recurring driver of homelessness impacting thousands of people annually. The coastal poor are the most susceptible to these impacts. A study by Kumar et al. (2022) suggested that a proper afforestation measures in the upper cathments of Brahmaputra basin might reduce soil erosion and subsequent impacts on the riverbank communities.

Bangladesh is considered as one of the most vulnerable countries to the impacts of climate change in the world, particularly sea-level rise (Nicholls et al., 2007; Sarwar and Khan, 2007; Davis et al., 2018). Moreover, future global warming and subsequent rising sea levels seriously threaten coastal populations in this part of the world. Additionally, as economically marginalized populations live in coastal Bangladesh, the magnitudes and severity of the affected people may affect the total economic growth of the country (Hossain et al., 2016). As a lower middle-class country like Bangladesh, with limited internal resources, it is hard to cope with catastrophic natural hazards like erosion and its related consequences (Poncelet et al., 2010). Additionally, disasters like coastal erosion create the acute problems of unemployment in coastal rural areas and thereby worsen the socio-economic condition of displaced people. Most of these displaced people become landless, which pushes them further into poverty and forces migration. Future climate change is more likely to impact the migration decisions of the people living in coastal Bangladesh in search of prosperous livelihoods (Call et al., 2017).

Due to coastal erosion, people living on the coast not only lose their valuable lands and houses but also infrastructure, communication systems, and most importantly their livelihood (Monirul Alam et al., 2017). A proper estimation of different types of land loss is crucial for better understanding of the impacts of shoreline movement. It is particularly important for proper planning and implementation of appropriate environmental practices. Land use and land cover analysis using satellite imagery is a cost-effective way to monitor long-term changes. Many different methods are used to classify land use and land cover. The maximum likelihood, random forest, support vector machine, and artificial neural network methods were found to be most applied method for LULC analysis (Otukei and Blaschke, 2010; Rodriguez-Galiano et al., 2012; Balha and Singh, 2022). It is well evident that in the recent decades, human activity has significantly influenced land use and land cover globally (Lambin and Geist, 2008). A significant portion of the global population lives near the coast. As a result, it is expected that the coastal ecosystem will change globally due to a large number of human footprints in the coastal region. For regions experiencing the loss or gain of land resources due to erosion/accretion processes, it is important to map existing land use and land cover (LULC) and to integrate resulting data products with information on future shoreline change.

Coastal landscapes are changing rapidly due to both natural and anthropogenic activities in Bangladesh and elsewhere (Muttitanon and Tripathi, 2005; Olaniyi et al., 2012; Abdullah et al., 2019; Ekumah et al., 2020). In Bangladesh, coastal landscape is changing over time due to many reasons. A recent study by Abdullah et al. (2019) found that the vegetation coverage in the coastal Bangladesh is declining day by day due to natural (e.g., flooding, cyclones, etc.) as well as human influenced alterations (e.g., shrimp farming). They also found that river areas have increased by 4.52 percent within 27 years (1990–2017). This indicates that, as this part of the country is the heart of the Ganges-Brahmaputra Meghna (GBM) delta, coastal areas of Bangladesh are experiencing erosion at alarming rates over the last few decades. Global warming and sea level rise is putting extra fuel on ever changing coastal landscape in Bangladesh. A similar study by (Rahman et al., 2017) found 26 percent increase in shrimp farm area from 1989–2015. During this 26 year of period, about 21% of bare lands declined. This is an indication that this highly dynamic coastal region of Bangladesh is changing rapidly.

With an aim to assess the impacts of historical and predicted shoreline change on different land use and land cover, this study estimated historical shoreline movement, predicted shoreline positions based on historical data, and quantified and assessed land loss due to historical and predicted shoreline movement. In our previous study, we assessed the predicted performance of shoreline movement (Islam and Crawford, 2022). We analyzed how prediction performance varies depending on the time depths of input historical shoreline data and the time horizons of predicted shorelines. Our results suggested that the higher the number of shorelines used in calculating and predicting shoreline change rates the better predictive performance was yielded. Though the prediction performance varied spatially, we found that prediction accuracies were substantially higher for the immediate future years compared to the more distant future. In this study, we assess how different LULC classes changed due to historical and predicted

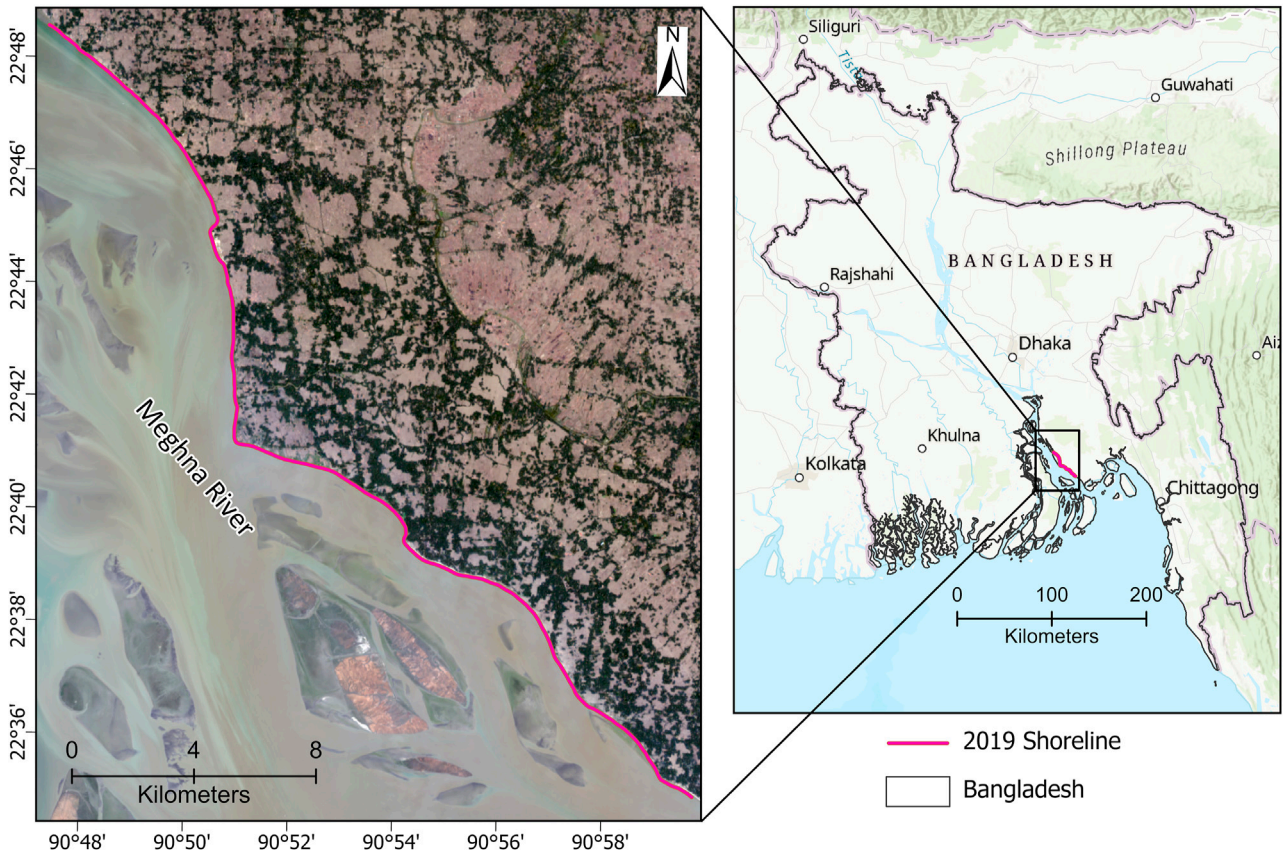

FIGURE 1
The location of study area in coastal Bangladesh. In the map, natural color band combinations (4, 3, 2) were used to show the actual landscape in this part of the coast.

shoreline movement. The specific goals of this study were to 1) assess historical land loss in the Lower Meghna river region of Bangladesh, 2) measure the amount of different LULC has been lost to erosion over defined time intervals, and 3) estimate how well predicted shorelines predict amounts of succeeding LULC resources lost to erosion.

2 Materials and methods

2.1 Study area

The area covered in this study consists of Ramgati and Kamalnagar upazilla of Lakshmipur district in Bangladesh. The upazillas are the second lowest elevation administrative units in Bangladesh. The study area covers approximately 885 km^2 with an estimated population of 490,000 (BBS, 2011). This area is located in coastal Bangladesh along the Lower Meghna river (Figure 1), which is highly prone to different natural hazards and disasters including coastal erosion, flooding, cyclones, etc. This area is a major hotspot of coastal erosion in the country (Crawford et al., 2021). Peoples living in this part of the coastal Bangladesh are mostly dependent on agriculture and fishing for their livelihood (Paul et al., 2021; Rahman et al., 2021, 2022).

2.2 Data

Multitemporal Landsat satellite imagery from 1988–2021 was used in this study. Landsat satellite data were obtained from the USGS Earth Explorer website (https://earthexplorer.usgs.gov/). Landsat imagery (30 m resolution) were used for both shoreline mapping and LULC classification. To avoid cloud issues, we obtained imagery only from the dry season. This allowed us to acquire cloud free scenes. Landsat imagery is widely used for quantification of coastal erosion and land use and land cover change (Ghoneim et al., 2015; Ahmed et al., 2018; Crawford et al., 2021). Additionally, this research used high resolution satellite imagery from Google Earth Pro for post classification accuracy assessment.

2.3 Shoreline extraction

After getting the imagery, multiple steps were followed to extract shorelines. First, the Modified Normalized Difference Water Index (MNDWI) was used to create an index that enhances the ability to distinguish between open water and non-open water sources (Xu, 2006). MNDWI makes use of the middle infrared and green bands. Values ranges from −1 to 1, where water pixels approach 1 and are

easily distinguishable from other pixels. It is a widely used method to separate water and non-water pixels (Singh et al., 2015; Crawford et al., 2021). Second, MNDWI images were used as an inputs with other Landsat bands to classify images into different classes. The ISO cluster unsupervised classification was used to classify the image into 10 classes. After getting the classification output, it was reclassified into two classes, water and non-water via visual interpretation. A similar approach was used to generate annual vector shorelines from 1988–2021. Shoreline uncertainty was assessed by considering different uncertainty terms, including georeferencing uncertainty, pixel uncertainty, digitizing uncertainty, and uncertainty due to tidal variation. Shoreline total uncertainty was assessed using the following equation provided by (Hapke et al., 2011).

$$\text{Utotal} = \sqrt{Ug^2 + Up^2 + Ud^2 + Ut^2} \quad (1)$$

Where, Utotal = total uncertainty, *Ug* = georeferencing uncertainty, *Up* = pixel uncertainty, *Ud* = digitizing uncertainty, and *Ut* = uncertainty associated with tide.

To assess shoreline uncertainty, we adopted a similar approach used in our previous research (Crawford et al., 2020; Islam and Crawford, 2022). The shoreline uncertainty analysis suggest that the mean uncertainty related to georeferencing (*Ug*), pixel (*Up*), digitizing (*Ud*), and tidal variation (*Ut*) were 4.72, 30, 0, and 7.32 m respectively. The mean total uncertainty (*Utotal*) was found to be 32.27 m.

2.4 Shoreline change rates calculation

Shoreline change rate was calculated using the DSAS (Digital Shoreline Analysis System), a software package for quantification of shoreline movement developed by United States Geological Survey (Thieler et al., 2009). There are several widely accepted methods for estimating coastal erosion rates including End Point Rate (EPR), Linear Regression Rate (LRR), Net Shoreline Movement (NSM), and Weighted Linear Regression (WLR) (Ciritci and Türk, 2020; Crawford et al., 2020, 2021). In this study, the LRR rates were used to estimate shoreline change rates. This method is the most used method for coastline change analysis (Kanwal et al., 2022). The LRR rate is calculated by fitting a least-squares regression line to all shoreline points for along digital transects that are cast orthogonal from an offshore or onshore baseline to the mapped shorelines. This method is applied to the set of transects such that each transect obtains a position-specific shoreline change rate and uncertainty value.

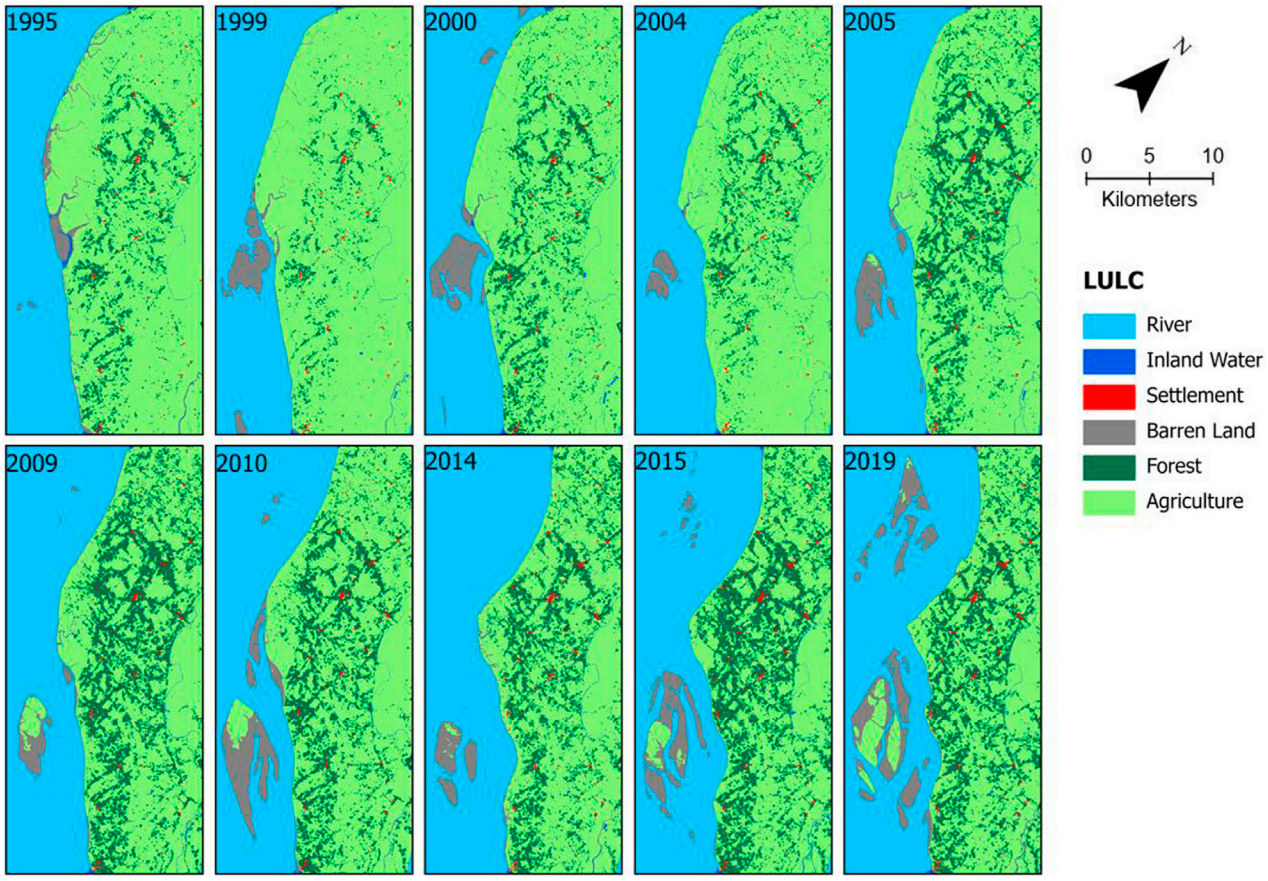

FIGURE 2
Land use and land cover (LULC) of the coastal Lakshmipur region.

2.5 Shoreline prediction

We used LRR rates to predict future shoreline position. Prediction involves a general two-step process. First, we generated shoreline change rates using the LRR method. Second, we used these rates as inputs for future shoreline prediction. Future shoreline prediction is implemented by simple extrapolation of historical rates deployed in ArcGIS via relevant geoprocessing tools and/or original scripts to automate processing. One of the essential aspects of this research was establishing a temporal strategy to predict future shorelines. Our strategy included two different variables: time depth and time horizon. Here, time depth means the number of years of shoreline data used in DSAS (e.g., 5 years means 5 years of annual shorelines as input to DSAS for estimates of transect-specific shoreline rates). Time horizon can be defined as the year of prediction in the future. For time depth, we used three different time depths of 5, 10, and 15 years; for time horizon we used four different time horizons of 1, 5, 10, and 20 years into the future. Using 5, 10, and 15-year time depths of shoreline rates, future shoreline positions were predicted for different time horizons (e.g., 1, 5, 10, and 20 years). After deriving the predicted shoreline movement rates for each transect (e.g., LRR), we created the predicted shoreline positions along the transect using the following equation.

$$(x_t, y_t) = \left(((1-t)x_0 + tx_1), ((1-t)y_0 + ty_1)\right) \quad (2)$$

Where, Start point = (x_0, y_0)

End point = (x_1, y_1)

Predicted Point = (x_t, y_t)

The distance between Start and End point, $d = \sqrt{(x_1 - x_0)^2 + (y_1 - y_0)^2}$

Distance ratio, $t = (d_t/d)$

Predicted distance = d_t

Finally, we used the geoprocessing functionality of ArcGIS Pro to create the predicted linear shorelines by connecting predicted shoreline points of sequentially adjacent transects created by the above equation.

2.6 Land use and land cover (LULC) classification and accuracy assessment

Based on the satellite images' spectral characteristics and familiarity with the study area's land use, we identified and classified six LULC categories for the years 1995, 1999, 2000, 2004, 2005, 2009, 2010, 2014, 2015, and 2019 (Figure 2). A detailed description of the LULC categories can be found in Table 1. We used the Random Forest (RF) and Support Vector Machine (SVM) algorithms to classify land use/cover. Random Forest is a robust machine learning classifier that balances ease of implementation and generalization ability (Rodriguez-Galiano et al., 2012). It is one of the most widely used land use land cover change classifiers (Rodriguez-Galiano et al., 2012; Zhou et al., 2020). The Support Vector Machine (SVM) algorithm is also found to be one of the most widely used algorithms in land use and land cover classification (Huang et al., 2002; Otukei and Blaschke, 2010). For a given land cover mapping task, it is often a good practice to examine multiple machine learning algorithms to compare and select a better performer (Ren et al., 2021).

Post-classification accuracy is an essential part of LULC analysis. After getting the classified image, an accuracy assessment was conducted using high-resolution imagery in Google Earth Pro. Our initial assessment found that the accuracy of the SVM classifier was slightly better. As a result, we used SVM-classified LULC products for all the subsequent analyses. After getting the classified data, we found that the urban pixels are overly estimated for most of the years and underestimated for several years. To make the urban pixels consistent, we fused the Urban Settlement Footprint (WSF) data product of the German Aerospace Center (Marconcini et al., 2020). The World Settlement Footprint (WSF) evolution is a 30 m resolution dataset of the global settlement extent. First, we mask out urban/built-up class using WSF results. Second, we classify the remaining study area based on our classification scheme. Finally, our classified image was fused with the WSF products using the raster calculator tool in ArcGIS Pro.

We assessed classification accuracy for the year 2015, first using the Create Accuracy Assessment Points tool in ArcGIS Pro to create 300 random points. Each land cover/use covers 60 random points. Accuracy was assessed using standard methods, including user's accuracy, producer's accuracy, overall classification accuracy, and the kappa coefficient. Our accuracy assessment result suggested that the 2015 LULC map had an overall accuracy of 86.67% and the Kappa statistic was 0.83 (Table 2). A high Kappa statistic value indicates that the relation between the predicted and actual land use is very strong. The user accuracy analysis suggested that all classes except built-up (75%) had greater than 80% accuracy. For producer accuracy, the barren and forest class had highest (96%) and lowest (75.68%) accuracy, respectively.

TABLE 1 Description of the LULC categories used for the classification.

LULC category	Description
River Water	Meghna river
Inland Water	Permanent and seasonal wetlands (e.g. ponds or lakes), river tributaries, canals, and other active hydrological features
Urban/Built-up	Commercial, residential, industrial, transportation and other areas with artificial structures
Barren land	Recently developed islands, dry canals or ponds, exposed soils
Forest area	Natural or Homestead forest, mixed forest lands
Agricultural land	Cultivated land, croplands, fallow lands, and vegetable fields

TABLE 2 Result of LULC accuracy assessment for the year 2015.

LULC category	Water	Urban	Barren	Forest	Agriculture	Total	UA (%)
Water	58	0	1	0	1	60	96.67
Urban	1	45	1	12	1	60	75.00
Barren	8	0	48	1	3	60	80.00
Forest	0	1	0	56	3	60	93.33
Agriculture	0	2	0	5	53	60	88.33
Total	67	48	50	74	61	300	
PA (%)	86.57	93.75	96.00	75.68	86.89		
OA (%)	86.67						
K	0.83						

Note: UA, User's Accuracy; PA, Producer's Accuracy; OA, Overall Accuracy; K, Kappa Coefficient

2.7 Impacts of shoreline change on land use and land cover calculation

Historical and predicted shorelines were overlaid with classified LULC to assess the impacts of coastal erosion on different land use and land cover. This provided historical estimation of LULC that has been impacted by coastal erosion, as well as the estimation of the future impacts. Using the actual and predicted shoreline, we created polygon to estimate the area lost. We used clip raster tool to extract area that is lost by overlaying the LULC and polygon layer. This allowed us to estimate both the total land loss and the land loss by LULC type. We used similar approach to estimate both the actual and predicted land loss for all the shoreline prediction scenarios. One goal of this overlay analysis was to quantify how well previously generated shoreline predictions perform in predicting lost or gained LULC in terms of lost area by LULC type. For example, for 2010 and 2015, we had the actual 2010 and 2015 shorelines and LULC for both years. Additionally, we produced predicted shorelines for 2015 based on the actual 2010 shoreline and using selected time depths of historical shorelines leading up to 2010 (e.g., 5 years, 10 years, and 15 years time depths). These results allowed for a comparison of the actual vs. predicted lost LULC due to erosion after the 2010 to 2015 study period. A similar approach was used for other years of assessment. A detailed description of the methodology followed for predicting future shorelines using different time depths and time horizons can be found in our previously published research (Islam and Crawford, 2022). Finally, the zonal statistics tool in ArcGIS Pro was used to extract the actual and predicted land use and land cover lost.

2.8 Land loss accuracy assessment

We used recall, precision, and F1 Score metrics to evaluate the predicted land use/cover lost accuracy. The recall, precision and F1 score are confusion matrix-based metrics. The F1 score metric is a more balanced metric than recall and precision (Chicco and Jurman, 2020). All these metrics are broadly used for assessing prediction accuracy (Tseng et al., 2022). The values of the metrics mentioned above range from 0 to 1. A higher value of a metric indicates higher prediction accuracy. The metrics were calculated using the following equations. In this case, true positive (TP) means overlapping areas of actual and predicted land loss. False positive (FP) and false negative (FN) means over-predicted and under-predicted land loss areas. Figure 3. Depicts a schematic diagram of land loss accuracy assessment.

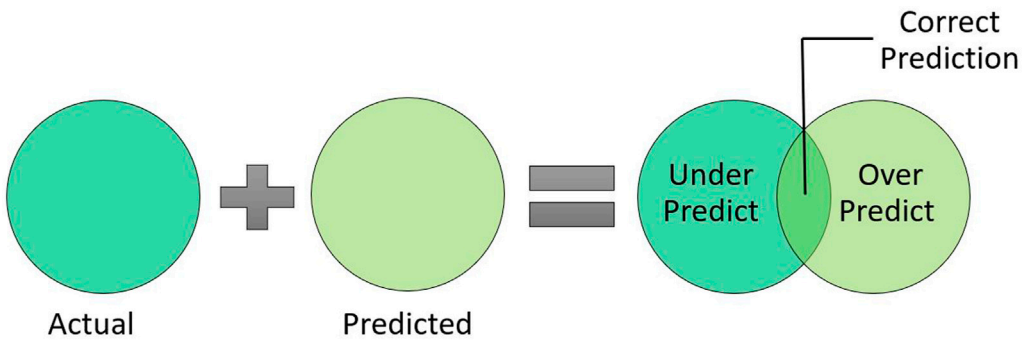

FIGURE 3
Schematic diagram of land loss accuracy assessment.

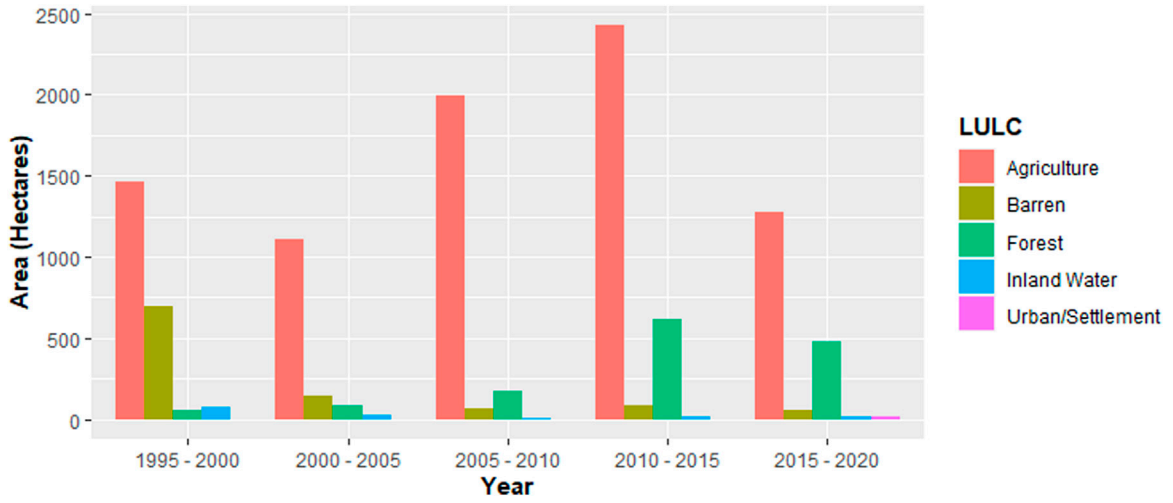

FIGURE 4
Historical land/LULC loss from 1995 to 2020.

$$Recall = \frac{Ture\ Positive\ (TP)}{True\ Positive\ (TP) + False\ Negative\ (FN)} \quad (3)$$

$$Precision = \frac{True\ Positive\ (TP)}{True\ Positive\ (TP) + False\ Positive\ (FP)} \quad (4)$$

$$F1\ score = 2^{*}\frac{Precision^{*}\ Recall}{Precision + Recall} \quad (5)$$

2.9 Statistical analysis

We used two non-parametric statistical Friedman test and Wilcoxon signed-rank test to assess the difference among models. The Friedman test is widely used for multiple comparisons of different models (Khosravi et al., 2018). We used a *p*-value less than 0.05 ($\alpha = 0.05$) to be statistically significant. In addition to the Friedman test, we used the Wilcoxon signed-rank test since Friedman does not provide a pairwise comparison of the models. The Wilcoxon signed-rank tests are typically used to check the statistical significance of pairwise comparisons of the models (Nhu et al., 2020). The probability of the hypothesis is assessed here: whether to accept or reject a null hypothesis. The null hypothesis is rejected if there is a significant difference between different models (Nickerson, 2000).

3 Results

3.1 Spatio-temporal patterns of land loss

The land loss due to erosion between 1995–2020 is shown in Figure 4. During the study period, agricultural land represented the LULC incurring the most loss (76.04%). This was expected, as agricultural land is the region's dominant land use/cover (Figure 2). Forest land accounted for approximately 12.93% of the total land loss. Other land cover types included barren, inland waterbodies, and settlements that were estimated to be lost at levels of 9.57%, 1.27%, and 0.19%, respectively. Previous studies suggest that most people living on this part of the coast depend on farming/agriculture and fishing for their livelihood (Paul et al., 2020; Rahman et al., 2021). As such, agricultural land loss forces people to migrate and threatens their livelihood. Among the different studied periods, the highest (3,137 ha) and lowest (1,367 ha) land losses were during 2010–2015 and 2000–2005. During 1995–2000, approximately 2,285.64 ha of land were lost. Land loss decreased in the following half-decade period (2000–2005). After that, it increased until the mid of the last decade. The latter half of the last decade experienced a decreased amount of land loss compared to the first half. Factors like upstream water discharge, wave energy, storm events, and heavy rainfall are possible drivers of these trends.

3.2 Model comparison—total land loss

Land loss prediction performance was evaluated by averaging the ranking of each metric. We followed a similar ranking approach to Moayedi et al. (2020) who evaluated the performance of different image classification algorithms. First, we ranked individual metrics (e.g., recall, precision, F1) based on the prediction performance. Second, we averaged the ranking of all metrics to get the final rank. The results of individual metric ranking indicate that the best-performing model for recall was 5 year time depth and 1 year time horizon; for precision it was 15 year time depth and 10 year time horizon, and for F1, 10 year time depth and 20 year time horizon (Table 3). Our final ranking system suggests that the best model was the 10 year time depth and 20 year time horizon, followed by the 5 year time depth and 20 year time horizon model. Our lowest-ranked model was the 15 year time depth and 1 year time horizon model. This indicates the performance was best while 10 years of shoreline data were used to predict shoreline positions 20 years in the future. This result also aligns with our previous research (Islam

TABLE 3 Ranks of different combinations of time depth and time horizon evaluation for total land loss.

Time Depth	Time Horizon	Count	Recall		Precision		F1		Total Rank	Final Rank
			Mean	Rank	Mean	Rank	Mean	Rank		
5	1	10	0.688	1	0.643	8	0.654	5	14	4
5	5	9	0.617	5	0.627	9	0.591	9	23	8
5	10	7	0.594	8	0.690	5	0.617	7	20	7
5	20	3	0.654	3	0.713	4	0.663	4	11	2
10	1	9	0.617	5	0.597	10	0.586	10	25	9
10	5	8	0.645	4	0.658	7	0.624	6	17	6
10	10	6	0.604	7	0.766	3	0.669	2	12	3
10	20	2	0.680	2	0.812	2	0.740	1	5	1
15	1	7	0.592	9	0.594	11	0.575	11	31	11
15	5	6	0.558	11	0.679	6	0.597	8	25	9
15	10	4	0.565	10	0.817	1	0.668	3	14	4

TABLE 4 Performance evaluations of different models using Friedman's test.

Models	Recall		Precision		F1	
	Mean Rank	*p*-Value	Mean Rank	*p*-Value	Mean Rank	*p*-Value
5TD_1TH	2.29	0.180	1.43	0.156	2.43	0.276
5TD_5TH	1.43		2.14		1.57	
5TD_10TH	2.29		2.43		2.00	
10TD_1TH	1.67	0.607	1.17	**0.042***	1.33	0.069
10TD_5TH	2.17		2.33		2.00	
10TD_10TH	2.17		2.50		2.67	
15TD_1TH	2.00	0.779	1.00	**0.039***	1.50	**0.050***
15TD_5TH	1.75		2.25		1.50	
15TD_10TH	2.25		2.75		3.00	

TD, Time Depth; TH, Time Horizon; *indicates $p < 0.05$

and Crawford, 2022), where we assessed the prediction performance of shoreline movement.

In addition to the ranking system, the model performance was also evaluated by the non-parametric Friedman test and Wilcoxon signed-rank test. As mentioned earlier, the null hypothesis is rejected if the *p*-value is less than 0.05 ($\alpha = 0.05$). If the *p*-value is less than 0.05, there is a statistically significant difference in model performance. The Friedman test results suggested a statistically significant difference in model performance for multiple models used. The lowest *p*-value of Friedman test was found to be 0.042, while difference in model performance was assessed using precision values for 10-year time depth and 1-year time horizon, 10-year time depth 5-year time horizon, and 10-year time depth and 10-year time horizon. The results of the Friedman's test are shown in Table 4.

The Friedman test does not provide any information on pairwise comparison. As a result, we used Wilcoxon signed rank test to discover the statistically significant performance difference between two models. The Wilcoxon test results suggest that multiple pairs of models exhibit statistically significant differences in prediction performance ($\alpha = 0.05$). Among different model pairs, 5-year time depth and 1-year time horizon *versus* 5-year time depth and 5-year time horizon exhibit a *p*-value less than 0.05 for precision and F1 score. Other significant pairs of models are 10-year time depth and 1-year time horizon *versus* 10-year time depth and 10-year time horizon with a *p*-value less than 0.05 ($\alpha = 0.05$) for both precision and F1 score. These statistically significant results of different pairs illustrate that there are multiple models where the results are significantly different from one another. Detailed results of Wilcoxon signed-rank tests can be found in Table 5.

TABLE 5 Performance of different models by Wilcoxon signed-rank test.

No.	Pairwise Comparison	Recall		Precision		F1	
		z-Value	*p*-Value	z-Value	*p*-Value	z-Value	*p*-Value
1	5TD1TH vs 5TD5TH	−1.836	0.066	−0.178	0.859	−2.310	**0.021***
2	10TD1TH vs 10TD5TH	−0.280	0.779	−0.980	0.327	−0.280	0.779
3	15TD1TH vs 15TD5TH	−0.405	0.686	−1.483	0.138	−0.405	0.686
4	5TD5TH vs 5TD10TH	−1.014	0.310	−0.676	0.499	−0.845	0.398
5	10TD5TH vs 10TD10TH	−0.314	0.753	−1.153	0.249	−1.153	0.249
6	15TD5TH vs 15TD10TH	−1.461	0.144	−1.826	0.273	−1.826	0.068
7	5TD1TH vs 5TD10TH	−0.507	0.612	−0.676	0.499	−0.676	0.499
8	10TD1TH vs 10TD10TH	−0.524	0.600	−1.992	**0.046***	−2.201	**0.028***
9	15TD1TH vs 15TD10TH	−0.365	0.715	−1.826	0.068	−1.826	0.068

TD, Time Depth; TH, Time Horizon; *indicates $p < 0.05$

TABLE 6 Rank of different combinations of time depths and time horizons evaluation for land loss by LULC type.

Time Depth	Time Horizon	Final Rank				
		Agricultural Land	Forested Land	Urban /Settlement	Waterbody	Barren Land
5	1	5	3	5	10	11
5	5	8	9	3	8	7
5	10	7	7	4	5	5
5	20	4	2	10	3	9
10	1	8	7	7	11	10
10	5	6	5	2	7	5
10	10	3	4	6	2	1
10	20	1	1	9	1	3
15	1	11	10	11	9	7
15	5	8	11	1	6	4
15	10	2	6	7	3	2

3.3 Model comparison—land loss by different LULC

Our results suggest that the model with 10 years time depth and 20 years time horizon performed the best for agricultural land, forest, and water body. The 15 years time depth and 5 years time horizon model performed the best for the urban class. In case of barren land loss prediction, the 10 years time depth and 10 years time horizon model performed the best. The 15 years time depth and 1 year time horizon model perfomed the worst for land cover classes of agricultural land and urban. For forest, waterbody and barren land, the worst performing models were found to be 15 years time depth and 5 years time horizon, 10 years time depth and 1 year time horizon, and 5 years time depth and 1 year time horizon model, respectively. Table 6 shows the ranking of land loss prediction performance by different LULC.

While evaluating results for individual metrics used for assessing prediction performance, we found that the F1 rank had the most influence on the final ranking. It is expected because among the metrics used the F1-score was found to be most balanced metric for accuracy assessment. Due to the nature of variables used in the accuracy metric equation, the ranking result varied. For instance, in case of agricultural land, the 5 years time depth and 1 year time horizon performed best for recall. On the other hand, the best performing models based on precision and F1 score are: 15-year time depth and 10-year time horizon and 10-year time depth and 20-year time horizon models, respectively. In case of forest land, we found that 5 years time depth and 1 year time horizon model performed best based on recall value, 15-year time depth and 10-year time horizon performed best for precision and 10-year time depth and 20-year time horizon model performed best based on F1 score ranking. A detailed ranking

for different metrics used can be found in Supplementary Tables S1–S5.

4 Discussion

In this study, land loss due to historical and predicted shoreline movement was quantified and assessed using Landsat satellite imagery from 1988–2021. This study used 34 years of data, enabling us to assess the land loss prediction performance for a rich time series of data. The study area is located in coastal Bangladesh along the eastern bank of Meghna river. Our previous studies found that this area is highly prone to erosion (Crawford et al., 2021; Islam and Crawford, 2022). This side of the riverbank is eroding at an alarming rate; thousands of economically marginalized inhabitants of the delta are continually displaced.

The study demonstrated that overall land loss decreased from the last half of the 1990 s to the mid of 2000 s (Figure 5). After 2005, the land loss increased until 2015, and afterward, it decreased again. The performance of 10-year time depth and 20-year time horizon model was found to be the best (Rank 1) for predicting future land loss. Among the different land use/cover predictions, the 10-year time depth and 20-year time horizon model was found to be the best model for predicting agricultural, forest, and inland waterbodies loss. In the urban and barren land loss prediction, the 15-year time depth and 5-year time horizon and 10-year time depth and 10-year time horizon models were found to be best performing models, respectively. Our analysis of Friedman and Wilcoxon signed-rank tests results suggests a statistically significant difference among the different model performances.

Compared to much of the coastal erosion literature, this work draws from a 34 years time series of satellite-derived shorelines at annual temporal resolution. This time depth enables us to employ a temporal design strategy expected to yield a robust characterization of space-time erosion patterns. It also enables us to empirically assess the performance of future land use/cover loss predictions by predicting future shoreline positions depending on the time depths of input historical shoreline data. This is a methodological innovation with the potential for prediction of future land use/cover loss, and is applicable to other deltas and vulnerable coastal areas globally. With the increasing availability of high spatial/temporal remote sensing data, our methods can be generalized to derive a robust database of shorelines. We advocate developing and calibrating shoreline predictions using longer time-series data. While empirical results are specific to the project's study area, results can inform the region's future land use/cover loss and associated mitigation and adaptation strategies.

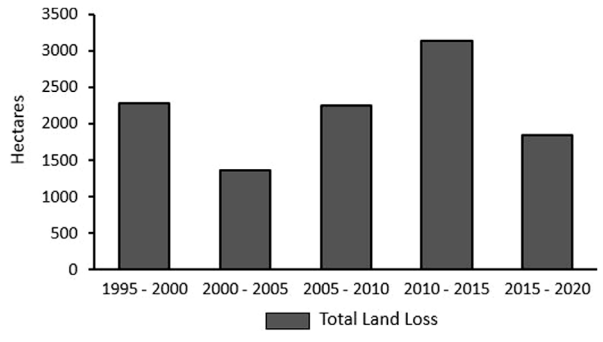

FIGURE 5
Total land loss in the studied area during 1995–2020.

4.1 Limitations of the study

Our analysis provides one of the first assessments of how well predicted shoreline movement predicts amounts of LULC resources lost to erosion. Nevertheless, this study has limitations that point to future research opportunities. First, we predicted future shoreline positions solely based on the extrapolation of historical erosion rates. We know that coastal erosion rates might differ over time due to factors including flooding, cyclones, sea level rise, sediment transportation, extreme rainfall events, wave intensity, height, etc. (Sanuy and Jiménez, 2019; Bamunawala et al., 2021). Since this study didn't consider these factors while predicting future shoreline positions, our prediction might get under or over-estimated for some years. Second, our analysis of LULC suggests that several classes were under or overestimated for some years. For example, urban classes were underestimated, primarily due to the built structure of these areas. Most of the houses in this part of the coast are located near/under homestead forest. As a result, we believe certain residential areas were classified as forest cover. Similar to the urban areas, water bodies like small ponds or narrow canals were classified as forest cover, and sometime even as barren land. On the other hand, we believe that the barren lands were overestimated for some years due to the depths of some wetlands or ponds being very shallow. Third, our study site is located in coastal Bangladesh where the rates of erosion are among the highest in the world. The prediction accuracy of future shoreline locations might vary based on the type, rates or location of the coast. Finally, we used Landsat imagery for both LULC and coastal erosion analysis. The pixel size of Landsat imagery is 30 m. High-resolution imagery might better and accurately detect shoreline movement and LULC. Where possible, future studies might be prioritized to investigate different types of coastal landscapes with differing erosion rates.

5 Conclusion

Coastal areas are impacted by erosion globally. The severity and magnitude of coastal erosion is often high in the deltaic environments. Due to erosion, people lose their households, agricultural lands, and livelihoods. In this study, we assess the impacts of historical and predicted shoreline change on different land use and land covers in Bangladesh's Lower Meghna estuary region. This area is highly susceptible to the damaging coastal erosion. Long-term time series data at an annual scale during

1988–2021 were used to assess the prediction performance of different land use/cover losses. We employed a temporal design strategy of three different time depths and four different time horizons to predict future land loss for different scenarios. Agricultural lands were the top most lost land use class (76.04% of total land loss). Our results suggest that the best-performing model for land loss prediction was 10-year time depth and 20-year time horizon (rank 1) followed by the 5-year time depth and 20-year time horizon model. Among the individual land cover loss prediction, 10-year time depth and 20-year time horizon model were best performing model for the agricultural, forested and inland waterbodies loss prediction. Though the results are specific to our study area located in coastal Bangladesh, they can inform and help refine other models to predict land loss due to erosion in other parts of the coastal and deltaic environment worldwide. The results of this study provide spatiotemporally specific evidence useful for targeted coastal land management by planners, policymakers, and other relevant stakeholders.

Data availability statement

The raw data supporting the conclusion of this article will be made available by the authors, without undue reservation.

Author contributions

Conceptualization, MSI and TWC; methodology, MSI, TWC, and YS; software, MSI; validation, TWC; formal analysis, MSI; data curation, MSI and TWC; writing—original draft preparation, MSI; writing—review and editing, MSI, TWC, and YS; visualization, MSI; supervision, TWC and YS; funding acquisition, TWC. All authors have read and agreed to the published version of the manuscript.

Funding

This research was funded by the U.S. National Science Foundation, grant number 1660447. The article processing costs were partially supported by Virginia Tech's Open Access Subvention Fund (OASF).

Acknowledgments

We would like to thank Munshi Khaledur Rahman for his contribution in generating shorelines for the initial years while working as a postdoctoral researcher in this project.

Conflict of interest

The authors declare that the research was conducted in the absence of any commercial or financial relationships that could be construed as a potential conflict of interest.

Publisher's note

Supplementary material

The Supplementary Material for this article can be found online at: https://www.frontiersin.org/articles/10.3389/fenvs.2023.1144686/full#supplementary-material

References

Abdullah, A. Y. M., Masrur, A., Adnan, M. S. G., Baky, M. A. A., Hassan, Q. K., and Dewan, A. (2019). Spatio-temporal patterns of land use/land cover change in the heterogeneous coastal region of Bangladesh between 1990 and 2017. *Remote Sens.* 11, 790. doi:10.3390/rs11070790

Ahmed, A., Drake, F., Nawaz, R., and Woulds, C. (2018). Where is the coast? Monitoring coastal land dynamics in Bangladesh: An integrated management approach using GIS and remote sensing techniques. *Ocean Coast. Manag.* 151, 10–24. doi:10.1016/j.ocecoaman.2017.10.030

Balha, A., and Singh, C. K. (2022). "Comparison of maximum likelihood, neural networks, and random forests algorithms in classifying urban landscape," in Application of remote Sensing and GIS in natural Resources and built infrastructure management *water science and technology library*. Editors V. P. Singh, S. Yadav, K. K. Yadav, G. A. Corzo Perez, F. Muñoz-Arriola, and R. N. Yadava (Berlin, Germany: Springer International Publishing), 29–38. doi:10.1007/978-3-031-14096-9_2

Bamunawala, J., Ranasinghe, R., Dastgheib, A., Nicholls, R. J., Murray, A. B., Barnard, P. L., et al. (2021). Twenty-first-century projections of shoreline change along inlet-interrupted coastlines. *Sci. Rep.* 11, 14038. doi:10.1038/s41598-021-93221-9

BBS (2011). *Statistical yearbook of Bangladesh*, Ministry of Planning, Dhaka, Bangladesh.

Brammer, H. (2014). Bangladesh's dynamic coastal regions and sea-level rise. *Clim. Risk Manag.* 1, 51–62. doi:10.1016/j.crm.2013.10.001

Call, M. A., Gray, C., Yunus, M., and Emch, M. (2017). Disruption, not displacement: Environmental variability and temporary migration in Bangladesh. *Glob. Environ. Change* 46, 157–165. doi:10.1016/j.gloenvcha.2017.08.008

Chicco, D., and Jurman, G. (2020). The advantages of the Matthews correlation coefficient (MCC) over F1 score and accuracy in binary classification evaluation. *BMC Genomics* 21, 6. doi:10.1186/s12864-019-6413-7

Ciritci, D., and Türk, T. (2020). Assessment of the Kalman filter-based future shoreline prediction method. *Int. J. Environ. Sci. Technol.* 17, 3801–3816. doi:10.1007/s13762-020-02733-w

Crawford, T. W., Islam, M. S., Rahman, M. K., Paul, B. K., Curtis, S., Miah, M. G., et al. (2020). Coastal erosion and human perceptions of revetment protection in the lower Meghna estuary of Bangladesh. *Remote Sens.* 12, 3108. doi:10.3390/rs12183108

Crawford, T. W., Rahman, M. K., Miah, M. G., Islam, M. R., Paul, B. K., and Curtis, S. (2021). Coupled adaptive cycles of shoreline change and households in deltaic Bangladesh: Analysis of a 30-year shoreline change record and recent population impacts. *Ann. Am. Assoc. Geogr.* 111, 1002–1024. doi:10.1080/24694452.2020.1799746

Davis, K. F., Bhattachan, A., D'Odorico, P., and Suweis, S. (2018). A universal model for predicting human migration under climate change: Examining future sea level rise in Bangladesh. *Environ. Res. Lett.* 13, 64030. doi:10.1088/1748-9326/aac4d4

Ekumah, B., Armah, F. A., Afrifa, E. K. A., Aheto, D. W., Odoi, J. O., and Afitiri, A. R. (2020). Assessing land use and land cover change in coastal urban wetlands of international importance in Ghana using Intensity Analysis. *Wetl. Ecol. Manage* 28, 271–284. doi:10.1007/s11273-020-09712-5

Ghoneim, E., Mashaly, J., Gamble, D., Halls, J., and AbuBakr, M. (2015). Nile Delta exhibited a spatial reversal in the rates of shoreline retreat on the Rosetta promontory

comparing pre- and post-beach protection. *Geomorphology* 228, 1–14. doi:10.1016/j.geomorph.2014.08.021

Hapke, C., Himmelstoss, E., Kratzmann, M., and Thieler, E. (2011). National assessment of shoreline change: Historical shoreline change along the new england and mid-atlantic coasts. https://digitalcommons.usf.edu/msc_facpub/2498.

Hossain, Md. S., Dearing, J. A., Rahman, M. M., and Salehin, M. (2016). Recent changes in ecosystem services and human well-being in the Bangladesh coastal zone. *Reg. Environ. Change* 16, 429–443. doi:10.1007/s10113-014-0748-z

Huang, C., Davis, L. S., and Townshend, J. R. G. (2002). An assessment of support vector machines for land cover classification. *Int. J. Remote Sens.* 23, 725–749. doi:10.1080/01431160110040323

Islam, M. S., and Crawford, T. W. (2022). Assessment of spatio-temporal empirical forecasting performance of future shoreline positions. *Remote Sens.* 14, 6364. doi:10.3390/rs14246364

Kanwal, S., Ding, X., Wu, S., and Sajjad, M. (2022). Vertical ground displacements and its impact on erosion along the karachi coastline, Pakistan. *Remote Sens.* 14, 2054. doi:10.3390/rs14092054

Khosravi, K., Pham, B. T., Chapi, K., Shirzadi, A., Shahabi, H., Revhaug, I., et al. (2018). A comparative assessment of decision trees algorithms for flash flood susceptibility modeling at Haraz watershed, northern Iran. *Sci. Total Environ.* 627, 744–755. doi:10.1016/j.scitotenv.2018.01.266

Kumar, A., Mondal, S., and Lal, P. (2022). Analysing frequent extreme flood incidences in Brahmaputra basin, South Asia. *PLOS ONE* 17, e0273384. doi:10.1371/journal.pone.0273384

Lal, P., Shekhar, A., Gharun, M., and Das, N. N. (2023). Spatiotemporal evolution of global long-term patterns of soil moisture. *Science of The Total Environment*, 867, 161470, doi:10.1016/j.scitotenv.2023.161470

Lambin, E. F., and Geist, H. J. (2008). *Land-use and land-cover change: Local processes and global impacts*. Springer Science & Business Media, Berlin, Germany.

Marconcini, M., Gorelick, N., Metz-Marconcini, A., and Esch, T. (2020). Accurately monitoring urbanization at global scale – The world settlement footprint. *IOP Conf. Ser. Earth Environ. Sci.* 509, 12036. doi:10.1088/1755-1315/509/1/012036

Mentaschi, L., Vousdoukas, M. I., Pekel, J.-F., Voukouvalas, E., and Feyen, L. (2018). Global long-term observations of coastal erosion and accretion. *Sci. Rep.* 8, 12876. doi:10.1038/s41598-018-30904-w

Moayedi, H., Jamali, A., Gibril, M. B. A., Kok Foong, L., and Bahiraei, M. (2020). Evaluation of tree-base data mining algorithms in land used/land cover mapping in a semi-arid environment through Landsat 8 OLI image; Shiraz, Iran. *Geomatics, Nat. Hazards Risk* 11, 724–741. doi:10.1080/19475705.2020.1745902

Monirul Alam, G. M., Alam, K., Mushtaq, S., and Clarke, M. L. (2017). Vulnerability to climatic change in riparian char and river-bank households in Bangladesh: Implication for policy, livelihoods and social development. *Ecol. Indic.* 72, 23–32. doi:10.1016/j.ecolind.2016.06.045

Muttitanon, W., and Tripathi, N. K. (2005). Land use/land cover changes in the coastal zone of Ban Don Bay, Thailand using Landsat 5 TM data. *Int. J. Remote Sens.* 26, 2311–2323. doi:10.1080/01431160512331326666

Nguyen, Q. H., and Takewaka, S. (2020). Land subsidence and its effects on coastal erosion in the Nam Dinh coast (vietnam). *Cont. Shelf Res.* 207, 104227. doi:10.1016/j.csr.2020.104227

Nhu, V.-H., Shirzadi, A., Shahabi, H., Singh, S. K., Al-Ansari, N., Clague, J. J., et al. (2020). Shallow landslide susceptibility mapping: A comparison between logistic model tree, logistic regression, naïve bayes tree, artificial neural network, and support vector machine algorithms. *Int. J. Environ. Res. Public Health* 17, 2749. doi:10.3390/ijerph17082749

Nicholls, R. J., Wong, P. P., Burkett, V., Codignotto, J., Hay, J., McLean, R., et al. (2007). Coastal systems and low-lying areas, https://ro.uow.edu.au/scipapers/164/.

Nickerson, R. S. (2000). Null hypothesis significance testing: A review of an old and continuing controversy. *Psychol. Methods* 5, 241–301. doi:10.1037/1082-989X.5.2.241

Olaniyi, A. O., Abdullah, A. M., Ramli, M. F., and Alias, M. S. (2012). Assessment of drivers of coastal land use change in Malaysia. *Ocean Coast. Manag.* 67, 113–123. doi:10.1016/j.ocecoaman.2012.05.029

Otukei, J. R., and Blaschke, T. (2010). Land cover change assessment using decision trees, support vector machines and maximum likelihood classification algorithms. *Int. J. Appl. Earth Observation Geoinformation* 12, S27–S31. doi:10.1016/j.jag.2009.11.002

Paul, B. K., Rahman, M. K., Crawford, T., Curtis, S., Miah, Md. G., Islam, R., et al. (2021). "Coping strategies of people displaced by riverbank erosion in the lower Meghna estuary," in Living on the edge: Char Dwellers in Bangladesh *springer Geography*. Editors M. Zaman and M. Alam (Berlin, Germany: Springer International Publishing), 227–239. doi:10.1007/978-3-030-73592-0_13

Paul, B. K., Rahman, M. K., Crawford, T., Curtis, S., Miah, M. G., Islam, M. R., et al. (2020). Explaining mobility using the community capital framework and place attachment concepts: A case study of riverbank erosion in the lower Meghna estuary, Bangladesh. *Appl. Geogr.* 125, 102199. doi:10.1016/j.apgeog.2020.102199

Poncelet, A., Gemenne, F., Martiniello, M., and Bousetta, H. (2010). "A country made for disasters: Environmental vulnerability and forced migration in Bangladesh," in *Environment, forced migration and social vulnerability*. Editors T. Afifi and J. Jäger (Berlin, Heidelberg: Springer), 211–222. doi:10.1007/978-3-642-12416-7_16

Radosavljevic, B., Lantuit, H., Pollard, W., Overduin, P., Couture, N., Sachs, T., et al. (2016). Erosion and flooding—threats to coastal infrastructure in the arctic: A case study from herschel island, yukon territory, Canada. *Estuaries Coasts* 39, 900–915. doi:10.1007/s12237-015-0046-0

Rahman, M. K., Crawford, T. W., Paul, B. K., Sariful Islam, Md., Curtis, S., Giashuddin Miah, Md., et al. (2021). "Riverbank erosions, coping strategies, and resilience thinking of the lower-meghna river basin community, Bangladesh," in Climate Vulnerability and Resilience in the global South: Human Adaptations for sustainable futures *climate change management*. Editors G. M. M. Alam, M. O. Erdiaw-Kwasie, G. J. Nagy, and W. Leal Filho (Berlin, Germany: Springer International Publishing), 259–278. doi:10.1007/978-3-030-77259-8_13

Rahman, M., Popke, J., and Crawford, T. W. (2022). Resident perceptions of riverbank erosion and shoreline protection: A mixed-methods case study from Bangladesh. *Nat. Hazards* 114, 2767–2786. doi:10.1007/s11069-022-05489-3

Rahman, M. T. U., Tabassum, F., Rasheduzzaman, Md., Saba, H., Sarkar, L., Ferdous, J., et al. (2017). Temporal dynamics of land use/land cover change and its prediction using CA-ANN model for southwestern coastal Bangladesh. *Environ. Monit. Assess.* 189, 565. doi:10.1007/s10661-017-6272-0

Ren, J., Shao, Y., Wan, H., Xie, Y., and Campos, A. (2021). A two-step mapping of irrigated corn with multi-temporal MODIS and Landsat analysis ready data. *ISPRS J. Photogrammetry Remote Sens.* 176, 69–82. doi:10.1016/j.isprsjprs.2021.04.007

Rodriguez-Galiano, V. F., Ghimire, B., Rogan, J., Chica-Olmo, M., and Rigol-Sanchez, J. P. (2012). An assessment of the effectiveness of a random forest classifier for land-cover classification. *ISPRS J. Photogrammetry Remote Sens.* 67, 93–104. doi:10.1016/j.isprsjprs.2011.11.002

Sanò, M., Jiménez, J. A., Medina, R., Stanica, A., Sanchez-Arcilla, A., and Trumbic, I. (2011). The role of coastal setbacks in the context of coastal erosion and climate change. *Ocean Coast. Manag.* 54, 943–950. doi:10.1016/j.ocecoaman.2011.06.008

Sanuy, M., and Jiménez, J. A. (2019). Sensitivity of storm-induced hazards in a highly curvilinear coastline to changing storm directions. The tordera delta case (NW mediterranean). *Water* 11, 747. doi:10.3390/w11040747

Sarwar, G. M., and Khan, M. H. (2007). sea level rise A threat to the coast of Bangladesh. *Int. Asienforum* 38, 375–397.

Singh, K. V., Setia, R., Sahoo, S., Prasad, A., and Pateriya, B. (2015). Evaluation of NDWI and MNDWI for assessment of waterlogging by integrating digital elevation model and groundwater level. *Geocarto Int.* 30, 650–661. doi:10.1080/10106049.2014.965757

Thieler, E. R., Himmelstoss, E. A., Zichichi, J. L., and Ergul, A. (2009). The digital shoreline analysis system (DSAS) version 4.0 - an ArcGIS extension for calculating shoreline change. Reston, VA, USA: US. Geol. Surv. doi:10.3133/ofr20081278

Tseng, H.-H., Yang, M.-D., Saminathan, R., Hsu, Y.-C., Yang, C.-Y., and Wu, D.-H. (2022). Rice seedling detection in UAV images using transfer learning and machine learning. *Remote Sens.* 14, 2837. doi:10.3390/rs14122837

Wei, L., Zhang, B., and Wang, M. (2007). Effects of antecedent soil moisture on runoff and soil erosion in alley cropping systems. *Agric. water Manag.* 94 (1-3), 54–62. doi:10.1016/j.agwat.2007.08.007

Woodroffe, C. D., Nicholls, R. J., Saito, Y., Chen, Z., and Goodbred, S. L. (2006). "Landscape variability and the response of asian megadeltas to environmental change," in Global Change and integrated coastal management: The asia-pacific region *coastal systems and continental margins*. Editor N. Harvey (Amsterdam, Netherlands: Springer Netherlands), 277–314. doi:10.1007/1-4020-3628-0_10

Xu, H. (2006). Modification of normalised difference water index (NDWI) to enhance open water features in remotely sensed imagery. *Int. J. Remote Sens.* 27, 3025–3033. doi:10.1080/01431160600589179

Zhang, K., Douglas, B. C., and Leatherman, S. P. (2004). Global warming and coastal erosion. *Clim. Change* 64, 41–58. doi:10.1023/B:CLIM.0000024690.32682.48

Zhou, L., Dang, X., Sun, Q., and Wang, S. (2020). Multi-scenario simulation of urban land change in Shanghai by random forest and CA-Markov model. *Sustain. Cities Soc.* 55, 102045. doi:10.1016/j.scs.2020.102045

frontiers | Frontiers in Environmental Science

TYPE Original Research
PUBLISHED 03 May 2023
DOI 10.3389/fenvs.2023.1137442

OPEN ACCESS

EDITED BY
Seth Munson,
U.S. Geological Survey, United States

REVIEWED BY
Xiankun Yang,
Guangzhou University, China
Wiwin Ambarwulan,
National Research and Innovation Agency (BRIN), Indonesia

*CORRESPONDENCE
Tianling Qin,
qintl@iwhr.com

RECEIVED 04 January 2023
ACCEPTED 14 April 2023
PUBLISHED 03 May 2023

CITATION
Liu F, Qin T, Liu S, Wang H and Nie H (2023), Spatial response of urban land use change and ecosystem service value in the lower reaches of the Yangtze River: A case study of Tongling, China. *Front. Environ. Sci.* 11:1137442. doi: 10.3389/fenvs.2023.1137442

Spatial response of urban land use change and ecosystem service value in the lower reaches of the Yangtze River: A case study of Tongling, China

Fang Liu[1], Tianling Qin[2]*, Shanshan Liu[2], Hao Wang[2] and Hanjiang Nie[3]

[1]College of Environmental Science and Engineering, Donghua University, Shanghai, China, [2]State Key Laboratory of Simulation and Regulation of Water Cycle in River Basin, China Institute of Water Resources and Hydropower Research (IWHR), Beijing, China, [3]Key Laboratory for Geographical Process Analysis and Simulation of Hubei Province, School of Urban and Environmental Sciences, Central China Normal University, Wuhan, China

Exploring the impact of urban land use change (LUC) on ecosystem services is significant for ensuring urban ecological security and realizing regional economic development. This study used land use data from 1985, 2000, 2014, and 2020 of Tongling city and the CA–Markov model to predict the LUC in 2025 and 2030. The spatio-temporal distribution characteristics of LUC during 1985–2030 were analyzed using the land use dynamics model and Sankey diagram. The vegetation-corrected ecological services value (ESV) equivalent was used to quantify the impact of LUC on ESV. Estimating the profit/loss value and spatial autocorrelation revealed ESV's spatial and temporal dynamics in Tongling city. The results show that: 1) The most obvious LUC in the study area during 1985–2030 is the conversion of cultivated land to built-up land, in which the proportion of cultivated land decreased by 9.6%, and built-up land increased by 12.2%. 2) During 1985–2030, the ESV in Tongling showed an increasing trend at the beginning and then decreased, reaching a maximum value of 274.74 billion yuan in 2000. Regarding individual ecosystem service functions, the hydrological regulation function significantly contributed to ESV changes. The area change in paddy fields and built-up land had the most significant impact on ESV. 3) The total addition of ESV in Tongling during 1985–2030 was 5.98 billion yuan; the total loss was 18.59 billion yuan, and the net loss was 12.6 billion yuan. The proportion of area with ESV gains relative to the whole city is getting smaller, and the proportion of area with ESV losses is growing. The spatial autocorrelation shows the presence of high aggregation in ESV profit and loss areas. Simulating future LUC in Tongling and exploring ESV's response is beneficial to developing new landscape patterns and ecological protection. It also provides a scientific basis for the extensive promotion of sustainable urban development in the future.

KEYWORDS

land use change, ecosystem service value, CA-Markov, characteristics, ESV profit and loss

1 Introduction

Urban land use change (LUC) is a direct manifestation of urbanization. Rapid urban development profoundly affects the changes in the structure and function of different types of urban ecosystems (Dewan and Yamaguchi, 2009; Chatterjee and Majumdar, 2022). Ecosystem services reflect the direct or indirect benefits humans derive from changes in ecosystem structure, processes, and functions (De Groot et al., 2010; Pueffel et al., 2018; Chatterjee et al., 2022). Ecological services value (ESV) is the value generated by natural ecosystems quantified in monetary terms (Vallecillo et al., 2019). Changes in ESV are due to LUC, and substantial LUC has become a major factor in weakening and destroying urban ESV (Rimal et al., 2019; Santos-Martín et al., 2019; Gao et al., 2021a). LUC is also the main driver of changes in the value of ecosystem goods and services (Kindu et al., 2016; Felipe-Lucia et al., 2020). Exploring the impact of urban LUC on ESV has important practical significance for identifying the characteristics of the urban ecological environment changes and optimizing the national landscape planning (Hu et al., 2019; Sun et al., 2020).

Since Costanza et al. pioneered the quantification of global ESV in 1997, ESV research gradually became a hot spot in ecological research and accumulated numerous research results on the impact of urban LUC on ESV (Costanza et al., 1998; Sonter et al., 2017; Himes-Cornell et al., 2018; Syrbe et al., 2018; He et al., 2021; Zhang et al., 2021). Based on this, domestic scholars Xie et al. (2003) developed a Chinese ecosystem service value per unit area scale. Their findings are widely used by scholars in China and abroad. As the research progressed, the direction shifted from global to local and regional scales. Analyzing finer scales and typical regions has prompted more attention to various research questions (Tammi et al., 2017; Sannigrahi et al., 2018). Most studies involve high ESV value areas such as lakes and forests ((Gao et al., 2021b; Schirpke et al., 2021)). The studies mainly focus on the drivers, spatial and temporal changes and influencing factors of ecosystem services (Hu et al., 2022; Devkota et al., 2023). The research methods are mainly based on spatial and statistical analyses (Kubiszewski et al., 2017; Houtven et al., 2019). For example, at a global scale, Nelson et al. (2010) modelled the effects of urban sprawl on ecosystem services. They found that urban sprawl was the main factor contributing to species habitat decline. At the regional scale, Delphin et al. (2016) modelled the effects of urban sprawl on forest ecosystem services in the lower Suwannee River. They found varying degrees of reduction in carbon storage and wood volume. At the local scale, Cao et al. (2021) studied the relationship between regional urbanization characteristics and ecosystem services in China from 2000 to 2015. They found that ESV was positively correlated with economic growth, with significant differences in ESV across ecosystem types.

Aided by remote sensing and GIS technology, many scholars have conducted studies on land use prediction using simulation models. The advantages and disadvantages of these models have also been examined. For example, the FLUS model has unique advantages in simulating complex non-linear problems, but its inherent uncertainty can adversely affect the simulation results (Liang et al., 2018; Liu et al., 2021). The PLUS model can simulate the plot-level changes of multiple land use types and effectively solve the probability of land conversion under the combined effect of natural and human factors. However, it has shortcomings in spatial optimization (Li et al., 2022; Gao et al., 2022). The CLUE-S model systematically simulates the spatial distribution of various land types based on the relationship between land use and driving factors. However, it can only predict land use scenarios for small-scale studies (Chasia et al., 2023; Kiziridis et al., 2023). The CA-Markov model combines the ability of CA models to simulate spatial changes in complex systems. The Markov models are advantageous for long-term prediction since they can effectively simulate urban land use patterns from both temporal and spatial perspectives. They can also accurately predict land use type conversions (Gashaw et al., 2018; Mansour et al., 2020).

Previous studies on the impacts of LUC on ESV have focused mainly on the impact of past land use changes on the current ESV (Clements et al., 2021; Wang and Nuppenau, 2021; Xiang et al., 2022). There is still room for research on potential future trends in ESV. The studies also lack a detailed assessment of the current and future ESV profits and losses. In addition, attention was not given to ESV's spatial differences caused by drastic changes in urban land use. In the context of implementing the Yangtze River conservation strategy and supporting the Yangtze River Economic Belt's green development, Tongling has a typical problem of an unbalanced relationship between urban development and ecological conservation (Peng et al., 2021; Qiao and Huang, 2022). In this study, the CA–Morkov model is used to predict the future land use scenario of Tongling city for 5–10 years. The hot spots of ecological changes and ecological restoration areas were effectively identified by analyzing past and future land use scenario changes and ESV responses. The findings provide a theoretical basis for restoring ecological spots in the city. In addition, identifying ecological spots can also help to understand the ecological evolution mechanism in similar regions and provide scientific reference for the government to develop sustainable land use measures for cities targeted in the national strategic development (Schirpke et al., 2020; Peng et al., 2021).

This study used land use data in 1985, 2000, 2014, and 2020 as the main data source. The CA–Markov model was employed to predict land use patterns in 2025 and 2030 by combining land use information and natural and social driving factors. The spatial and temporal distribution of LUCs from 1985 to 2030 were analyzed using the dynamic LUC model and Sankey diagram. ESV equivalent per unit area was corrected using the normalized difference vegetation index (NDVI). The correction helps to identify ESV's spatial and temporal response to LUC. The profit and loss analysis and spatial autocorrelations were also used to characterize profit and loss changes during 1985–2030. We expect this research to be of practical significance for effective urban planning and the realization of ecological security in Tongling city. The research also provides scientific support for restoring ecological space per the national strategic plan.

2 Study area

Tongling (30°20′–31°09′N, 117°05′–118°10′E) is located in Anhui Province, China (Figure 1). It is located at the intersection of the Yangtze River plains and the mountains of

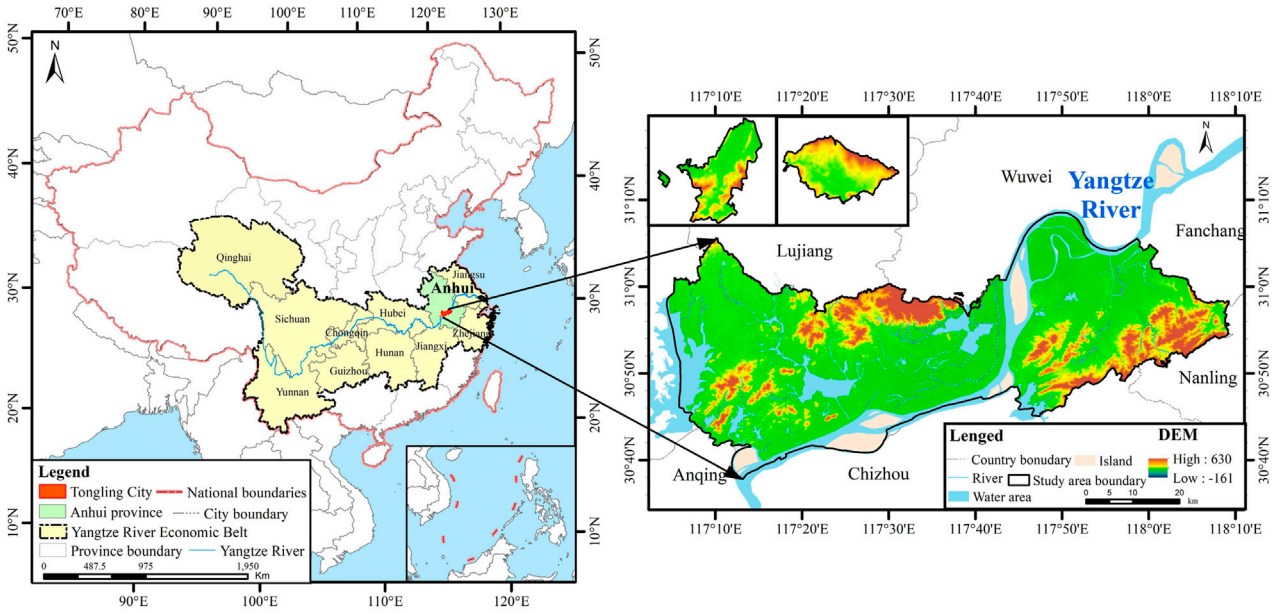

FIGURE 1
The location of the study area.

southern Anhui. The main stream of the Yangtze River is 142.6 km long in Tongling. The section is the most curved and branched section in the middle and lower reaches of the Yangtze River. Tongling is situated in a plain landscape in south-central Anhui, and the city's total area is 2993.81 km^2. The altitude ranges between 100 and 350 m. The city's flat plains, basins and hills account for 63.67%, 14.43%, and 21.9% of the total land area. A humid subtropical monsoon climate with an average temperature of 16.2°C characterizes Tongling. It receives total annual sunshine hours of 2000–2050 h and annual precipitation of 1,247–1,558 mm. The rainfall is concentrated from May to September, accounting for approximately 60% of the annual rainfall. By the end of 2020, Tongling had a resident population of 1,312,000 and a gross regional product of 1003.7 million yuan. In addition, the vegetation cover ≥0.78 area accounted for 82% of the whole city in recent year, indicating the extensive green area and high degree of vegetation cover in Tongling.

3 Materials and methods

3.1 Data sources and processing

The data used in this study include digital elevation model (DEM), slope, land use, remote sensing imagery, socioeconomic, road and meteorological data. The details of these datasets are shown in Table 1. The land use data of Tongling in 1985, 2000, 2014, and 2020 are the main data sources. The data were obtained from the Environmental Science Data Center of the Chinese Academy of Sciences with a spatial resolution of 30 m. The classification accuracy of this data is more than 90%. Following the global land use classification systems such as International Geosphere-Biosphere Programme (IGBP), Food and Agriculture Organization of the United Nations (FAO) and the University of Maryland, the land uses were divided into 6 categories: cultivated land, forest, grassland, water area, built-up land and unused land (Zuo, 2016; Lei et al., 2020). The land covered by human infrastructure and urban construction is defined as built-up land. Considering the local situation of Tongling, the cultivated land and forest classes were further classified into detailed classes. Consequently, the cultivated land is subdivided into dryland and paddy fields, and the forest is subdivided into the broad-leaved forest and shrub wood.

Slope information was obtained from DEM (30 m spatial resolution) using the surface analysis module of ArcGIS10.2 software. The NDVI data were retrieved from the Geospatial Data Cloud, which contains two products, GIMMS and MODIS. This study uses the GIMMS NDVI (8 km spatial resolution) for 1985–2000 and the MODIS NDVI (1 km spatial resolution) for 2001–2020. The remote sensing data from the two sources were downscaled to obtain NDVI data with 30 m spatial resolution. Spatial interpolation of precipitation for 1960–2020 was performed using the spatial interpolation module in ArcGIS10.2 software to obtain the multi-year average surface rainfall in Tongling with 30 m spatial resolution. The food crops' socioeconomic information was obtained from the statistical yearbook of Tongling city. The spatial distribution of the population and gross domestic product (GDP) of Tongling (30 m spatial resolution) was obtained by downscaling the 1 km grid dataset of China's population and GDP. The road data were obtained from the National Center for Basic Geographic Information, and the raster data of highway, expressway and railway with 30 m spatial resolution were generated using ArcGIS10.2 software. The above data were used as drivers for predicting future land use patterns.

TABLE 1 Data types and sources.

Datatype	Main data	Year	Source
Topography	DEM	2002	National Geomatics Center of China http://www.ngcc.cn/ngcc/html/1/index.html
	Slope	—	
Land use	Different land use type	1985, 2000, 2014, and 2020	Resource and Environment Data Cloud Platform of Chinese Academy of Sciences http://www.resdc.cn/
Remote sensing image	NDVI	1985–2020	Geospatial Data Cloud https://www.gscloud.cn/
Climate	Precipitation	1960–2020	National Meteorological Information Center http://www.cma.gov.cn/2011qxfw/2011qsjgx/
Socioeconomic data	Types of food crops	1985, 2000, 2014, and 2020	Bureau of Statistics in Tongling city https://tjj.tl.gov.cn/
	National average price of food crops		
	Grain crop yield per unit area		
	Planting area of grain crops		
	Total acreage of food crops		
	GDP		Resource and Environment Data Cloud Platform of Chinese Academy of Sciences http://www.resdc.cn/
	Population		
Road	Highway	2014 and 2020	The National Center for Basic Geographic Information http:/www.ngcc.cn/
	Expressway		
	Railway		

3.2 Methods

3.2.1 Research ideas

This study simulates the LUC in 2025 and 2030 using the CA–Markov model and five periods of land use data in Tongling. Elevation, slope, precipitation, road, population and GDP data were used as drivers. The dynamic LUC model and Sankey diagram were utilized to characterize each land use type's spatial and temporal changes. Based on the ESV assessment system proposed by previous studies, the equivalence table of each ESV for different land use types in Tongling was constructed. The NDVI was used to correct the ESV equivalents of paddy fields, dryland, broad-leaved forest and shrub wood. Moreover, the equivalence factor method was used to analyze the distribution of ESV of each land use type from 1985 to 2030. In addition, the spatial and temporal dynamics of ESV profit and loss were analyzed using spatial autocorrelation (Figure 2).

3.2.2 Analysis methods

3.2.2.1 CA–Markov model

The CA–Markov model in IDRISI software has been widely used in LUCC simulation studies (Matlhodi et al., 2021; Wang and Wang, 2022). The cellular automata (CA) in land use simulations can generate potential transition maps considering spatial structure and neighborhood states. At the same time, the Markov model can provide a time-varying LUCC transition zone matrix based on time variation. The initial probabilities of the different states of the system and the transfer probabilities between states are used to determine each state's trend at each future moment. The CA–Markov model combines Markov and CA models to compensate for the deficiencies of each model. It can achieve dual prediction of land use types and their spatial distribution. The simulation process is as follows.

1) Complete merging, cropping, adjusting coordinate system and resolution of land use data using ArcGIS software. Then convert the datasets to IDRISI identifiable data.
2) Set the error parameters and interval years based on the land use data for 2014 and 2020. The land use transfer area and transfer probability matrix were obtained using the Markov model in the study area during 2014–2020.
3) Produce the suitability atlas using the "Decision Wizard" module of IDRISI software. This study selected eight factors that greatly impact LUC to create the suitability atlas. They are DEM, slope, average annual precipitation, roads, highways, railroads, population, and GDP.
4) Import the land use transfer area and transfer probability matrix into CA–Markov model with the suitability atlas to simulate the land use scenarios in 2025 and 2030.

In this paper, the Kappa coefficient is used as the evaluation index for the simulation accuracy assessment of the CA–Markov model. When the Kappa coefficient is greater than 0.75, it indicates high simulation accuracy. When the Kappa coefficient is less than 0.4, the simulation results are less consistent with the actual condition (Aksoy and Kaptan, 2021; Cunha et al., 2021). The expressions are:

$$k = \frac{x_{p,i} - x_{a,i}}{x_{a,i}} \times 100\%$$

Where k is the error precision. $x_{p,i}$ is the predicted area of the type i. $x_{a,i}$ is the actual area of the type i.

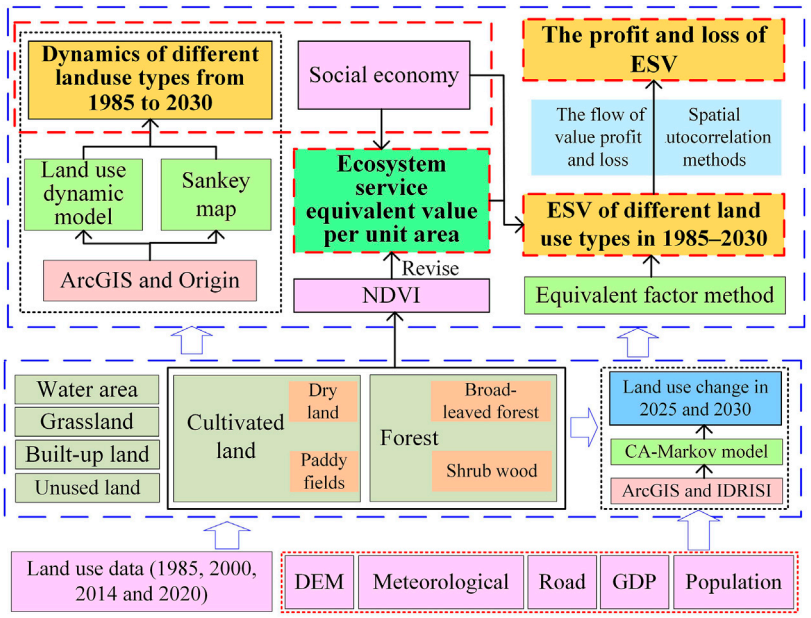

FIGURE 2
Research ideas.

3.2.2.2 Analysis of LUC characteristics

(1) The following land use dynamic models were used to describe the LUC characteristics quantitatively.

$$S_{in} = \frac{\Delta_{in}}{A_{(i,t_1)}} \times \frac{1}{t_2 - t_1} \times 100\% \quad (1)$$

$$S_{out} = \frac{\Delta_{out}}{A_{(i,t_1)}} \times \frac{1}{t_2 - t_1} \times 100\% \quad (2)$$

$$V_i = \frac{\Delta_{in} + \Delta_{out}}{A_{(i,t_1)}} \times \frac{1}{t_2 - t_1} \times 100\% \quad (3)$$

$$V = \frac{\sum_{i=1}^{n} \Delta_{out}}{A_{(i,t_1)}} \times \frac{1}{t_2 - t_1} \times 100\% \quad (4)$$

Where Δ_{in} refers to the area converted from other land use types to a certain type (km^2). Δ_{out} is the area converted from a certain type of land use to other types (km^2). $A_{(i,t_1)}$ is the area of type t_1 in year i (km^2). S_{in} and S_{out} is the area change rate of a certain type in t_1–t_2 years (%). V_i is the dynamic degree of single land use (%). V is the dynamic degree of comprehensive land use (%)

(2) The Sankey diagram was made by origin software to reveal the conversion characteristics of the various land use types in different years (Zhang et al., 2019). The map depicts a network between start and end states, while the different branching lines inside the network represent the conversion of land use types. The width of the stacked bars proportionally shows the percentage of area occupied by this conversion method. The heights at the nodes represent the area of each land use type.

3.2.2.3 Assessment of ESV

1) The value equivalent of various ecosystem services of land use types in Tongling City was assigned following the "China Terrestrial Ecosystem Service Value Equivalent Table per Unit Area" evaluation system. The system was a revision by Xie following the ESV assessment system proposed by Costanza et al. (1998) (Costanza et al., 1998; Xie et al., 2015) (Table 2). Eqs 5, 6 were used to calculate the ESV of Tongling City.

$$ESV = \sum_{i=1}^{m} A_i \times VC_i \quad (5)$$

$$VC_i = \sum_{j=1}^{k} EC_j \times E_a \quad (6)$$

Where ESV is ecosystem service value (yuan/a). i is the type of land use. j is the type of ecosystem service. A_i is the area of land use type (hm^2). VC_i is the ecosystem service value per unit area of land use type i (yuan $hm^{-2}a^{-1}$). EC_j is the value equivalent of ecosystem services for a certain type of land use type item j. E_a is the economic value of 1 unit of ecosystem services (yuan $hm^{-2}a^{-1}$).

The equivalent of ecosystem services for the study area was computed using Eq. 7 below. The economic value of farmland natural grain production in Tongling City in 2014 was calculated, and the economic value of 1 unit of ecosystem services was found to be 3083.8 yuan $hm^{-2}a^{-1}$.

$$E_a = \frac{1}{7} \sum_{g=1}^{n} \frac{w_g p_g q_g}{M} \times MCI \quad (7)$$

where g is the type of food crops. M is the total planted area of food crops (hm^2). w_g is the national average price of the grain crop g

TABLE 2 Ecosystem service equivalent value per unit area for Tongling.

Ecosystem services		Cultivated land		Grassland	Forestland		Water area	Unused land
Primary classification	Secondary classification	Dry land	Paddy fields		Broad-leaved forest	Shrub wood		
Provisioning services	Food production	0.85	1.36	0.38	0.29	0.19	0.8	0
	Raw material production	0.4	0.09	0.56	0.66	0.43	0.23	0
	Water supply	0.02	−2.63	0.31	0.34	0.22	8.29	0
Regulating services	Gas conditioning	0.67	1.11	1.97	2.17	1.41	0.77	0.02
	climatic conditioning	0.36	0.57	5.21	6.5	4.23	2.29	0
	Purify the environment	0.1	0.17	1.72	1.93	1.28	5.55	0.1
	Hydrological regulation	0.27	2.72	3.82	4.74	3.35	102.24	0.03
Supporting services	Soil conservation	1.03	0.01	2.4	2.65	1.72	0.93	0.02
	Maintain nutrient cycling	0.12	0.19	0.18	0.2	0.13	0.07	0
	Biodiversity	0.13	0.21	7.87	2.41	1.57	2.55	0.02
Cultural services	Aesthetic landscape	0.06	0.09	4.73	1.06	0.69	1.89	0.01

(yuan/ kg). p_g is the unit yield of grain crop g (kg/hm^2). q_g is the planted area of grain crop g (hm^2). MAC is the farmland multiple cropping index, and the value of Tongling City is 1.41.

To study the spatial distribution of ESV, we selected the vegetation coverage index (Eq. 8) as the revision index of grid-scale ESV. We used Eqs 9, 10 to revise grid-level ESV. Due to the scarcity of vegetation in the water bodies, the NDVI value for these land use types is ≤0. This study made further revisions for the cultivated land, forest and grassland.

$$f = \frac{NDVI - NDVI_{min}}{NDVI_{max} - NDVI_{min}} \tag{8}$$

$$f_{vi} = \frac{f_{ir}}{\overline{f_r}} \tag{9}$$

$$Ef_{vi} = E_i \times f_{vi} \tag{10}$$

Where f is the vegetation coverage index. i is the grid cell number. r refers to the type of ecosystem, which refers to five types: dry land, paddy field, grassland, broad-leaved forest and shrubbery. f_{vi} is the vegetation coverage revision coefficient of cell i. f_{ir} is the vegetation coverage of type r ecosystem in cell i. $\overline{f_r}$ is the average vegetation coverage of type r ecosystem in the study area. Ef_{vi} is the value equivalent of ecosystem services revised by vegetation cover for cell i. E_i is the regionally revised ecosystem service value equivalent in cell i.

(2) The degree of impact of LUC on ESV was identified through analysis of ESV profit and loss (Ling et al., 2016). Using ArcGIS's fish net creation tool, Tongling City was divided into 1.25×10^4 grid units of 0.5 km × 0.5 km. The spatial autocorrelation analysis of ESV profit and loss was done using Geoda software.

$$PL_{ij} = \left(VC_j - VC_i\right) \times A_{ij} \tag{11}$$

$$IM_i = \frac{\sum\left(PL_{ij} + PL_{ji}\right)}{2PL} \times 100\% \tag{12}$$

Where PL_{ij} is the ESV profit and loss after the conversion of the category i land use type to the category j land use type. VC_i and VC_j are the ESV coefficients of land use types i and j, respectively. A_{ij} is the area of land use type i converted to land use type j (hm^2). IM_i is the impact of LUC on ecosystem service value (%). PL is the profit and loss of ESV.

4 Results

4.1 Simulation of land use scenario in 2025 and 2030 in Tongling

Before the simulation of land use scenarios in 2025 and 2030 in Tongling, the model's accuracy was tested. The land use data for 2014 and 2020 were imported in IDRISI software, the number of cycles was set to 6 years, and a standard 5 × 5 adjacency filter was applied to obtain the LUCC simulated map for 2020. The Kappa index between the simulated and measured maps in 2020 is calculated to be 0.87. The error in cultivated land and forest area is about 5%. The error in the built-up land area is about 4%, and the error in grassland, water area and unused land is less than 3%. The results prove that the CA–Markov model meets the simulation requirements. Based on the 2020 land use data again, the number of cycles was set to 5 and 10 years. The standard 5 × 5 adjacency filter was also applied to obtain land use scenario maps for 2025 and 2030 (Figure 3).

4.2 Characteristics of LUC in Tongling from 1985 to 2030

The most significant aspect of the LUC in Tongling from 1985 to 2020 is the decrease in cultivated land and the increase in built-up land. The area of built-up land in 2020 is three times larger than in

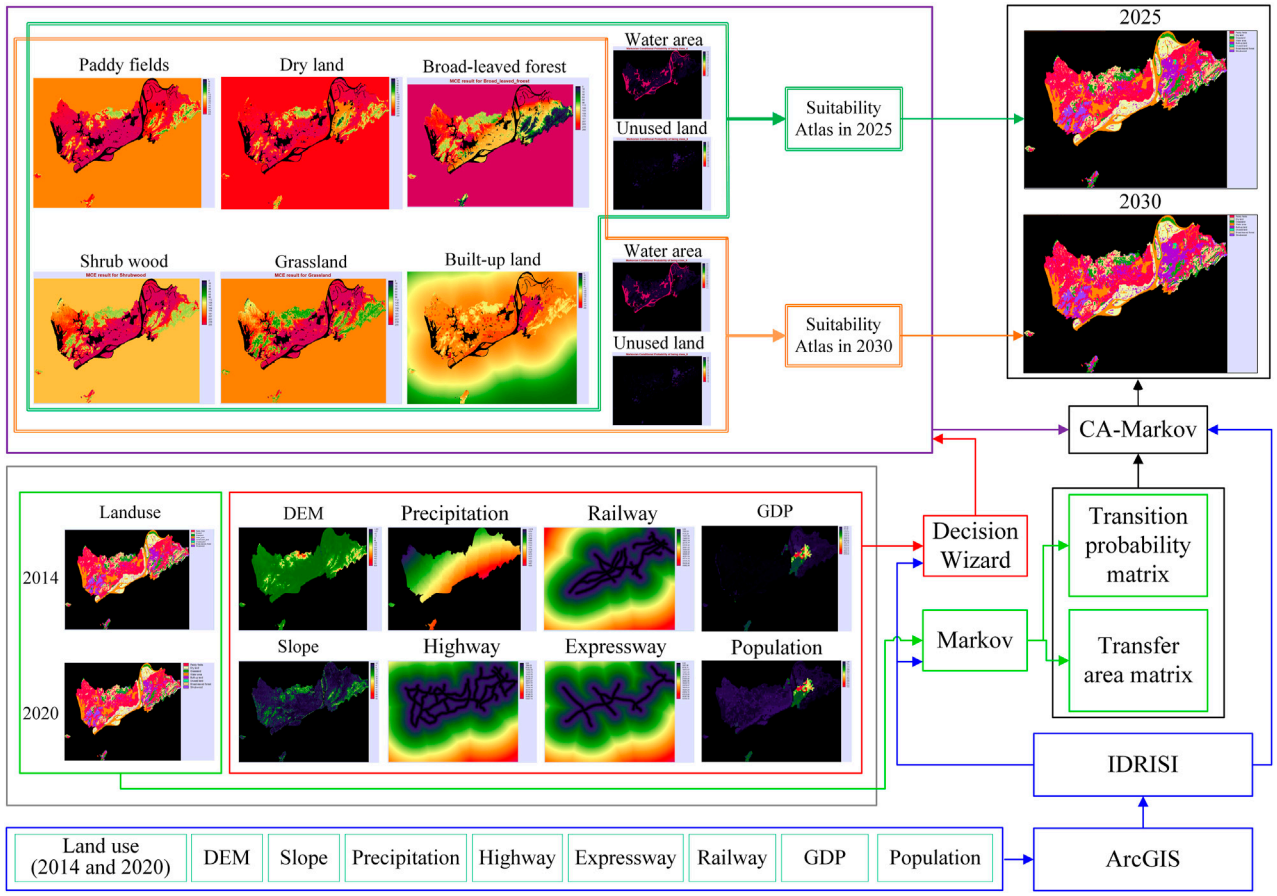

FIGURE 3
Simulation process of land use scenario in 2025 and 2030 with CA-Markov model in Tongling.

1985 (9.25×10^3 hm^2) (Figure 4). The increased area is derived from the conversion of 54.35% of cultivated land, 6.52% of forest and 4.8% of grassland. The built-up land continues to increase by 1.84×10^4 hm^2 in 2020–2030. 72.16% of the area comes from the conversion of cultivated land, and 21.26% and 9.76% of the area comes from forest and grassland, respectively. Generally, the LUC in Tongling from 1985 to 2030 is the conversion between cultivated and built-up land. By 2030, the proportion of cultivated land area in the city will decrease by 9.6%; the proportion of built-up land area will increase by 12.2%; the proportion of forest and grassland area will reduce by 1.4%; and the proportion of both water area and the unused land area will increase by 0.2%.

During 1985–2030, each period's comprehensive land use dynamics fluctuated with an increasing trend. The largest change was observed during 2025–2030 (0.22%), indicating that this period has the most drastic LUC in Tongling (Figure 5). Regarding the individual land use types, all of them maintain an increasing trend except for the built-up and unused land. Built-up land decreased during 1985–2025 and shows an increase during 2025–2030. The change was the largest during 1985–2000 (5.59%) and the smallest during 2020–2025 (0.69%). These two periods are important as the built-up area shows a significant change. The unused land use type increased during 1985–2020 and decreased from 2020 to 2030. The maximum value (6.32%) was obtained during 2014–2020. The result indicates that unused land undergoes the most drastic change during this period, with a threefold increase in area (258.2 hm^2).

4.3 Characteristics of change in ESV in Tongling from 1985 to 2030

4.3.1 Spatial and temporal characteristics in ESV in Tongling from 1985 to 2030

The ESV in Tongling fluctuated from 1985 to 2030, reaching a maximum of 274.74 billion yuan in 2000. The ESV showed an increase of 5.08 billion yuan compared to 1985s (Table 3). The ESV decreased by 27 billion yuan during 2000–2030, with the largest decreases observed in grassland (28.21%), paddy fields (25.22%), and broad-leaved forests (20.96%). The total reduction in ESV from 1985 to 2030 is 15.91 billion yuan. The ESV of cultivated land decreased by 5.27 billion yuan (paddy fields accounted for 80.5%); the ESV of grassland decreased by 4.33 billion yuan; the ESV of forest decreased by 4.96 billion yuan (broad-leaved forest accounted for 65.77%); the ESV of water area decreased by 1.35 billion yuan, and unused land changed very little. In terms of ecosystem service types, from 1985 to 2030, except for the service value of water supply, which

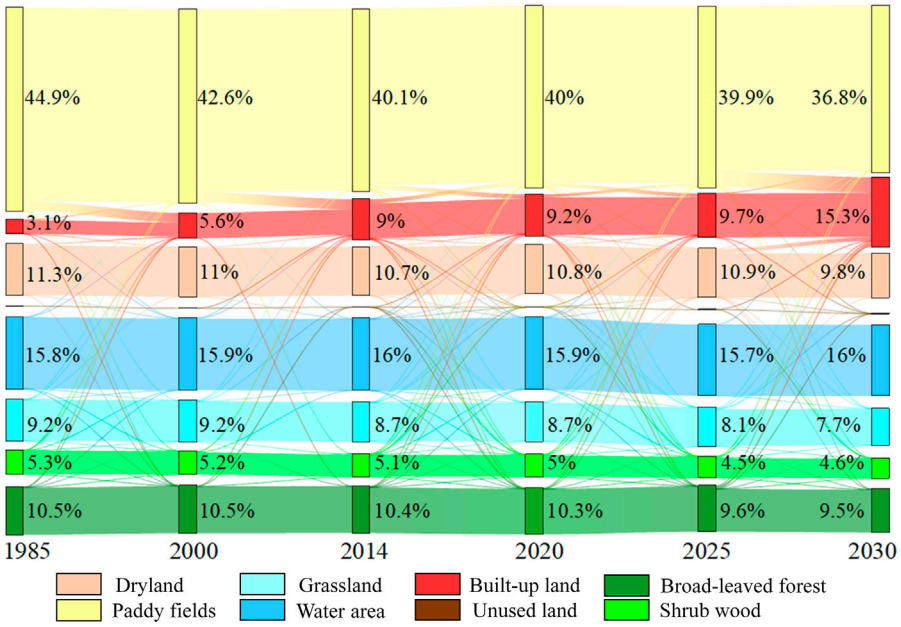

FIGURE 4
The Sankey map of LUC in Tongling from 1985 to 2030.

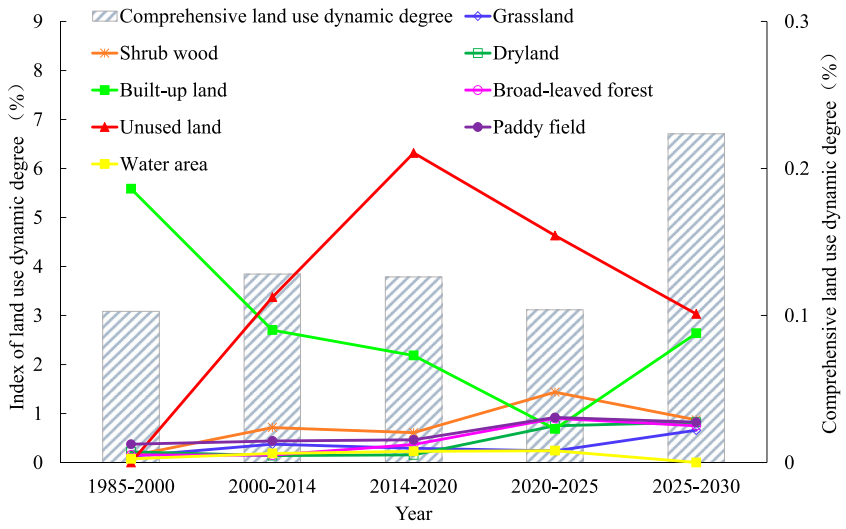

FIGURE 5
The dynamics degrees of different land use types in Tongling during 1985–2030.

increased (266 billion yuan), the service value of other ecosystem types decreased (Figure 6). The hydrological regulation function of the ecosystem contributed the most to ESV, but the variation trends varied greatly. From 1985 to 2020, the ESV of all ecological services increased, and the ESV of hydrological regulation increased the most (2.21 billion yuan). The ESV reduction of hydrological regulation reached the largest during 2020–2030 (7.96 billion yuan) and 1985–2030 (5.75 billion yuan). From 1985 to 2030, changes in the area of paddy fields and built-up land have the most significant impact on ESV (Figure 7). The average impact degree of the paddy field is 12.14%. The average impact degree of built-up land is −42.35%, indicating that its area's increase (decrease) will lead to a decrease (increase) in ESV. The average impacts of woodland and grassland on ESV are negative (−13.42% and −8.03%); The average impact of dryland on ESV is 1.36%, and the unused land has almost no impact.

TABLE 3 Variations of ecological services value (ESV) of different land use types in Tongling (billion yuan).

Years	Cultivated land		Grassland	Forestland		Water area	Unused land	Total
	Dry land	Paddy fields		Broad-leaved forest	Shrub wood			
1985	4.67	17.51	26.20	23.67	8.04	183.55	0.001	263.63
2000	5.10	20.07	29.49	26.07	8.96	185.04	0.001	274.74
2014	5.04	18.07	27.32	25.00	8.45	185.68	0.001	269.56
2025	3.34	11.43	21.01	20.56	6.84	186.44	0.005	249.62
2030	4.22	12.35	20.85	20.18	6.52	186.12	0	250.24
2000–2030 ΔESV	−0.88	−7.72	−8.64	−5.89	−2.44	1.07	0	−24.5
2014–2030 ΔESV	−0.82	−5.72	−6.54	−6.47	−4.82	−1.93	0	−19.32
1985–2030 ΔESV	−0.45	−5.16	−5.35	−3.49	−1.52	2.57	0	−13.4

FIGURE 6
Variations of different types of ESV of Tongling. Note: Bar charts with the same color represent ecosystem service functions of the same classification level. Blue indicates the provisioning service function, including three secondary classification ecosystem service functions: food production, raw material production and water supply. Yellow indicates supporting service functions, including three secondary classification ecosystem services: soil conservation, maintaining nutrient cycling and biodiversity. Green indicates the regulation service function, including four secondary classification ecosystem services: gas conditioning, climatic conditioning, purifying the environment and hydrological regulation. Pink represents the aesthetic landscape in the cultural service function. The abscissa in the line chart represents the 11 ecosystem service functions. The serial order of the functions is as follows: food production, raw material production, water supply, gas conditioning, climatic conditioning, purifying the environment, hydrological regulation, soil conservation, maintaining nutrient cycling, biodiversity and aesthetic landscape.

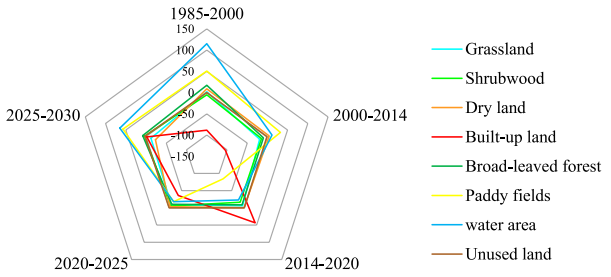

FIGURE 7
The influence degree from different land use types to ESV in Tongling.

4.3.2 Characteristics of ESV profit and loss in Tongling from 1985 to 2030

From 1985 to 2030, the total addition of ESV in Tongling was 5.98 billion yuan. The total loss was 18.59 billion yuan, and a net loss of 12.6 billion yuan (Table 4). The largest contribution to the net loss came from the conversion of cultivated land and forest to built-up land, accounting for 20.03% and 19.04% of the total loss, respectively. The conversion of paddy fields to the water area and shrub forest to the broad-leaved forest are the main sources of value gain, accounting for 30.24% and 42.98% of the total gain in the region. During 1985–2000, the spatial distribution of ESV in Tongling was relatively uniform. With the rapid development of the social economy and the rapid increase in population, the flat right bank of the Yangtze River has been developed into urban centers, significantly increasing the built-up land area. The rapid urbanization forced the low-value areas of ESV to expand from the original sporadic distribution to a large city area. As a result, from 1985 to 2030, the area of ESV gain declined, and the value loss area increased. The loss ultimately led to an increase in the proportion of high-loss ranges. The city's gain area decreased from 0.93% to 0.44%, and the proportion of loss area increased from 6.82% to 7.33% during 2020–2030 compared to 1985–2020 (Figure 8).

The spatial autocorrelation analysis of ESV profit and loss shows that the global Moran's I > 0, $p < 0.001$ in the three periods and the ESV profit and loss scatter points were mainly distributed in the first and third quadrants (Figure 9). It shows that the ESV profit and loss in Tongling has a high spatial correlation, relatively consistent distribution and high aggregation. For 1985–2020 and 2020–2030, the "high-high" and "low-low" aggregation areas of ESV profit and loss are more widely distributed. From 1985 to 2030, the ESV profit and loss of Tongling showed a "low-low" accumulation, mainly in the central urban areas. The "high-high" aggregation occurred in the water area.

5 Discussion

5.1 Simulation of land use scenario with CA-Markov model

In this study, the driving factors for LUC changes were selected from both natural and social attributes to predict the urban land use pattern of Tongling City in the next 5–10 years based on CA–Markov model. The driving factors in natural attributes include elevation, slope and precipitation. Related studies have shown that elevation and slope are crucial factors affecting the layout of cultivated land. As their values increase, they have a negative effect on cropland layout (Mansour et al., 2020). Precipitation affects woodland changes by influencing soil water content, transpiration, and air humidity (Venkatesh et al., 2022). The driving factors in social attributes include road information, population and GDP. They are important factors in limiting the development pattern and changing trends of urban spatial layout, especially in low and medium-density cities (Fu et al., 2018). Using the CA–Markov model, this study predicts an agricultural and forestry area of 2.03×10^5 hm^2 and a built-up land area of 4.87×10^4 hm^2 in Tongling by 2030. The prediction results are consistent

TABLE 4 Loss and profit matrix of ESV in Tongling during 1985–2030 (10^4 yuan).

Land use type in 1985	Land use type in 2030								
	Grassland	Shrub wood	Dryland	Built-up land	Broad-leaved forest	Paddy field	Water area	Unused land	Total
Grassland	−12600.95	−1200.36	−190.87	−21699.15	−1351.52	−5398.80	186.68	−0.85	−42255.82
Shrubwood	65.25	0	−7.94	−13912.58	25688.56	−1009.91	284.81	−92.41	11015.78
Dryland	58.26	27.48	−4027.32	−5367.46	81.10	−105.84	4778.15	0	−4555.64
Built-up land	24.27	0.84	29.49	0	12.74	149.31	240.55	0.03	457.24
Broad-leaved forest	282.16	−119.20	−1.13	−21470.88	−12051.02	−5989.11	1219.38	0	−38129.79
Paddy field	2212.49	1334.14	−1.15	−31866.76	4770.25	−10784.83	18072.51	−646.42	−16909.77
Water area	−1349.29	−585.18	−2480.56	−22053.74	−378.95	−8989.50	0	−73.09	−35910.33
Unused land	242.65	3.75	0	−1.30	0	0	0	0	245.10
Total	−11065.17	−538.52	−6679.48	−116371.88	16771.17	−32128.68	24782.09	−812.74	−126043.22

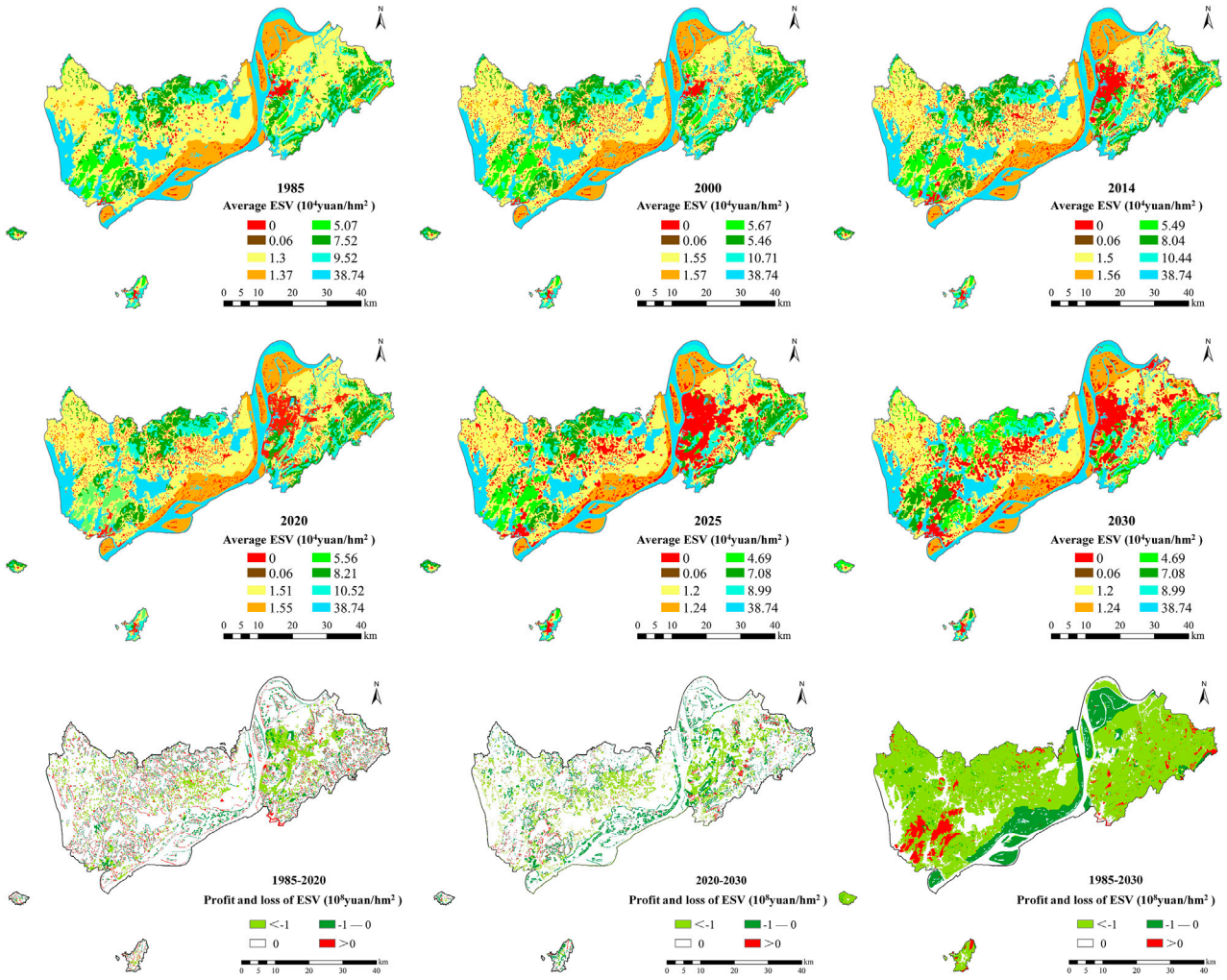

FIGURE 8
Spatial distribution pattern and the profit and loss of ESV in Tongling during 1985–2030.

with the provisions of the Tongling City Urban Master Plan (2016–2030) for agricultural and forestry area (1.94×10^5 hm^2) and built-up land area (4.9×10^4 hm^2). The finding shows that the selected drivers and the predicted land use layouts are reasonable.

5.2 Characteristics of LUC

This study found that in the past 35 years, the most significant change in Tongling City is the three-fold increase in the built-up land area, mainly from the transformation of cultivated land, forest land and grassland. Tongling is an important city in the Yangtze River Economic Belt. Since 2000, the efficiency of urban land use in the Yangtze River Economic Belt has increased annually. With rapid industrialization and urbanization, land use has also changed rapidly (Zhang and Sun, 2016). In particular, economic values were overly pursued in past land use development. All these factors have led to the rapidly expanding of the built-up land area. Scholars such as Cao et al. (2021), Yuan et al. (2018) and Wang et al. (2017) have verified that this problem exists in different scales and different cities. By forecasting the pattern of urban land use in the next 5–10 years, it is found that the area of built-up land will still increase, mainly due to the conversion of cultivated land. Although China's population will decline slightly by 2021, China's urbanization rate has been growing rapidly from 1990 to 2021, rising from 26.44% (1990) to 64.72% (2021) (Cao et al., 2021). A comprehensive analysis of the five levels of commercial resource agglomeration, urban hub, urban population activity, lifestyle diversity, and future plasticity found that Tongling is a city with relatively slow development in China (Zhang and Sun, 2016). Many factories and enterprises were introduced and developed to promote the development of Tongling City into a more prosperous city. In addition, relying on the golden waterway of the Yangtze River, from the perspective of sustainable development, it is proposed to build an urban green and ecological corridor to create a "win-win" pattern of ecology and economy (Zhai et al., 2021). As a result, the types of forest land and water area did not change much.

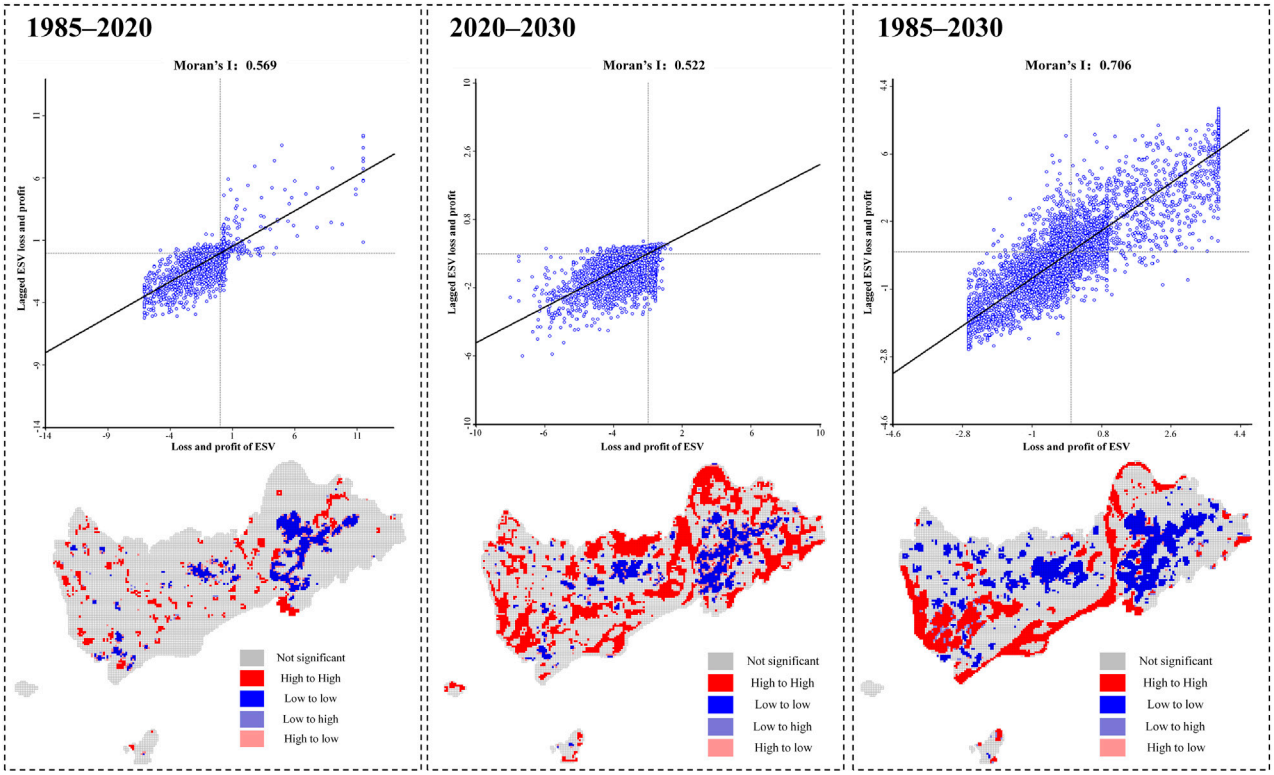

FIGURE 9
Moran scatter diagram and spatial autocorrelation map of ESV profit and loss in Tongling during 1985–2030.

5.3 Characteristics of ESV

In this paper, the equivalent factor method is adopted. Usually, this method can only reflect the overall situation of the study area, and there is no way to reflect its change characteristics in space. Therefore, the value equivalent per unit area of cultivated land, forest land, and grassland types is corrected cell by cell using the NDVI in each period (Jia et al., 2021; Cao et al., 2021). The value equivalent in 2025 and 2030 is the average value equivalent of the corrected value equivalent of NDVI from 1985 to 2020. This method improves the accuracy of the results to a certain extent. This study found that the ESV of Tongling increased at the beginning and then decreased, reaching the maximum value in 2000 (274.74 billion yuan). Although the biggest change in land use from 1985 to 2000 was the conversion of paddy fields to built-up land, ESV did not decrease. The reason is the influence of ESV on value equivalent correction. The grid-by-grid NDVI values of cultivated land, grassland, and woodland in 2000 were all higher than those in 1985, especially for the forest. Even though the area decreased, the NDVI was higher (Chu et al., 2022). Therefore, reasonably determining the ESV correction coefficient is important in estimating the true response to ESV changes in the study area (Barrera et al., 2016; Fenta et al., 2020). After 2000, a large amount of cultivated land was transferred to built-up land, and the area of forest land also decreased to a certain extent, which greatly reduced the service capacity of the ecosystem.

According to statistics, by 2020, the forest coverage rate and afforestation area in Tongling City decreased by 8.59% and 6.56%, respectively, and the pressure on the ecological environment increased (Wu et al., 2017). These reductions eventually led to a year-on-year decrease in ESV, which is consistent with the continuous decrease in ESV caused by the development of most cities in China during the same period (Rong et al., 2017; Liu et al., 2021). From 1985 to 2030, the total addition of ESV in Tongling was 5.98 billion yuan, and the total loss was 1.859 billion yuan. The ESV profit and loss in Tongling are closely related to urban spatial structure and topography. The loss of ESV in the flat south bank of the Yangtze River has gradually increased with urbanization and cultivated land conversion into built-up land (Li et al., 2022). In the forest land types on the north bank of the Yangtze River, the ESV increased significantly due to the transformation from shrub wood to the broad-leaved forest. This transformation makes the ESV profit and loss show significant positive spatial autocorrelation characteristics on the global scale.

5.4 Strategies to increase ESVs in urban development

Studies have shown that woodlands and watersheds are important aspects of the ESV, illustrating the value of lucid waters and lush mountains for sustainable development (Qiao and Huang, 2022). Tongling is an important city along the

Yangtze River that relies on the Yangtze River's golden waterway to achieve a sustainable economy and ecological environment. In the future, the ecological environment protection of Tongling could focus on forest land and water areas. Under the background of decreasing cultivated land and increasing built-up land, the urban spatial layout needs to be optimized from three aspects.

1) The area of urban green space could be increased, and the interplanting structure of understory land could be optimized. It is recommended to develop urban ecological corridors considering the key water areas along the river.
2) The reduction of cultivated land will reduce the value of food production services. The optimum area of cultivated land could be strictly controlled. Furthermore, advanced technology could be introduced to increase grain yield to ensure food security further.
3) The effective utilization of existing built-up land area could be maximized and planned rationally. The occupation of water bodies and forests could be minimized. The industrial structure could also be adjusted to increase the city's carrying capacity.

In this paper, advanced remote sensing observation combined with the CA–Markov model is used to predict the land use of Tongling city in the next 5–10 years. The method integrates the effects of natural, economic and social factors on LUC, and establishes a model of land use evolution under the combination of different influencing factors and different decision makers. It not only improves the accuracy of the simulation, but also the reasonableness of the land use development scenario prediction. The NDVI was incorporated to revise the ESV coefficients. It is the most widely applied method in China at present. Firstly, the method of accounting for NDVI is mature and the accuracy of remote sensing images used for calculation is high, which increases the accuracy of ESV accounting from the source. Secondly, compared with other vegetation indices, the NDVI can accurately reflect the intra- or inter-annual variation characteristics of vegetation cover on forest, grassland and cultivated land. Furthermore, the research results can provide a theoretical reference for the land use and ecological development of urban areas in the Yangtze River Economic Belt.

However, the limitations of the study that need to be pointed out include four aspects.

1) The main driving mechanisms of urban LUC include five aspects: urbanization, economic development, industrial structure, technological development and land marketization. More drivers need to be considered in forecasting future urban growth from the above five aspects, especially the adjustment of industrial structure and layout.
2) This study has uncertainties in predicting the change of the ESV equivalent in 2025 and 2030. The economic value in 2020 is used for the prediction, which may lead to an under- or overestimation of the ESV. In follow-up research, the future value equivalent of changes in ecosystem services will be carefully evaluated to improve the accuracy of ESV predictions.
3) This study summarizes the types of ecosystem services into four primary categories: provisioning, regulating, supporting and cultural, with a total of 11 secondary categories. But it narrowly defines the types of ecosystem services and lacks thinking about more types of the services, such as: wildlife habitat, healthy functioning soils, number of trees, etc.
4) Future land use pattern is predicted based on the current development trend only. We did not consider other land use scenarios. In follow-up research, we will set up various development scenarios. Further research on the process and mechanism of small-scale LUC could be undertaken to improve understanding of ESV, the trade-offs and the synergistic relationship of various ecosystem services.

6 Conclusion

This study considers actual situations to predict the land use scenario of the study area in the next 5–10 years and correct the ESV equivalent factor. Furthermore, the space-time distribution of LUC, ESV and ESV profit and loss are analyzed. The main conclusions are as follows.

1) During 1985–2030, the most obvious LUC in Tongling was the transformation of cultivated land to built-up land. The proportion of cultivated land decreased by 9.6%, built-up land increased by 12.2%, while other types of land did not change much. Regarding the dynamics of various land use types, the most pronounced changes are observed in built-up and unused lands.
2) During 1985–2030, the ESV of Tongling showed an increasing trend at the beginning and then decreased. It reached a maximum value of 274.74 billion yuan in 2000 and then decreased to 247.73 billion yuan in 2030. The overall ESV showed a downward trend. Regarding the individual ecosystem service functions, the hydrological regulation function greatly contributed to ESV changes.
3) During 1985–2030, the total addition of ESV in Tongling was 5.98 billion yuan; the total loss was 1.859 billion yuan, and the net loss was 1.26 billion yuan. The largest contribution to the net loss comes from converting cultivated land (20.03%) and forest (19.04%) to built-up land. The conversion of paddy fields into water areas and shrub forests to broad-leaved forests are the main sources of value gain, accounting for 30.24% and 42.98% of the total gain, respectively. From 1985 to 2030, the ESV profit showed fewer gain areas and more loss areas. The proportion of high-loss areas increased during this period as well. ESV profit and loss showed a significant spatial correlation on the global scale, showing a high degree of aggregation.

Data availability statement

Publicly available datasets were analyzed in this study. This data can be found here: http://www.ngcc.cn/ngcc/html/1/index.html; https://tjj.tl.gov.cn/; https://zrzyhghj.tl.gov.cn/3227/3262/cxghj; http://www.cma.gov.cn/2011qxfw/2011qsjgx/; http://www.ngcc.cn/ngcc/html/1/index.html; http://www.resdc.cn/.

Author contributions

Conceptualization and methodology, FL; validation, HW; data curation, SL; writing—original draft, FL and HN; writing—review and editing, FL and TQ; supervision, SL; funding acquisition, TQ.

All authors have read and agreed to the published version of the manuscript.

Funding

This study was supported by the National Science Fund Project (Grant No. 52130907).

Acknowledgments

We are very grateful to Dr. Sintayehu A. Abebe and Ms. Juan Chen for revising the English language of the article. We are also grateful to reviewers for their helpful comments on the manuscript.

Conflict of interest

The authors declare that the research was conducted in the absence of any commercial or financial relationships that could be construed as a potential conflict of interest.

Publisher's note

All claims expressed in this article are solely those of the authors and do not necessarily represent those of their affiliated organizations, or those of the publisher, the editors and the reviewers. Any product that may be evaluated in this article, or claim that may be made by its manufacturer, is not guaranteed or endorsed by the publisher.

References

Aksoy, H., and Kaptan, S. (2021). Monitoring of land use/land cover changes using GIS and CA-markov modeling techniques: A study in northern Turkey. *Environ. Monit. Assess.* 193, 507. doi:10.1007/s10661-021-09281-x

Barrera, F. D. L., Rubio, P., and Banzhaf, E. (2016). The value of vegetation cover for ecosystem services in the suburban context. *Urban. For. Urban. Gree.* 16, 110–122. doi:10.1016/j.ufug.2016.02.003

Cao, G., Liu, Y., Song, X., Chen, Y., Zhang, Z., and Wu, D. (2021a). Study on the response mechanism of ecosystem services to urban land expansion by dynamic equivalent factor method: A case of wuhan, China. *IOP Conf. Ser. Earth Environ. Sci.* 651, 042039. doi:10.1088/1755-1315/651/4/042039

Cao, Y., Kong, L., Zhang, L., and Ouyang, Z. (2021b). The balance between economic development and ecosystem service value in the process of land urbanization: A case study of China's land urbanization from 2000 to 2015. *Land. use. Pol.* 108, 105536. doi:10.1016/j.landusepol.2021.105536

Chasia, S., Olang, L. O., and Sitoki, L. (2023). Modelling of land-use/cover change trajectories in a transboundary catchment of the Sio-Malaba-Malakisi Region in East Africa using the CLUE-s model. *Ecol. Model.* 476, 110256. doi:10.1016/j.ecolmodel.2022.110256

Chatterjee, S., Dutta, S., Dutta, I., and Das, A. (2022). Ecosystem services change in response to land use land cover dynamics in Paschim Bardhaman District of West Bengal, India. *RSASE* 27, 100793. doi:10.1016/j.rsase.2022.100793

Chatterjee, U., and Majumdar, S. (2022). Impact of land use change and rapid urbanization on urban heat island in Kolkata city: A remote sensing based perspective. *J. Urban Manag.* 11 (1), 59–71. doi:10.1016/j.jum.2021.09.002

Chu, D., Shen, H. F., Guan, X. B., and Li, X. H. (2022). An L1-regularized variational approach for NDVI time-series reconstruction considering inter-annual seasonal similarity. *Int. J. Appl. Earth. Obs.* 114, 103021. doi:10.1016/j.jag.2022.103021

Clements, H. S., Vos, A. D., Bezerra, J. C., Coetzer, K., Maciejewski, K., Mograbi, P. J., et al. (2021). The relevance of ecosystem services to land reform policies: Insights from South Africa. *Land. use. Pol.* 100, 104939. doi:10.1016/j.landusepol.2020.104939

Costanza, R., D'Arge, R., De Groot, R. D., Farber, S., Grasso, M., Hannon, B., et al. (1998). The value of the world's ecosystem services and natural capital. *Ecol. Econ.* 25 (1), 3–15. doi:10.1016/S0921-8009(98)00020-2

Cunha, E. R. D., Santos, C. A. G., Silva, R. M. D., Bacani, V. M., and Pott, A. (2021). Future scenarios based on a CA-Markov land use and land cover simulation model for a tropical humid basin in the Cerrado/Atlantic forest ecotone of Brazil. *Land. use. Pol.* 101, 105141. doi:10.1016/j.landusepol.2020.105141

De Groot, R. S., Alkemade, R., Braat, L., Hein, L., and Willemen, L. (2010). Challenges in integrating the concept of ecosystem services and values in landscape planning, management and decision making. *Ecol. Complex.* 7, 260–272. doi:10.1016/j.ecocom.2009.10.006

Delphin, S., Escobedo, F. J., Abd-Elrahman, A., and Cropper, W. P. (2016). Urbanization as a land use change driver of forest ecosystem services. *Land. use. Pol.* 54, 188–199. doi:10.1016/j.landusepol.2016.02.006

Devkota, P., Dhakal, S., Shrestha, S., and Shrestha, U. B. (2023). Land use land cover changes in the major cities of Nepal from 1990 to 2020. *Environ. Sustain. Indic.* 17, 100227. doi:10.1016/j.indic.2023.100227

Dewan, A. M., and Yamaguchi, Y. (2009). Land use and land cover change in greater dhaka, Bangladesh: Using remote sensing to promote sustainable urbanization. *Appl. Geogr.* 29 (3), 390–401. doi:10.1016/j.apgeog.2008.12.005

Felipe-Lucia, M. R., Soliveres, S., Penone, C., Fischer, M., Allan, E., Boch, S., et al. (2020). Land-use intensity alters networks between biodiversity, ecosystem functions, and services. *Proc. Natl. Acad. Sci.* 117 (45), 28140–28149. doi:10.1073/pnas.2016210117

Fenta, A. A., Tsunekawa, A., Haregeweyn, N., Tsubo, M., Yasuda, H., Shimizu, K., et al. (2020). Cropland expansion outweighs the monetary effect of declining natural vegetation on ecosystem services in sub-Saharan Africa. *Ecosyst. Serv.* 45, 101154. doi:10.1016/j.ecoser.2020.101154

Fu, X., Wang, X. H., and Yang, Y. J. (2018). Deriving suitability factors for CA-Markov land use simulation model based on local historical data. *J. Environ. Manage.* 206, 10–19. doi:10.1016/j.jenvman.2017.10.012

Gao, L., Tao, F., Liu, R., Wang, Z., Leng, H., and Zhou, T. (2022). Multi-scenario simulation and ecological risk analysis of land use based on the PLUS model: A case study of nanjing. *Sustain. Cities. Soc.* 85, 104055. doi:10.1016/j.scs.2022.104055

Gao, X., Shen, J. Q., He, W. J., Zhao, X., Li, Z. C., Hu, W. F., et al. (2021b). Spatial-temporal analysis of ecosystem services value and research on ecological compensation in Taihu Lake Basin of Jiangsu Province in China from 2005 to 2018. *J. Clean. Prod.* 317, 128241. doi:10.1016/j.jclepro.2021.128241

Gao, X., Wang, J., Li, C. X., Shen, W. N., Song, Z. Y., Nie, C. J., et al. (2021a). Land use change simulation and spatial analysis of ecosystem service value in Shijiazhuang under multi-scenarios. *Environ. Sci. Pollut. Res.* 28, 31043–31058. doi:10.1007/s11356-021-12826-9

Gashaw, T., Tulu, T., Argaw, M., Worqlul, A. W., TolessaKindu, T., M., and Kindu, M. (2018). Estimating the impacts of land use/land cover changes on Ecosystem Service Values: The case of the Andassa watershed in the Upper Blue Nile basin of Ethiopia. *Ecosyst. Serv.* 31, 219–228. doi:10.1016/j.ecoser.2018.05.001

He, F., Jin, J., Zhang, H., and Yuan, L. (2021). The change of ecological service value and the promotion mode of ecological function in mountain development using InVEST model. *Arab. J. Geosci.* 14, 510. doi:10.1007/s12517-021-06869-y

Himes-Cornell, A., Pendleton, L., and Atiyah, P. (2018). Valuing ecosystem services from blue forests: A systematic review of the valuation of salt marshes, sea grass beds and mangrove forests. *Ecosyst. Serv.* 30, 36–48. doi:10.1016/j.ecoser.2018.01.006

Houtven, G. V., Phelan, J., Clark, C., Sabo, R. D., Buckley, J., Thomas, R. Q., et al. (2019). Nitrogen deposition and climate change effects on tree species composition and ecosystem services for a forest cohort. *Ecol. Monogr.* 89 (2), 13–45. doi:10.1002/ecm.1345

Hu, M. M., Li, Z. T., Wang, Y. F., Jiao, M. Y., Li, M., and Xia, B. C. (2019). Spatio-temporal changes in ecosystem service value in response to land-use/cover changes in the Pearl River Delta. *Resour. Conserv. Recy.* 149, 106–114. doi:10.1016/j.resconrec.2019.05.032

Hu, S., Yang, Y., Li, A., Liu, K., Mi, C., and Shi, R. (2022). Integrating ecosystem services into assessments of sustainable development goals: A case study of the beijing-tianjin-hebei region, China. *Front. Environ. Sci.* 10, 897792. doi:10.3389/fenvs.2022.897792

Jia, Y., Liu, Y., and Zhang, S. (2021). Evaluation of Agricultural Ecosystem Service Value in Arid and Semiarid Regions of Northwest China Based on the Equivalent Factor Method. *Environ. Process* 8 (2), 713–727. doi:10.1007/s40710-021-00514-2

Kindu, M., Schneider, T., Teketay, D., and Knoke, T. (2016). Changes of ecosystem service values in response to land use/land cover dynamics in Munessa-Shashemene landscape of the Ethiopian highlands. *Sci. Total Environ.* 547, 137–147. doi:10.1016/j.scitotenv.2015.12.127

Kiziridis, D. A., Mastrogianni, A., Pleniou, M., Tsiftsis, S., Xystrakis, F., and Tsiripidis, L. (2023). Improving the predictive performance of CLUE-S by extending demand to land transitions: The trans-CLUE-S model. *Ecol. Model.* 478, 110307. doi:10.1016/j.ecolmodel.2023.110307

Kubiszewski, I., Costanza, R., Anderson, S., and Sutton, P. (2017). The future value of ecosystem services: Global scenarios and national implications. *Ecosyst. Serv.* 26, 289–301. doi:10.1016/j.ecoser.2017.05.004

Lei, J. R., Chen, Z. Z., Chen, X. H., Li, W. L., and Wu, T. T. (2020). Spatio-temporal changes of land use and ecosystem services value in Hainan Island from 1980 to 2018. *Acta. Ecol. Sin.* 40 (14), 4760–4773. doi:10.5846/stxb201907261580

Li, X., Fu, J. Y., Jiang, D., Lin, G., and Cao, C. L. (2022a). Land use optimization in Ningbo City with a coupled GA and PLUS model. *J. Clean. Prod.* 375, 134004. doi:10.1016/j.jclepro.2022.134004

Li, X. M., Wang, Y., and Song, Y. (2022b). Unraveling land system vulnerability to rapid urbanization: An indicator-based vulnerability assessment for Wuhan, China. *Environ. Res.* 211, 112981. doi:10.1016/j.envres.2022.112981

Liang, X. L., Liu, X. P., Li, X., Chen, Y. M., Tian, H., and Yao, Y. (2018). Delineating multi-scenario urban growth boundaries with a CA-based FLUS model and morphological method. *Landsc. Urban. Plan.* 177, 47–63. doi:10.1016/j.landurbplan.2018.04.016

Ling, H. E., Chao, L. I., and Jia, Q. (2016). Profit and loss analysis on ecosystem services value based on land use change in coastal land. *Ecol. Econ.* 25 (8), 256–261. doi:10.3969/j.issn.1002-6819.2009.08.046

Liu, P. J., Hu, Y. C., and Jia, W. T. (2021). Land use optimization research based on FLUS model and ecosystem services–setting Jinan City as an example. *Urban. Clim.* 40, 100984. doi:10.1016/j.uclim.2021.100984

Mansour, S., Al-Belushi, M., and Al-Awadhi, T. (2020). Monitoring land use and land cover changes in the mountainous cities of Oman using GIS and CA-Markov modelling techniques. *Land. use. Pol.* 91, 104414. doi:10.1016/j.landusepol.2019.104414

Matlhodi, B., Kenabatho, P. K., Parida, B. P., and Maphanyane, J. G. (2021). Analysis of the future land use LandCover changes in the gaborone dam catchment using CA-markov model: Implications on water resources. *Remote. Sens.* 13, 2427. doi:10.3390/rs13132427

Nelson, E., Sander, H., Hawthorne, P., Conte, M., Ennaanay, D., Wolny, S., et al. (2010). Projecting global land-use change and its effect on ecosystem service provision and biodiversity with simple models. *PloS One* 5, e14327. doi:10.1371/journal.pone.0014327

Peng, K., Jiang, W., Ling, Z., Hou, P., and Deng, Y. (2021). Evaluating the potential impacts of land use changes on ecosystem service value under multiple scenarios in support of sdg reporting: A case study of the wuhan urban agglomeration. *J. Clean. Prod.* 307, 127321. doi:10.1016/j.jclepro.2021.127321

Pueffel, C., Haase, D., and Priess, J. A. (2018). Mapping ecosystem services on brownfields in Leipzig, Germany. *Ecosyst. Serv.* 30, 73–85. doi:10.1016/j.ecoser.2018.01.011

Qiao, W. Y., and Huang, X. J. (2022). The impact of land urbanization on ecosystem health in the Yangtze River Delta urban agglomerations, China. *Cities* 130, 103981. doi:10.1016/j.cities.2022.103981

Rimal, B., Sharma, R., Kunwar, R., Keshtkar, H., Stork, N. E., Rijal, S., et al. (2019). Effects of land use and land cover change on ecosystem services in the Koshi River Basin, Eastern Nepal. *Ecosyst. Serv.* 38, 100963. doi:10.1016/j.ecoser.2019.100963

Rong, Y., Li, C., Xu, C., and Yan, Y. (2017). Ecosystem service values and spatial differentiation changes during urbanization: A case study of Huanghua City. *Chinese Journal of Ecology* 36 (5), 1374–1381. doi:10.13292/j.1000-4890.201705.001

Sannigrahi, S., Bhatt, S., Rahmat, S., Paul, S. K., and Sen, S. (2018). Estimating global ecosystem service values and its response to land surface dynamics during 1995–2015. *J. Environ. Manage.* 223, 115–131. doi:10.1016/j.jenvman.2018.05.091

Santos-Martín, F., Zorrilla-Miras, P., Palomo, I., Montes, C., Benayas, J., and Maes, J. (2019). Protecting nature is necessary but not sufficient for conserving ecosystem services: A comprehensive assessment along a gradient of land-use intensity in Spain. *Ecosyst. Serv.* 35, 43–51. doi:10.1016/j.ecoser.2018.11.006

Schirpke, U., Ebner, M., Pritsch, H., Fontana, V., and Kurmayer, R. (2021). Quantifying ecosystem services of high mountain lakes across different socio-ecological contexts. *Sustainability* 13, 6051–6122. doi:10.3390/su13116051

Schirpke, U., Tscholl, S., and Tasser, E. (2020). Spatio-temporal changes in ecosystem service values: Effects of land-use changes from past to future (1860–2100). *J. Environ. Manage.* 272, 111068. doi:10.1016/j.jenvman.2020.111068

Sonter, L. J., Johnson, J. A., Nicholson, C. C., Richardson, L. L., Watson, K. B., and Ricketts, T. H. (2017). Multi-site interactions: Understanding the offsite impacts of land use change on the use and supply of ecosystem services. *Ecosyst. Serv.* 23, 158–164. doi:10.1016/j.ecoser.2016.12.012

Sun, Y. X., Liu, S. L., Shi, F. N., An, Y., Li, M. Q., and Liu, Y. X. (2020). Spatio-temporal variations and coupling of human activity intensity and ecosystem services based on the four-quadrant model on the Qinghai-Tibet Plateau. *Sci. Total Environ.* 743, 140721. doi:10.1016/j.scitotenv.2020.140721

Syrbe, R. U., Schorcht, M., Grunewald, K., and Meinel, G. (2018). Indicators for a nationwide monitoring of ecosystem services in Germany exemplified by the mitigation of soil erosion by water. *Ecol. Indic.* 94, 46–54. doi:10.1016/j.ecolind.2017.05.035

Tammi, I., Mustajärvi, K., and Rasinmäki, J. (2017). Integrating spatial valuation of ecosystem services into regional planning and development. *Ecosyst. Serv.* 26, 329–344. doi:10.1016/j.ecoser.2016.11.008

Vallecillo, S., La Notte, A., Zulian, G., Ferrini, S., and Maes, J. (2019). Ecosystem services accounts: Valuing the actual flow of nature-based recreation from ecosystems to people. *Ecol. Model.* 392, 196–211. doi:10.1016/j.ecolmodel.2018.09.023

Venkatesh, K., John, R., Chen, J. Q., Xiao, J. F., Amirkhiz, R. G., Giannico, V., et al. (2022). Optimal ranges of social-environmental drivers and their impacts on vegetation dynamics in Kazakhstan. *Sci. Total Environ.* 847, 157562. doi:10.1016/j.scitotenv.2022.157562

Wang, Q., and Wang, H. J. (2022). Correction to: An integrated approach of logistic-MCE-CA-Markov to predict the land use structure and their micro-spatial characteristics analysis in Wuhan metropolitan area, Central China. *Environ. Sci. Pollut. Res.* 29 (20), 30054–30053. doi:10.1007/s11356-022-18735-9

Wang, X., Dong, X., Liu, H., Wei, H., Fan, W., Lu, N., et al. (2017). Linking land use change, ecosystem services and human well-being: A case study of the manas river basin of xinjiang, China. *Ecosyst. Serv.* 27, 113–123. doi:10.1016/j.ecoser.2017.08.013

Wang, X. L., and Nuppenau, E. A. (2021). Modelling payments for ecosystem services for solving future water conflicts at spatial scales: The Okavango River Basin example. *Ecol. Econ.* 184, 106982. doi:10.1016/j.ecolecon.2021.106982

Wu, J. J., and He, R. H. (2017). Coordination degree between land use and eco-environment in Tongling City of Anhui Province. *Journal of Yunnan Agricultural University (Social Science)* 11 (5), 29–34. doi:10.3969/j.issn.1004-390X(s).2017.05.006

Xiang, M., Yang, J., Li, W., Song, Y., Wang, C., Liu, Y., et al. (2022). Spatiotemporal evolution and simulation prediction of ecosystem service function in the western sichuan plateau based on land use changes. *Front. Environ. Sci.* 10, 890580. doi:10.3389/fenvs.2022.890580

Xie, G. D., Lu, C. X., Leng, Y. F., Zheng, D., and Li, S. C. (2003). Ecological assets valuation of the Tibetan Plateau. *J. Nat. Resour.* 18 (2), 189–196. doi:10.11849/zrzyxb.2003.02.010

Xie, G. D., Zhang, C. X., Zhang, L. M., Chen, W. H., and Li, S. M. (2015). Improvement of the evaluation method for ecosystem service value based on per unit area. *J. Nat. Resour.* 12, 1243–1254. doi:10.11849/zrzyxb.2015.08.001

Yuan, Y., Wu, S., Yu, Y., Tong, G., Mo, L., Yan, D., et al. (2018). Spatiotemporal interaction between ecosystem services and urbanization: Case study of Nanjing City, China. *Ecol. Indic.* 95, 917–929. doi:10.1016/jecolind.2018.07.056

Zhai, H., Lv, C., Liu, W., Yang, C., Fan, D., Wang, Z., et al. (2021). Understanding spatio-temporal patterns of land use/land cover change under urbanization in Wuhan, China, 2000–2019. *Remote Sens.* 13 (16), 3331. doi:10.3390/rs13163331

Zhang, G. Y., and Sun, W. (2016). Research on the practice path of crossing river development in tongling city based on the adjustment of regionalization. *China Int. Bus.* 10, 36–40. doi:10.19516/j.cnki.10-1438/f.2016.21.013

Zhang, H., Yang, Q., Zhang, H., Zhou, L., and Chen, H. (2021). Optimization of land use based on the source and sink landscape of ecosystem services: A case study of fengdu county in the three gorges reservoir area, China. *Land* 10, 1242. doi:10.3390/land10111242

Zhang, Y. Q., Liu, S. L., Hou, X. Y., Cheng, F. Y., and Shen, Z. Y. (2019). Landscape- and climate change-induced hydrological alterations in the typically urbanized Beiyun River basin, Beijing, China. *Stoch. Environ. Res. Risk. Assess.* 33, 149–168. doi:10.1007/s00477-018-1628-8

Zuo, Y. (2016). Dynamic changes in land cover and landscape patterns of Anhui province based on global land cover products. dissertation. China (Anhui): Anhui University.

frontiers | Frontiers in Environmental Science

TYPE Original Research
PUBLISHED 09 May 2023
DOI 10.3389/fenvs.2023.1118953

OPEN ACCESS

EDITED BY
Chang Huang,
Northwest University, China

REVIEWED BY
Qingsong He,
Huazhong University of Science and Technology, China
Shi Qiu,
Chinese Academy of Sciences (CAS), China
Yan Xia,
Institutes of Science and Development, Chinese Academy of Sciences, China
Kailan Tian,
Chinese Academy of Sciences (CAS), China

*CORRESPONDENCE
Xiaowei Nie,
xwnie@itpcas.ac.cn

RECEIVED 08 December 2022
ACCEPTED 25 April 2023
PUBLISHED 09 May 2023

CITATION
Li J, Peng B, Liu S, Ye H, Zhang Z and Nie X (2023), An accurate fringe extraction model of small- and medium-sized urban areas using multi-source data. *Front. Environ. Sci.* 11:1118953. doi: 10.3389/fenvs.2023.1118953

An accurate fringe extraction model of small- and medium-sized urban areas using multi-source data

Jianfeng Li[1,2,3,4], Biao Peng[1,4], Siqi Liu[1,4], Huping Ye[2], Zhuoying Zhang[3,5] and Xiaowei Nie[3,6]*

[1]Technology Innovation Center for Land Engineering and Human Settlements, Shaanxi Land Engineering Construction Group Co., Ltd. and Xi'an Jiaotong University, Xi'an, China, [2]State Key Laboratory of Resources and Environmental Information System, Institute of Geographic Sciences and Natural Resources Research, Chinese Academy of Sciences, Beijing, China, [3]State Key Laboratory of Tibetan Plateau Earth System, Environment and Resources (TPESER), Institute of Tibetan Plateau Research, Chinese Academy of Sciences, Beijing, China, [4]Institute of Land Engineering and Technology, Shaanxi Provincial Land Engineering Construction Group Co., Ltd., Xi'an, China, [5]Academy of Mathematics and Systems Science, Chinese Academy of Sciences, Beijing, China, [6]College of Science, Tibet University, Tibet, China

Urban fringes are of great significance to urban development as connecting hubs between urban and rural areas. However, there are many problems in urban fringes, including disorderly spatial layout, waste of social resources, and low quality of human settlements. Rapid and accurate identification of urban fringes has important practical significance for optimizing urban spatial layout, controlling urban unlimited expansion, and protecting land resources. Given the lack of suitable and high-quality fringe extraction models for small- and medium-sized urban areas, this study was based on Gaofen-2 (GF-2) imagery, Suomi National Polar-orbiting Partnership Visible Infrared Imager Radiometer Suite (NPP-VIIRS) imagery, point of interest (POI) data, and WorldPop data, taking the landscape disorder degree, POI kernel density, and night light intensity as urban feature factors and constructing a fringe extraction model of small- and medium-sized urban areas (FEM-SMU). Taking Hantai District in China as the study area, the results of the model were compared to the landscape disorder degree threshold method and POI kernel density breakpoint analysis method, while the generality of the model was further tested in Shangzhou and Hanbin Districts. The results show that the FEM-SMU model has evident improvements over the conventional methods in terms of accuracy, detail, and integrity, and has higher versatility, which can better meet the research needs of small- and medium-sized urban fringes.

KEYWORDS

landscape disorder degree, kernel density estimation (KDE), night light intensity, geographical detector (Geodetector), urban fringe

1 Introduction

Since the reform and opening up, China has experienced unprecedented growth of urbanization and completed the great transformation from a country dominated by an agricultural population to an urban population (Chen et al., 2018; Feng et al., 2019). Rapid urbanization not only promotes the implementation of urban-rural integration development strategies, but also provides unprecedented development opportunities

for urban fringes (Whitehand and Gu, 2017; Liu et al., 2018). The urban fringe is a region located at the outer boundaries of a city and serves as a transition zone between urban and rural areas, encompassing suburban developments and rural lands undergoing urbanization (Simon et al., 2004). As the connecting hub between urban and rural areas, urban fringes are the areas with the fastest change in land use and spatial structure in the process of urban expansion, with the characteristics of diversity, dynamics, and transition (Seto et al., 2010; Gant et al., 2011; Wadduwage et al., 2017). However, many problems have arisen in the urban fringe during the process of urbanization in China, including disorderly spatial layout, deterioration of ecological environment, waste of land resources and so on (Zhao and Zhang, 2018; Ahani and Dadashpoor, 2021; Lyu et al., 2022). Rapid and accurate identification of urban fringes is of great practical significance for optimizing urban spatial layout, protecting land resources, and promoting urban and rural integration.

With the development of remote sensing (RS) and geographic information system (GIS) technology in recent years, the recognition of the urban fringe has broken through the early empiricism of fuzzy definition and gradually changed into a scientism of accurate identification (Peng et al., 2016; Wadduwage et al., 2017; Wang Y. et al., 2021). Most existing studies constructed index systems using elements closely relevant to urban development to identify the urban fringe through mathematical models (Chang et al., 2018; Wang Y. et al., 2021; Dong et al., 2022). The identification methods of urban fringe mainly include the urban-rural gradient view, threshold, mutation/breakpoint analysis methods, and so on (Peng et al., 2014; van Vliet et al., 2019; Yang et al., 2021). The urban-rural gradient view method mainly identifies the urban fringe according to the spatial gradient changes in regional land use, socioeconomic status, and population density (van Vliet et al., 2019). It is generally well accepted that the gradient change of land use can determine the difference in landscape structure between urban and rural areas and reduce the subjectivity of land use variability measurements (Warren et al., 2011; Wadduwage et al., 2017). Moreover, the gradient changes in the social economy and population density can well reflect the differences between urban and rural areas (Vizzari and Sigura, 2015). However, the urban-rural gradient view method has difficulty in overcoming the subjectivity in determining the dividing point in areas with a scattered landscape structure (Peng et al., 2016; Sharaf El Din, 2020). As an alternative, the threshold method determines the urban fringe according to the threshold range of indicators such as distance from the built-up area, population density, building proportion, and information entropy (Imhoff et al., 2010; Peng et al., 2016; Yang et al., 2017). The threshold method is simple and practical, but the determination of the threshold usually requires repeated experiments, which has some problems, such as low efficiency, discontinuous results, and poor universality (Gao et al., 2014; Peng et al., 2014; Yang et al., 2017). As the current mainstream option, the mutation/break point analysis method is used to determine the urban fringe by calculating the mutation/break values of single or comprehensive indexes such as night light intensity, the impervious surface index, and the landscape

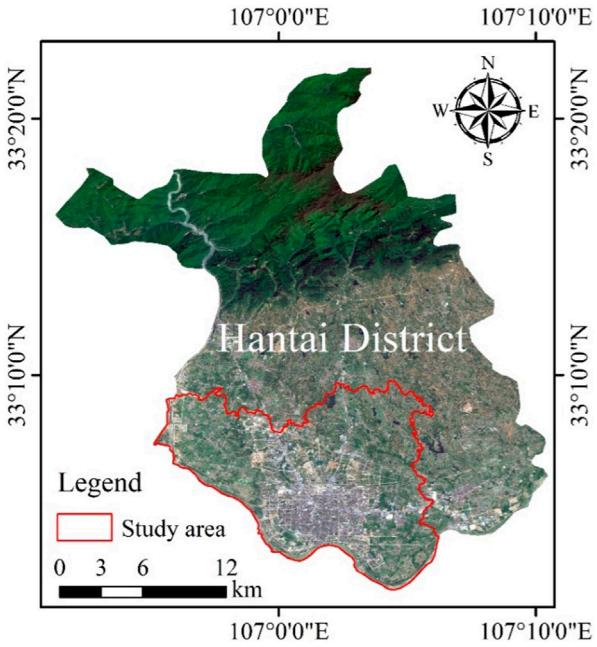

FIGURE 1
Location of the study area.

disorder degree in different directions through the model (Peng et al., 2016; Yang et al., 2017; Peng et al., 2018; Yang et al., 2021).

At present, research on the identification of urban fringe is mainly focused on larger cities (Peng et al., 2014; Peng et al., 2016; Cai et al., 2017; Yang et al., 2017; Yang et al., 2021), while the extraction model suitable for small- or medium-sized urban fringes is rare. The fringes of large cities have higher population density and more economic activities, while the fringes of small and medium-sized cities are more remote and rural (Long et al., 2022). At the same time, the fringes of small- and medium-sized urban areas are smaller, and the spatial resolution of available data related to urban development (economy, population, lighting images, etc.) is lower. The existing models designed for large cities are difficult to accurately identify the fringes of small- and medium-sized urban. In recent years, the rapid development of 3 S (i.e., GIS, RS, and global positioning system (GPS)) technology has resulted in a large amount of urban spatial data, including POI data, GPS data, and population migration data (Li et al., 2019; Fang et al., 2020; Tu et al., 2020). These spatial data can reflect the activity law of residents and the spatial characteristics of the city, which is conducive to urban fringe studies. At the same time, high-resolution RS satellite images such as GF and Systeme Probatoire d'Observation dela Tarre (SPOT) improve the richness of obtaining surface spatial information (Su, 2019; Tong et al., 2020). This study was based on GF-2 imagery, NPP-VIIRS imagery, POI data, and WorldPop data, taking the landscape disorder degree, POI kernel density, and night light intensity as urban feature factors, and proposing an accurate fringe extraction model for small and medium-sized urban areas, hereafter FEM-SMU.

TABLE 1 The specific information of data.

Data type	Date	Resolution/m	Website
GF-2 image	07/08/2020	1	http://www.gscloud.cn/
POI data	2020	—	https://lbs.amap.com/
Woldpop data	07/2020	100	https://www.worldpop.org.uk/
NPP/VIIRS image	07/2020	500	http://ladsweb.nascom.nasa.gov/data/
Administrative boundary	2020	—	http://www.dsac.cn/

2 Materials and methods

2.1 Study area

The study area of this study is Hantai District which is located in the center of the Hanzhong Basin in the southwest of Shaanxi Province in China, with the Hanjiang River to the south and the Qinling Mountains to the north. The terrain of Hantai District is high in the north and low in the south, and the north belongs to the Qinling Mountains, with an elevation of 700–2000 m, accounting for 34% of the total area; the central part is a hilly area, with an elevation of 541–700 m, accounting for 28% of the total area; and the south is the Hanjiang alluvial plain, accounting for 38% of the total area (Wang L. et al., 2021). Hantai District is the largest commodity distribution center in southern Shaanxi and the core area of the Qinling and Bashan mountains, which has important economic and ecological value. Since the urban construction in Hantai District is mainly concentrated in the south, the study area is composed of the administrative boundaries of nine towns in the south (Figure 1).

2.2 Data

This study utilized five types of data: GF-2 imagery, NPP-VIIRS imagery, POI data, WorldPop data, and administrative boundaries. The GF-2 satellite is the first civil optical RS satellite with a spatial resolution better than 1 m independently developed by China, which achieves sub-meter spatial resolution and multi-spectral comprehensive RS data acquisition (Zhou et al., 2021). It has the characteristics of high positioning accuracy, high spatial resolution, and high time resolution. Four GF-2 images covering the study area in July 2020 were used.

The data of POI comprises geographical objects that can be abstracted as points, especially some geographical entities closely related to people's lives (Wenhao and Tinghua, 2015). In this study, the POI map data was divided into 18 service categories: automobile, motorcycle, catering, shopping, life, sports and leisure, healthcare, accommodation, scenic spots, commercial residences, government institutions and social organizations, science and education, transportation facilities, financial and insurance, company enterprises, road ancillary facilities, place name address information, and public facilities. Given road ancillary facilities and place names usually represent non-substantive information, such as road section identification, administrative place names, natural place names, and traffic place names, they were not selected.

The NPP-VIIRS data were obtained from the National Geophysical Data Center (NGDC) of the United States and were detected by the Suomi NPP satellite with a visible infrared imaging radiation instrument (Shi et al., 2014). The monthly data of lighting products in July 2020 were selected with a spatial resolution of 500 m.

The WorldPop project, hosted by the Department of Geography and the Institute of New Pathogens at the University of Florida, aims to provide spatial population data sets for Central and South America, Africa, and Asia to support development, disaster response, and health applications (Tatem, 2017). Table 1 lists the specific information of all the data used in this study.

2.3 Object-oriented support vector machines (SVM) classification method

SVM is a classification algorithm based on the VC dimension theory of statistical learning theory and the structural risk minimization principle (Cortes and Vapnik, 1995). Compared with traditional classification ideas based on neural networks or statistics, SVM controls the complexity of the model through the number of vectors and does not need to reduce the feature variables through dimensionality reduction processing to control the complexity of the model (Thaseen and Kumar, 2017). Therefore, in the classification process, the SVM classifier will not lose the feature information of ground objects and reduces the occurrences of some over-fitting phenomena.

The basic principle of SVM is to transform the original feature vector into a high-dimensional feature space and to solve the optimal classification hyperplane in a high-dimensional space. The classification accuracy depends on the distance between the hyperplane and the boundary plane on both sides of the hyperplane. The larger the distance, the higher the accuracy of the classifier and the smaller the error. Given a sample set (x_i, y_i), i is 1, 2, 3.N, $x_i \epsilon R^n$, $y_i \epsilon \{-1, 1\}$, the classification line is $H = \omega \cdot x + b = 0$. ω is the normal vector, x is the training sample, and b is the offset. The optimal classification line needs to have the maximum classification interval, that is, the maximum distance of $\frac{2}{\|\omega\|}$ between the two types of samples, equivalent to finding the minimum value of the function.

$$\varphi(\omega) = \frac{1}{2}\|\omega\|^2 \tag{1}$$

The classification of land use belongs to the linear inseparable problem, so it is necessary to introduce the relaxation variable ξ_i and

the penalty parameter c into the above expression, which can then be expressed as:

$$min\left[\frac{1}{2}\|\omega\|^2 + c\sum_{i=1}^{l}\left(\xi_i + \xi_i^*\right)\right], \quad \xi_i \geq 0\ (i = 1, 2, \ldots N)$$
$$s.t.\begin{cases} ((\omega x_i) + b - y_i) \leq \varepsilon + \xi_i \\ y_i - ((\omega x_i) + b) \leq \varepsilon + \xi_i^* \\ \xi_i, \xi_i^* \geq 0 \end{cases} \quad (2)$$

where ε is the insensitive loss coefficient, and its value affects the number of support vectors; ξ_i and ξ_i^* are relaxation variables, indicating the extent to which the sample deviates from the ε-insensitive region.

For optimization problems, it needs to be transformed into the dual problem of the Lagrangian operator, and the final expression of SVM is:

$$f(x) = \sum_{i=1}^{n}(\alpha_i - \alpha_i^*)k(x_i, x) + b \quad (3)$$

where $k(x_i, x)$ is the kernel function, α and α^* are Lagrange multipliers.

The object-oriented classification method breaks through the limitation of the traditional classification method which takes a single pixel as the basic classification and processing unit, classifies the image from the object level, and reduces the loss rate of semantic information contained in the traditional pixel-based classification method (Stumpf and Kerle, 2011). The object-oriented SVM classification method takes into account the advantages of object-oriented multi-scale segmentation and SVM. Firstly, multi-scale segmentation is carried out according to the properties of the object region on the image, which not only considers the spectral information of the image, but also adds features such as texture, geometric shape, and spatial topological relations, and then uses training samples for SVM classification. The object-oriented SVM classification method has obvious advantages in accuracy, generalization, and high-dimensional data processing, and thus has been widely used in RS image classification (Li et al., 2010; Lin et al., 2018; Shen et al., 2020). To obtain the land use types in the study area, this research utilized the object-oriented SVM classification method to classify remote sensing images.

2.4 Landscape disorder degree

The landscape disorder degree can indicate the degree of fragmentation and dispersion of urban landscapes, as well as reflect the heterogeneity and homogeneity of landscape space (Dong et al., 2010). The higher the heterogeneity of land use patches per unit area, the greater the degree of landscape disorder. Urban and rural areas usually have a single type of land, mostly for construction or agricultural use, and the degree of their landscape disorder is low. Since the urban fringe is an active expansion zone between the urban landscape and agricultural hinterland, it has various types of land use and a high degree of landscape disorder (Scott et al., 2013; Yang et al., 2017; Sharaf El Din, 2020). Therefore, the scope of the urban fringe can be determined by the differences in landscape disorder. The formula for the landscape disorder degree is as follows:

$$W = -\sum_{n=1}^{N} X_n \ln(X_n)\ (\text{Vranken et al., 2015}) \quad (4)$$

Where W is the value of the degree of landscape disorder, X_n represents the ratio of a certain type of land in the unit area, and n is the number of land use type patches per unit area.

2.5 Kernel density estimation (KDE)

The KDE calculation is often used to evaluate the density value of the neighborhood of point or line elements, and to simulate the spatial distribution of elements, which is widely used in geospatial analyses (Lin et al., 2021). Its main principle is that the estimated density of elements decreases with an increase in distance within a certain bandwidth. The kernel density at the center of the feature is the highest, and the kernel density at the edge of the bandwidth is 0. As KDE obeys the law of spatial correlation, the closer the distance is, the greater the correlation is, hence the POI data also conform to this law. The kernel density formula is as follows:

$$\lambda_{(s)} = \sum_{l=1}^{n}\frac{1}{\pi r^2}\varphi\left(\frac{d_{ls}}{r}\right) \quad (5)$$

where $\lambda_{(s)}$ is the estimated density at region s, r is the bandwidth set by the kernel density function, n is the total number of elements involved in the calculation, d_{ls} is the distance between POI points l and s, and φ is the weight of the distance.

2.6 Geographical detector (Geodetector)

Geodetectors are a group of statistical methods used to detect spatial diversity and explain the driving force behind it, including factor, interaction, risk, and ecological detectors (Wang et al., 2010). The main principle of the geodetector is to assume that the study area is divided into several sub-regions; if the sum of the variance of the sub-region is less than the total variance of the region, there is a spatial difference; if the spatial distribution of the two variables tends to be consistent, there is a statistical correlation between the two variables. Geodetectors can evaluate spatial differentiation, detect explanatory factors, and analyze the interaction between variables, and therefore have been widely used in nature, environmental science, human health, and other fields (Wang et al., 2010; Cao et al., 2013; Liu et al., 2020). Based on the factor detector, this study obtained the degree of landscape disorder, POI kernel density, and night light intensity to explain the spatial distribution of population.

Of the detector components, the factor detector detects the spatial differentiation of attribute Y and the explanatory power of factor X to attribute Y, which is measured by q value. Given population density is closely related to urban development (Liu et al., 2012; Yue et al., 2013; Li et al., 2019), this study determined the weight of each factor according to the explanatory power of landscape disorder degree, POI kernel density, and night light intensity on population spatial distribution. The value q can be defined as:

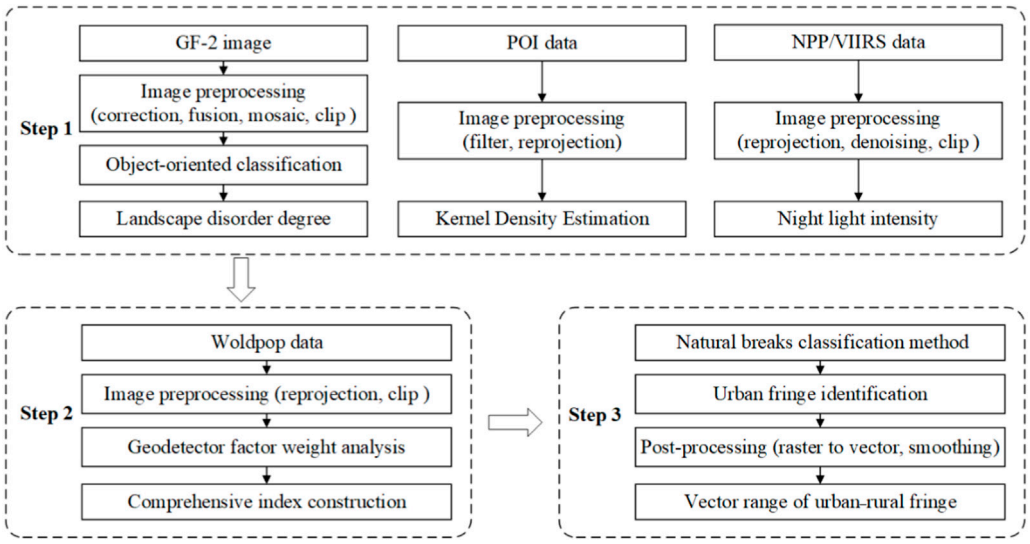

FIGURE 2
The implementation process of the FEM-SMU model.

$$q = 1 - \frac{\sum_{h=1}^{L} N_h \sigma_h^2}{N\sigma^2} = 1 - \frac{SSW}{SST} \quad (h = 1, 2 \ldots)$$
$$SSW = \sum_{h=1}^{L} N_h \sigma_h^2, SST = N\sigma^2 \tag{6}$$

where L is the stratification of variable Y or factor X, that is, classification or partition ; N_h and N are the numbers of units in layer h and the whole region, respectively; σ_h^2 and σ^2 are the variances of layer h and Y values of the whole region, respectively; and SSW and SST are the sums of the variance of the layer and the variance of the whole region, respectively.

2.7 Fringe extraction model of small and medium-sized urban areas (FEM-SMU)

Taking the landscape disorder degree, POI kernel density, and night light intensity as urban characteristic factors, this study proposes the FEM-SMU model (Figure 2). The spatial distribution of population density in an urban area is reflective of the differences between the urban center, urban fringe, and rural areas (Simon, 2008). The explanatory power of individual factors (landscape disorder degree, POI kernel density, night light intensity) on population distribution can reflect their explanatory power on the differences in urban center, urban fringe, and rural characteristics. Therefore, the relative weights of the various factors can be established based on the ratio of the explanatory power of a single factor to the sum of the explanatory power of all factors. The implementation process of the model is divided into the following three steps.

The first step was to calculate the degree of landscape disorder, POI kernel density, and night light intensity. For the calculation of landscape disorder degree: First, Envi 5.3 software was used to perform atmospheric correction, fusion, mosaic, and cropping operations on GF-2 images in the study area, then the object-oriented SVM method was used for land use classification, and finally, Eq. 4 was used to calculate the degree of landscape disorder. For the calculation of POI kernel density: First, the POI data were filtered and reprojected using ArcGIS 10.3 software, and then the kernel density tool was used to evaluate the kernel density. For the calculation of night light intensity: First, the NPP-VIIRS data of the study area were reprojected, denoised, and cropped using ArcGIS 10.3, and then the DN value of pixels was obtained to represent the night light intensity. It should be noted that the degree of landscape disorder, POI kernel density, and night light intensity should be normalized and resampled to a resolution of 10 m after calculation to ensure accurate analysis.

The second step was to build a comprehensive index. First, the Wordpop data were reprojected and cropped using ArcGIS 10.3. Second, the explanatory power of the landscape disorder degree, POI kernel density, and night light intensity on population spatial distribution was determined based on the factor detector. Finally, the comprehensive index was established after the weight was determined according to the ratio of the explanatory power degree of a single factor to all explanatory power degrees.

The third step was to extract the fringe of small- and medium-sized urban areas. First, the comprehensive index grid was divided into three categories by using the Natural Breaks Classification (NBC) method, which represents the urban core, urban fringe, and rural hinterland, and then the classified results were transformed into vectors and smoothed to obtain the range of the urban fringe. It is worth mentioning that this paper determines the NBC method as the classification method for the composite index through comparison of the accuracy of equal interval method, NBC method, and standard deviation method, and reference to literature (Xu et al., 2013; Xiao et al., 2020).

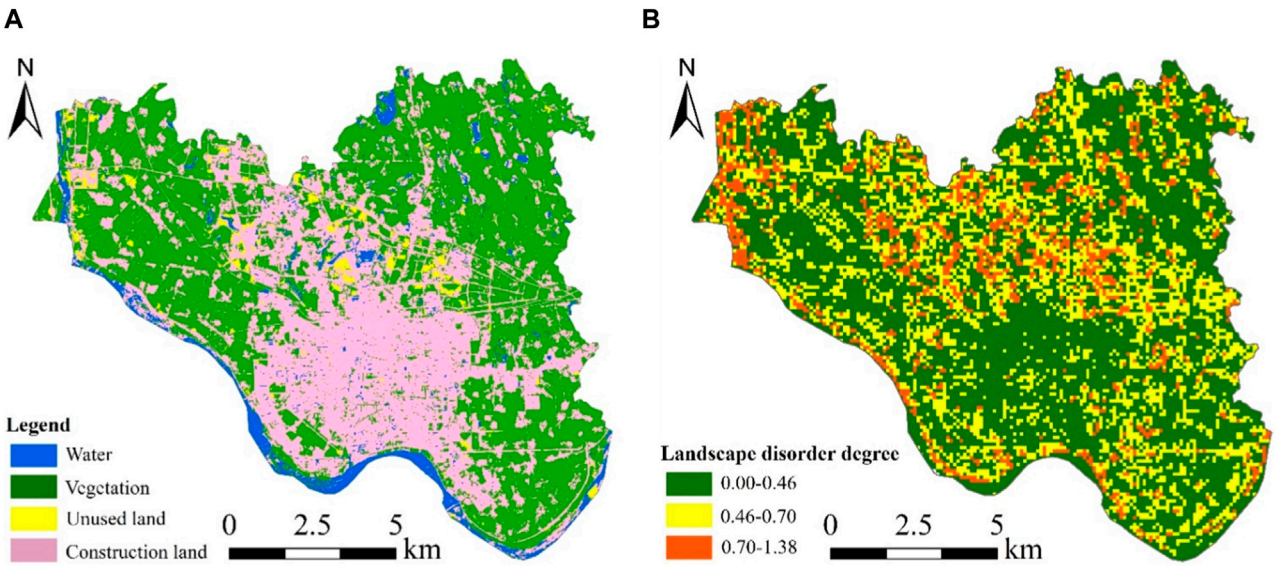

FIGURE 3
(A) Results of land use classification based on the object-oriented SVM method. **(B)** Results of the landscape disorder degree threshold method.

3 Results

3.1 Results of landscape disorder degree threshold method

Based on the preprocessed GF-2 imagery of the study area, the land use was divided into four categories: vegetation (cultivated land, forest land, and grassland), construction land, water, and unused land, using the object-oriented SVM classification method (Figure 3A). It can be seen from the figure that the construction land was mainly distributed in the middle and south of the study area, the water was distributed along the southern boundary, the unused land was mainly distributed in the north, and the vegetation was mainly distributed in the northwest, northeast, and southeast. According to statistics, the vegetation area of the study area was 80.34 km^2, the construction land area was 60.83 km^2, the water area was 6.95 km^2, and the unused land area was 3.31 km^2.

To highlight the circular structure of landscape disorder in the study area, a grid of 100 × 100 m was constructed as the scale unit of spatial calculation. ArcGIS 10.3 was applied to calculate the area ratios of vegetation, construction land, water, and unused land in the cell grid, and the degree of landscape disorder in the study area was calculated using Eq. 4; (Figure 3B). As can be seen from the figure, the landscape structure characteristics of the urban core area were prominent, the landscape disorder degree was low, and there were concentrated and contiguous low-value areas. After repeated experiments, a threshold value of less than 0.46 was used as the symbol to identify the urban core area. However, if there was a large range of green spaces in the urban core area, the degree of landscape disorder was higher, and the landscape disorder degree threshold method could not identify the complete urban core area. The difference in the degree of landscape disorder between the urban fringe and rural hinterland was not obvious, and the degree of landscape disorder was higher. We consider that, compared with larger cities, small- and medium-sized cities have fewer populations and smaller villages; further, the study area is located in the Hanzhong Plain, where villages are relatively concentrated and cultivated land is relatively scattered. These circumstances resulted in a higher degree of landscape disorder between the urban fringe and rural hinterland. Although the landscape disorder degree threshold method is currently widely used in the identification of metropolitan fringes (Huang et al., 2016; Wang Y. et al., 2021; Liu, 2021), in this study, the common shortcomings of this as a single-factor threshold method, which include discontinuity, lack of detail, and poor versatility, were amplified obviously in the process of urban fringe identification in the study area. Therefore, we conclude that the landscape disorder degree threshold method is not suitable for the identification of small- and medium-sized urban fringes.

3.2 Results of the POI kernel density breakpoint analysis method

The setting of the bandwidth in KDE has an important influence on the results. After referring to previous research results (Heidenreich et al., 2013; Lin et al., 2021), the distances of 500 m, 1000 m, and 1,500 m were selected for KDE analysis (Figures 4A–C). It can be seen from the figure that with the shortest bandwidth of 500 m, the KDE results were fragmented and discontinuous, and the overall distribution of urban POI was not obvious. On the other end of the spectrum, with a bandwidth of 1,500 m, the local characteristics of the overall distribution trend of urban POI were difficult to show, and the details were insufficient. Finally, with the medium

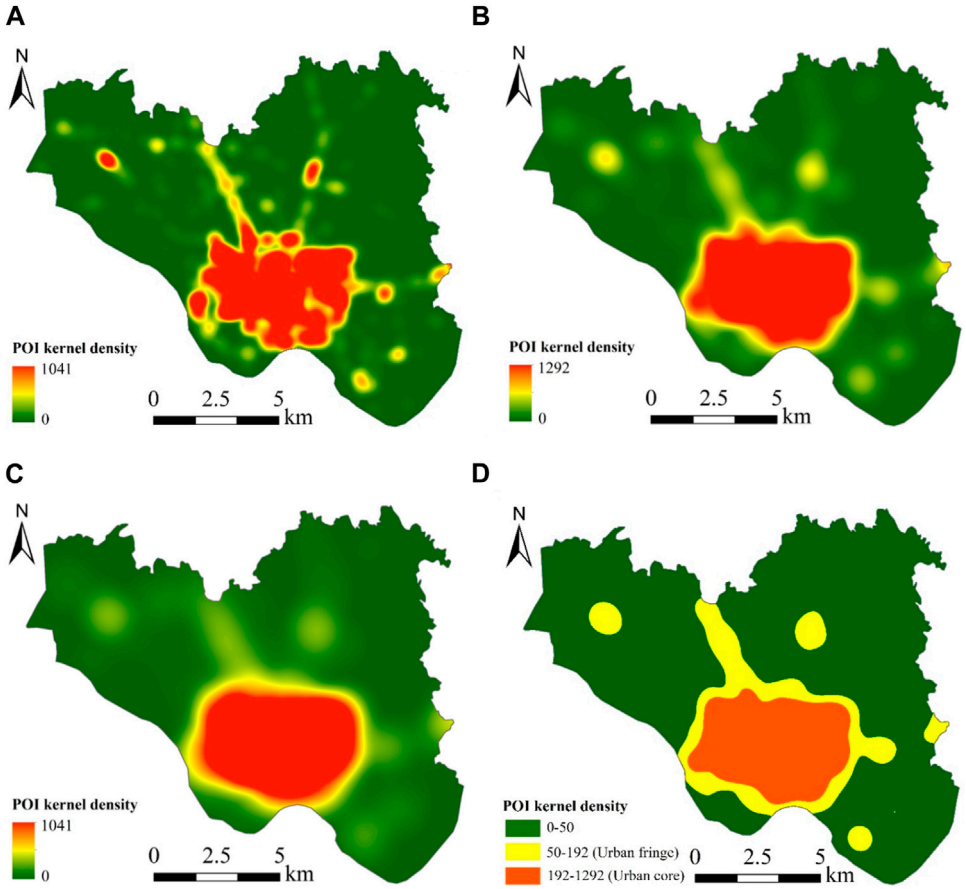

FIGURE 4
(A–C) The KDE results with bandwidths of 500 m, 1,000 m, and 1,500 m, respectively. **(D)** Results of dividing the POI kernel density with a bandwidth of 1,000 m into three categories by the NBC method.

bandwidth of 1,000 m, the KDE results had good stability and an obvious overall distribution, which can meet the analysis needs of the urban fringe in the study area.

Taking this selected bandwidth, Figure 4D shows the result of dividing the POI kernel density with a bandwidth of 1,000 m into three categories by the NBC method. As can be seen from Figures 4B, D, the POI kernel density showed an obvious circular structure distribution. The urban core area had a large area of continuous high-density area, the density of the urban fringe was low, and the density of most rural areas was close to 0. Compared with the landscape disorder degree threshold method, the results of the POI kernel density breakpoint analysis method can clearly and completely identify the urban core area; however, both of them had poor recognition results for the urban fringe area. Moreover, the POI kernel density breakpoint analysis method identifies well-developed villages with a large number of POIs as urban fringes. As the urban fringe was in the stage of development, with less POI data and slow updating speed, this led to obvious errors between the results and the actual urban fringe. Different from larger cities, the POI data integrity of small- and medium-sized urban fringe was lower and the update speed was relatively slow, so we conclude that the POI kernel density breakpoint analysis method had too much difficulty in accurately extracting the urban fringe of the study area.

3.3 Results of the FEM-SMU model

Finally, the urban fringe of the study area was extracted using the FEM-SMU model proposed in this study. First, the degree of landscape disorder, POI kernel density, and night light intensity were calculated. Then, the weight of each factor was determined by combining the Geodetector and WorldPop data (landscape disorder degree: 0.10, POI kernel density: 0.51, night light intensity: 0.39) to construct a comprehensive index. Finally, the urban fringe was identified by the NBC method, and the results were post-processed.

Figure 5A shows the result of dividing the comprehensive index into three categories by the NBC method, and Figure 5B shows the final result of the FEM-SMU model. As can be seen from the figure, the FEM-SMU model could accurately and completely identify the urban fringe of the study area. The urban fringe was mainly concentrated in the north and east, with an area of approximately 39 km^2. Compared with the two single-factor extraction methods, the performance of the FEM-SMU model was a great improvement, especially for the results of the outer boundary of the urban fringe. The overall pattern of the inner boundary of the urban fringe (urban core area) extracted by the FEM-SMU model and POI kernel density breakpoint analysis was more consistent, and further, the former was more detailed. The

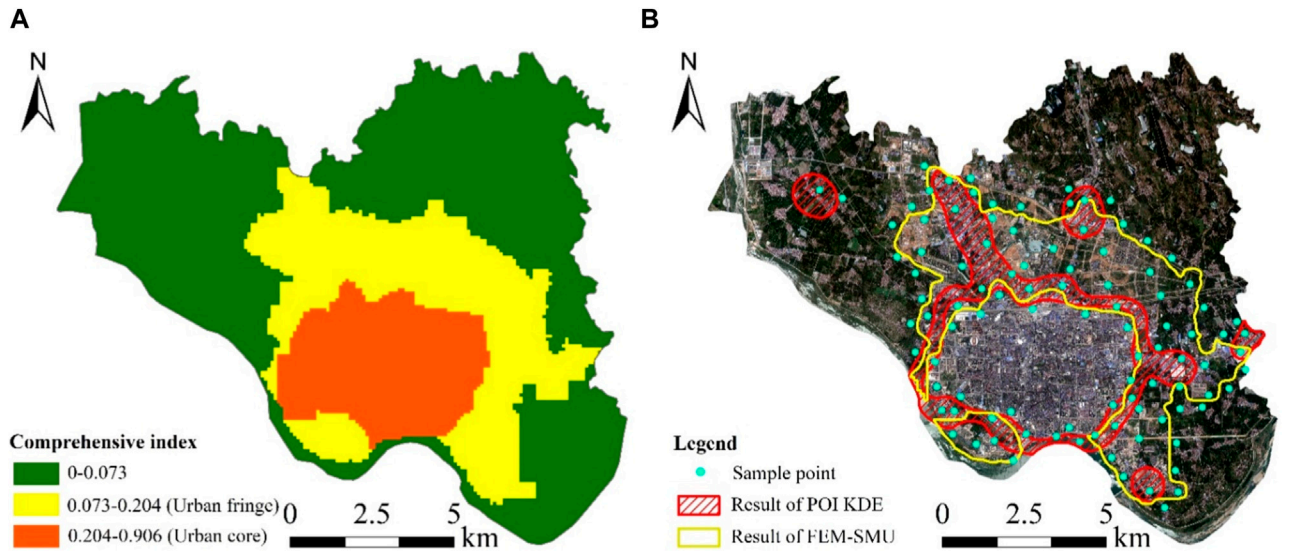

FIGURE 5
(A) Results of dividing the comprehensive index into three categories by the NBC method. **(B)** Final results of the FEM-SMU model.

TABLE 2 Extraction accuracy of different methods.

Analysis method	Error quantity	Correct quantity	Overall accuracy/%
POI kernel density breakpoint analysis method	33	67	67
FEM-SMU	2	98	98

difference between the results of the two methods was mainly concentrated in the southwest in the Hanjiang New Area which is still in the stage of rapid development with rapidly changing landscape patterns, and the POI data updated slowly. Therefore, there is a partial error between the inner boundary of the urban fringe extracted by the POI kernel density breakpoint analysis and the actual boundary. Nevertheless, the FEM-SMU model focuses on the comprehensive performance of the regional landscape disorder degree, POI kernel density, and night light intensity, and is less dependent on the performance of a single factor, thus it can more accurately identify the urban fringe.

4 Discussion

4.1 Accuracy evaluation of the FEM-SMU model

As the landscape disorder degree threshold method makes it difficult to identify the urban fringe of the study area, this study only evaluates the accuracy of the POI kernel density breakpoint analysis method and FEM-SMU model. Through detailed visual analysis in Section 4, we found that the FEM-SMU model was significantly stronger than the POI kernel density breakpoint analysis method in detail and integrity. To further evaluate the extraction accuracy of different methods, field verification and landscape pattern index evaluations were used in this study. A total of 100 sample points were evenly selected along the road around the urban fringe (Figure 5B), and the accuracy of the extraction results was analyzed by field verification (Table 2). It can be seen from the table that the overall accuracy of the FEM-SMU model was significantly higher than that of POI kernel density breakpoint analysis method, reaching 98%. The POI kernel density breakpoint analysis method had a relatively large number of errors, with an overall accuracy of only 67%.

As another validation method, the landscape pattern index is often used to evaluate the extraction accuracy of urban fringes (Peng et al., 2016). After referring to previous research results (Vizzari and Sigura, 2015; Yang et al., 2021), patch density (PD) and the Shannon diversity index (SHDI) were selected to evaluate the accuracy of the two methods at the grade and landscape levels. The PD value indicates the degree of landscape fragmentation, and SHDI represents the degree of richness and complexity of landscape types. Generally speaking, the PD and SHDI in urban fringes should be higher, while those in urban centers and rural areas should be lower. Table 3 shows the PD and SHDI values of the two methods in different regions calculated by the Fragstats 4.2 software. It can be seen from the table that the PD and SHDI values of the FEM-SMU model were significantly higher than those of the POI kernel density breakpoint analysis method in the urban fringe. This shows that the degree of landscape fragmentation, complexity, and diversity in the urban fringe extracted by the former was higher than

TABLE 3 PD and SHDI values in different regions.

Region	Method	PD				SHDI
		Vegetation	Water	Construction land	Unused land	
Urban fringe	POI KDE	28.66	6.34	11.28	4.22	0.87
	FEM-SMU	34.01	6.68	11.80	6.93	0.92
Urban core	POI KDE	44.64	9.30	2.37	2.14	0.42
	FEM-SMU	44.23	9.23	2.24	2.20	0.42
Rural	POI KDE	10.82	5.82	15.89	4.63	0.76
	FEM-SMU	7.03	5.64	14.25	3.33	0.70

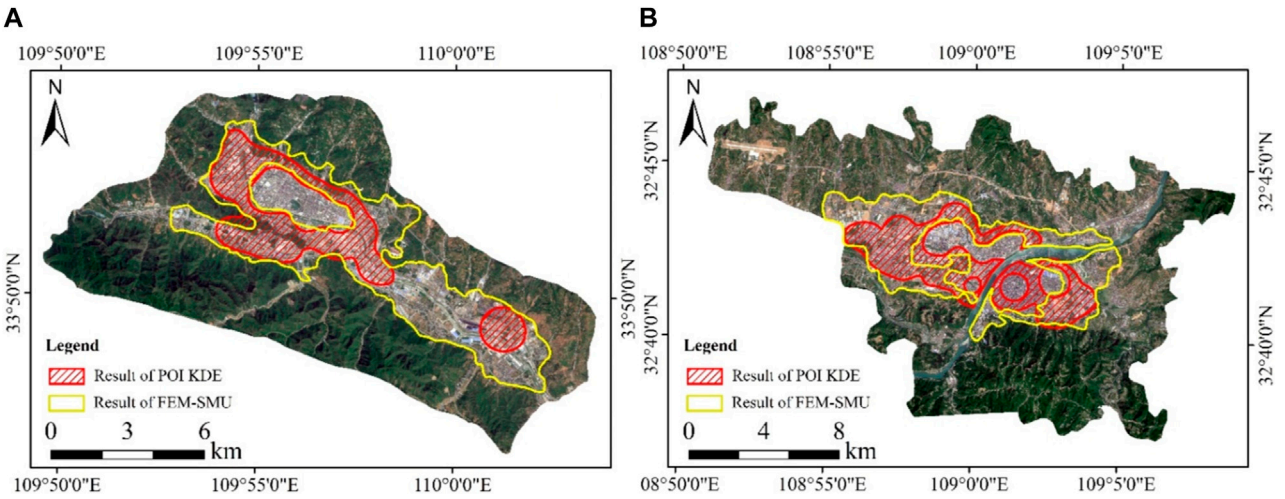

FIGURE 6
(A) Urban fringe of Shangzhou District extracted using different methods. **(B)** Urban fringe of Hanbin District extracted using different methods.

that of the latter, which can better reflect the characteristics of the urban fringe. In the rural hinterland, the PD and SHDI values of the FEM-SMU model were significantly lower than those of the POI kernel density breakpoint analysis method. However, the PD and SHDI values are approximate in the urban core areas because of the relatively small difference between the boundaries extracted by the two methods. In conclusion, the two evaluation methods show that the FEM-SMU model has higher accuracy and can accurately extract the urban fringe of the study area.

4.2 Generality analysis of the model

To further verify the applicability of the model proposed in this study in different regions and different types of small- and medium-sized cities, urban fringe identification was completed for Shangzhou District in Shangluo City and Hanbin District in Ankang City (Figure 6). Shangzhou District is a typical banded urban structure, which is severely limited by resource conditions. As shown in Figure 6A, the extraction result of the POI kernel density breakpoint analysis method is incomplete, especially in the southeast. The reason for this is likely that the southeast part of Shangzhou District is mainly an industrial park, and the number of POIs is small and scattered, which is not enough to support the identification of the urban fringe. Hanbin District is separated from the middle by the Hanjiang River, with the old urban area in the southeast and the new urban area in the northwest, which is a multi-center urban structure. As can be seen from Figure 6B, the extraction result of the POI nuclear density breakpoint analysis was poor, especially in the old urban area of the southeast. The main reason for this is likely that the single-factor method requires high data quality when extracting the fringe of multi-center cities, while the development of the old urban area is relatively backward, the population distribution is concentrated, and the POI data are not complete. As a better option, the FEM-SMU model identifies the urban fringe according to the comprehensive performance differences of regional landscape disorder degree, POI kernel density, and night light intensity combined, and is less dependent

on the performance of a single factor, thus it can adapt to different regions and different types of small- and medium-sized cities.

5 Conclusion

This study proposes a FEM-SMU taking the landscape disorder degree, POI kernel density, and night light intensity as urban feature factors. The extraction results of the FEM-SMU model, landscape disorder degree threshold method, and POI kernel density breakpoint analysis method in Hantai District, China were compared through experiments, and the generality of the model was tested in Shangzhou and Hanbin districts, also in China. The results show that although the landscape disorder degree threshold method could reflect the landscape characteristics of urban core areas, the recognition results of the rural hinterland and urban fringe were poor. The overall pattern characteristics of urban core areas extracted by the POI kernel density breakpoint analysis method and FEM-SMU model were consistent, but the former was poor in extracting urban fringe. In contrast, the urban fringe extracted by FEM-SMU had obvious advantages in accuracy, detail, and integrity, and can be applied to different areas and different types of small- and medium-sized urban areas. The research results have important practical significance for optimizing urban spatial layout, controlling unlimited urban expansion, and protecting land resources.

Data availability statement

The original contributions presented in the study are included in the article/supplementary material, further inquiries can be directed to the corresponding author.

Author contributions

JL contributed by processing the data and wrote the main part of the manuscript. BP and SL contributed to writing and collecting data. HY, ZZ, and XN contributed to the research design and gave constructive comments and suggestions.

Funding

This research was supported by the National Natural Science Foundation of China (No.71874183), the Technology Innovation Center for Land Engineering and Human Settlements, Shaanxi Land Engineering Construction Group Co., Ltd and Xi'an Jiaotong University (No. 2021WHZ0090), the Scientific Research Item of Shaanxi Provincial Land Engineering Construction Group (DJNY-YB-2023-33, DJTD-2023-2, DJTD-2022-4), and Shaanxi Key laboratory of land consolidation (No. 300102352502).

Acknowledgments

We greatly appreciate the POI data provided by Gaode, the NPP/VIIRS data provided by NGDC and the Worldpop data provided by the Department of Geography and the Institute of New Pathogens at the University of Florida.

Conflict of interest

Authors JL, BP, and SL were employed by the company Shaanxi Provincial Land Engineering Construction Group Co., Ltd.

The remaining authors declare that the research was conducted in the absence of any commercial or financial relationships that could be construed as a potential conflict of interest.

The authors declare that this study received funding from Shaanxi Provincial Land Engineering Construction Group Co., Ltd. The company had the following involvement in the study: design, data collection and analysis.

Publisher's note

References

Ahani, S., and Dadashpoor, H. (2021). A review of domains, approaches, methods and indicators in peri-urbanization literature. *Habitat Int.* 114, 102387. doi:10.1016/j.habitatint.2021.102387

Cai, J., Huang, B., and Song, Y. (2017). Using multi-source geospatial big data to identify the structure of polycentric cities. *Remote Sens. Environ.* 202, 210–221. doi:10.1016/j.rse.2017.06.039

Cao, F., Ge, Y., and Wang, J.-F. (2013). Optimal discretization for geographical detectors-based risk assessment. *GIScience Remote Sens.* 50 (1), 78–92. doi:10.1080/15481603.2013.778562

Chang, S., Jiang, Q., Wang, Z., Xu, S., and Jia, M. (2018). Extraction and spatial–temporal evolution of urban fringes: A case study of changchun in jilin province, China. *ISPRS Int. J. Geo-Information* 7 (7), 241. doi:10.3390/ijgi7070241

Chen, M., Liu, W., Lu, D., Chen, H., and Ye, C. (2018). Progress of China's new-type urbanization construction since 2014: A preliminary assessment. *Cities* 78, 180–193. doi:10.1016/j.cities.2018.02.012

Cortes, C., and Vapnik, V. (1995). Support-vector networks. *Mach. Learn.* 20 (3), 273–297. doi:10.1007/bf00994018

Dong, C., Man-Chun, L., Zhen-jie, C., Fei-xue, L., and Wei, W. (2010). "A method of division of urban fringe based on message entropy:----A case study in Nanjing Cit," in Proceedings of the 2009 joint urban remote sensing event, May 2009, Shanghai, China, doi:10.1109/URS.2009.5137553

Dong, Q., Qu, S., Qin, J., Yi, D., Liu, Y., and Zhang, J. (2022). A method to identify urban fringe area based on the industry density of POI. *ISPRS Int. J. Geo-Information* 11 (2), 128. doi:10.3390/ijgi11020128

Fang, L., Huang, J., Zhang, Z., and Nitivattananon, V. (2020). Data-driven framework for delineating urban population dynamic patterns: Case study on Xiamen Island, China. *Sustain. Cities Soc.* 62, 102365. doi:10.1016/j.scs.2020.102365

Feng, W., Liu, Y., and Qu, L. (2019). Effect of land-centered urbanization on rural development: A regional analysis in China. *Land Use Policy* 87, 104072. doi:10.1016/j.landusepol.2019.104072

Gant, R. L., Robinson, G. M., and Fazal, S. (2011). Land-use change in the 'edgelands': Policies and pressures in London's rural–urban fringe. *Land use policy* 28 (1), 266–279. doi:10.1016/j.landusepol.2010.06.007

Gao, Y., Feng, Z., Wang, Y., Liu, J.-L., Li, S.-C., and Zhu, Y.-K. (2014). Clustering urban multifunctional landscapes using the self-organizing feature map neural network model. *J. Urban Plan. Dev.* 140 (2), 05014001. doi:10.1061/(asce)up.1943-5444.0000170

Heidenreich, N.-B., Schindler, A., and Sperlich, S. (2013). Bandwidth selection for kernel density estimation: A review of fully automatic selectors. *AStA Adv. Stat. Analysis* 97 (4), 403–433. doi:10.1007/s10182-013-0216-y

Huang, J., Zhou, Q., and Wu, Z. (2016). Delineating urban fringe area by land cover information entropy—An empirical study of guangzhou-foshan metropolitan area, China. *ISPRS Int. J. Geo-Information* 5 (5), 59. doi:10.3390/ijgi5050059

Imhoff, M. L., Zhang, P., Wolfe, R. E., and Bounoua, L. (2010). Remote sensing of the urban heat island effect across biomes in the continental USA. *Remote Sens. Environ.* 114 (3), 504–513. doi:10.1016/j.rse.2009.10.008

Li, H., Gu, H., Han, Y., and Yang, J. (2010). Object-oriented classification of high-resolution remote sensing imagery based on an improved colour structure code and a support vector machine. *Int. J. remote Sens.* 31 (6), 1453–1470. doi:10.1080/01431160903475266

Li, J., Li, J., Yuan, Y., and Li, G. (2019). Spatiotemporal distribution characteristics and mechanism analysis of urban population density: A case of xi'an, Shaanxi, China. *Cities* 86, 62–70. doi:10.1016/j.cities.2018.12.008

Lin, A., Sun, X., Wu, H., Luo, W., Wang, D., Zhong, D., et al. (2021). Identifying urban building function by integrating remote sensing imagery and POI data. *IEEE J. Sel. Top. Appl. Earth Observations Remote Sens.* 14, 8864–8875. doi:10.1109/jstars.2021.3107543

Lin, Q., Guo, J., Yan, J., and Heng, W. (2018). Land use and landscape pattern changes of Weihai, China based on object-oriented SVM classification from Landsat MSS/TM/OLI images. *Eur. J. Remote Sens.* 51 (1), 1036–1048. doi:10.1080/22797254.2018.1534532

Liu, C., Li, W., Zhu, G., Zhou, H., Yan, H., and Xue, P. (2020). Land use/land cover changes and their driving factors in the northeastern Tibetan plateau based on geographical detectors and google earth engine: A case study in gannan prefecture. *Remote Sens.* 12 (19), 3139. doi:10.3390/rs12193139

Liu, H. (2021). Apply fringe identification to understand urban economic development in China: In case of wuhan. *Arabian J. Geosciences* 14 (13), 1295–1314. doi:10.1007/s12517-021-07629-8

Liu, Y., Li, J., and Yang, Y. (2018). Strategic adjustment of land use policy under the economic transformation. *Land Use Policy* 74, 5–14. doi:10.1016/j.landusepol.2017.07.005

Liu, Y., Song, Y., and Arp, H. P. (2012). Examination of the relationship between urban form and urban eco-efficiency in China. *Habitat Int.* 36 (1), 171–177. doi:10.1016/j.habitatint.2011.08.001

Long, Y., Luo, S., Liu, X., Luo, T., and Liu, X. (2022). Research on the dynamic evolution of the landscape pattern in the urban fringe area of wuhan from 2000 to 2020. *ISPRS Int. J. Geo-Information* 11 (9), 483. doi:10.3390/ijgi11090483

Lyu, Y., Wang, M., Zou, Y., and Wu, C. (2022). Mapping trade-offs among urban fringe land use functions to accurately support spatial planning. *Sci. Total Environ.* 802, 149915. doi:10.1016/j.scitotenv.2021.149915

Peng, J., Liu, Y., Ma, J., and Zhao, S. (2018). A new approach for urban-rural fringe identification: Integrating impervious surface area and spatial continuous wavelet transform. *Landsc. Urban Plan.* 175, 72–79. doi:10.1016/j.landurbplan.2018.03.008

Peng, J., Ma, J., and Yuan, Y. (2014). Research progress and prospect on the identification of urban fringe. *Prog. Geogr.* 33 (8).

Peng, J., Zhao, S., Liu, Y., and Tian, L. (2016). Identifying the urban-rural fringe using wavelet transform and kernel density estimation: A case study in beijing city, China. *Environ. Model. Softw.* 83, 286–302. doi:10.1016/j.envsoft.2016.06.007

Scott, A., Carter, C., Reed, M., Larkham, P., Adams, D., Morton, N., et al. (2013). Disintegrated development at the rural–urban fringe: Re-Connecting spatial planning theory and practice. *Prog. Plan.* 83, 1–52. doi:10.1016/j.progress.2012.09.001

Seto, K. C., Sánchez-Rodríguez, R., and Fragkias, M. (2010). The new geography of contemporary urbanization and the environment. *Annu. Rev. Environ. Resour.* 35, 167–194. doi:10.1146/annurev-environ-100809-125336

Sharaf El Din, E. (2020). A novel approach for surface water quality modelling based on Landsat-8 tasselled cap transformation. *Int. J. Remote Sens.* 41 (18), 7186–7201. doi:10.1080/01431161.2020.1754497

Shen, G., Yang, X., Jin, Y., Luo, S., Xu, B., and Zhou, Q. (2020). Land use changes in the zoige plateau based on the object-oriented method and their effects on landscape patterns. *Remote Sens.* 12 (1), 14. doi:10.3390/rs12010014

Shi, K., Huang, C., Yu, B., Yin, B., Huang, Y., and Wu, J. (2014). Evaluation of NPP-VIIRS night-time light composite data for extracting built-up urban areas. *Remote Sens. Lett.* 5 (4), 358–366. doi:10.1080/2150704x.2014.905728

Simon, D., McGregor, D., and Nsiah-Gyabaah, K. (2004). The changing urban-rural interface of african cities: Definitional issues and an application to kumasi, Ghana. *Environ. urbanization* 16 (2), 235–248. doi:10.1177/095624780401600214

Simon, D. (2008). Urban environments: Issues on the peri-urban fringe. *Annu. Rev. Environ. Resour.* 33, 167–185. doi:10.1146/annurev.environ.33.021407.093240

Stumpf, A., and Kerle, N. (2011). Object-oriented mapping of landslides using Random Forests. *Remote Sens. Environ.* 115 (10), 2564–2577. doi:10.1016/j.rse.2011.05.013

Su, T. (2019). Scale-variable region-merging for high resolution remote sensing image segmentation. *ISPRS J. Photogrammetry Remote Sens.* 147, 319–334. doi:10.1016/j.isprsjprs.2018.12.003

Tatem, A. J. (2017). WorldPop, open data for spatial demography. *Sci. data* 4 (1), 170004–4. doi:10.1038/sdata.2017.4

Thaseen, I. S., and Kumar, C. A. (2017). Intrusion detection model using fusion of chi-square feature selection and multi class SVM. *J. King Saud University-Computer Inf. Sci.* 29 (4), 462–472. doi:10.1016/j.jksuci.2015.12.004

Tong, X.-Y., Xia, G.-S., Lu, Q., Shen, H., Li, S., You, S., et al. (2020). Land-cover classification with high-resolution remote sensing images using transferable deep models. *Remote Sens. Environ.* 237, 111322. doi:10.1016/j.rse.2019.111322

Tu, W., Zhu, T., Xia, J., Zhou, Y., Lai, Y., Jiang, J., et al. (2020). Portraying the spatial dynamics of urban vibrancy using multisource urban big data. *Comput. Environ. Urban Syst.* 80, 101428. doi:10.1016/j.compenvurbsys.2019.101428

van Vliet, J., Verburg, P. H., Grădinaru, S. R., and Hersperger, A. M. (2019). Beyond the urban-rural dichotomy: Towards a more nuanced analysis of changes in built-up land. *Comput. Environ. Urban Syst.* 74, 41–49. doi:10.1016/j.compenvurbsys.2018.12.002

Vizzari, M., and Sigura, M. (2015). Landscape sequences along the urban–rural–natural gradient: A novel geospatial approach for identification and analysis. *Landsc. Urban Plan.* 140, 42–55. doi:10.1016/j.landurbplan.2015.04.001

Vranken, I., Baudry, J., Aubinet, M., Visser, M., and Bogaert, J. (2015). A review on the use of entropy in landscape ecology: Heterogeneity, unpredictability, scale dependence and their links with thermodynamics. *Landsc. Ecol.* 30, 51–65. doi:10.1007/s10980-014-0105-0

Wadduwage, S., Millington, A., Crossman, N. D., and Sandhu, H. (2017). Agricultural land fragmentation at urban fringes: An application of urban-to-rural gradient analysis in adelaide. *Land* 6 (2), 28. doi:10.3390/land6020028

Wang, J. F., Li, X. H., Christakos, G., Liao, Y. L., Zhang, T., Gu, X., et al. (2010). Geographical detectors-based health risk assessment and its application in the neural tube defects study of the Heshun Region, China. *Int. J. Geogr. Inf. Sci.* 24 (1), 107–127. doi:10.1080/13658810802443457

Wang, L., Wu, L., and Zhang, W. (2021a). Impacts of land use change on landscape patterns in mountain human settlement: The case study of Hantai District (Shaanxi, China). *J. Mt. Sci.* 18 (3), 749–763. doi:10.1007/s11629-020-6236-7

Wang, Y., Han, Y., Pu, L., Jiang, B., Yuan, S., and Xu, Y. (2021b). A novel model for detecting urban fringe and its expanding patterns: An application in harbin city, China. *Land* 10 (8), 876. doi:10.3390/land10080876

Warren, P. S., Ryan, R. L., Lerman, S. B., and Tooke, K. A. (2011). Social and institutional factors associated with land use and forest conservation along two urban gradients in Massachusetts. *Landsc. Urban Plan.* 102 (2), 82–92. doi:10.1016/j.landurbplan.2011.03.012

Wenhao, Y., and Tinghua, A. (2015). The visualization and analysis of POI features under network space supported by kernel density estimation. *Acta Geod. Cartogr. Sinica* 44 (1), 82.

Whitehand, J., and Gu, K. (2017). Urban fringe belts: Evidence from China. *Environ. Plan. B Urban Anal. City Sci.* 44 (1), 80–99. doi:10.1177/0265813515608849

Xiao, W., Lv, X., Zhao, Y., Sun, H., and Li, J. (2020). Ecological resilience assessment of an arid coal mining area using index of entropy and linear weighted analysis: A case study of shendong coalfield, China. *Ecol. Indic.* 109, 105843. doi:10.1016/j.ecolind.2019.105843

Xu, W., Yu, W., Jing, S., Zhang, G., and Huang, J. (2013). Debris flow susceptibility assessment by GIS and information value model in a large-scale region, Sichuan Province (China). *Nat. hazards* 65, 1379–1392. doi:10.1007/s11069-012-0414-z

Yang, J., Dong, J., Sun, Y., Zhu, J., Huang, Y., and Yang, S. (2021). A constraint-based approach for identifying the urban–rural fringe of polycentric cities using multi-sourced data. *Int. J. Geogr. Inf. Sci.* 36, 114–136. doi:10.1080/13658816.2021.1876236

Yang, Y., Ma, M., Tan, C., and Li, W. (2017). Spatial recognition of the urban-rural fringe of Beijing using DMSP/OLS nighttime light data. *Remote Sens.* 9 (11), 1141. doi:10.3390/rs9111141

Yue, W., Liu, Y., and Fan, P. (2013). Measuring urban sprawl and its drivers in large Chinese cities: The case of Hangzhou. *Land use policy* 31, 358–370. doi:10.1016/j.landusepol.2012.07.018

Zhao, P., and Zhang, M. (2018). Informal suburbanization in Beijing: An investigation of informal gated communities on the urban fringe. *Habitat Int.* 77, 130–142. doi:10.1016/j.habitatint.2018.01.006

Zhou, L., Tu, W., Wang, C., Ma, W., and Li, Q. (2021). A heterogeneous access meta-model for efficient IoT remote sensing observation management: Taking precision agriculture as an example. *IEEE Internet Things J.* 9, 8616–8632. doi:10.1109/jiot.2021.3118024

frontiers | Frontiers in Environmental Science

TYPE Original Research
PUBLISHED 23 May 2023
DOI 10.3389/fenvs.2023.1120704

OPEN ACCESS

EDITED BY
Jiren Xu,
University of Glasgow, United Kingdom

REVIEWED BY
Yuhong Zhang,
Harbin Normal University, China
Lei Wang,
Northeast Forestry University, China

*CORRESPONDENCE
Jing Ning,
jning@neau.edu.cn
Huimei Zhang,
2857852358@qq.com

RECEIVED 10 December 2022
ACCEPTED 09 May 2023
PUBLISHED 23 May 2023

CITATION
Ning J, Zhang H, Shi D and Du G (2023), Analysis of trade-offs/synergies in land use function changes in Bin County, China.
Front. Environ. Sci. 11:1120704.
doi: 10.3389/fenvs.2023.1120704

Analysis of trade-offs/synergies in land use function changes in Bin County, China

Jing Ning[1]*, Huimei Zhang[1]*, Dongwei Shi[2] and Guoming Du[1]

[1]School of Public Administration and Law, Northeast Agriculture University, Harbin, China, [2]Pingquan Natural Resources and Planning Bureau, Pingquan, China

Land use function has become an important part in land change science. More attention should be given to multifunctional land to achieve land structure optimization and sustainable land use. This study takes Bin County in Heilongjiang province of China as the research area and investigates the spatiotemporal pattern and trade-off synergistic relationship of land functions from 2000 to 2020. Land functions were quantitatively measured by the spatiotemporal method of statistical data, INVEST model, CASA, RUSLE, and other models. The results showed that 1) during 2000–2020, the production function showed an overall trend of enhancement. Living function remained enhanced except in the southeast and north. The water conservation function was weakened in most areas, while the carbon fixation function was strengthened in the southeast and weakened in the central and northern parts. Soil conservation function decreased first and then increased significantly in the southwest. 2) There was a synergistic relationship between production and living functions and trade-off relationships between ecology and production functions and ecology and living functions from 2000 to 2020. 3) The production and living functions are mainly coordinated in space, and the collaborative agglomeration types are mainly distributed in Tangfang town, Manjing town, and other areas. The spatial distribution of trade-offs and synergies between ecological and productive functions and ecological and living functions was similar. The trade-off and agglomeration types were scattered, and the synergies were distributed in Binxi town and Juren town.

KEYWORDS

land use function, trade-offs, synergies, spatiotemporal variation, Bin County

1 Introduction

The land is a complex system of ecology–economy–society, carrying all social and economic activities of human beings and providing space bearing and material foundation for human beings (Huang et al., 2017; LUO, 2019). With the deepening of land use research, its scope has been gradually extended to land use function evaluation, relationship, mechanism, and zoning. Influenced by human behavior and activities, the interaction between different land use functions is complex, but it mainly shows two kinds of relationships: mutual checks and balances and mutual promotion. Based on these, we can identify and coordinate the relationship between different land use functions and their spatial and temporal distribution patterns is a meaningful way to realize the optimal allocation and sustainable use of land resources to provide a broader perspective for managers to use the land better.

Studying the spatiotemporal pattern of land use function and its trade-off and synergy is a hot topic in land science and geographical science. Meng et al. (2021), Zhu et al. (2018), and Peng et al. (2016) adopted the correlation analysis method to identify the service function relationship and its intensity change (Sun et al., 2018; Xu et al., 2018). Liu et al. (2019), Feng et al. (2017), and Fang et al. (2018) used the root mean square error method to analyze the trade-off and synergy between ecosystem services and cultivated multifunctional land. Yang et al. (2019), Lester et al. (2013), Cavend-Bares et al. (2015), and Verhagen et al. (2018) have quantitatively described the abstract relationship of ecosystem services by drawing the possible productive boundary. Zhang et al. (2019) and Liu et al. (2018) studied and analyzed the relationship between land use function, urban expansion, and cultivated land protection. Wang and Tang (2018), Liu et al. (2021), and Willemen et al. (2010), respectively, took the Chongqing Municipality, Beijing Municipality, and the countryside of the Netherlands as examples to analyze the coupling relationship of rural functional trade-offs. Xin et al. (2019) and Ren et al. (2019) used statistical analysis to explore the interaction of land use functions in time and used spatial analysis to describe the trade-off synergistic relationships of land use functions in space. Pan et al. (2013) used bivariate spatial autocorrelation to analyze the spatial trade-off of multiple ecosystem supplies. Qi et al. (2020) identified ecosystem service clusters in northeast China and divided them into ecological functional areas. Kang et al. (2021) and Zhang et al. (2019) analyzed and showed the characteristics of land use function evolution and trade-off synergistic relationships based on a comprehensive evaluation model and mechanical model.

From the perspective of domestic and foreign research, there was some progress in the research of land use function. However, there is still significant room for progress in applying land use functions to evaluate content and results. The following are the shortcomings: 1) in research content, studies mainly focus on constructing a function evaluation index system, the spatial and temporal distribution of functions, and analyzing the influencing factors. In analyzing spatial and temporal patterns of land use functions, there is a lack of spatial correlation analysis and research on the spatiotemporal dynamics and heterogeneity of land use functions. 2) In terms of research and application, the combination of research conclusion and practical application is not potent, and the typical research cases are few and concentrated in regions that have no reference value for the research of land use function in other regions in China. In the future, the research scope should be expanded, especially to regions with high comprehensive research value of land use function, to provide method cases for improving the multifunctional level of land use within the regional scope. Based on this, this work takes Bin County, a typical black soil area with land use characteristics, as the study area to conduct a multifunctional study of land use. With the help of the statistical spatial data method, INVEST model, CASA model, and RUSLE model, this work quantitatively measures the spatial–temporal distribution patterns of land use production, and living and ecological functions. This study uses the correlation coefficient and bivariate local spatial autocorrelation methods to study the characteristics of the trade-off synergistic relationships between land use functions from the perspective of space and time to reveal the dynamic and spatial heterogeneity and provide a reference for land use, development, and construction.

2 Study area

Bin County is in the south of Heilongjiang province, under the jurisdiction of Harbin city. Its geographical location is between 126°55′–128°19′E and 45°30’–46°01′N, as shown in Figure 1. It has a flat and narrow shape, and the total area is about 3,843.16 km^2. Bin County is high in the southeast and low in the northwest, with an average elevation of 405 m. It has a cold temperate continental climate, with an average annual temperature of 4.5°C and an average annual precipitation of 570 mm. The territory has eight major rivers with complex hydrogeological conditions, and the annual average surface runoff is 4.11 m^3 × 108 m^3. Bin County is a major grain-producing county in the country. Arable land is the main land use type, accounting for 61.31% of the county area. The second is forest and grass. The county has a total forest area of 1,180 km^2, a grassland comprehensive vegetation coverage of 81.3%, and rich forest and grass, which is an important cornerstone for developing the ecological function. There are mainly eight soil types in Bin County, among which the high-quality soil resources, such as black soil and meadow soil in the plain and hilly areas, are a good foundation for agricultural cultivation.

3 Materials and methods

3.1 Data sources

This study mainly includes 1) socioeconomic statistical data from the statistical yearbook of the Heilongjiang province, the statistical yearbook of Bin County (2000–2020), and the bulletin of water resources of Bin County. The missing statistics are obtained by calculating the average annual growth rate and other methods. 2) Natural environment data such as remote sensing data, topographic data, meteorological data, soil data, etc. 3) Reference data used for setting relevant parameters in model calculation (Table 1).

Among these, the collection of land use data is to extract the land use data of Bin County from 2000 to 2020 through the ENVI 5.3 software combined with human–computer interactive visual interpretation and modify the interpretation results by combining the Google Earth software and field investigation to meet the accuracy requirements. In order to facilitate the quantitative measurement of the functional model used for land use functional evaluation, preliminary data processing was carried out. All raster and vector data were projected to the ArcGIS10.5 software platform, where the coordinates were unified as WGS_1984_UTM_Zone_52N, and the mask was cut with the administrative boundary of Bin County in 2020, and the accuracy was unified.

3.2 Methodology

3.2.1 Production function

Net primary production (NPP) is the difference between the total amount of organic matter produced by the green vegetation

TABLE 1 Data sources and descriptions.

Data type	Data source	Resolution	Notes
Land use data	Geospatial data cloud (http://www.gscloud.cn)	30 m × 30 m	Through the interpretation of Landsat remote sensing images, the land use is divided into six categories, such as arable land
Digital elevation data (DEM)			Aster GDEM data: used to calculate slope coefficient s, slope length coefficient L, and soil conservation function
Normalized vegetation index (NDVI)	NASA (https://www.nasa.gov/)	250 m × 250 m	Modis products, MOD13Q116 days data are synthesized monthly to calculate the net primary productivity of vegetation (NPP)
Night light data	National Oceanic and Atmospheric Administration (https://www.ngdc.noaa.gov)	1 km × km	Used for calculating non-agricultural economic output value and residential load-bearing function
Meteorological data	National Meteorological Information Center (http://data.cma.cn/)	Weather station	Precipitation, sunshine hours, temperature, relative humidity, wind speed
Soil data	Scientific Data Center for cold and arid regions (http://westdc.westgis.ac.cn/)	1:1 million	It mainly includes soil types (gravel, clay, silt, organic matter content), soil depth, and so on
Socio-economic data	Heilongjiang statistical yearbook, Bin County, Heilongjiang Resource Water Bulletin	County/township (town) level	Includes population, grain output, economic output value of secondary and tertiary industries, surface runoff
Reference data	Liu et al. (2020) and Zhang and Ren (2015)		Root depth coefficient and vegetation evapotranspiration coefficient

TABLE 2 Vegetation evapotranspiration coefficient and root depth coefficient.

	Cultivated land	Forest land	Meadow	Water area	Construction land	Unused land
Kcx	0.65	1	0.65	1	0.1	0.6
Root depth (mm)	300	3,000	500	1	1	1

TABLE 3 Types of multifunctional land use trade-off/synergistic relationships.

	Production function–living function	Production function–ecological function	Living function–ecological function
High–high aggregation	Production–living high–high synergy type	Production–ecology high–high synergy type	Living–ecology high–high synergy type
Low–low aggregation	Production–living low–low synergy type	Production– ecology low–low synergy type	Living–ecology low–low synergy type
Low–high aggregation	Living–production trade-offs	Ecology–production trade-offs	Ecology–living trade-offs
High–low aggregation	Production–living trade-offs	Production–ecology trade-offs	Living–ecology trade-offs

through photosynthesis and consumption due to respiration of the vegetation per unit time and area, that is, the organic mass accumulated by the vegetation (Jiang, 2020). Therefore, vegetation NPP can reflect the production capacity of different vegetation crops in arable land and can be used as a standard to measure the production capacity of different crops. Based on this, according to the functional measurement model of food production proposed by Fan (2019), this study allocates the statistical data of grain crop yield in townships to the cultivated land grid through NPP to realize the spatialization of grain supply function and analyze the changes of the grain supply function. Combined with the land use vector data, the cultivated land vector layer is extracted, which is based on the l km vector grid in the research region. The NPP data for the entire study area is then input using the ArcGIS spatial analysis tool. The intersecting NPP raster layer is extracted by putting the cultivated land vector layer as a mask. The grain crop yield at the grid scale is quantitatively quantified in conjunction with the statistics on the grain yield of the administrative region, and the regional production function is thoroughly characterized. The specific calculation formula is as follows:

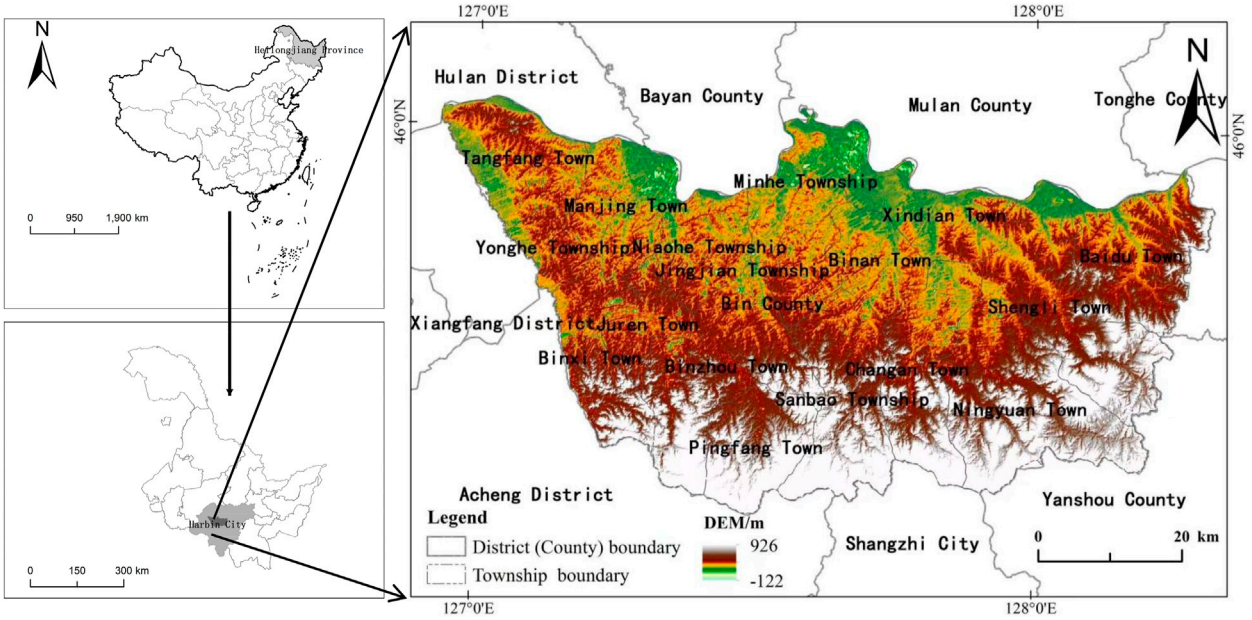

FIGURE 1
Location and elevation of the study area.

$$\frac{Yield_m}{Yield_j} = \frac{NPP_m}{Npp_j}. \quad (1)$$

where $Yield_m$ is the grain yield of the MTH grid and $Yield_j$ is the grain yield of the township where the MTH grid is. NPP_m is the NPP of the MTH grid and NPP_j is the total NPP of the township where the MTH grid is. The unit is t/km^2.

3.2.2 Living function

Based on the relationship between night light data, non-agricultural economic output value, and population residence, the spatial expression of the 1 km grid scale is realized by combining land use type, night light index, and residential density, and based on the population data of the administrative region and the value of secondary and tertiary industries (Han et al., 2012). The calculation formula is as follows:

Non-agricultural output value:

$$GDP_{23_m} = \sum_m^3 (A_{mn} \times NL_{mn} + B_{mn} \times NU_{mn} + C_{mn} \times LE_{mn}). \quad (2)$$

where GDP_{23m} is the value of non-agricultural industries (secondary and tertiary industries) in the NTH grid; NL_{mn}, NU_{mn}, and LE_{mn} are the three land lighting parameters of the MTH secondary land type in the construction land in the grid; and A_{mn}, B_{mn}, and C_{mn} are the corresponding weights of the three parameters of the MTH land use type in the grid. The unit is ten thousand yuan/km^2.

Living load:

$$\frac{Pop_m}{Pop} = \frac{M_m}{M}. \quad (3)$$

where Pop_m is the population number of the MTH grid, Pop is the demographic value of the administrative region where the MTH grid is, and Mm and m are the total weight of land use type, night light index, and residential density of the administrative region where the MTH grid is. The unit is person/km^2.

3.2.3 Ecological function

3.2.3.1 Water conservation

Water yield is the ability to represent the water supply and guarantee it in the region. The difference between precipitation and actual evapotranspiration in grid cell x is the water yield in the selected INVEST model (Liu et al., 2020; Pan et al., 2020). The INVEST water conservation model utilizes grid unit parameters to calculate water yield, which includes surface or groundwater runoff, soil water content, water holding capacity of the withered objects, and canopy interception. These parameters cover precipitation, plant transpiration, surface evaporation, plant root depth, plant available water, and soil maximum root burial depth. The calculation formula is as follows:

$$Y_x = \left(1 - \frac{AET_x}{P_x}\right) \times P_x. \quad (4)$$

$$\frac{AET_x}{P_x} = 1 + \frac{PET_x}{P_x} - \left[1 + \left(\frac{PET_x}{P_x}\right)^{\omega}\right]^{1/\omega}. \quad (5)$$

$$\omega_x = \frac{AWC_x \times Z}{P_x} + 1.25. \quad (6)$$

$$PET_x = Kc_x \times ETO_x. \quad (7)$$

$$ETO_x = 0.0013 \times 0.0408 \times SR_x \times (T_x + 17) \times (T_{dvx} - 0.0123P_{mx}). \quad (8)$$

$$AWC_x = Min(Rest.layer.depth, root.deepth) \times PAWC_x. \quad (9)$$

$$PAWC = 54.509 - 0.132Sand - 0.003(Sand)^2 - 0.055Silt - 0.006(Silt)^2 - 0.738Clay + 0.007(Clay)^2 - 2.699Om + 0.501(Om)^2. \quad (10)$$

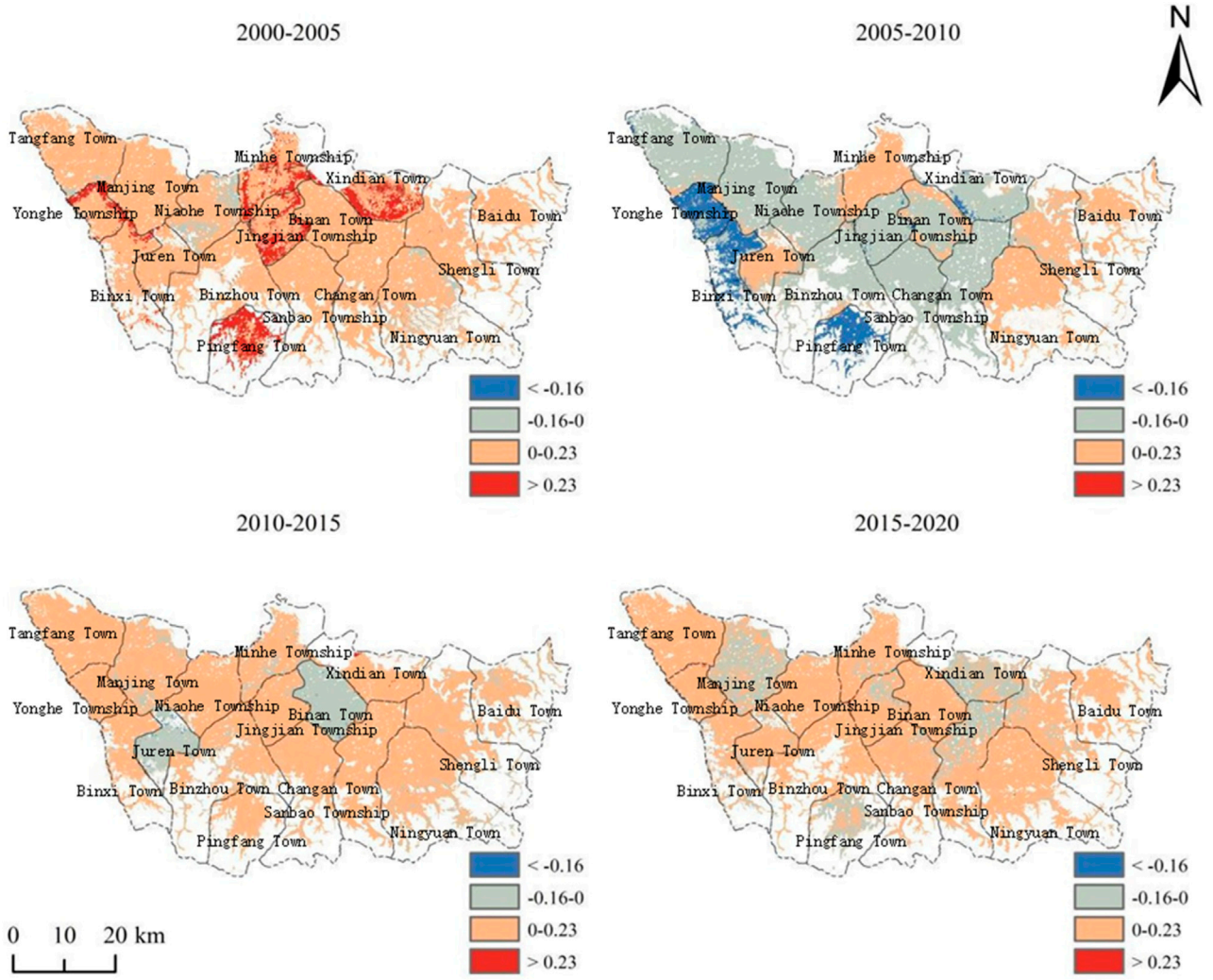

FIGURE 2
Spatial and temporal patterns of production functions in Bin County.

In Eq. 4, Y_x, AET_x, and P_x are the average annual water yield (mm), average annual actual evapotranspiration (mm), and average annual precipitation (mm) of x in each grid cell in the study area, respectively. In Eq. 5, PET_x is the potential evapotranspiration (mm), and ω is a non-physical parameter. In Eq. 6, AWC_x is the available soil water content (mm) of x in each grid cell, Z is an empirical constant, ranging from 1 to 10, Z equals 4.12 through linear fitting according to the surface runoff in the water resources bulletin of Bin County. In Eq. 7, Kc_x is the plant evapotranspiration coefficient of x in each grid cell, which is set in Table 2. ETO_x is the reference crop evapotranspiration of x in each grid cell, which is obtained by the Penman–Monteith formula. In Eq. 8, SR_x is solar radiation, Tx is the daily average temperature, Tdv_x is the difference between the highest and lowest temperatures of the day, and Pm_x is the monthly average precipitation. In Eq. 9, root depth is the root coefficient, and parameter settings are shown in Table 2; $PAWC_x$ is the available water content of vegetation in x of each grid cell. In Eq. 10, Sand is soil sand content, Silt is soil silt content, Clay is soil clay content, and Om is soil organic matter content.

3.2.3.2 Carbon fixation

Carbon fixation is an important ecological function to measure the gas balance and temperature regulation in a region, which refers to the process of carbon fixation and oxygen release through photosynthesis during vegetation growth (Zhang and Ren, 2015). This project intends to use the improved CASA model to calculate NPP, which can be converted into carbon fixation through the photosynthesis equation. The calculation formula is as follows:

$$NPP(x,t) = APAR(x,t) \times \varepsilon(x,t). \quad (11)$$

$$APAR(x,t) = SOL(x,t) \times FPAR(x,t) \times 0.5. \quad (12)$$

$$\varepsilon(x,t) = T_{\varepsilon 1}(x,t) \times T_{\varepsilon 2}(x,t) \times W_{\varepsilon}(x,t) \times \varepsilon_{max}. \quad (13)$$

$$Mc = Nc \times \beta \times \sum NPP(x,t). \quad (14)$$

In Eq. 11, APAR(x, t) is the photosynthetically absorbed active radiation (MJ/m^2/month), and ε (x, t) is the actual light energy utilization rate (gC/MJ). In Eq. 12, SOL(x, t) is the total solar radiation (MJ/m_2/month), where the solar radiation is calculated by the sunshine hours, and FPAR(x, t) is the effective radiation ratio

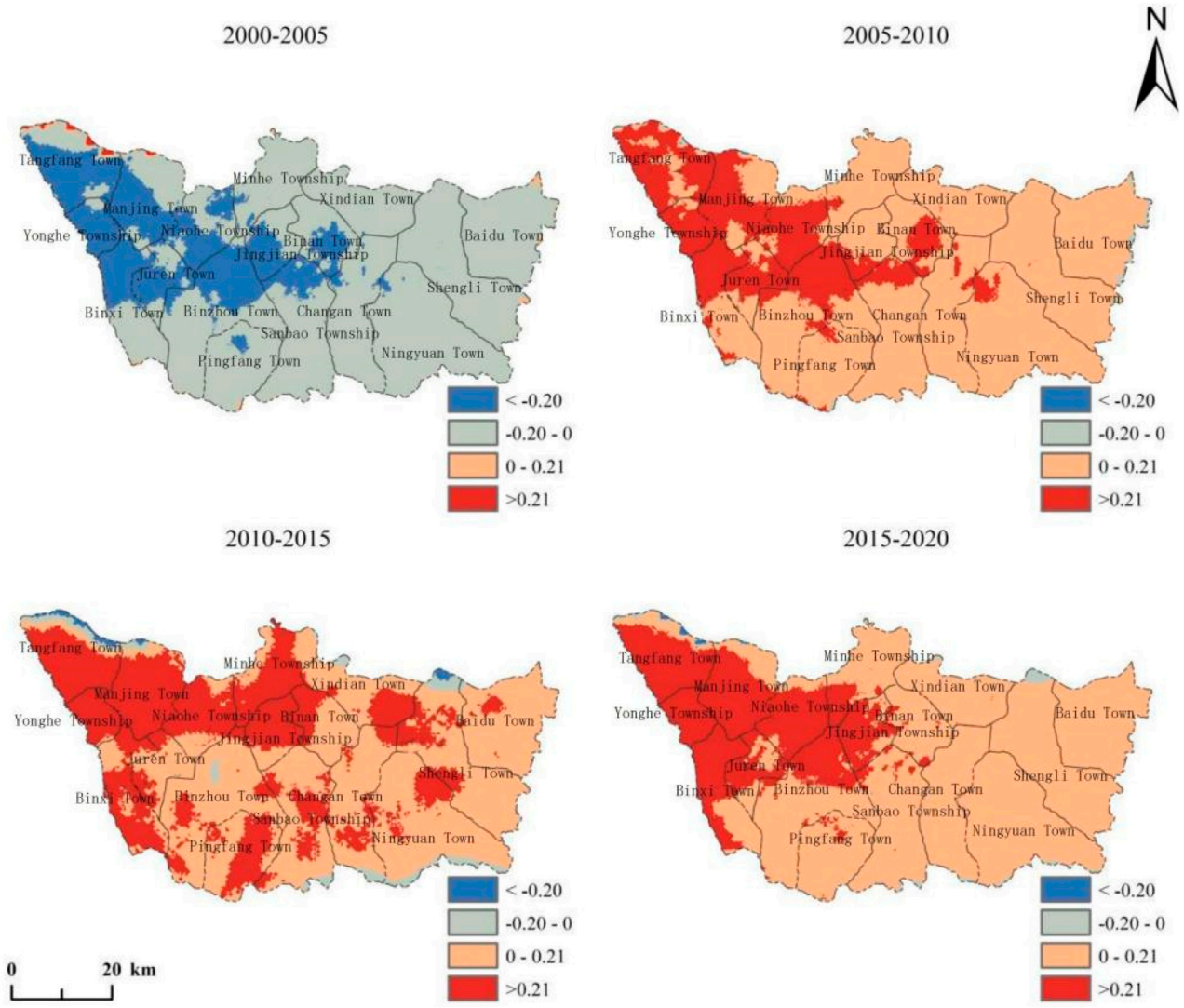

FIGURE 3
Spatial and temporal patterns of living functions in Bin County.

of vegetation to incident light cooperation. In Eq. 13, $T_{\varepsilon 1}(x, t)$ and $T_{\varepsilon 2}(x, t)$ are the effects of high temperature and low temperature stress on light energy utilization, $W\varepsilon(x, t)$ is the effect of water conditions on light energy utilization, and ε_{max} is the maximum light energy utilization (gC/MJ). ε, NDVImax, and NDVImin are set according to Zhu Wenquan's modified CASA model (Zhu et al., 2006a; Zhu et al., 2006b; Zhu et al., 2007). In Eq. 14, Mc is the carbon content of CO_2 in the atmosphere fixed by vegetation, and Nc is the content of C in CO_2, namely, 27.27%; β = 1.63, indicating that 1.63 kg CO_2 will be fixed for every 1 kg organic matter produced by the vegetation.

3.2.3.3 Soil conservation

The soil conservation function represents the ability of green vegetation to protect the soil and its fertility. In this study, the modified Universal Soil Erosion Model (RUSLE) was used to estimate the soil conservation in Bin County (Peng et al., 2017), and the calculation formula is as follows:

$$\begin{aligned} Ac &= Ap - Ar \\ Ap &= R \times K \times LS \\ Ar &= R \times K \times LS \times C \times P. \end{aligned} \quad (15)$$

where Ac is the annual soil conservation (t/hm^2/a), and it is the difference between the potential erosion Ap and actual erosion Ar. The potential soil erosion refers to soil erosion without any water conservation engineering measures (t/hm^2/a), whereas the actual soil erosion refers to soil erosion (Peng et al., 2017) based on the vegetation cover within the scope and the utilization of soil and water conservation measures (t/hm^2/a). R is the annual average precipitation erosivity factor, which is obtained by the Wischmeier empirical formula. K is the soil erosion factor, which is calculated by the EPIC model. LS in the given equations represents the slope length and slope factor, respectively, which are calculated by the method of Zhang et al. (2015) and is dimensionless. C is the vegetation coverage and management factor. P is the water and soil conservation management factor.

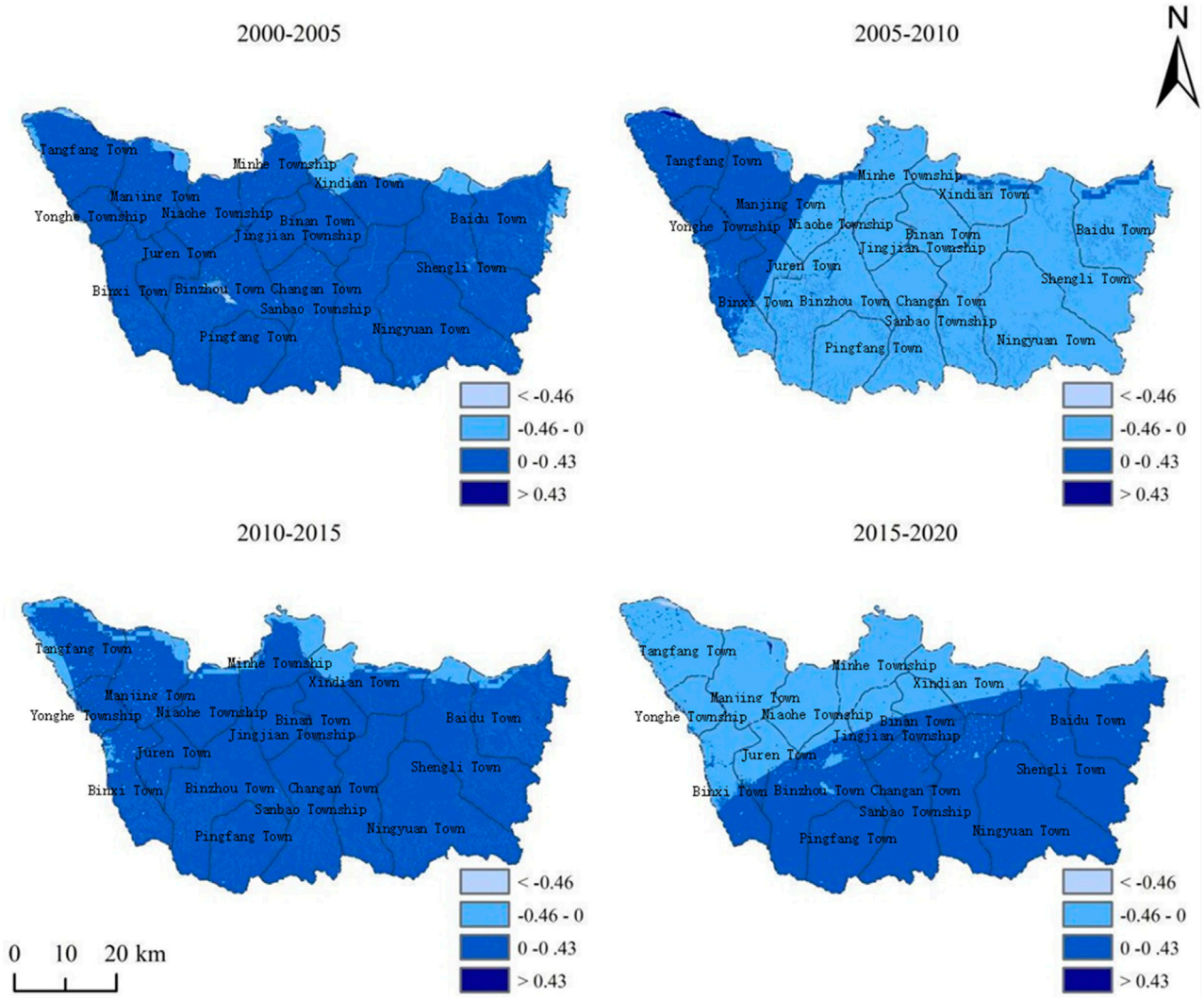

FIGURE 4
Spatial and temporal patterns of ecological functions of water conservation in Bin County.

3.2.3.4 Analysis of tradeoff and synergy

The dynamic changes of the synergistic relationship in time were weighed, and the correlation coefficient method was used to explore the correlation between production, living, and ecological functions at different time points and their intensity, under the scale of a 1 km grid from 2000 to 2020. When the correlation coefficient was positive, it indicated that the functional relationship of the two land use functions was in the same direction, which is a synergistic relationship; when the correlation coefficient was negative, it indicated that the functional relationship of the two land use functions was in the opposite direction, which is a trade-off relationship. The synergies and trade-off of the land use functions change with the absolute quantity of the correlation value (Fan, 2019).

Using bivariate local spatial autocorrelation can achieve the dynamic change of the trade-off synergistic relationship at the spatial scale, which can realize the distribution pattern of the trade-off synergistic relationship between two land use functions. Using different agglomeration types in the bivariate LISA cluster map can represent the trade-off or synergy area. There are five categories: high–high agglomeration synergy area, low–low agglomeration synergy area, high–low agglomeration trade-off area, low–high agglomeration trade-off area, and insignificant area (Cheng et al., 2021).

4 Results

4.1 Analysis of spatial–temporal pattern change of land use function

4.1.1 Spatial and temporal variation pattern of a production function

From the perspective of time characteristics, from 2000 to 2005, the production function of Bin County showed an overall trend of enhancement, and the enhanced area was about 218.60 km^2

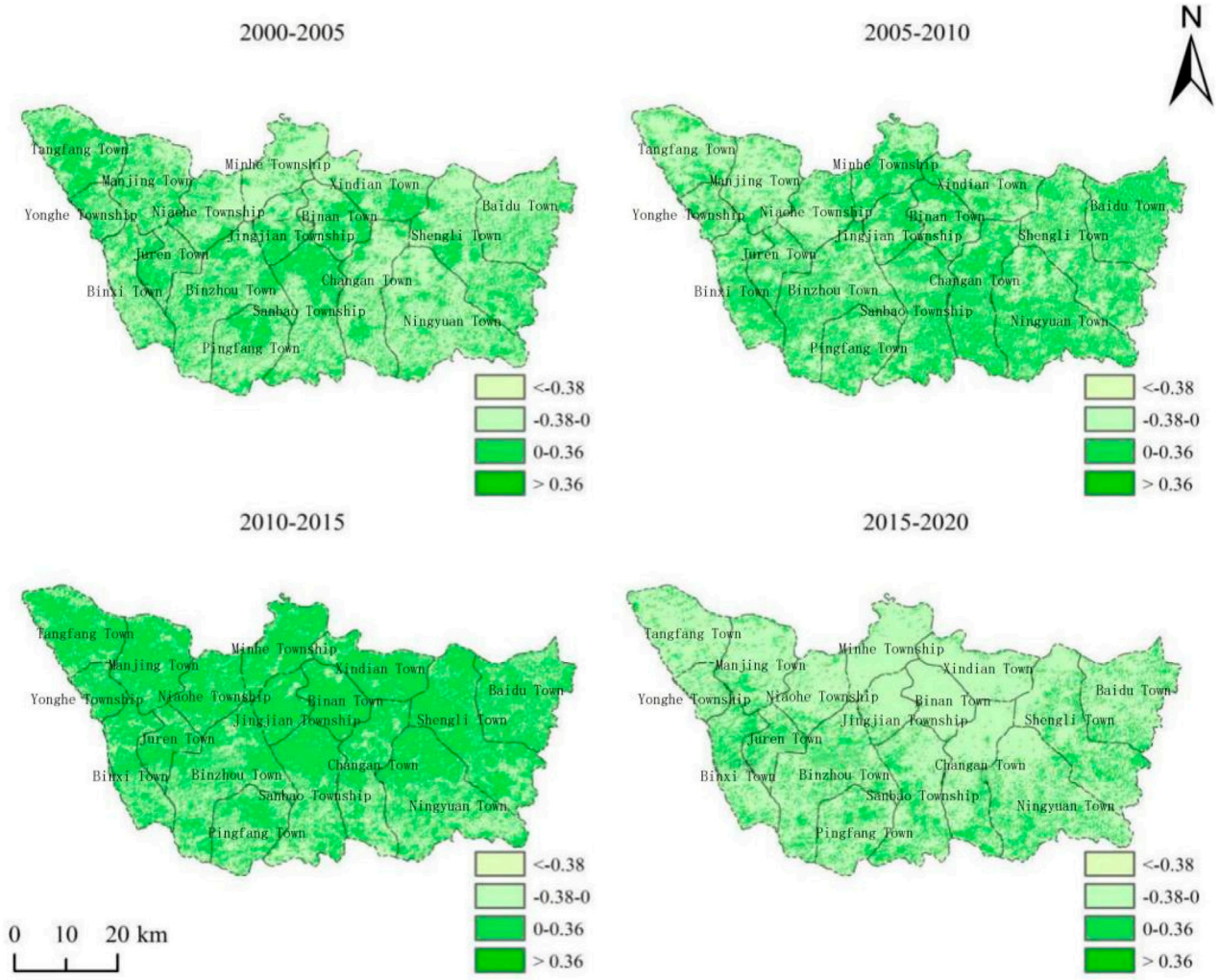

FIGURE 5
Spatial and temporal patterns of ecological functions of carbon fixation in Bin County.

(Figure 2). From 2005 to 2010, the production function decreased, mainly due to the low precipitation and grain yield in 2010. From 2010 to 2015, the production function of most regions had enhanced, and the area of the enhanced function area was about 1958.86 km^2. From 2015 to 2020, the production function of Bin County did not change, and from the area of functional changes, the area of the enhanced region was similar to that of the weakened one. From the change in spatial distribution of the production function, it shows that the enhanced area is mainly in the north of Binzhou town, Ningyuan town, and Baidu town, while the weakened area is mainly in the north of Pingfang town, Xindian town, and Changan town.

4.1.2 Spatial and temporal change pattern of land use living function

From the perspective of time, from 2000 to 2005, the overall living function of Bin County showed a weakening trend, and the enhanced area only accounted for 0.84% of the county area (Figure 3). From 2005 to 2010, and from 2010 to 2015, the living function of Bin County showed an increasing trend, with an area of 3,705.57 km^2 and 3,822.02 km^2, respectively. From 2015 to 2020, the overall living function of Bin County was still enhanced to a large extent, showing a centralized distribution. The change in the spatial distribution of production function shows that the enhanced area is mainly in the north of Binzhou town, Ningyuan town, and Baidu town, while the weakened area is mainly in the north of Pingfang town, Xindian town, and Changan town.

4.1.3 Spatial and temporal change pattern of land use ecological function

4.1.3.1 Ecological functions of water conservation

From 2000 to 2020, according to the distribution of water yield in each township, Ningyuan town, Changan town, Binan town, and Baidu town had relatively high water yields (Figure 4). From 2000 to 2005, precipitation increased and water conservation function was enhanced in most areas, accounting for 92.34% of the county's total area. From 2005 to 2010, the enhanced area of water conservation decreased, and the weakened area was about 1,106.45 km^2, concentrated in the central and eastern areas of Bin County.

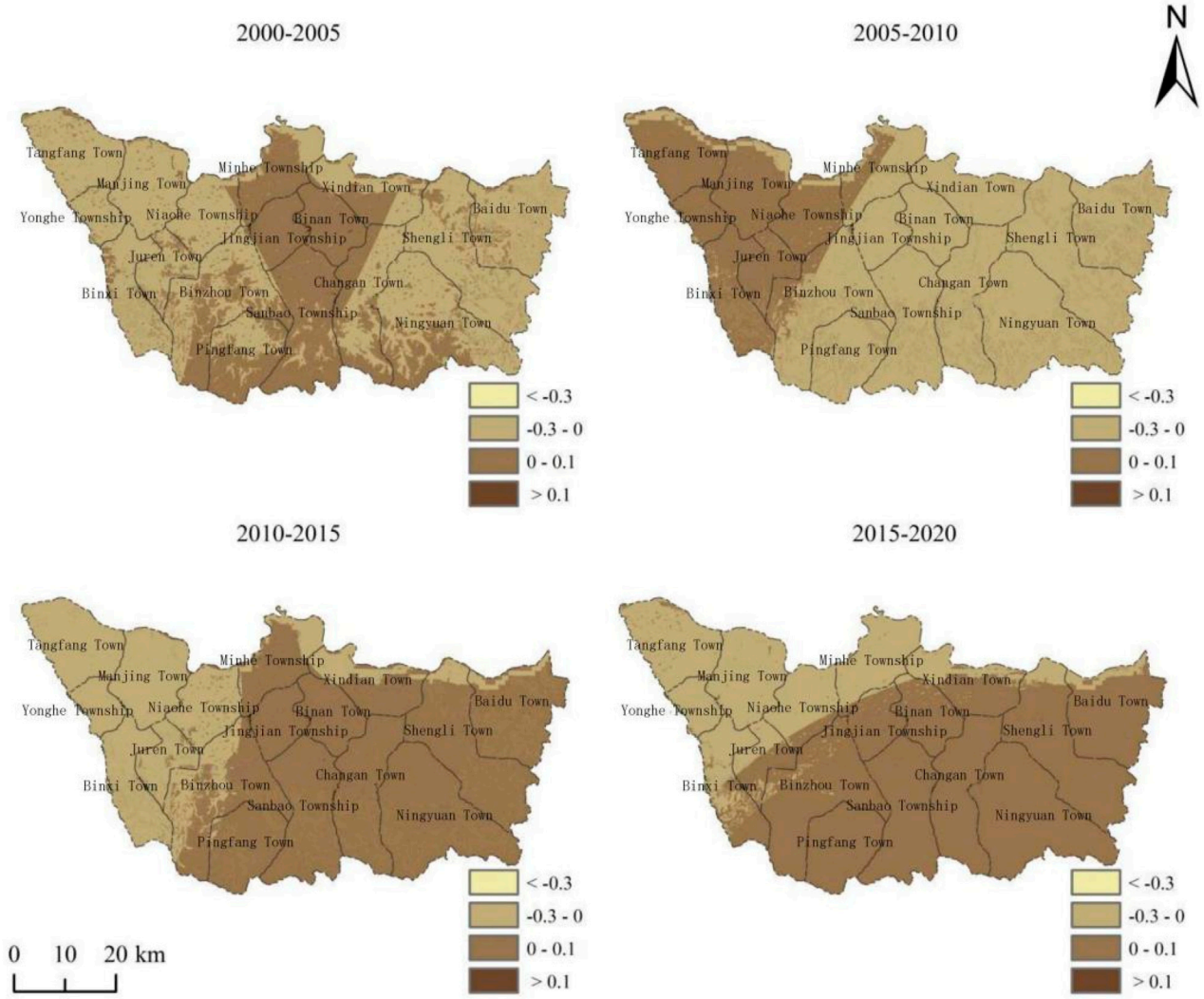

FIGURE 6
Spatial and temporal patterns of ecological functions of soil conservation in Bin County.

From 2010 to 2015, the precipitation increased significantly when compared with the previous period. In addition, due to the perfect construction of soil and water conservation facilities and good vegetation production, the vegetation was fixed and stable, the surface runoff increased, and the water yield showed an overall increasing trend. From 2015 to 2020, due to the influence of typhoon "Bawei" 2020, the summer precipitation was abundant, which resulted in increased defoliation and dead leaves, weakened vegetation evapotranspiration, and decreased the temperature in the southeastern mountainous area. Therefore, the regions with increased water sources are distributed chiefly in the southeastern region.

4.1.3.2 Ecological functions of carbon fixation

In terms of time, from 2000 to 2005, the area with enhanced carbon fixation function was 1700.21 km^2, accounting for 44.24%. From 2005 to 2010, the enhanced and weakened carbon function areas were similar, accounting for 50.15% and 49.85%, respectively. From 2010 to 2015, most areas of carbon fixation function showed an extended growth trend, and the enhanced area expanded by about 2,840.86 km^2. However, from 2015 to 2020, the carbon fixation function decreased. Regarding space, the carbon fixation enhancement areas were mainly concentrated in Tangfang town, Yonghe town, Xindian town, Pingfang town, and Juren village, while the carbon fixation reduction areas were scattered in various townships (Figure 5).

4.1.3.3 Ecological functions of soil conservation

From 2000 to 2005, the changes in soil conservation function showed a trend of decreasing on both sides and increasing in the middle, namely, in the middle of Bin County, Sanbao township, Binan township, Jingjian township, Minhe township, and some other areas showed an increasing trend of function, and the proportion of enhanced areas was about 44.24% (Figure 6). From 2010 to 2015, most regions showed a weak, increasing trend, and the functional enhancement part showed a patchy distribution. The

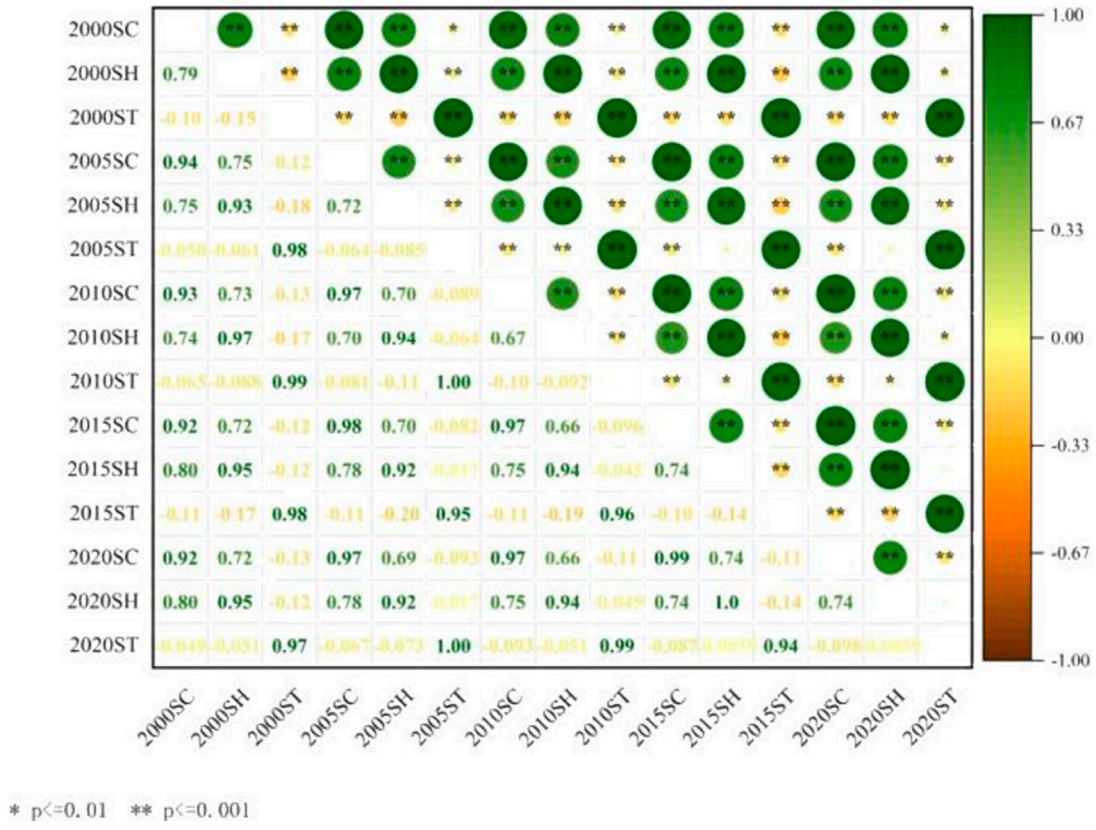

FIGURE 7
Correlation between production, living, and ecological functions in Bin County.

change in soil function in 2005–2010 and 2015–2020 was consistent with the spatial distribution trend of the water conservation function because the change in water conservation is directly related to the level of soil and water conservation capacity, which is a significant positive correlation. The surface runoff accelerates the soil surface loss, which is not conducive to soil conservation.

4.2 Synergistic analysis of land use function trade-off in Bin County

4.2.1 Temporal variation analysis of land use function trade-off and synergy

It can be seen from Figure 7 that the correlation coefficients of the production and living functions in Bin County at the five time points of 2000, 2005, 2010, 2015, and 2020 are all greater than zero, with values between 0.671 and 0.789, indicating a significant positive correlation, that is, a stable synergistic relationship between the two. Overall, the average correlation coefficient was 0.619, indicating a high degree of synergy. However, from the perspective of changes, the synergetic relationship changed with the advance of time, indicating that the trade-off synergetic relationship between land use functions was volatile and dynamic.

As seen from Figure 7, from 2000 to 2020, the production and ecological functions of Bin County always showed a negative correlation, and the average value of the correlation coefficient was −0.094, indicating that the trade-off degree changed stably. In general, from 2000 to 2020, the correlation coefficient between the production and ecological functions in Bin County first increased, then decreased, and again increased. In 2005, the trade-off relationship between production and ecological functions weakened significantly, and the trade-off relationship was enhanced.

From 2000 to 2020, the living and ecological functions in Bin County showed different degrees of negative correlation at five different time points. During the study period, the absolute value of the correlation coefficient showed a trend of first decreasing, then increasing, and again decreasing, indicating that the trade-off relationship between the two functions also showed corresponding fluctuations. In summary, from 2000 to 2020, the degree of trade-off between the living and ecological functions in Bin County was continuously weakened, and the correlation coefficient decreased by 0.148 during the 20 years. The trade-off relationship between the living and ecological functions in Bin County changed significantly during 2000–2005 and 2015–2020.

4.2.2 Spatial change analysis of land use function trade-off and synergy

The specific trade-offs and synergies among production, living, and ecological functions are shown in Table 3, and the spatial distribution pattern is shown in Figure 8.

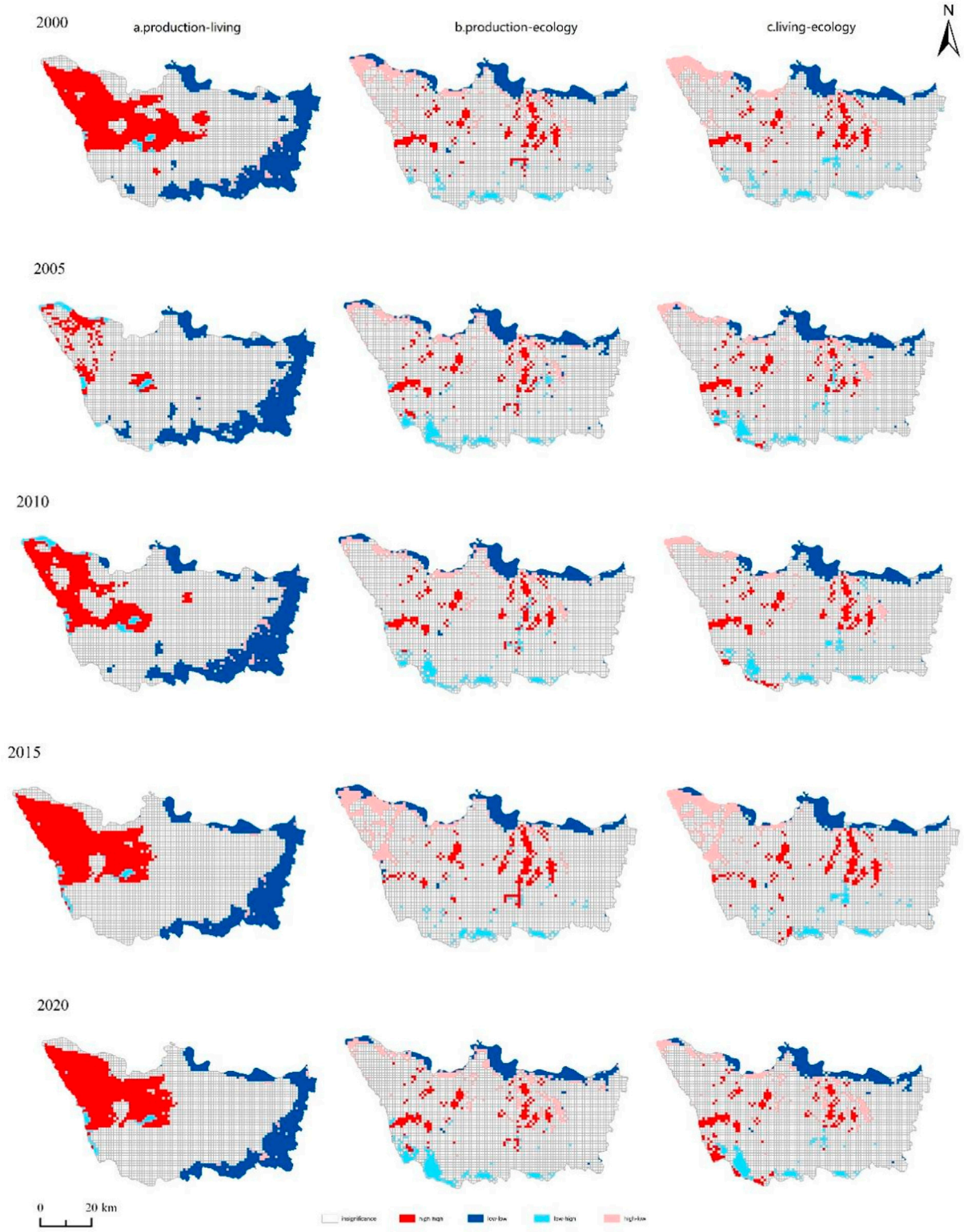

FIGURE 8
Spatial distribution pattern of functional trade-offs/synergistic relationships of land use in Bin County in 2000–2020.

4.2.2.1 Production and living functions

From 2000 to 2020, the trade-off synergistic relationship between production and living functions in Bin County has apparent spatial heterogeneity. In 2000, the relationship between production and living functions was mainly characterized by production–living high–high synergy and low–low synergy. The production–living trade-off (high–low) and the living–production trade-off (low—high) showed an irregular spatial pattern. In 2005,

the number of high–high agglomeration units decreased from 936 in 2000 to 229, and the number of low–low agglomeration units was stable, indicating that the communal area decreased, the low–high agglomeration and high–low agglomeration units increased from 85 to 110, and the trade-off area increased slightly. From 2010 to 2020, the spatial trade-off/synergy between production and living functions changed stably, and mainly manifested as a synergy relationship. The number of agglomeration units in 2010, 2015 and 2020 accounted for 36.44%, 38.99% and 38.57%, respectively. High–high agglomeration grid cells accounted for 39.90%, 55.02%, and 55.18% of the cooperative relationship, indicating that the cooperative relationship was gradually dominated by high–high agglomeration in space.

4.2.2.2 Production and ecological functions

From 2000 to 2020, the spatial distribution of the trade-off synergistic relationships between production function and ecology function in Bin County was stable. The production-ecology low-low synergy type was mainly distributed in the northern valley plain area of Bin County, while the production-ecology high-high synergy type was mainly distributed in Binxi town, Niaohe township, Binan town and the northern area of Ningyuan town. The high–low agglomeration (production–ecological trade-off) type with trade-off relationship was scattered in some areas of Tangfang town, Xindian town, and Binan town, and the low–high agglomeration (eco–production trade-off) type was mainly distributed in the low hilly areas of southern Bin County.

4.2.2.3 Living and ecological functions

From 2000 to 2020, the living and ecological functions in Bin County mainly characterized the living–ecology high–high synergy (high–high) and living–ecology low–low synergy (low–low), among which the low–low agglomeration type accounted for 59.24%, 63.08%, 60.24%, 58.3%, and 59.39% of the synergistic relationship. It indicates that the synergy relationship dominated the low–low agglomeration type. On the other hand, the trade-off types showed a decreasing trend, and high–low agglomeration (living–ecological trade-off) types accounted for 69.47%, 56.11%, 56.90%, 73.70%, and 61.56% of the trade-off relationships, indicating that high–low agglomeration types dominated the trade-off relationship. According to the spatial distribution pattern of the trade-off and synergy regions between living and ecological functions, the trade-off areas were distributed in Tangfang town, Yonghe town, Sanbao township, and the southern mountain area of Penn town in the northwest of Bin County.

5 Conclusion

This study takes Bin County as the research area to analyze the dynamic change of multifunctional land use and explore the spatiotemporal change patterns of trade-offs and synergies among various land use functions, aiming to provide scientific reference for optimizing the multifunctional land use in Bin County.

(1) Based on the literature research and the development characteristics of Bin County, the land use function was divided into production, living, and ecological functions. From 2000 to 2020, the production function of Bin County showed an overall trend of enhancement. Living function enhanced except in the southeastern mountainous area of Bin County and along the Songhua river in the north. The water conservation function weakened in most areas of the county, and the carbon fixation function was enhanced in southeastern Bin County but weakened in the central hills and the northern plain area. The soil conservation function showed a trend of decreasing first and then increasing, and the function improved significantly in southwestern Bin County.

(2) The trade-offs and synergies of land use function in Bin County in 2000, 2005, 2010, 2015, and 2020 were measured from two dimensions of time and space, and the spatiotemporal evolution trend of land use function in the 1 km grid scale was analyzed. During the study period, the production and living functions in Bin County always showed a significant synergistic relationship, and the production and ecological functions, as well as the living and ecological functions were significant trade-offs. From 2000 to 2020, the production and living functions of Bin County mainly showed a collaborative relationship in space, and the clustering type of collaborative relationship was distributed in Tangfang town, Manjing town, and other areas. The spatial distribution of trade-offs and synergies among production, living, and ecological functions was similar, and the clustering types of trade-offs showed an irregular distribution pattern. These types of synergies were mainly distributed in Binxi town, Juren village, and other areas.

Data availability statement

The raw data supporting the conclusion of this study will be made available by the authors, without undue reservation.

Author contributions

JN was responsible for data processing, model calculation, writing of manuscript, and verifying. HZ was responsible for writing of manuscript and verifying. DS was responsible for data processing and model calculation. All authors contributed to the article and approved the submitted version.

Funding

This research was funded by The National Natural Science Foundation of China, grant No. 41971217; the National Key R&D Program of China, grant No. 2021YFD1500101.

Conflict of interest

The authors declare that the research was conducted in the absence of any commercial or financial relationships that could be construed as a potential conflict of interest.

Publisher's note

References

Cavender-Bares, J., Polasky, S., King, E., and Balvanera, P. (2015). A sustainability framework for assessing trade-offs in ecosystem services. *Ecol. Soc.* 20, art17. doi:10.5751/es-06917-200117

Cheng, H., Meng, J., and Zhu, L. (2021). Spatial-temporal pattern and tradeoff of land versatility in the middle reaches of Heihe River based on multi-source geographic data fusion. *Arid. Land Geogr.* 44 (01), 208–220. doi:10.12118/j.issn.1000–6060.2021.01.22

Fan, Y. (2019). *Study on the trade-off and coordination of land use functions in rapid urbanization areas*. Nanjing, China: Nanjing University.

Fang, Y., Wang, J., Kong, X., Wu, R., Li, B., and Liu, J. (2018). Measurement and zoning optimization of multifunctional trade-off of cultivated land use: A case study in henan province. *China Land Sci.* 32 (11), 57–64. doi:10.11994/zgtdkx.20181019.151512

Feng, Q. W., Fu, B., Ding, J., and Wang, S. (2017). Ecosystem service trade-offs and their influencing factors: A case study in the loess plateau of China. *Sci. Total Environ.* 607, 1250–1263. doi:10.1016/j.scitotenv.2017.07.079

Han, X., Zhou, Y., Wang, S., Liu, R., and Yao, Y. (2012). Spatialization of GDP based on night light and land use data. *Remote Sens. Technol. Appl.* 27 (03), 396–405.

Huang, A., Xu, Y., Jinmin, H., Sun, P., Liu, C., and Zheng, W. (2017). Research progress and prospect of multi-functional evaluation of land use. *China Land Sci.* 31 (04), 88–97. doi:10.11994/zgtdkx.20170315.133056

Jiang, Y. (2020). *Change of cultivated land use and its impact on farmland productivity in black soil region of Heilongjiang Province*. Harbin, China: Northeast Agricultural University.

Kang, Q., Guo, Q. X., Ding, Y., Zhang, Y., Hu, Y., and Chen, S. Y. (2021). Spatial-temporal differentiation and influencing factors of "three living" functions in Shanxi Province, 2005-2018. *Bull. Soil Water Conservation* 41 (05), 327–337. doi:10.13961/j.cnki.stbctb.2021.05.042

Lester, S., Costello, C., Halpern, B. S., Gaines, S. D., White, C., and Barth, J. A. (2013). Evaluating tradeoffs among ecosystem services to inform marine spatial planning. *Mar. Policy* 38, 80–89. doi:10.1016/j.marpol.2012.05.022

Liu, J. H., Li, W. F., Zhou, W. Q., Han, L. J., and Qian, Y. G. (2018). Scenario analysis of optimal allocation of land use in Beijing-Tianjin-Hebei urban agglomeration based on urban expansion, cultivated land protection and ecological benefits. *Acta Ecol. Sin.* 38 (12), 4341–4350. doi:10.5846/stxb201712312369

Liu, L., Wang, Z., Wang, Y., Zhang, Y., Shen, J., Qin, D., et al. (2019). Trade-off analyses of multiple mountain ecosystem services along elevation, vegetation cover and precipitation gradients: A case study in the taihang mountains. *Ecol. Indic.* 103, 94–104. doi:10.1016/j.ecolind.2019.03.034

Liu, Y. Y., Liu, X. Y., Zhang, B., and Li, M. Y. (2020). Spatial characteristics of water conservation function in hilly region of Loess Plateau based on INVEST model. *Acta Ecol. Sin.* 40 (17), 6161–6170. doi:10.5846/stxb201910102108

Liu, Y., Gao, Y. B., Pan, Y. C., Tang, L. N., and Tu, M. G. (2021). Spatial characteristics of rural functions based on multi-source data and measurement of trade-offs and synergies. *Geogr. Res.* 40 (07), 2036–2050. doi:10.11821/dlyj020201140

Luo, G. (2019). *Spatial-temporal differentiation and influencing factors of land use versatility in Chongqing*. Chongqing, China: Southwest University.

Meng, H. B., Zhou, Q. G., Li, M. H., Zhou, L., Liu, X. W., and Peng, C. H. (2021). Spatial and temporal changes of ecosystem services and their trade-offs and synergies in the Three Gorges Reservoir Area. *J. Ecol. Rural Environ.* 37 (05), 566–575. doi:10.19741/j.issn.1673-4831.2020.0814

Pan, Y., Xu, Z., and Wu, J. (2013). Spatial differences of the supply of multiple ecosystem services and the environmental and land use factors affecting them. *Ecosyst. Serv.* 5, 4–10. doi:10.1016/j.ecoser.2013.06.002

Pan, X., Shi, P.-ji, and Wu, Na (2020). Ecological risk assessment and priority area identification based on ecosystem service balance: A case study of lanzhou city. *Chin. J. Environ. Sci.* 40 (02), 724–733. doi:10.13671/j.hjkxxb.2019.0437

Peng, J., Liu, Z. C., Liu, Y. X., Chen, X., and Zhao, H. J. (2016). Evaluation of landscape versatility of county cultivated land in Beijing-Tianjin-Hebei region. *Acta Ecol. Sin.* 36 (8), 12. doi:10.5846/stxb201509091856

Peng, J., Liu, Y., Liu, Z., and Yang, Y. (2017). Mapping spatial non-stationarity of human-natural factors associated with agricultural landscape multifunctionality in Beijing–Tianjin–Hebei region, China. *Agric. Ecosyst. Environ.* 246, 221–233. doi:10.1016/j.agee.2017.06.007

Qi, N., Zhao, J., Yang, Y.g, Gou, R. K., Chen, J. Q., Zhao, P. X., et al. (2020). Ecosystem service trade-offs and synergies based on service clusters in Northeast China. *Acta Ecol. Sin.* 40 (09), 2827–2837. doi:10.5846/stxb201903310620

Ren, G., Liu, L., Li, H.g, and Yuan, C. C. (2019). *Trans. Chin. Soc. Agric. Eng.* 35 (23), 273–285. doi:10.11975/j.issn.1002-6819.2019.23.034

Sun, X., Lu, Z., Li, F., and Crittenden, J. C. (2018). Analyzing spatio-temporal changes and trade-offs to support the supply of multiple ecosystem services in Beijing, China. *Ecol. Indic.* 94, 117–129. doi:10.1016/j.ecolind.2018.06.049

Verhagen, W., van der Zanden, E. H., Strauch, M., van Teeffelen, A. J., and Verburg, P. H. (2018). Optimizing the allocation of agri-environment measures to navigate the trade-offs between ecosystem services, biodiversity and agricultural production. *Environ. Sci. Policy* 84, 186–196. doi:10.1016/j.envsci.2018.03.013

Wang, C., and Tang, N. (2018). Spatial and temporal characteristics and pattern evolution of the coupling and coordination of rural three-livelihood spatial function in Chongqing. *Geogr. Res.* 37 (06), 1100–1114. doi:10.11821/dlyj201806004

Willemen, L., Hein, L., van Mensvoort, M. E. F., and Verburg, P. H. (2010). Space for people, plants, and livestock? Quantifying interactions among multiple landscape functions in a Dutch rural region. *Ecol. Indic.* 10, 62–73. doi:10.1016/j.ecolind.2009.02.015

Xin, L., Fang, B., Yin, R., and Hui-fang, R. (2019). Spatial-temporal change and collaboration/trade-off relationship of production-living-ecological functions in county area of Jiangsu province. *J. Nat. Resour.* 34 (11), 2363–2377. doi:10.31497/zrzyxb.20191109

Xu, X., Yang, G., Tan, Y., Liu, J., and Hu, H. (2018). Ecosystem services trade-offs and determinants in China's yangtze river economic belt from 2000 to 2015. *Sci. Total Environ.* 634, 1601–1614. doi:10.1016/j.scitotenv.2018.04.046

Yang, W., Jin, Y., Sun, L.n, Sun, T., and Shao, D. D. (2019). Ecosystem service tradeoff intensity in the Yellow River Delta wetland based on production possibility boundary. *J. Nat. Resour.* 34 (12), 2516–2528. doi:10.31497/zrzyxb.20191203

Zhang, C., and Ren, Z. (2015). Dynamic assessment of carbon sequestration and oxygen release value in land ecosystem in northern Shaanxi Province. *Geogr. Res.* 34 (08), 1522–1534. doi:10.11821/dlyj201508010

Zhang, L., Fu, B., Lü, Y., and Zeng, Y. (2015). Balancing multiple ecosystem services in conservation priority setting. *Landsc. Ecol.* 30 (3), 535–546. doi:10.1007/s10980-014-0106-z

Zhang, Y., Long, H., Tu, S., Ge, D., Ma, L., and Wang, L. (2019). Spatial identification of land use functions and their tradeoffs/synergies in China: Implications for sustainable land management. *Ecol. Indic.* 107, 105550. doi:10.1016/j.ecolind.2019.105550

Zhu, W., Pan, Y., Liu, X., and Wang, A. (2006). Spatio-temporal distribution of net primary productivity along the Northeast China Transect and its response to climatic change. *J. For. Res.* 17 (02), 93–98. doi:10.1007/s11676-006-0022-4

Zhu, W., Pan, Y., He, H., Yu, D., and Hu, H. (2006). Simulation of maximum light utilization rate of typical vegetation in China. *Chin. Sci. Bull.* (06), 700–706. doi:10.3321/j.issn:0023-074X.2006.06.014

Zhu, W., Pan, Y., and Zhang, J. (2007). Estimation of net primary productivity of terrestrial vegetation in China by remote sensing. *Acta Phytoecol. Sin.* (03), 413–424. doi:10.3321/j.issn:1005-264X.2007.03.010

Zhu, Q., Hu, W., and Zhao, Z. (2018). Dynamic analysis of spatial and temporal patterns of multifunctional trade-off and synergy of cultivated land: A case study in hubei province. *Econ. Geogr.* 38 (07), 143–153. doi:10.15957/j.cnki.jjdl.2018.07.018

frontiers | Frontiers in Environmental Science

TYPE Original Research
PUBLISHED 30 May 2023
DOI 10.3389/fenvs.2023.1134917

OPEN ACCESS

EDITED BY
Li Wen,
NSW Department of Planning, Industry and Environment, Australia

REVIEWED BY
Lunche Wang,
China University of Geosciences Wuhan, China
Kaibo Wang,
Chinese Academy of Sciences (CAS), China

*CORRESPONDENCE
Zhouping Shangguan,
shangguan@ms.iswc.ac.cn

RECEIVED 31 December 2022
ACCEPTED 19 May 2023
PUBLISHED 30 May 2023

CITATION
Mao S and Shangguan Z (2023), Evolution of spatiotemporal patterns in vegetation net primary productivity and the driving forces on the Loess Plateau.
Front. Environ. Sci. 11:1134917.
doi: 10.3389/fenvs.2023.1134917

Evolution of spatiotemporal patterns in vegetation net primary productivity and the driving forces on the Loess Plateau

Shenglin Mao and Zhouping Shangguan*

State Key Laboratory for Soil Erosion and Dryland Farming on the Loess Plateau, Northwest A&F University, Xianyang, Shaanxi, China

In this study, we determined whether changes in vegetation net primary productivity (NPP) can be used to characterize the quality of terrestrial ecosystems, which is critical for global change and carbon balance. We first explored the spatial correlation of NPP and its impact on vegetation restoration. MOD17A3 remote sensing products were used to analyze the temporal and spatial changes in NPP on the Loess Plateau (LP) over the last two decades (2000–2020). The resulting spatial autocorrelation indices identified cold and hot spots in the spatial clustering patterns. The effects of climate change and human activities on the anomalous clustering of NPP were assessed using Pearson correlation analysis and multi-temporal land use land cover data. The results indicate that i) Temporally, from 2000 to 2020, the NPP of the LP increased significantly by 6.88 $gCm^{-2}yr^{-1}$ and so did the proportion of revegetated land area >400 $gCm^{-2}yr^{-1}$ from 4% to 37%. Spatially, NPP showed an increasing trend from northwest to southeast. ii) The vegetation NPP on the LP showed a strong positive global spatial autocorrelation ($p< 0.01$). The hot and cold regions were polarized; the cold spots were clustered in the northwest, while the hot spots in the south and east. The spatial clustering patterns were dominated by high-high (HH) and low-low (LL) clusters. Abnormal patterns existed mainly in the transition areas between HH and LL clusters and insignificant regions, which were jointly affected by human activities and climate change. iii) Precipitation was the dominant climatic factor (86%) affecting the NPP variation in the LP, with the annual minimum precipitation showing a significantly positive relationship with the interannual variability in NPP, while the maximum precipitations greatly influenced the variation in local spatial anomaly patterns. This suggests that climatic extremes affect vegetation. Our study helps to facilitate green ecological management and high-quality development in the LP.

KEYWORDS

net primary productivity, spatial autocorrelation, climate change, human activities, land use land cover, Loess Plateau

1 Introduction

Global warming has significantly affected the structure, processes, and functions of terrestrial ecosystems and regional ecological environment. As an important component of terrestrial ecosystems, vegetation provides essential materials for humans and plays an inestimable role in regulating climate change, supporting ecological environments, maintaining a carbon balance, and developing renewable resources. Vegetation net

primary productivity (NPP) refers to the amount of organic carbon fixed by plant photosynthesis (GPP) minus the amount consumed by its respiration and growth (Goldewijk and Leemans, 1995; Yuan et al., 2021). NPP is an important index to measure the structure and function of terrestrial ecosystems and has been used in global and regional ecological environment monitoring and crop yield estimation (Wu et al., 2020; Zhang et al., 2022). Increasing carbon storage capacity may be the most effective way to limit global warming to 1.5°C. As a major factor in evaluating carbon sources and sinks, quantitative assessment of the dynamic changes in NPP not only expand our understanding of the interactions between climate change and ecosystems but also provides theoretical support for early realization of "carbon peaking" and "carbon neutrality" in ecologically fragile areas (Lei et al., 2020).

With the rapid development of remote sensing technology, the estimation of NPP may extend from sample plots to a regional or global scale. It is possible to evaluate the NPP of terrestrial ecosystems using field measurements and model validation; however, the cost of field surveys may be a major limitation. NPP has been a research hot spot at the regional level (Wu et al., 2014; Guo et al., 2021). Currently, the CASA model of the light energy utilization model (parametric model) and the MOD17A3HGF remote sensing product calculated using the BIOME-BGC model have been widely used (Wang et al., 2020; Li et al., 2021; Xiao et al., 2022). Guided by various international conventions on global climate change, the prohibition of deforestation has become a legal provision, and productivity estimates can only be obtained either directly from the field or via remote sensing data. Although the CASA model has recently been improved (Zhu et al., 2007; Pei et al., 2018), and the MOD17A3 HGF data have been refined from 500 m to 250 m, their reliability warrants improvement. In different natural environmental conditions in other regions, the application scope varies, while our understanding of the mechanism regulating various interactions of NPP remains rudimentary, thereby hindering parameter regulations (Kolby Smith et al., 2016). Therefore, there are errors in NPP estimations. A common method used in ecology and geology is the linear regression from the regional to pixel-by-pixel scale to reveal the temporal and spatial changes in vegetation NPP and its response to climate change. Cui et al. (2018) analyzed the growth trend in vegetation NPP in China from 1982 to 2011 based on the GLOPEM-CEVSA model, revealing a growth rate of 5.66 $gCm^{-2}(10yr)^{-1}$. Previous studies have combined simple and multiple linear regression models to explore the spatial-temporal evolution and driving factors of NPP in national park vegetation restorations (Yang et al., 2023) and urbanization development (Peng et al., 2016). Additionally, methods such as partial correlation analysis and the Mann-Kendall trend test better reveal the spatiotemporal variation and driving forces in regional NPP (Pan and Dong, 2018; Wei et al., 2022). Classic statistical analysis suggests that spatiotemporal variation and driving forces of NPP are generally defined as "first-order effects" (Huang et al., 2013). However, spatial pattern changes can also be the result of local effects. Presently, the potential changes and effects of spatial heterogeneity and spatial autocorrelation of vegetation NPP in the Loess Plateau (LP) remains unclear. Therefore, to clarify the spatial pattern in vegetation NPP, we used the first law of geography with spatial autocorrelation to characterize the spatial dependence and spatial heterogeneity of vegetation NPP and explore the convergence and divergence between spatially adjacent location data, i.e., "second-order effect" (Huang et al., 2013; Fan and Myint, 2014). This can better show the spatial variation laws of NPP in different regions.

LP is an important ecological barrier in China, which has one of the most serious soil erosion areas. Prior to the 1990s, China controlled soil erosion by constructing terraces and silt dams and implementing management projects for slopes and small watersheds. Since 2000, China has initiated large-scale projects such as the Grain for Green Project (GGP), gully control, and land reclamation. Thus, the rate of vegetation coverage increased from 31.6% in 1999 to 65% in 2017. In 2016, China has launched the first batch of pilot projects for the ecological protection of mountains, rivers, forests, fields, and lakes. State policies have continuously promoted the construction of rural revitalization and ecological civilization projects. Improving the vegetation coverage of the LP through natural restoration has achieved remarkable results. Although the Grain for Green Project has been implemented to alleviate the problems caused by human activities and natural factors, the local ecological environment remains very fragile, and problems such as insufficient vegetation carrying capacity are becoming increasingly prominent (He et al., 2006; Fu et al., 2011). Vegetation restoration has had several effects on this ecosystem (Lü et al., 2012; Zhao et al., 2013; Zhang et al., 2018), and the vegetation NPP of the LP has evident spatial heterogeneity with interannual variation. Prior to 1990, many scholars explored the changes in vegetation on LP in historical periods using pollen data and other technologies (Liu et al., 1996; Jiang and Ding, 2005). Given the severe soil and water loss, the correlation between vegetation restoration and soil environment after afforestation has been investigated using sample plots (Shangguan and Zheng, 2006). After 2000, remote sensing methods were used to reveal the changes in vegetation cover in the LP, and their association with climate and social factors and also analyze the influencing factors of vegetation change (Chen et al., 2007). At the plot scale, the interaction and mechanism between vegetation and soil erosion, soil and water conservation and organic carbon has attracted attention. The relationship between water and vegetation has been well demonstrated. How to limit the dry layer of soil and sustainably manage regional vegetation has become a hot research topic (Zhang et al., 2016; Ma et al., 2022).

Data on the spatial autocorrelation of vegetation NPP on the LP are limited. We hypothesize that the vegetation NPP on LP has a spatial autocorrelation and correlates with natural factors and human activities. Therefore, we aimed to (1) reveal the temporal and spatial distribution patterns and NPP variation on the LP from 2000 to 2020, (2) explore the spatial dependence and heterogeneity of NPP in the LP from 2000 to 2020 by exploiting global and local autocorrelations, and (3) quantify the impact and contribution of climatic factors and human activities on NPP using Pearson correlation analysis and the land use transition matrix. Our results provide important information to better manage ecological resources for successful vegetation restoration in various regions of the LP and can help to facilitate high-quality development in the LP.

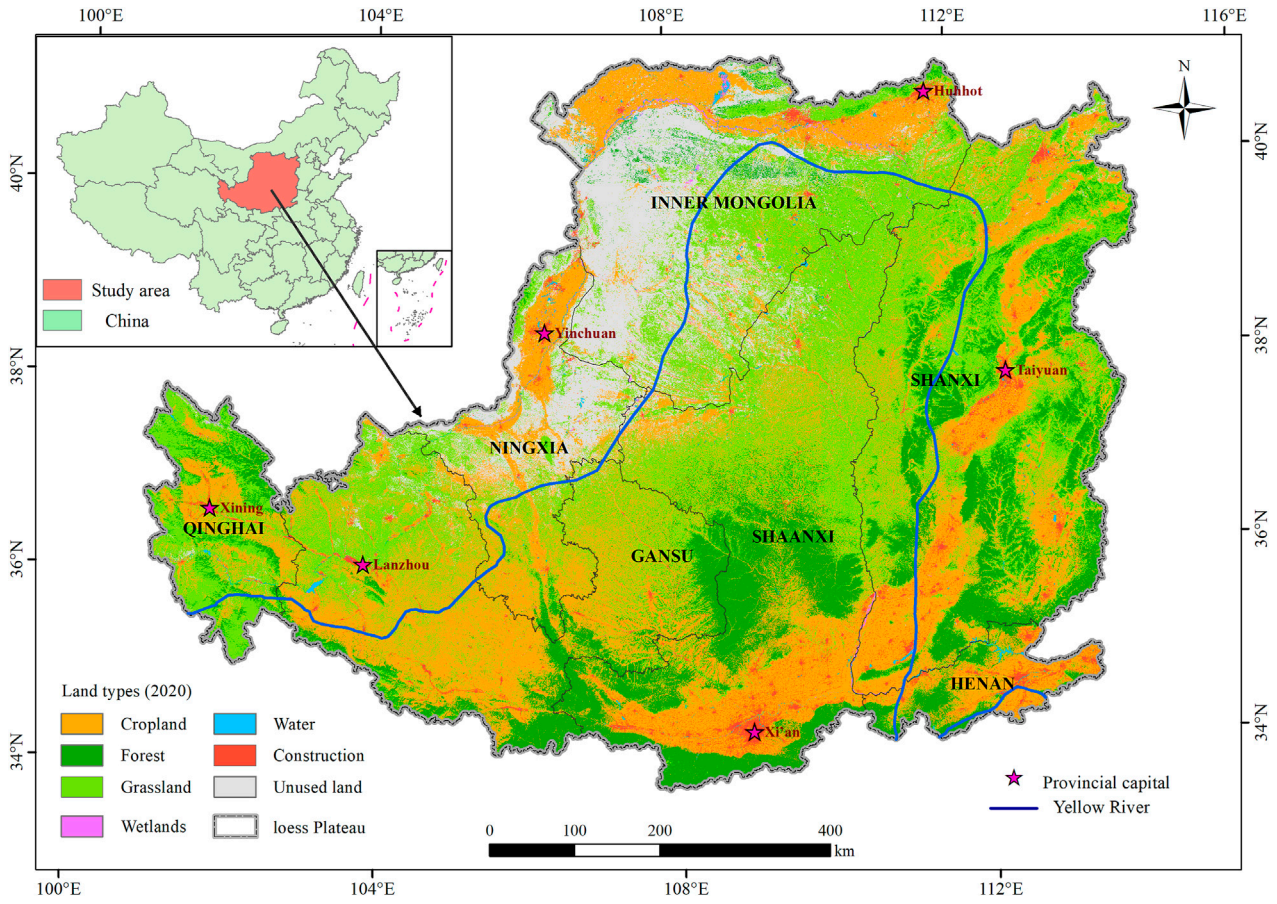

FIGURE 1
Topographic map of the Loess Plateau (LP). Note: the spatial distribution map of land use classification is the vegetation type map of the LP in 2020 with a resolution of 30 m.

2 Materials and methods

2.1 Study area

The LP is located in the middle of the Yellow River basin (33°41′–41°16′N, 100°52′–114°31′E), with a total area of approximately 6.4 × 10^5 km^2, spanning the provinces of Gansu, Henan, Inner Mongolia, Ningxia, Qinghai, Shanxi, and Shaanxi in China (Figure 1). The overall topography of the LP presents a downward trend of high in the northwest and low in the southeast. It is located in the semi-humid and semi-arid regions of China, with typical temperate continental monsoon climate characteristics. The multi-year average temperature and precipitation are approximately 8°C and 400 mm, respectively. The heavy and concentrated rainstorms in summer, coupled with high evaporation, high sediment content in the water system, and loose loess soil, cause serious soil erosion. According to the national classification standard of China, we used the land use data set of 2000–2020 produced by Zhang et al. (2021), and divide the land use types of LP into grassland, cultivated, forest, and unused lands, construction land, and wetland and water areas. In recent decades, the implementation of restoration projects (such as the Grain for Green project), rapid urbanization, and global warming have significantly altered the vegetation cover and land structure of the LP (Song et al., 2014), impacting the regional ecological environment.

2.2 Data description and preprocessing

2.2.1 NPP

The NPP data are based on the MODIS satellite-generated MOD17A3HGF V006 product provided by NASA (https://lpdaac.usgs.gov/products), which provides annual NPP information at the 500-m pixel resolution. Annual NPP was derived from the addition of all 8-day net photosynthesis (PSN) products (MOD17A2H) for a given year, calculated using the BIOME-BGC model to derive the global terrestrial vegetation NPP interannual data. Previous research has verified the reliability of the MOD17A3 NPP data with the measured data used in the analysis of the study area (Liu et al., 2018; Li et al., 2020). We used the MODIS Reprojection Tool (MRT) and ArcGIS 10.8 software to eliminate outliers and invalid values, and uniformly cropped data from the LP area. Due to the elimination of cloud pollution, we used the nearest neighbor method to resample a 1 km dataset in our analysis.

TABLE 1 Classification of the land use land cover (LULC) dataset used in this study.

Primary classes	Sub-classes
Cropland	Rainfed cropland
	Herbaceous cover
	Irrigated cropland
Forest	Open evergreen broadleaved forest
	Closed evergreen broadleaved forest
	Open deciduous broadleaved forest (0.15 < fc < 0.4)
	Closed deciduous broadleaved forest (fc > 0.4)
	Open evergreen needle-leaved forest (0.15 < fc < 0.4)
	Closed evergreen needle-leaved forest (fc > 0.4)
	Closed deciduous needle-leaved forest (fc > 0.4)
	Shrubland
	Deciduous shrubland
Unused land	Bare areas
	Unconsolidated bare areas
	Permanent ice and snow
	Sparse vegetation (fc < 0.15)
Grassland	Grassland
Wetlands	Wetlands
Impervious surfaces	Impervious surfaces
Water	Waterbody

2.2.2 Meteorological data

The meteorological data (1 km × 1 km) were originated from the LP Sub Center, National Earth System Science Data Center of China (http://loess.geodata.cn), which generates monthly temperature and precipitation data for China from 2000 to 2020 busing a Delta spatial downscaling scheme. The LP region was generated via mask extraction.

2.2.3 Land use land cover (LULC)

The multi-temporal land use land cover dataset was obtained from the Institute of Aerospace Information Research, Chinese Academy of Sciences (https://doi.org/10.5194), which produces global 30-m land-cover results every 5 years, from 1985 to 2020 on the Google Earth Engine platform using all Landsat satellite data from 1984 to 2020. The overall accuracy of this dataset is >80% (Zhang et al., 2021); hence, we used it in this study. We selected land-cover data from 2000 to 2020 (i.e., 2000, 2005, 2010, 2015, and 2020) for the dynamic study of NPP on LP by tailoring the data. A field investigation combined with the actual land types of the LP enabled us to divide the dataset into the seven categories, with an overall validation accuracy of 96.4% (Table 1). According to the classification standard of Zhang et al.'s data set and the actual land types of the LP, we reclassified the land types into seven types.

2.3 Methods

The fishing net (10 km × 10 km) was created using the processed NPP data, following which the NPP of each matrix unit was assigned using the partitioned table. Finally, the global spatial autocorrelation test was performed in ArcGIS on the NPP data of the LP from 2000 to 2020. If the results showed a significant global correlation, then a local spatial autocorrelation analysis was performed.

2.3.1 Global spatial autocorrelation

The global Moran's I index and high/low clustering (Getis-Ord General G) characterized whether the NPP of the LP from 2000 to 2020 had clustered or outliers in space (Swetnam et al., 2015; Cheniti et al., 2021). The formula for calculating the global Moran's I index is as follows:

$$I = \frac{\left\{\sum_{i=1}^{n}\sum_{j\neq i}^{n} w_{ij}(x_i-\bar{x})(x_j-\bar{x})\right\}}{S^2\sum_{i=1}^{n}\sum_{j\neq i}^{n} w_{ij}}, \quad (1)$$

$$S^2 = \sum_i (x_i-\bar{x})^2 \Big/ n, \quad (2)$$

where n is the total number of observation elements, x_i and x_j are the pixel values of NPP at positions i and j ($i \neq j$), $\bar{x} = \left(\sum_i^n x_i\right)/n$, i is a variance, and w_{ij} is a symmetric spatial weight matrix element; if i is adjacent to j, then w_{ij} is 1, otherwise w_{ij} is 0.

To test the significance of the spatial autocorrelation relationship, the standardized statistic Z value was introduced. The calculation formula of Z is:

$$Z = \frac{(I-E(I))}{\sqrt{VAR(I)}}, E(I) = -\frac{1}{(n-1)}, \quad (3)$$

where $E(I)$ is the expected value of I (compared with Moran's I index), $VAR(I)$ is the variance of the variable I, $VAR(I) = E(I^2) - E(I)^2$. Moran's I index is generally between −1 and 1. A Moran's I index and Z value greater than 0 and significant (with a p-value within the given significance level) indicates a positive spatial correlation. Therefore, similar observations (high or low) tend to be spatially clustered. When the values are equal to 0, the values are independent and randomly distributed.

The General G and its expected value $E(G)$ and Z-score are calculated as follows:

$$G = \frac{\left(\sum_{i=1}^{n}\sum_{j=1}^{n} w_{ij}x_ix_j\right)}{\sum_{i=1}^{n}\sum_{j\neq i}^{n} x_ix_j},,$$

$$Z = \frac{\{G-E(G)\}}{\sqrt{VAR(G)}}. \quad (4)$$

If General G is greater than $E(G)$, and the Z-score is positive, then the high NPP values will cluster within the region. If General G is less than $E(G)$, and the Z-score is negative, then the low NPP values will tend to cluster.

2.3.2 Local spatial autocorrelation

To explore whether the high and/or low local spatial observations were concentrated, we used the Hot Spot Analysis (Getis-Ord Gi*) and Anselin Local Moran's I tools in ArcGIS 10.8 to perform a local spatial autocorrelation analysis. Getis-Ord Gi* identified statistically significant hot and cold

spots (Getis and Ord, 2010). Anselin Local Moran's I identified spatial clusters of features with high or low values, as well as spatial outliers (Anselin, 1995; Liu K. et al., 2022).

The Getis-Ord Gi* is as follows:

$$G_i^* = \frac{\left(\sum_{j=1}^{n} w_{ij}x_j - \bar{X}\sum_{j=1}^{n} w_{ij}\right)}{S\sqrt{\left[n\sum_{j=1}^{n} w_{ij}^2 - \left(\sum_{j=1}^{n} w_{ij}x_j\right)^2\right]/(n-1)}}, \quad (5)$$

$$\bar{X} = \frac{\left(\sum_{j=1}^{n} x_j\right)}{n}, \quad (6)$$

$$S = \sqrt{\frac{\left(n\sum_{j=1}^{n} x_j\right)}{n} - (\bar{X})^2}, \quad (7)$$

where x_i is the same as the Formula (1), and the G_i^* statistic uses the z-score. For statistically significant values, positive and highest z-score indicates that the areas with high NPP are more closely clustered (hot spots). Conversely, a negative and low z-score means that the areas with low NPP are more tightly clustered (cold spots). The Anselin Local Moran's I statistic is defined as:

$$I_i = \frac{\left[(x_i - \bar{x})\sum_{j=1, j\neq i}^{n} w_{ij}(x_i - \bar{x})\right]}{S_i^2}, \quad (8)$$

$$S_i^2 = \frac{\left(\sum_{j=1, j\neq i}^{n} w_{ij}\right)}{(n-1)} - \bar{X}^2. \quad (9)$$

The standardized statistic for the Anselin Local Moran's I statistical test is similar to the global Moran's I index and distinguishes statistically significant clusters of high values (HH), clusters of low values (LL), outliers (HL) where high values are mostly surrounded by low values, and outliers (LH) where low values are mostly surrounded by high values.

2.3.3 Pearson correlation analysis

Pearson correlation analysis is used to determine the linear correlation between multiple variables and ranges from −1 to 1 (Gbagir et al., 2022). The MATLAB R2021 software generated the codes to analyze the pixel-by-pixel correlations between NPP temperature and NPP rainfall, as well as the regional contribution of temperature and rainfall to NPP. The correlations were combined with spatial autocorrelations to analyze the spatial anomalous changes in vegetation NPP. The correlation coefficient r_{xy} is calculated as follows:

$$r_{xy} = \frac{\{\sum_{i=1}^{n}[(x_i - \bar{X})(y_i - \bar{Y})]\}}{\sqrt{\sum_{i=1}^{n}(x_i - \bar{X})^2\sum_{i=1}^{n}(y_i - \bar{Y})}}, \quad (10)$$

where, n is the number of years in the monitoring period ($n = 21, i = 1, 2, \cdots, 21$), x_i is NPP of the 1 km raster data in different years, $\bar{X}$ is the average of 21 years of NPP raster data, y_i is the raster data of temperature or precipitation in different years, and y_i is the raster data of the annual average rainfall or temperature.

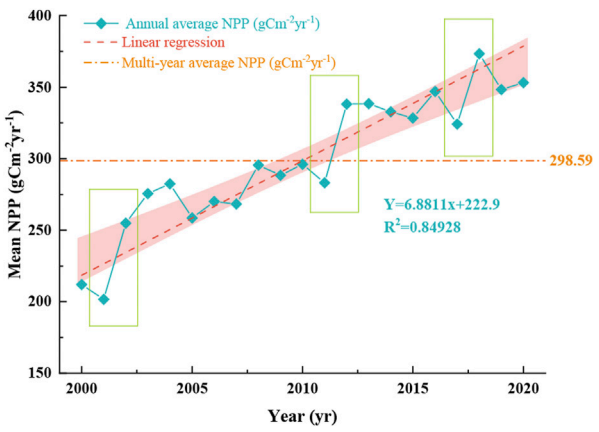

FIGURE 2
Annual trend in the net primary productivity variation on the Loess Plateau from 2000 to 2020.

3 Results

3.1 Temporal and spatial distribution pattern of NPP in the Loess Plateau

The annual mean value of vegetation NPP on the LP from 2000 to 2020 followed a fluctuating upward trend ($p < 0.05$), with a growth rate of 6.88 $gCm^{-2}yr^{-1}$. The increases prior to 2010 (3.61%) were more pronounced than those after (1.75%). The multi-year average NPP was 298.59 $gCm^{-2}yr^{-1}$. The total volume of NPP increased from 127.12 Tg (in 2000) to 212 Tg (in 2020), with an annual growth rate of 4.05 Tg/yr. The mean NPP varied in different years, with 2002 being the lowest at only 201.64 $gCm^{-2}yr^{-1}$, while the highest was in 2018. Before 2012, the average annual NPP of the LP was lower than the multi-year average; however, in 2012, it increased sharply to 338.13 $gCm^{-2}yr^{-1}$ (Figure 2).

Three obvious mutation periods were more intense than other years, namely 2001 to 2002, 2011 to 2012, and 2017 to 2018. The average annual NPP of each province in the LP from 2000 to 2020 is listed in Table 2. Henan Province had the highest average annual NPP (391.57 $gCm^{-2}yr^{-1}$) and the largest growth rate (+11.60 $gCm^{-2}yr^{-1}$), followed by Shaanxi, Shanxi, Gansu, Ningxia, Inner Mongolia, and Qinghai (with a growth rate of 5.10 $gCm^{-2}yr^{-1}$). The NPP of each province showed rapid growth from 2000 to 2020, and the time points of NPP mutation in the LP, aligned with the implementation of the Grain for Green project in 1999. All provinces actively responded to the Grain for Green project with rapid vegetation restoration on the LP, achieving remarkable results.

The inter-annual NPP of the LP presented a spatial distribution pattern of low in the northwest and high in the southeast. The areas with the highest NPP were situated primarily in the central and southeast LP (Figure 3). Approximately 16%–55% of the total area had an average annual NPP below 200 $gCm^{-2}yr^{-1}$, which decreased annually, but the regional annual average NPP did not vary and remained at 200–400 $gCm^{-2}yr^{-1}$. The proportion of NPP with an average of 400–600 $gCm^{-2}yr^{-1}$ varied significantly between years, encompassing only 4% in 2000 compared with the 37% in 2020, demonstrating significant improvements over time (Figure 4).

TABLE 2 Annual average net primary productivity of each province in the Loess Plateau from 2000 to 2020 ($gCm^{-2}yr^{-1}$).

Year	Henan	Shaanxi	Shanxi	Gansu	Qinghai	Ningxia	Inner Mongolia
2000	320.42	228.24	276.56	215.11	252.84	122.88	111.82
2001	281.25	221.75	229.47	238.26	270.01	134.42	101.29
2002	317.77	293.96	277.45	301.17	303.83	179.85	143.15
2003	402.07	316.04	333.88	288.42	293.88	181.09	153.17
2004	419.64	323.01	349.29	290.74	285.99	179.73	158.93
2005	365.51	300.65	303.10	296.23	302.84	156.06	128.13
2006	400.08	317.67	327.60	290.50	304.47	158.59	135.79
2007	374.77	315.27	301.30	303.58	324.43	172.11	144.22
2008	397.02	344.23	357.23	328.79	323.41	170.00	154.30
2009	387.30	345.69	342.54	311.01	321.94	172.80	152.16
2010	384.23	366.80	334.74	329.26	332.21	201.29	147.30
2011	359.81	346.13	341.58	303.46	309.21	181.71	136.08
2012	436.90	404.03	396.57	365.32	315.07	229.35	196.28
2013	370.08	407.89	392.81	385.80	341.97	224.63	183.65
2014	370.86	401.49	386.14	377.79	316.25	236.59	179.20
2015	452.12	410.42	377.65	372.73	302.86	209.22	165.26
2016	424.77	407.33	426.40	357.69	341.23	221.98	204.56
2017	411.21	393.01	376.62	356.51	321.38	215.23	177.82
2018	487.61	448.47	429.72	423.61	355.85	255.01	201.51
2019	384.19	410.11	381.09	412.45	358.75	251.88	205.03
2020	475.10	420.87	420.78	399.85	339.85	226.78	178.95
Mean	391.57	353.50	350.62	330.88	315.16	194.34	159.93

Our results also indicated that before 2002, there were almost no areas with an average NPP above 600 $gCm^{-2}yr^{-1}$, which has gradually increased over the past 20 years. Therefore, the implementation of ecological construction projects (such as the project of grain for green project) has improved the vegetation on the LP and the ecological environment has achieved remarkable results.

The land cover variations impacted the terrestrial ecosystem structure. The variations in NPP of different vegetation types from 2000 to 2020 are illustrated in Figure 5. The mean NPP values of different vegetation types (from high to low) were: forest (447.87 $gCm^{-2}yr^{-1}$) > cropland (317.20 $gCm^{-2}yr^{-1}$) > impervious surface (301.61 $gCm^{-2}yr^{-1}$) > grassland (256.81 $gCm^{-2}yr^{-1}$) > water (197.79 $gCm^{-2}yr^{-1}$) > wetlands (162.56 $gCm^{-2}yr^{-1}$) > unused land (194 $gCm^{-2}yr^{-1}$). All types showed a significant increasing trend from 2000 to 2020. Among them, the annual average NPP of the forest was much higher than that of other land types, indicating that the forest ecosystem is a large carbon sink (Figure 5). Moreover, there were significant discrepancies in the total annual NPP among different vegetation types. The annual total NPP of cropland, forest, and grassland increased rapidly above 40 TgC, while the total NPP of unused land was much higher than that of the remaining land, which suggests the carbon sequestration potential of unused land is enormous.

3.2 Spatial autocorrelation analysis

3.2.1 Global autocorrelation variations of NPP

Global spatial autocorrelations explore the spatial agglomeration characteristics of carbon sequestration of vegetation NPP on the LP. As listed in Table 3, we calculated the global Moran's I index, General G, and their z-scores, expectation values, variance, and *p*-value of NPP from 2000 to 2020. The annual global Moran's I index varied from 0.95 to 0.97, and the Moran's I index of the multi-year average NPP was 0.961, extremely close to 1. At the same time, the Z-score of each year was positive and above 106 (Z(I) > 2.58), indicating that the NPP of the LP in 2000–2020 showed a very significant agglomeration effect on the interannual spatial distribution and had a strong positive spatial correlation ($p< 0.01$). Correspondingly, the annual General G was greater than E(G) (p-value <0.001), and Z(d) was also much higher than 2.58 [P(G) < 0.01], which

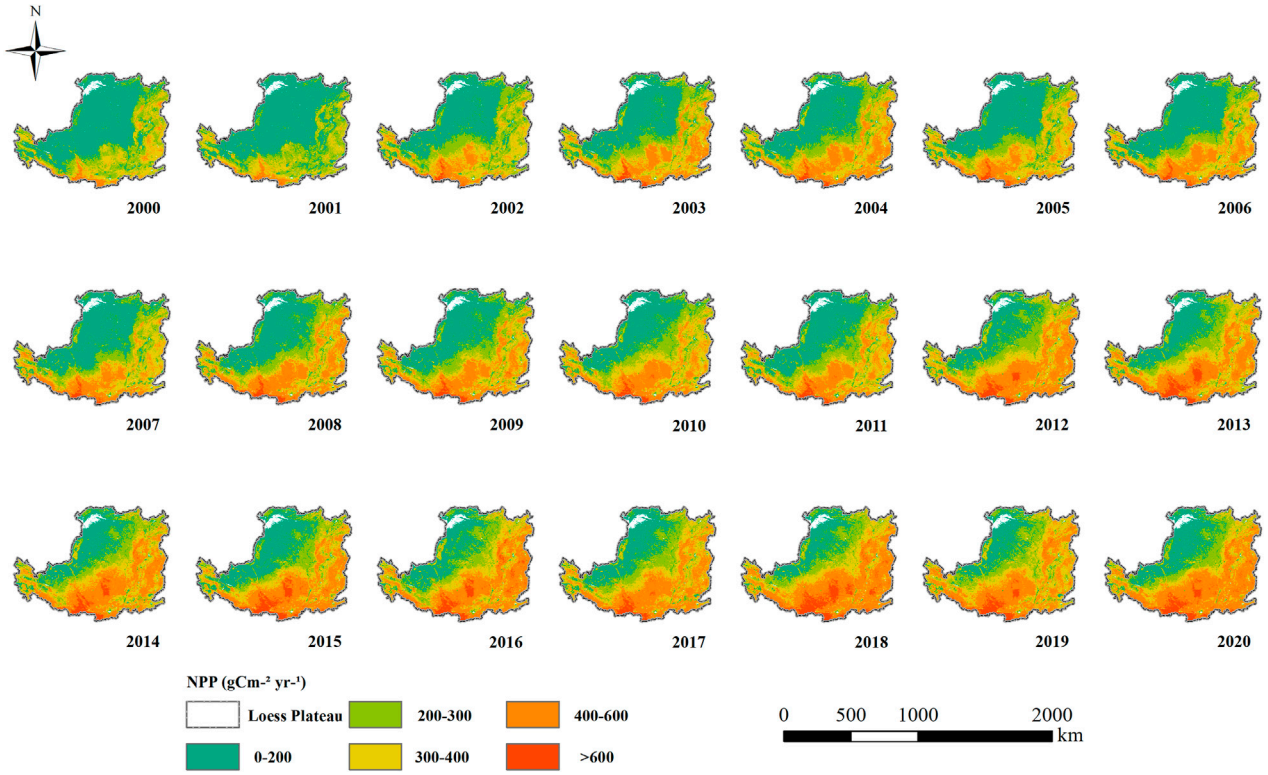

FIGURE 3
Spatial distribution of vegetation net primary productivity on the Loess Plateau from 2000 to 2020.

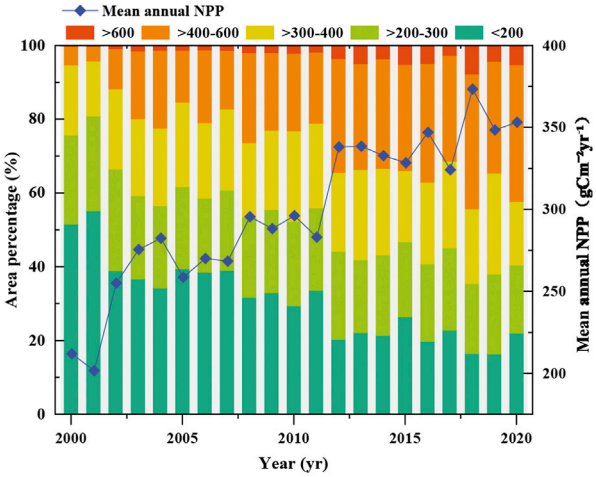

FIGURE 4
Ratio of the average annual area of net primary productivity in the Loess Plateau from 2000 to 2020.

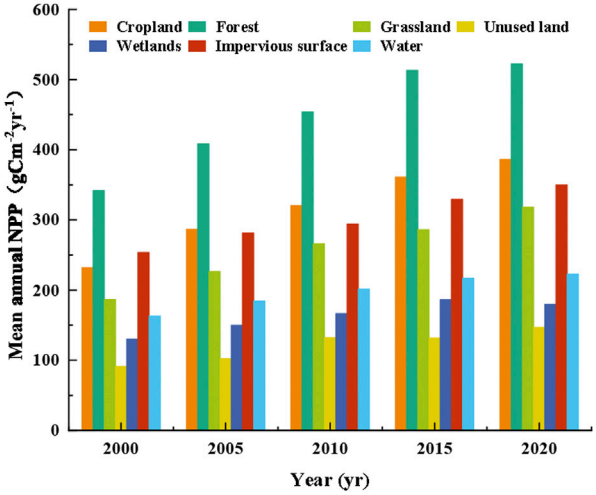

FIGURE 5
Distribution of mean net primary productivity for different land cover types.

indicated that the overall spatial distribution pattern of NPP in the study area had high clustering. The global autocorrelation did not reveal the specific clustering pattern at the fine scale; therefore, the local Moran's I was needed to further identify the spatial clustering pattern of NPP.

3.2.2 Hot spot analysis and local autocorrelation of NPP

The hot spot analysis tool identified the statistically significant hot and cold areas of NPP in the LP. The hot and

TABLE 3 Global autocorrelation of net primary productivity in the Loess Plateau from 2000 to 2020.

Year	Moran's I	Z (I)	*p*-value	General G	E(G)	Z(d)	P(G)
2000	0.953	106.837	<0.01	0.000192	0.000153	102.359	<0.01
2001	0.947	106.215	<0.01	0.000191	0.000153	101.847	<0.01
2002	0.950	106.530	<0.01	0.000183	0.000153	100.919	<0.01
2003	0.952	106.826	<0.01	0.000186	0.000153	101.643	<0.01
2004	0.957	107.323	<0.01	0.000185	0.000153	102.026	<0.01
2005	0.962	107.857	<0.01	0.000191	0.000153	103.292	<0.01
2006	0.962	107.942	<0.01	0.000191	0.000153	103.363	<0.01
2007	0.958	107.494	<0.01	0.000186	0.000153	102.333	<0.01
2008	0.962	107.934	<0.01	0.000187	0.000153	102.755	<0.01
2009	0.958	107.414	<0.01	0.000186	0.000153	102.258	<0.01
2010	0.962	107.900	<0.01	0.000185	0.000153	102.483	<0.01
2011	0.960	107.715	<0.01	0.000187	0.000153	102.662	<0.01
2012	0.962	107.922	<0.01	0.000179	0.000153	101.458	<0.01
2013	0.964	108.144	<0.01	0.000183	0.000153	102.397	<0.01
2014	0.956	107.178	<0.01	0.000180	0.000153	100.874	<0.01
2015	0.965	108.285	<0.01	0.000188	0.000153	103.265	<0.01
2016	0.956	107.211	<0.01	0.000178	0.000153	100.616	<0.01
2017	0.959	107.519	<0.01	0.000179	0.000153	101.104	<0.01
2018	0.969	108.638	<0.01	0.000179	0.000153	101.932	<0.01
2019	0.954	107.056	<0.01	0.000176	0.000153	99.730	<0.01
2020	0.970	108.742	<0.01	0.000182	0.000153	102.760	<0.01
Mean	0.961	107.373	<0.01	0.000184	0.000153	101.424	<0.01

cold spot areas were polarized. The cold spots were mainly distributed in the northwest of Ningxia, Inner Mongolia (Ordos and Bayannur), and Gansu (Lanzhou and Baiyin), while the hot spots were distributed in the southern and eastern regions, mainly covering Gansu (Tianshui, Pingliang, Qingyang), central Shaanxi, and Henan (Sanmenxia, Luoyang).

From 2000 to 2020, the overall distribution pattern of the cold spot areas did not vary, but the area containing an NPP with a 99% confidence level gradually expanded and incorporated Ordos City, Inner Mongolia. In addition, the cold spot area of the Yulin City started to gradually disappear in 2009, while the cities of Bayannur and Shizuishan changed from insignificant to cold spot areas. There were also local anomalies in Lanzhou's NPP in 2007, 2018, and 2019 (Figure 6).

The cold spot area (at the 99% confidence level) showed an increasing trend and its proportion increased to 15%. The cold spot area gradually decreased at 95% and 90% confidence levels. However, the insignificant areas remained dominant, accounting for 41%–50%. Conversely, the hot spot areas were stable at the 99%, 95%, and 90% confidence levels, accounting for approximately 11%, 8.5%, and 5.4%, respectively, indicating that the hot spot areas were transferred into different spatial locations. For instance, the NPP in the south of the hot spot area gradually expanded from 2000 to 2020, from Tianshui, Baoji, and Xi'an to Xianyang, Pingliang, and Yan'an. Other hot spots were sporadically distributed in Shanxi and Henan Province, and the high NPP pattern in the eastern region (Changzhi, Jincheng, Jinzhong City) almost disappeared in 2002, 2007, 2010, and 2019. Generally, the hot spots of NPP in the eastern region are likely to continue to shrink.

To further identify the specific clustering patterns of hot and cold areas, clustering and outlier analyses were performed. The NPP had spatial heterogeneity in the spatial distribution and the inter-annual local spatial pattern was dominated by the HH and LL clustering patterns; the clustering model of the multi-year average vegetation NPP was similar to each year (Figure 7). HH was mainly distributed in southeastern Gansu, southern Shaanxi, and central Henan (which encompasses 16%–22% of the area of the LP). The LL was concentrated in the Inner Mongolia Autonomous Region, northern Ningxia, northwestern Gansu, and northeastern Shaanxi (23%–30%). The gray areas were insignificant, accounting for 50%–60%, revealing no spatial autocorrelation patterns (Figure 7).

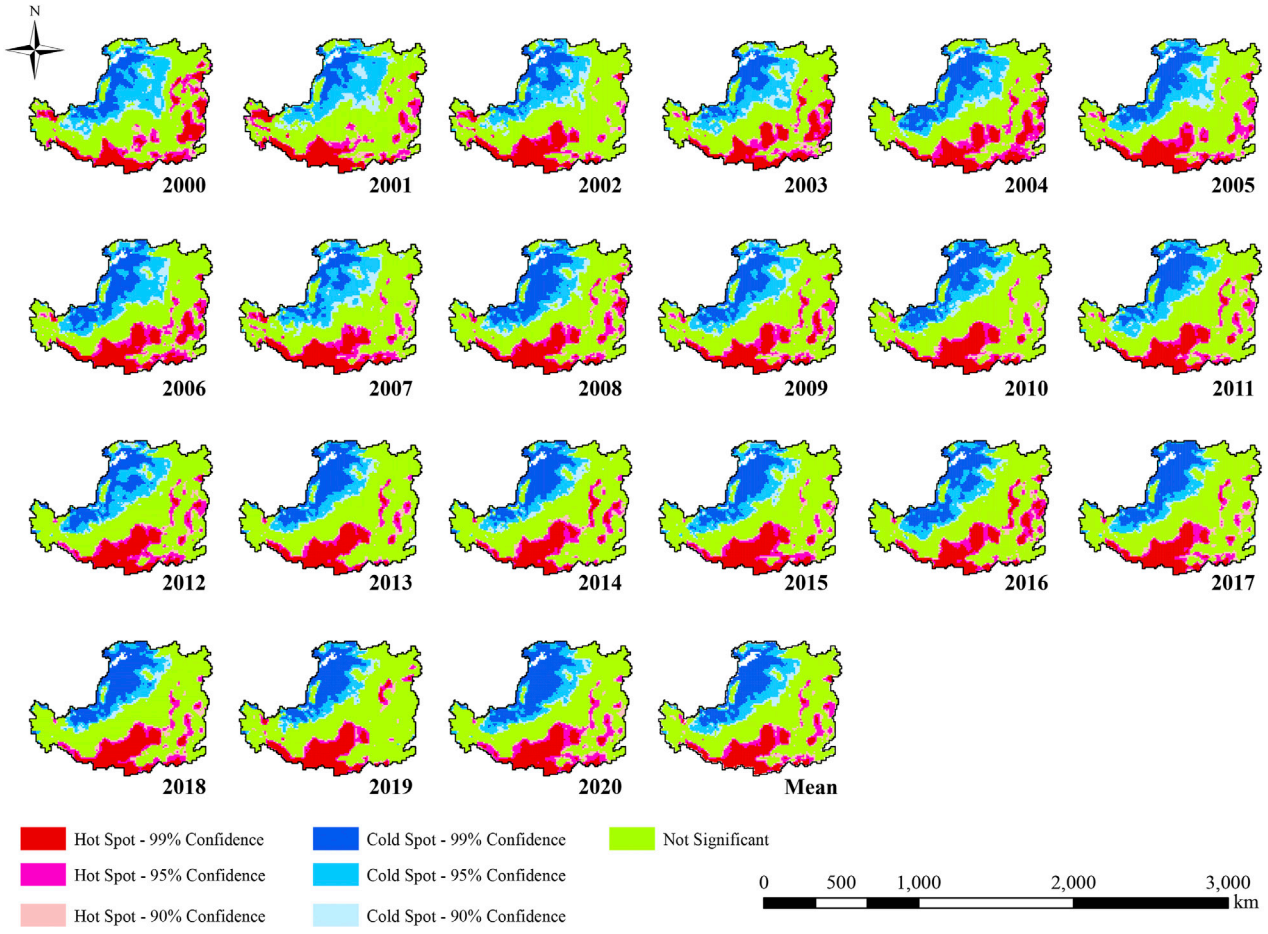

FIGURE 6
Spatiotemporal variation characteristics of net primary productivity cold and hot spots in the Loess Plateau from 2000 to 2020.

3.3 Climatic factors affecting vegetation NPP changes

To further explore the spatial-temporal variations and spatial anomalous clustering changes in vegetation NPP, we analyzed the responses of precipitation and temperature to vegetation NPP.

There was a positive correlation between NPP and precipitation in 94.09% of the LP, with only approximately 5.91% of the region revealing a negative correlation (Figure 8). A total of 58.92% of the regions had a significant positive correlation, mainly in Inner Mongolia, Ningxia and Shaanxi, southern Gansu and western Shanxi, and 35.17% of the regions showed significant irrelevance. Conversely, 5.90% of the regions showed no significant negative correlation, these areas were concentrated in Xi'an, southeastern Baoji in Shaanxi, and Sanmenxia and Luoyang in Henan, there were almost no significant negative correlations.

Compared with the variations in response to precipitation, the temperature influences on vegetation NPP in the LP were not obvious over many years. In terms of spatial distribution, 76.99% of the regions showed a positive correlation, while 23.01% showed a negative correlation. There were almost no significant positive or negative correlations in the LP, as demonstrated in Figure 9.

In the study area, 73.73% of the regions showed an insignificant positive correlation, mainly in the southeast of Gansu Province, Ningxia, and Shanxi Province. Conversely, 22.86% of the region showed an insignificant negative correlation, in Yan 'an, Xianyang, and Xi 'an in the Shaanxi Province (Figure 9). The results indicate the impact of temperature rise on vegetation NPP has not had significant effects.

To further quantitatively explore the contributing factors to the vegetation NPP on the LP, we used correlation analyses. We compared the *p*-values of the correlation coefficients of precipitation and temperature; the least significant correlation coefficient was extracted as the highest value correlation coefficient (Figure 10). The two climatic factors (temperature and precipitation) on the LP and the highest significant NPP correlation revealed significant correlations in 48.96% of the regions, mainly in the northwest and northeastern Shanxi, with no significance in the southeast LP. A total of 48.96% of the NPP on LP was significantly influenced by temperature and precipitation, mainly in the northwest and northeast of Shanxi, while the influence of climatic factors was insignificant on NPP in the south and east

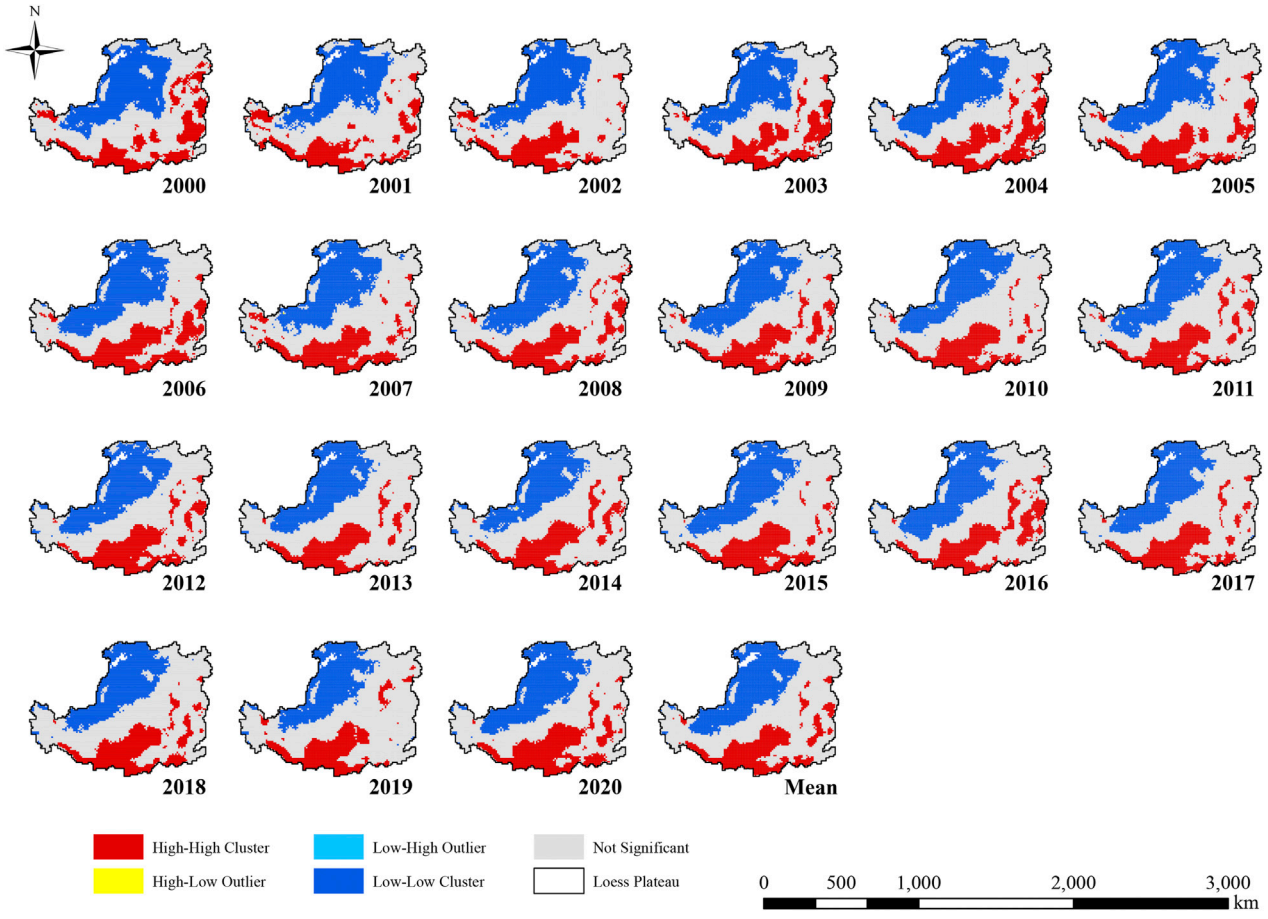

FIGURE 7
Local clustering and outlier changes in the Loess Plateau from 2000 to 2020.

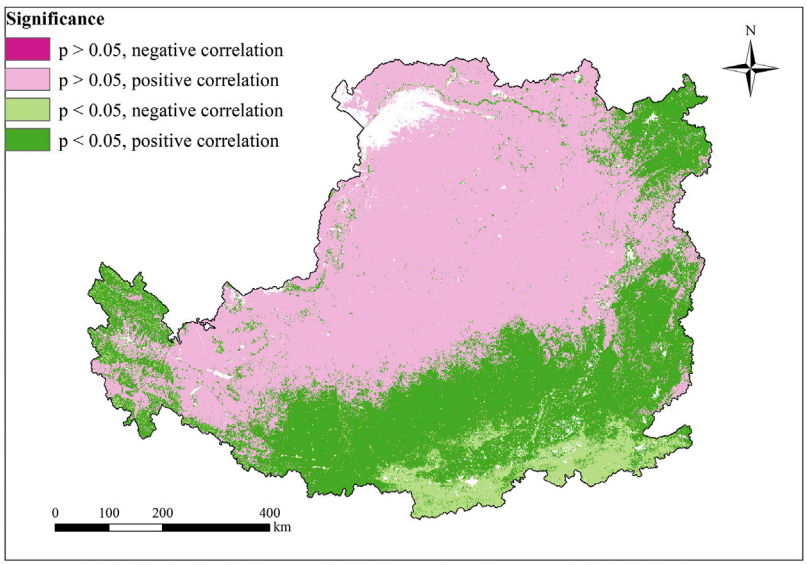

FIGURE 8
Spatial distribution of the Pearson correlation results between net primary productivity and precipitation in the Loess Plateau from 2000 to 2020.

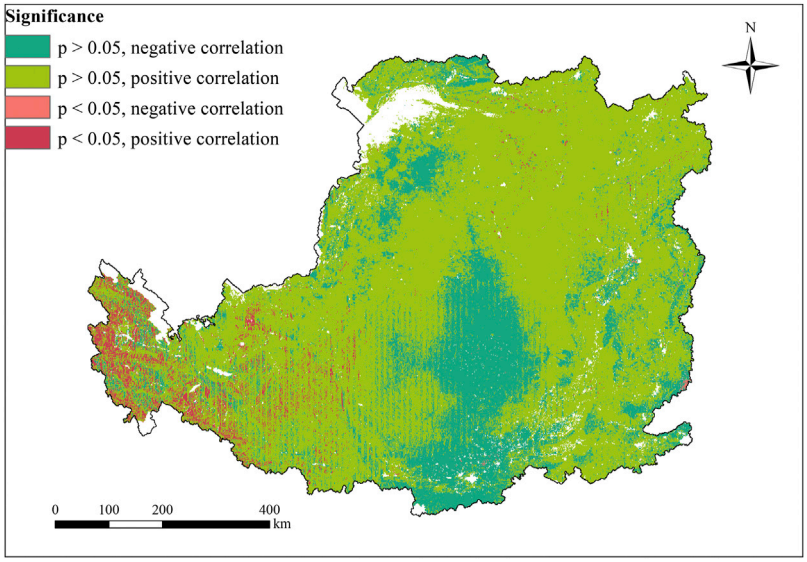

FIGURE 9
Spatial distribution of the Pearson correlation results between net primary productivity and temperature in the Loess Plateau from 2000 to 2020.

of the LP (Figure 10A). On the LP, 86.31% of the area is heavily dependent on precipitation for vegetation NPP, whereas only 13.70% of the area relies mainly on temperature. Therefore, precipitation is the main climatic factor affecting variations in vegetation NPP on the LP (Figure 10B). Moreover, for provinces and cities, the areas mainly influenced by temperature were the Shaanxi Province (Xianyang, Tongchuan, Baoji, Xi'an), Guyuan City in Ningxia, Pingliang City in Gansu, Xining City in Qinghai, and Sanmenxia City in Henan, while other areas were mainly influenced by precipitation factors.

4 Discussion

4.1 Spatiotemporal variation in vegetation NPP

The interannual variation in NPP had "multi-peak" fluctuation increases since the implementation of the Grain for Green project on the LP. These peaks may be attributed to ecological engineering coupled with the effects of climate change and human activities. With global warming over the past 20 years, the climate of the LP has gradually increased in temperature and humidity; temperature and precipitation play an important role in vegetation growth (Sun et al., 2020). Additionally, many ecological construction projects have been implemented, including the natural forest protection project, the comprehensive management of small watersheds, and the Grain for Green Project. From artificial afforestation to natural restoration, the LP has an obvious "greening" trend (Li et al., 2017; Zhao et al., 2018; Deng and ShangGuan, 2021), thereby enhancing the carbon sequestration capacity of the vegetation. Our results are in line with previous findings (Feng et al., 2013; Jiang et al., 2019).

Interestingly, there are three distinct spikes in the NPP (2001–2002, 2011–2012, and 2017–2018). On the regional scale, the sudden increase in NPP from 2001 to 2002 corresponded with the pilot projects in Shaanxi and Gansu in 1999. After 2000, the pilot projects of returning farmland to forests were expanded to include 17 provinces in the central and western regions. The wave of forestry projects has continued, and vegetation growth improved as plants develop. The extreme NPP during 2011–2012 may be due to two factors, the implementation of a new round of Grain for Green Projects and sudden change in extreme temperatures which accelerated vegetation growth and abundance, improving NPP (Liu P. et al., 2022). In 2017, the State Council approved the conversion of Cropland to forests and grasslands in 17 provinces to expand the scale of agriculture and forestry in the region. The State Council also initiated rural revitalization and the mountains-rivers-forests-farmlands-lakes-grasslands program has favorably promoted the grand vision of "green waters and green mountains" (Li and Liu, 2022), which led to a sudden rise in NPP from 2017 to 2018. Moreover, the extreme precipitation levels correlated with NPP, especially the P-min with NPP, indicating that extreme precipitation may have strongly influenced the sudden increase in NPP (Figure 11). Similarly, at the provincial scale, the timing of sudden increases in vegetation NPP in each province also clustered with the three stages of distinct spikes. For example, the NPP in Shaanxi Province increased by 72.21 $gCm^{-2}yr^{-1}$ from 2001 to 2002, indicating that increased vegetation effectively controlled soil erosion, reduced carbon loss from the ecosystem, and enhanced carbon fixation.

The annual average vegetation NPP on the LP had a significant gradient from southeast to northwest. The area with an NPP above 400 $gCm^{-2}yr^{-1}$ gradually increased, and moved northward, with the main concentration in northern Shaanxi and southeastern Gansu and the Lüliang mountains in Shanxi. These results are in line with those of Zhang et al.

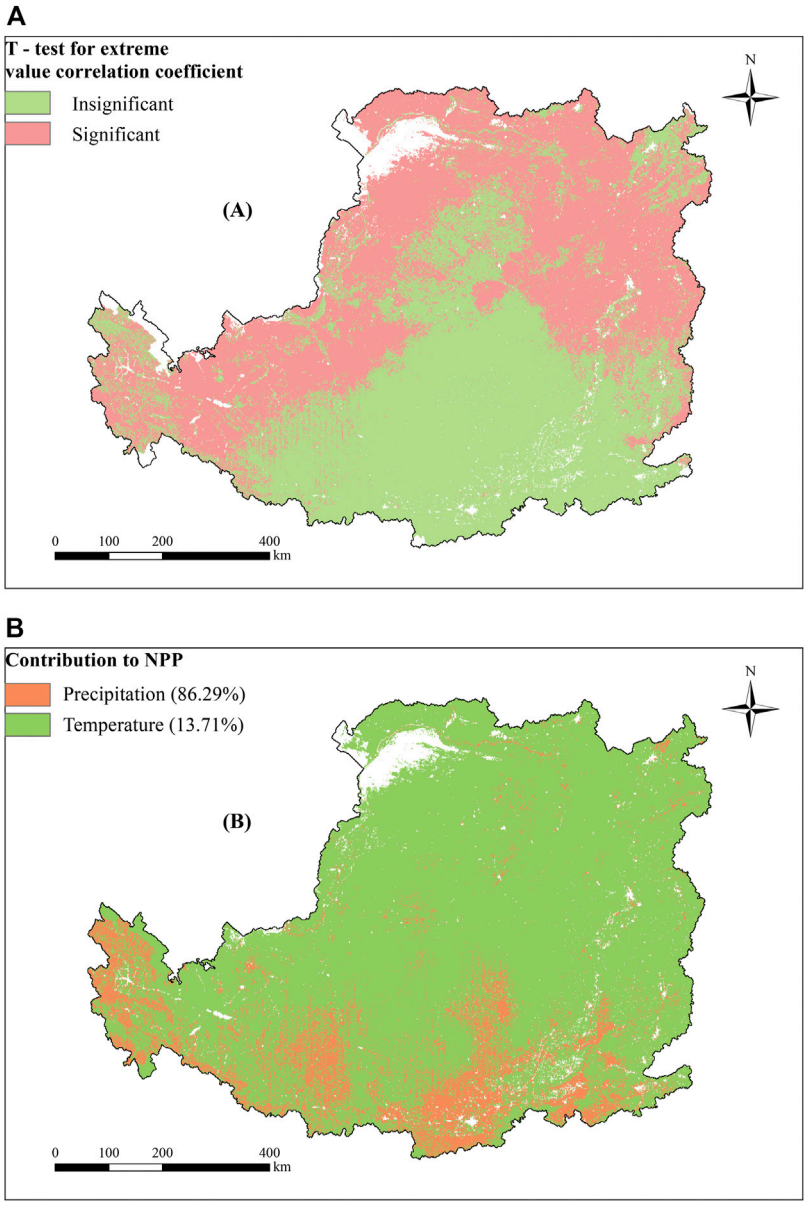

FIGURE 10
Spatial distribution **(A)** of the most significant correlation coefficients from the *t*-test results with precipitation and temperature; **(B)** contributions of precipitation and temperature to the significant net primary productivity results on the Loess Plateau for 2000–2020.

(2016). The higher NPP locations are the key restoration areas of the early pilot sites of the Grain for Green project. The pilot areas focused on the sub-region with warm temperate deciduous oak forest, with relatively superior site conditions as identified through superb afforestation technology, to ensure vegetation restoration success. However, the poor natural conditions, lack of water resources, severe drought, and planting a vegetation monoculture (single species) have allowed unused land to occupy most of the LP, impacting afforestation attempts in Inner Mongolia, Gansu, and Ningxia, resulting in slow NPP growth. In general, a series of large-scale ecological construction projects implemented over the past 21 years has changed the ecological environment of the LP and promoted the sustainable development of the Yellow River Basin; the effect of the extensive vegetation restoration work was also outstanding.

4.2 Effects of spatial autocorrelation on climate and human activities

Most previous studies have focused on the linear relationship and driving factors based on the "first-order effect," ignoring the advantage of spatial autocorrelation which can remove the assumption of sample independence in classical statistics and performs well with potentially dependent samples. Presently, few studies have used the spatial

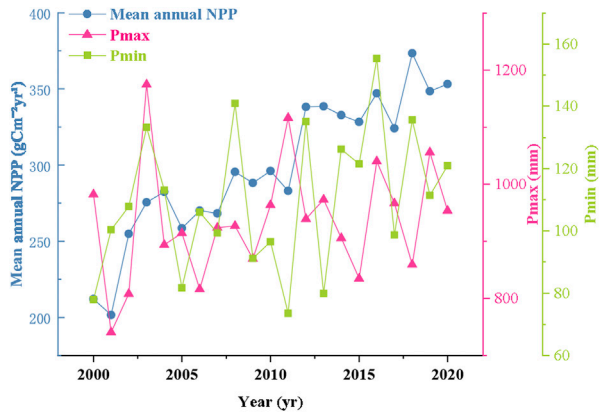

FIGURE 11
Association between vegetation net primary productivity and extreme precipitation levels on the Loess Plateau from 2000 to 2020.

autocorrelation method to analyze spatial variation in NPP (Ren et al., 2020). Therefore, we used the "second-order effect" via spatial grid to explore the spatial correlation and heterogeneity of NPP in the LP. Our results reveal that the NPP of the LP from 2000 to 2020 had a strong spatial positive correlation ($p< 0.01$), and an agglomeration effect, indicating that the ecosystems between the regions are not independent, yet interrelated with a tendency to gather. To avoid global autocorrelation masking local anomalies or instability, we explored the degree of local spatial aggregation on the LP and observed obvious polarization of cold and hot spots. The local spatial pattern of the LP is dominated by HH and LL clustering patterns, with a prominent hot spot area ($p< 0.01$), which is similar to previous research (Wang and Gong, 2022). The HH is dominated by forests and cultivated land with vast carbon storage and is located in the warm temperate zone, which allows for an effective carbon sequestration. Focused conversion of farmland to forests involved sloping farmland converted into forest and grassland; the net forest area increased to 4,726 km^2 in 2020 (Table 4). Forests promote the accumulation of forest carbon and areas with high forest cover have significantly higher NPP than other habitats. In the past 21 years, Ordos and Bayannur (cities in Inner Mongolia, northern Ningxia) and Baiyin City in the Gansu Province remain a LL district (cold spot), as previously indicated (Ren et al., 2020). The carbon sequestration services of ecosystems in the northwest of the LP remain low, with the fragile ecological environments impacting the success of vegetation restoration in this area.

The transfer matrix revealed the worst land categories (unused land and grassland) in Inner Mongolia, which accounted for 79.58% (Table 4) of this land category. In addition, the location is a temperate desert steppe zone with serious desertification of Mu Us sandy land. The ongoing coal mining in the Ordos City has also adversely impacted local vegetation and caused soil erosion.

Recently, the government has improved the area through ecological restoration, although vegetation rehabilitation remains slow (Wu et al., 2022).

To further explore the heterogeneity in the clustering patterns, we calculated the clustering patterns between counties and combined the annual average NPP of each county with LULC data to explore the abnormal changes between HH and LL and the significance levels of each stage.

The main reason for the disappearance of the LL in Ansai, Wuqi, Yanchang County, and Yan'an City in the Shaanxi Province and Shanxi (Xi and Yonghe County) from 2000 to 2005 was the transformation of sloping farmland into forest and grassland and of unused land into grassland, which increased the vegetation cover. The reason for the disappearance of the HH in Shanxi Province may be attributed to the conversion of grassland to cultivated land and the expansion of cultivated land to impervious surfaces, including the transfer of 76 km^2 in Yuanping County (from 2000 to 2005).

The main reason for the disappearance of HH from 2005 to 2010 was the transfer of cropland and grassland to impervious surfaces in some counties in Shanxi Province. For example, 11 km^2 of cropland and grassland in Gaoping County was changed to impervious surfaces. The expansion of urban construction has accelerated urbanization, thereby reducing the ability for vegetation to sequester carbon in many arable lands and grasslands. The emergence of LL is mainly the degradation of grassland. For example, the grassland was converted into unused land in Hangjin Banner in Inner Mongolia, creating an additional

TABLE 4 Land use transfer matrix of the Loess Plateau from 2000 to 2020 (km^2).

Land use type		2020						
		Cropland	Forest	Grassland	Unused land	Wetlands	Impervious surface	Water
2000	Cropland	181,132	1,383	7,279	1,796	654	4,712	464
	Forest	276	90,253	308	53	7	30	11
	Grassland	11,439	2,880	206,731	4,161	431	1,688	261
	Unused land	7,976	1,140	12,596	74,454	509	815	153
	Wetlands	58	3	4	33	1,228	4	18
	Impervious surface	0	0	0	0	0	8,706	0
	Water	37	5	11	4	58	4	1,414

90 km^2 of unused land from 2005 to 2010. The conversion of unused land to forest and grassland (in 2010–2015) was the main reason for the disappearance of the LL. Other clusters were less affected by land use changes. The disappearance of the LL in 2015–2020 and the expansion of the HH may be related to the transfer of grassland to cropland.

The local spatial anomaly of the NPP in the LP is driven by human-land relationship and natural factors. The effect of temperature on NPP was much smaller than that of precipitation, which is consistent with the results of Xie et al. (2014), however, Xie et al. (2014) did not provide the specific spatial distribution of NPP which is affected by climate indicators. This study revealed a positive correlation between NPP and precipitation in 94.09% on the LP, which indicates that precipitation has a strong synergy with plant photosynthesis and vegetation growth. The increased precipitation in the Qinling Mountains did not correspondingly increase the NPP or reduce vegetation resilience. Northwest China (especially Inner Mongolia, Gansu, and Shaanxi) is in arid and semi-arid areas. The lack of precipitation weakens the net primary production capacity of the vegetation, which might have caused consistent LL in the area. The quantitative results of the extreme value analysis revealed that the contribution of precipitation to NPP reached 86.31%; therefore, precipitation was the dominant climatic factor affecting variations in NPP in the LP. Combined with spatial autocorrelation analysis, the cold spot area was mainly influenced by precipitation, while the temperature had a stronger correlation with the hot spot area. This suggests that precipitation plays a decisive role in vegetation change in arid and semi-arid areas in the northwest of the LP, which is consistent with previous research on the impact of climate change on vegetation NPP in China (Ge et al., 2021). The southeast LP is in a warm temperate zone with abundant precipitation where vegetation growth is strongly affected by light conditions.

Our analysis of precipitation impacts identified a very close synergistic relationship between the interannual variation in NPP mean and minimum precipitation levels on the LP. There is both coordination and a tradeoff between the minimum and maximum precipitation.

The year of the tradeoff between the NPP and maximum precipitation almost coincides with the abnormal year in the local clustering model in the Shanxi and Henan provinces, which indicates that the heterogeneity of this spatial clustering model was affected by P-max (Figure 11). Hence, future studies should focus on the impact of extreme precipitation on vegetation restoration (Fischer et al., 2013).

The spatial autocorrelation model is based on the first law of geography and regularly applied in various industries. However, in ecology (especially in the application of remote sensing data) some mechanistic discussions have not been fully investigated. For example, Geoda and ArcGIS software is superior to previous ecological research which has not clearly defined data distance and the selection and rationality of thresholds, such as NPP. This study focused on a single variable in the spatial autocorrelations to reveal the spatial variation in vegetation NPP on the LP. Future studies should combine multivariate spatial correlation analysis with economic, natural, and other indicators to explore the high and low clustering relationship between the factors and vegetation NPP to advise effective ecological construction.

Global warming remains a major global challenge. As an ecologically fragile area, we focused on temperature and rainfall as the natural factors influencing LP and identified gaps in the land cover data in a specific year. There may be deficiencies in our selection of indicators. Previous research has suggested that altitude and species diversity can also impact vegetation NPP. In the future, we will increase the diversity of valuable indicators in our exploration of the driving forces in vegetation carbon sequestration capacity to achieve the dual-carbon goal in China and the world.

In general, the vegetation NPP in the LP possessed a strong spatial autocorrelation. This spatial heterogeneity and dependence are driven by both natural factors and human activities. The results reveal that extreme NPP are a response to natural factors and violent disturbances by human activities and clarify the driving mechanism underlying vegetation carbon sequestration on the LP, revealing the spatial dependence of vegetation NPP and relationships between regions to support ecological management plans and provide suggestions to formulate double carbon plans. Future studies and relevant government departments should focus on fragile areas for vegetation restoration and, using the results of this study, accurately identify these vulnerable locations. By exploring the driving factors in vegetation restoration in each county, the correlations between the vegetation restoration impacts on the adjacent areas in space can be comprehensively explored. The potential future risks are predicted so that measures can be taken to prevent them. Reasonable regulation of land resources should solve issues of optimal allocation of space resources, which is especially important in the northwest region which has a weak vegetation carbon sequestration capacity, due to the inferior local conditions for ecological construction. Our results support the realization of ecological protection and high-quality development in the LP.

5 Conclusion

The average annual NPP of the LP showed an increasing trend with varying degrees. There was a sharp increase in the NPP over three periods. The spatial distribution pattern of NPP increased mainly in the middle and southeast of the LP. Furthermore, the average annual NPP of different types of vegetation increased significantly, while the unused land had great potential for carbon sequestration. The NPP of vegetation in the study area has a strong spatial correlation ($p< 0.01$), and

the spatial clustering model is mainly HH and LL. HH accounts for 16%–22% of the LP, whereas LL accounts for 23%–30%.

Climate has a strong influence on vegetation NPP; however, recently the frequent land transformation due to human activities has greatly disturbed the spatial distribution of vegetation ecosystems. Additionally, changes among HH, LL, and insignificant areas are greatly affected by LUCC. The contribution of precipitation to regional NPP is much higher than temperature. Moreover, there is a strong synergistic relationship between the minimum value of precipitation and annual NPP. Future ecological management and decision makers should consider land planning and the important role of water resource allocation on vegetation growth. Finally, addressing problems such as the insufficient vegetation carrying capacity in the LP, and providing feasible schemes for green, low-carbon, and high-quality development of the LP remain to be accomplished.

Data availability statement

The original contributions presented in the study are included in the article/Supplementary Material, further inquiries can be directed to the corresponding author.

Author contributions

SM: conceptualization, methodology, formal analysis, investigation, data curation, writing—original draft. ZS: conceptualization, methodology, validation, supervision, writing—review and editing, funding acquisition. All authors contributed to the article and approved the submitted version.

Funding

This study was funded by the Major projects of the National Social Science Fund of China (22&ZD083).

Acknowledgments

We would like to thank Editage (www.editage.cn) for English language editing.

Conflict of interest

The authors declare that the research was conducted in the absence of any commercial or financial relationships that could be construed as a potential conflict of interest.

Publisher's note

All claims expressed in this article are solely those of the authors and do not necessarily represent those of their affiliated organizations, or those of the publisher, the editors and the reviewers. Any product that may be evaluated in this article, or claim that may be made by its manufacturer, is not guaranteed or endorsed by the publisher.

Supplementary material

The Supplementary Material for this article can be found online at: https://www.frontiersin.org/articles/10.3389/fenvs.2023.1134917/full#supplementary-material

References

Anselin, L. (1995). Local indicators of spatial association—lisa. *Geogr. Anal.* 27, 93–115. doi:10.1111/j.1538-4632.1995.tb00338.x

Chen, L. D., Huang, Z. L., Gong, J., Fu, B. J., and Huang, Y. L. (2007). The effect of land cover/vegetation on soil water dynamic in the hilly area of the loess plateau, China. *CATENA* 70, 200–208. doi:10.1016/j.catena.2006.08.007

Cheniti, H., Cheniti, M., and Brahamia, K. (2021). Use of GIS and Moran's I to support residential solid waste recycling in the city of Annaba, Algeria. *Environ. Sci. Pollut. Res.* 28, 34027–34041. doi:10.1007/s11356-020-10911-z

Cui, L. L., Shi, J., and Xiao, F. J. (2018). Impacts of climatic factors and El Niño/La Niña events on the changes of terrestrial ecosystem NPP in China. *Acta Geogr. Sin.* 73, 53–66. doi:10.11821/dlxb201801005

Deng, L., and ShangGuan, Z. P. (2021). High quality developmental approach for soil and water conservation and ecological protection on the Loess Plateau. *Front. Agr. Sci. Eng.* 8, 501–511. doi:10.15302/j-fase-2021425

Fan, C., and Myint, S. (2014). A comparison of spatial autocorrelation indices and landscape metrics in measuring urban landscape fragmentation. *Landsc. Urban Plann.* 121, 117–128. doi:10.1016/j.landurbplan.2013.10.002

Feng, X. M., Fu, B. J., Lu, N., Zeng, Y., and Wu, B. F. (2013). How ecological restoration alters ecosystem services: An analysis of carbon sequestration in China's Loess Plateau. *Sci. Rep.* 3, 1–5. doi:10.1038/srep02846

Fischer, E. M., Beyerle, U., and Knutti, R. (2013). Robust spatially aggregated projections of climate extremes. *Nat. Clim. Change* 3, 1033–1038. doi:10.1038/NCLIMATE2051

Fu, B. J., Liu, Y., Lü, Y. H., He, C. S., Zeng, Y., and Wu, B. F. (2011). Assessing the soil erosion control service of ecosystems change in the Loess Plateau of China. *Ecol. Complex.* 8, 284–293. doi:10.1016/j.ecocom.2011.07.003

Gbagir, A. M. G., Sikopo, C. S., Matengu, K. K., and Colpaert, A. (2022). Assessing the impact of wildlife on vegetation cover change, northeast Namibia, based on MODIS satellite imagery (2002-2021). *Sensors* 22.4006 doi:10.3390/s22114006

Ge, W. Y., Deng, L. Q., Wang, F., and Han, J. Q. (2021). Quantifying the contributions of human activities and climate change to vegetation net primary productivity dynamics in China from 2001 to 2016. *Sci. Total Environ.* 773, 145648. doi:10.1016/j.scitotenv.2021.145648

Getis, A., and Ord, J. K. (2010). *The analysis of spatial association by use of distance statistics, Perspectives on spatial data analysis*. Berlin, Germany Springer. pp 127-145.

Goldewijk, K. K., and Leemans, R. (1995). *Systems models of terrestrial carbon cycling*. Berlin, Germany: Springer Berlin Heidelberg. pp 129-151.

Guo, D., Song, X. N., Hu, R. H., Cai, S. H., Zhu, X. M., and Hao, Y. B. (2021). Grassland type-dependent spatiotemporal characteristics of productivity in Inner Mongolia and its response to climate factors. *Sci. Total Environ.* 775, 145644. doi:10.1016/j.scitotenv.2021.145644

He, X. B., Zhou, J., Zhang, X. B., and Tang, K. L. (2006). Soil erosion response to climatic change and human activity during the Quaternary on the Loess Plateau. *China. Reg. Environ. Change.* 6, 62–70. doi:10.1007/s10113-005-0004-7

Huang, Y., Wang, Y. J., Li, X. S., Hu, Z. L., and Liu, G. P. (2013). Graphic analysis of spatio-temporal effect for vegetation disturbance caused by coal mining: A case of datong coal mine area. *Acta Ecol. Sin.* 33, 7035–7043. doi:10.5846/stxb201207080952

Jiang, H. C., and Ding, Z. L. (2005). Temporal and spatial changes of vegetation cover on the Chinese Loess Plateau through the last glacial cycle: Evidence from spore-pollen records. *Rev. Palaeobot. Palyno* 133, 23–37. doi:10.1016/j.revpalbo.2004.08.003

Jiang, X. D., Shen, W., and Bai, X. Y. (2019). Response of net primary productivity to vegetation restoration in Chinese Loess Plateau during 1986-2015. *PLoS ONE* 14.e0219270 doi:10.1371/journal.pone.0219270

Kolby Smith, W., Reed, S. C., Cleveland, C. C., Ballantyne, A. P., Anderegg, W. R. L., Wieder, W. R., et al. (2016). Large divergence of satellite and Earth system model estimates of global terrestrial CO2 fertilization. *Nat. Clim. Change* 6, 306–310. doi:10.1038/NCLIMATE2879

Lei, T., Feng, J., Lv, J., Wang, J., Song, H., Song, W., et al. (2020). Net Primary Productivity Loss under different drought levels in different grassland ecosystems. *J. Environ. Manage.* 274, 111144. doi:10.1016/j.jenvman.2020.111144

Li, C. H., Wang, Y. T., Wu, X. D., Cao, H. J., Li, W. P., and Wu, T. H. (2021). Reducing human activity promotes environmental restoration in arid and semi-arid regions: A case study in northwest China. *Sci. Total Environ.* 768, 144525. doi:10.1016/j.scitotenv.2020.144525

Li, H. W., Ding, J. H., Zhang, J., Yang, Z. N., Yang, B., Zhu, Q., et al. (2020). Effects of land cover changes on net primary productivity in the terrestrial ecosystems of China from 2001 to 2012. *Land-Basel* 9. doi:10.3390/land9120480

Li, J. J., Peng, S. Z., and Li, Z. (2017). Detecting and attributing vegetation changes on China's Loess Plateau. *Agric. For. Meteorol.* 247, 260–270. doi:10.1016/j.agrformet.2017.08.005

Li, S. D., and Liu, M. C. (2022). The development process, current situation and prospects of the conversion of farmland to forests and grasses project in China. *J. Resour. Ecol.* 13, 120–128. doi:10.5814/j.issn.1674-764x.2022.01.014

Liu, H. X., Zhang, A. B., Jiang, T., Zhao, A. Z., Zhao, Y. L., and Wang, D. L. (2018). Response of vegetation productivity to climate change and human activities in the shaanxi-gansu-ningxia region, China. *J. Indian Soc. Remote* 46, 1081–1092. doi:10.1007/s12524-018-0769-z

Liu, K., Liu, W. R., Wu, J. L., Chen, Z. F., Zhang, W., and Liu, F. (2022a). Spatial differences and influencing factors of urban water utilization efficiency in China. *Front. Environ. Sci.* 10, 593. doi:10.3389/fenvs.2022.890187

Liu, P., Zhao, X. N., Gao, X. D., Yu, L. Y., and Ren, M. (2022b). Characteristics of extreme temperature variation in the Loess Plateau and its correlation with average temperature. *Chin. J. Appl. Ecol.* 33, 1975–1982. doi:10.13287/j.1001-9332.202207.024

Liu, T. S., Guo, Z. T., Wu, N. Q., and Lu, H. Y. (1996). Prehistoric vegetation on the Loess Plateau: Steppe or forest? *J. S. Asian Earth* 13, 341–346. doi:10.1016/0743-9547(96)00041-4

Lü, Y. H., Fu, B. J., Feng, X. M., Zeng, Y., Liu, Y., Chang, R. Y., et al. (2012). A policy-driven large scale ecological restoration: Quantifying ecosystem services changes in the Loess Plateau of China. *PLoS ONE* 7, e31782. doi:10.1371/journal.pone.0031782

Ma, R. X., Wang, D. C., Cui, X. M., Yao, X. J., Li, S. S., Wang, H. S., et al. (2022). Distribution and driving force of water use efficiency under vegetation restoration on the Loess Plateau. *Remote Sens-Basel* 14. doi:10.3390/rs14184513

Pan, J. H., and Dong, L. L. (2018). Spatio-temporal variation in vegetation net primary productivity and its relationship with climatic factors in the Shule River basin from 2001 to 2010. *Hum. Ecol. Risk. Assess.* 24, 797–818. doi:10.1080/10807039.2017.1400373

Pei, Y. Y., Huang, J. L., Wang, L. H., Chi, H., and Zhao, Y. j. (2018). An improved phenology-based CASA model for estimating net primary production of forest in central China based on Landsat images. *Int. J. Remote Sens.* 39, 7664–7692. doi:10.1080/01431161.2018.1478464

Peng, J., Shen, H., Wu, W. H., Liu, Y. X., and Wang, Y. L. (2016). Net primary productivity (NPP) dynamics and associated urbanization driving forces in metropolitan areas: A case study in beijing city, China. *Landsc. Ecol.* 31, 1077–1092. doi:10.1007/s10980-015-0319-9

Ren, H. R., Shang, Y. J., and Zhang, S. (2020). Measuring the spatiotemporal variations of vegetation net primary productivity in Inner Mongolia using spatial autocorrelation. *Ecol. Indic.* 112, 106108. doi:10.1016/j.ecolind.2020.106108

Shangguan, Z. P., and Zheng, S. X. (2006). Ecological properties of soil water and effects on forest vegetation in the Loess Plateau. *Int. J. Sustain. Dev. World Ecol.* 13, 307–314. doi:10.1080/13504500609469682

Song, X. Z., Peng, C. H., Zhou, G. M., Jiang, H., and Wang, W. F. (2014). Chinese grain for green program led to highly increased soil organic carbon levels: A meta-analysis. *Sci. Rep.* 4, 1–7. doi:10.1038/srep04460

Sun, R., Chen, S. H., and Su, H. B. (2020). Spatiotemporal variation of NDVI in different ecotypes on the Loess Plateau and its response to climate change. *Geogr. Res.* 39, 1200–1214. doi:10.11821/dlyj020190399

Swetnam, T. L., Lynch, A. M., Falk, D. A., Yool, S. R., and Guertin, D. P. (2015). Discriminating disturbance from natural variation with LiDAR in semi-arid forests in the southwestern USA. *Ecosphere* 6. 1-22. doi:10.1890/Es14-00384.1

Wang, T. F., and Gong, Z. W. (2022). Evaluation and analysis of water conservation function of ecosystem in Shaanxi Province in China based on "Grain for Green" Projects. *Environ. Sci. Pollut. Res.* 29, 1–19. doi:10.1007/s11356-022-21730-9

Wang, Y. W., Yue, H. B., Peng, Q., He, C., Hong, S., and Bryan, B. A. (2020). Recent responses of grassland net primary productivity to climatic and anthropogenic factors in Kyrgyzstan. *Land Degrad. Dev.* 31, 2490–2506. doi:10.1002/ldr.3623

Wei, X. D., Yang, J., Luo, P. P., Lin, L. G., Lin, K. L., and Guan, J. M. (2022). Assessment of the variation and influencing factors of vegetation NPP and carbon sink capacity under different natural conditions. *Ecol. Indic.* 138, 108834. doi:10.1016/j.ecolind.2022.108834

Wu, D. H., Piao, S. L., Zhu, D., Wang, X. H., Ciais, P., Bastos, A., et al. (2020). Accelerated terrestrial ecosystem carbon turnover and its drivers. *Glob. Change Biol.* 26, 5052–5062. doi:10.1111/gcb.15224

Wu, Q. Y., Yao, X. J., Liang, J., Zhang, S. L., Yang, Y. J., and Hou, H. P. (2022). Spatial and temporal intensity of vegetation cover improvement and degradation in coal mining areas of Erdos city. *J. Arid Land Resour. Environ.* 36, 101–109. doi:10.13448/j.cnki.jalre.2022.205

Wu, S. H., Zhou, S. L., Chen, D. X., Wei, Z. Q., Dai, L., and Li, X. G. (2014). Determining the contributions of urbanisation and climate change to NPP variations over the last decade in the Yangtze River Delta, China. *Sci. Total Environ.* 472, 397–406. doi:10.1016/j.scitotenv.2013.10.128

Xiao, F. J., Liu, Q. F., and Xu, Y. Q. (2022). Estimation of terrestrial net primary productivity in the Yellow River Basin of China using light use efficiency model. *Sustainability* 14. 7399 doi:10.3390/su14127399

Xie, B. N., Qin, Z. F., Wang, Y., and Chang, Q. R. (2014). Spatial and temporal variation in terrestrial net primary productivity on Chinese Loess Plateau and its influential factors. *Trans. Chin. Soc. Agric. Eng.* 30, 244–253. doi:10.3969/j.issn.1002-6819.2014.11.030

Yang, A. L., zhang, X. P., Li, Z. S., li, Y. C., and Nan, F. S. (2023). Quantitative analysis of the impacts of climate change and human activities on vegetation NPP in the Qilian Mountain National Park. *Acta Ecol. Sin.* 43, 1–9. doi:10.5846/stxb202202050295

Yuan, Z., Wang, Y. Q., Xu, J. J., and Wu, Z. G. (2021). Effects of climatic factors on the net primary productivity in the source region of Yangtze River, China. *Sci. Rep.* 11. 1-11. doi:10.1038/s41598-020-80494-9

Zhang, B. Q., He, C. S., Burnham, M., and Zhang, L. H. (2016). Evaluating the coupling effects of climate aridity and vegetation restoration on soil erosion over the Loess Plateau in China. *Sci. Total Environ.* 539, 436–449. doi:10.1016/j.scitotenv.2015.08.132

Zhang, M., Yuan, N. Q., Lin, H., Liu, Y., and Zhang, H. Q. (2022). Quantitative estimation of the factors impacting spatiotemporal variation in NPP in the Dongting Lake wetlands using Landsat time series data for the last two decades. *Ecol. Indic.* 135, 108544. doi:10.1016/j.ecolind.2022.109478

Zhang, S. L., Yang, D. W., Yang, Y., Piao, S. L., Yang, H. B., Lei, H. M., et al. (2018). Excessive afforestation and soil drying on China's Loess Plateau. *J. Geophys. Res. Biogeosci.* 123, 923–935. doi:10.1002/2017JG004038

Zhang, T., Peng, J., Liang, W., Yang, Y. T., and Liu, Y. X. (2016). Spatial–temporal patterns of water use efficiency and climate controls in China's Loess Plateau during 2000–2010. *Sci. Total Environ.* 565, 105–122. doi:10.1016/j.scitotenv.2016.04.126

Zhang, X., Liu, L. Y., Chen, X. D., Gao, Y., Xie, S., and Mi, J. (2021). GLC_FCS30: Global land-cover product with fine classification system at 30 m using time-series Landsat imagery. *Earth Syst. Sci. Data* 13, 2753–2776. doi:10.5194/essd-13-2753-2021

Zhao, G. J., Mu, X. M., Wen, Z. M., Wang, F., and Gao, P. (2013). Soil erosion, conservation, and eco-environment changes in the Loess Plateau of China. *Land Degrad. Dev.* 24, 499–510. doi:10.1002/ldr.2246

Zhao, H. F., He, H. M., Wang, J. J., Bai, C. Y., and Zhang, C. J. (2018). Vegetation restoration and its environmental effects on the Loess Plateau. *Sustainability* 10, 4676. doi:10.3390/su10124676

Zhu, W. Q., Pan, Y. Z., and Zhang, J. S. (2007). Estimation of net primary productivity of Chinese terrestrial vegetation based on remote sensing. *Chin. J. Plant Ecol.* 31, 413. doi:10.3321/j.issn:1005-264X.2007.03.010

frontiers | Frontiers in Environmental Science

TYPE Original Research
PUBLISHED 20 June 2023
DOI 10.3389/fenvs.2023.1139264

OPEN ACCESS

EDITED BY
Xiaoyang Zhang,
South Dakota State University,
United States

REVIEWED BY
Ionut Cristi Nicu,
Norwegian Institute for Cultural Heritage Research, Norway
Isaac Sarfo,
Nanjing University of Information Science and Technology, China

*CORRESPONDENCE
Mexoese Nyatuame,
doga_nyatuame@yahoo.com

RECEIVED 06 January 2023
ACCEPTED 02 June 2023
PUBLISHED 20 June 2023

CITATION
Nyatuame M, Agodzo S, Amekudzi LK and Mensah-Brako B (2023), Assessment of past and future land use/cover change over Tordzie watershed in Ghana. *Front. Environ. Sci.* 11:1139264. doi: 10.3389/fenvs.2023.1139264

Assessment of past and future land use/cover change over Tordzie watershed in Ghana

Mexoese Nyatuame[1,2]*, Sampson Agodzo[1], Leonard Kofitse Amekudzi[1] and Bismark Mensah-Brako[2]

[1]Kwame Nkrumah University of Science and Technology, Kumasi, Ghana, [2]Ho Technical University, Ho, Ghana

Land use/ land cover (LULC) change has been identified as the main driving force of global change. The study investigated LULC change in Tordzie watershed in Ghana and predicted the future development. The supervised classification procedure was applied to Landsat images of 1987, 2003, and 2017. The cellular automata–Markov model embedded in IDRISI 17 software was employed to model LULC for the years 2030 and 2050. The trend of LULC change was exploited from 1987 to 2003, from 2003 to 2017, and projected to 2030 and 2050. Settlement and crop land, respectively, increased from 2.68% to 16.46% in 1987 to 3.65% and 53.47% in 2003 and finally to 20.61% and 58.52% in 2017. Vegetation cover declined from 23.2% in 1987 to 13.9% in 2003 and finally to 11.3% in 2017. The annual rate of change was determined. In 2030 and 2050, the dominant land use type will be crop land (56%). However, it decreased between 2017 and 2030 by −1.73%. The findings of the study are very relevant to land and water resource planners, policy formulators and implementers, and environmental and climate change advocates. Sustainable land use policy and its implementation are recommended.

KEYWORDS

land use, land cover, rate of change, Tordzie watershed, Ghana

1 Introduction

The anthropogenic modification of the surface of the Earth by human activities induced land use/land cover (LULC) changes. Although the modification of the Earth's surface by people existed since time immemorial to support livelihood for humankind's continual existence on Earth, the current state of LULC changes is alarming with its attendant degradation of the ecosystem due to increasing population. The current LULC changes are carried out in an unsustainable manner and thus negatively endangering posterity. The mentioned changes are the driving forces behind the local, regional, and global changes in the climate. The extreme climate events such as flush floods and droughts could also be attributed to LULC (Nyatuame and Agodzo, 2017) since LULC modifies the hydrology of a watershed or a catchment area.

The global change has become a topical issue and has attracted the attention of the world leaders and scientists. In the study and analysis of global change, the LULC plays an essential role. The data available on LULC changes and the rate of change provide critical information to aid in decision-making of ecological management and environmental planning for the future (Chowdhury et al., 2018; Mengist et al., 2022). The change detection procedure has an objective of identifying LULC changes on digital images that provide change features between

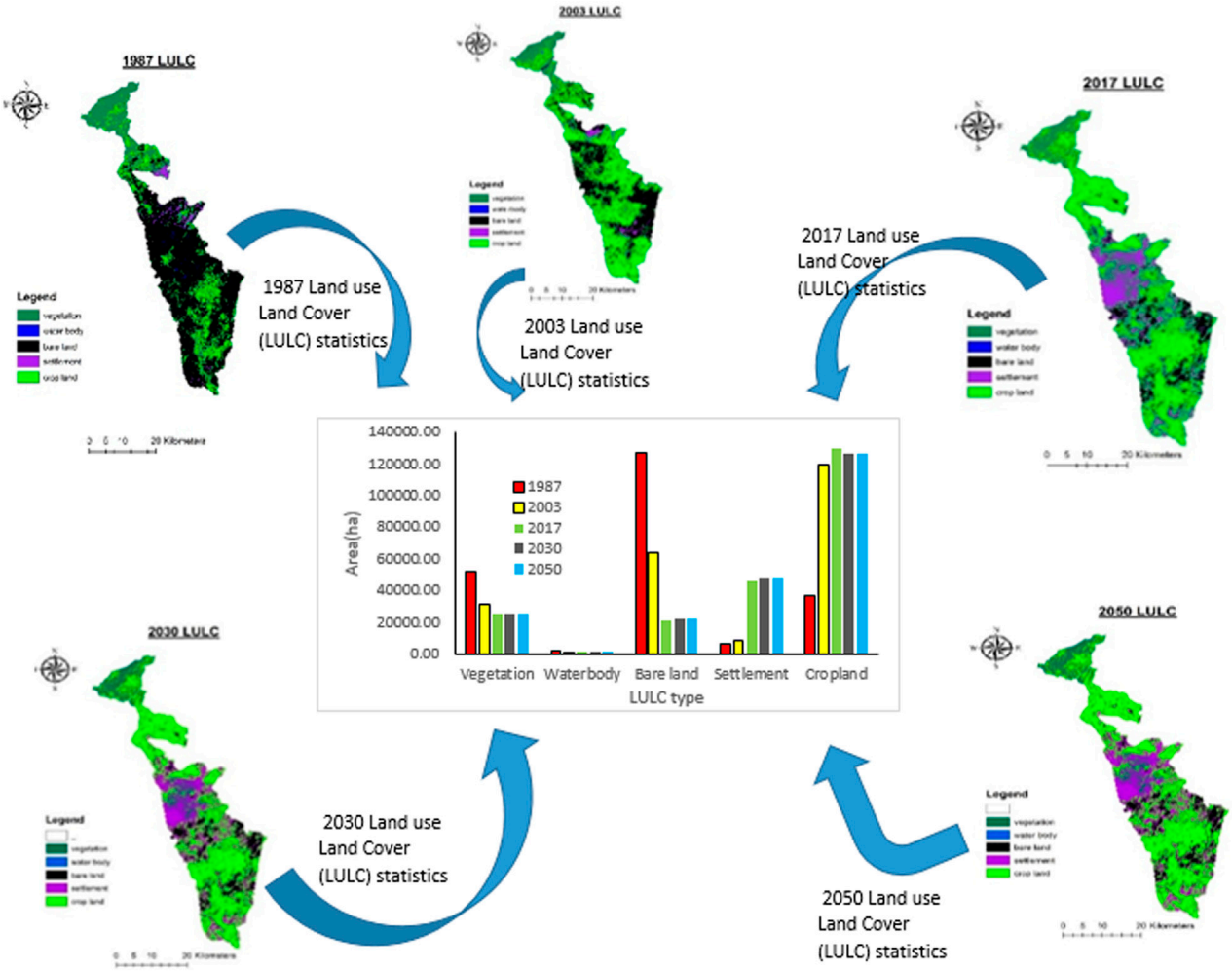

GRAPHICAL ABSTRACT

different timelines (Lu et al., 2019). Minale (2013) pointed out that the increase in LULC changes is alarming and its implication is enormous at local, regional, and global levels with high negative consequences. Schulp et al. (2018) employed the mapping and modeling technique to assess the impact of the past and future changes in LULC on Europe's cultural landscape. The study was aimed to decipher the threats to future cultural landscape as a result of LULC changes.

LULC changes have direct and indirect impact on the hydrological cycle and climate on the local, regional, and global scale (Butt et al., 2015; Nyatuame et al., 2020). LULC does not only impact the hydrological cycle but also biodiversity (Rawat and Kumar, 2015) and land productivity. The hydrological cycle is impacted by deforestation locally as trees with extensive root networks and capable of accessing deep reservoirs of moisture are replaced with pasture or crop land (Bagley, 2011). According to Mengist et al. (2022), deforestation has a bio-geophysical impact on the energy balance. Bagley (2011) reported the previous finding leads to a sharp reduction in latent heat flux as a consequence and a small reduction in net radiation. In addition, Bagley (2011) argued that there is moderate increment in sensible heat flux and storage of surface energy. Coe et al. (2011) further argued that runoff increases as a consequence of deforestation to balance the excess moisture, which alters the basin flow.

Remote sensing (RS) and geographical information systems (GIS) are powerful tools employed to acquire accurate and timely information on the spatial distribution of LULC changes (Das et al., 2021). GIS offered an environment for gathering, storing, presenting, and examining digital data for change discovery (Liping et al., 2018; Kafy et al., 2020). Nicu and Stoleriu (2019) employed RS and GIS techniques to land use changes and dynamics over a century around churches of Moldavia, Bukovina, and Northern Romania to ascertain the challenges and future perspectives of LULC. The study of Nicu and Stoleriu (2019) found out that the land use dynamic was dominated by anthropogenic phenomena and therefore recommended the deployment of the sustainable land use policy and the conservation of the cultural landscape's biocultural diversity.

Remotely sensed data are normally employed for differencing of image, post-classification comparison (PCC), and vegetation index differencing (Alam et al., 2020). The images from different periods are compared independently so as to distinguish changes in land cover (Kalra et al., 2013). The images from different dates are

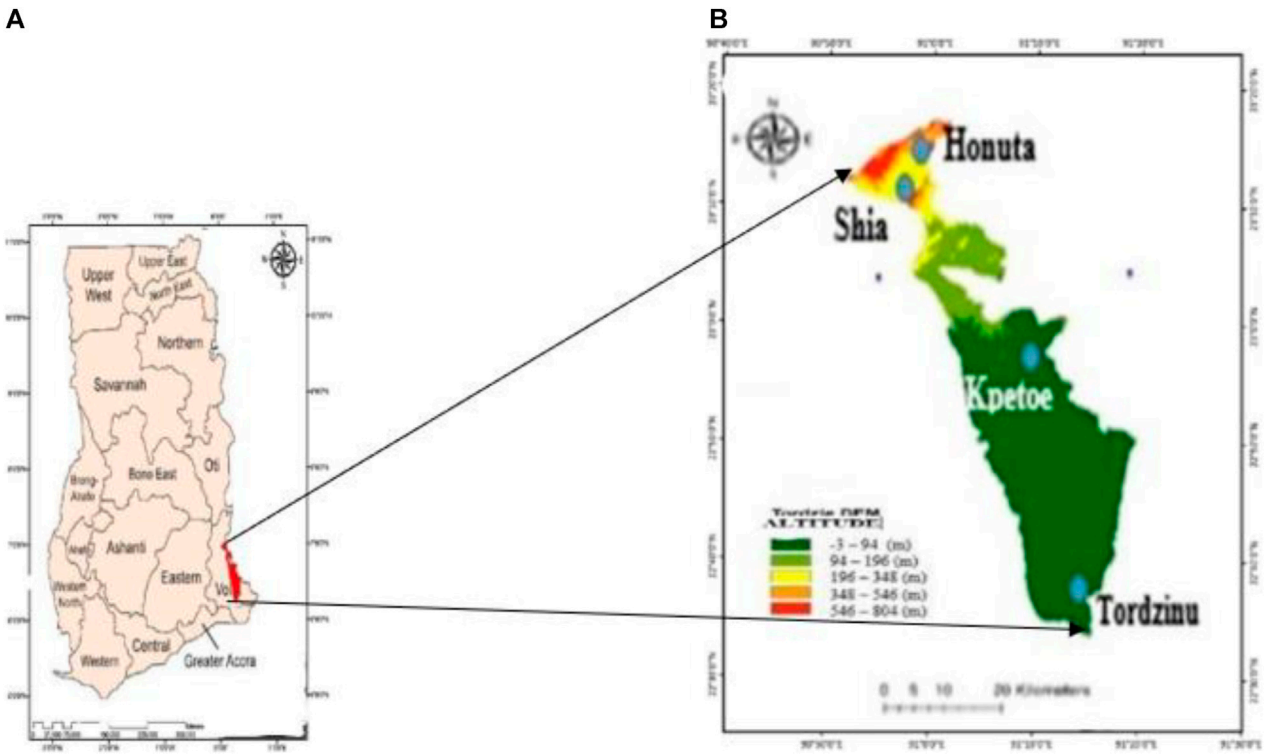

FIGURE 1
Map of Ghana in relation to the Volta region **(A)**, Tordzie watershed, and DEM **(B)**.

classified separately, which do not require modification for direct comparison (Cheruto et al., 2016).

In Ghana, a number of studies have been conducted in recent times to analyze LULC changes using the techniques of RS and GIS to assess the changes of LULC both at the national and watershed levels (Appiah et al., 2015; Basommi et al., 2016). It has been reported by most researchers that human activities like illegal lumbering, urbanization, and agricultural land expansion are responsible for the LULC (Awotwi et al., 2018; Forkuor, 2014). Sarfo et al.(2023) also conducted a study in south-eastern Ghana on class dynamics and relationship between land use systems and temperature, employing geospatial technologies on satellite images and found out the drivers of LULC as political, social, economic, scientific, and biophysical in nature.

However, a search of the literature revealed the gap of no LULC change analysis employing remote sensing-based technology at the microclimate level of Tordzie watershed. The LULC dynamics is not expected to be the same across board but vary from one location to another with its implications. Therefore, a study of LULC dynamics in Tordzie watershed is justified. The Tordzie basin is an important basin in the Volta region of Ghana. It has enormous economic benefits to its catchment dwellers. The water from the basin serves for domestic use, and for agricultural and industrial purposes among others (Nyatuame et al., 2022). As has been established, LULC changes influence the hydrology and the LULC assessment of Tordzie is essential because of the implications for water availability and others. Tordzie watershed encompasses key towns such as Shia, Kpedze, Honuta, Kpetoe, and Tordzinu besides other smaller towns. The 2021 national housing and population census in Ghana estimated the population at Kpedze to be around 27,000, Shia to be around 2000, Honuta estimated to be 1800, Kpetoe to be around 40,000, and Tordzinu also estimated to be 20,000. According to GSS (2021), the population around the watershed is increasing at the rate of 2.5% per annum; therefore, the future LULC situation could be precarious if the future scenario is not known and measures are adopted to ensure sustainability. Against the aforementioned background, this study seeks to assess the LULC and analyze its futuristic ramifications. The findings of this research will guide the environmental policy formulators and implementers by churning out valuable information, the way forward and the adoption of more sustainable development plans as a strategy in lines with sustainable development goals (SDGs) 11, 13, and 15. Again, the scientific knowledge and understanding of LULC dynamics are very essential for both medium- and long-term watershed restoration and management, as well as developing a strategy for soil and water resource conservation plan.

For posterity's sake, the historical LULC evaluation would be accompanied with future development analysis. A modeling technique is the answer to the quest for future demand and supply analysis. A number of working models have been employed by the scientists in modeling LULC changes (Karimi et al., 2018). An example of such a model is the cellular automata (CA) (Arunyawat and Shrestha, 2016) and Markov chain (Awotwi et al., 2018) model used for the prediction of LULC change. In this study, the CA–Markov model was employed to model the future LULC change and analysis. The primary reason for choosing the

TABLE 1 Characteristics of satellite images used.

Named year	Path 193 row 56	Path 193 row 55	Landsat type	Band/colour	Resolution (m)	Source
1987	08-02-1987	23-01-1987	Landsat 4	TM multispectral	30	USGS-GloVis
2003	29-12-2003	29-12-2003	Landsat 7	ETM + Multispectral	30	USGS-GloVis
2017	25-01-2017	25-01-2017	Landsat 8	Multispectral	15	USGS-GloVis

CA–Markov model for this research is because of reports of its high accuracy and other advantages over other models (Gidey et al., 2017). It is also universal and effective. The CA–Markov model was adopted by Luo et al (2015) to study the dynamics of landscape in Central Asia. Matlhodi et al. (2021) also employed the same model to analyze future land use and cover change in Botswana and its implication for water resources.

The objective of the study is to investigate historical LULC changes using satellite imagery and GIS in Tordzie watershed and predict future LULC.

2 Materials and methods

2.1 Study area

The study was carried out in Tordzie watershed in Ghana, Figure 1. The geocodes of stations in Tordzie watershed were Honuta (6°83′0″N, 0°53′0″E), Kpetoe (6°33′0″N, 0°69′0″E), and Tordzinu (5°5′0″N, 0°45′0″E). The digital elevation model (DEM) of the watershed is shown in Figure 1. Tordzie is a trans-boundary basin; the area in Ghana constitutes 83.7%, and the remaining in Togo is 16.3% (WRC, 2010); however, the current study is conducted in the area within Ghana.

2.2 Data used

A cloud-free Landsat multispectral scanner (MSS) and Enhanced Thematic Mapper Plus (ETM+) imageries obtained on January and February 1987, December 2003, and January 2017 were downloaded from the USGS–EROS archive and used. The summary of the Landsat imagery details is presented in Table 1. The Landsat images used for processing were based on what is available and its quality for the area of the study for the chosen years. The limitation with the data was the unequal interval of good-quality Landsat images available for the study area for analysis.

2.3 Image preprocessing

Image pre-processing was carried out to obtain useful data from the satellite images. Data were pre-processed in ENVI 5.0 for geo-referencing, mosaicking, and sub-setting of the image on the basis of the area of interest (AOI). The pre-processing involves actions like geometric corrections, image enhancement, noise removal, and topographic corrections. The acquired data were stacked into composite images as the first step. The layers were stacked to create a multispectral image after combining the required bands. To make the data compatible with each other, projection transformation was carried out and assigned UTM WGS-84,30N projection. The AOI was extracted from the images using the subset option by employing a second-degree polynomial to rectify the scene. The images were taken to ArcMap 10.2.2 for the clipping of the AOI, which is the Tordzie basin. The changes in the LULC type were detected on pixel count from the analysis in ArcMap.

2.4 Image classification

The image classification has the objective of automatically categorizing all pixels in an image into land cover classes. In this study, the images were classified into thematic maps using supervised classification. A band combination of visible and infrared color composites was prepared by delineating the training areas. Signatures and overlapping signatures were merged into one using a histogram tool to compare them. This assisted in avoiding overlapping spectral signatures and thus clearly representing the cover classes distinctly without any ambiguity. The maximum likelihood algorithm (MLA)-supervised classification procedure was adopted as it has more advantages (Talukdar et al., 2020).

2.5 Post-classification

In order to improve the classification accuracy to avoid misclassification, Google Earth Explorer was used to cross-check or validate the classification on the ground. Based on the ground verification, the necessary corrections were made.

2.6 Assessment of accuracy

In order for the classified land use classes to be dependable and useful for analysis of changes, it is required that the accuracy assessment for individual classification be performed. The accuracy assessment technique of classification, which is the most popular, is the error matrix. Kappa is a measure of agreement between pre-defined producer ratings and user assigned ratings. Kappa statistic was computed for the classification using error matrices. It is calculated by the following formula:

$$K = \frac{P(A) - P(E)}{1 - P(E)}, \quad (1)$$

where $P(A)$ is the number of times the k raters agree and $P(E)$ is the number of times the k raters are expected to agree only by chance (Flight and Julious, 2015).

TABLE 2 LULC-type description.

S/N	Land cover	Description
1	Vegetation	This is the area with evergreen trees largely developing naturally in the land, along the streams and on the slopes, grass land cover and bush land areas with sparse trees and shrubs
2	Crop land	This cover type is mostly utilized for growing food crops such as maize, green vegetables, beans, and cassava
3	Water bodies	This land cover type denotes the areas covered with water either along the river bed or man-made earth dams, filled sand dams, and ponds
4	Bare land	This type covers the land without a vegetation cover. This is occasioned by an abandoned crop field, ploughed field not planted and burn grasslands, paths eroded, construction sites, excavation sites, solid waste landfills, open space, and uncovered soil
5	Settlement	This represents the land covered with buildings in the countryside and urban areas. It comprises commercial, residential, industrial, and transportation infrastructures

Adopted from Olaleye *et al.*(2012).

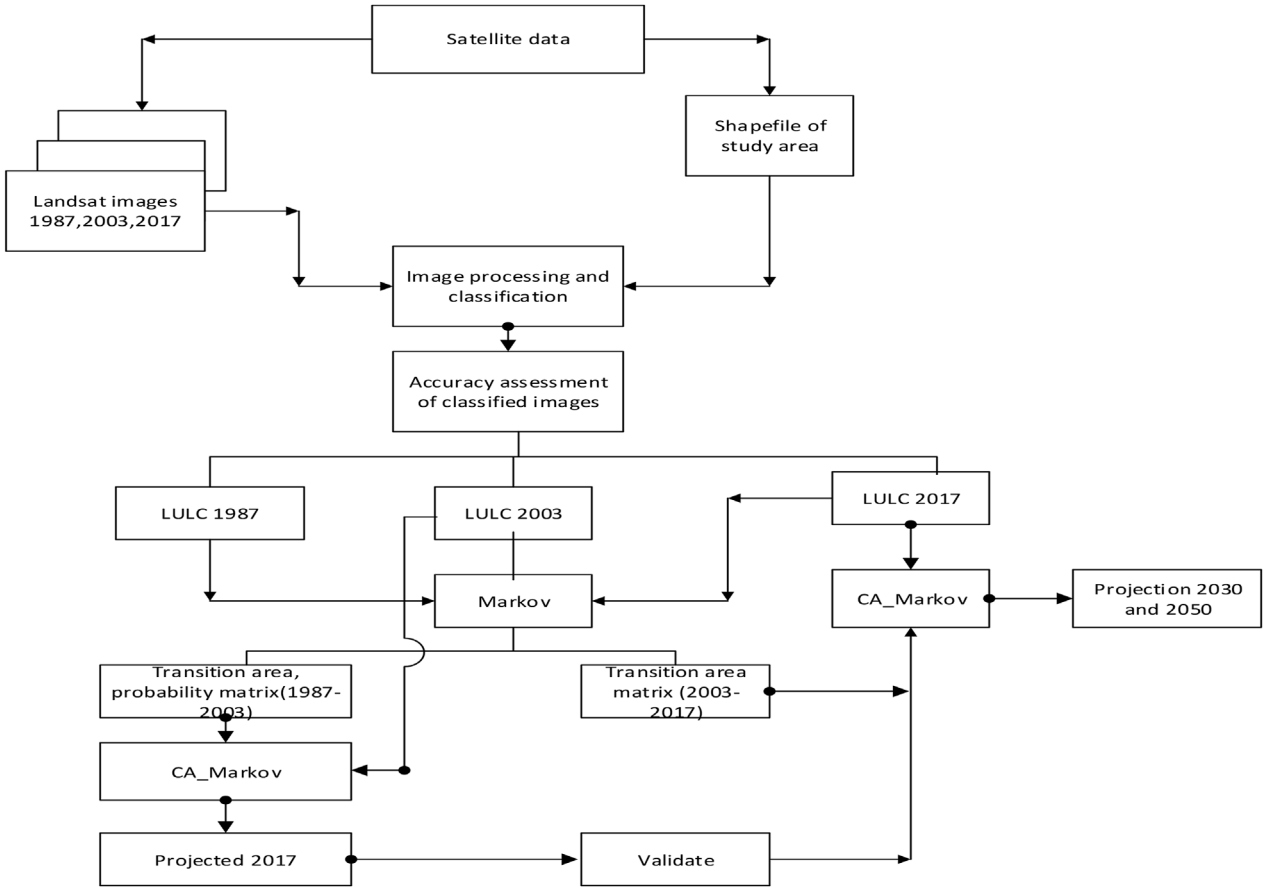

FIGURE 2
Summary of LULC and the cellular automata (CA)–Markov model.

2.7 LULC change detection

LULC identification is the procedure of recognizing changes in the state of an object or phenomenon by observing it at different times. Thus, a new thematic layer was also produced from the two five-class maps, containing different combinations of "from–to" change classes. The general procedure for LULC detection employs the PCC method by comparing the state of the land imagery at two different independent dates (Hassan et al., 2016). The LULC-type classification employed in the study is presented in Table 2. In addition, the flow chart showing procedures followed in LULC detection, quantification, and projection is displayed in Figure 2.

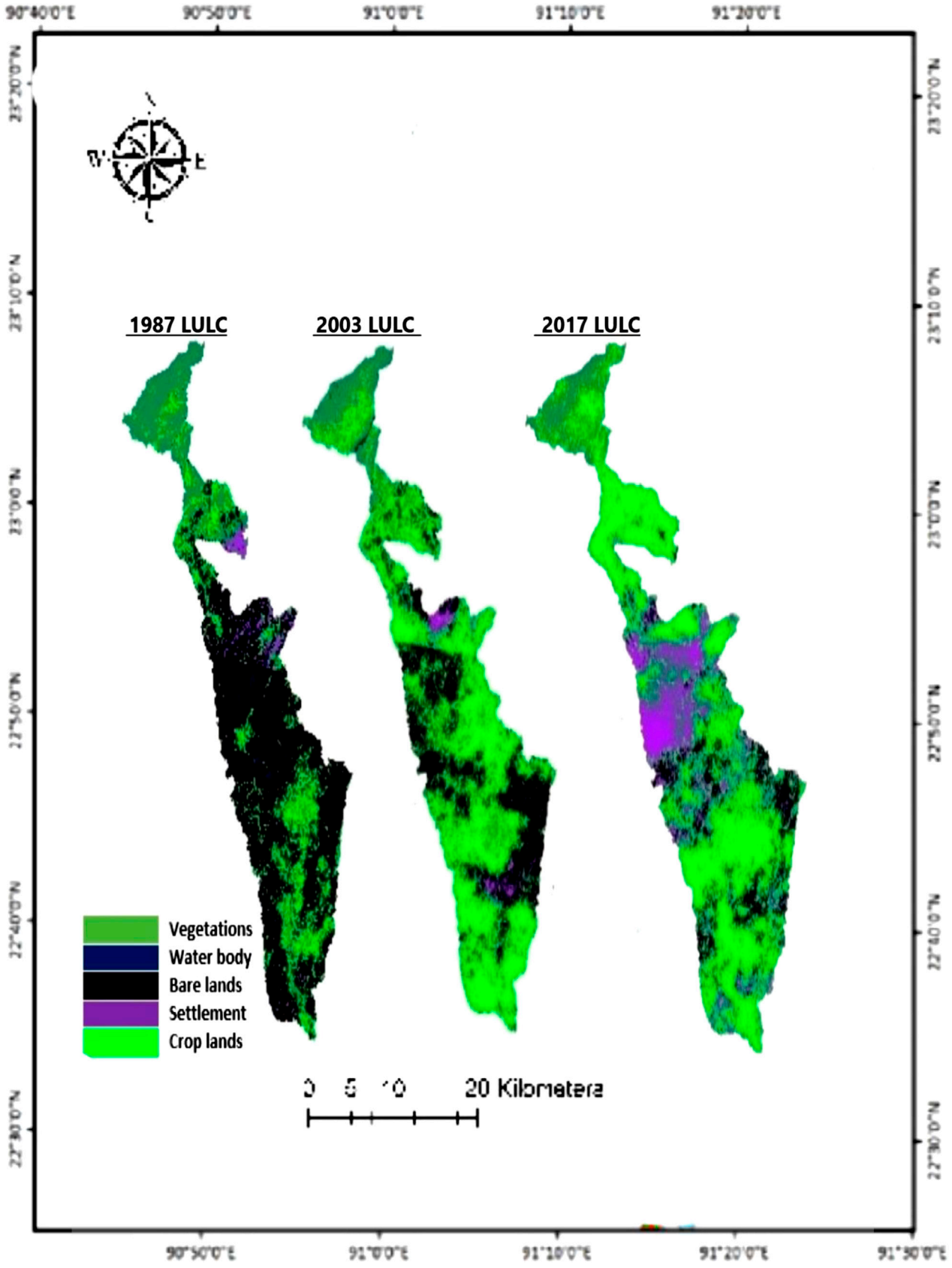

FIGURE 3
LULC maps for Tordzie watershed.

TABLE 3 Accuracy assessment statistics.

Statistics	1987	2003	2017
Overall accuracy (%)	93.13	93.28	96.22
Kappa coefficient	0.90	0.90	0.95

2.8 LULC-type computation

Subsequent to image classification, according to Meshesha et al (2016), the geographical extent in hectares for the LULC type must be calculated for each time period and the extent of change in the LULC type within and between periods compared. The variation in the LULC type was performed using ArcGIS 10.2.2 software. In the analysis of the change, relation (2) was used to compute the rate of change in hectares (ha) per year (ha/y.) and the percentage (%) share of each class type in the period of study.

$$\delta A\ (\%) = \frac{A_{t2} - A_{t1}}{A_{t1}}\ x100, \tag{2}$$

where δA represents the % change in the area of the LULC type between the initial time A_{t1} and time period A_{t2}, A_{t1} represents the area of the LULC type at initial time, and A_{t2} represents the area of the LULC type at final time according to (Shiferaw, 2011).

The rate of change of the LULC cover type was computed using relation (3):

$$\Delta R = \left(\frac{ha}{year}\right) = \frac{K - P}{T}, \tag{3}$$

where ΔR represents the rate of change, K represents the recent area of the LULC type in ha, P represents the previous area of the LULC type in ha, and T represents the time interval between K and P in years.

For the purpose of achieving the objective of evaluating the LULC change in Tordzie watershed, three land cover maps were created with a blend of satellite image bands. With the aim of limiting classification blunder and dissimilarities in the vegetation development consistently, all data were gathered for the periods of December, January, and February with the cloud cover set to zero.

2.9 Land use modeling in the CA–Markov model

IDRISI 17 embedded with land change modeling (LCM) was employed to predict the future LULC for analysis. The following procedures were followed: analysis of change, transition potential modeling, prediction of change, and validation of the model.

2.9.1 Transition potential modeling

A number of transition maps were developed arising out of location of change. The transition maps denote the suitability of a pixel count to turn to other LULC classes in each transition. The transition probability matrix was generated from the transition maps to quantify the likelihood of a particular land use type transitioning into another type in the future.

2.9.2 Change prediction

The change rates calculated previously with the LCM were employed in addition to the transitional potential maps produced subsequently to predict the scenario of future 2030 and 2050. The land use map of 1987–2003 was used to predict the LULC map of 2017. The simulated LULC map of 2017 was compared with the LULC map of 2017 classified as a way of validation. The LULC map of 2017 was employed as the baseline for future prediction.

2.9.3 Model validation

The aim of the validation process was to determine the quality of the map predicted in 2007 in relation to the 2017 LULC map. Kappa indices of agreement (KIA) were employed to compare the spatial proximity of land cover classes between two models. The validation module in IDRISI was employed for validating the model resulting in the parameters listed as K_{no} = 0.8302, $K_{location}$ = 0.7899, and $K_{standard}$ = 0.6935. According to Mishra et al. (2018), K_{no} is the most important parameter for the accuracy assessment of the simulation. $K_{location}$ is the ability of the simulation to identify the location.

TABLE 4 LULC change statistics.

Land cover class	1987		2003		2017		Change 1987–2003		Change/annum (1987–2003) (%)	Change 2003–2017		Change/annum (2003–2017) (%)
	Area (ha)	(%)	Area (ha)	(%)	Area (ha)	(%)	Area (ha)	(%)		Area (ha)	%	
Vegetation	51,726.48	23.22	31,048.24	13.94	25,181.60	11.30	27,333.79	−12.27	−0.77	13,322.43	−5.98	−0.43
Water body	1,554.78	0.70	169.23	0.08	29.15	0.01	1,825.55	−0.82	−0.05	318.09	−0.14	−0.01
Bare land	126,875.38	56.95	64,327.44	28.87	21,275.68	9.55	82,587.59	−37.07	−2.32	97,761.91	−43.88	−3.13
Settlement	5,978.09	2.68	8,122.34	3.65	45,926.36	20.61	2,799.08	+1.26	+0.08	85,843.92	+38.53	+2.75
Crop land	36,665.27	16.46	119,132.76	53.47	130,387.21	58.52	108,254.00	+48.59	+3.04	25,553.65	+11.47	+0.82

NB (−) decrease and (+) increase in land use from the first year.

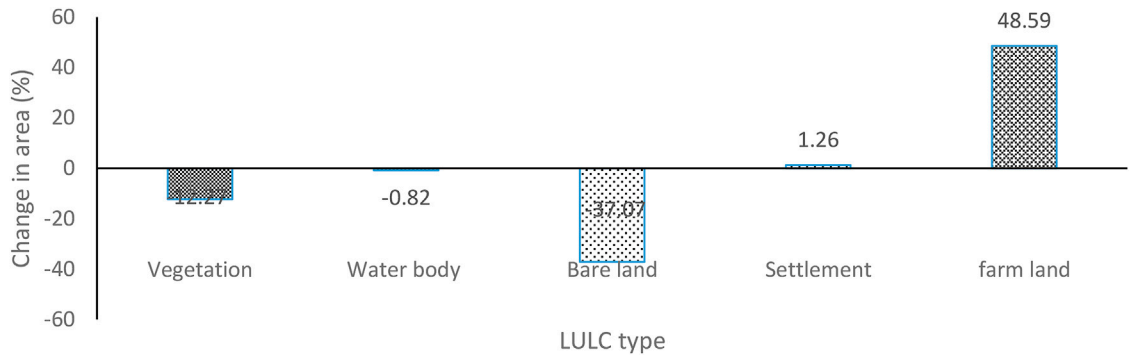

FIGURE 4
Land gain/loss from 1987 to 2003.

$K_{location}$ of 1 is perfect for predicting the future LULC. As observed, with a $K_{location}$ of 0.7899, it means there is uncertainty with the future prediction with the CA–Markov model.

3 Results and discussion

The LULC maps for the years of 1987, 2003, and 2017 are shown in Figure 3. The assessment of accuracy of the LULC-type classification was carried out using Kappa coefficient for different years, as presented in Table 3.

3.1 The dynamics of LULC

The land cover, change rate, and the rate of change per annum are summarized in Table 4 in area and in percentage for Tordzie watershed. In the year 1987, the bare land was the main LULC type with 57% (126,875.38 ha) of the total land area. The mentioned LULC type was followed by vegetation (23.22%), crop land with 16.46% (36,665.27 ha), settlement (2.68%), and finally water bodies (0.70%). The vegetation cover, water bodies, and bare lands progressively decreased from 23.22%, 0.70%, and 56.95% in 1987 to 13.94%, 0.08%, and 28.87% in 2003 and lastly to 11.30%, 0.01%, and 9.55%, respectively, in 2017. However, the settlement and crop land, respectively, increased from 2.68% to 16.46% in 1987 to 3.65% and 53.47% in 2003 and finally to 20.61% and 58.52% in 2017. When vegetation cover and water bodies reduced at the given percentages mentioned, there was an increment in settlement and the agricultural land area under production. These observations are in line with the similar studies in other jurisdictions (Awotwi et al., 2018). The implications of the vegetation cover decline are enormous such as the loss of biodiversity and reduction in land productivity among others (Rawat and Kumar, 2015).

3.2 The rate of LULC change

The rate of change of the LULC type is indicated in Table 4. The rate of vegetation loss per annum from 1987 to 2003 was −0.77% and from 2003 to 2017 was −0.43%. The loss of bare land from 1987 to 2003 was −2.32% per annum and −3.13% per annum from 2003 to 2017 and that of the water body for the same stated period were −0.05% and −0.01%, respectively, per annum. On the other hand, the rate of land gain by settlement and crop land for the mentioned period were +0.08% and +2.75%, and +3.04 and +0.82%, respectively, per annum. The result implies the intensive gain in the settlement and crop land is at the expense of massive loss of vegetation and bare land. The result obtained is in agreement with Appiah et al. (2015) and Basommi et al. (2016), who conducted a similar study at different parts of Ghana.

3.3 Implication of LULC changes

The implication of the conversion of vegetation to crop land and settlement is the modification of the evapotranspiration regime, thus impacting the precipitation. This is because vegetation or forest has high evaporation, which contributes to atmospheric circulation. Thus, deforestation reduces evapotranspiration due to vegetation loss with the consequences of reduction in atmospheric moisture circulation and leads to declining precipitation. The aforementioned assertion is buttressed by the contemporary literature (Snyder, 2010; Spracklen et al., 2012).

The aforementioned scientific consensus on the negative impact of deforestation is further supported by Aragao (2012). He stated that the canopy of forest reprocesses water more efficiently through evapotranspiration than sparsely vegetated surfaces like farmlands. There is also an associated flood risk as a result of loss of vegetation. This is because the canopies of forest intercept rainfall, increase soil infiltration capacity, lower runoff, and reduce evaporation of water from the canopy. The aforesaid deduction agrees with Fonseca et al. (2022), who revealed in their study that 10% decrease in natural forest is responsible for increased flood frequency of between 4% and 28%. Lobell et al. (2011) related declining rainfall and rising temperatures to de-vegetation, leading to a reduction in crop yield with an estimated 10% decline in crop yield due to 1% rise in temperature.

The reduction in the vegetation cover also has a health implication as the quality of air is deteriorated because plants give oxygen and absorb carbon dioxide. A typical example is

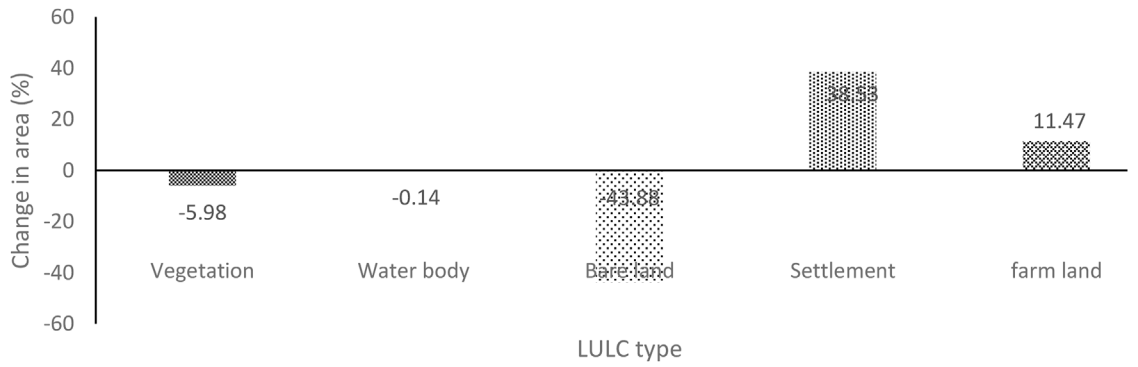

FIGURE 5
Land gain/loss from 2003 to 2017.

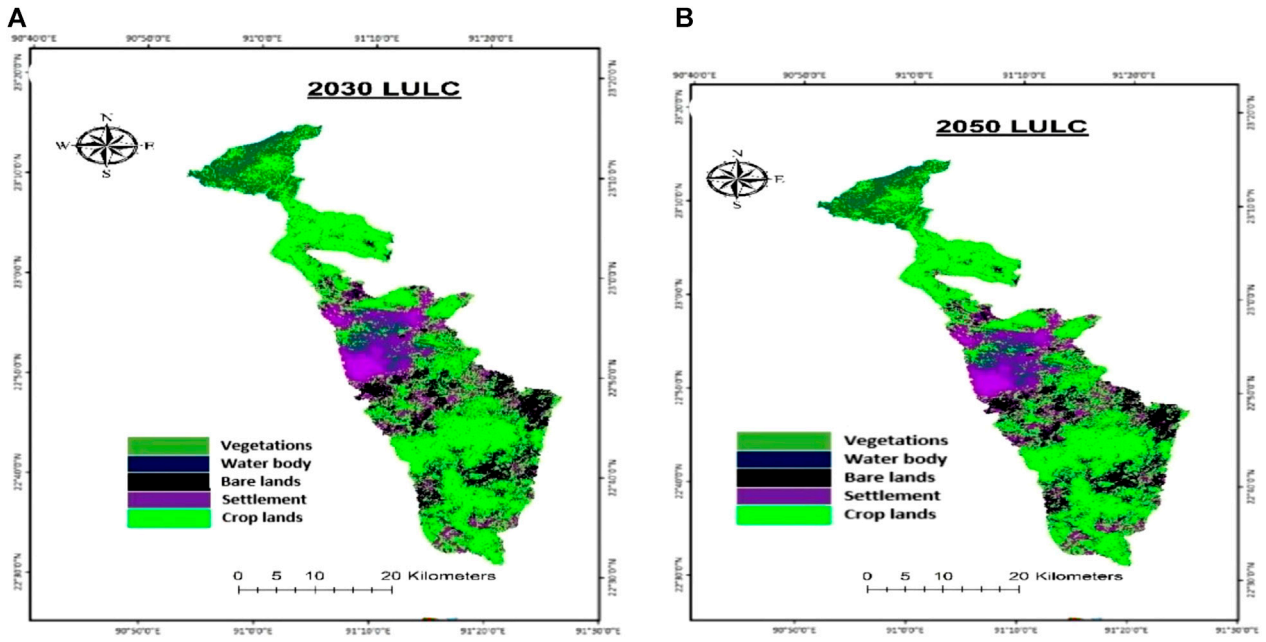

FIGURE 6
Projected LULC map of 2030 **(A)** and 2050 **(B)**.

where slash and burn are employed in converting vegetation to farm land; air pollution results from emission of smokes. This smoke includes carbon particles smaller than 1.5 μm in size, which is harmful to human health.

3.4 Land loss/land gain

The trend of the LULC change generally is a shift of vegetation, bare lands, and water bodies to crop land and settlement. When the vegetative cover of the land is being lost together with the water bodies and bare lands, there is a gain for the farmland and settlement. The magnitude of the change from 1987 to 2003 and 2003 to 2017 is illustrated in Figures 4, 5. The total vegetation loss from 1987 to 2017 was −26544.88 ha (−11.92%) and that of the bare land was −105599.7 ha (−47.4%). The gain in settlement and crop land for the same period was +39,948.27 ha (+17.93%) and +93,721.94 ha (+42.06%), respectively. The trend of the reduction of vegetation cover corresponded with the expansion of the settlement area and agricultural land to cater for the food security needs of the burgeoning population. The negative and positive trends in LULC detection corresponded to the gain or loss of the specific land cover.

The implication of the fast rate of the vegetation decline and the sprawl of urbanization is that climate change impacts will be

TABLE 5 Markov Chain transition probability matrix for periods 1987–2003 and 2003–2017.

Year	Vegetation	Water body	Bare land	Settlement	Cropland
Vegetation 1987–2003	0.4289	0.0012	0.0719	0.0057	0.4923
2003–2017	0.4415	0.0000	0.0041	0.0108	0.5437
Water body 1987–2003	0.0181	0.0361	0.5170	0.0358	0.3931
2003–2017	0.0000	0.0000	0.1216	0.5454	0.3330
Bare land 1987–2003	0.0254	0.0004	0.3388	0.0443	0.5910
2003–2017	0.0390	0.0004	0.1569	0.3211	0.4827
Settlement 1987–2003	0.0180	0.0000	0.2379	0.1105	0.6336
2003–2017	0.0145	0.0000	0.1758	0.2556	0.5542
Crop land 1987–2003	0.0935	0.0005	0.3162	0.0579	0.5319
2003–2017	0.0757	0.0001	0.0890	0.2564	0.5788

TABLE 6 Projected LULC statistics.

LULC type	2030		2017–2030	2050		2030–2050
	Area (ha)	Area (%)	Change (%)	Area (ha)	(%)	Change (%)
Vegetation	25,526.06	11.46	0.15	25,714.09	11.54	0.08
Water body	43.91	0.02	0.01	43.77	0.02	~0.00
Bare land	22,014.04	9.88	0.33	22,245.60	9.98	0.10
Settlement	48,688.44	21.85	1.24	48,711.43	21.86	0.01
Crop land	126,527.60	56.79	−1.73	126,085.10	56.59	−0.20

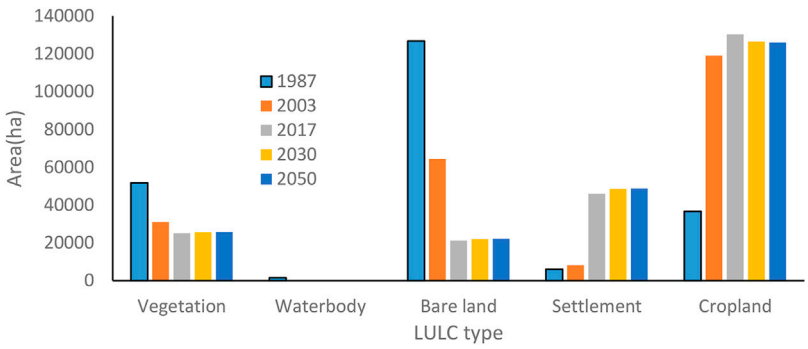

FIGURE 7
LULC variations.

exacerbated. As the urbanization sprawl, it leads to the destruction of the natural ecosystem, water quality, and the impairment of biodiversity due to development of the area. Urbanization, as a result of vegetation loss, culminates in the loss of terrestrial carbon stored in vegetation biomass and thus increase carbon footprint in the ecosystem, which contribute to climate change (Seto et al., 2012).

3.5 Prognosis of LULC based on the CA–Markov Chain model

Land cover change has substantial influence on the functioning of social, economic, and ecological systems and enormous benefits for its sustenance (Mahmoud and Alazba, 2015). Predicting the future impacts of land cover changes on an area necessitates an

understanding of the effects that historic land cover changes have exerted on the environment. The projected land cover in 2030 and 2050 is shown in Figures 6A, B, respectively.

3.6 Transition probability matrix analysis

A significant part of detecting change is to determine what is really changing and which LULC type is changing to the other. Table 5 provides the probability that each land cover type will change to the other type. Table 5 shows that the rows indicate the older land cover types, while the columns represent the newer types. The derived probability matrix was employed in predicting the LULC of 2030 and 2050. For instance, between 2003 and 2017, the probability of vegetation changing to crop land was 0.5437 or 54.37% and the converse was 0.0757 or 7.57%. The probability of vegetation converting to crop land has increased from 0.4923 in 1987–2003 to 0.5437 in 2003–2017. The transition probability matrix assists in knowing which changed land use type is due to be converted to another land use type and thus aids in better decision-making for mitigative strategies to manage the ecosystem.

3.7 The driving force of LULC change

Rapid deforestation, as a result of urbanization, may be due to the increase in population, which is leading to change in the land use pattern. According to GSS (2021), population is increasing at the rate of 2.5% per annum and may be playing a significant role in the LULC dynamics. The implications of population increase are many and thus put pressure on the use of natural land resources. The cutting of trees for fuel wood, bush fires, and other economic activities of high market value are the main causes of accelerated deforestation in the watershed. This occurs as there is no alternate livelihood support for rural dwellers who depend a lot on the natural resources for survival. Thus, an increase in population drives the increase in the agricultural land area and the settlement area since there is the need to produce food in response to growing population and the demand for settlement. Evidence abounds in the literature to buttress the point that human activities are the main causes of LULC change dynamics (Shiferaw, 2011). Again, it was also reported by Toma et al. (2023) that population growth, agricultural expansion, illegal wood extraction, increase in the settlement area or built-up area, urbanization, and environmental policy gaps are the major drivers of LULC. The drivers of LULC have been categorized into natural causes and human-induced or anthropogenic stresses. The anthropogenic stresses in relation to biophysical factors may be contributing to the LULC.

The anthropogenic stresses of LULC are further classified as direct causes and underlying causes according to Sarfo et al. (2023). According to Sarfo et al. (2023), five primary drivers of LULC, namely, political, social, economic, scientific, and environmental factors, are considered to be the underlying influencers on human-induced factors.

In 2030 and 2050, the crop land will be 56.8% (126,527.6 ha) and 56.6% (126,085.10 ha), respectively, of the watershed. However, there is a reduction in the crop land between 2017 and projected 2030 by −3,859.61 ha (−1.73%) with a decreasing rate of −0.13% per annum for the stated period. The settlement will increase by 2.4% for the same period. The settlement area projected will continue to increase until 2030 and 2050, and it will be 21.85% (48,688.44 ha) and 21.86% (48,711.43 ha) of the LULC type in the watershed, respectively. The detail projected statistics are presented in Table 6 and Figure 7. The loss from the crop land in the projected will be gained by settlement, bare land, and vegetation. Nonetheless, the net change analysis reveals a decrease in the vegetation area from 1987 to the projected 2030 and 2050.

3.8 Implication of the projected LULC change in the watershed

The changes in LULC in the future as simulated, especially the increase in settlement and decline in the agricultural land area, might impact the local population in several ways. It may lead to overexploitation of the ecosystem and natural resources due to socioeconomic factors, such as population increase, which drives the settlement increase. The overexploitation of natural resources may lead to resource use conflict as these resources get scantier and there is a scramble for them.

As a vegetation cover, which serves as a carbon sink, decreases, it may lead to the rise in temperature and reduction in rainfall and its variability. The increasing temperatures may result in thermal discomfort as heat waves are on the rise as a consequence. In order to mitigate the excessive heats at homes, people may have to resort to the use of air conditionings in their homes and thus may lead to an increase in the energy cost.

The increase in settlement, virtually robbing the crop land, may come with its challenges. The conversion of agricultural land to non-agricultural uses may bring serious consequences of food insecurity.

It may also bring about unemployment among the users of agricultural lands and migration of the users to big cities for better opportunities. The conversion of crop land to vegetation may have implications for ecosystem services including providing habitat and biodiversity (Lawler et al., 2014).

Since forest serves as a carbon sink, thus a comparatively small crop land conversion to vegetation may have an enormous impact on the net GHG emissions. However, overall, vegetation has decreased from 1987 to the projected 2050. The marginal increase in the projected bare land could be as a result of the expected increase in road infrastructure, construction sites, and landfill sites due to the increase in the settlement area as a consequence of the expected population rise.

The negative environmental consequences of LULC will worsen if business as usual (BAU) is continued in the future. The detrimental impact on the soil and water resources (water scarcity) in the watershed will be heightened.

The aforementioned LULC changes and implications historically have not been severe, as is expected in the projected LULC changes. The loss of biodiversity associated with the decline in vegetation as simulated may be more severe in the future compared to the historical changes, along with drought severity, intensity, amount, and duration, as projected by Nyatuame and Agodzo (2017), as a result of rainfall variability due to climate and land cover change.

The local population may be severely impacted as there is land productivity decrease, affecting their livelihood, since the local economy is agrarian.

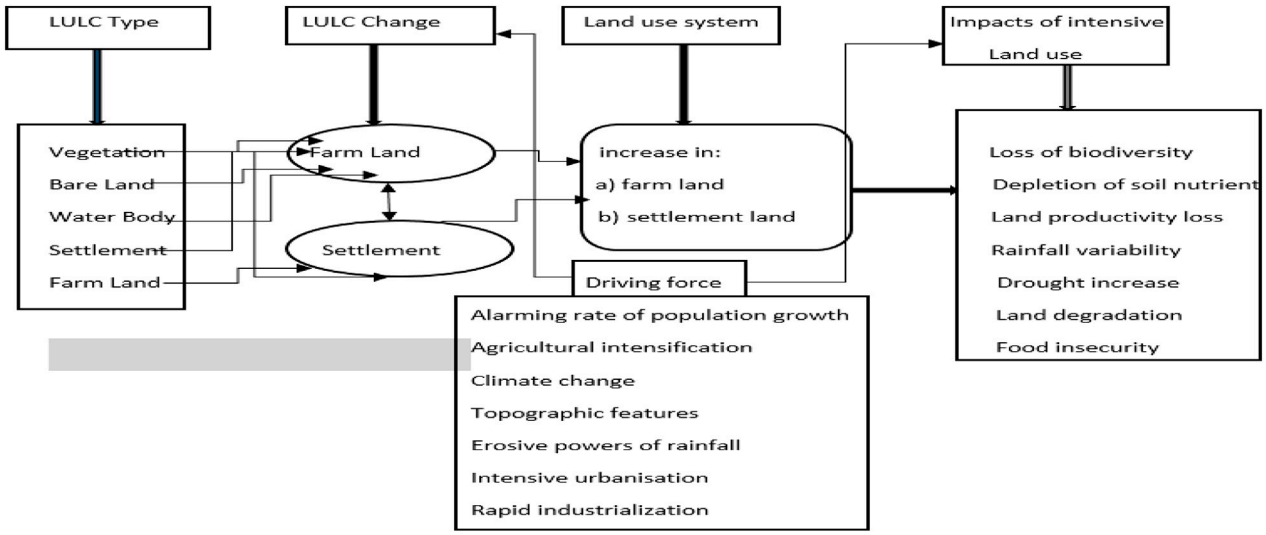

FIGURE 8
Conceptual framework of the LULC dynamics. Adopted from Maitima et al. (2009) and Shiferaw (2011).

3.9 LULC dynamics, the need for policy intervention

In line with SDGs 13 and 15, and the protection of biodiversity and ecosystem, there need to be a policy to guide the use of natural resources with posterity in mind, which includes the following:

- Vertical development that maximizes the land area instead of horizontal development.
- Planting of indigenous tree species to forestall de-vegetation and to restore the ecosystem benefits of afforestation.
- Obtaining permission from relevant authorities before felling of trees.
- Replacement plan provided and executed to the letter.
- Policy on the land use plan.
- Use of liquefied petroleum gas (LPG) instead of fuel wood.
- Alternative livelihood means instead of lumbering.

Figure 8 illustrates LULC changes and consequences of the change. It also summarizes the drivers of the LULC and the impacts of LULC.

4 Conclusion

LULC change has been acknowledged as the main driving force of the climate change and variability. The study revealed a progressive decrease in the land cover of vegetation, water bodies, and bare land from 1987 to 2003 through to 2017. The vegetation cover, water bodies, and bare lands progressively decreased from 23.22%, 0.70%, and 56.95% in 1987 to 13.94%, 0.08%, and 28.87% in 2003 and lastly to 11.30%, 0.01%, and 9.55%, respectively, in 2017. However, the settlement area and crop land, respectively, increased from 2.68% to 16.46% in 1987 to 3.65% and 53.47% in 2003 and finally to 20.61% and 58.52% in 2017. The projected LULC indicated that in 2030 and 2050, the dominant land use type will be crop land (56%). The findings of this research are relevant to environmental policy formulators and implementers, as well as urban and water resource planners.

The limitation to this current study is the images of different time intervals due to the difficulty of obtaining good-quality Landsat images from the study area for the periods under study.

The recourse to land use policy and its effective implementation is recommended to curtail the alarming LULC in Tordzie watershed and its environs. The study also recommends adapted mitigation strategies to protect vegetation (forest cover) and improve the green spaces around the built-up areas by planting more trees. It is further recommended that technology be adopted in farming to increase productivity instead of increasing the farm size. The urbanization in relation to temperature rise, energy cost, and LULC is recommended for further study by the future researchers.

Data availability statement

Publicly available datasets were analyzed in this study. These data can be found at: https://earthexplorer.usgs.gov/.

Author contributions

MN conceptualized the study, designed and analyzed the literature, wrote the manuscript and revised it. SA and LKA reviewed and edited the manuscript. BM-B worked on the

figures. All authors contributed to the article and approved the submitted version.

Acknowledgments

The authors acknowledge the authors whose works have been reviewed and duly cited. The authors are especially thankful to the Shuttle Radar Topography Mission (SRTM) for DEM data and the United State Geographical Survey department of the Earth Resources Observation Service (USGS-EROS) for the satellite imageries. The authors would like to thank the editors and the reviewers for the relevant comments and suggestions, which significantly improved the quality of the manuscript.

Conflict of interest

The authors declare that the research was conducted in the absence of any commercial or financial relationships that could be construed as a potential conflict of interest.

Publisher's note

References

Alam, A., Bhat, M. S., and Maheen, M. (2020). Using Landsat satellite data for assessing the land use and land cover change in Kashmir valley. *GeoJournal* 85 (6), 1529–1543. doi:10.1007/s10708-019-10037-x

Appiah, D. O., Schröder, D., Forkuo, E. K., and Bugri, J. T. (2015). Application of geo-information techniques in land use and land cover change analysis in a peri-urban district of Ghana. *ISPRS Int. J. Geo-Information* 4 (3), 1265–1289. doi:10.3390/ijgi4031265

Aragao, L. E. (2012). Environmental science: The rainforest's water pump. *Nature* 489 (7415), 217–218. doi:10.1038/nature11485

Arunyawat, S., and Shrestha, R. P. (2016). Assessing land use change and its impact on ecosystem services in northern Thailand. *Sustainability* 8, 768. doi:10.3390/su8080768

Awotwi, A., Anornu, G. K., Quaye-Ballard, J. A., and Annor, T. (2018). Monitoring land use and land cover changes due to extensive gold mining, urban expansion, and agriculture in the Pra River Basin of Ghana, 1986–2025. *Land Degrad. Dev.* 29 (10), 3331–3343. doi:10.1002/ldr.3093

Bagley, J. E. (2011). *Impact of land cover change, energy regulation, bread basket production and precipitation*. PhD Thesis. University of Wisconsin-Madison.

Basommi, L. P., Guan, Q. F., Cheng, D. D., and Singh, S. K. (2016). Dynamics of land use change in a mining area: A case study of nadowli district, Ghana. *J. Mt. Sci.* 13 (4), 633–642. doi:10.1007/s11629-015-3706-4

Butt, A., Shabbir, R., Ahmad, S. S., and Aziz, N. (2015). Land use change mapping and analysis using remote sensing and GIS: A case study of simly watershed, islamabad, Pakistan. *Egypt. J. Remote Sens. Space Sci.* 18 (2), 251–259. doi:10.1016/j.ejrs.2015.07.003

Cheruto, M. C., Kauti, M. K., Kisangau, D. P., and Kariuki, P. C. (2016). *Assessment of land use and land cover change using GIS and remote sensing techniques: A case study of makueni county*. Kenya.

Chowdhury, M., Hasan, M. E., and Abdullah-Al-Mamun, M. M. (2018). Land use/land cover change assessment of Halda watershed using remote sensing and GIS. *Egypt. J. Remote Sens. Space Sci.* 23, 63–75. doi:10.1016/j.ejrs.2018.11.003

Coe, M. T., Latrubesse, E. M., Ferreira, M. E., and Amsler, M. L. (2011). The effects of deforestation and climate variability on the streamflow of the Araguaia River, Brazil. *Biogeochemistry* 105 (1-3), 119–131. doi:10.1007/s10533-011-9582-2

Das, N., Mondal, P., Sutradhar, S., and Ghosh, R. (2021). Assessment of variation of land use/land cover and its impact on land surface temperature of Asansol subdivision. *Egypt. J. Remote Sens. Space Sci.* 24 (1), 131–149. doi:10.1016/j.ejrs.2020.05.001

Flight, L., and Julious, S. A. (2015). The disagreeable behaviour of the kappa statistic. *Pharm. Stat.* 14 (1), 74–78. doi:10.1002/pst.1659

Fonseca, C. A. B. D., Al-Ansari, N., Silva, R. M. D., Santos, C. A. G., Zerouali, B., Oliveira, D. B. D., et al. (2022). Investigating relationships between runoff–erosion processes and land use and land cover using remote sensing multiple gridded datasets. *ISPRS Int. J. Geo-Information* 11 (5), 272. doi:10.3390/ijgi11050272

Forkuor, G. (2014). *Agricultural land use mapping in West Africa using multi-sensor satellite imagery,PhD thesis*. Germany: University of Wuerzburg.

Ghana Statistical Service (GSS) (2021). *National population and housing census*.

Gidey, E., Dikinya, O., Sebego, R., Segosebe, E., and Zenebe, A. (2017). Cellular automata and Markov chain (CA_Markov) model-based predictions of future land use and land cover scenarios (2015–2033) in Raya, northern Ethiopia. *Model. Earth Syst. Environ.* 3 (4), 1245–1262. doi:10.1007/s40808-017-0397-6

Hassan, Z., Shabbir, R., Ahmad, S. S., Malik, A. H., Aziz, N., Butt, A., et al. (2016). Dynamics of land use and land cover change (LULCC) using geospatial techniques: A case study of islamabad Pakistan. *Springer plus* 5, 812. doi:10.1186/s40064-016-2414-z

Kafy, A. A., Rahman, M. S., Hasan, M. M., and Islam, M. (2020). Modelling future land use land cover changes and their impacts on land surface temperatures in Rajshahi, Bangladesh. *Remote Sens. Appl. Soc. Environ.* 18, 100314. doi:10.1016/j.rsase.2020.100314

Kalra, K., Goswami, A. K., and Gupta, R. (2013). A comparative study of supervised image classification algorithms for satellite images. *Int. J. Electr. Electron. data Commun.* 1 (10), 10–16.

Karimi, H., Jafarnezhad, J., Khaledi, J., and Ahmadi, P. (2018). Monitoring and prediction of land use/land cover changes using CA-markov model: A case study of ravansar county in Iran. *Arabian J. Geosciences* 11 (19), 592–599. doi:10.1007/s12517-018-3940-5

Lawler, J. J., Lewis, D. J., Nelson, E., Plantinga, A. J., Polasky, S., Withey, J. C., et al. (2014). Projected land-use change impacts on ecosystem services in the United States. *Proc. Natl. Acad. Sci. U. S. A.* 111, 7492–7497. doi:10.1073/pnas.1405557111

Liping, C., Yujun, S., and Saeed, S. (2018). Monitoring and predicting land use and land cover changes using remote sensing and GIS techniques—a case study of a hilly area, jiangle, China. *PloS one* 13 (7), e0200493. doi:10.1371/journal.pone.0200493

Lobell, D. B., Schlenker, W., and Costa-Roberts, J. (2011). Climate trends and global crop production since 1980. *Science* 333 (6042), 616–620. doi:10.1126/science.1204531

Lu, Y., Wu, P., Ma, X., and Li, X. (2019). Detection and prediction of land use/land cover change using spatiotemporal data fusion and the Cellular Automata–Markov model. *Environ. Monit. Assess.* 191 (2), 68–19. doi:10.1007/s10661-019-7200-2

Luo, G., Amuti, T., Zhu, L., Mambetov, B. T., Maisupova, B., and Zhang, C. (2015). Dynamics of landscape patterns in an inland river delta of Central Asia based on a cellular automata-Markov model. *Reg. Environ. change* 15 (2), 277–289. doi:10.1007/s10113-014-0638-4

Mahmoud, S. H., and Alazba, A. A. (2015). Hydrological response to land cover changes and human activities in arid regions using a geographic information system and remote sensing, *Plos One* 10, e0125805. doi:10.1371/journal.pone.0125805

Maitima, J. M., Mugatha, S. M., Reid, R. S., Gachimbi, L. N., Majule, A., Lyaruu, H., et al. (2009). The linkages between land use change, land degradation and biodiversity across East Africa. *Afr. J. Environ. Sci. Technol.* 3 (10).

Matlhodi, B., Kenabatho, P. K., Parida, B. P., and Maphanyane, J. G. (2021). Analysis of the future land use land cover changes in the gaborone dam catchment using ca-markov model: Implications on water resources. *Remote Sens.* 13 (13), 2427. doi:10.3390/rs13132427

Mengist, W., Soromessa, T., and Feyisa, G. L. (2022). Forest fragmentation in a forest Biosphere Reserve: Implications for the sustainability of natural habitats and forest management policy in Ethiopia. *Resour. Environ. Sustain.* 8, 100058. doi:10.1016/j.resenv.2022.100058

Meshesha, T. W., Tripathi, S. K., and Khare, D. (2016). Analyses of land use and land cover change dynamics using GIS and remote sensing during 1984 and 2015 in the Beressa Watershed Northern Central Highland of Ethiopia. *Model. Earth Syst. Environ.* 2, 1–12. doi:10.1007/s40808-016-0233-4

Minale, A. S. (2013). Retrospective analysis of land cover and use dynamics in Gilgel Abbay Watershed by using GIS and remote sensing techniques, Northwestern Ethiopia. *Int. J. Geosciences* 4 (07), 1003–1008. doi:10.4236/ijg.2013.47093

Mishra, V. N., Rai, P. K., Prasad, R., Punia, M., and Nistor, M. M. (2018). Prediction of spatio-temporal land use/land cover dynamics in rapidly developing varanasi district of Uttar Pradesh, India, using geospatial approach: A comparison of hybrid models. *Appl. Geomatics* 10 (3), 257–276. doi:10.1007/s12518-018-0223-5

Nicu, I. C., and Stoleriu, C. C. (2019). Land use changes and dynamics over the last century around churches of Moldavia, Bukovina, Northern Romania–Challenges and future perspectives. *Habitat Int.* 88, 101979. doi:10.1016/j.habitatint.2019.04.006

Nyatuame, M., and Agodzo, S. (2017). Analysis of extreme rainfall events (drought and flood) over Tordzie Watershed in the Volta Region of Ghana. *J. Geoscience Environ. Prot.* 5 (9), 275–295. doi:10.4236/gep.2017.59019

Nyatuame, M., Amekudzi, L. K., and Agodzo, S. K. (2020). Assessing the land use/land cover and climate change impact on water balance on Tordzie watershed. *Remote Sens. Appl. Soc. Environ.* 20, 100381. doi:10.1016/j.rsase.2020.100381

Nyatuame, M., Agodzo, S., and Amekudzi, L. (2022). Analysis of rainfall and temperature trend and variability of the Tordzie Watershed. *Ghana J. Sci. Technol. Dev.* 8 (1), 1–17. doi:10.47881/271.967x

Olaleye, J. B., Abiodun, O. E., and Asonibare, R. O. (2012). Land use and land cover ananlysis of Ilorin Emirate between 1986 and 2006 using landsat imageries. *Afr. J. Environ. Sci. Technol.* 6 (4), 189–198.

Rawat, J. S., and Kumar, M. (2015). Monitoring land use/cover change using remote sensing and GIS techniques: A case study of hawalbagh block, district almora, uttarakhand, India. *Egypt. J. Remote Sens. Space Sci.* 18 (1), 77–84. doi:10.1016/j.ejrs.2015.02.002

Sarfo, I., Bi, S., Kwang, C., Yeboah, E., Addai, F. K., Nkunzimana, A., et al. (2023). Class dynamics and relationship between land-use systems and surface temperature in south-eastern Ghana. *Environ. Earth Sci.* 82 (4), 104. doi:10.1007/s12665-023-10755-z

Schulp, C. J., Levers, C., Kuemmerle, T., Tieskens, K. F., and Verburg, P. H. (2019). Mapping and modelling past and future land use change in Europe's cultural landscapes. *Land use policy* 80, 332–344. doi:10.1016/j.landusepol.2018.04.030

Seto, K. C., Güneralp, B., and Hutyra, L. R. (2012). Global forecasts of urban expansion to 2030 and direct impacts on biodiversity and carbon pools. *Proc. Natl. Acad. Sci.* 109 (40), 16083–16088. doi:10.1073/pnas.1211658109

Shiferaw, A. (2011). Evaluating the land use and land cover dynamics in borena woreda of south wollo highlands, Ethiopia. *J. Sustain. Dev. Afr.* 13 (1).

Snyder, P. K. (2010). The influence of tropical deforestation on the Northern Hemisphere climate by atmospheric teleconnections. *Earth Interact.* 14 (4), 1–34. doi:10.1175/2010ei280.1

Spracklen, D. V., Arnold, S. R., and Taylor, C. M. (2012). Observations of increased tropical rainfall preceded by air passage over forests. *Nature* 489 (7415), 282–285. doi:10.1038/nature11390

Talukdar, S., Singha, P., Mahato, S., Pal, S., Liou, Y. A., Rahman, A., et al. (2020). Land-use land-cover classification by machine learning classifiers for satellite observations—a review. *Remote Sens.* 12 (7), 1135. doi:10.3390/rs12071135

Toma, M. B., Belete, M. D., and Ulsido, M. D. (2023). Historical and future dynamics of land use land cover and its drivers in Ajora-Woybo watershed, Omo-Gibe basin, Ethiopia. *Nat. Resour. Model.* 36 (1), e12353. doi:10.1111/nrm.12353

WRC (2010). *Water resources commission, annual report.*

frontiers | Frontiers in Environmental Science

TYPE Original Research
PUBLISHED 04 July 2023
DOI 10.3389/fenvs.2023.1179328

OPEN ACCESS

EDITED BY
George Xian,
United States Department of the Interior,
United States

REVIEWED BY
José Maria Santos,
University of Lisbon, Portugal
Michael Nones,
Polish Academy of Sciences, Poland

*CORRESPONDENCE
Roy E. Petrakis,
rpetrakis@usgs.gov

RECEIVED 03 March 2023
ACCEPTED 21 June 2023
PUBLISHED 04 July 2023

CITATION
Petrakis RE, Norman LM and Middleton BR (2023), Riparian vegetation response amid variable climate conditions across the Upper Gila River watershed: informing Tribal restoration priorities.
Front. Environ. Sci. 11:1179328.
doi: 10.3389/fenvs.2023.1179328

Riparian vegetation response amid variable climate conditions across the Upper Gila River watershed: informing Tribal restoration priorities

Roy E. Petrakis*, Laura M. Norman and Barry R. Middleton

U. S. Geological Survey, Western Geographic Science Center, Tucson, AZ, United States

Riparian systems across the Southwest United States are extremely valuable for the human and ecological communities that engage with them. However, they have experienced substantial changes and stresses over the past century, including non-native vegetation expansion, vegetation die-offs, and increased fire activity. Vegetation management approaches, such as ecological restoration, may address some of these stressors as well as reduce the risk of future impacts. We apply remote sensing to inform restoration priorities along the upper Gila River within the San Carlos Apache Reservation and Upper Gila River watershed. First, we develop a spatially and temporally explicit trend analysis across three observed climate periods (1985–1993, 1993–2014, 2014–2021) using the Landsat-derived indices to quantify changes in riparian vegetation conditions. These maps can be used to identify areas potentially more at risk for degradation. Second, we analyze changes in riparian vegetation within a climate framework to better understand trends and the potential effect of climate change. Vegetation greenness has largely increased throughout the watershed despite intensifying drought conditions across our study period, though areas within the lower watershed have shown increased stress and higher rates of wildfire and other disturbances over the past 5-years. Nevertheless, small-scale restoration activities appear to show improving vegetation conditions, suggesting efficacy of these restoration activities. Results from this study may be integrated with restoration objectives to develop a restoration plan that will help riparian vegetation communities adapt to change.

KEYWORDS

riparian vegetation, remote sensing, Sen's slope, climate periods, indigenous science, riparian restoration, riparian wildfire

1 Introduction

The Upper Gila River watershed is an ecologically important riverine system in the Southwest United States (US) that is being impacted by natural and anthropogenic stressors, including invasion by non-native plants, flooding, wildfire, urban encroachment, and various land- and water-use activities (Banister et al., 2014; Orr et al., 2014). Draining from western New Mexico into eastern Arizona, the Gila River and its primary tributaries flow nearly unobstructed from the headwaters to the San Carlos Reservoir at the western edge of the watershed (Huckleberry, 1996). The watershed provides numerous ecosystem

services including water for human and agricultural uses, habitat for endangered species such as the southwestern willow flycatcher (*Empidonax traillii extimus*), and recreational opportunities (Banister et al., 2014; Eppehimer et al., 2021).

The riparian vegetation is highly complex and dynamic throughout the Upper Gila River watershed and is comprised of numerous native and non-native tree, shrub, and grass species (Orr et al., 2014). Primarily, non-native and invasive tamarisk (*Tamarix*) serves as the dominant vegetation type across much of the lower portion of the Upper Gila River watershed and outcompetes native vegetation (Orr et al., 2014). Tamarisk is widely viewed as a principal restoration objective because of its threat to the biodiversity of riparian systems (Harms and Hiebert, 2006). However, many native species such as Fremont cottonwood (*Populus fremontii*), Goodding's willow (*Salix gooddingii*), and mesquite (*Prosopis*), among others are also present. In the upper portion of the watershed, native species primarily dominate (Kindscher, 2011).

The Southwest US experiences a bi-modal precipitation regime, consisting of a cold winter precipitation season running from December through March and a hot summer monsoon season from July through September (Adams and Comrie, 1997; Jacobs et al., 2005). Winter storms originating in the Pacific Ocean typically provide longer-term, light rainfall events while summer storms during the monsoon season generally provide short-term, isolated, high-intensity precipitation events (Orr et al., 2014). The spring and fall are typically warm and dry (Eppehimer et al., 2021). Numerous wet and dry periods have occurred across the Southwest US and the Upper Gila Watershed over the past century. However, the Southwest US has experienced extended and intensifying drought conditions over the past 2 decades resulting in reductions in both areal surface water and groundwater resources (MacDonald et al., 2008; Seager et al., 2013; Cook et al., 2015; Williams et al., 2020; Petrakis et al., 2022).

Land within the Upper Gila River Watershed is owned and managed by numerous organizations and private landowners, including federal organizations such as the U.S. Forest Service (USFS) and Bureau of Land Management (BLM), the state land offices of Arizona and New Mexico, the San Carlos Apache Tribe, and private owners, among others (BLM, 2020). This has resulted in numerous approaches to land management over time throughout the watershed, though several mandates across federal, state, and local jurisdictions including the Clean Water Act, the National Environmental Policy Act, and the Endangered Species Act, govern both water and environmental uses (UArizona WRRC, 2022). Local Non-Governmental Organizations (NGOs) are also engaged in restoration within the watershed with the purpose of either re-establishing and planting of native species, controlling the impacts of invasive plant species, improving water quality, or addressing ecosystem water stress (Stillwater Sciences and UArizona WRRC, 2018; Eppehimer et al., 2021).

Sitting within a scrub-grassland basin with headwaters located in the forested uplands of the Gila Mountains, agriculture is, and has been since the mid-20th century, a primary land use across large portions of the Gila River floodplain (Orr et al., 2014), including near the urban centers of San Carlos (AZ), Safford (AZ), Duncan (AZ), and Gila (NM) (NLCD, 2016).

Remote sensing can support analyses of long-term changes on the landscape at a broad scale and advance our knowledge of the direct relationship between climate conditions and the ecosystem (Kerr and Ostrovsky, 2003; Pettorelli et al., 2014; AghaKouchak et al., 2015). For instance, riparian vegetation has been effectively monitored using satellite imagery and other remotely sensed data analyses and sources (Macfarlane et al., 2017; Petrakis et al., 2017; Hartfield et al., 2020; Huylenbroeck et al., 2020; Norman et al., 2006). Recent developments in cloud computing environments have allowed for broadened studies to assess land changes across large areas over extended time periods (Gorelick et al., 2017; Wang et al., 2020). The full suite of Landsat satellite imagery, for instance, is available through Google Earth Engine (GEE) (Google Earth Engine, 2022b). These data can be analyzed to provide an overview of multitemporal conditions across numerous disciplines (Tamiminia et al., 2020).

On the San Carlos Apache Reservation, riparian areas provide significant cultural and natural value but are at risk of degradation resulting from changes in climate and land use. We collaborate with the San Carlos Apache Tribe (hereafter Tribe or Tribal) to apply a research approach that can inform riparian restoration planning by developing products that show: i) recent trends (i.e., 1985 through 2021): in vegetation conditions identifying areas potentially more at risk for degradation and ii) the associated relationship between riparian vegetation dynamics and climate conditions. Additionally, based on discussions with employees of the Tribe, we identified three resource management and disturbance-themed case studies that directly associate vegetation dynamics with climate. Once the effects of varied climatic events are correlated with riparian response over time, adjustments in the management of the riparian corridor can be developed in response to expected future climatic stimuli. Informing riparian vegetation response based on historical data, tribal insight, and climate adaptation could serve as an early-warning system to benefit the management of the natural and cultural resources they provide and help the landscape become more resilient.

2 Methods

2.1 Study site

Our analysis is focused on a suite of riparian zones within the Upper Gila River level-4 Hydrologic Unit Code (HUC-4) watershed (Seaber et al., 1987; USGS NHD, 2020) (Figure 1; Table 1). Specifically, our primary study site is the riparian zones located along both the San Carlos River and Gila River within the San Carlos Apache Reservation (hereafter San Carlos and Bylas Reach, respectively) (Figure 1). In addition, we include select riparian zones along the Gila River and main tributaries within the Upper Gila River watershed for comparison of broad conditions (Figure 1). Each primary and comparison riparian zone (n = 8) is described in Table 1.

Similarities can be drawn between the collection of study reaches based on their vegetative and geographic properties. For instance, agricultural activity surrounds a large portion of the riparian zone along the Safford and Duncan reaches; agriculture can also be found, though less prevalent, across portions of the San Carlos, Upper Gila, and Upper San Francisco reaches (Dewitz and USGS, 2021).

Non-native tamarisk is also present throughout many of the reaches and is the dominant species across the Bylas and Safford reaches (Orr et al., 2014). We found tamarisk to be dominant across portions of the San Carlos and Duncan reaches, though not

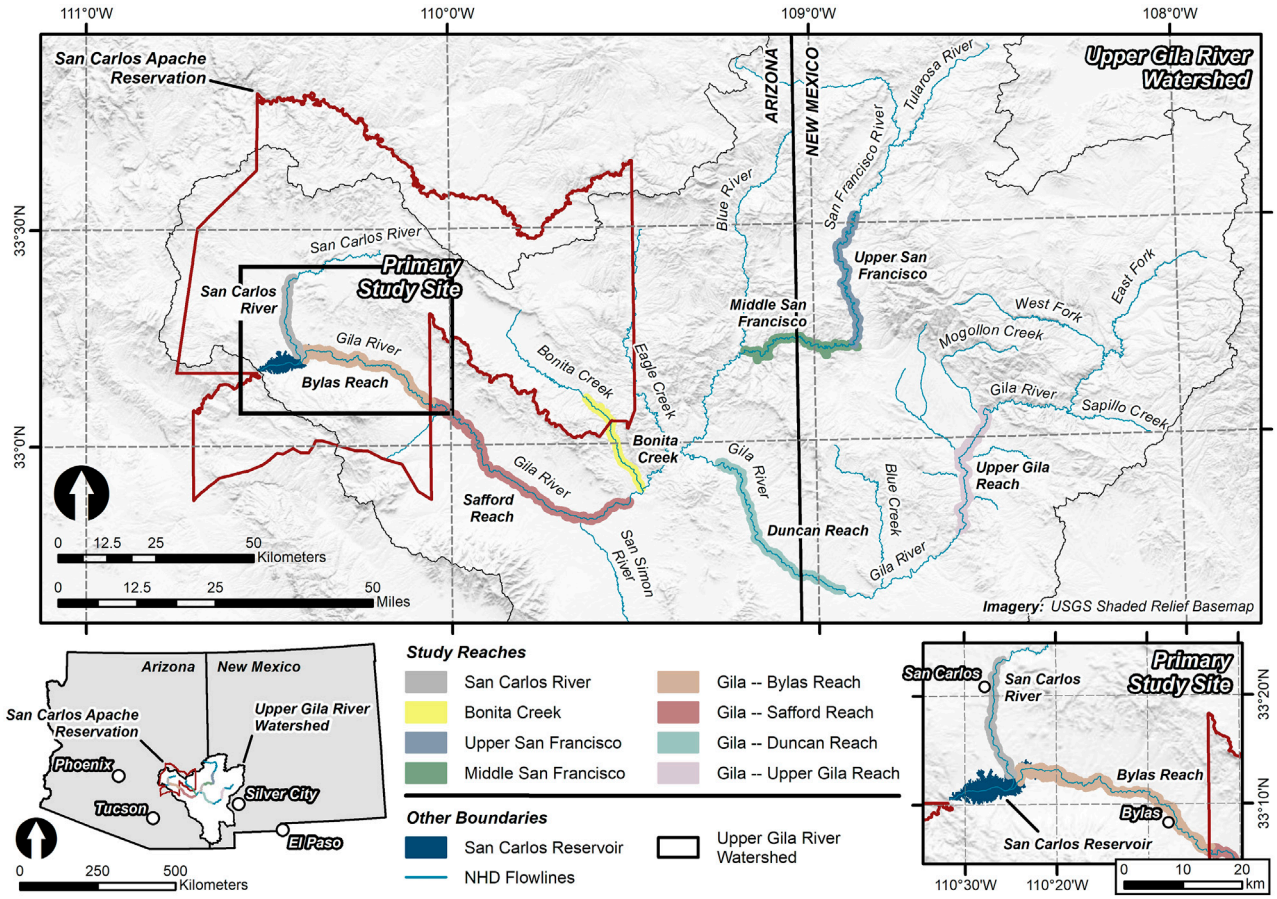

FIGURE 1
A map showing the primary study site, including the San Carlos River and Bylas Reach of the Gila River. Other study reaches along the Upper Gila River, the San Francisco River, and Bonita Creek within the Upper Gila River watershed were also addressed in this study. Flowlines and the boundary for the Upper Gila River watershed were produced by the National Hydrography Dataset (NHD) (USGS NHD, 2020).

universally, via a visual analysis of high-resolution U.S. Department of Agricultural National Agriculture Imagery Program (NAIP; ~0.6 m resolution) imagery (USDA, 2021). In addition, native cottonwood-willow deciduous gallery forests are identified across many of the reaches, including the San Carlos and Duncan reaches. Similarly, both San Francisco reaches, Bonita Creek, and the Upper Gila Reach are characterized as having dominant native gallery forests within the riparian zone.

Transverse geographic profiles, based on a 30-m Digital Elevation Model (DEM) layer (USGS, 2017), were used to define these reaches, where some reaches have wide floodplains with generally low slopes (i.e., broad valley systems) (Green, 2007). This includes the Safford, Bylas, Duncan, and San Carlos reaches, where mean slope within 1 km extending from the edge of the riparian zone is 2°, 4.2°, 5°, and 5.1°, respectively (USGS, 2017). Other reaches are characterized as being surround by canyon-like structures with narrow floodplains (i.e., confined systems) (Green, 2007), including the Middle San Francisco (mean slope = 24.9°), Bonita Creek (16.3°), and the Upper San Francisco River (13°) reaches (USGS, 2017). We identified the Upper Gila Reach has having moderate mean slope (10.4°), though much of the riparian zone consists of lower slope landscapes using the DEM (USGS, 2017). This contrast in geographic profile can have implications on vegetation traits, hydrologic flows, and surrounding land use such as agriculture and urban development (Naiman and Décamps, 1997; Green, 2007).

Lastly, wildfire has become a prominent disturbance across the San Carlos, Bylas, and Safford reaches over the past several years (San Carlos Apache Tribe, personal communication, January 2022). In addition, the tamarisk beetle (*Diorhabda*), which defoliates the non-native tamarisk vegetation (Kennard et al., 2016), has been identified throughout portions of the Upper Gila River watershed (RiversEdge West, 2021), though there is no formal documentation of the beetle within the Reservation during our study period (San Carlos Apache Tribe, personal communication, January 2023). Wildfire and beetle disturbances could impact the results of this remote sensing study by directly affecting vegetation conditions (Dennison et al., 2009; Fairfax and Whittle, 2020).

2.2 Discussions with tribal members and employees

Input from San Carlos Apache Tribe members and employees of Tribal departments, including the Forest Resources Program, the

TABLE 1 Names, locations, and descriptions of the comparison and primary riparian zones considered in this study.

Reach Name	Location	Description
Gila River		
Safford Reach	Upstream of the boundary of the San Carlos Apache Reservation to the exit of the Gila Box	Widespread agriculture; dominant tamarisk presence; recent wildfire activity; broad valley system
Duncan Reach	~2 miles upstream of the Arizona/New Mexico border to the entrance to the Gila Box	Widespread agriculture; semi-dominant tamarisk presence; native cottonwood-willow deciduous gallery forests are present; broad valley system
Upper Gila Reach	The confluence of the Gila River and Mogollon Creek downstream to ~5 miles downstream of the confluence with Mangas Creek	Dominant native cottonwood-willow deciduous gallery forests; limited agriculture; generally broad valley system
Bonita Creek		
Bonita Creek	Extending ~20 miles upstream to the confluence with the Gila River	Confined system; dominant native cottonwood-willow deciduous gallery forests
San Francisco River		
Middle San Francisco	Confluence of the San Francisco River and the Big Dry Creek downstream to the confluence with the Blue River	Confined system: dominant native cottonwood-willow deciduous gallery forests
Upper San Francisco	Confluence of the San Francisco River and the Big Dry Creek upstream to ~5 miles upstream of the confluence with Copper Creek	Confined system; native cottonwood-willow deciduous gallery forests; limited agriculture
Primary Sites		
San Carlos River	Downstream of Talkalai Lake to the San Carlos Reservoir	Limited agriculture; semi-dominant tamarisk presence; native cottonwood-willow deciduous gallery forests are present; broad valley system; recent wildfire activity
Bylas Reach	Upstream from the San Carlos Reservoir to the boundary of the San Carlos Apache Reservation boundary	Dominant tamarisk presence; recent wildfire activity; broad valley system

Department of Environmental Protection, and the Range Program, was used to structure research objectives and restoration priorities. Specifically, we held multiple virtual and in-person meetings with Tribal members that were structured to meet the following two objectives: i) provide an update on the status of this project and ii) identify and discuss issues and/or concerns voiced by employees and leaders of the Tribal programs related to the study thus far, the landscape, and/or the management. Following the update, an open discussion was held focusing on issues related to Tribal concerns. Based on feedback from Tribal natural resource employees and leaders, we structured site-specific analyses on potential restoration and management applications as well as previous degradation of the San Carlos and Gila River riparian vegetation. We present these as the case studies within this analysis.

2.3 Assessment of recent vegetation trends

2.3.1 Climate analysis

We use the Standardized Precipitation Evapotranspiration Index (SPEI) to quantify climate variability across the study period. The SPEI is a water balance index which calculates evaporative demand through precipitation and reference evapotranspiration—using the Penman-Monteith method by applying temperature, dewpoint temperature, windspeed, and surface radiation (Abatzoglou, 2013)—to develop a robust drought severity metric (Vicente-Serrano et al., 2010; Beguería et al., 2014). Conditions from the cumulative prior *n* months, generally ranging from 1 to 60, are compared to the same respective period, applying a standardization, over the prior years to identify the index value (Vicente-Serrano et al., 2010; Beguería et al., 2014). Values less than 0 denote drought conditions while values greater than 0 signify wetter than normal conditions. For this study, we are using a 12-month, or 1-year, timeframe to compare annual conditions.

The Gridded Surface Meteorological (GRIDMET) Drought dataset provides a spatially explicit SPEI product in GEE at a 5-day interval and a spatial resolution of 4-km (Abatzoglou, 2013; Google Earth Engine, 2022a). Using the 1-year SPEI product from GRIDMET Drought available in GEE (Google Earth Engine, 2022a), we produce mean values across the watershed for each 5-day period from January 1980 to December 2021. Using R Software (R Core Team, 2022), we reduced the 5-day values to represent monthly mean values and constrained the analysis to water year 1981 (i.e., October 1980) through water year 2021 (i.e., October 2021).

Using the monthly timeseries, we completed the breakpoint analysis using the R Software breakpoint package (Priyadarshana and Sofronov, 2015) to identify breaks within the SPEI timeseries. Detecting a shift within a climate timeseries at a point in time, also referred to as changepoint detection, is widely used across climate research (Reeves et al., 2007; Strong et al., 2020), including with SPEI timeseries data (Wang et al., 2019). The breakpoint algorithm identifies a seasonal pattern within the timeseries. When the seasonal pattern deviates, a breakpoint is then detected. These multiple breaks can be used to frame unique climate periods in the timeseries.

2.3.2 Remote sensing metrics

All remote sensing products use the Landsat satellite imagery catalog in GEE (Cohen and Goward, 2004; NASA, 2021; Google

TABLE 2 The Tasseled Cap (Kauth and Thomas, 1976) coefficient values are multiplied against the surface reflectance value for each band for each metric. Coefficients for Landsat 4, 5, and 7 are provided in A) (DeVries et al., 2016), while coefficients for Landsat 8 are provided in B) (Zhai et al., 2022).

Metric	Blue	Green	Red	NIR	SWIR-1	SWIR-2
(A) Tasseled Cap Coefficients for Landsat 4, 5, and 7 Surface Reflectance						
Brightness	0.2043	0.4158	0.5524	0.5741	0.3124	0.2303
Greenness	−0.1603	0.2819	−0.4934	0.7940	−0.0002	−0.1446
Wetness	0.0315	0.2021	0.3102	0.1594	−0.6806	−0.6109
(B) Tasseled Cap Coefficients for Landsat 8 Surface Reflectance						
Brightness	0.3690	0.4271	0.4689	0.5073	0.3824	0.2406
Greenness	−0.2870	−0.2685	−0.4087	0.8145	0.0637	−0.1052
Wetness	0.0382	0.2137	0.3536	0.2270	−0.6108	−0.6351

Earth Engine, 2022b). Landsat has a spatial resolution of 30-m and data available from 1985 to present-day with a repetition rate of 16-day for each sensor (NASA, 2021), with fewer days between repeat images when multiple sensors are functioning simultaneously. We use imagery acquired by the following Landsat sensors in this analysis: i) Landsat 4 Thematic Mapper (TM) (1985 through 1993), ii) Landsat 5 TM (1985 through 2011), iii) Landsat 7 Enhanced Thematic Mapper Plus (ETM+) (1999 through 2003), and iv) Landsat 8 Optical Land Imager (OLI) (2013 through 2021). Results from 2012 were not considered due to Landsat 5 being decommissioned. All Landsat sensors collect data across the 6 bands used in this analysis: i) Blue, ii) Green, iii) Red, iv) Near Infrared (NIR), v) Shortwave Infrared-1 (SWIR-1), and vi) SWIR-2 bands. Additionally, a pixel quality attributes band (i.e., pixel-qa) produced across all Landsat images was used to identify and mask cloud cover (Foga et al., 2017).

We complete the remote sensing analysis using the GEE online cloud computing platform, which allows for complex calculations and processing (Gorelick et al., 2017). The Landsat imagery series is available within GEE (Google Earth Engine, 2022b). All images were from Landsat Collection-2/Level-2/Tier-1, which required a scaling factor applied to all bands using the following equation to obtain surface reflectance (USGS, 2022):

$$\textit{Landsat Surface Reflectance Scaling Factor} = (\textit{Band} * \mathbf{0.0000275}) - \mathbf{0.2}$$

We apply two primary indices to monitor the characteristics of the vegetation. First, the Normalized Difference Vegetation Index (NDVI) is a commonly used vegetation index that quantifies relative greenness of the vegetation based on the plant's photosynthetic activity, measured as a ratio between the NIR and Red bands (Tucker, 1979). The NDVI has a range of −1 to 1, where dense green vegetation is represented with values closer to 1 while barren soil, rock, and less-dense surface vegetation has values closer to 0. Values below 0 often represent water due to its unique reflective characteristics.

Second, the Tasseled Cap (TC) transformation is used to transform satellite imagery into a collection of spectral metrics that can quantify various aspects of the vegetation and soil surfaces (Kauth and Thomas, 1976). Specifically, the TC transformation develops 6 separate metrics, though we only consider the three primary metrics: i) brightness (transformation 1), ii) greenness (transformation 2), and iii) wetness (transformation 3). The metrics are calculated using a series of coefficients multiplied across reflectance values for the suite of Landsat bands, then summed across each metric. Because bandwidths differ slightly between Landsat 4, 5, 7 and Landsat 8 (Google Earth Engine, 2022b), we use two sets of coefficients (Table 2) and complete the calculation separately before combining the collections into a single series of images (DeVries et al., 2016; Zhai et al., 2022).

To reduce the effects of cloud cover and outlier values on our results that could occur when using a single cloud-affected image and to supplement our analysis by addressing seasonal vegetation dynamics (Adams et al., 2020), we combine multiple Landsat images into seasonal mean composites for NDVI and TC metrics from 1985 to 2021. This reduces cloud-based artifacts and outlier values and simplifies measurements for analysis and presentation of results. The following "seasons" were constrained by 2-month intervals across each year: i) spring (March/April), ii) late-spring (May/June), iii) summer (July/August), and iv) fall (September/October) and represent the effects from climate variation throughout the year. Each season is also characterized by unique temperature and precipitation regimes. For instance, the spring is generally cooler and wetter, while the late-spring is characteristically hot and dry across the watershed. The summer is generally hot and overlaps with the North American Monsoon, in which there is an enhancement in the presence of short-term high-precipitation events, with increased intensity in the higher elevations (Adams and Comrie, 1997). The fall remains warm, but typically begins to dry out.

All four indices (i.e., NDVI and TC brightness, greenness, wetness) were produced using three temporal resolutions: i) seasonal products from spring 1985 to fall 2021 (i.e., one image per year for each season), ii) Sen's slope trends across the climate periods for each season (i.e., one image per season for each climate period), and iii) monthly images across various timelines to address both phenology and case studies, discussed below, as needed. For the Sen's slope analysis, we modified the approach established by the Google Earth Engine Developers Community (Google Earth Engine Community, 2021). The seasonal products can be applied to review conditions at a single point in time, while Sen's slope trends provide a quantification of the linear rate of change across each climate period. All products are spatially and temporally explicit (Petrakis et al., 2023).

2.3.3 Phenology

Phenology is the natural shift in the timing of plant life in response to changing seasonality (Cleland et al., 2007; USA NPN, 2022). Establishing the remote sensing analysis within a phenological framework supports observations of plant dynamics which can help differentiate between various riparian plant types present within the study site (Diao and Wang, 2016). Furthermore, when considering these seasonal dynamics within the phenological framework, we will be able to relate shifts in the seasonal timing of vegetation response within the riparian floodplain to vegetation dynamics. For instance, deciduous gallery forest vegetation, typically consisting of a collection of native species, including cottonwood, willow (*Salix*), Arizona black walnut (*Juglans major*), mesquite

(*Prosopis*), sycamore (*Platanus occidentalis*), desert willow (*Chilopsis linearis*), and others (Kindscher, 2011; Orr et al., 2014; Smith and Finch, 2014), experiences a transition from leaf-off to leaf-on between the winter (i.e., January/February) and spring (i.e., March/April), respectively, resulting in a relative increase in NDVI in the spring (Braatne et al., 1996). This vegetation type often reaches peak greenness in April or May. Hereafter we refer to this group of vegetation as cottonwood-willow, or deciduous, gallery forest. In contrast, saltcedar (e.g., Tamarisk; *Tamarix*), an invasive species commonly found throughout riparian ecosystems across the southern and western US (Glenn and Nagler, 2005), typically begins blooming and greening-up in late-spring (April/May) through early-summer (June/July) and reaches a peak greenness in June and July (Stevens and Siemion, 2012; Diao and Wang, 2016). Hereafter, we refer to this vegetation type as non-native tamarisk. This seasonal contrast can supplement the identification and separation of native deciduous forest and non-native tamarisk over time. Similarly, grassland composition (i.e., primarily C4 species—produces 4-carbon molecules), which comprises a large portion of the understory vegetation, characteristically responds to moisture and heating, and experiences both a slight increase in greenness during the early-spring (March/April) and an elevated increase in greenness following monsoon-season precipitation during the summer (August/September) (Edwards et al., 2010; Gremer et al., 2015). The increase in greenness during the spring is usually followed by a decline in the late-spring (May/June).

To develop a multi-temporal phenological signature for the different vegetation types within the primary study site, we completed a sampling analysis. We placed sample points (n = 246), virtually in ArcMap 10.8.1 (ESRI, 2020), at reference locations that subjectively represented pure visual samples, using NAIP imagery (USDA, 2021), of three unique plant types within the San Carlos and Bylas Reach riparian zones, including: i) cottonwood-willow gallery forest, ii) tamarisk, and iii) understory vegetation (i.e., primarily grassland). We then collected values for each month across the third climate period (i.e., 2014 through 2020; 2021 was not considered because of widespread wildfire) for NDVI and TC greenness at each point, and averaged across years. This produced an average monthly value for each vegetation type. The monthly images are available at Petrakis et al. (2023).

2.3.4 Data analysis and interpretation

Vegetation and surface characteristics of the riparian floodplain are analyzed using a combination of the vegetation indices (i.e., NDVI and TC brightness, greenness, wetness) across the phenological framework and structured within the climate period approach. Each index records unique properties of the vegetation. For example, NDVI provides a general overview of vegetation condition and can be used to inform on changes related to disturbances, vegetation growth, productivity, or even slight changes in surface and ground hydrology (Chen et al., 2004; Fu and Burgher, 2015; Vicente-Serrano et al., 2016; Shammi and Meng, 2021). The TC is a multi-dimensional transformation of the Landsat imagery, where each metric is interrelated and can provide distinctive information on conditions within a vegetation ecosystem. Brightness primarily measures soil reflectance or changes in overall surface reflectance. Greenness is highly correlated with NDVI and similarly measures the vegetation greenness and health. Finally, wetness informs on both plant and soil moisture. A combination of the three TC metrics provides a robust assessment of various aspects of the vegetation, including the canopy coverage, overall condition, and general density, and can be used to supplement NDVI.

Vegetation stress or degradation can be characterized numerous ways based on our multi-temporal analysis of the vegetation indices. For instance, stress can be qualified as declines in vegetation greenness or wetness over time (Cohen, 1991; Jin and Sader, 2005). Specifically, we would observe either decreasing or increasing greenness and wetness within the year-to-year seasonal images or though the climate period Sen's slope trend. However, declining trends may also represent transitions between vegetation types, such as from one vegetation type that is greener to one that is less green. Therefore, we must also consider the phenological traits which can inform on seasonal shifts over time. Examples of this may include leaf transitions (i.e., leaf-on and leaf-off) in cottonwood-willow gallery forest or understory vegetation seasonality, particularly whether greening primarily occurs in the spring (as with C3 grasses—produces 3-carbon molecules) or after the onset of monsoonal rains in the summer (as with C4 grasses) (Munson et al., 2022). Analogously, vegetation degradation or disturbance may present similarly as a decline in greenness and wetness, yet also as an increase in brightness (Healey et al., 2005). This combination of metrics would suggest more open soil or loss of vegetation canopy cover. Wildfire is a prime example of a disturbance that could result in an increase in brightness due to loss of canopy cover. Finally, an important consideration with this study is the transition of native cottonwood-willow gallery forests to non-native tamarisk. This transition would likely characterize as an increase in NDVI, greenness, and wetness in the late-spring.

Monitoring the spectral properties and multi-temporal signatures of the vegetation is inherently challenging due to the complexity of riparian systems. However, the indices that we include, within a seasonal framework, can inform on numerous aspects of the vegetation.

2.4 Case studies

We develop three case studies based on conversations with San Carlos Apache Tribal program employees that are structured to directly relate the vegetation response to changes in both climate and management. Each case study was specifically requested and is designed to address either resource and management objectives or known disturbances that have occurred both during and prior to the study period.

2.4.1 Prior riparian restoration application

The first case study addresses a prior restoration application that was applied on the San Carlos River. We are not revealing the location of this restoration work to protect Tribal cultural and ecological values. Much of the restoration is believed to have taken place between 2006 and 2009, with the objectives to both remove non-native vegetation and plant native cottonwood. These objectives were designed to establish native cottonwood vegetation and reduce the presence of non-native tamarisk. Tamarisk was cleared while cottonwoods were planted using pole planting

throughout the restoration area (San Carlos Apache Tribe, personal communication, May 2022).

We test the efficacy of these restoration approaches using monthly NDVI products that we produced in GEE for the restoration area from January 1985 through December 2021. Our hypotheses are: i) that native vegetation would increase in overall canopy cover following the restoration application, evidenced by an increase in the rate of positive change in early-spring NDVI (i.e., the respective leaf-on period—February through April) and ii) that non-native tamarisk cover would decrease immediately following the restoration application as a result of the targeted removal of the vegetation type, evidenced by a decrease in the rate of positive change in NDVI during the late-spring and early-summer (i.e., April through June).

To compare conditions from before restoration to after restoration, we assess NDVI across the four following periods: i) historic—1992 through 1995, ii) pre-restoration—2003 through 2006, iii) restoration (during)—2008 through 2010, and iv) post-restoration—2018 through 2021. To account for naturally occurring yearly variability in vegetation conditions, we average monthly NDVI values across multiple years for each month. Additionally, the multi-year periods were selected to include mostly continuous data, while years with missing data because of cloud cover or issues with the Landsat sensor, were largely removed from the analysis (i.e., 1988 through 1992, 2007, 2011 through 2013).

2.4.2 Historic phreatophyte vegetation removal

Between 1967 and 1971, the Bureau of Indian Affairs (BIA) cleared phreatophyte vegetation, defined as deep rooted plants that draw a large amount of the water they require from groundwater sources when precipitation is deficient (Naumburg et al., 2005), throughout the riparian floodplain along a 9-mile stretch of the San Carlos River and a 26-mile stretch (i.e., 15,800 acres) of the Gila River within the San Carlos Apache Reservation (Park et al., 1978). This project was referred to, shorthand, as the "Gila River Channel Improvements" project (Park et al., 1978). Clearing of the vegetation was completed using both mechanical-eradication methods (i.e., root plowing using a bulldozer, uprooting, mowing) and chemical-eradication (i.e., Silvex—a dioxin-based biological agent related to "Agent Orange") (Park et al., 1978). The clearing treatments primarily targeted phreatophyte species including tamarisk (*Tamarix pentandra*), which was the dominant vegetation species across the area, as well as mesquite (*Prosopis*) and cottonwood, which was also present in the floodplain (Park et al., 1978). In addition to the BIA clearing the vegetation, the USGS initiated the Gila River Phreatophyte Project (hereafter "Phreatophyte Project") to study the impacts of the clearing on hydrologic properties along the Gila River, including evapotranspiration and surface water flow (Culler et al., 1970; 1982; Park et al., 1978). Specific details were published within a set of USGS scientific reports published between 1970 and 1982 (see USGS Scientific Report 665, series A through P) (Culler et al., 1982).

To assess the long-term response of the vegetation, we mirror aspects of the Phreatophyte Project by defining the spatial extent of our analysis using boundaries of areas included in the initial project. For the Phreatophyte Project, the floodplain was divided into four subreaches: 1, 2a, 2, and 3 (Figure 2) (Culler et al., 1982). Furthermore, we included two additional subreaches to supplement our assessment of the vegetation response. Subreach 0, extending east from subreach 1 to the reservation boundary, was cleared during the Gila River Channel Improvements project. Subreach 4, located outside and upstream of the Reservation boundary, serves as a control subreach to monitor untreated vegetation conditions.

The subreaches are defined by the amount of surface flooding and other geologic, hydrologic, and vegetative properties (Culler et al., 1982). Subreaches 2 and 3 were affected by sediment deposited during maximum storage of the San Carlos Reservoir and have gradual slopes. These subreaches also consist of dense tamarisk-dominant vegetation. Subreaches 0, 1, and 2a, are above the maximum water level of the reservoir and did not experience reservoir-induced surface water flooding during either the Phreatophyte Project or during our study (Culler et al., 1982). These subreaches may be subject to short-term surface flooding from large hydrologic flows along the Gila River, though such flows were not considered in this study. Subreach 2a does not experience reservoir-induced flooding, and consists of more dense tamarisk vegetation. Subreaches 0, 1, and the control subreach (i.e., 4) have generally lower density vegetation, in addition to a greater presence of native mesquite (Park et al., 1978). Lastly, it was noted that there is high salinity concentration in an area that largely extends throughout subreach 0 (San Carlos Apache Tribe, personal communication, May 2022). High salinity, in general, limits cottonwood pole planting (Shafroth et al., 1995) and may have killed young cottonwoods within the Gila River system (San Carlos Apache Tribe, personal communication, May 2022).

To monitor the vegetation response following the Phreatophyte Project timeline, we group the subreaches into four generalized classes defined by surface flooding and vegetation properties, including: i) group 1—reservoir-induced surface flooding/high-density vegetation (i.e., subreaches 2 and 3), ii) group 2—no surface flooding/high-density vegetation (i.e., subreach 2a), iii) group 3—no surface flooding/low-density vegetation (i.e., subreaches 0 and 1), and iv) group 4—untreated with no surface flooding/low-density vegetation (i.e., subreach 4) (Figure 2A).

For each subreach group, we assess both Sen's slope across climate periods as well as the yearly timeseries for the TC metrics. We average Sen's slope trends across each subreach for the three climate periods (i.e., 1985 to 1993, 1993 to 2014, 2014 to 2021) for each season. Vegetation was significantly affected by a series of wildfires that burned during the third climate period across all subreach groups, including the i) Bottom Fire (June 28—18 August 2021; ~5,998 acres), ii) the Salt Fire (April 8—11 May 2021; ~4,423 acres), iii) the Light Fire (August 28—11 September 2020; ~971 acres), and iv) the Bylas Fire (June 8—10 July 2019; ~636 acres) (San Carlos Apache Tribe, personal communication, January 2022) (Figure 2B). Therefore, results across all subreach groups within the third climate period will be driven by these fire disturbances. Additionally, we average the yearly TC metrics seasonally for each subreach to identify the temporal response of the vegetation and identify differences between locations on the river and time from clearing disturbance.

2.4.3 Pre- and post-wildfire analysis

Numerous fires have recently burned along the Gila River. For this case study, we focus on two fires, i) the Bottom Fire and ii) the Bylas Fire, that burned along the Gila River within the San Carlos

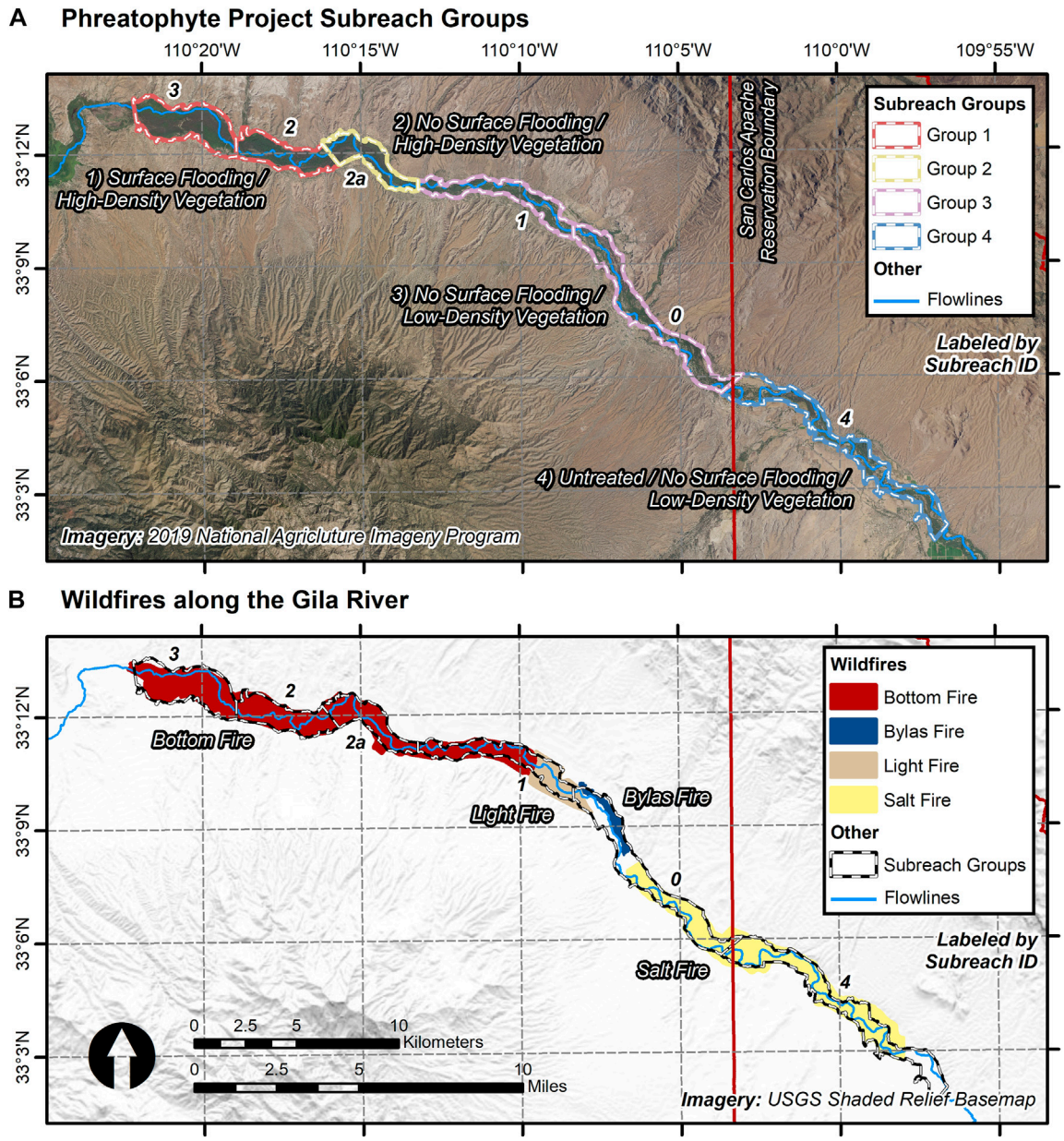

FIGURE 2
(A) shows the location of the four subreach groups, based on boundaries originally identified by (Culler et al., 1970), ranging from the furthest upstream subreach group on the San Carlos Apache Reservation, 1 (red/white stripes), to the furthest downstream subreach group, 4, which is just outside of the Reservation and serves as a control (blue/white stripes). Each subreach group consists of subreaches (n = 6), identified by their ID number (black text with white outline). Panel **(B)** shows the locations of the four wildfires (San Carlos Apache Tribe, personal communication, January 2022) that burned along this portion of the Gila River between 2019 and 2021.

Apache Reservation (Figure 2B). The Bottom Fire (2021) aligns with the current end of the third climate period and allows us to quantify pre-fire conditions. The Bylas Fire (2019) allows us to quantify short-term post-fire response (i.e., 2019 through 2022).

To assess pre-fire conditions, we consider both the Sen's slope products as well as the multi-year NDVI and TC metric images. In addition, we include a post-fire burn severity product developed by the Burned Area Emergency Response (BAER) program (USGS BAER, 2022a). BAER has developed a collection of burn severity products that quantify relative rates of burn severity of large-scale wildfires, called the differenced Normalized Burn Ratio (dNBR) (USGS BAER, 2022b). We collect pixel values for each raster product using a collection of sample points (n = 1,335). The points were randomly selected to represent 5% of Bottom Fire area and were tested for autocorrelation using R software (R Core Team, 2022). First, we assess the seasonal timeseries for each vegetation metric across the second and third climate periods to identify both short- and long-term transitions in response to the climate conditions. Second, we correlate remotely sensed burn severity to both Sen's slope trends for the third climate period and the 2021 pre-fire values

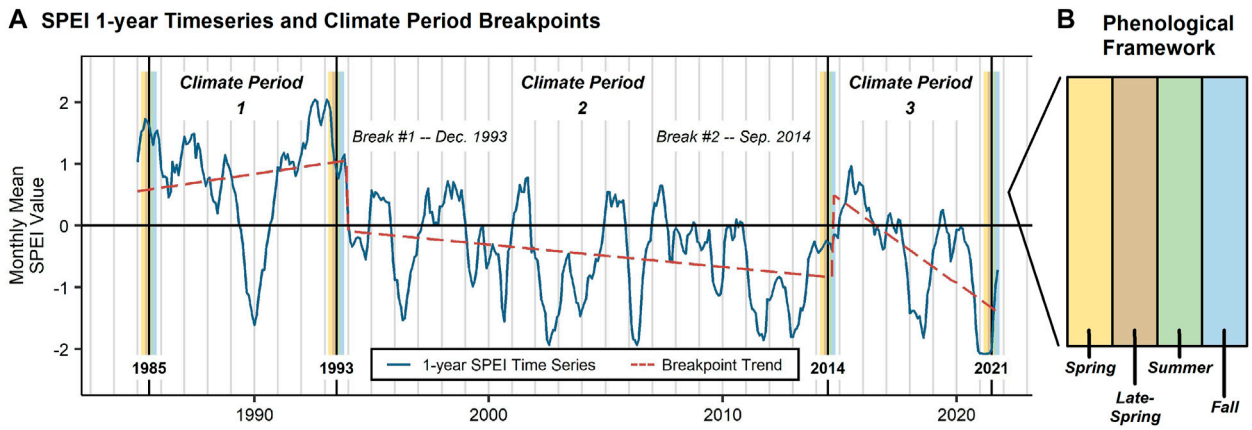

FIGURE 3
Showing the **(A)** 1-year Standardized Precipitation Evapotranspiration Index (SPEI) timeseries (Google Earth Engine, 2022a), the breakpoint trend (Priyadarshana and Sofronov, 2015), the four climate breaks, and the three climate periods that represent our study period. Each climate break is assessed using a **(B)** phenological framework, which includes the following four 2-month seasons: i) spring (March/April), ii) late-spring (May/June), iii) summer (July/August), and iv) fall (September/October). The structure of the **(B)** phenological framework, which is applied at each climate breakpoint, is shown on the right.

for each of the vegetation metrics for the spring and late-spring. We produce Pearson correlations and scatter plots in R Software (R Core Team, 2022) to assess these relationships.

To assess post-fire response within the Bylas Fire boundary, we develop a timeseries of NDVI across the third climate period, including temporarily extending our study period to June 2022 within the Bylas Fire boundary, to collect supplementary information on the temporal response of the vegetation. We also assessed a nearby control site over the same time period, which notably consists of generally less dense tamarisk vegetation based a review of high-resolution NAIP imagery (USDA, 2021), to allow for comparison to an unburned site. We averaged NDVI values across the fire and control site boundaries. Image products for January 2014 through June 2022 were developed using GEE, and are included in the data release (Petrakis et al., 2023). This NDVI timeseries can provide information on trends leading up to the fire, as well as a summary of general vegetation response following the fire.

3 Results

3.1 Climate breakdown

Fluctuating wet (i.e., above 0) and dry (i.e., below 0) periods were observed within the 1-year SPEI timeseries (Figure 3). Despite year-to-year variability, the breakpoint algorithm identifies two breaks. The first break occurs in December 1993, in which there is a transition between predominantly wet and dry conditions. A second break occurs in September 2014, where there is a short-term transition between dry and wet conditions (~3-year). This length deviates from the seasonal pattern that was established in 1993, thus resulting in a break in the timeseries. This 2014 break also separates an earlier extended dry period with a subsequent period of intensifying drought conditions.

Using the breakpoint breaks, in addition to the beginning (1985) and ending (2021) years of our study period, we identify three climate periods: i) 1985 through 1993, ii) 1993 through 2014, and iii) 2014 through 2021 (Figure 3A). We use the breakpoint linear trendline to characterize the long-term climate trends. The first climate period is characterized by generally wet conditions (i.e., SPEI >0). There was a period of short-term drought conditions (i.e., SPEI <0) between 1989 and 1990, however, wet conditions soon returned. Following the break in 1993, a long-term period of drier conditions was present within the watershed. Though the trendline implies intensifying drought conditions, driven by a significant and extended dry period between 2011 and 2013, a series of short-term above-average SPEI periods were present, including from 1997 to 1999, 2001 to 2002, and 2005 to 2006 (Gregg Garfin, Director—UArizona AIR Science Translation and Outreach; Professor and Extension Specialist—UArizona School of Natural Resources and the Environment, personal communication, August 2021). Nevertheless, we characterize the second climate period as having largely consistent drought conditions. Following this break, conditions have become even more dry, allowing us to characterize the third climate period as having intensifying drought conditions (Williams et al., 2020), with the 2021 being measured as the hottest summer on record across much of the Southwest—including the area of the Upper Gila River watershed (Osman et al., 2022).

At each climate period break, we assess the vegetation conditions using a phenological framework as discussed in Section 2.3.3 *Phenology*. The phenological framework breakdown is portrayed in Figure 3B.

3.2 Vegetation response within a phenological framework

We identified important seasonal contrasts in the phenological timeseries in NDVI and greenness for each of the primary vegetation

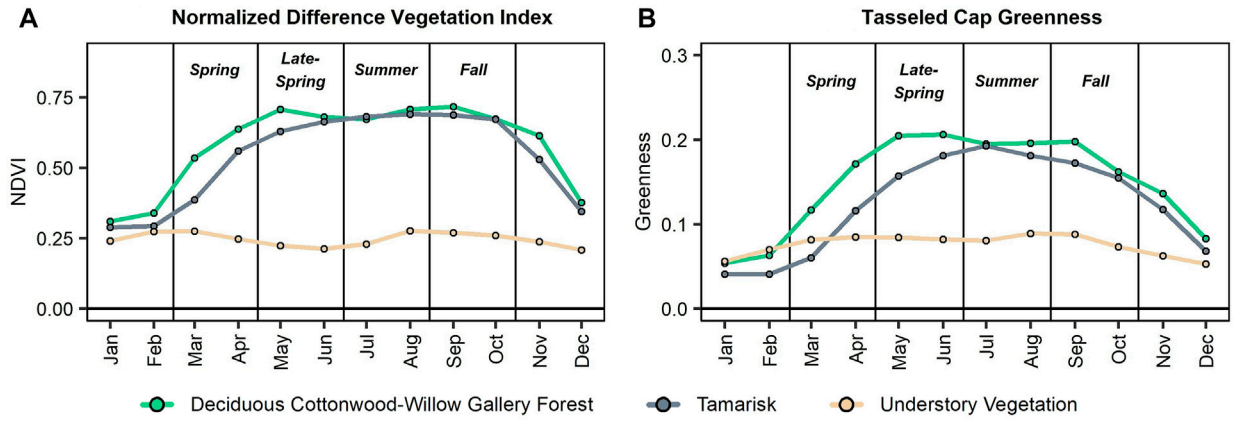

FIGURE 4
Showing the phenological patterns of three vegetation types, i) deciduous cottonwood-willow gallery forest, ii) tamarisk, and iii) understory vegetation, for **(A)** Normalized Difference Vegetation Index (NDVI) (Tucker, 1979) and **(B)** Tasseled Cap (TC) greenness (Kauth and Thomas, 1976). Values represent monthly means across the vegetation sample points.

types (Figure 4). Specifically, deciduous cottonwood-willow gallery forests and tamarisk have unique seasonal patterns. Deciduous gallery forests typically increase in NDVI and greenness at a greater rate during the spring (i.e., February through April). Additionally, the vegetation type experiences a secondary green-up during the late-summer and early-fall (i.e., August and September) due to increased moisture from the monsoon season. On the other hand, tamarisk greens-up at a greater rate, when compared to the gallery forests, during the late-spring and into the early-summer (i.e., April through June). Understory vegetation has much lower values across most of the year, particularly from the late-spring through the fall.

3.3 Vegetation timeseries across climate periods

Across the primary and comparison study reaches, the directionality of change in NDVI did not always mirror the SPEI timeseries trend for each climate period (Figure 5). For instance, though the first climate period is characterized as a wet period, NDVI values were relatively lower, compared to conditions across the second and third climate periods, and remained generally stable across most reaches. Both increasing and decreasing NDVI trends were identified but were locationally and seasonally specific. During the second climate period, which is characterized as having largely consistent drought conditions, NDVI increased across all reaches for all four seasons. This period saw widespread vegetation growth throughout the watershed. Finally, during the third climate period, characterized as having intensifying drought conditions, NDVI timeseries were largely variable based on season and location. Some areas (i.e., San Carlos River, Bylas Reach, Safford Reach) had generally decreasing NDVI values, while other reaches (i.e., Upper Gila Reach, Middle and Upper San Francisco Reaches) had seasonally specific increasing NDVI values.

We also identified subreach groups based on similarities in the vegetation signatures. First, the primary subreaches, the San Carlos River (Figure 5A) and Bylas Reach (**5B**), experienced significant green-ups during the second climate period, particularly for the late-spring, summer, and fall. During this period, reservoir-induced surface flooding from the San Carlos Reservoir had ended, resulting in significant growth of vegetation within areas that had been previously flooded (Park et al., 1978). The Bylas Reach then experienced a widespread decline in NDVI during the third climate period. This was primarily due to large-scale wildfires, which we present as a case study. However, declining NDVI was observed for the spring and late-spring during the third climate period for both reaches, as well, despite no impacts from wildfire.

Second, NDVI across the Gila River Safford Reach (**5C**), Gila River Duncan Reach (**5D**), and Bonita Creek (**5E**) had analogous patterns. Specifically, this pattern was defined by relatively consistent NDVI values across the first climate period, increasing NDVI across the second climate period, and relatively stable values across the third climate period. In all 3 reaches, NDVI declined slightly in the spring, late-spring, and summer and increased during the fall for the first and third climate periods. It is notable that the Safford and Duncan reaches have widespread agriculture surrounding the riparian zone (NLCD, 2016), while Bonita Creek is primarily a gallery forest with mixed native (i.e., cottonwood-willow gallery forest) and non-native (i.e., tamarisk) species and surrounding open areas and grasslands.

Finally, the Gila River Upper Gila Reach (**5F**) and both reaches along the San Francisco River—the Middle Reach (**5G**) and Upper Reach (**5H**)—had similar temporal signatures in NDVI. This pattern can be characterized as having seasonally unique trends during the first climate period, slightly increasing NDVI during the second climate period, and larger increasing NDVI during the late-spring, summer, and fall for the third climate period. All three of these reaches have widespread riparian forest vegetation, both native and non-native, as well as open areas and grasslands. The Upper Gila Reach also has minimal agriculture surrounding the riparian zone. Most notable of these trends is that NDVI increased the greatest amount across the second and third climate periods during the

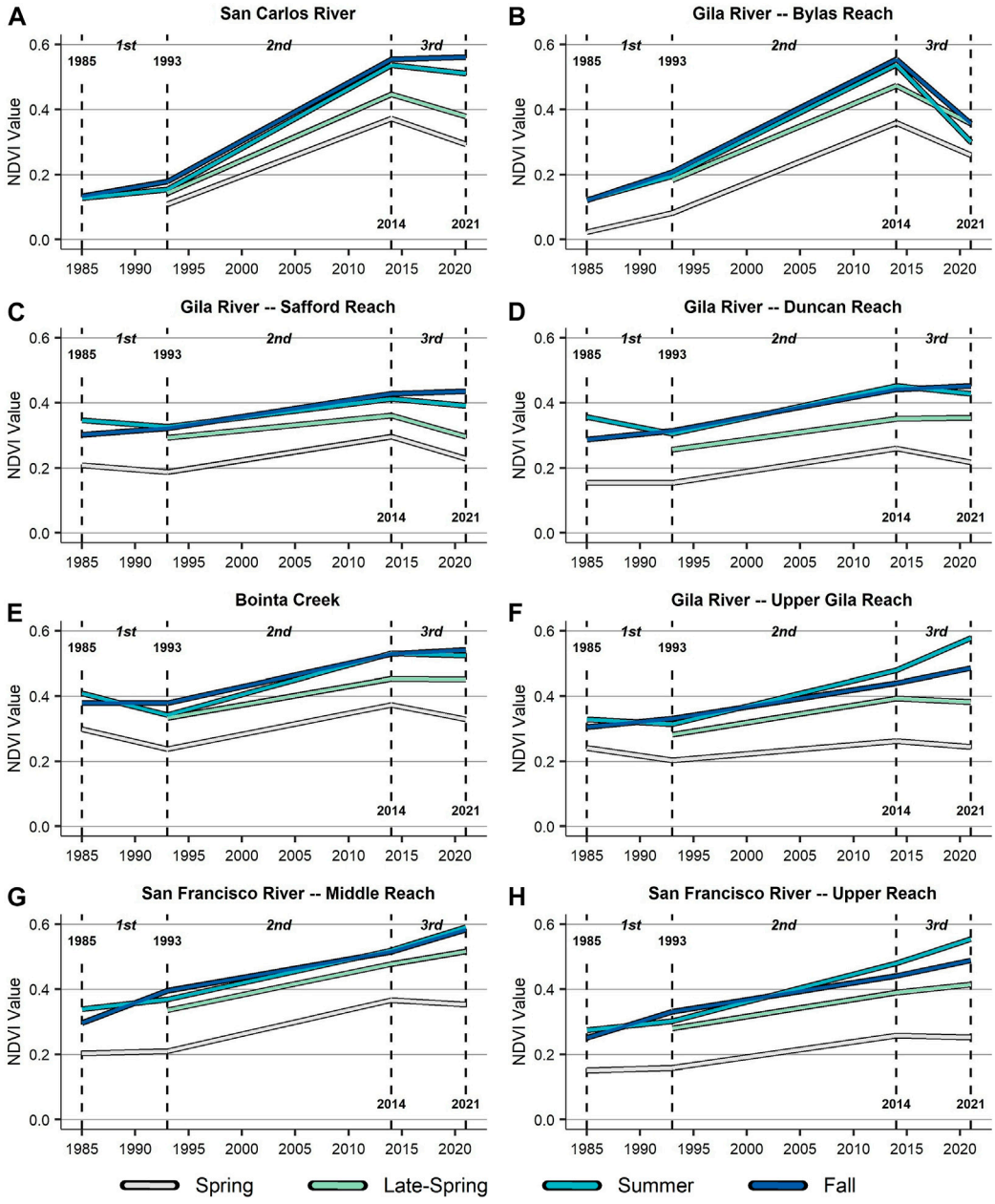

FIGURE 5
Showing snapshots of average annual Normalized Difference Vegetation Index (NDVI) (Tucker, 1979) values at each climate period break (i.e., 1985, 1993, 2014, 2021) for each season (i.e., spring, late-spring, summer, fall) across the eight primary and comparison subreaches (**(A)** through **(H)**). Imagery was unavailable in 1985 during the late-spring for all reaches as well as during the spring for the San Carlos River.

summer, with the most significant rate of increase occurring during the third climate period. Based on the phenological timeseries assessment, this aligns with a green-up for deciduous gallery forest class in the summer season, though it occurred despite intensifying drought conditions.

In short, the main riparian zones along the San Carlos River and Bylas Reach of the Gila River, within the San Carlos Apache Reservation, are experiencing different relative changes in NDVI compared to upstream reaches of the Gila River and other Gila River tributaries. Bonita Creek, with the headwaters and upstream portion of the riparian zone located in the Reservation, is generally more stable (as measured via NDVI) across the full study period.

3.4 Case studies

3.4.1 Effects of the prior riparian restoration application

Various patterns can be identified within the timeseries of NDVI within the restoration area based on metrics before, during, and after

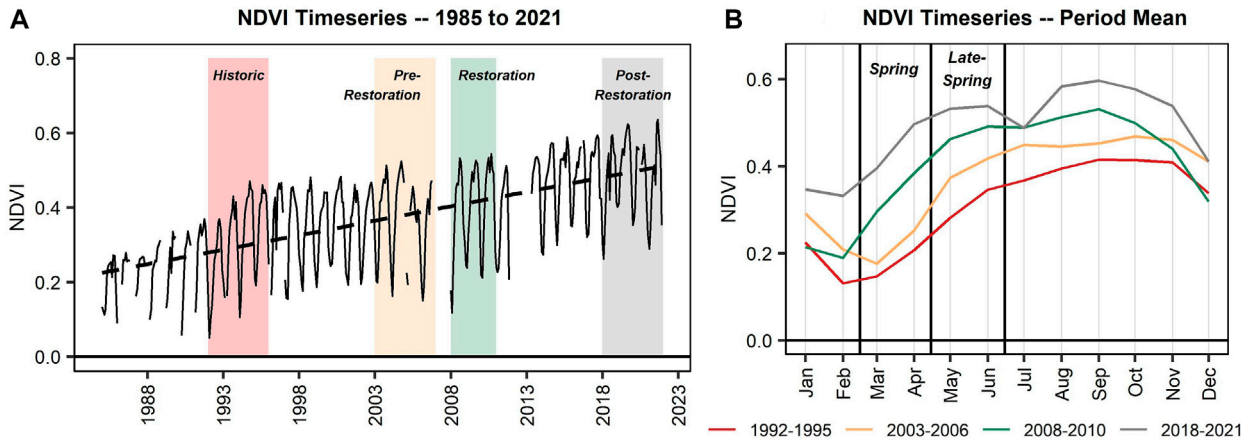

FIGURE 6
Showing **(A)** the full timeseries of the Normalized Difference Vegetation Index (NDVI) (Tucker, 1979) for the restoration area from 1985 to 2021 and **(B)** the monthly timeseries averaged across each multi-year period, representing historic conditions (1992–1995), conditions prior to the restoration activities (2003–2006), conditions during the restoration period (2008–2010), and post-restoration conditions (2018–2021). The spring (March/April) and late-spring (May/June) seasons are boxed.

the restoration activities. First, this region experienced a consistent and large increase in NDVI across the study period (Figure 6A), pointing to an overall increase in vegetation canopy cover across the second and third climate periods. Additionally, the minimum NDVI increased during and following the restoration activities, signaling that more widespread or dense understory and perennial riparian forested vegetation may be present.

The post-restoration period (i.e., 2018 through 2021) had the highest monthly NDVI values, while the historic period (i.e., 1992 through 1995) had the lowest NDVI values (Figure 6B), matching results from Figure 6A. Notably, NDVI had a larger increase from February to March and March to April, during the spring, for the post-restoration period when compared to the historic period (February to March Δ: historic = 0.016, post-restoration = 0.063; March to April Δ: historic = 0.06, post-restoration = 0.101). A large increase in NDVI is also present during the restoration period. Conversely, NDVI change nearly stabilized for the post-restoration period when compared to the historic period for the late-spring (April to May Δ: historic = 0.074, post-restoration = 0.035; May to June Δ: historic = 0.065, post-restoration = 0.007). Though tamarisk has somewhat returned since the restoration activities ended, as noted by Tribal employees, less non-native tamarisk is present currently than prior to the restoration, whereas numerous native riparian vegetation species (i.e., willow, Arizona black walnut, mesquite, sycamore, desert willow) have been documented to have returned. Overall, this system is described as a "healthier system" (San Carlos Apache Tribe, personal communication, May 2022) and the remote sensing metrics support this observation.

3.4.2 Implications of the phreatophyte vegetation removal

Results from the multi-temporal analysis show differences across the subreach groups for the climate period Sen's slope and timeseries metrics from 1985 through 2021 (Figure 7). Across the timeseries, subreach groups 1 and 2 (e.g., higher-density non-native vegetation; history of reservoir-induced surface water flooding) had similar temporal signatures, as did subreach groups 3 and 4 (e.g., lower-density vegetation; no reservoir-induced flooding). Subreach groups 1 and 2 generally have higher NDVI, greenness, and wetness values compared to subreach groups 3 and 4. This contrast largely began in the late-spring, while signatures were more similar between all subreach groups during the spring.

The contrast in timeseries trends between subreach groups 1 and 2 and subreach groups 3 and 4 are generally mirrored by changes (i.e., Δ) for the Sen's slope products across the climate periods (Figure 8). Notably, for NDVI (Figures 8A, D, G, J) there is variability between subreach groups 1 and 2 as well as groups 3 and 4 for the second and third climate periods. However, a large increase in NDVI is noted for group 1 during the first climate period for all four seasons (i.e., ΔNDVI >0; spring = 0.019; late-spring = 0.023; summer = 0.017; fall = 0.014), driven by the increase of vegetation in formerly flooded locations. For the second climate period, groups 3 and 4 increase (i.e., ΔNDVI >0; Group 3: spring = 0.001; late-spring = 0.003; summer = 0.004; fall = 0.004; Group 4: spring = 0.001; late-spring = 0.004; summer = 0.004; fall = 0.005) while groups 1 and 2 remain relatively stable or even decrease, not including the spring (ΔNDVI≤0; Group 1: late-spring = 0; summer = 0; fall = 0.001; Group 2: late-spring = −0.006; summer = −0.004; fall = −0.002). For the third climate period, groups 1 and 2 have higher decreasing ΔNDVI values (Figure 8) compared to groups 3 and 4. This is partially a result of fire activity (Section 3.3. Vegetation Timeseries Across Climate Periods), where fire impacts appear to be more significant in the downstream groups (i.e., 1 and 2).

Greenness (Figures 8B, E, H, K) and wetness (Figures 8C, F, I, L) generally follow similar patterns. Specifically, groups 1 and 2 decrease for all seasons during the second climate period for both greenness and wetness, while groups 3 and 4 largely increase or remain relatively stable, except for spring greenness (**8B, 8E, 8H,**

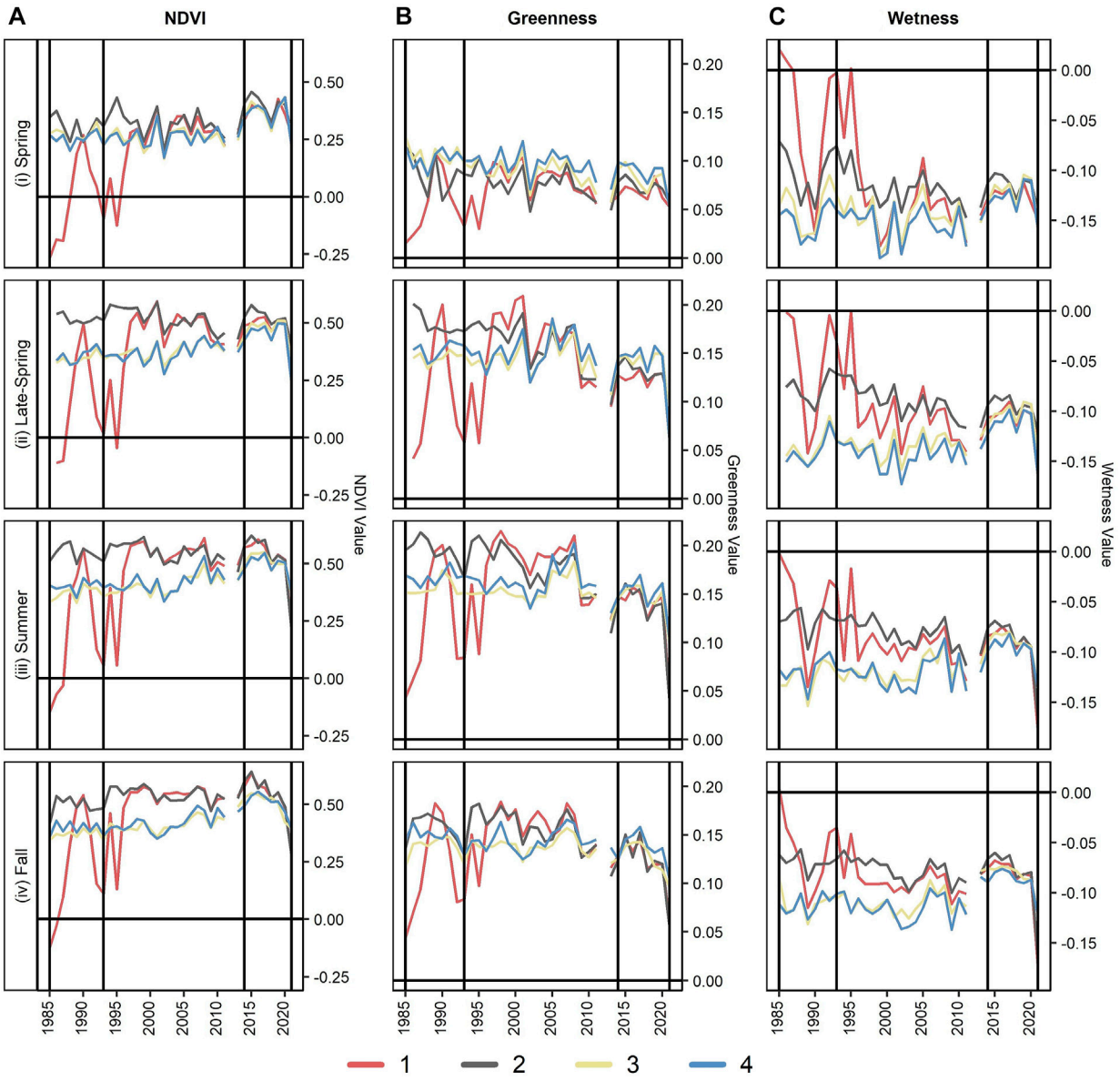

FIGURE 7
Showing the timeseries of **(A)** Normalized Difference Vegetation Index (NDVI) (Tucker, 1979), **(B)** Tasseled Cap (TC) greenness, and **(C)** TC wetness (Kauth and Thomas, 1976) for each of subreach groups of the Phreatophyte Project (i.e., 1 through 4) from 1985 through 2021. Vertical black lines in 1993 and 2014 show the breaks between the climate periods.

8K). During the third climate period, groups 1 and 2 experience large declines in wetness for all seasons, while groups 3 and 4 increase or remain stable during the spring and late-spring and decrease at a comparatively lower rate during the summer and fall (**8C, 8F, 8I, 8L**).

3.4.3 Results of the pre- and post-wildfire assessment

Timeseries of NDVI and the TC metrics averaged across the Bottom Fire for the second and third climate periods show a combination of both short- and long-term changes occurring prior to the fire (Figure 9). Direct impacts of the Bottom Fire are visualized through notable short-term declines for the summer and fall from 2020 through 2021 for (**9A**) NDVI (ΔNDVI from 2020 to 2021: summer = −0.28; fall = −0.19) (**9C**) greenness (ΔGreenness from 2020 to 2021: summer = −0.1; fall = −0.06), and (**9D**) wetness (ΔWetness from 2020 to 2021: summer = −0.08; fall = −0.08), in addition to a slight increase in (**9B**) brightness in 2021 (ΔBrightness from 2020 to 2021: summer = 0.001; fall = 0.05). Though not as large of changes when compared to the summer and fall, additional declines are documented for NDVI (ΔNDVI from 2020 to 2021: spring = −0.11; late-spring = −0.11), greenness (ΔGreenness from 2020 to 2021: spring = −0.02; late-spring = −0.03), and wetness (ΔWetness from 2020 to 2021: spring = −0.02; late-spring = −0.03) for the spring and late-spring seasons of 2021, indicative of short-term vegetation degradation prior to the fire.

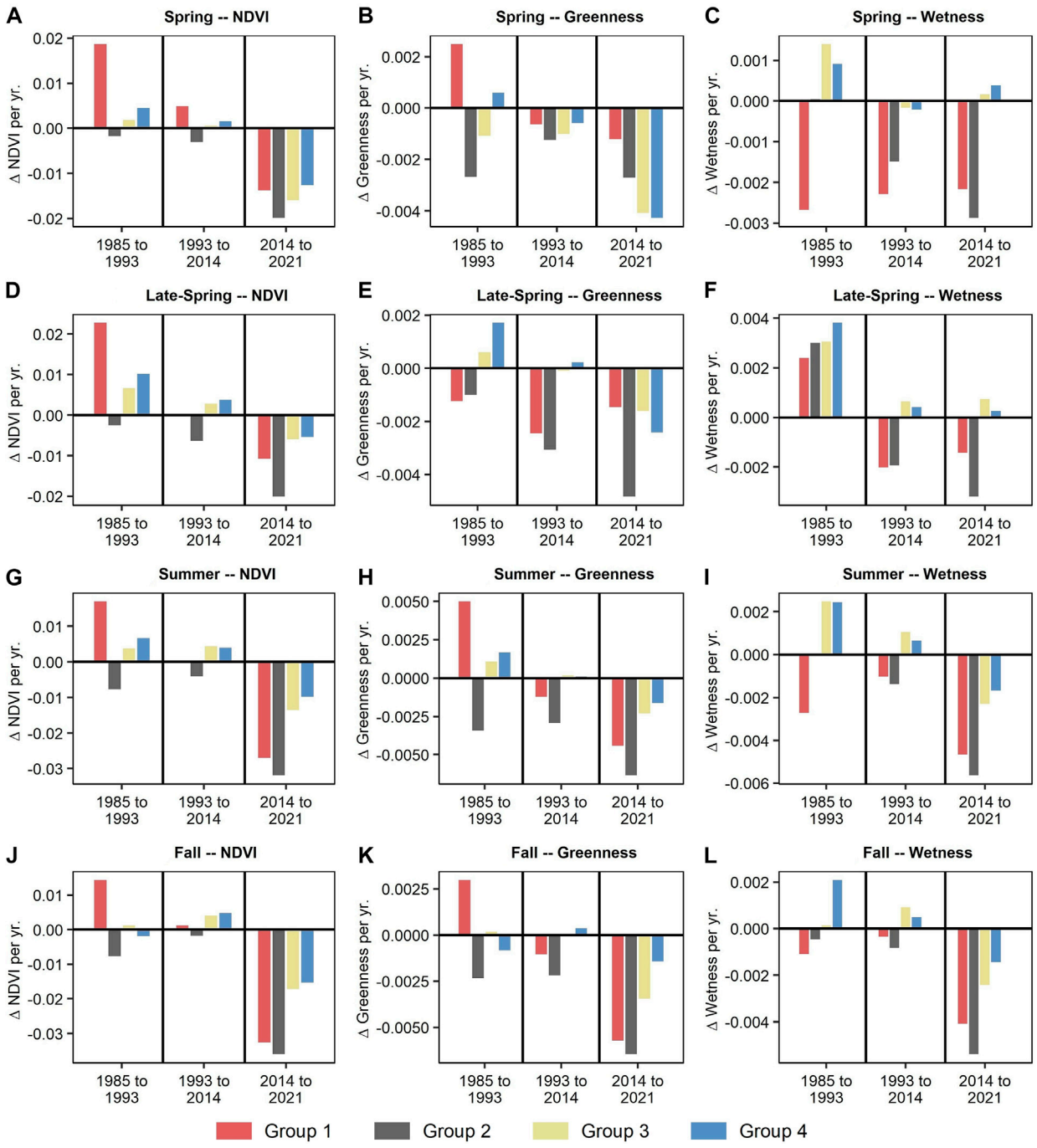

FIGURE 8
Showing the mean Sen's slope across the four subreach groups for the Normalized Difference Vegetation Index (NDVI) (Tucker, 1979) and the Tasseled Cap (TC) metrics greenness and wetness (Kauth and Thomas, 1976) for each of the four seasons: first row **(A–C)** = spring; second row **(D–F)** = late-spring; third row **(G–I)** = summer; fourth row **(J–L)** = fall. Values represent change in value per year (i.e., Δ).

One notable long-term change is a decrease in greenness between 2008 and 2009 for the late-spring, summer, and fall (**9C**). This drop in greenness is not directly aligned in the NDVI (**9A**) timeseries. Rather, NDVI shows a slight increase compared to prior years beginning in 2013, particularly in the spring. However, both summer and fall NDVI values decrease from roughly 2015 through 2020. Similar to the NDVI timeseries, a slight increase occurs in wetness (**9D**) for the spring, summer, and fall. Wetness also had higher values in 1993 and 1995 from surface flooding from the San Carlos Reservoir. Following the surface flooding of 1995, values across all metrics began to stabilize in 1997.

Correlations show a direct and statistically significant (p-value <0.05) relationship between burn severity and Sen's slope trends across the third climate period for many of the pre-

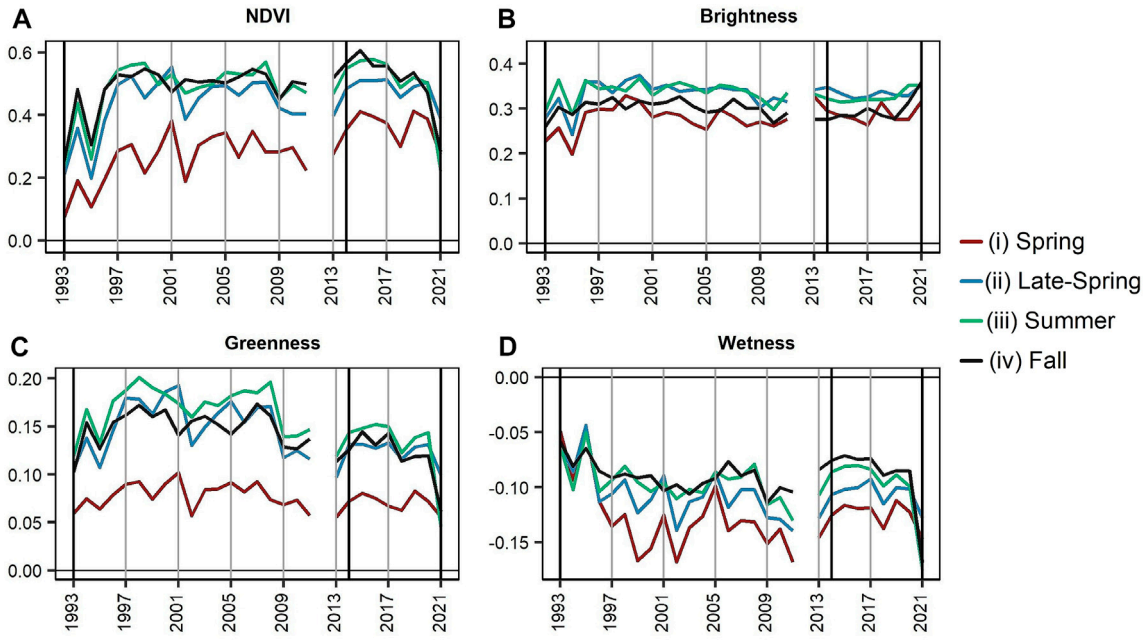

FIGURE 9
Graphs showing the yearly timeseries of **(A)** Normalized Difference Vegetation Index (NDVI) (Tucker, 1979) **(B)** Tasseled Cap (TC) brightness **(C)** TC greenness, and **(D)** TC wetness (Kauth and Thomas, 1976) for the area within the Bottom Fire boundary from 1993 through 2021 for each season—i) spring, ii) late-spring, iii) summer, and iv) fall. There are no data available for 2012.

fire (i.e., spring and late-spring) vegetation metrics (i.e., NDVI, TC brightness, TC greenness, TC wetness) (Figure 10A, **a–h**). The strongest correlations, through generally moderate in strength, were between dNBR and spring NDVI (**10a**), greenness (**10e**), and wetness (**10g**) (correlations: NDVI = −0.37; greenness = −0.38; wetness = −0.33), which denotes that higher fire severity occurred within areas that have higher decreasing rates of NDVI, greenness, and wetness in the spring (i.e., increasing severity and declining metrics). However, correlations were weaker for late-spring greenness and wetness, −0.19 and −0.08, respectively (**10f, 10h**). A positive correlation (correlation value = 0.14) for spring brightness (**10c**) implies areas with increasing brightness experienced higher fire severity. Late-spring NDVI and brightness (**10b, 10d**) were not significant.

Correlations between fire severity and 2021 pre-fire conditions reveal significant (p-value <0.05) relationships (Figure 10B**; i-p**). NDVI had the strongest relationship between pre-fire conditions and fire severity, with correlation values of 0.67 and 0.69 for the spring and late-spring, respectively (**10i, 10j**). Brightness had significant negative correlations with fire severity (**10k, 10l**). For the spring and late-spring, strong negative correlations indicate that areas with lower brightness, likely comprised of more dense vegetation canopies, burned more severely while brighter areas that likely consist of greater open soil or grassland coverage burned less severely. Greenness results were similar to NDVI, as expected (**10m, 10n**). Strong positive correlations between pre-fire greenness and burn severity imply that higher fire severity occurred within greener areas, particularly measured as late-spring greenness. Wetness had a positive correlation with burn severity for both the spring and late-spring (**10o, 10p**). However, because wetness is measured with negative values, this correlation implies that wetter areas burned more severely than drier areas; this aligns with the assumption that greener areas are wetter due to higher vegetation and moisture.

In short, areas that were experiencing a greater negative Sen's slope rate in NDVI, greenness, and wetness in the spring and late-spring prior to the Bottom Fire burned at a higher severity (i.e., higher dNBR values) (Figure 10). Furthermore, greener and wetter areas in the spring and late-spring for 2021 also burned at a higher severity. However, it is notable that some areas (i.e., Bottom Fire sample points) had higher late-spring NDVI (**10j**), greenness (**10n**), and wetness (**10p**) and burned with lower severity than the liner relationship would suggest. Corresponding evidence of this was identified in the high-resolution 2021 post-fire NAIP imagery (USDA, 2021), where an area immediately surrounding the active flow channel within the Bottom Fire boundary was not severely impacted by the wildfire. This vegetation was wetter and greener prior to the fire activity. This implies there is a threshold of moisture in which the vegetation is protected from wildfire.

The 2019 Bylas Fire provides an opportunity to review short-term response following a wildfire within a tamarisk dominant system. The timeseries of NDVI (Figure 11) displays a relatively consistent pattern from 2014 through May 2019 for the Bylas Fire area, though the peak value is declining moderately year-to-year (0.63 in September 2014 to 0.55 in September 2018; ΔNDVI = 0.08). A similar decline is documented in the nearby control site (0.53 in September 2014 to 0.47 in September 2018; ΔNDVI = 0.06). For the Bylas Fire timeseries, an immediate and substantial drop in NDVI is observed following the fire in June (i.e., May NDVI = 0.55; June NDVI = 0.30; ΔNDVI = −0.25), followed by a minimal increase in

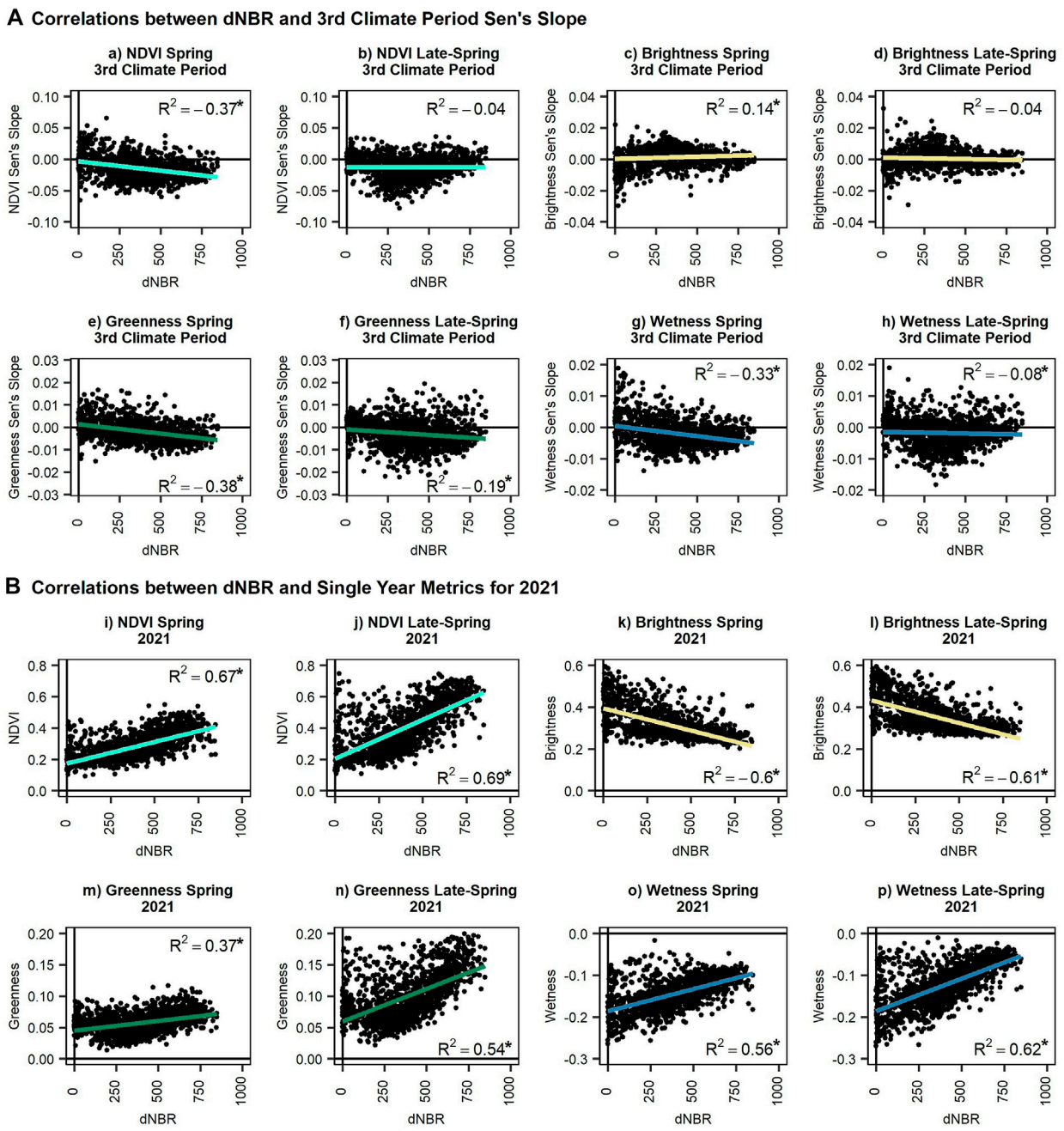

FIGURE 10
Scatter plots between the differenced Normalized Burn Ratio (dNBR) (USGS BAER, 2022b) and the vegetation metrics for the spring and late-spring for the **(A)** third climate period slope and **(B)** the single year metrics for 2021. The metrics include (a/b/i/j) Normalized Difference Vegetation Index (NDVI) (Tucker, 1979) (c/d/k/l) Tasseled Cap (TC) brightness (e/f/m/n) TC greenness, and (g/h/o/p) TC wetness (Kauth and Thomas, 1976) for points within the Bottom Fire boundary. Correlation values are provided in either the upper or lower right corners of the graphs. Significant correlations (*p*-value <0.05) are identified using "*".

summer 2020. However, in July through September 2021, following a relatively wet monsoon season, a moderate recovery in NDVI is documented. This aligns with discussions with Tribal employees and members, in which it was noted that tamarisk immediately recovers following fire activity on the Reservation (San Carlos Apache Tribe, personal communication, May 2022). Yet despite increases in 2021, NDVI has not shown a large increase by June 2022, which was the most recent data Landsat imagery available.

4 Discussion

4.1 Summary of restoration potential

Based on the full suite of analyses, including i) a comparison of vegetation conditions in response to climate trends within the primary study site and at the comparison watershed study reaches and ii) three case studies addressing environmental- and

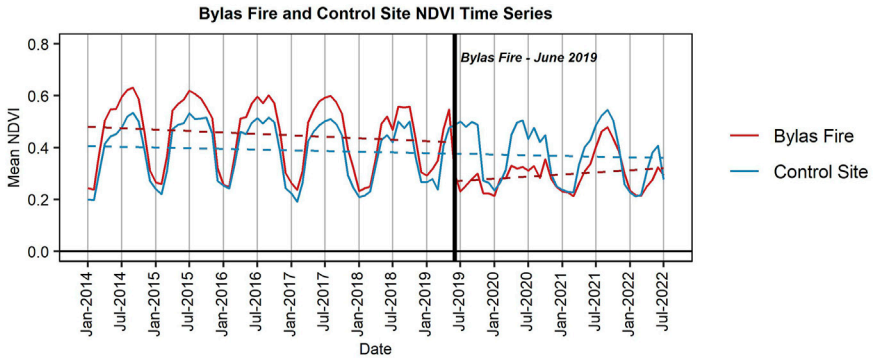

FIGURE 11
The graph shows the Normalized Difference Vegetation Index (NDVI) (Tucker, 1979) timeseries within the Bylas Fire boundary (red) and a nearby control site (blue) from January 2014 through July 2022. The Bylas Fire burned in June 2019, indicated by the black vertical line. Linear trend lines show the trend before and after the fire for the Bylas fire, while the trend line for the control site is not divided at the time of the fire.

management-based themes including prior restoration efforts, prior vegetation removal, wildfire, as well as climate- and disturbance-based vegetation change, we have developed a summary of vegetation change along the San Carlos River and Bylas Reach of the Gila River that could be used to identify restoration potential for future planning. Specifically, we focus on areas that have been effectively restored as well as areas that show degradation tied to an increase in wildfire presence and scale, post-fire restoration, and restoration of the native gallery forests in the watershed.

4.1.1 Where restoration is occurring

Our analysis shows that the restoration approach applied within the restoration area was largely effective at both removing non-native tamarisk as well as developing native deciduous gallery forest vegetation. The remote sensing metrics show that early-spring greenness has increased likely because of an increase in the presence and overall coverage of native vegetation species, such as the cottonwood trees were planted during the restoration application (San Carlos Apache Tribe, personal communication, May 2022). NDVI shows a declining rate in the amount of positive increase between the months of April, May, and June, in addition to a near stabilization of NDVI values during the averaged post-restoration period. This suggests that non-native vegetation may have less areal extent and reduced growth within the restoration area when compared to historic conditions. Additionally, Tribal employees and members described a healthier native riparian system with many important native riparian vegetation species (i.e., willow, Arizona black walnut, mesquite, sycamore, desert willow) known to be present in this location likely became more prevalent following the restoration activities. Overall, the restoration application appeared to have met the primary objectives determined by the Tribe.

In upper reaches of the watershed (i.e., San Francisco Reaches and Upper Gila Reach), which is known to have a lower prevalence of tamarisk vegetation (Carolyn Koury, Hydrologist—U.S. Forest Service Gila National Forest, personal communication, October 2022), native deciduous gallery forests have widely increased in NDVI, greenness, and wetness despite recent climate conditions (i.e., second and third climate periods). Similar conditions are observed, though not as widespread, throughout the full watershed, including on subreaches not addressed in this study though mapped in the spatially explicit products (i.e., Eagle Creek, the Bule River, the Gila Box, and others) (Petrakis et al., 2023). It is possible that a warm and wet summer monsoon season in 2021 may be influencing this response. However, Davis et al. (2022) suggests that increases in atmospheric carbon stocks may be tied to increasing wood volume, including for cottonwood forests in the western US.

Providing an assessment of the requirements needed to establish native vegetation is beyond the scope of this study. However, prior studies suggest that overbanking flows support the establishment of native cottonwood-willow trees (Poff et al., 1997; Stromberg et al., 2007). Natural Infrastructure in Dryland Streams (NIDS) (Norman et al., 2022), such as rock detention structures (i.e., one rock dams, trincheras, etc.), beaver dams, and their analogs, have been shown to be effective at increasing baseflows and overall flow volume (Norman et al., 2015), vegetation greenness and moisture both upstream and downstream (Norman et al., 2014; Wilson and Norman, 2018), surface water and riparian wetland habitat (Gibson and Olden, 2014; Norman et al., 2014; 2022; Wilson and Norman, 2018; Norman, 2020) and fire resistance within riparian systems by retaining water and increasing greenness and moisture in the riparian vegetation (Fairfax and Whittle, 2020; Norman et al., 2022). It is plausible that greater use of these structures could help establish native riparian species.

4.1.2 Areas that show degradation

We identified sizable contrast between subreach groups structured in the Phreatophyte Project, which was likely a derivative of the vegetation and the historic presence of reservoir-induced surface-water flooding. For instance, densely vegetated stands that have greater declining rates in NDVI, greenness, and wetness across the second and third climate periods (i.e., drought and intensifying drought conditions) potentially represent widespread declines in vegetation health, and potentially even limited mortality of tamarisk (Nagler et al.,

2018). Pre-existing conditions prior to the Phreatophyte Project treatments portray cycles of tamarisk invasion, where previous vegetation was killed by reservoir-induced surface flooding from the San Carlos Reservoir. After the surface flooding receded, high rates of vegetation growth incurred (Section 3.3 and 3.4.2). The greater decline in overall condition of vegetation in these subreaches could be resulting from drought intensification and reduced reservoir levels.

Additionally, we concluded in our post-fire analysis of the 2019 Bylas Fire that, i) the NDVI response in 2020, 2021, and 2022 was lower than pre-fire conditions and ii) the post-fire vegetation temporal signature did not follow a typical non-native tamarisk signature and increased in NDVI at a much slower rate, particularly from July through August. A very wet 2021 monsoon (CLIMAS, 2021) likely contributed to the increase in NDVI during the summer, while winter and spring droughts for 2021 and 2022 (NOAA and NIDIS, 2022; Seager et al., 2022) may have contributed to minimal growth during the spring and early-summer. In short, it is likely that only limited re-vegetation occurred within 1 year (i.e., 2020), though the rate of re-vegetation appeared to increase following summer rain in 2021. Nevertheless, this implies that non-native tamarisk has not fully re-vegetated up to 3-year following the Bylas Fire. Several studies suggest that the plant specific growth rate is dependent on various factors such as the amount and type of surrounding vegetation, structure of the plant, climate conditions, and tamarisk beetle impacts (Lesica and Miles, 2001; Snyder and Scott, 2020); therefore it is possible that full recovery of the tamarisk stand following a wildfire would take several years. However, Smith et al. (2006) observed tamarisk sprouts reflowering following a wildfire in as little as 3-month. This response has also been documented elsewhere following wildfire (Busch, 1995; Smith et al., 2009), in addition to defoliation events caused by the tamarisk beetle, though not universally (Snyder and Scott, 2020). Despite an initial response, this may allow for a period of restoration following wildfire events, such as the 2021 Bottom Fire, before tamarisk returns as the dominant vegetation species within the system. We hypothesize that climate conditions during this period, specifically below average rainfall, were not conducive to vegetation recovery, and that years with average or above-average rainfall would result in faster recovery of the vegetation. Continued monitoring of the vegetation response may help inform post-fire recovery within this ecosystem as more imagery becomes available.

For the Bottom Fire, declining trends in pre-fire vegetation condition, identified in our Sen's slope analysis, may have led to increased fire risk. Similar relationships aligning drier climate and vegetation conditions with intensifying wildfire patterns have been documented elsewhere (Leblon et al., 2007; Halofsky et al., 2020). However, immediate pre-fire vegetation conditions also showed that greener and wetter areas were burning with higher fire severity. Combined, this suggests that stressed vegetated areas may be at greater risk of fire, however, greener areas, which likely provide higher fuel loads, may burn more severely (Drus, 2013). We can only speculate as to intensifying drought conditions driving this decline, though there is a possibility that the tamarisk beetle may have arrived in the Reservation, without formal documentation, by 2021 (San Carlos Apache Tribe, personal communication, January 2023). Nevertheless, we hypothesize that riparian vegetation conditions, due to effects from historic surface flooding from the San Carlos Reservoir coupled with observations of declining vegetation metrics during the third climate period, may lead to higher fire risk within the lower San Carlos River. If surface water levels within the San Carlos Reservoir remain low because of extended drought conditions, areas that would historically be considered portions of the San Carlos Reservoir may experience widespread non-native tamarisk growth in those drying floodplains and be subject to similar wildfire-inducing conditions in the future.

In short, it may be both appropriate and logical to draw parallel conclusions in areas throughout the watershed to conditions from the Phreatophyte Project along the Gila River to inform restoration priorities. Specifically, locations along the lower San Carlos River north of the San Carlos Reservoir, are experiencing widespread decline in NDVI and TC greenness across the third climate period. Both hydrologic and vegetation properties of this region are likely very similar to conditions observed within lower portions of the Phreatophyte Project, where numerous occasions of reservoir-induced surface water flooding occurred leading to high amounts of sediment, low slopes, and likely high salinization in the soil. Though not widespread and driven by localized factors, it is plausible that other locations throughout the larger watershed could be experiencing similar conditions. This may include the Safford and Duncan reaches of the Gila River, as well as portions of Bonita Creek. Even though generalized trends show increasing metrics (i.e., NDVI, greenness, wetness) along other reaches, the spatially explicit products can identify localized areas experiencing declines in overall vegetation metrics (Petrakis et al., 2023).

4.2 Challenges and benefits of remote sensing within riparian zones

Applications of remote sensing using both satellite- and aerial-based imagery sources have been widely used for the semi-continuous monitoring of the vegetation at a broad-scale on the San Carlos Apache Reservation (Petrakis et al., 2016; 2018; Wu et al., 2016; Norman et al., 2018; Middleton and Norman, 2021). However, riparian zones are extremely dynamic and complex systems structurally, and cover only a small portion of the landscape (Naiman and Décamps, 1997). Site-specific conditions are more likely driven by micro-scale factors that could vary across (i.e., transverse) and along (i.e., longitudinal) the riparian floodplain, such as distance to groundwater, fire history, vegetation type, elevation and orientation, as well as human activities and disturbances (Bendix, 1994; Wilson and Norman, 2022). We hypothesize that other micro-scale factors may also be impacting changes, such as climate variability (i.e., temperature and precipitation regimes), proximity to agriculture, and geomorphic-based shading effects we observed in the spatially explicit raster products. These detailed changes can be challenging when analyzing satellite imagery (Middleton and Norman, 2021). We largely generalized conditions across various reaches of the San Carlos and Gila Rivers. We also averaged Landsat data into seasonal means to monitor changes occurring more consistently at different periods across the 37-year study

period, which could result in loss of data that would be available if we were using single-date Landsat imagery. In general, it is possible this approach could result in the loss of spatially explicit, small-scale changes occurring within the vegetation.

However, remote sensing allows for a wide-scale assessment for an extended period. It has a capacity to measure vegetation dynamics using spectral response. Because of this, we were able to quantify general trends across subreaches within the larger riparian system, with some additional analyses related to pixel-scale conditions. Our multi-scaled approach primarily addressed conditions across the larger watershed by comparing reaches, addressing restoration impacts, and reviewing historic management impacts, but also included highly detailed pixel-based analyses when addressing pre- and post-fire impacts. This variability in scale helps identify unique properties of the vegetation response to climate conditions. Additionally, we monitor long-term changes scaled across multiple climate periods to focus on generalized patterns in climate rather than short-term weather driven events. As a result, the changes that we document using the vegetation indices can be directly tied to long-term climate patterns and future trend predictions (Yang et al., 2016).

Lastly, we applied a phenological framework to gain more information on generalized plant types that are important when considering riparian restoration efforts—specifically, native deciduous (i.e., cottonwood-willow dominant) gallery forests and non-native tamarisk. This four-season approach allows us to monitor changes more directly across plant types based on the differences in seasonality of the vegetation types. Spatially explicit products derived seasonally can show where and when changes occur across the landscape. Using these products, we can conduct analyses that may help inform restoration and management decisions in the future.

4.3 Generalizations of southwestern riparian systems

Though we hypothesize that trends in the vegetation metrics would mirror the directionality of the trends in the climate conditions, that was not the case for all climate periods. Vegetation conditions (i.e., NDVI) during the first climate period remained relatively stable. Though we can characterize the climate period as being relatively wet, we chose to use SPEI because it expands on other metrics, such as the Standardized Precipitation Index (SPI), by including sensitivity to temperature-driven evaporative demand to estimate drought conditions (Vicente-Serrano et al., 2010; Stagge et al., 2014). A slight transition to drier, and possibly warmer, conditions appears to have occurred during this period; vegetation conditions largely aligned with that characterization. During the third climate period, in which intensifying drought conditions were present, NDVI largely declined. This appears to be a result of both drought conditions, identified using the SPEI timeseries (Section 3.1 Climate Breakdown), and an increasing presence of wildfire in the riparian zone (Section 2.4.3 Pre- and Post-Wildfire Analysis). However, climate and vegetation conditions largely diverged during the second climate period. Despite dry conditions occurring during this time, as measured by SPEI, much of the riparian zone experienced increasing NDVI, greenness, and wetness, aligning with vegetation filling into formally flooded areas. This was the most apparent in areas upstream of the San Carlos Reservoir that had experienced reservoir-induced surface water flooding during the first climate period. Furthermore, it is possible that either intra-period or intra-annual variability between wet and dry conditions that supersede the breakpoint trend could also be driving vegetation response throughout the watershed.

Despite our generalization of these climate periods, localized variability was present in the spatially explicit raster images (Petrakis et al., 2023). For instance, many of the native gallery forested locations in the upper comparison subreaches of the watershed appear to increase in NDVI during the third climate period despite drought conditions. Similarly, the restoration area also increased in greenness and wetness during this time. This pattern could be representative of increasing greenness within the native cottonwood-willow gallery forests, which is known to respond positively to summer rain and hydrologic flows. Conversely, during the second climate period which we generalize as having an increase in overall greenness, declines in the vegetation metrics were noted in understory vegetation plots along the San Carlos River. These localized vegetation dynamics can directly impact restoration priorities and objectives though they may not be identified using generalizations across riparian zones and climate periods.

We also observed a large increase in fire presence and scale, particularly beginning in 2019. Fire severity for the Bottom Fire, in particular, was relatively high compared to other riparian wildfires across the southwestern US over the past 2 decades (USGS BAER, 2022b), likely driven by a combination of extremely dense tamarisk, drought, and a lack of prior fire activity within this region. The high severity burns within the Bottom Fire had direct impacts on local infrastructure, including damaging a railroad bridge and a USGS stream gaging system (Kurt Ehrenberg, Supervisory Hydrologic Technician—U.S. Geological Survey Arizona Water Science Center, personal communication, February 2023). The extent and impact of these wildfires was largely unanticipated because of the expectation that riparian zones are not historically prone to wildfire, though riparian fire dynamics, such as frequency and severity, are believed to be tied to changes in vegetation composition, geomorphology, and climate and streamflow, among other factors (Busch, 1995; Dwire and Kauffman, 2003; Webb et al., 2019). We hypothesize that this increase in wildfire in the Upper Gila River watershed riparian areas, which occurred almost entirely during the third climate period, was fundamentally climate driven. For instance, a significant portion of the Gila River riparian zone within the reservation boundary burned during this time. Our remote sensing metrics identified both long- and short-term declines in the vegetation prior to the Bottom Fire, particularly within the densely vegetated non-native tamarisk. Similar conditions were also likely present within the Salt Fire boundary, which also burned in 2021, though we did not assess pre-fire conditions for this fire.

Along the San Carlos River, recent fires have burned into the native gallery forest, though we did not investigate whether these fires started in the stressed tamarisk communities or in the native gallery forest vegetation. Nevertheless, this could have ramifications

regarding the extent of native gallery forests in the future depending on how the forests recover after the fires. Recent studies suggest that some cottonwood species (i.e., *Populus deltoides*, *Populus wislizenii*) regenerated well following wildfire in Kansas and New Mexico, though many local factors, such as stand conditions, fire intensity, timing, and climate, may have been determinants in the response (Smith et al., 2009; Wonkka et al., 2018). Likewise, restoration treatments using NIDS can reverse post-fire degradation and promote riparian climate resilience (Long and Davis, 2016; Fairfax and Whittle, 2020; Norman et al., 2022).

4.4 Future applications

We streamline our climate analysis using the robust SPEI drought metric. However, additional metrics could be considered in future analysis. For example, hydrology, specifically measurements of river discharge, can provide an assessment of direct water availability for the riparian vegetation. Cottonwood-willow vegetation, for instance, is dependent on occasional overbank flooding, especially during periods of establishment (Poff et al., 1997; Rood et al., 2007; Stromberg et al., 2007). Tamarisk, on the other hand, can establish without overbanking of floodwaters (Stromberg et al., 2007). Understanding the dynamics of seasonal overbanking flows and overall baseflow availability could help supplement the climate framework.

The rise in both the presence and severity of riparian wildfire has also become a developing resource management challenge, necessitating consideration in future research. For instance, with many of the fires occurring primarily during the later years of this study, we were unable to address long-term fire response tied to applications of restoration. We hope to assess long-term impacts tied to fire severity and seasonal post-fire riparian vegetation response in future research. Additionally, we observed areas directly along the active flow channel that experienced lower fire severity coupled with greener and wetter conditions, identified using the vegetation metrics. Though determining thresholds of either greenness or wetness that protect a particular riparian zone from wildfire was beyond the scope of this study, quantifying these thresholds may provide a reference for possible restoration applications that support reaching these thresholds of moisture within the overall system to increase resilience to wildfire.

Further enhancements of the remote sensing techniques could better inform our results. For example, improvements in the identification of tamarisk extent by using other imagery sources and image dates could benefit management of the species. Studies show that tamarisk identification is more accurate when identifying a period of senescence in the fall when the rest of the native riparian vegetation is in leaf-off condition (Diao and Wang, 2018). Additionally, higher spatial resolution sources, such as imagery from the European Space Agency (ESA) Sentinel satellite series (i.e., 10-m resolution) (ESA, 2023) and the NAIP aerial imagery are becoming more useful (i.e., NAIP imagery's NIR band, etc.) (USDA, 2021) and more frequently available, and are actively used to map vegetation dynamics (Wu et al., 2019; Misra et al., 2020; Segarra et al., 2020). Similarly, Moderate Resolution Imaging Spectroradiometer (MODIS) satellites, though with lower spatial resolution (i.e., 250 m for MODIS) which limits the ability to precisely measuring smaller riparian zone vegetation dynamics, has twice-daily overpasses (NASA, 2023). These satellite and aerial sources can be used to monitor non-native vegetation with greater spatial and even temporal (i.e., Sentinel with combined 5-day revisit period) accuracy (Huylenbroeck et al., 2020).

Data availability statement

The datasets presented in this study can be found in online repositories. The names of the repository/repositories and accession number(s) can be found below: RP, LN, BM, 2023. Mapping Riparian Vegetation Response to Climate Change on the San Carlos Apache Reservation and Upper Gila River Watershed to Inform Restoration Priorities: 1935 to Present—Database of Trends in Vegetation Properties and Climate Adaptation Variables. https://doi.org/10.5066/P9HL0N5T.

Author contributions

Conceptualization of idea—RP, LN, and BM; Formal analysis and investigation—RP; Resources and outreach—RP, LN, and BM; Writing and preparation of the original draft—RP; Review and editing of manuscript—LN, and BM; Visualizations and figures—RP; Supervision and project administration—LN; Funding acquisition and proposal development—RP, LN, and BM. All authors contributed to the article and approved the submitted version.

Funding

This research was supported through funding from the Land Change Science (LCS) Program of the U.S. Geological Survey (USGS) and the USGS Southwest Climate Adaptation Science Center (Southwest CASC). The article processing charges were funded by the USGS.

Acknowledgments

We would like to thank employees of program and departments of the San Carlos Apache Tribe, including the San Carlos Tribal Forest Resources Program, the Department of Environmental Protection, the Range Program, and the Archaeology Department, for providing input, time, and expertise pertaining to the history, condition, and concerns of the riparian vegetation. We would like to thank Michael Crimmins (Professor and Climate Science Extension Specialist—UArizona Department of Soil, Water and Environmental Science) and Seth Munson (Research Ecologist—U.S. Geological Survey Southwest Biological Science Center) for their detailed and thoughtful reviews of the manuscript. Lastly, we would also like to thank the U.S. Geological Survey (USGS) Land Change Science Program and the USGS Southwest Climate Adaptation Science Center for their financial support and assistance in this research.

Conflict of interest

The authors declare that the research was conducted in the absence of any commercial or financial relationships that could be construed as a potential conflict of interest.

Publisher's note

All claims expressed in this article are solely those of the authors and do not necessarily represent those of their affiliated organizations, or those of the publisher, the editors and the reviewers. Any product that may be evaluated in this article, or claim that may be made by its manufacturer, is not guaranteed or endorsed by the publisher.

Author disclaimer

Any use of trade, firm, or product names is for descriptive purposes only and does not imply endorsement by the U.S. Government.

References

Abatzoglou, J. T. (2013). Development of gridded surface meteorological data for ecological applications and modelling. *Int. J. Climatol.* 33, 121–131. doi:10.1002/joc.3413

Adams, B., Iverson, L., Matthews, S., Peters, M., Prasad, A., and Hix, D. M. (2020). Mapping forest composition with Landsat time series: An evaluation of seasonal composites and harmonic regression. *Remote Sens.* 12, 610. doi:10.3390/rs12040610

Adams, D. K., and Comrie, A. C. (1997). The North American monsoon. *Bull. Am. Meteorological Soc.* 78, 2197–2213. doi:10.1175/1520-0477(1997)078<2197:TNAM>2.0.CO;2

AghaKouchak, A., Farahmand, A., Melton, F. S., Teixeira, J., Anderson, M. C., Wardlow, B. D., et al. (2015). Remote sensing of drought: Progress, challenges and opportunities: Remote sensing of drought. *Rev. Geophys.* 53, 452–480. doi:10.1002/2014RG000456

Banister, K., Chan, D., Driscoll, J. M., Fullerton, C., Lien, A., and Mott Lacriox, K. (2014). *Atlas of the upper Gila River Watershed*. Arizona Water Resources Research Center.

Beguería, S., Vicente-Serrano, S. M., Reig, F., and Latorre, B. (2014). Standardized precipitation evapotranspiration index (SPEI) revisited: Parameter fitting, evapotranspiration models, tools, datasets and drought monitoring. *Int. J. Climatol.* 34, 3001–3023. doi:10.1002/joc.3887

Bendix, J. (1994). Scale, direction, and pattern in riparian vegetation-environment relationships. *Ann. Assoc. Am. Geogr.* 84, 652–665. doi:10.1111/j.1467-8306.1994.tb01881.x

BLM (2020). BLM national surface management agency area polygons - national geospatial data asset (NGDA). Bureau of land management geospatial business platform. Available at: https://gbp-blm-egis.hub.arcgis.com/datasets/blm-national-surface-management-agency-area-polygons-national-geospatial-data-asset-ngda/about.

Braatne, J. H., Rood, S. B., and Heilman, P. E. (1996). "Chapter 3: Life history, ecology, and conservation of riparian cottonwoods in North America," in *Biology of Populus and its implications for management and conservation* (NRC Press).

Busch, D. E. (1995). Effects of fire on southwestern riparian plan community structure. *Southwest. Nat.* 40, 259–267. doi:10.1007/s10021-007-9048-5

Chen, Z. M., Babiker, I. S., Chen, Z. X., Komaki, K., Mohamed, M. A. A., and Kato, K. (2004). Estimation of interannual variation in productivity of global vegetation using NDVI data. *Int. J. Remote Sens.* 25, 3139–3159. doi:10.1080/0143116032000160435

Cleland, E., Chuine, I., Menzel, A., Mooney, H., and Schwartz, M. (2007). Shifting plant phenology in response to global change. *Trends Ecol. Evol.* 22, 357–365. doi:10.1016/j.tree.2007.04.003

CLIMAS (2021). 2021 SW monsoon recap. CLIMAS: Climate assessment for the Southwest. Available at: https://climas.arizona.edu/swco/southwest-climate-outlook-october-2021/sw-monsoon-tracker-oct-2021.

Cohen, W. B., and Goward, S. N. (2004). Landsat's role in ecological applications of remote sensing. *BioScience* 54, 535. doi:10.1641/0006-3568(2004)054[0535:LRIEAO]2.0.CO;2

Cohen, W. B. (1991). *Response of vegetation indices to changes in three measures of leaf water stress*. Photogrammetric Engineering and Remote Sensing.

Cook, B. I., Ault, T. R., and Smerdon, J. E. (2015). Unprecedented 21st century drought risk in the American southwest and central plains. *Sci. Adv.* 1, e1400082. doi:10.1126/sciadv.1400082

Culler, R. C., Burkham, D. E., Collings, M. R., Davidson, E. S., Laney, R. L., Leppanen, O. E., et al. (1970). Objectives, methods, and environment Gila River Phreatophyte project, graham county, Arizona. United states department of the interior. Available at: https://pubs.usgs.gov/pp/0655a/report.pdf.

Culler, R. C., Hanson, R. L., Myrick, R. M., Turner, R. M., and Kipple, F. P. (1982). Evapotranspiration before and after clearing phreatophytes, Gila River flood plain, graham county, Arizona. United states department of the interior. Available at: https://pubs.usgs.gov/pp/0655p/report.pdf.

Davis, E. C., Sohngen, B., and Lewis, D. J. (2022). The effect of carbon fertilization on naturally regenerated and planted US forests. *Nat. Commun.* 13, 5490. doi:10.1038/s41467-022-33196-x

Dennison, P. E., Nagler, P. L., Hultine, K. R., Glenn, E. P., and Ehleringer, J. R. (2009). Remote monitoring of tamarisk defoliation and evapotranspiration following saltcedar leaf beetle attack. *Remote Sens. Environ.* 113, 1462–1472. doi:10.1016/j.rse.2008.05.022

DeVries, B., Pratihast, A. K., Verbesselt, J., Kooistra, L., and Herold, M. (2016). Characterizing forest change using community-based monitoring data and Landsat time series. *PLoS ONE* 11, e0147121. doi:10.1371/journal.pone.0147121

Dewitz, J.USGS (2021). *National land cover Database (NLCD) 2019 products (ver. 2.0, June 2021). ScienceBase data repository: U.S. Geological Survey*. Available at. doi:10.5066/P9KZCM54

Diao, C., and Wang, L. (2016). Incorporating plant phenological trajectory in exotic saltcedar detection with monthly time series of Landsat imagery. *Remote Sens. Environ.* 182, 60–71. doi:10.1016/j.rse.2016.04.029

Diao, C., and Wang, L. (2018). Landsat time series-based multiyear spectral angle clustering (MSAC) model to monitor the inter-annual leaf senescence of exotic saltcedar. *Remote Sens. Environ.* 209, 581–593. doi:10.1016/j.rse.2018.02.036

Drus, G. M. (2013). "Fire ecology of Tamarix," in *Tamarix: A case study of ecological change in the American west* (Oxford University Press). Available at. doi:10.1093/acprof:osobl/9780199898206.001.0001

Dwire, K. A., and Kauffman, J. B. (2003). Fire and riparian ecosystems in landscapes of the Western USA. *For. Ecol. Manag.* 178, 61–74. doi:10.1016/S0378-1127(03)00053-7

Edwards, E. J., Osborne, C. P., Strömberg, C. A. E., Smith, S. A., Grasses Consortium, C., Bond, W. J., et al. (2010). The origins of C4 grasslands: Integrating evolutionary and ecosystem science. *Science* 328, 587–591. doi:10.1126/science.1177216

Eppehimer, D., Fard, E., Kemper, J., Sierks, M., Morrisett, C., Sturtevant, J., et al. (2021). *Climate adaptation planning to support ecosystems and people in the Gila River Watershed*. Arizona.

ESA (2023). Sentinel-2 MSI user guide. Available at: https://sentinel.esa.int/web/sentinel/user-guides/sentinel-2-msi.

ESRI (2020). ArcMap desktop. Available at: https://www.esri.com/en-us/arcgis/products/arcgis-desktop/resources.

Fairfax, E., and Whittle, A. (2020). Smokey the beaver: Beaver dammed riparian corridors stay green during wildfire throughout the Western United States. *Ecol. Appl.* 30, e02225. doi:10.1002/eap.2225

Foga, S., Scaramuzza, P. L., Guo, S., Zhu, Z., Dilley, R. D., Beckmann, T., et al. (2017). Cloud detection algorithm comparison and validation for operational Landsat data products. *Remote Sens. Environ.* 194, 379–390. doi:10.1016/j.rse.2017.03.026

Fu, B., and Burgher, I. (2015). Riparian vegetation NDVI dynamics and its relationship with climate, surface water and groundwater. *J. Arid Environ.* 113, 59–68. doi:10.1016/j.jaridenv.2014.09.010

Gibson, P. P., and Olden, J. D. (2014). Ecology, management, and conservation implications of North American beaver (*Castor canadensis*) in dryland streams. *Aquat. Conserv. Mar. Freshw. Ecosyst.* 24, 391–409. doi:10.1002/aqc.2432

Glenn, E. P., and Nagler, P. L. (2005). Comparative ecophysiology of Tamarix ramosissima and native trees in Western U.S. riparian zones. *J. Arid Environ.* 61, 419–446. doi:10.1016/j.jaridenv.2004.09.025

Google Earth Engine Community (2021). Non-parametric trend analysis. Available at: https://developers.google.com/earth-engine/tutorials/community/nonparametric-trends.

Google Earth Engine (2022a). Gridmet drought: CONUS drought indices. Earth engine data catalog. Available at: https://developers.google.com/earth-engine/datasets/catalog/GRIDMET_DROUGHT#description.

Google Earth Engine (2022b). Landsat collections. Earth engine data catalog. Available at: https://developers.google.com/earth-engine/datasets/catalog/landsat/.

Gorelick, N., Hancher, M., Dixon, M., Ilyushchenko, S., Thau, D., and Moore, R. (2017). Google earth engine: Planetary-scale geospatial analysis for everyone. *Remote Sens. Environ.* 202, 18–27. doi:10.1016/j.rse.2017.06.031

Green, D. (2007). "Chapter 5: Biological processes in riparian areas," in *Arizona's riparian areas* (University of Arizona College of Agricluture and Life Sciences: UArizona CALS). Available at: https://cals.arizona.edu/extension/riparian/pub/UARA_07-17-07_chapter5.pdf.

Gremer, J. R., Bradford, J. B., Munson, S. M., and Duniway, M. C. (2015). Desert grassland responses to climate and soil moisture suggest divergent vulnerabilities across the southwestern United States. *Glob. Change Biol.* 21, 4049–4062. doi:10.1111/gcb.13043

Halofsky, J. E., Peterson, D. L., and Harvey, B. J. (2020). Changing wildfire, changing forests: The effects of climate change on fire regimes and vegetation in the pacific northwest, USA. *fire Ecol.* 16, 4. doi:10.1186/s42408-019-0062-8

Harms, R. S., and Hiebert, R. D. (2006). Vegetation response following invasive tamarisk (Tamarix spp) removal and implications for riparian restoration. *Restor. Ecol.* 14, 461–472. doi:10.1111/j.1526-100X.2006.00154.x

Hartfield, K., Leeuwen, W. J. D. V., and Gillan, J. K. (2020). Remotely sensed changes in vegetation cover distribution and groundwater along the lower Gila River. *Land* 9, 326. doi:10.3390/land9090326

Healey, S., Cohen, W., Zhiqiang, Y., and Krankina, O. (2005). Comparison of Tasseled Cap-based Landsat data structures for use in forest disturbance detection. *Remote Sens. Environ.* 97, 301–310. doi:10.1016/j.rse.2005.05.009

Huckleberry, G. (1996). Historical geomorphology of the Gila River. Arizona geological Survey. Available at: https://repository.arizona.edu/handle/10150/629787.

Huylenbroeck, L., Laslier, M., Dufour, S., Georges, B., Lejeune, P., and Michez, A. (2020). Using remote sensing to characterize riparian vegetation: A review of available tools and perspectives for managers. *J. Environ. Manag.* 267, 110652. doi:10.1016/j.jenvman.2020.110652

Jacobs, K. L., Garfin, G. M., and Morehouse, B. J. (2005). Climate science and drought planning: The Arizona experience. *J. Am. Water Resour. Assoc.* 41, 437–446. doi:10.1111/j.1752-1688.2005.tb03747.x

Jin, S., and Sader, S. A. (2005). Comparison of time series tasseled cap wetness and the normalized difference moisture index in detecting forest disturbances. *Remote Sens. Environ.* 94, 364–372. doi:10.1016/j.rse.2004.10.012

Kauth, R. J., and Thomas, G. S. (1976). The tasselled cap -- A graphic description of the spectral-temporal development of agricultural crops as seen by landsat. *Symposium Mach. Process. Remote. Sensed Data - Conf. Proc.* 13. Available at: https://ntrs.nasa.gov/citations/19770032233

Kennard, D., Louden, N., Gemoets, D., Ortega, S., González, E., Bean, D., et al. (2016). Tamarix dieback and vegetation patterns following release of the northern tamarisk beetle (Diorhabda carinulata) in Western Colorado. *Biol. Control* 101, 114–122. doi:10.1016/j.biocontrol.2016.07.004

Kerr, J. T., and Ostrovsky, M. (2003). From space to species: Ecological applications for remote sensing. *Trends Ecol. Evol.* 18, 299–305. doi:10.1016/S0169-5347(03)00071-5

Kindscher, K. (2011). *Vegetation and habitat along the Gila River in southwestern New Mexico*, 5.

Leblon, B., García, P. A. F., Oldford, S., Maclean, D. A., and Flannigan, M. (2007). Using cumulative NOAA-AVHRR spectral indices for estimating fire danger codes in northern boreal forests. *Int. J. Appl. Earth Observation Geoinformation* 9, 335–342. doi:10.1016/j.jag.2006.11.001

Lesica, P., and Miles, S. (2001). Tamarisk growth at the northern margin of its naturalized range in Montana, USA. *U. S. A. Wetl.* 21, 240–246. doi:10.1672/0277-5212(2001)021[0240:TGATNM]2.0.CO;2

Long, J. W., and Davis, J. (2016). Erosion and restoration of two headwater wetlands following a severe wildfire. *Ecol. Rest.* 34, 317–332. doi:10.3368/er.34.4.317

MacDonald, G. M., Stahle, D. W., Diaz, J. V., Beer, N., Busby, S. J., Cerano-Paredes, J., et al. (2008). Climate warming and 21st-century drought in southwestern north America. *Eos Trans. AGU* 89, 82. doi:10.1029/2008EO090003

Macfarlane, W. W., McGinty, C. M., Laub, B. G., and Gifford, S. J. (2017). High-resolution riparian vegetation mapping to prioritize conservation and restoration in an impaired desert river: Conservation and restoration site prioritization. *Restor. Ecol.* 25, 333–341. doi:10.1111/rec.12425

Middleton, B. R., and Norman, L. M. (2021). Remote sensing analysis to quantify change in woodland canopy cover on the san Carlos Apache reservation, Arizona, USA (1935 vs. 2017). *Land* 10, 393. doi:10.3390/land10040393

Misra, G., Cawkwell, F., and Wingler, A. (2020). Status of phenological research using sentinel-2 data: A review. *Remote Sens.* 12, 2760. doi:10.3390/rs12172760

Munson, S. M., Bradford, J. B., Butterfield, B. J., and Gremer, J. R. (2022). Primary production responses to extreme changes in North American Monsoon precipitation vary by elevation and plant functional composition through time. *J. Ecol.* 110, 2232–2245. doi:10.1111/1365-2745.13947

Nagler, P. L., Nguyen, U., Bateman, H. L., Jarchow, C. J., Glenn, E. P., Waugh, W. J., et al. (2018). Northern tamarisk beetle (Diorhabda carinulata) and tamarisk (Tamarix spp) interactions in the Colorado River basin: Northern tamarisk beetle and tamarisk interactions. *Restor. Ecol.* 26, 348–359. doi:10.1111/rec.12575

Naiman, R. J., and Décamps, H. (1997). The ecology of interfaces: Riparian zones. *Annu. Rev. Ecol. Syst.* 28, 621–658. doi:10.1146/annurev.ecolsys.28.1.621

NASA (2021). Landsat science. The Landsat program. Available at: https://landsat.gsfc.nasa.gov/(Accessed January 26, 2021).

NASA (2023). MODIS moderate resolution imaging spectroradiometer. Available at: https://modis.gsfc.nasa.gov/.

Naumburg, E., Mata-gonzalez, R., Hunter, R. G., Mclendon, T., and Martin, D. W. (2005). Phreatophytic vegetation and groundwater fluctuations: A review of current research and application of ecosystem response modeling with an emphasis on great basin vegetation. *Environ. Manag.* 35, 726–740. doi:10.1007/s00267-004-0194-7

NLCD (2016). Multi-resolution land characteristics (MRLC) consortium national land cover Database. Available at: https://www.mrlc.gov/.

NOAANIDIS (2022). Southwest drought briefing – a focus on snowpack: April 5, 2022. Drought.gov. Available at: https://www.drought.gov/webinars/southwest-drought-briefing-focus-snowpack-april-5-2022.

Norman, L. M., Brinkerhoff, F., Gwilliam, E., Guertin, D. P., Callegary, J., Goodrich, D. C., et al. (2015). Hydrologic response of streams restored with check dams in the chiricahua Mountains, Arizona. *River Res. Appl.* 32, 519–527. doi:10.1002/rra.2895

Norman, L. M. (2020). Ecosystem services of riparian restoration: A review of rock detention structures in the madrean archipelago ecoregion. *Air, Soil Water Res.* 13, 117862212094633. doi:10.1177/1178622120946337

Norman, L. M., Gishey, M., Gass, L., Yanites, B., Pfeifer, E., and Simms, R. (2006). Processed 1938 Aerial Photography for Selected Areas of the Lower Colorado River, Southwestern United States. *U.S. Department of the Interior: U.S. Geological Survey*. Available at: https://pubs.usgs.gov/of/2006/1141/

Norman, L. M., Lal, R., Wohl, E., Fairfax, E., Gellis, A. C., and Pollock, M. M. (2022). Natural infrastructure in dryland streams (NIDS) can establish regenerative wetland sinks that reverse desertification and strengthen climate resilience. *Sci. Total Environ.* 849, 157738. doi:10.1016/j.scitotenv.2022.157738

Norman, L. M., Middleton, B. R., and Wilson, N. R. (2018). Remote sensing analysis of vegetation at the San Carlos Apache Reservation, Arizona and surrounding area. *J. Appl. Rem. Sens.* 12, 1. doi:10.1117/1.JRS.12.026017

Norman, L. M., Villarreal, M., Pulliam, H. R., Minckley, R., Gass, L., Tolle, C., et al. (2014). Remote sensing analysis of riparian vegetation response to desert marsh restoration in the Mexican Highlands. *Ecol. Eng.* 70, 241–254. doi:10.1016/j.ecoleng.2014.05.012

Orr, B. K., Leverich, G. T., Diggory, Z. E., Dudley, T. L., Hatten, J. R., Hultine, K. R., et al. (2014). *Riparian restoration framework for the upper Gila River, Arizona*. Safford, AZ: Gila Watershed Partnership of Arizona.

Osman, M., Zaitchik, B. F., and Winstead, N. S. (2022). Cascading drought-heat dynamics during the 2021 southwest United States heatwave. *Geophys. Res. Lett.* 49. doi:10.1029/2022GL099265

Park, D. M., Culler, R. C., and Turner, R. M. (1978). *Management of flood-plain vegetation, 1967 to 1972, san Carlos Indian reservation, Arizona*. U.S. Geological Survey. Available at. doi:10.3133/ofr78412

Petrakis, R. E., Norman, L. M., and Middleton, B. R. (2023). *Mapping riparian vegetation response to climate change on the san Carlos Apache reservation and upper Gila River Watershed to inform restoration priorities: 1935 to present - Database of trends in vegetation properties and climate adaptation variables*. USGS ScienceBase Data Repository. Available at. doi:10.5066/P9HL0N5T

Petrakis, R. E., Soulard, C. E., Waller, E. K., and Walker, J. J. (2022). Analysis of surface water trends for the conterminous United States using MODIS satellite data. *Water Resour. Res.* 58, 2003–2019. doi:10.1029/2021WR031399

Petrakis, R. E., van Leeuwen, W., Villarreal, M. L., Tashjian, P., Dello Russo, R., and Scott, C. (2017). Historical analysis of riparian vegetation change in response to shifting management objectives on the Middle rio grande. *Land* 6, 29. doi:10.3390/land6020029

Petrakis, R. E., Villarreal, M. L., Wu, Z., Hetzler, R., Middleton, B. R., and Norman, L. M. (2018). Evaluating and monitoring forest fuel treatments using remote sensing applications in Arizona, U.S.A. *For. Ecol. Manag.* 413, 48–61. doi:10.1016/j.foreco.2018.01.036

Petrakis, R. E., Wu, Z., McVay, J., Middleton, B., Dye, D., and Vogel, J. (2016). Vegetative response to water availability on the San Carlos Apache Reservation. *For. Ecol. Manag.* 378, 14–23. doi:10.1016/j.foreco.2016.07.012

Pettorelli, N., Laurance, W. F., O'Brien, T. G., Wegmann, M., Nagendra, H., and Turner, W. (2014). Satellite remote sensing for applied ecologists: opportunities and challenges. *J. Appl. Ecol.* 51, 839–848. doi:10.1111/1365-2664.12261

Poff, N. L., Allan, J. D., Bain, M. B., Karr, J. R., Prestegaard, K. L., Richter, B. D., et al. (1997). The Natural Flow Regime. *BioScience* 47, 769–784. doi:10.2307/1313099

Priyadarshana, W. J. R. M., and Sofronov, G. (2015). R Package breakpoint. Available at: https://cran.r-project.org/web/packages/breakpoint/index.html.

R Core Team (2022). R Software. Available at: https://www.r-project.org/.

Reeves, J., Chen, J., Wang, X. L., Lund, R., and Lu, Q. Q. (2007). A Review and Comparison of Changepoint Detection Techniques for Climate Data. *J. Appl. Meteorology Climatol.* 46, 900–915. doi:10.1175/JAM2493.1

RiversEdge West (2021). What is the Tamarisk Beetle? RiversEdge West Tamarisk Beetle. Available at: https://riversedgewest.org/services/tamariskbeetle (Accessed February 4, 2021).

Rood, S. B., Goater, L. A., Mahoney, J. M., Pearce, C. M., and Smith, D. G. (2007). Floods, fire, and ice: disturbance ecology of riparian cottonwoodsThe review is one of a selection of papers published in the Special Issue on Poplar Research in Canada. *Can. J. Bot.* 85, 1019–1032. doi:10.1139/B07-073

Seaber, P. R., Kapinos, F. P., and Knapp, G. L. (1987). *Hydrologic unit maps*. U.S. Geological Survey. Water-Supply Paper 2294.

Seager, R., Ting, M., Alexander, P., Nakamura, J., Liu, H., Li, C., et al. (2022). Mechanisms of a Meteorological Drought Onset: Summer 2020 to Spring 2021 in Southwestern North America. *J. Clim.* 35, 7367–7385. doi:10.1175/JCLI-D-22-0314.1

Seager, R., Ting, M., Li, C., Naik, N., Cook, B., Nakamura, J., et al. (2013). Projections of declining surface-water availability for the southwestern United States. *Nat. Clim. Change* 3, 482–486. doi:10.1038/nclimate1787

Segarra, J., Buchaillot, M. L., Araus, J. L., and Kefauver, S. C. (2020). Remote Sensing for Precision Agriculture: Sentinel-2 Improved Features and Applications. *Agronomy* 10, 641. doi:10.3390/agronomy10050641

Shafroth, P. B., Friedman, J. M., and Ischinger, L. S. (1995). Effects of Salinity on Establishment of Populus Fremontii (Cottonwood) and Tamarix Ramosissima (Saltcedar) in Southwestern United States. *Gt. Basin Nat.* 55, 58–65. doi:10.2307/41712864

Shammi, S. A., and Meng, Q. (2021). Use time series NDVI and EVI to develop dynamic crop growth metrics for yield modeling. *Ecol. Indic.* 121, 107124. doi:10.1016/j.ecolind.2020.107124

Smith, D. M., Finch, D. M., Gunning, C., Jemison, R., and Kelly, J. F. (2009). Post-Wildfire Recovery of Riparian Vegetation during a Period of Water Scarcity in the Southwestern USA. *fire Ecol.* 5, 38–55. doi:10.4996/fireecology.0501038

Smith, D. M., and Finch, D. M. (2014). Use of Native and Nonnative Nest Plants by Riparian-Nesting Birds along Two Streams in New Mexico. *River Res. Applic* 30, 1134–1145. doi:10.1002/rra.2713

Smith, D. M., Kelly, J. F., and Finch, D. M. (2006). Wildfire, Exotic Vegetation, and Breeding Bird Habitat in.

Snyder, K. A., and Scott, R. L. (2020). Longer term effects of biological control on tamarisk evapotranspiration and carbon dioxide exchange. *Hydrol. Process.* 34, 223–236. doi:10.1002/hyp.13639

Stagge, J. H., Tallaksen, L. M., and Xu, C.-Y. (2014). "Standardized precipitation-evapotranspiration index (SPEI): Sensitivity to potential evapotranspiration model and parameters," in *Hydrology in a changing world: Environmental and human dimensions proceedings of FRIEND-water 2014*.

Stevens, L. E., and Siemion, G. (2012). Tamarisk Reproductive Phenology and Colorado River Hydrography, Southwestern USA. *J. Arizona-Nevada Acad. Sci.* 44, 46–58. doi:10.2181/036.044.0106

Stillwater Sciences, and UArizona WRRC (2018). Upper Gila River Watershed Assessment Draft Report. Available at: https://www.gwpaz.org/uploads/b/9d52ff60-b669-11ea-86c9-437433cc9a75/Watershed-Assessment-GWP_WFF-FINAL.pdf.

Stromberg, J. C., Beauchamp, V. B., Dixon, M. D., Lite, S. J., and Paradzick, C. (2007). Importance of low-flow and high-flow characteristics to restoration of riparian vegetation along rivers in arid south-Western United States. *Freshw. Biol.* 52, 651–679. doi:10.1111/j.1365-2427.2006.01713.x

Strong, C., McCabe, G. J., and Weech, A. (2020). Step Increase in Eastern U.S. Precipitation Linked to Indian Ocean Warming. *Geophys. Res. Lett.* 47. doi:10.1029/2020GL088911

Tamiminia, H., Salehi, B., Mahdianpari, M., Quackenbush, L., Adeli, S., and Brisco, B. (2020). Google Earth Engine for geo-big data applications: A meta-analysis and systematic review. *ISPRS J. Photogrammetry Remote Sens.* 164, 152–170. doi:10.1016/j.isprsjprs.2020.04.001

Tucker, C. J. (1979). Red and Photographic Infrared Linear Combinations for Monitoring Vegetation. *Remote Sens. Environ.* 8, 127–150. doi:10.1016/0034-4257(79)90013-0

UArizona WRRC (2022). Key Regulations Impacting Land and Water Use. The University of Arizona Water Resources Research Center. Available at: https://wrrc.cals.arizona.edu/programs/water-rapids/projects/watershed-planning-upper-gila-watershed/guide-landowners-upper-30.

USA NPN (2022). Why Phenology? USA National Phenology Network. Available at: https://www.usanpn.org/about/why-phenology.

USDA (2021). NAIP Imagery. National Agriculture Imagery Program (NAIP). Available at: https://naip-usdaonline.hub.arcgis.com/(Accessed January 26, 2021).

USGS (2017). 1 Arc-second Digital Elevation Models (DEMs) - USGS National Map 3DEP Downloadable Data Collection. USGS ScienceBase Data Repository: U.S. Geological Survey. Available at: https://www.sciencebase.gov/catalog/item/4f70aa71e4b058caae3f8de1.

USGS BAER (2022a). Burned Area Emergency Response (BAER). Available at: https://burnseverity.cr.usgs.gov/baer/.

USGS BAER (2022b). Mapping Burn Severity for Burned Area Emergency Response (BAER) and Monitoring Trends in Burn Severity (MTBS). Available at: https://www.mtbs.gov/baer.

USGS (2022). How do I use a scale factor with Landsat Level-2 science products? Available at: https://www.usgs.gov/faqs/how-do-i-use-scale-factor-landsat-level-2-science-products#:~:text=Surface%20Temperature%20Landsat%20Collection%202%20surface%20temperature%20has,302.6%20Kelvin%20after%20the%20scale%20factor%20is%20applied.

USGS NHD (2020). National Hydrography Dataset. Available at: https://www.usgs.gov/national-hydrography/national-hydrography-dataset.

Vicente-Serrano, S. M., Beguería, S., and López-Moreno, J. I. (2010). A Multiscalar Drought Index Sensitive to Global Warming: The Standardized Precipitation Evapotranspiration Index. *J. Clim.* 23, 1696–1718. doi:10.1175/2009JCLI2909.1

Vicente-Serrano, S. M., Camarero, J. J., Olano, J. M., Martín-Hernández, N., Peña-Gallardo, M., Tomás-Burguera, M., et al. (2016). Diverse relationships between forest growth and the Normalized Difference Vegetation Index at a global scale. *Remote Sens. Environ.* 187, 14–29. doi:10.1016/j.rse.2016.10.001

Wang, L., Diao, C., Xian, G., Yin, D., Lu, Y., Zou, S., et al. (2020). A summary of the special issue on remote sensing of land change science with Google Earth engine. *Remote Sens. Environ.* 248, 112002. doi:10.1016/j.rse.2020.112002

Wang, Y., Liu, G., and Guo, E. (2019). Spatial distribution and temporal variation of drought in Inner Mongolia during 1901–2014 using Standardized Precipitation Evapotranspiration Index. *Sci. Total Environ.* 654, 850–862. doi:10.1016/j.scitotenv.2018.10.425

Webb, A. D., Falk, D. A., and Finch, D. M. (2019). *Fire ecology and management in lowland riparian ecosystems of the southwestern United States and northern Mexico*, 140.

Williams, A. P., Cook, E. R., Smerdon, J. E., Cook, B. I., Abatzoglou, J. T., Bolles, K., et al. (2020). Large contribution from anthropogenic warming to an emerging North American megadrought. *Science* 368, 314–318. doi:10.1126/science.aaz9600

Wilson, N. R., and Norman, L. M. (2018). Analysis of vegetation recovery surrounding a restored wetland using the normalized difference infrared index (NDII) and normalized difference vegetation index (NDVI). *Int. J. Remote Sens.* 39, 3243–3274. doi:10.1080/01431161.2018.1437297

Wilson, N. R., and Norman, L. M. (2022). Five Year Analyses of Vegetation Response to Restoration using Rock Detention Structures in Southeastern Arizona, United States. *Environ. Manag.* 71, 921–939. doi:10.1007/s00267-022-01762-0

Wonkka, C. L., Twidwell, D., Bielski, C. H., Allen, C. R., and Stambaugh, M. C. (2018). Regeneration and invasion of cottonwood riparian forest following wildfire: Cottonwood restoration following wildfire. *Restor. Ecol.* 26, 456–465. doi:10.1111/rec.12577

Wu, Q., Lane, C. R., Li, X., Zhao, K., Zhou, Y., Clinton, N., et al. (2019). Integrating LiDAR data and multi-temporal aerial imagery to map wetland inundation dynamics using Google Earth Engine. *Remote Sens. Environ.* 228, 1–13. doi:10.1016/j.rse.2019.04.015

Wu, Z., Velasco, M., McVay, J., Middleton, B. R., Vogel, J., and Dye, D. (2016). MODIS Derived Vegetation Index for Drought Detection on the San Carlos Apache Reservation. *Int. J. Adv. Remote Sens. GIS* 5, 1524–1538. doi:10.23953/cloud.ijarsg.44

Yang, Z., Dominguez, F., Gupta, H., Zeng, X., and Norman, L. (2016). Urban Effects on Regional Climate: A Case Study in the Phoenix and Tucson Sun Corridor. *Earth Interact.* 20, 1–25. doi:10.1175/EI-D-15-0027.1

Zhai, Y., Roy, D. P., Martins, V. S., Zhang, H. K., Yan, L., and Li, Z. (2022). Conterminous United States Landsat-8 top of atmosphere and surface reflectance tasseled cap transformation coefficients. *Remote Sens. Environ.* 274, 112992. doi:10.1016/j.rse.2022.112992

frontiers | Frontiers in Environmental Science

TYPE Original Research
PUBLISHED 24 July 2023
DOI 10.3389/fenvs.2023.1084764

OPEN ACCESS

EDITED BY
Xiaoyang Zhang,
South Dakota State University,
United States

REVIEWED BY
Gautam Talukdar,
Wildlife Institute of India, India
Anthony Gidudu,
Makerere University, Uganda

*CORRESPONDENCE
Ce Zhang,
c.zhang9@lancaster.ac.uk

RECEIVED 30 October 2022
ACCEPTED 11 July 2023
PUBLISHED 24 July 2023

CITATION
Ojoatre S, Zhang C, Yesuf G and Rufino MC (2023), Mapping deforestation and recovery of tropical montane forests of East Africa.
Front. Environ. Sci. 11:1084764.
doi: 10.3389/fenvs.2023.1084764

Mapping deforestation and recovery of tropical montane forests of East Africa

Sadadi Ojoatre[1,2,3], Ce Zhang[1,4]*, Gabriel Yesuf[5] and Mariana C. Rufino[1,2]

[1]Lancaster Environment Centre, Faculty of Science & Technology, Lancaster University, Lancaster, United Kingdom, [2]Centre for International Forestry Research (CIFOR), World Agroforestry Centre (ICRAF), Nairobi, Kenya, [3]BeZero Carbon, Shoreditch Exchange, London, United Kingdom, [4]UK Centre for Ecology & Hydrology, Lancaster, United Kingdom, [5]Department of Geography and Environmental Science, University of Reading, Reading, United Kingdom

Deforestation poses a major threat to the tropical montane forest ecosystems of East Africa. Montane forests provide key and unique ecological and socio-economic benefits to the local communities and host diverse flora and fauna. There is evidence of ongoing deforestation and forest clearance in these montane forests although estimates diverge among different sources suggesting rates of 0.4%–3% yr^{-1}. Quantifying deforestation rates and forest disturbance is critical to design conservation and sustainable management policies for forest management. This study quantified the rate of deforestation and forest recovery over the last three decades for the Mau Forest Complex and Mount Elgon forests in Kenya and Uganda using Landsat time-series satellite imagery. With the analysis, classification accuracies of 86.2% and 90.5% (kappa 0.81 and 0.88) were achieved for the Mau Forest Complex and the Mt Elgon forests, respectively. 21.9% (88,493 ha) of the 404,660 ha of Mau forest was lost at an annual rate of −0.82% yr^{-1} over the period between 1986 and 2017. More positively, 18.6% (75,438 ha) of the forest cover that was disturbed during the same period and is currently undergoing recovery. In Mt Elgon forest, 12.5% (27,201 ha) of 217,268 ha of the forest cover was lost to deforestation at an annual rate of −1.03% yr^{-1} for the period between 1984–2017 and 27.2% (59,047 ha) of the forest cover disturbed is undergoing recovery. The analysis further demonstrated agriculture (both smallholder and commercial) was the main driver of forest cover loss in Mau forest, accounting for 81.5% (70,612 ha) of the deforestation, of which 13.2% was due to large scale and 68.3% was related to the smallholders. For the Mt Elgon forest, agriculture was also the main driver accounting for 63.2% (24,077 ha) of deforestation followed by the expansion of human settlements that contributed to 14.7% (5,597 ha) of forest loss. This study provides accurate and novel estimates of the rate of deforestation for the Mau forest complex and Mt Elgon forest ecosystems. These rates are higher than previously estimated and recent deforestation has been identified, which provides a quantitative basis for forest restoration programs and to design conservation policies.

KEYWORDS

deforestation, forest clearance, montane tropical forests, land use change, forest recovery

1 Introduction

Deforestation poses a global challenge to humanity. This is due to its vast contribution towards greenhouse gas (GHG) emissions to the atmosphere and the impact that forest loss has on the hydrological cycle globally. These impacts include disruption of movement of water in the atmosphere, shifts in precipitation and hence leading to draught among others. Forests regulate water flows in catchments by playing an important role in the interception of rainfall, reducing runoff, attracting rainfall through their high evapotranspiration rates, and contributing to condensation (Sheil and Murdiyarso, 2009; Sheil, 2018). Forests also contribute to cloud formation by releasing biogenic volatile compounds into the atmosphere, which further accelerate condensation (Ellison et al., 2017), contrarily deforestation increases the surface temperature leading to increased evaporation and reduced evapotranspiration (Lawrence and Vandecar, 2015). Since 1990, an estimated total of 420 million hectares of forests have been lost globally because of conversion to other land uses, most notably agriculture and human settlements (FAO and UNEP, 2020). Between 2015 and 2020, the global rate of deforestation was estimated at 10 million ha yr^{-1} down from 16 million ha yr^{-1} in the 1990s (FAO and UNEP, 2020). Between 2001 and 2019, forest clearing resulted in global gross GHG emission of 8.1 ± 2.5 GtCO2e yr^{-1}, yet tropical forests contribute most (5.3 ± 2.4 GtCO2e yr^{-1}) to the removal of atmospheric carbon dioxide (CO_2) emissions (Harris et al., 2021).

Despite the importance of tropical forests in regulating climate and supporting the hydrological systems, their cover has dropped from 1,966 million ha in 1990 to 1,770 million ha in 2015 (FAO, 2015a; Keenan et al., 2015; MacDicken, 2015). Large areas of tropical forests have been deforested between 2000 and 2012, amongst which 20% were in sub-Saharan Africa (Kim, Sexton, and Townshend, 2015; Mitchard, 2018). The tropical forests in sub-Saharan Africa are facing a rapid loss to deforestation and degradation at an estimated annual conversion rate of approximately 0.4%–0.5% yr^{-1} (Mayaux et al., 2005; FAO, 2015b). The increasing demand for land for agriculture and human settlements means that forests are the main target for conversion (Kissinger et al., 2012; Curtis et al., 2018). The forest loss rates have been reported over global and continental scales, such as through the Global Forest Change (GFC) platform and Global Forest Watch (Hansen et al., 2013). The GFC data shows forest gain and loss from 2001 and these forest cover change estimates provide the global perspective of the forest cover change with accuracy that differs across regions. The usefulness of global datasets at a local scale has not been examined closely for East Africa (Hamunyela et al., 2020), although literature suggest that GFC underestimates forest loss rates at a local scale and varies spatially (Milodowski, Mitchard and Williams, 2017; Yesuf, Brown and Walford, 2019). Specifically, the GFC dataset provides estimates of the scale and magnitude of forest cover change as a gain or loss (Hansen et al., 2013), and although these estimates are valuable there is a need to distinguish permanent losses due to deforestation and to identify areas under-recovery over time through forest clearing events, i.e., fragmentation, logging, shifting cultivation or fires (Curtis et al., 2018; Grantham et al., 2020). Reliable estimates for the rates of deforestation for Africa are lacking at both national and regional levels (Achard et al., 2014). Understanding the magnitude and spatial distribution of deforestation hotspots is essential to monitor, protect and manage tropical forest ecosystems sustainably (Hansen et al., 2008). Quantifying the rates of deforestation and understanding the underlying causes is a critical component for designing and developing evidence-based policies to tackle forest cover loss, in order to support the implementation of national or international programs such as REDD+ (Entenmann et al., 2014).

In East Africa, the annual rates of deforestation at the national level are under debate and estimated at 0.05% yr^{-1} (Kenya) for the period 1990–2010 and 0.4%–3% yr^{-1} (Uganda) in 2016 (Mwangi et al., 2018). These rates are contentious and disparity in estimates arises from different forest types, measurements, definition of forest cover, and reporting methods (MacDicken, 2015). This research aims to establish robust estimates of forest change for East African montane forests, focusing on two important forests in Kenya and Uganda (Mau Forest Complex and Mt Elgon forest) with respects to their ecological and socio-economic values (WWF, 2007; Cavanagh, 2017; KEFRI, 2018). The estimates of deforestation in these two important forests involve the forest cover change, the underlying drivers, as well as the extent of forest recovery.

Previous research on montane forests focused on land-use change over specific blocks of Mau forest complex and Mt Elgon forests (e.g., Baldyga et al., 2007; Were et al., 2013). Although some studies assessed land use and land cover change and the underlying drivers for the Mau forest complex (e.g., Ayuyo and Sweta, 2014; Kimutai and Watanabe, 2016; Swart, 2016), the rates of deforestation, forest clearing, and the rates of forest recovery were not investigated.

Different remote sensing tools and methods are used to detect, monitor, and map forest loss due to deforestation and other forms of forest Clearance. For example, Breaks For Additive Season and Trend (BFAST) uses Landsat time-series data (DeVries et al., 2015), TimeSync (Cohen et al., 2010), spectral forest recovery trajectories (Frazier et al., 2015), and change detection approach (Margono et al., 2012). In this study we use the freely available satellite data (Landsat time-series) and carry out change detection to map deforestation and recovery resulting from forest clearance. We defined deforestation according to Hirata et al. (2012) as "direct human-caused conversion of forested land to non-forested land". Therefore, our main goal was to determine the rate of deforestation (loss) and forest recovery (gain) in Mau forest complex and Mt Elgon forest by analysing spectral differences in Landsat imagery from 1984 to 2017.

The specific research objectives include.

(i) to identify the areas where deforestation has occurred.
(ii) to detect when the first and last deforestation took place.
(iii) to quantify the annual rate of deforestation and recovery for montane forests.

To achieve these objectives, the study used the existing and available Landsat time-series from L4/5 TM, Landsat 7 and Landsat 8 OLI data collected between December–March each year from 1984 to 2017 for the Mt Elgon forest and 1986 to 2017 for Mau forest complex to examine forest cover change. Due to limitation of images for some years, the average for the available data was used. Maximum likelihood classification was undertaken, and change detection was carried out between the available time spans.

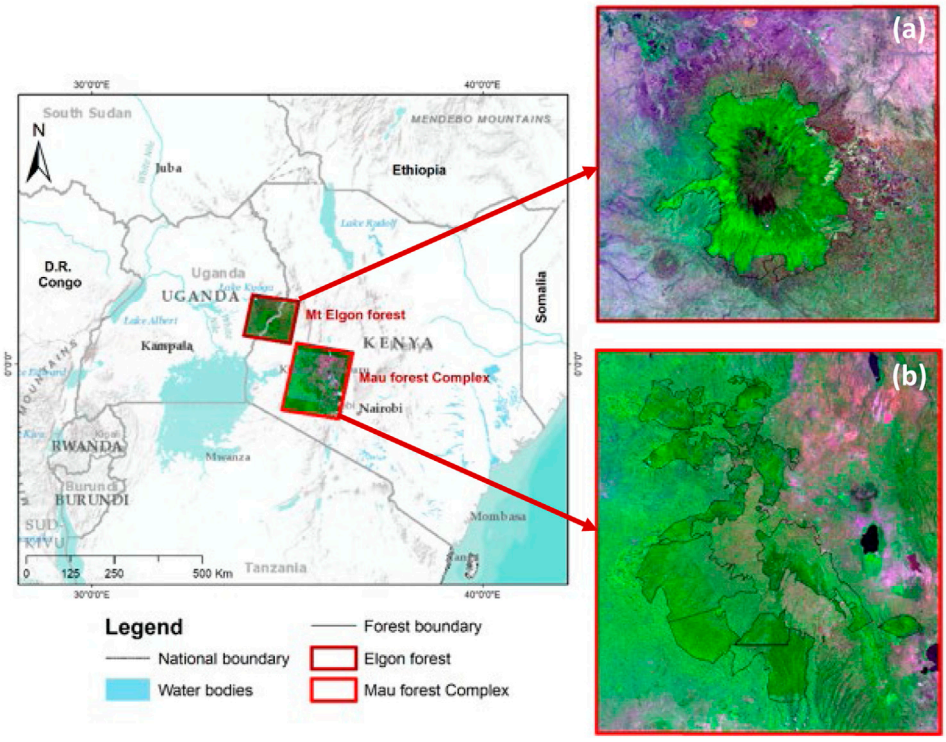

FIGURE 1
Location of the Mau forest complex and Elgon forest in East Africa. **(A)** Map showing the official boundaries of the Mt Elgon forests (Scott, 1998) and **(B)** Map showing the official boundaries of the Mau forest complex (Government of Kenya, 2017).

2 Methodology

2.1 Study area

The study was carried out in the Mt Elgon forest and Mau forest complex as indicated in Figures 1A, B respectively which are classified as tropical montane forest and are collectively referred to as the Water Towers of East Africa. The tropical montane forests are forest with varying elevation and are characterized with Afroalpine vegetation from over 1,000 m elevation (White, 1983). The Mau forest Complex is approximately 1,800–3,000 m elevation and the ecosystem is approximately 4,088.93 km^2 (408,893 ha) and comprises several forest blocks (22 blocks) such as Narok, Masaya Mau, Eastern, and Western Mau, Southern to Southwest Mau, and Transmara regions among others (Crafford et al., 2012; Chrisphine et al., 2015a). Mau forest complex is classified as an Afromontane vegetation type comprising both closed deciduous forest in the lower elevation and afro alpine vegetation such as Fern and moorland at the top of the mountain (Ojoatre, 2022). This forest is the major catchment area for 12 rivers draining into Lake Baringo, Nakuru, Turkana, Natron, and the Trans-boundary Lake Victoria shared by Kenya, Uganda, and Tanzania and therefore has been referred to as the Water Tower of East Africa (Olang and Kundu, 2011; Chrisphine et al., 2015b).

Mt Elgon forest is located approximately 100 km northeast of Lake Victoria (Penny Scott, 1998) and it is a protected area that covers approximately 2,045 km^2 (Mukadasi et al., 2007). It is a volcanic mountain with five (5) major peaks located in Eastern Uganda and Western Kenya as shown in Figure 1A. The 5 major peaks include Wagagai with 4,321 m above sea level, Mubiyi (4,211 m), Masaba (4,161 m) all these are predominantly located in Uganda meanwhile Koitobos (4,222 m) is in Kenya and Sudek which stands at (4,302 m) is located on the Kenya/Uganda border (Wielochowski and West Col Productions., 1989). Mt Elgon forest is classified as a dense closed canopy montane forest at the lower elevations and the top is characterized as moorland. Uganda Wildlife Authority currently manages Mt Elgon forest and the Nation Park since the merging of the Uganda National Parks (UNP) with the Game department. On the Kenya side, the forest is co-managed by Kenya Wildlife Service (KWS) focusing on the wildlife and Kenya Forest Service (KFS) that focuses on the forest reserve (Ongugo, et al., 2001).

The East African montane forests are found in moderate to high altitudes comprising of several separate mountain areas above 2,000 m spanning from South Sudan through Uganda and Kenya to Northern Tanzania along the Rift valley (EAC, UNEP, and GRID-Arendal, 2016).

2.2 Data sources and processing

Landsat satellite imagery acquired from the USGS archives for the study area from Path/Raw 170/59 (for Mt Elgon forest), and 169/60–61 for the Mau forest complex as indicated in Table 1. Available data from Landsat 4 and 5 Thematic Mapper [TM], Landsat 7 Enhanced Thematic Mapper Plus

TABLE 1 Landsat time-series data for the Mt Elgon forest area and Mau forest complex.

Mt. Elgon forest		Mau forest complex	
Date of acquisition	Sensor	Date of acquisition	Sensor
31/12/1984	L5 TM	28/01/1986	L5 TM
08/03/1986	L5 TM	01/03/1989	L4 TM
27/03/1987	L5 TM	21/01/1995	L5 TM
18/02/1988	L4 TM	12/02/2000	L7 ETM+
12/01/1995	L5 TM	14/02/2001	L7 ETM+
06/03/2000	L7 ETM+	01/02/2002	L7 ETM+
05/02/2001	L7 ETM+	04/02/2003	L7 ETM+
07/01/2002	L7 ETM+	30/01/2010	L5 TM
10/01/2003	L7 ETM+	26/02/2014	L8 OLI
21/01/2010	L5 TM	17/03/2015	L8 OLI
05/03/2014	L8 OLI	16/02/2016	L8 OLI
03/01/2015	L8 OLI	17/01/2017	L8 OLI
23/02/2016	L8 OLI		
09/02/2017	L8 OLI		

10.3389/fenvs.2023.1084764

TABLE 2 Land cover classes and the scheme used in the study adopted from similar reported studies in the same current study area as well as the reported vegetation classification in Eastern Africa.

Land cover/land use class	Description (FAO/National classification and vegetation map for Africa)
Forest (F)	Trees with closed canopy visible on high-resolution imagery. With height >2 m, canopy cover of >30%
Agriculture large-scale (LA)	Large scale commercial agriculture including tea estates of >2 ha, large scale irrigated and mechanized agriculture
Agriculture smallholder (SA)	Smallholder agriculture (Small-scale) mainly rainfed with fields of <2 ha for subsistence farming purposes
Rangeland (R)	This involves open land cultivated with pasture and grasslands
Settlements/urban (SU)	Bare land, developed with high density especially urban areas, infrastructure, and markets with limited farmlands
Moorland (M)	Extensive low-growing vegetation characterized with heath in high altitude >1,500 m above sea level commonly referred to as Afro-alpine vegetation
Water (W)	Areas that are occupied with open water bodies (both natural and man-made) such as lakes

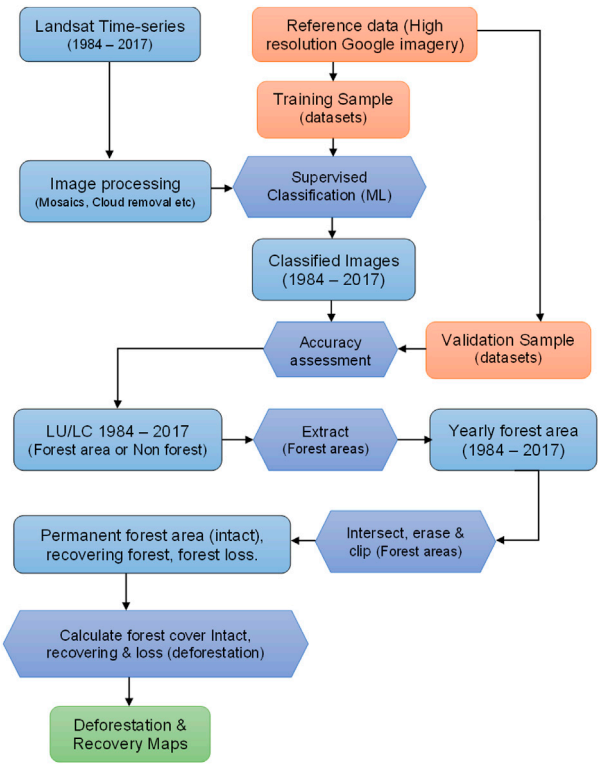

FIGURE 2
Flow chart showing a summary of the methodology that was undertaken in the current study.

[ETM+], and Landsat 8 OLI from 1984 to 2017 (Mt Elgon forest) and 1986 to 2017 (Mau forest Complex) were collected during dry months (from December to March) for both sites obtained. The images for the years from 1989 to 1994, 1996 to 1999 for the two-study areas generally are missing from the USGS archives. From 2004 to 2009, images from Landsat 7 were affected by SLC failure which rendered the images with a data loss (Andréfouët et al., 2003). For the images missing from Landsat 8, were largely because of cloud cover in the study area.

Forest boundaries created in 2009 for the Mau forest Complex were obtained from the Kenya Forest Service (KFS) and for the Mt Elgon forest from the National Forestry Authority (NFA) for the part of Mt Elgon forest located in Uganda. The Mt Elgon forest boundary was demarcated in 1968 for the Kenyan side and in 1992 for the Uganda side (Scott, 1998).

The Landsat data were processed and classified using the steps indicated in Figure 2. The processing software used was ArcGIS for Desktop and ENVI Software. After the classification process indicated in Figure 2. The yearly forest areas were extracted from the classified imagery and analysed using Microsoft excel software. The maps were produced using the ArcGIS software.

Global Forest Change (GFC) dataset from 2000 to 2017 (version 1.5) was also used (http://earthenginepartners.appspot.com/science-2013-global-forest; Hansen et al., 2013). The results of the GFC data were compared with the results for the forest loss from supervised classification results of the Landsat time-series for the period 2001–2017 which corresponds with the GFC data.

GFC quantifies the trend in forest cover change (gain and loss) from the year 2000. GFC datasets have being reported to present limitations at the local scale (Sannier et al., 2016; Hamunyela et al., 2020). In this study, the classification results for years from 2000 were extracted to be assessed with corresponding findings from GFC for the Mau forest Complex and Mt Elgon forest.

2.3 Image analysis and classification

The images were classified in to 7 (seven) classes, namely: Forest, Non forest, Agriculture (Smallholder and Large scale), Rangeland among others. Supervised classification with the Maximum Likelihood (ML) algorithm was undertaken and change detection was performed to assess forest cover change. The ML classifier considers the centers of the clusters (class), shape size, and the orientation of the clusters by calculating the statistical distance based on the mean values and covariance matrix of the clusters (Tolpekin and Stein, 2012). The acquired Landsat imagery shown in Table 1. Were processed, classified, analyzed and the results were compared with the forest cover change from GFC data for the corresponding period. The supervised classification approach used in the current study requires reference data

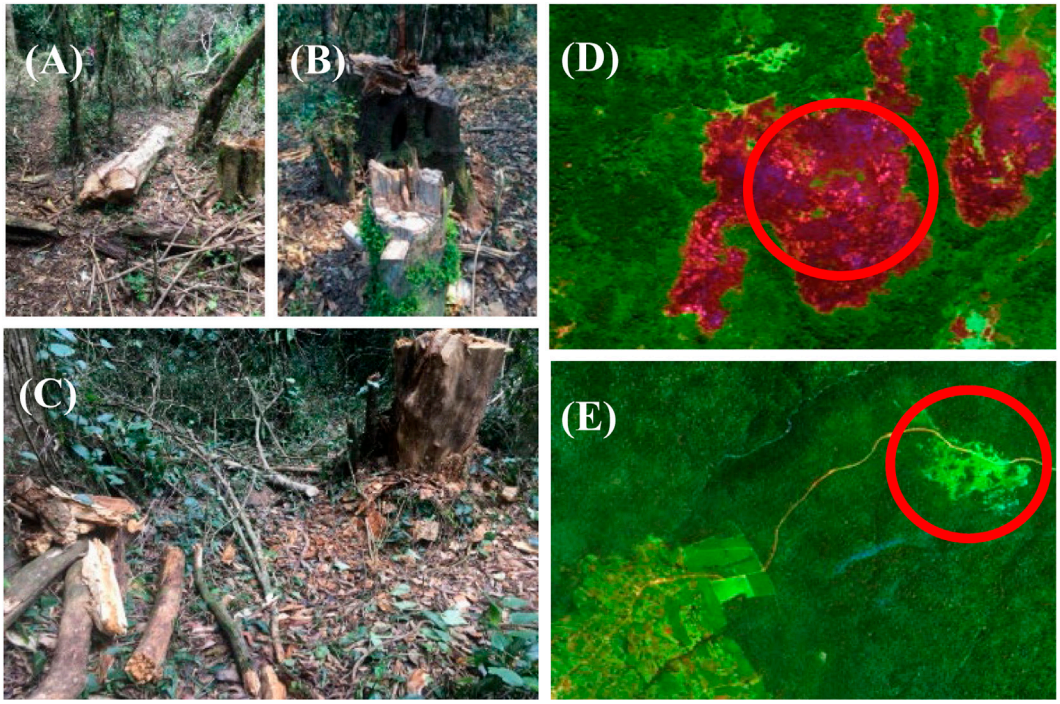

FIGURE 3
Examples from Mau forest complex of areas that show deforestation as a result of clearance for logs and firewood **(A–C)**. Deforestation resulting from fire indicated by the red circle **(D)**, forest recovery following clearance from encroachment **(E)**. The high-resolution Google imagery showing **(D, E)** are dated February 2017.

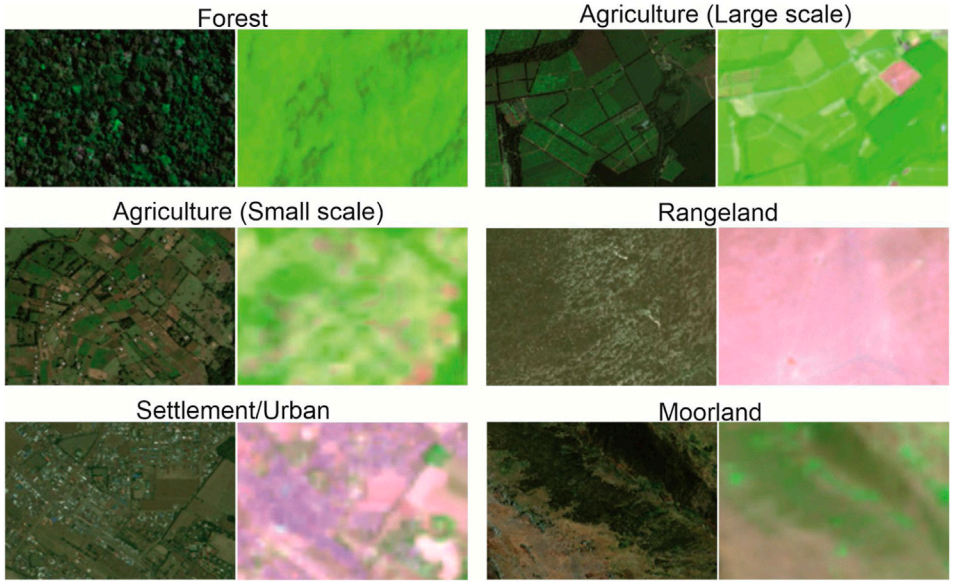

FIGURE 4
Training and validation samples based on visual interpretation from High-resolution Google imagery and Multispectral Landsat images. The figure shows the Land cover class identification and sample from the high-resolution imagery and Landsat TM, ETM+ (5-4-3 spectral band combination), and Landsat 8 OLI (6-5-4 spectral band combination) for each land cover class used for the classification scheme.

for training and validation. High-resolution Google Earth imagery dated February 2017 available shown in Figures 3D, E, together with field survey (Figures 3A–C) was used to acquire the reference data for training and validation of the classified Landsat data (Fortier et al., 2011; Zhu, Woodcock and Olofsson, 2012; Rutkowska et al., 2014).

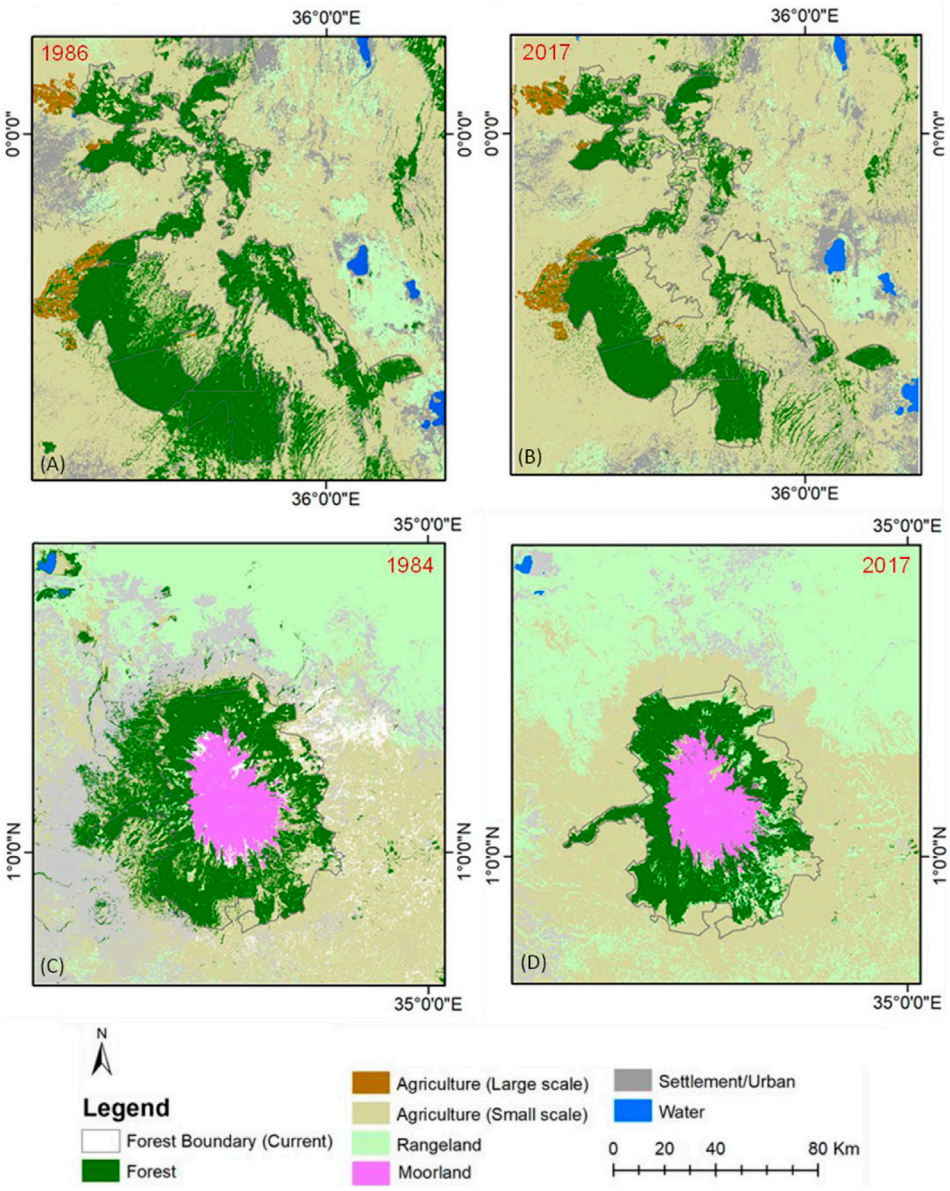

FIGURE 5
Land cover map 1986 **(A)**, 2017 **(B)** for the Mau forest complex, 1984 **(C)** and 2017 **(D)** for the Mt Elgon forest showing forest cover change within and outside the official boundaries of the two montane forests.

Classification accuracy was assessed using the error matrix (confusion Matrix) with the high resolution (50 cm) Google Earth images used as the reference data (Strahler et al., 2006; Olofsson et al., 2014; Vogelmann et al., 2017).

To map forest cover change, seven land cover classes (with the corresponding land use) were defined, including forest, agriculture (large scale), agriculture (small scale), rangelands, settlement/urban, and moorland as described in Table 2. The land use and land cover classes were defined based on classification schemes in previous studies (Houghton et al., 2012; Sassen et al., 2013; Ayuyo and Sweta, 2014; FAO, 2014; Mugagga et al., 2015). Additionally, the vegetation map of the Eastern Africa region (VECEA Team, 2020) was used for the class definition alongside the previous studies.

Visual interpretation of the high-resolution Google imagery and the Landsat multispectral image (Figure 4) was undertaken to obtain 500 training and validation samples (split into 60% for training and 40% for validation) for the supervised classification of the multispectral Landsat images.

2.4 Forest cover change, deforestation and recovery

Forest cover changes were quantified from the classified satellite images for the two study areas. The classification was undertaken on selected images with at least <10% cloud cover during the dry months (December to March) for the available images from 1986 to 2017 for the

TABLE 3 Accuracy assessment for the supervised classification of the Mau forest complex (a) and the Mt Elgon forest (b).

(a) The Mau forest complex									
Overall accuracy = 86.2%, kappa coefficient = 0.81									
Class	F	AL	SA	R	B	W	Total	P (%)	U (%)
F	89.96	0.52	0.21	0.00	0.00	0.00	21.23	89.96	99.45
AL	0.12	88.19	0.93	0.00	0.80	0.00	6.16	88.19	93.42
SA	9.83	4.19	91.51	36.01	0.08	0.00	42.91	91.51	82.87
R	0.00	0.24	4.03	44.51	0.00	0.00	7.48	44.51	78.86
B	0.09	6.86	3.32	19.48	99.12	0.07	6.27	99.12	30.64
W	0.00	0.00	0.00	0.00	0.00	99.93	15.96	99.93	100.0
(b) Mt Elgon forest									
Overall Accuracy = 90.50%, Kappa Coefficient = 0.87									
Class	F	A	R	M	B	W	Total	P (%)	U (%)
F	100	0.00	0.00	0.00	0.00	0.00	19.45	100.0	100.0
A	0.00	67.16	0.55	0.00	1.54	0.00	18.88	67.16	98.92
R	0.00	22.66	99.45	0.00	3.82	0.00	31.44	99.45	79.45
M	0.00	0.88	0.00	100	0.00	0.00	20.29	100.0	98.80
B	0.00	9.30	0.00	0.00	94.64	0.00	6.59	94.64	60.77
W	0.00	0.00	0.00	0.00	0.00	100	3.35	100.0	100.0

F, Forest; AL, Agriculture (Largescale); SA, Agriculture (Smallholder); R, Rangeland; B, Bare land (Open Land) and W, Water; P, Producer accuracy and U, User accuracy.
F, Forest; AL, Agriculture (Largescale); SA, Agriculture (Smallholder); R, Rangeland; B, Bare land (Open Land) and W, Water; P, Producer accuracy and U, User accuracy.

Mau forest complex and 1984 to 2017 for the Mt Elgon forest shown in Table 1. To quantify forest cover change over time, the multispectral images and the high-resolution imagery were visually interpreted. The areas showing deforestation (loss) and forest recovery (gain) were identified as shown in Figures 3D, E and Figure 4. The visual interpretation process was then followed by the supervised classification using the classification scheme and classes that were developed as shown in Table 2.

From the classified imagery, forest class for each year was extracted. The forest area for 1986 (Mau forest complex) and 1984 (Mt Elgon forest) were used as masks. The masks were then used to identify and calculate (i) areas that were lost and never recovered (deforestation), (ii) areas that were lost or disturbed at some point in the time series but and were under-recovery by 2017, and (iii) forest areas that stayed forest since the beginning of the time series as permanent (intact) forest. To further quantify the areas that were permanent, recovering, and deforested, the current forest boundaries for the Mau forest complex and Mt Elgon forest were used to clip and estimate area changes within the forest boundary for both forests.

2.5 Rate of deforestation

The rate of deforestation was calculated from the yearly detected change in forest cover. This study adopts the method by Puyravaud (2003), who proposed the use of the mean annual rate of change of forest cover over time. The method has been widely used to quantify the rate of deforestation and land cover change across the tropics (e.g., Schulz et al., 2010; Grinand et al., 2013; Reimer et al., 2015). The rate of deforestation (Eqn. 1) is based on the change analysis and the method accounts for variations in date for the image acquisitions.

Equation 1: Rate of deforestation

$$r = \left(1/\left(T_2 - T_1\right)\right) \times \ln\left(A_2/A_1\right)$$

where: r = the deforestation rate per year (% yr^{-1}).

T_1 = Year for the beginning of the time step (initial year).

T_2 = Year for the end of the time step (final year).

A_1 = Forest area at the beginning of the time step (initial year).

A_2 = Forest area at the end of the time step (final year).

Classified images for the Mau forest Complex and Mt Elgon forest were used to determine the change in land cover from forest to the other land cover/land use types (gross loss) and Other Land covers to forest (gross gain), the net change was calculated by subtracting the Gross Loss from the Gross Gain for the timespans based on the available imagery. To determine the transition of change from forest to other land covers/land use types, a matrix table for the classified land cover/use types was generated and the change areas were obtained. To determine the rate of deforestation, the current official forest boundaries for

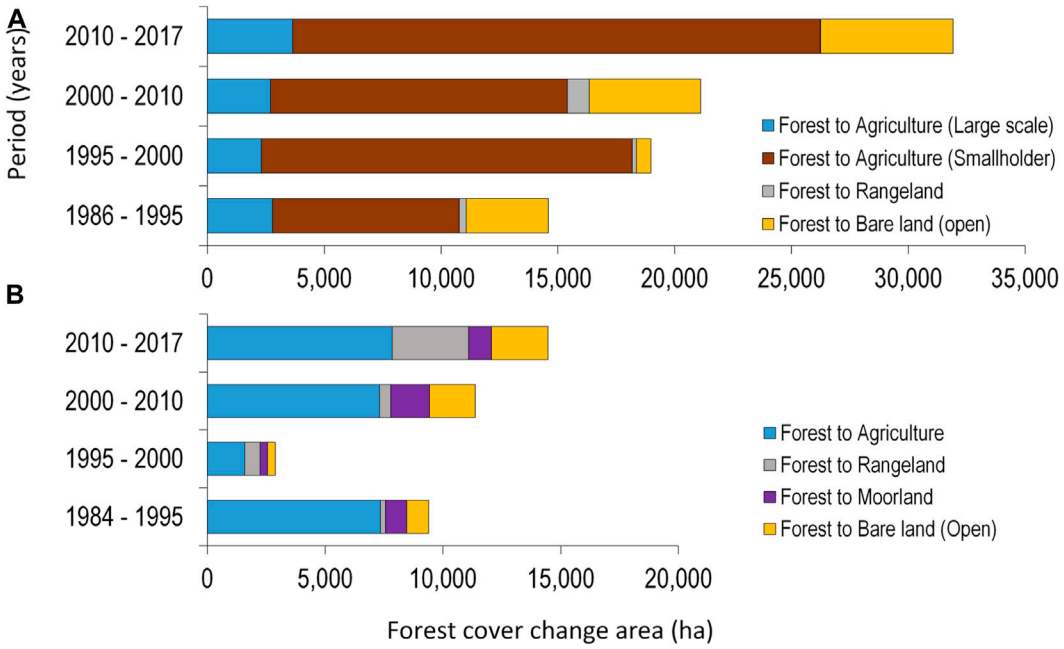

FIGURE 6
Land use change transitions from forest to other land cover, i.e., agriculture (large scale), agriculture (small-scale), rangeland, moorland, and bare land (open) in **(A)** the Mau forest complex and **(B)** Mt Elgon forest.

both Mt Elgon forest and the Mau forest complex were used to carry out change detection to identify areas that were deforested.

3 Results and analysis

3.1 Land cover classification and forest cover change

Land cover and forest cover change in the Mau forest complex are presented for the period 1986–2017 and the Mt Elgon forest for the period 1984–2017 (Figure 5). Seven land cover classes were identified based on classification scheme in Table 2. Overall classification accuracy of 86.2% with Kappa coefficient of 0.81 was attained for the Mau forest complex and 90.5% (Kappa coefficient of 0.87) for the Mt Elgon forest as indicated in Tables 3A, B. In the Mau forest complex, rangelands were classified with the lowest producer accuracy (P) of 44.51% and the Settlements/Urban were classified with a lower user accuracy (U) of 30.64%. For the Mt Elgon forest, agriculture (A) had the lowest producer accuracy of 67.16% and the open/bare land class had the lowest user accuracy of 60.77%. The low producer accuracy of Rangeland was largely because the images used in the classification were obtained during the dry months of the study area hence rangelands appear bare because the grasses have dried, and some areas are burnt. While the user accuracy of the bare is high because areas that are rangelands because the dry season would sometimes appear like bare land with no vegetation. This is why the producer for rangelands is low and user accuracy for bare land were also low. Meaning areas that are rangelands are seen as bare in the classification and areas that are rangeland are classified as bare.

The analysis shows that in the Mau forest complex, forest areas that existed outside the current forest boundary of 2009 were converted to mainly agriculture both small and large scale. For the Mt Elgon forest, agriculture was also the main land cover/use to which forest area was lost.

The results show that 81.5% (70,612 ha) of forest cover was lost mainly to agriculture between 1986 and 2017, of which 13.2% (11,440 ha) can be attributed to large scale agriculture and 68.3% (59,172 ha) to smallholder agriculture in the Mau forest complex as shown in Figure 6A. For the Mt Elgon forest, agriculture was also the main land cover to which forest was lost accounting for 63.2% (24,077 ha) followed by settlement at 14.7% (5,597 ha) as indicated in Figure 6B.

From the gross changes (loss and gain), net forest cover change was established for all the years based on the available imagery for the Mau forest complex as shown in Figure 7A and for the Mt Elgon forest as indicated in Figure 7A.

3.2 Forest cover change from supervised classification

The forest cover loss in the Mau forest complex was assessed for the period 1986 to 2017 and the Mt Elgon forest for the period 1984 to 2017 using supervised classification (maximum likelihood classifier) and compared to the estimates from GFC for the period 2000–2017 for the same period as the GFC datasets are only available from the year 2000. The results indicate that in the period 2000–2017, GFC detected a loss of 17.0% (68,848 ha) out of the 404,660 ha of forest cover loss in the Mau forest complex and

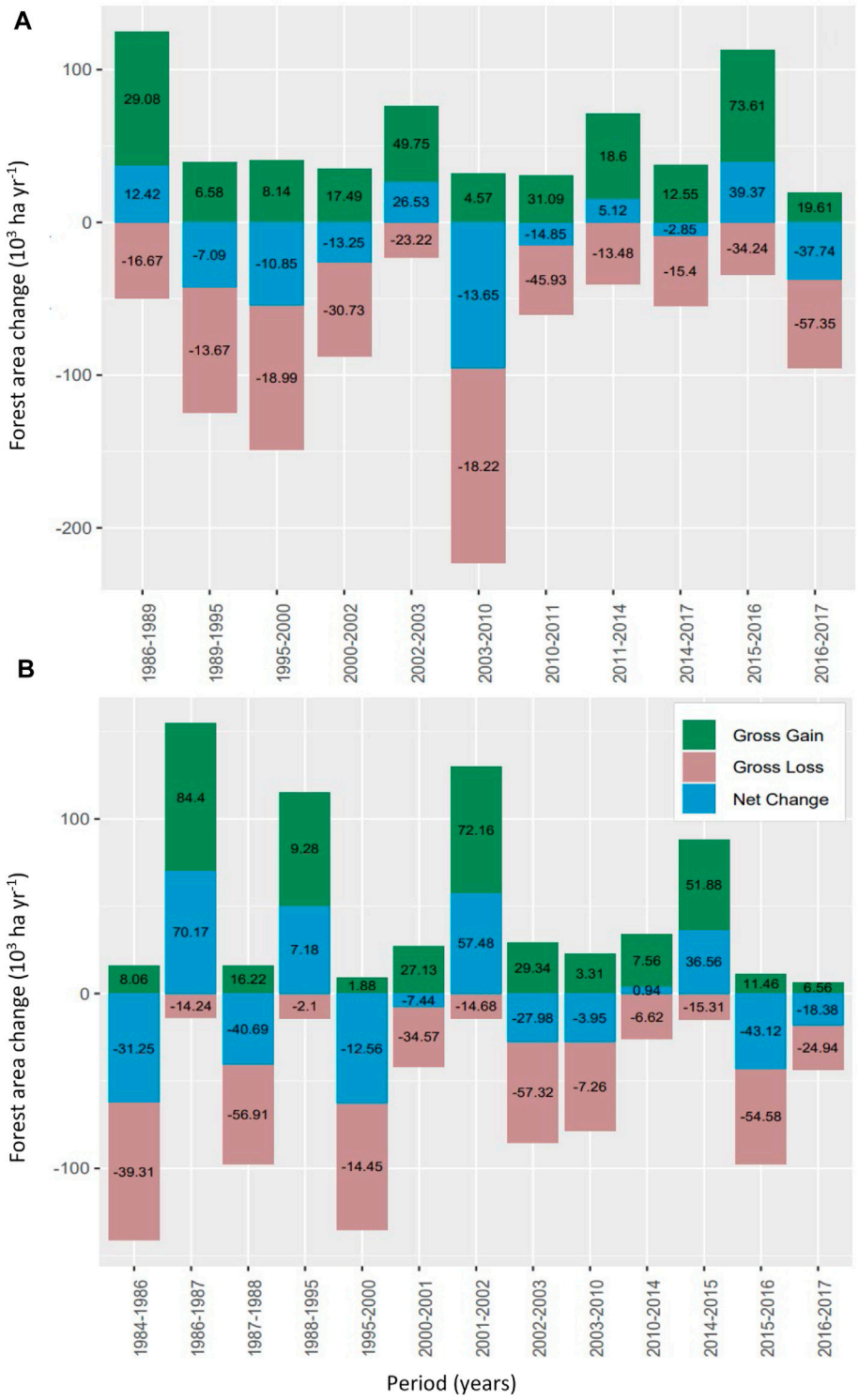

FIGURE 7
Changes in forest area for the various periods (1984/1986–2017) for the Mau forest complex **(A)** and Mt Elgon forest **(B)**. Net change (in blue) is the difference between Gross gain and Gross loss. The bars represent the total change for each period while the values represent the annual change within the periods. A negative net result indicates overall forest conversion to other land covers.

5.3% (11,501 ha) of the 217,268 ha of forest loss in the Mt Elgon forest. The analysis conducted in this study with supervised classification from the same period (2000–2017) estimated similar overall figures for the Mau forest complex with 16.8% (68,155 ha) and larger forest loss with 7.6% (16,496 ha) for the Mt Elgon forest as presented in Table 4.

TABLE 4 Estimates of forest cover loss using Supervised Classification (ML) compared to the GFC data for the Mau forest complex (a) and the Mt Elgon forest (b) for the period 2000–2017.

Period (2000–2017)	Mau forest complex				Mt Elgon forest			
	ML		GFC		ML		GFC	
	Area (ha)	%	Area (ha)	%	Area (ha)	%	Area (ha)	%
Deforestation	68,155	16.8	68,848	17.0	16,496	7.6	11,501	5.3
Remained forest	282,779	69.9	276,446	68.3	120,497	55.5	166,356	76.6
Non-forest	53,668	13.3	59,308	14.7	80,275	37.0	39,411	18.1
Total	404,602	100	404,602	100	217,268	100	217,268	100

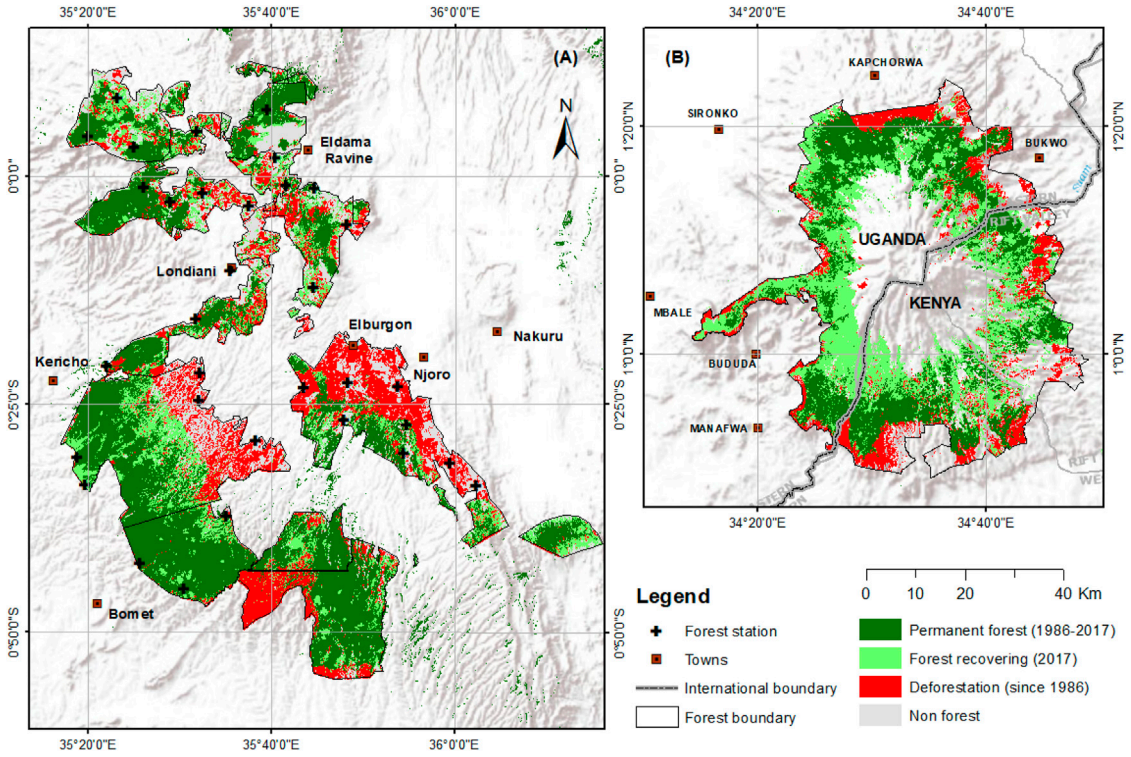

FIGURE 8
Forest cover change from 1984 (Mt Elgon forest) and 1986 (Mau forest Complex) to 2017 showing areas that remained forest throughout the time series analyzed, the forest that was disturbed and is currently undergoing recovery by 2017, and forest that has been permanently lost to deforestation in the Mau forest complex **(A)** and the Mt Elgon forest **(B)**.

TABLE 5 Forest cover change in the Mau forest Complex and Mt Elgon forest calculated from classified Landsat imagery from 1984 to 2017 (Mt Elgon forest) and 1986–2017 (Mau forest complex) using the supervised classification and change detection method.

Forest cover	Mau forest complex		Mt Elgon forest	
	Area (ha)	%	Area (ha)	%
Permanent forest (1984–2017)	172,250	42.6	52,369	24.1
Deforested area (2017)	88,493	21.9	27,201	12.5
Forest under recovery (2017)	75,438	18.6	59,047	27.2
Non-forest	68,479	16.9	78,651	36.2
Total	**404,660**	**100**	**217,268**	**100**

TABLE 6 Observed forest cover loss in Mau forest complex (a) and Mt Elgon forest (b) within the official forest boundaries for the Mau Forest Complex and Mt Elgon forest.

Time [T1]	Time [T2]	Period (T2-T1)	Area (ha) [A1]	Area (ha) [A2]	Def [period] (ha)	Deforestation rate yr^{-1} [%]
Mau forest complex (a)						
1986	1989	3	336,181.3	334,563.3	1,618.0	−0.2
1989	1995	6	334,308.3	330,095.2	4,213.0	−0.2
1995	2003	8	330,095.2	285,342.4	44,752.8	−1.8
2003	2010	7	285,342.4	257,817.4	27,525.0	−1.5
2010	2014	4	257,817.4	253,223.4	4,594.0	−0.5
2014	2017	3	253,223.4	247,688.0	5,535.4	−0.7
Average						−0.8
Mt Elgon forest (b)						
1984	1988	4	138,350.0	118,904.4	19,445.6	−3.8
1988	1995	7	118,904.4	116,699.6	2,204.8	−0.3
1995	2003	8	116,699.6	121,138.5	−4,438.9	0.5
2003	2010	7	121,138.5	121,732.9	−594.4	0.1
2010	2014	4	121,732.9	116,552.9	5,180.0	−1.1
2014	2017	3	116,552.9	111,149.0	5,403.9	−1.6
Average						−1.0

TABLE 7 Observed forest cover gain (recovery) in the Mau forest complex and Mt Elgon forest within the official forest boundaries for the Mau Forest Complex and Mt Elgon forest.

Ecosystem (forest)	Time [T1]	Time [T2]	Period (T2 - T1)	Area recovered/Gain (ha)	Recovery rate yr^{-1} [%]
Mau forest Complex	1986	1989	3	7,710.20	3.41
	1989	1995	6	3,803.70	0.84
	1995	2003	8	18,573.10	3.08
	2003	2010	7	10,565.10	2.00
	2010	2014	4	15,562.90	5.16
	2014	2017	3	19,222.90	8.49
Mt Elgon forest	1984	1988	4	8,239.40	3.49
	1988	1995	7	6,353.90	1.54
	1995	2003	8	19,850.40	4.20
	2003	2010	7	9,075.80	2.20
	2010	2014	4	6,825.20	2.89
	2014	2017	3	8,702.40	4.91

3.3 Forest cover change, deforestation, and recovery

Forest cover changes from 1986 to 2017 for the Mau forest complex and the Mt Elgon forest from 1984 to 2017 within their respective official forest boundaries are shown in Figure 8. The hotspots, forest blocks, and areas that are more pronouncedly affected by deforestation were the Southwestern Mau, Eastern Mau, Londiani (Western Mau), and Maasai Mau. For the Mt Elgon forest, deforestation was more pronounced in the Kapchorwa area of Uganda and the Southern part of the Mt Elgon forest on the Kenyan side of the forest. The result also revealed the specific areas in the two montane forests where forest cover was lost to other land cover types (deforestation) within the study period and areas that were undergoing forest recovery.

The analysis of the area change in Figure 8, shows that during the 1986–2017 period, 42.6% (172,250 ha) of the Mau forest complex remained forest, 21.9% (88,493 ha) of the forest area was lost to deforestation and 18.6% (75,438 ha) was disturbed and is currently at different stages of recovery as shown in Table 5. For the Mt Elgon forest, 24.1% (52,369 ha) of the forest remained forest between 1984 and 2017, and 12.08% (26,250 ha) of the forest area was deforested and 27.6% (59,998 ha) was disturbed and is currently undergoing recovery as indicated in Table 5.

3.4 Rates of deforestation and recovery

The multi-temporal assessment of the rate of deforestation covers 31 years (the Mau forest complex) and 33 years for Mt Elgon forest as shown in Tables 6A, B respectively. The results indicate that an estimated 88,493 ha of the Mau forest complex was lost to deforestation at an annual rate of −0.86% for the period 1986–2017 and an estimated 27,201 ha for the Mt Elgon forest at a rate of −1.03% during the same period. The recovery rates for the Mau forest complex and the Mt Elgon forest were estimated at an average of 2,434 ha yr^{-1} and 1,789 ha yr^{-1}, respectively presented in Table 7.

Deforestation rates were higher for the Mau forest Complex between 1995 and 2003 where 44,753 ha were lost and in the period between 2003 and 2010 when 27,525 ha of the forest cover were lost as shown Table 6A. For the Mt Elgon forest, deforestation was high between 1984–1988 when 19,446 ha of the forest were lost as shown in Table 6B.

4 Discussion

4.1 Mapping and classification of forest cover change

This study produced a new set of maps that show the extent of intact forest and degraded forest following clearance since 1984 for the two montane forests in East Africa. The study estimated the forest area that stayed as from the beginning of the time series (1984) until 2017, identified areas that were lost due to deforestation and those that are undergoing recovery. Supervised image classification with maximum likelihood (ML) algorithm was used with an accuracy of 86.20% (Kappa coefficient of 0.81) for the Mau forest complex was attained and 90.50% (Kappa coefficient of 0.88) was obtained for the Mt Elgon forest and deforestation was determined using the change detection method (Margono et al., 2012). The classification accuracy in this study for the Mau forest complex is comparable with a related classification that was undertaken by Were et al. (2013) with a reported accuracy of 80%, with which land cover and land-use change were assessed in the Eastern Mau forest reserve, a section of the Mau forest complex for the years 1986, 2000, and 2011. However, the results from Were et al. (2013) were only for a small section of the Mau forest complex. In this study, the training and validation samples for the maximum likelihood classification were obtained from the available high-resolution Google images for the two study areas, an approach that conforms with the best practices described by Olofsson et al. (2014). Several factors contribute to the accuracy of the classification of which the reliability associated with the use of the high-resolution Google image with a slight difference in the dates of acquisition introduces potential errors into the class definition and allocation especially when the changes occur after the acquisition of the Google Imagery. Using ML for land cover mapping and carrying out change detection provides a challenge in class identification and definition given the images were collected during the dry months of the study area to be able to segregate forest cover from other land cover types. For example, small-scale agricultural land where harvesting has taken place could be assigned to the settlement and *vice versa*. ML assigns classes based on likelihood, and the classes assigned are used to assess the forest cover change at each time step. However, these challenges were minimized by using the forest masks to focus the changes within the areas that had been forest at the beginning of the time series.

The study further shows that the forest cover loss detected compared with the GFC data by Hansen et al. (2013) for the period 2000–2017. GFC results indicate gross forest loss of 17.0% (68,848 ha) for the Mau forest complex and 5.3% (11,501) for the Mt Elgon forest. These estimates from GFC for the period (2000–2017) are comparable to the results from the classification in this current study which revealed 16.8% (68,155 ha) and 7.6% (16,496 ha) forest cover loss for the Mau forest complex and Mt Elgon forest respectively for the same period. The variations could be associated with differences in method, scales, and thresholds used as well as the processes involved. For example, ML is operator-based with a focus on the changes in the spectral value in different periods, while GFC uses the canopy cover percentage and determines change using the bagged decision tree in Google Earth Engine with images collected during the growing season (Arjasakusuma et al., 2018).

4.2 Spatio-temporal forest cover change and drivers of deforestation and forest disturbance

A comprehensive assessment of the forest cover changes due to deforestation and the following forest recovery for the two largest montane forests of East Africa covering together 621,928 ha (404,660 ha for the Mau forest complex and 217,268 ha for Mt Elgon forest) was undertaken. Over the period from 1984–2017, this study showed that 21.9% (88.493 ha) and 12.5% (27,201 ha) of the Mau forest and Mt Elgon forest respectively were lost to deforestation. It also revealed that 18.6% (75,438 ha) for the Mau forest complex and 27.2% (59,047 ha) of Mt Elgon forest are currently undergoing different stages of recovery as indicated in Figure 8. Despite the losses to deforestation and clearance, the two montane forests have been regarded as the largest closed-canopy forest in East Africa playing a significant role in carbon sequestration, regulation of rainfall and nutrient cycling, soil formation, and support to biodiversity (Gichuhi, 2013; Otieno, 2016; Plumptre et al., 2019; Omoding et al., 2020). These montane forests are also very important ecosystems and water catchments to the East African region (Muhweezi et al., 2007; Hesslerová and Pokorný, 2011; Chrisphine et al., 2015). Due to various factors ranging from natural to anthropogenic, these montane forests have faced large-scale deforestation and

disturbance (Landmann and Dubovyk, 2014; Mutugi and Kiiru, 2015) which conforms to the findings of the current study. In the Mau forest complex, our findings demonstrate that deforestation has been attributed largely to agriculture with the largest losses in forest cover resulting from the conversion of forest to small-scale agriculture 59,172 ha (68.3%). While in Mt Elgon forest, agriculture was also the main driver of forest cover loss accounting for 63.2% (24,077 ha) of the loses quantified. Previous studies also reported agriculture as the main driver of the land cover changes, for example, 4,500 ha of Mt Elgon forest that has been converted to other land uses (Petursson et al., 2013), and a total of 145,850 ha (1,458.5 km^2) of the Mau forest complex has been lost to other land uses as reported by Swart, (2016). Our findings also agrees with the findings of Were et al. (2013) for the Eastern Mau forest and Lake Nakuru basin sections of the Mau forest complex, which revealed that there was an increase in cropland expansion and built-up area by an annual rate of 6% and 16% and a decrease in the forest cover as a consequence for the period from 1973 to 2011. Kissinger et al. (2012) associated forest cover loss with increasing demand for land to expand agriculture at a global level, this study confirms these claims as the study demonstrates that most of the forest cover was lost to agriculture for both the study areas. Curtis et al. (2018) reported deforestation rates in Africa being driven by shifting agriculture, i.e., small to medium-scale forest and shrubland conversion for agriculture that is later abandoned and followed by subsequent forest regrowth. However, this study determined that smallholder agriculture contributed to 68.31% of forest loss and large scale agriculture to 13.2%, and most of this area remains under agriculture, making it the main driver of forest cover loss as suggested by Hosonuma et al. (2012); Albertazzi et al. (2018). The current study further showed that deforestation in the Mau forest complex and Mt Elgon forest occurs in small patches of less than 1 ha, which may be associated with the activities of farming communities adjacent to the forest as reported by the empirical studies by Sassen et al. (2013); Brandt et al. (2018). The finding of this study demonstrates that most of the areas deforested were mainly at the edges of agricultural lands both smallholder and large scale tea farms.

4.3 Rate of deforestation and recovery in the montane forest of East Africa

Deforestation has been reported to be pervasive in sub-Saharan Africa especially in the Democratic Republic of Congo (DRC) rainforests and the Miombo woodlands due to smallholder agriculture and increasingly commodity crop cultivation (Song et al., 2018), however, the rates are largely for lowland tropical rainforests. This study quantified the rate of deforestation and recovery for the two east African montane ecosystems which revealed 88,493 ha reduction in the forest cover from 336,181.3 ha at an annual rate of −0.82% yr^{-1} for the Mau Forest Complex. While in the Mt Elgon forest, forest cover reduced by 27,201 ha from 138,350 ha in 1984 to 111,149 ha by 2017 at an annual rate of −1.03% yr^{-1} as indicated in Table 6. Comparing the rates of deforestation from this study with other reported rates can be challenging because of differences in datasets used, scale, and boundaries of the study areas. Most studies for the Mau forest complex do not quantify forest cover changes for the whole forest but in selected specific blocks out of the 22 blocks. For example, Were et al. (2013) estimated changes for the Lake Nakuru basin, Kinyanjui et al. (2013) calculated changes for the Southwestern and Transmara blocks of the Mau forest complex, and Swart, (2016) assessed the land cover change in the region that includes the Mau forest complex. These previous studies focused on the land-use change and the main drivers within specific blocks, whereas the current study covers the quantification of the rate of forest cover change and recovery across all the blocks of the Mau forest complex.

This study shows that the rate of deforestation in the Mau forest complex is also higher than the nationally reported annual rates by the Food and Agriculture Organization of the United Nations (FAO) for Kenya and Uganda at the national level since there are no site-specific reported rates of deforestation for the period 1990 to 2010 at 0.32% per year for Kenya and the findings for the Mt Elgon forest are below the national reported annual rate of 0.4%–3% per year for Uganda for the period 1990 to 2010 (FAO, 2013). In comparison with the regional studies that have assessed rates of deforestation, the annual rates for the Mau forest complex and Mt Elgon determined in this study were slightly higher than the findings of Brink et al. (2014) that indicated an increase in the annual rate of deforestation from 0.2% in the period from 1990–2000 to 0.4% from 2000–2010. It should be noted that the study by Brink et al. (2014) used the images from the DMC Deimos imagery with ground resolution of 22 m and the standard imager resolution of 32 m collecting images in 3 spectral bands.

The current study provides spatio-temporal information regarding forest cover change. This provides the basis for future research to investigate the key drivers of the forest cover change and how these can be controlled in order to plan, implement and monitor the restoration and conservation programs for the tropical montane forest of East Africa. Previous studies have cited agriculture (both smallholder and Large scale as the key driver of change, however the magnitude and scale were not clearly stated. Our findings clearly show both the magnitude and scale of the drives from historical spatial data which can therefore provide much needed basis for further investigation into the drivers of change and how they can be managed. Other remote sensing methods can also be applied to test their robustness in determining forest cover change in the Eastern Africa region in general.

Future research work could involve the assessment of community perception regarding forest disturbance and develop citizen science tools to engage the community into the monitoring of the forest disturbance, with focus to areas that have been identified as deforested.

5 Conclusion

Deforestation has been a major problem facing the Mau forest Complex and Mt Elgon forests in Kenya and Uganda, yet the annual rate of deforestation over time has not been quantified previously. This study provides a detailed multi-temporal and extensive spatial analysis of these two important forests thus providing an annual rate of forest loss to deforestation and the rate of recovery. The results provide a basis and spatial-temporal status of the forest for the development of effective monitoring of the two forest ecosystems

from the areas that are currently deforested and those that are undergoing recovery. The study findings also provide the relevant scientific evidence on the trends of forest cover loss due to deforestation and forest cover clearance in the Mau forest complex and Mt Elgon forest and add to the limited information regarding the changes in montane forest ecosystems. The use MLC approach for assessing the rate of deforestation and forest recovery in the Mau forest complex and Elgon forest benchmarks the wider use and application of these datasets for assessing deforestation and forest recovery in the East African forests.

Data availability statement

The original contributions presented in the study are included in the article/Supplementary Material, further inquiries can be directed to the corresponding author.

Author contributions

SO: Data curation, Formal analysis, Investigation, Methodology, Software, Visualization, Writing—original draft, Writing—review and editing. CZ: Conceptualization, Formal analysis, Methodology, Writing—review and editing, Project Administration. GY: Formal analysis, Investigation, Visualization. MR: Conceptualization, Writing—review and editing, Supervision, Project Administration. All authors contributed to the article and approved the submitted version.

Funding

This study was part of a PhD research (Ojoatre, 2022) funded by the Federal Ministry for Economic Cooperation and Development (BMZ) (Grant 81206682 "The Water Towers of East Africa: policies and practices for enhancing co-benefits from joint forest and water conservation") through Centre for International Forestry Research (CIFOR). This study forms part of the CGIAR Research Program Forest, Trees and Agroforestry (FTA), led by CIFOR. CZ was supported in part by the Natural Environment Research Council (grant number NE/T004002/1).

Conflict of interest

Author SO was employed by company BeZero Carbon.

The remaining authors declare that the research was conducted in the absence of any commercial or financial relationships that could be construed as a potential conflict of interest.

Publisher's note

References

Achard, F., Beuchle, R., Mayaux, P., Stibig, H., Bodart, C., Brink, A., et al. (2014). Determination of tropical deforestation rates and related carbon losses from 1990 to 2010. *Glob. Change Biol.* 20 (8), 2540–2554. doi:10.1111/gcb.12605

Albertazzi, S., (2018). *Relations of power driving tropical deforestation: A case study from the Mau forest (Kenya)*. Belgium: Belgeo National Committee of Geography of Belgium/Société Royale Belge de Géographie. doi:10.4000/belgeo.24223

Andréfouët, S., Bindschadler, R., Brown De Colstoun, E. C., Choate, M., Chomentowski, W., Christopherson, J., et al. (2003). Preliminary assessment of the value of Landsat 7 ETM+ data following scan line corrector malfunction. *Science*, 1–86.

Arjasakusuma, S., Kamal, M., Hafizt, M., and Forestriko, H. F. (2018). Local-scale accuracy assessment of vegetation cover change maps derived from global forest change data, ClasLite, and supervised classifications: Case study at part of riau province, Indonesia. *Springer Berl. Heidelb.* 10 (3), 205–217. doi:10.1007/s12518-018-0226-2

Ayuyo, O. I., and Sweta, L. (2014). Land cover and land use mapping and change detection of mau complex in Kenya using geospatial technology. *Int. J. Sci. Res.* 3 (3).

Baldyga, T. J., Miller, S. N., Driese, K. L., and Gichaba, C. M. (2007). Assessing land cover change in Kenya's Mau Forest region using remotely sensed data. *Afr. J. Ecol.* 46 (1), 46–54. doi:10.1111/j.1365-2028.2007.00806.x

Brandt, P., Hamunyela, E., Herold, M., de Bruin, S., Verbesselt, J., and Rufino, M. C. (2018). Sustainable intensification of dairy production can reduce forest disturbance in Kenyan montane forests. *Agric. Ecosyst. Environ.* 265, 307–319. doi:10.1016/j.agee.2018.06.011

Brink, A. B., Bodart, C., Brodsky, L., Defourney, P., Ernst, C., Donney, F., et al. (2014). Anthropogenic pressure in East Africa-Monitoring 20 years of land cover changes by means of medium resolution satellite data. *Int. J. Appl. Earth Observation Geoinformation* 28, 60–69. doi:10.1016/j.jag.2013.11.006

Cavanagh, C. (2017). "Paying for carbon at Mount Elgon: Two contrasting approaches at a transboundary park in East Africa," in *Co-Investment in ecosystem services: Global lessons from payment and incentive schemes*. Editors S. Namirembe, B. Leimona, and M, M. P. van Noordwijk (Nairobi, Kenya: World Agroforestry Centre), 1–10.

Chrisphine, M. O., Maryanne, A. O., and Mark, B. K. (2015). 'Assessment of hydrological impacts of mau forest, Kenya', journal of waste water treatment and analysis. *OMICS Int.* 7 (1), 1–7. doi:10.4172/2157-7587.1000223

Cohen, W. B., Yang, Z., and Kennedy, R. (2010). Detecting trends in forest disturbance and recovery using yearly Landsat time series: 2. TimeSync — tools for calibration and validation. *Remote Sens. Environ.* 114 (12), 2911–2924. doi:10.1016/j.rse.2010.07.010

Crafford, J., (2012). *The role and contribution of montane forests and related ecosystem services to the Kenyan economy*. Nairobi, Kenya: United Nations Environment Programme UNEP.

Curtis, P. G., Slay, C. M., Harris, N. L., Tyukavina, A., and Hansen, M. C. (2018). Classifying drivers of global forest loss. *Am. Assoc. Adv. Sci.* 361 (6407), 1108–1111. doi:10.1126/science.aau3445

DeVries, B., Verbesselt, J., Kooistra, L., and Herold, M. (2015). Robust monitoring of small-scale forest disturbances in a tropical montane forest using Landsat time series. *Remote Sens. Environ.* 161, 107–121. doi:10.1016/j.rse.2015.02.012

Eac, U. N. E. P., and Grid-Arendal (2016). Sustainable mountain development in EastEast Africa in a changing climate - mountain adaptation outlook series. Available at: https://www.weadapt.org/sites/weadapt.org/files/maos_eastafrica_screen.pdf (Accessed November 10, 2020).

Ellison, D., (2017). Trees, forests and water: Cool insights for a hot world. *Glob. Environ. Change* 43, 51–61. doi:10.1016/j.gloenvcha.2017.01.002

Entenmann, S. K., Schmitt, C. B., and Konold, W. (2014). REDD+-related activities in Kenya: Actors' views on biodiversity and monitoring in a broader policy context. *Biodivers. Conservation* 23 (14), 3561–3586. doi:10.1007/s10531-014-0821-4

Fao (2015a). *Global forest resources assessment 2015*. Rome, Italy: FAO. doi:10.1002/2014GB005021

Fao (2015b). *Global forest resources assessment 2015*. Rome, Italy: FAO. doi:10.1002/2014GB005021

Fao (2014). Global forest resources assessment 2015 country report Kenya. Rome. Available at: http://www.fao.org/3/a-az251e.pdf (Accessed January 23, 2018).

Fao and Unep (2020). *The state of the world's forests 2020*. Rome, Italy: FAO. doi:10.4060/ca8642en

Fortier, J., Rogan, J., Woodcock, C. E., and Runfola, D. M. (2011). Utilizing temporally invariant calibration sites to classify multiple dates and types of satellite imagery. *Am. Soc. Photogrammetry Remote Sens.* 77 (2), 181–189. doi:10.14358/PERS.77.2.181

Frazier, R. J., Coops, N. C., and Wulder, M. A. (2015). Boreal Shield forest disturbance and recovery trends using Landsat time series. *Remote Sens. Environ.* 170, 317–327. doi:10.1016/j.rse.2015.09.015

Gichuhi, M. (2013). Ecological management of the Mau catchment area and its impact on Lake Nakuru national park. *J. Agric. Sci. Technol.*, 81–101.

Government of Kenya (2017). Forest management information system, Kenya forest Service (KFS). Available at: http://www.kenyaforestservice.org/index.php?option=com_content&view=article&id=472&Itemid=633 (Accessed: November 7, 2020).

Grantham, H. S., (2020). "Modification of forests by people means only 40% of remaining forests have high ecosystem integrity," in *bioRxiv* (Laurel Hollow, New York, USA: Cold Spring Harbor Laboratory). 10017. doi:10.1101/2020.03.05.978858

Grinand, C., Rakotomalala, F., Gond, V., Vaudry, R., Bernoux, M., and Vieilledent, G. (2013). Estimating deforestation in tropical humid and dry forests in Madagascar from 2000 to 2010 using multi-date Landsat satellite images and the random forests classifier. *Remote Sens. Environ.* 139, 68–80. doi:10.1016/j.rse.2013.07.008

Hamunyela, E., Brandt, P., Shirima, D., Do, H. T. T., Herold, M., and Roman-Cuesta, R. M. (2020). Space-time detection of deforestation, forest degradation and regeneration in montane forests of Eastern Tanzania. *Int. J. Appl. Earth Observation Geoinformation* 88, 102063. doi:10.1016/j.jag.2020.102063

Hansen, M. C., Potapov, P. V., Moore, R., Hancher, M., Turubanova, S. A., Tyukavina, A., et al. (2013). High-resolution global maps of 21st-century forest cover change. *Am. Assoc. Adv. Sci.* 342 (6160), 850–853. doi:10.1126/science.1244693

Hansen, M. C., Stehman, S. V., Potapov, P. V., Loveland, T. R., Townshend, J. R. G., DeFries, R. S., et al. (2008). Humid tropical forest clearing from 2000 to 2005 quantified by using multitemporal and multiresolution remotely sensed data. *Proc. Natl. Acad. Sci. U. S. A.* 105 (27), 9439–9444. doi:10.1073/pnas.0804042105

Harris, N. L., Gibbs, D. A., Baccini, A., Birdsey, R. A., de Bruin, S., Farina, M., et al. (2021). Global maps of twenty-first century forest carbon fluxes. *Nat. Clim. Change* 11, 234–240. doi:10.1038/s41558-020-00976-6

Hesslerová, P., and Pokorný, J. (2011). "Effect of mau forest clear cut on temperature distribution and hydrology of catchment of lakes nakuru and naivasha: Preliminary study," in *Water and nutrient management in natural and constructed wetlands* (Dordrecht, Netherlands: Springer Netherlands), 263–273. doi:10.1007/978-90-481-9585-5_19

Hirata, Y., (2012). in *REDD-plus Cookbook, how to measure and monitor forest carbon, REDD-plus Cookbook, how to measure and monitor forest carbon* (Ibaraki, Japan: Forestry and Forest Products Research Institute REDD Research and Development Center).

Hosonuma, N., Herold, M., De Sy, V., De Fries, R. S., Brockhaus, M., Verchot, L., et al. (2012). An assessment of deforestation and forest degradation drivers in developing countries. *Environ. Res. Lett.* 7, 044009. doi:10.1088/1748-9326/7/4/044009

Houghton, R., (2012). Carbon emissions and the drivers of deforestation and forest degradation in the tropics. *Curr. Opin. Environ. Sustain.* 4, 597–603. doi:10.1016/j.cosust.2012.06.006

Keenan, R. J., Reams, G. A., Achard, F., de Freitas, J. V., Grainger, A., and Lindquist, E. (2015). Dynamics of global forest area: Results from the FAO global forest resources assessment 2015. *For. Ecol. Manag.* 352, 9–20. doi:10.1016/j.foreco.2015.06.014

Kefri (2018). Economic value of the mau forest complex, cherangany hills and Mt. Elgon water towers in Kenya; supporting decision making and conservation of Kenya's important ecosystems. Available at: www.kefri.org (Accessed: November 10, 2020).

Kim, D., Sexton, J. O., and Townshend, J. R. (2015). Accelerated deforestation in the humid tropics from the 1990s to the 2000s: Accelerated pan-tropical deforestation. *Geophys. Res. Lett.* 42, 3495–3501. doi:10.1002/2014gl062777

Kimutai, D. K., and Watanabe, T. (2016). Forest-cover change and participatory forest management of the lembus forest, Kenya. *Kenya', Environ. - MDPI* 3 (3), 20–18. doi:10.3390/environments3030020

Kissinger, G., Herold, M., and De Sy, V. (2012). Drivers of deforestation and forest degradation: A synthesis report for REDD+ policymakers. Vancouver Canada. Available at: http://www.forestbonds.net/sites/default/files/userfiles/1file/6316-drivers-deforestation-report.pdf (Accessed September 25, 2017).

Lawrence, D., and Vandecar, K. (2015). Effects of tropical deforestation on climate and agriculture. *Nat. Clim. Change* 5, 27–36. doi:10.1038/nclimate2430

Landmann, T., and Dubovyk, O. (2014). Spatial analysis of human-induced vegetation productivity decline over eastern Africa using a decade (2001-2011) of medium resolution MODIS time-series data. *Int. J. Appl. Earth Observation Geoinformation* 33 (1), 76–82. doi:10.1016/j.jag.2014.04.020

MacDicken, K. G. (2015). Global forest resources assessment 2015: What, why and how? *For. Ecol. Manag.* 352, 3–8. doi:10.1016/j.foreco.2015.02.006

Margono, B. A., Turubanova, S., Zhuravleva, I., Potapov, P., Tyukavina, A., Baccini, A., et al. (2012). Mapping and monitoring deforestation and forest degradation in Sumatra (Indonesia) using Landsat time series data sets from 1990 to 2010. *Environ. Res. Lett.* 7 (3), 034010. doi:10.1088/1748-9326/7/3/034010

Mayaux, P., Holmgren, P., Achard, F., Eva, H., Stibig, H. J., and Branthomme, A. (2005). Tropical forest cover change in the 1990s and options for future monitoring. *Philosophical Trans. R. Soc. B Biol. Sci.* 360 (1454), 373–384. doi:10.1098/rstb.2004.1590

Milodowski, D. T., Mitchard, E. T. A., and Williams, M. (2017). Forest loss maps from regional satellite monitoring systematically underestimate deforestation in two rapidly changing parts of the Amazon. *Environ. Res. Lett.* 12 (9), 094003. doi:10.1088/1748-9326/aa7e1e

Mitchard, E. T. A. (2018). The tropical forest carbon cycle and climate change. *Nature* 559 (7715), 527–534. doi:10.1038/s41586-018-0300-2

Mugagga, F., (2015). The effect of land use on carbon stocks and implications for climate variability on the slopes of Mount Elgon, eastern Uganda. *Int. J. Regional Dev.* 2 (1), 58. doi:10.5296/ijrd.v2i1.7537

Muhweezi, A. B., Sikoyo, G. M., and Chemonges, M. (2007). Introducing a transboundary ecosystem management approach in the Mount Elgon region. *Mt. Res. Dev.* 27 (3), 215–219. doi:10.1659/0276-4741(2007)27[215:IATEMA]2.0.CO;2

Mutugi, M., and Kiiru, W. (2015). Biodiversity, local resource, national heritage, regional concern, and global impact: The case of Mau forest. *Kenya', Eur. Sci. J. ESJ* 11 (10). doi:10.19044/ESJ.2015.V11N10P%P

Mwangi, E., Cerutti, P., Doumenge, C., and Nasi, R. (2018). *The current state of Eastern Africa's forests*. Luxembourg: European Union. doi:10.2760/512555

Ojoatre, S. (2022). "Deforestation and recovery of the tropical montane forests of East Africa,". PhD (England: Lancaster University). doi:10.17635/lancaster/thesis/1627

Olang, L. O., and Kundu, P. M. (2011). Land degradation of the mau forest complex in eastern Africa: A review for management and restoration planning, environmental monitoring. Available at: http://etd-library.ku.ac.ke/handle/123456789/11626 (Accessed September 4, 2017).

Olofsson, P., Foody, G. M., Herold, M., Stehman, S. V., Woodcock, C. E., and Wulder, M. A. (2014). Good practices for estimating area and assessing accuracy of land change. *Remote Sens. Environ.* 148, 42–57. doi:10.1016/j.rse.2014.02.015

Omoding, J., Walters, G., Andama, E., Carvalho, S., Colomer, J., Cracco, M., et al. (2020). Analysing and applying stakeholder perceptions to improve protected area governance in Ugandan conservation landscapes. *Land* 9 (6), 207. doi:10.3390/LAND9060207

Ongugo, P., Njuguna, J., Obonyo, E., and Sigu, G. (2001). *Livelihoods, natural resource entitlements and protected areas: The case of Mt.* Kenya: Elgon forest in Kenya, 11.

Otieno, K. O. (2016). Forestry carbon sequestration and trading: A case of mau forest complex in Kenya forest change detection and carbon trading. Available at: https://www.diva-portal.org/smash/get/diva2:882491/FULLTEXT02.pdf (Accessed November 10, 2020).

Petursson, J. G., Vedeld, P., and Sassen, M. (2013). An institutional analysis of deforestation processes in protected areas: The case of the transboundary Mt. Elgon, Uganda and Kenya. *Elgon, Uganda Kenya', For. Policy Econ.* 26, 22–33. doi:10.1016/j.forpol.2012.09.012

Plumptre, A. J., Ayebare, S., Behangana, M., Forrest, T. G., Hatanga, P., Kabuye, C., et al. (2019). Conservation of vertebrates and plants in Uganda: Identifying Key Biodiversity Areas and other sites of national importance. *Conservation Sci. Pract.* 1 (2), e7. doi:10.1002/csp2.7

Puyravaud, J.-P. (2003). Standardizing the calculation of the annual rate of deforestation. *For. Ecol. Manag.* 177 (1–3), 593–596. doi:10.1016/S0378-1127(02)00335-3

Reimer, F., Asner, G. P., and Joseph, S. (2015). Advancing reference emission levels in subnational and national REDD+ initiatives: A CLASlite approach. *Carbon Balance Manag.* 10 (1), 5. doi:10.1186/s13021-015-0015-8

Rutkowska, M., Dubalska, K., Bajger-Nowak, G., Konieczka, P., and Namieśnik, J. (2014). Organomercury compounds in environmental samples: Emission sources, toxicity, environmental fate, and determination. *Toxic. Environ. Fate, Determination', Crit. Rev. Environ. Sci. Technol.* 44 (6), 638–704. doi:10.1080/10643389.2012.728825

Sannier, C., McRoberts, R. E., and Fichet, L. V. (2016). Suitability of Global Forest Change data to report forest cover estimates at national level in Gabon. *Remote Sens. Environ.* 173, 326–338. doi:10.1016/j.rse.2015.10.032

Sassen, M., Sheil, D., Giller, K. E., and ter Braak, C. J. (2013). Complex contexts and dynamic drivers: Understanding four decades of forest loss and recovery in an East African protected area. *Biol. Conserv.* 159, 257–268. doi:10.1016/J.BIOCON.2012.12.003

Schulz, J. J., Cayuela, L., Echeverria, C., Salas, J., and Rey Benayas, J. M. (2010). Monitoring land cover change of the dryland forest landscape of Central Chile (1975-2008). *Appl. Geogr.* 30 (3), 436–447. doi:10.1016/j.apgeog.2009.12.003

Scott, P. (1998). 'From conflict to collaboration: People and forests at Mount Elgon, Uganda', from conflict to collaboration: People and forests at Mount Elgon. Available at: https://www.iucn.org/content/conflict-collaboration-people-and-forests-mount-elgon-uganda (Accessed: January 25, 2021).

Sheil, D. (2018). Forests, atmospheric water and an uncertain future: The new biology of the global water cycle. *For. Ecosyst.* 5, 19. doi:10.1186/s40663-018-0138-y

Sheil, D., and Murdiyarso, D. (2009). 'How forests attract rain: An examination of a new hypothesis'. *BioScience* 59 (4), 341–347. doi:10.1525/bio.2009.59.4.12

Song, X. P., Hansen, M. C., Stehman, S. V., Potapov, P. V., Tyukavina, A., Vermote, E. F., et al. (2018). 'Global land change from 1982 to 2016'. *Nature* 560 (7720), 639–643. doi:10.1038/s41586-018-0411-9

Strahler, A. H., Boschetti, L., Foody, G. M., Friedl, M. A., Hansen, M. C., Herold, M., et al. (2006). *Global land cover validation: Recommendations for evaluation and accuracy assessment of global land cover maps*. Luxemburg: Office for Official Publications of the European Communities. http://nofc.cfs.nrcan.gc.ca/gofcgold/Report Series/GOLD_25.pdf.

Swart, R. (2016). *Monitoring 40 years of land use change in the Mau Forest Complex, Kenya a land use change driver analysis*. Wageningen, Netherlands: Wageningen University.

Tolpekin, V., and Stein, A. (2012). *The core of GIScience: A systems-based approach*. Hengelosestraat, Enschede, Netherlands: Enschede: The International Institute for Geo-Information Science and Earth Observation ITC.

Vecea Team (2020). *Potential vegetation map for eastern Africa, Potential vegetation map for eastern Africa*. Available at: https://vegetationmap4africa.org/Home.html (Accessed: February 10, 2021).

Vogelmann, J., Khoa, P., Shermeyer, J., Shi, H., Wimberly, M., et al. (2017). Assessment of forest degradation in vietnam using Landsat time series data. *Forests* 8 (7), 238. doi:10.3390/f8070238

Were, K. O., Dick, T. B., and Singh, B. R. (2013). Remotely sensing the spatial and temporal land cover changes in Eastern Mau forest reserve and Lake Nakuru drainage basin Kenya. *Appl. Geogr.* 41, 75–86. doi:10.1016/j.apgeog.2013.03.017

White, F. (1983). *A descriptive memoir to accompany the Unesco/AETFAT/UNSO vegetation map of Africa*. Paris, France: United Nations Educational, Scientific and Cultural Organization.

Wwf Eastern Africa Programme (2007). Water towers of eastern Africa Policy, issues and vision for community-based protection and management of montane forests. Available at: www.panda.org/earpo.

Yesuf, G., Brown, K. A., and Walford, N. (2019). "Assessing regional-scale variability in deforestation and forest degradation rates in a tropical biodiversity hotspot," in *Remote sensing in ecology and conservation*. Editors N. Pettorelli, and M. Wegmann (Hoboken, New Jersey, United States: John Wiley and Sons, Ltd), 346–359. doi:10.1002/rse2.110

Zhu, Z., Woodcock, C. E., and Olofsson, P. (2012). Continuous monitoring of forest disturbance using all available Landsat imagery. *Remote Sens. Environ.* 122, 75–91. doi:10.1016/J.RSE.2011.10.030

frontiers | Frontiers in Environmental Science

TYPE Original Research
PUBLISHED 07 September 2023
DOI 10.3389/fenvs.2023.1146346

OPEN ACCESS

EDITED BY
Xiaoyang Zhang,
South Dakota State University,
United States

REVIEWED BY
Rui Manuel Vitor Cortes,
University of Trás-os-Montes and Alto Douro, Portugal
Wakjira Dibaba,
Jimma University Jimma Institute of Technology, Ethiopia

*CORRESPONDENCE
Michael Nones,
mnones@igf.edu.pl

RECEIVED 17 January 2023
ACCEPTED 28 August 2023
PUBLISHED 07 September 2023

CITATION
Regasa MS and Nones M (2023), SWAT model-based quantification of the impact of land use land cover change on sediment yield in the Fincha watershed, Ethiopia.
Front. Environ. Sci. 11:1146346.
doi: 10.3389/fenvs.2023.1146346

SWAT model-based quantification of the impact of land use land cover change on sediment yield in the Fincha watershed, Ethiopia

Motuma Shiferaw Regasa and Michael Nones*

Department of Hydrology and Hydrodynamics, Institute of Geophysics, Polish Academy of Science, Warsaw, Poland

In recent years, Ethiopia is facing problems due to soil erosion, mainly because of the conversion of natural vegetation into cultivated land to answer to increasing human pressure. Such changes in coverage are fostering soil erosion, which is also affecting dam reservoirs, because of the increasing sediment yield entering the lake. The present study focuses on the Ethiopian Fincha watershed and takes advantage of the potentiality of the Soil and Water Assessment Tool (SWAT) model, to investigate how land use land cover changes impact soil erosion and the consequent sediment yield entering the Fincha Dam. The SWAT model was calibrated and validated using time series data of stream flow and sediment covering the period 1986-2008, and its performance was evaluated by looking at the coefficient of determination, Nash-Sutcliffe simulation efficiency, and per cent bias. Once validated, the SWAT model was applied to derive sediment yield for the future 30 years, based on forecasted land use land cover conditions. The results show that the mean annual soil loss rate increased from 32.51 t ha^{-1} in 1989 to 34.05 t ha^{-1} in 2004, reaching 41.20 t ha^{-1} in 2019. For the future, a higher erosion risk should be expected, with the annual soil loss rate forecasted to be 46.20 t ha^{-1} in 2030, 51.19 t ha^{-1} in 2040, and 53.98 t ha^{-1} in 2050. This soil erosion means that sediments transported to the Fincha Dam, located at the watershed outlet, increased significantly in the last 30 years (from 1.44 in 1989 to 2.75 mil t in 2019) and will have the same trend in the future (3.08–4.42 mil t in 2020 and 2050, respectively), therefore highly affecting the Fincha reservoir services in terms of reduction of water volume for irrigation and hydroelectric power generation. By providing possible medium/long-term scenarios, the present work can help land planners and decision-makers in developing future land management strategies based on actual projections, eventually aiming to reduce soil erosion at the watershed scale and guarantee the sustainable development of the Fincha region and its key hydraulic infrastructures.

KEYWORDS

Ethiopia, Fincha watershed, sediment yield, SWAT model, land use land cover (LULC)

1 Introduction

Globally, 75 billion tons of soil are eroded every year (Dissanayake et al., 2019). Research performed at the continental scale pointed out that the United States experience a loss rate of around 15-18 t ha^{-1} year^{-1}, while Europe has a range of 10–20 t ha^{-1} year^{-1}. Less developed countries like Asia, Africa, and South America can reach rates of even 20-40 t ha^{-1} year $^{-1}$

(Deore, 2005). For example, as reported by Kidane and Alemu, (2015), transboundary rivers originating from the highlands of Ethiopia convey around 1.3 billion tons of sediment annually, while the Blue Nile only transports about 131 million tons per year. Changes in land use land cover (LULC) can cause soil erosion, which eventually contributes to increasing the quantity of sediments entering waterbodies and dam reservoirs. This process is evident in arid and semi-arid environments (e.g., Pulighe et al., 2019; Sharma et al., 2022; Negewo and Sarma, 2023), where soil degradation can generate cascading effects like drought and famine (Yesuf et al., 2015). To counteract the erosion process and guarantee suitable development, effective management strategies and policies, and implementation of best management practices with the active involvement of all stakeholders are needed. To guarantee proper outcomes in the medium to long term, the selection of such management actions should be evidence-driven, and therefore based on modelling approaches, able to provide reliable results in data-scarce regions (Tegegne et al., 2017; Degife et al., 2021).

Nowadays, the Ethiopian economy and population are taking advantage of the presence of multiple dams and reservoirs, providing the availability of a large amount of water resources and suitable topography (Assfaw, 2019). However, these reservoirs are highly impacted by soil erosion, with consequent severe problems of sedimentation even beyond their dead storage capacity, which is a clear sign of poor land use practices and improper land management. Many studies have shown that main factors contributing to soil erosion include the type of soil, the topography of the basin, the types of land uses and vegetation cover, and the amount of rainfall (e.g., Setegn et al., 2008; Betrie et al., 2011; Kidane et al., 2019; Aneseyee et al., 2020) The reduction of storage volume due to sedimentation negatively impacts the capacity to produce hydroelectric power, increasing production and maintenance costs, reducing the availability of water for concurrent uses like irrigation, and eventually shortening the reservoir life.

Past investigations have shown a large variety of hydrological models used for evaluating and predicting changes in water balance (Aredo et al., 2023) and soil erosion both worldwide (Zeiger and Hubbart, 2016; Gharibdousti et al., 2019) and in Ethiopian watersheds (Miheretu and Yimer, 2018), but most of them used the Soil and Water Assessment Tool (SWAT) (see, among many others, Gessese and Yonas, 2008; Senti et al., 2014; Yesuf et al., 2015; Ebabu et al., 2019; Megersa et al., 2019; Gebretekle et al., 2022; Mariye et al., 2022; Anteneh et al., 2023).

SWAT was chosen for the present investigation due to its free availability, simple integration with GIS-based interfaces, and connectivity to tools for sensitivity, calibration, and uncertainty analysis. Moreover, the opportunity to easily integrate GIS information in SWAT constitute an advantage in studying area with a scarcity of data, such as the Fincha watershed. These studies confirmed that poor land use practices, improper land management and absence of appropriate soil conservation measures have been major causes of soil erosion and land degradation problems, with consequent sedimentation in Ethiopian reservoirs (Tefera and Streak, 2010; Ayana et al., 2012; Dibaba et al., 2021; Anteneh et al., 2023).

During the past decades, the Fincha watershed, part of the Blue Nile River basin, has experienced dynamic LULC changes including the degradation of natural woodlands (Dibaba et al., 2021; Regasa et al., 2021). According to Leta et al. (2021a) and Kenea et al. (2021), such LULC variations can have both long- and short-term temporal and spatial effects on the watershed hydrology, and consequently on the soil erosion and sediment yield entering the dam reservoirs located in the watershed (Dibaba et al., 2021).

It is worth noting that these studies focused on the local scale, and investigated the impact of past LULC on the watershed hydrology. However, very reduced literature exists on predicting the impact of future LULC changes, both in terms of changes in watershed hydrology and the connected production of sediment. The present investigation aims to address this knowledge gap by evaluating the impact of LULC change on sediment yield entering the Fincha reservoir, looking at past trends (1989, 2004, 2019 years) and predicting future scenarios (2030, 2040, 2050 years). LULC scenarios were developed based on historical data and future predictions (Regasa and Nones, 2022), while hydrological changes and consequent sediment yield were computed by applying the SWAT model, given its reliability in modelling water and sediment loading (Gassman et al., 2007; Ang et al., 2023). The present findings contribute to a better understanding of soil erosion processes and consequences in a poorly gauged basin, giving useful insights on future management strategies and mitigation measures that can be applied for reducing sediments entering the Fincha reservoir, eventually contributing to assuring a long service life.

The study area is presented in the next section, together with the available dataset and a short overview of the methods used for data processing. This is followed by a thorough description of the SWAT model and the assumptions made for running it, along with a sensitivity analysis. Results are reported in Section 3, and focus on both the calibration and validation process, as well as the estimation of sediment yield and the localization of areas affected by the erosion process. The study assumptions and the obtained results are then discussed in light of the available literature to point out the study's novelty, as well as the pros and cons of applying SWAT in ungauged watersheds.

2 Materials and methods

2.1 Study area

The Fincha watershed is in Ethiopia's Horroo Guduruu Wallaggaa Oromiyaa Regional State, in the Upper Blue Nile Basin, about 300 km from Addis Ababa. It is geographically located between latitudes 9°9′53″ N to 10°1′00″ N and longitudes 37°00′25″ E to 37°33′17″ E, as shown in the map (Figure 1). The Fincha watershed covers an area of. 300,505 ha.

The region is defined by four distinct seasons: Summer, June to August, with heavy rains; Harvest season occurs from September to November, winter, which lasts from December to February, is illustrated by morning frost, particularly in January. Spring, from March to May, is the hottest season, with showers on occasion. The annual rainfall in the study area ranges from 1,367 to 1842 mm, with the Northern lowlands receiving the least rain and the Southern and Western highlands receiving more than 1,500 mm (Regasa and Nones, 2022). The main rainy season is from June to September, where the average precipitation is around 1,604 mm with peaks between July to August.

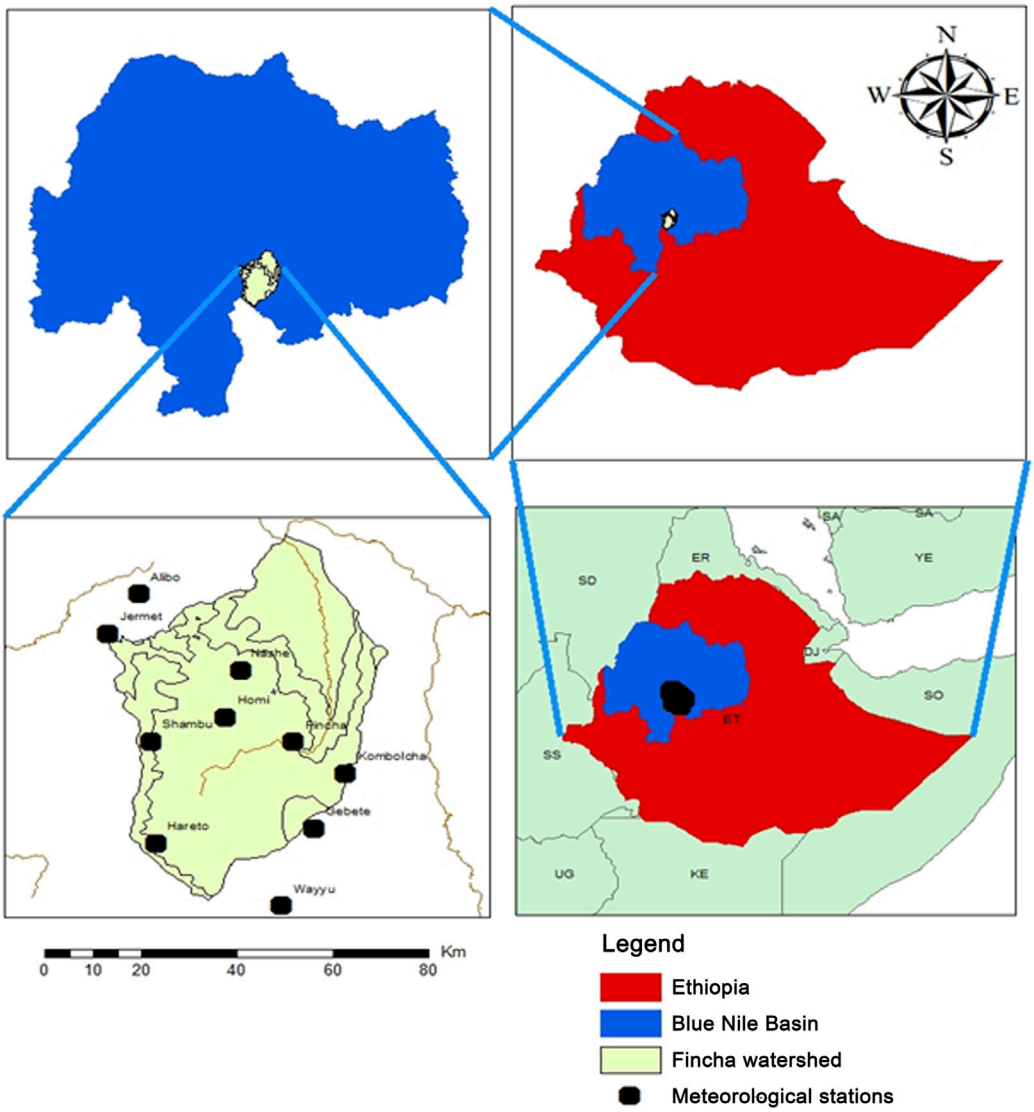

FIGURE 1
Location of the Fincha watershed, Blue Nile Basin, Ethiopia.

Three hydropower dams are present in the study area (Figure 1). This investigation focuses on the Fincha Dam, which was built in 1973, with an initial reservoir volume of 185 million m^3. In 1987, the Amarti River was diverted into the lake, increasing the reservoir capacity to 460 million m^3, which guarantees a current hydropower production of 127 MW (Tefera and Sterk, 2008).

According to previous studies (e.g., Leta et al., 2021b; Debela, 2022; Regasa and Nones, 2022), natural resources such as the Fincha, Amarti, and Nashe lakes not only contribute to the national economy by generating hydroelectric power, but are also used to irrigate crop and extensive sugar cane fields (Kitila et al., 2015). Because of its downstream connection to the Nile basin and intensive agriculture, the area is of national and international interest in hydro politics. Indeed, as suggested by various authors (e.g., Obengo, 2016; Chekol, 2019; Hailu, 2022), there are increased ambitions to control the Nile water resources, including controlling the river water sources and the hydropower reservoirs located in the watershed.

2.2 Available dataset

The SWAT model requires multiple pieces of information, which come from different sources (Table 1). In detail, the model inputs are Digital Elevation Model (DEM), LULC maps, soil data, weather data (relative humidity, precipitation, solar radiation, temperature, and wind speed), water flow and sediment data. For the sake of brevity, only a summary of the key data used in this research and their processing is reported here, while more details can be found in the cited literature.

2.2.1 Meteorological data

The data were obtained from the Metrological National Agency of Ethiopia. Their analysis was performed using daily observed weather data covering the period 1986-2019. These data include precipitation, maximum and minimum temperatures, solar radiation, wind speed and relative humidity of ten gauging

TABLE 1 Available data and sources.

Type	Data	Resolution/year/scale	Source
Spatial data	Digital elevation Model (DEM)	30m/2019	Ministry of Water, Irrigation, Energy (MOWIE), Ethiopia
	Land use land cover	30m/1989, 2004, 2019, 2030, 2040, 2050	1989, 2004, 2019 derived from Landsat images
			2030, 2040, 2050 predicted by Land Change Modeler Regasa and Nones. (2022)
	Soil	1:50,000	Ministry of Water, Irrigation and Energy (MOWIE), Ethiopia
Meteorological data	Precipitation, Temperature, Relative humidity, Solar radiation, Wind speed	1986–2019	National Meteorological Agency and Ministry of Water, Irrigation and Energy (MOWIE), Ethiopia
Hydrological data	Stream flow	1986-2008 (daily measurements)	Ministry of Water, Irrigation, and Energy (MOWIE), Ethiopia
Sediment data	Recorded sediment	1986-2008 (daily measurements)	Ministry of Water, Irrigation, and Energy (MOWIE), Ethiopia

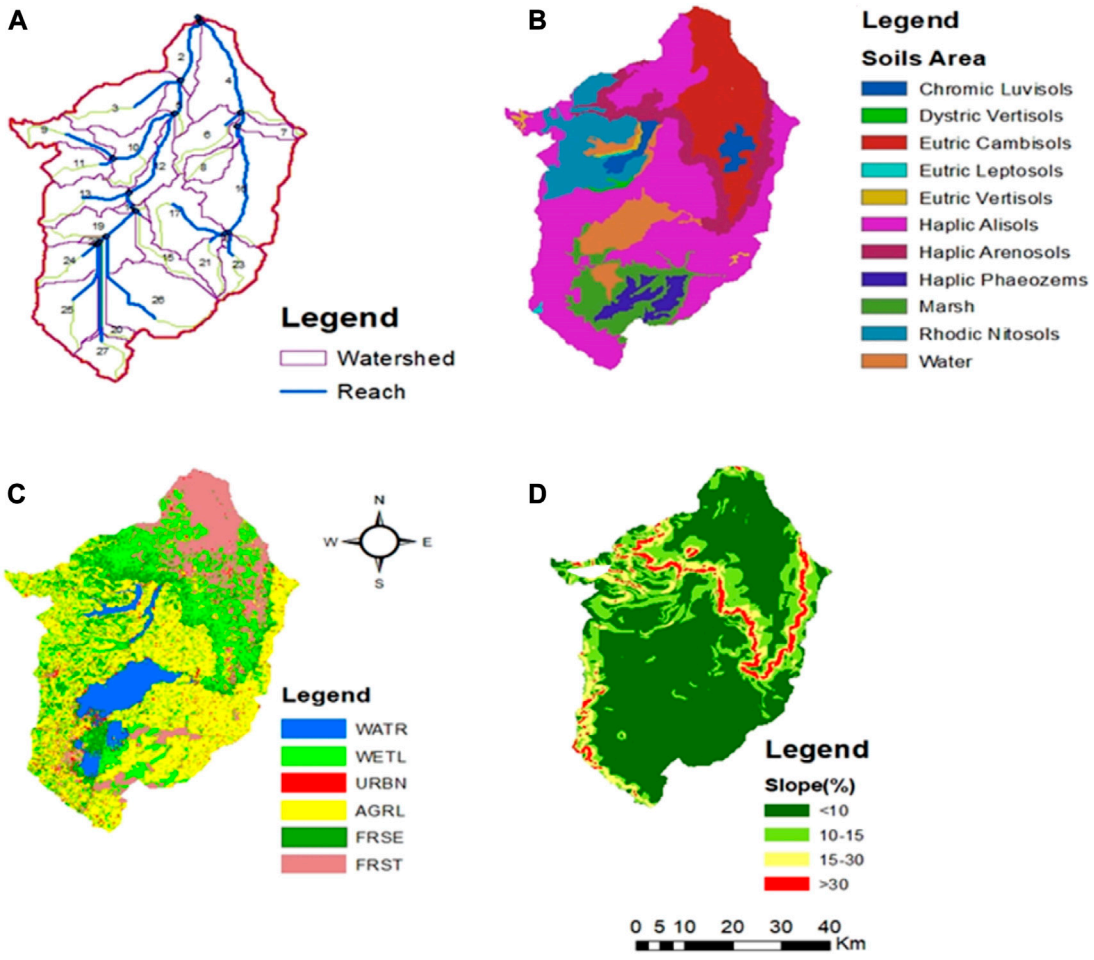

FIGURE 2
Main characteristics of the study area: **(A)** river system and sub-watersheds; **(B)** soil types; **(C)** Land Use Land Cover of 2019; **(D)** terrain slope.

stations, and were collected from the Ethiopian metrological agencies of Alibo, Fincha, Gebete, Hareto, Homi, Jermet, Kombolcha, Nashe, Shambu and Wayyu. The statistical software Xlstat was used to fill in missing data.

2.2.2 Soil data

Soil data were obtained from the Ethiopian Ministry of Water, Irrigation and Energy (MOWIE), and they were pre-processed to follow the Food and Agricultural Organization (FAO) guidelines as

stated in Pennock (2019). Ten soil types can be recognized in the Fincha watershed: Dystric Vertisols, Eutric Cambislos, Eutric Leptosols, Eutric Vertisols, Haplic Alisols, Haplic Arenosols, Haplic Phaeozems, Rhodic Nitisols, Chromic Luvisols, Water and Marsh (Figure 2B).

2.2.3 Land use land cover

Land use is a key SWAT model input that influences surface runoff, evapotranspiration, erosion, nutrients and pesticide load in a watershed. The LULC data used in the present research were previously described by Regasa and Nones (2022), who, using satellite imagery and Geographic Information Systems, investigated LULC changes in past (1989, 2004, 2019) and future (2030, 2040, 2050) years. In their study, ground truth data, key informant interviews and focal group discussions were also considered to reduce uncertainties associated with deriving LULC from remote sensing.

The Fincha watershed was classified into six classes: waterbody, grass/swamp, built-up, agricultural land, forest, and shrub (Figure 2C). The LULC data set was reclassified into six major land classes as it is for use in SWAT. This reclassification was conducted because the SWAT model needs standard names such as WATR, WETL, URBN, AGRL, FRSE, and FRST as indicated in the legend of Figure 2C for waterbody, grass/swamp, built-up, agricultural land, forest, and shrub, respectively.

2.2.4 Slope

Multiple slope classes were defined and then used to delineate SWAT HRU having the same slope, based on a 30 m × 30 m DEM of the Fincha watershed and using the Arc-GIS spatial analysis tool. When defining the hydrologic response unit, Arc-SWAT allows the integration of up to five slope classes. In addition, the SWAT model allows to select a single or multiple slope class. As a result, the slope classes used in this study were broken down into four classes (10%, 15%, 25%, >30%) to represent the variation in the topography of the Fincha watershed (Figure 2D).

2.2.5 Sediment rating curve

The sediment rating curve is generally used to estimate the sediment yield from the flow measurements and sediment concentrations (Asselman, 2000). To overcome the lack of continuous measurements, a sediment rating curve was developed to relate daily stream flow to sediment data recorded at the outlet of the Fincha Dam. Such a curve can show how stream flow affects the rate of sediment movement (Assfaw, 2020; Tilahun et al., 2023), but its reliability highly depends on the available dataset. Moreover, because of the difficulties in measuring sediment transport in high-flow conditions, generally, sediment rating curves are generally more reliable for low to medium flows (Sadeghi and Saeidi, 2010; Tomkins, 2014; Pomázi and Baranya, 2022).

To simulate sediment yield and stream flow, SWAT needs, as model input, sediment, and stream flow data with a continuous time step. Due to the lack of continuous sediment data, these were derived by applying an empirical sediment rating curve to the simulated 1 stream flow. Such an approach is generally used when there are few long-term and trustworthy records of sediment concentrations (Jilo et al., 2019).

Following literature evidence (e.g., Asselman, 2000; Horowitz, 2003; Franzoia and Nones, 2017; Assfaw, 2019; Temiz et al., 2022), a general relationship between sediment concentrations and river discharge can be written as:

$$Q_s = aQ_f{}^b \tag{1}$$

where Q_s is the sediment load in ton day^{-1}, Q_f represents the stream flow in m^3 s^{-1}, while a and b are regression constants to be determined from a regression between measured sediment and water flows.

In the study case, the obtained sediment data (four times in 1990, specifically in February, March April and May), in 1991 two times (October and August), in 1995 (one time in August) and in 1996 (one time in May) was in mg l^{-1}. The concentration was converted to ton day^{-1} via Eq. 2:

$$Q_s = 0.0864 * C * Q_f \tag{2}$$

where C indicates the suspended sediment concentration in mg l^{-1}.

Using the data obtained from MOWIE and reporting flow and sediment data measured at the Fincha gauging station between 1986 and 2008, a sediment rating was created (Figure 3). The regression constants a and b were found to be 2.9508 and 1.2056, respectively.

2.3 Soil and water assessment tool model description and setup

The Soil and Water Assessment Tool (SWAT) was developed by the United States Department of Agriculture (USDA) and is a continuous-time, semi-distributed, process-based watershed model. It was initially developed to predict the impact of land management practices on water, sediment and chemical yields in agricultural watersheds (Arnold et al., 1998; Winchell et al., 2007; Anteneh et al., 2023) but, since then, it has been widely used to understand the hydrological cycle in general, simulating the effect of land use hydrology, water quality and ecosystem services, to eventually derive sediment yield and soil management practices (e.g., Qiu and Wang, 2014; Xue et al., 2014; Dibaba et al., 2021; Kenea et al., 2021; Lin et al., 2022). There is ample literature proving the validity of SWAT in modelling soil erosion and transport processes (see, among many others, Setegn et al., 2010; Phuong et al., 2014; Cousino et al., 2015; Djebou, 2018; Dakhlalla and Parajuli, 2019; Khanchoul et al., 2020).

SWAT divides a watershed into sub-watersheds, connected through a stream channel. Further, each sub-watershed is divided into Hydrologic Response Units (HRUs), which represent a unique combination of soil, land use and slope type in a sub-watershed (Arnold et al., 2012; Rathjens and Oppelt, 2012). In SWAT, hydrology and sediment are simulated at the HRU level, and then the outputs are summarized first at the sub-watershed level, and then at the watershed level, routing these quantities through the stream network (Neitsch et al., 2011). SWAT can account for that, simulating all the effects of soil erosion and climate change on water supply properly (Krysanova and White, 2015; Boru et al., 2019).

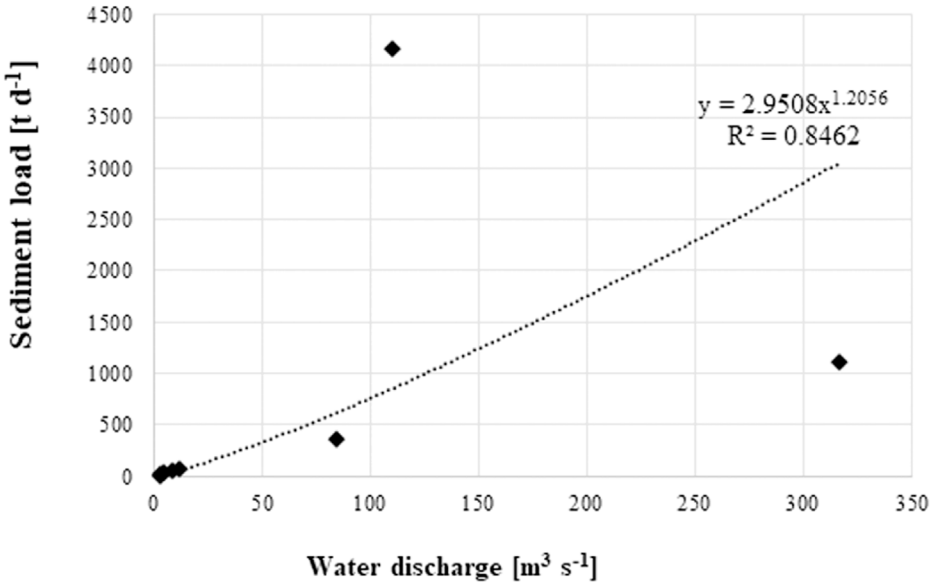

FIGURE 3
Sediment rating curve for the period 1986-2008. Data were measured at the Fincha gauging station (source: MOWIE).

From the SWAT website (swat.tamu.edu), Arc-SWAT version 2012.10 4.19 was downloaded, and its interface was linked to Arc-GIS 10.3.1 for the modelling. This latter process involves setting up a SWAT project, defining the spatial extent of the analysis (watershed, sub-watersheds, HRUs), writing and editing SWAT input, and performing the simulations. Following the collection of data, all input data were prepared, the watershed and the HRUs were defined, and the classification of land use, soil, and slope was included in the model.

Based on the water balance equation (Swami and Kulkarni, 2016), SWAT simulates the hydrological cycle:

$$SW_t = SW_o + \sum_{i=1}^{t}\left(R_{day} - Q_{surf} - E_a - W_{seep} - Q_{gw}\right) \quad (3)$$

where SW_t is the last soil water content [mm], SW_o is the first soil water content on day i [mm], t indicates the time [days], R_{day} is the amount of precipitation on day i [mm], Q_{surf} represents the amount of surface runoff on day i [mm], W_{seep} is the amount of water entering vadose zone from the soil profile on day i [mm], E_a is the amount of evapotranspiration on day i [mm] and Q_{gw} indicates the amount of return flow on day i [mm].

In our study, the SWAT model was applied to estimate hydrological components such as surface run-off, evapotranspiration, and sediment yield. Sediment yield was estimated at the HRU level, through a Modified Universal Soil Loss Equation (MUSLE) (e.g., Khelifa et al., 2017; Ayele et al., 2021; Sahar et al., 2021)

$$Sed = 11.8\left(Q_{surf} * q_{peak} * Area_{HRU}\right)^2 * K * C * P * LS * CFRG \quad (4)$$

where Sed is sediment yield in metric tons per day, Qsurf is the surface runoff volume [mm], q_{peak} is the peak run-off rate [$m^3\ s^{-1}$], $Area_{HRU}$ is the area of HRU [ha], K is the soil erodibility factor and depends on the type of soil, C is the factor and crop management factor, P is the practice support factor usually only apply to cropland or land that is managed to conserve soil, while L and S factors indicate the length and steepness of the slope, respectively. $CFRG$ is the course fragment factor.

2.3.1 Watershed delineation

The watershed and the sub-watersheds were delineated by using the 30 m-resolution DEM of the Fincha watershed, via defining the stream network in SWAT and considering flow accumulation and water flow direction. SWAT model enables users to delineate watersheds and sub-watersheds using Digital Elevation Models (DEMs) by expanding the Arc-GIS and spatial analyst extension function. Watershed and sub-watershed delineation was accomplished through a series of steps, including DEM setup, stream definition, inlet outlet definition, watershed outlet selection and definition, and finally watershed parameter calculation (Figure 2A).

The Arc SWAT model interface by default proposes the minimum and maximum watershed area, as well as the size of the sub-watershed in hectares to define the minimum drainage area required to form the stream's origin. The smaller the threshold area, the more detail of the drainage network, the greater the number of sub-watersheds, and the higher the number of HRUs. However, more processing time and computer space are required. As a result, the model's proposed threshold was used to determine the optimal size of the threshold area.

2.3.2 Hydrologic response units

HRUs were defined based on the topographical characteristics of the terrain as derived from the DEM and assigned to each sub-watershed based on a threshold value for LULC, soil, and slope categories. According to Megersa et al. (2019), a threshold of 10% was imposed in defining HRUs, to exclude areas characterized by small land uses and slope classes. Consequently, the Fincha watershed was divided into 27 sub-watersheds and then

subdivided into 234 HRUs. It is worth reminding that only 9 of these sub-watersheds are located upstream of the Fincha Dam, and are therefore contributing to the sediment yield entering the dam.

2.3.3 Model calibration and validation

A sensitivity analysis is needed to investigate the model's capacity to adequately predict water stream flow and sediment yield (Anaba et al., 2016), and this was done via the SWAT Calibration and Uncertainty Procedures (SWAT-CUP) interface (Mekuriaw, 2019) combined with the SUFI-2 approach (Leta et al., 2021a). For that, seven parameters connected to sediment processes and nine parameters representing stream flow were selected, following literature evidence (Khelifa et al., 2017; Daramola et al., 2019; Yuan and Forshay, 2019; Kenea et al., 2021).

SWAT Calibration and Uncertainty Procedures (SWAT-CUP), a program for integrated sensitivity analysis, calibration, and validation, was used to analyze the uncertainties of SWAT model prediction (Dibaba et al., 2021). In this investigation, the sensitivity analysis was performed using the SUFI-2 techniques and looking at the water discharge - sediment load data measured at the outlet of the Fincha Reservoir (at Fincha Dam) during the period 1986-2008.

To perform model calibration and validation, the stream flow and sediment data were divided into two periods, and an initial warm-up period was also taken into consideration. The initial three (1986–1988) years were chosen as the warm-up period, while the calibration was performed for the 1989-2002 period, and 2003-2008 was utilized to validate the SWAT model. To test the goodness of fit between monthly simulated and observed values, the model's performance was assessed using the coefficient of determination (R^2), the Nash-Sutcliffe simulation efficiency (*NSE*), and the per cent bias (*PBIAS*).

Determination coefficients can range from 0 (inadequate model) to 1 (the model perfectly fits the data), and, typically, values R^2 larger than 0.6 indicate good correlation (Leta et al., 2021b). The *NSE* values can reach a maximum of 1 (perfect fit), while a negative *NSE* value indicates that the model's performance is inferior to that obtained using the observations' mean as a predictor (Jilo et al., 2019). The simulation efficiency is classified as unsatisfactory, satisfactory, good, or very good if $NSE < 0.50$, $0.5 < NSE < 0.65$, $0.65 < NSE < 0.75$, $0.75 < NSE < 1$, respectively (Leta et al., 2021a).

PBIAS assesses the typical tendency of the simulated data to differ from the observed data in size or frequency, and lower *PBIAS* values indicate better simulation results. Moriasi et al. (2012) define *PBIAS* positive values as a model underestimation, while negative values as a model overestimation.

According to Yasir et al. (2020) and Dibaba et al. (2021), the following equations were applied to determine R^2 (Eq. 5), *NSE* (Eq. 6) and *PBIAS* (Eq. 7):

$$R^2 = \left[\frac{\sum_{i=1}^{n}(Q_{Obs} - \bar{Q}_{Obs})(Q_{cal} - \bar{Q}_{Cal}}{\sum_{i=1}^{n}(Q_{Obs} - \bar{Q}_{Obs})^2 \sum_{i=1}^{n}(Q_{Cal} - \bar{Q}_{Cal})^2}\right]^2 \quad (5)$$

$$A = 1 - \frac{\sum_{i=1}^{n}(Q_{Obs} - Q_{Cal})^2}{\sum_{i=1}^{n}(Q_{Obs} - \bar{Q}_{Obs})^2} \quad (6)$$

$$PBIAS = \frac{\sum_{i=1}^{n}(Q_{Obs} - Q_{Calc})*100}{\sum_{i=1}^{n} Q_{Obs}} \quad (7)$$

where Q_{Obs} is the actual variable, $\bar{Q}_{Obs}$ is the time average of the variable Q_{Obs}, Q_{Cal} is the simulated variable and $\bar{Q}_{Cal}$ is its time average. It is worth noticing that these equations are valid for both water flow and sediment data.

2.4 Scenarios simulation

Using scenario-based simulations, the effects of current and future LULC changes on watershed sediment yield were assessed for the period 1989-2050. This was done by creating six scenarios (historical reference years 1989, 2004, 2019; future predicted 2030, 2040, 2050) accounting for different LULC conditions (Regasa and Nones, 2022). A fixing-changing method was applied to investigate the effects of LULC change (Leta et al., 2021b): SWAT was run with changing LULC maps, but all the other modelling parameters were kept constant as derived from the model validation (Gessesse et al., 2015). The sediment yield was computed separately for the entire Fincha watershed (27 sub-watersheds) and the region upstream of the Fincha Dam (9 sub-watersheds). Pearson's correlation method (Aga et al., 2020) was used to assess the variations in LULC classes and the sediment yields, while the pair-wise Pearson correlation matrix was applied to detect linear correlations.

2.5 Sensitivity analysis

The sensitivity analysis was based on the SUFI-2 algorithm techniques (Arnold et al., 2013). The *p*-value and the t-stat value were used to assess the sensitivity of each parameter and then rank it, with rank 1 indicating the most sensitive parameter. Statistically, bigger absolute *t*-stats and lower *p*-values mean that a parameter is significant. On the other part, a high *p*-value indicates that there is no correlation between changes in the predictor values and the response variable (Pandey et al., 2021).

3 Results

3.1 Sensitivity analysis

As reported in Tables 2, 3, the performed sensitivity analysis shows that the top three most sensitive parameters for stream flow are 1) groundwater delay (V_GW_DELAY.gw), 2) threshold water depth in the shallow aquifer required for return flow to occur (V_GWQMN.gw), and iii) Manning's roughness value for the main channel (R_CH_N2.rte). In the case of sediments, the top three most sensitive are 1) exponential factor for channel sediment routing (R_SPEXP.bsn), 2) sediment concentration in lateral and groundwater flow (R_LAT_SED.hru), and iii) channel cover factor (R_CH_COV2.rte).

3.2 Soil and water assessment tool calibration and validation

Most of the studies performed using SWAT divided stream flow and sediment data for calibration and validation equally. However, according to the study conducted by Arnold et al. (2012), in the case

TABLE 2 Stream flow parameters with range and fitted value, as derived from the sensitivity analysis performed using SUFI-2. Their rank is based on the *p*-value.

Parameter	Description	Range	Fitted value	Calibration		
				t-stat	*p*-value	Rank
V_GW_DELAY.gw	Groundwater delay [days]	0–500	21.25	−9.891	0.000	1
R_CN2.mgt	SCS runoff curve number II	−25–25	−15.625	2.391	0.018	2
V_GWQMN.gw	Threshold depth of water in the shallow aquifer required for return flow to occur [mm H2O]	0–5,000	2012.5	−2.022	0.045	3
R_CH_N2.rte	Manning's "n" value for the main channel	0–1	0.7575	0.717	0.474	4
R_SOL_AWC(1).sol	Available water capacity of the 1st soil layer [mm H2O mm soil^{-1}]	−25–25	6.875	0.699	0.486	5
R_SOL_K (1).sol	Saturated hydraulic conductivity at the 1st soil layer [mm h^{-1}]	−25–25	9.875	0.255	0.799	6
R_SLSUBBSN.hru	Average slope length [m]	0–150	133.875	0.153	0.878	7
R_RCHRG_DP.gw	Deep aquifer percolation fraction	0–1	0.6475	−0.099	0.921	8
V_ALPHA_BF.gw	Base flow alpha factor [day^{-1}]	0–1	0.3125	0.060	0.952	9

TABLE 3 Sediment parameters with range and fitted value, as derived from the sensitivity analysis performed using SUFI-2. Their rank is based on the *p*-value.

Parameter	Description	Range	Fitted value	Calibration		
				t-stat	*p*-value	Rank
R_SPEXP.bsn	Exponential factor for channel sediment routing	0–2	1.71	−9.85	0.00	1
R_LAT_SED.hru	Sediment concentration in lateral and groundwater flow	1–1,000	242.50	−5.07	0.00	2
R_CH_COV2.rte	Channel cover factor	0–1	0.56	−3.06	0.00	3
R_SPCON.bsn	Linear factor for channel sediment routing	0–0.01	0.005	−1.95	0.05	4
R__CH_COV1.rte	Channel erodibility factor	0.01–0.06	0.11	−1.53	0.13	5
R__PSP.bsn	Peak rate adjustment factor for sediment routing in the sub-basin (tributary channels)	0–1	0.88	−0.42	0.67	6
R__USLE_P.mgt	USLE support Practice factor	0–1	0.208	−0.31	0.75	7

of watersheds characterized by a scarcity of data, most of them should be used for calibration, while a minor part of the data is for validation. As an example, Ait M'Barek et al. (2023) used 75% of hydrological data for calibration and 25% for validation.

As the Fincha watershed is also characterized by data scarcity, a similar approach was followed, using the observed monthly stream flow and sediment at the Fincha reservoir close to the Fincha Dam outlet from 1986 to 2008. The warm-up period spanned from 1986 to 1988, and was used to reduce the impact of the model's initial conditions, while the calibration period lasted from 1989 to 2002, and the validation period from 2003 to 2008.

The model is very effective at simulating the stream flow (Figure 4), while more uncertainties are connected with the simulation of sediment load during high-flow conditions (Figure 5). In both cases, SWAT slightly overestimates peak conditions during the calibration phase, while more consistent results characterize the validation phase.

The capability of the SWAT model in reproducing observed stream flow and sediment load was evaluated with a few statistics, which are summarized in Table 4. In this case, it is possible to observe that, on average, SWAT is able to adequately reproduce the observed phenomena, and it is considered reliable in simulating future conditions (Section 3.3).

A positive PBIAS for both periods indicates that the overall expected sediment production had been slightly underestimated, especially during the validation period, mainly due to problems in detecting water and sediment peaks (Figure 5).

3.3 Soil erosion and sediment yield

The SWAT model was applied to simulate sediment yield in 27 sub-watersheds (see Section 2.2). Based on the approach proposed by Dibaba et al. (2021), these sub-watersheds were classified in terms of soil loss (Table 5).

This classification pointed out significant dissimilarities across the Fincha watershed (Figure 6), which are mainly connected with the different LULC situations of each sub-watershed, as discussed in the next sections.

The simulated annual sediment yield in the Fincha watershed varies significantly over space and time, ranging from 0.36 to 183.80 t ha^{-1} (Table 6), with an average of 32.51, 34.05, 41.20, 46.20, 51.19, 53.98 t ha^{-1} for 1989, 2004, 2019, 2030, 2040, and 2050, respectively. This indicates an increment of soil loss of 8.69 t ha^{-1} from 1989 to 2009, while the increase forecasted for

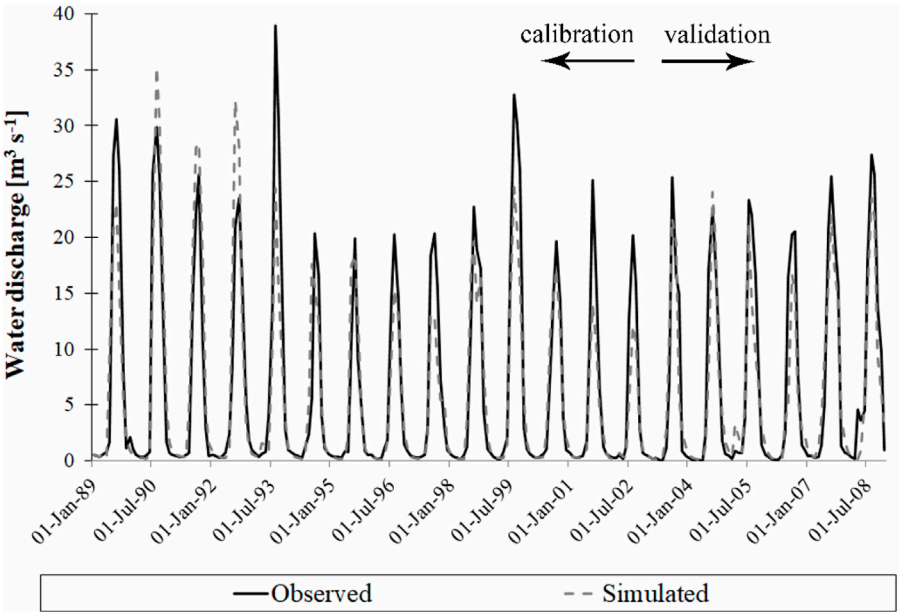

FIGURE 4
Comparison between computed and measured water discharge at the Fincha Dam outlet, during the calibration (1989–2002) and validation (2003–2008) phases.

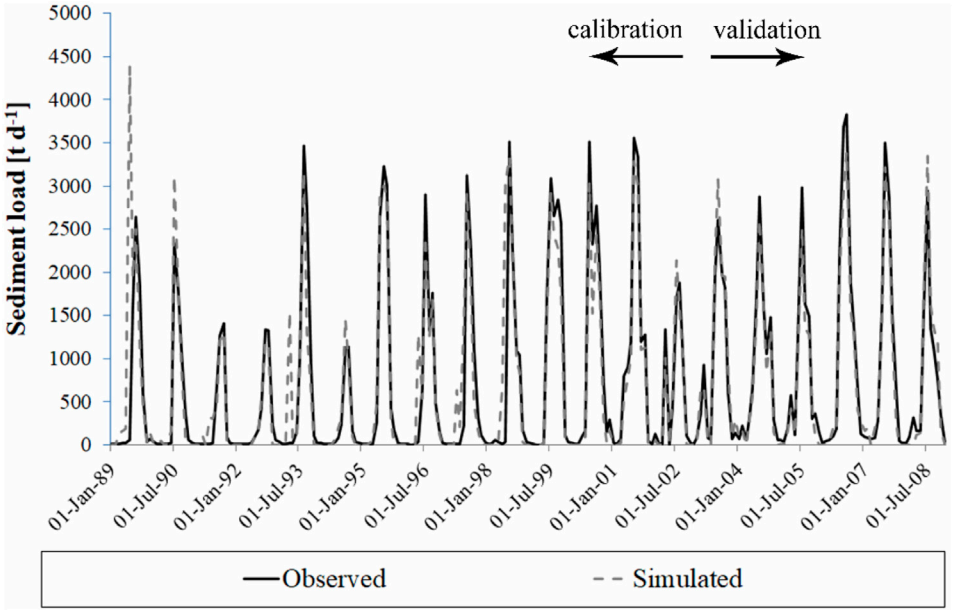

FIGURE 5
Comparison between computed and measured sediment load at the Fincha Dam outlet, during the calibration (1989–2002) and validation (2003–2008) phases.

the next 30 years (2019–2050) will be even more significant, reaching an annual sediment yield of 12.78 t ha^{-1}.

Focusing only on the nine sub-watersheds upstream of the Fincha Dam, and therefore contributing to feeding the reservoir with sediments, the average annual sediment yield magnitude reduces, but a similar spatiotemporal variability is still visible (Table 6). The annual average sediment yield is expected to increase from 6.71 t ha^{-1} in 1989 to 15.19 t ha^{-1} in 2050.

Even if the average annual sediment yield of sub-watersheds located upstream of the Fincha Dam is lower than the average annual sediment yield of the whole watershed, the sediment amount entering the reservoir annually is still very high. In detail, 1.44, 1.85,

TABLE 4 Monthly stream flow and sediment statistics for calibration (1989–2002) and validation (2003–2008).

	Statistical test	R^2	NSE	PBIAS
Stream flow	Calibration	0.83	0.83	8.3
	Validation	0.84	0.76	12.2
Sediment	Calibration	0.83	0.63	10.9
	Validation	0.86	0.72	14.2

2.75, 3.08, 3.27, and 3.42 million tons in 1989, 2004, 2019, 2030, 2040, and 2050, respectively, can enter the Fincha dam lake which has a storage capacity of 660 million m^3 (Duressa and Jubir, 2018; Duressa and Regasa, 2021). As shown in Figure 7, the sediment that can enter the Fincha Lake increases in time, following the expansion of agriculture, urbanization and deforestation.

4 Discussion

The observed and simulated water and sediment discharges at the Fincha Dam showed an overall good agreement, indicating the reliability of the SWAT model in simulating these parameters in data-scarce regions. However, the model was unable to adequately reproduce the peaks in both water discharge and sediment yield. The underestimation of peak water flows generally results in an underestimation of the sediment peaks (Akoko et al., 2021), and such an underestimation is also a significant source of error in defining the overall sediment load of the watershed.

Moreover, the reliability of SWAT in estimating sediment yield is highly dependent on the availability of long-term datasets. In Ethiopia, long-term monitoring data are very rare, in particular in terms of sediment information. In the present work, a sediment rating curve was developed on the basis of the suspended sediment concentration measured occasionally at the Fincha Dam outlet. Even if based on a limited dataset, this curve is characterized by a strong correlation (R^2 = 0.86) between recorded sediment and water flow data. However, uncertainties connected with using such a rating curve increase with the increase in water discharge, as only a few points were measured in high flow conditions (Figure 3). Despite the lack of data, the obtained curve is in line with similar investigations (Debela, 2022), at least for lower discharges.

The difference in peak sediment yields between observed and simulated data is comparable to the difference in estimating the peak flow. This problem, pointed out in similar studies, might be connected to the used model. For example, Leta et al. (2023) argue that the SWAT model's underestimation of peak flows results in an underestimation of sediment peak. In their work, Dibaba et al. (2021) show errors in predicting sediment yield connected to the difficulties of the SWAT model in predicting second storm effects.

For the entire Fincha watershed, the mean annual soil loss rate was calculated as 32.51 t ha^{-1}, 34.05 t ha^{-1}, 41.20 t ha^{-1}, 46.20 t ha^{-1}, 51.19 t ha^{-1}, 53.98 t ha^{-1} in 1989, 2004, 2019, 2030, 2040, 2050, respectively. This translates into an increase of annual soil loss of 8.69 t ha^{-1} during the last 30 years (1989–2019), and a forecasted increase of 12.78 t ha^{-1} for the next 3 decades, which will further negatively impact the overall watershed as well as the reservoirs located therein (Fincha, Amerti and Nashe). According to the study conducted on the Fincha watershed by Regasa and Nones (2022), for the last 30 years, deforestation, agriculture and urbanization have increased and this increment is expected for the future and is the reason for the increase of soil erosion and connected severity (Table 5).

As pointed out by Dibaba et al. (2021), tolerable soil loss is needed for maintaining ecosystem services without compromising the soil's ability to continue providing those services in the future. The maximum tolerable soil loss (<11 t ha^{-1} $year^{-1}$) estimated for Ethiopian watersheds is much lower than the estimated mean annual soil loss rate in the current study area (Girmay et al., 2020; Ayalew and Bharti, 2022), pointing out that the Fincha watershed is at very high of soil erosion. On the other part, the Fincha soil erosion rates are much lower than other local scale studies, which estimated an annual soil loss rate of 377.26 t ha^{-1} in the Chogo watershed, located very close to the current study area (Negash et al., 2021).

The mean annual sediment yields of the nine sub-watersheds located upstream of the Fincha Dam span will increase from 13.42 t ha^{-1} in 1989 to 30.38 t ha^{-1} in 2050. As the estimated mean annual soil loss rate is considerably higher than the maximum tolerable soil loss limit of 11 t ha^{-1}, also this area is threatened by high erosion, with consequent negative effects on the socio-economy (Dibaba et al., 2021).

The proportion of area Fincha watershed at low erosion risk covered around 18% of the watershed during the past (reference

TABLE 5 Annual soil erosion and its severity for past and future scenarios of Fincha reservoir.

Annual soil loss [t ha^{-1} $year^{-1}$]	Severity	Area in hectare [ha]						Area in per cent [%]					
		1989	2004	20,019	2030	2040	2050	1989	2004	2019	2030	2040	2050
<11	Low	14,348	14,348	14,348	6,996	6,996	6,996	17.77	17.77	17.77	8.66	8.66	8.66
11–18	Moderate	23,132	14,740	0	7,352	7,352	7,352	28.64	18.25	0.00	9.10	9.10	9.10
18–25	High	34,044	25,472	0	0	0	0	42.16	31.54	0.00	0.00	0.00	0.00
25–50	Very high	9,232	26,196	57,176	57,176	40,212	25,472	11.43	32.44	70.80	70.80	49.79	31.54
50–75	Severe	0	0	9,232	9,232	26,196	40,936	0.00	0.00	11.43	11.43	32.44	50.69
>75	Very severe	0	0	0	0	0	0	0.00	0.00	0.00	0.00	0.00	0.00

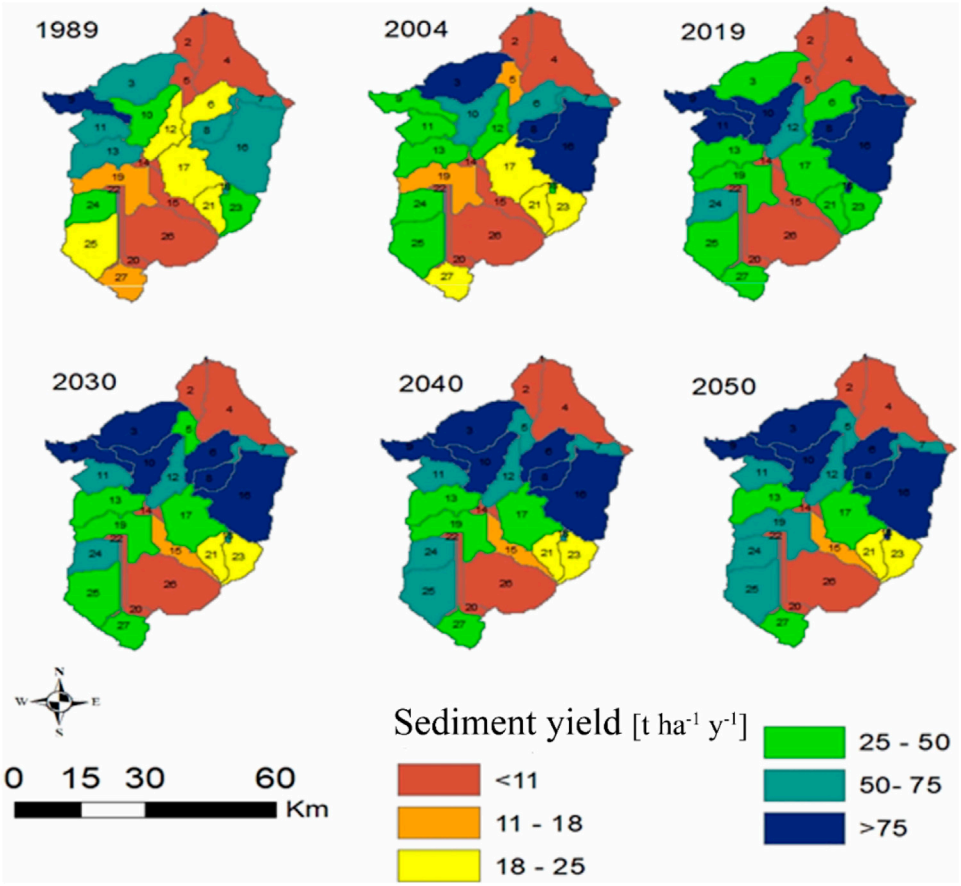

FIGURE 6
Spatial distribution of the sediment yield, subdivided for each sub-watershed.

TABLE 6 Simulated sediment yield for the six scenarios, for both the overall Fincha watershed and the nine sub-watersheds upstream of the Fincha Dam.

	Scenario	Annual sediment yield range [t ha^{-1}]	Average annual sediment yield [t ha^{-1}]
Fincha watershed	1989	0.36–83.74	32.51
	2004	0.80–113.72	34.05
	2019	0.28–121.96	41.20
	2030	0.48–117.92	46.20
	2040	1.06–162.96	51.19
	2050	1.12–183.80	53.98
sub-watershed upstream Fincha Dam	1989	0.36–40.06	6.71
	2004	0.40–48.96	8.49
	2019	0.28–61.72	12.30
	2030	0.94–64.42	13.69
	2040	1.06–68.78	14.57
	2050	1.12–69.94	15.19

years 1989, 2004, 2019) while a decrease is forecasted for the future (around 9% in 2030, 2040, 2050). On the other part, areas exposed to high erosion risk will increase, mainly because of deforestation in favour of agricultural land, expansion of urban areas and grassland, and growth and relocation of the population as stated (Regasa and Nones, 2022). This dynamic and rate of soil loss is a characteristic of

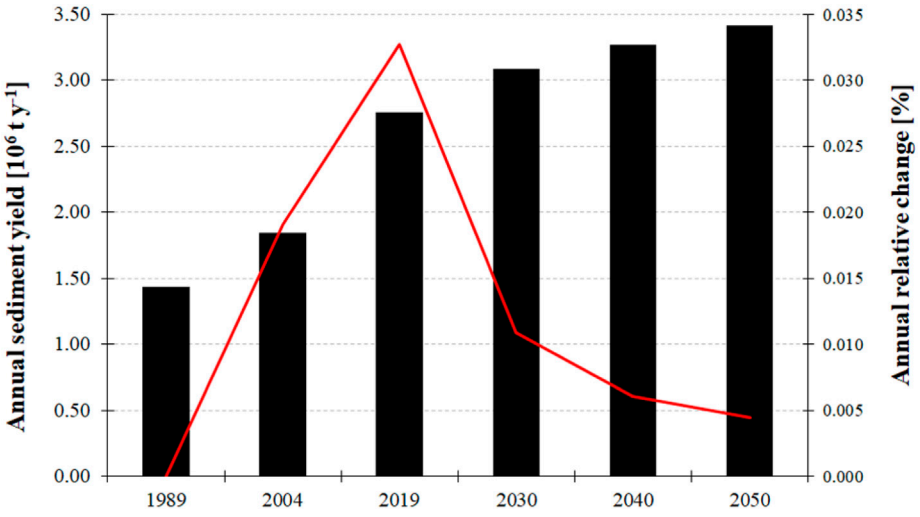

FIGURE 7
Annual sediment yield entering the Fincha Dam reservoir from the sub-watersheds located upstream (black bars). A slowdown in the annual sediment yield entering the Dam is observable by looking at the relative changes (red line).

many highland areas in Ethiopia (Weldu Woldemariam and Edo Harka, 2020), pointing out that the problem of soil erosion should be tackled at the national level, rather than with very local policies. The soil erosion risk showed a high spatial variation across the study landscape (Figure 6): low-risk areas were predicted downstream of the Fincha Dam, while areas characterized by the highest erosion risk are in the northwestern and eastern parts of the Fincha watershed. The evaluation of SY changes according to spatial location helps in pinpointing hotspot areas and areas where soil loss may be within acceptable limits.

Brhane and Mekonen (2009) focused on planning soil conservation strategies in the Medego watershed in Northern Ethiopia, using the Revised Universal Soil Loss Equation (RUSLE) to capture the annual soil loss. In their work, they pointed out that an acceptable soil loss is around 2 t ha^{-1} $year^{-1}$. This value agrees with Dibaba et al. (2021), who estimated that the manageable soil loss in different Ethiopian watersheds ranges between 2 and 18 t ha^{-1} $year^{-1}$.

Relatively less eroded areas were situated at lower elevations in the eastern and western parts of the sub-watershed, where the slope inclination is below 10% the above-mentioned factors made the area generate high soil loss risks. Similar results have been reported by earlier studies that directly correlated soil loss rate to terrain slope (Dibaba et al., 2021). The Nashe watershed, located in the Blue Nile region in Ethiopia, was the subject of a comparable study (Leta et al., 2023). In this work, the slope gradient, the percentage of farmland, and the amount of rainfall are all strongly correlated with the mean sediment production and the erosion hotspot zones. A high amount of sediment output was observed in steep sub-catchments with large amounts of land covered by agricultural activities and affected by high precipitation. Moreover, the authors have shown that, on slopes of less than 8%, the risk of erosion is typically low, while it increases for steeper slopes, especially in agricultural areas.

According to Regasa et al. (2021), the communities displaced from the reservoir areas were forced to resettle downstream of the dam, in areas characterized by lower soil loss. However, these communities were forced to relocate without receiving fair compensation because of the expansion of the number and dimension of reservoirs for hydropower production, taking them away from their farmland (Dibaba et al., 2020). Residents found it difficult to stay and were compelled to relocate due to the increased resettlement on unproductive lands and the relative depreciation of agricultural land, which resulted in further increasing soil erosion.

This study pointed out that most of the sub-watersheds of the Fincha watershed are highly threatened by soil erosion, and therefore require management and mitigation strategies to safeguard the environment and reduce the sediment yield entering the Fincha reservoir. However, such strategies could be costly and time-consuming, and cannot be applied at the same time all over the watershed. In this respect, the present investigation can provide information on what areas should be prioritized, but more studies are needed to propose effective management strategies to reduce soil erosion that also account for the sustainable socio-economic development of the area.

Despite the several assumptions made in this study, it is worth stressing here that the present results are consistent with the information reported by independent organizations such as UNESCO. Indeed, the sediment yield calculated at Addis Abeba in 2018 was around 67.53 t ha^{-1} $year^{-1}$ (UNESCO WINS, 2023), indicating that the overall Ethiopia region is subjected to significant erosion.

Looking at similar studies performed worldwide, one can notice that Ethiopia is highly impacted by soil erosion. For example, Ait M'Barek et al. (2023) estimated the average annual soil loss of 4.71 t ha^{-1} $year^{-1}$ in the El Grou watershed, located in north-central Morocco. In another study (Li et al., 2021), the authors show that the East African Highlands of Kagera Basin, located in Burundi (23% of the basin), Rwanda (34%), Tanzania (35%), and Uganda (8%), has an average soil erosion rate of 10.54 t ha^{-1} $year^{-1}$ (Li et al., 2021).

The lack of appropriate monitoring of watershed-wide soil erosion, and, more importantly, the quantity of sediments

entering and outgoing the Fincha reservoir, does not allow for a precise estimation of the lake sedimentation, therefore key questions connected to expected reservoir life and decrease of hydropower production connected with sedimentation remain unanswered, calling for additional research. To overcome the lack of in-field data, a potential option to be investigated in the next years is the use of remotely sensed data, taking advantage of examples developed in international projects such as HYPOS (hypos-project.eu). It is worth reminding that field information is still needed for calibrating and validating remote information, so more effort should be made in developing *in-situ* monitoring networks.

5 Conclusion

Using the Fincha watershed as a case study, the present research focused on understanding, via a modelling approach, the impact of LULC changes on soil erosion, comparing historical trends with future predictions. As pointed out by Regasa and Nones (2022), favouring agricultural land and settlements over natural forests might have a detrimental impact on soil erosion. In this work, it was demonstrated, via a numerical approach, that LULC changes are the major driver of soil erosion in the Fincha watershed, as it increased from 32.51 t ha^{-1} year^{-1} in 1989 to 41.20 t ha^{-1} year^{-1} in 2019, and it forecast to further increase till 53.98 t ha^{-1} year^{-1} in 2050 at the watershed scale. Such soil loss translates into sediment yield transported in the Fincha Dam reservoir, which was estimated to be around 1.44 million tons in 1989 and to increase to 3.42 million tons by 2050, eventually reducing the lifetime of the dam and negatively affecting the local socio-economy, which is largely connected with the functioning of the dam for hydropower and agricultural purposes.

Based on the estimated rate of mean annual soil loss, the erosion risk was classified into six classes, pointing out that the majority of the watershed is threatened by very high erosion risk, with severe erosion located in the central, northeastern, and northwestern sub-watersheds. As soil erosion represents a major threat to the current socio-economic development of the area, the classification proposed here could serve as a basis to prioritize future management strategies, aiming to reduce the impact of soil loss on the local environment and population.

Despite the uncertainties connected with the lack of data about soil erosion across the Fincha watershed and the assumption of LULC changes as the unique driver for soil erosion, neglecting additional drivers like climate change, the results proposed in this research are in line with literature evidence, and can provide practical implications for future land use management schemes. Indeed, the modelled scenarios can be used to guide water authorities, decision-makers, land managers, planners, and other interested parties to investigate potential management practices to reduce soil loss, particularly in areas characterized by high and severe erosion rates. This might result in improving the socio-economy in the Fincha watershed, eventually alleviating food scarcity and biodiversity losses.

Data availability statement

The datasets presented in this study can be found in online repositories. The names of the repository/repositories and accession number(s) can be found below: https://dataportal.igf.edu.pl/group/fincha-dam-ethiopia-ncn.

Author contributions

Conceptualization, MR and MN; writing—original draft preparation, MR and MN; literature review, MR and MN; modelling, MR; data analysis, MR; supervision, MN; project administration, MN; funding acquisition, MN. All authors contributed to the article and approved the submitted version.

Funding

This research was funded by NCN National Science Centre Poland–call PRELUDIUM BIS-1, Grant Number 2019/35/O/ST10/00167. Project website: https://sites.google.com/view/lulc-fincha/home.

Conflict of interest

The authors declare that the research was conducted in the absence of any commercial or financial relationships that could be construed as a potential conflict of interest.

Publisher's note

All claims expressed in this article are solely those of the authors and do not necessarily represent those of their affiliated organizations, or those of the publisher, the editors and the reviewers. Any product that may be evaluated in this article, or claim that may be made by its manufacturer, is not guaranteed or endorsed by the publisher.

References

Aga, A. O., Melesse, A. M., and Chane, B. (2020). An alternative empirical model to estimate watershed sediment yield based on hydrology and geomorphology of the basin in data-scarce rift valley lake regions, Ethiopia. *Geosciences* 10 (1), 31. doi:10.3390/geosciences10010031

Ait M'Barek, S., Bouslihim, Y., Rochdi, A., and Miftah, A. (2023). Effect of LULC data resolution on hydrological and erosion modeling using SWAT model. *Model. Earth Syst. Environ.* 9 (1), 831–846. doi:10.1007/s40808-022-01537-w

Akoko, G., Le, T. H., Gomi, T., and Kato, T. (2021). A review of SWAT model application in Africa. *Water* 13 (9), 1313. doi:10.3390/w13091313

Anaba, L. A., Banadda, N., Kiggundu, N., Wanyama, J., Engel, B., and Moriasi, D. (2016). Application of SWAT to assess the effects of land use change in the Murchison Bay catchment in Uganda. *Comput. Water, Energy Env. Eng.* 6 (1), 24–40. doi:10.4236/cweee.2017.61003

Aneseyee, A. B., Elias, E., Soromessa, T., and Feyisa, G. L. (2020). Land use/land cover change effect on soil erosion and sediment delivery in the Winike watershed, Omo Gibe Basin, Ethiopia. *Sci. Total Environ.* 728, 138776. doi:10.1016/j.scitotenv.2020.138776

Ang, R., Kinouchi, T., and Zhao, W. (2023). Sediment load estimation using a novel regionalization sediment-response similarity method for ungauged catchments. *J. Hydrology* 618, 129198. doi:10.1016/j.jhydrol.2023.129198

Anteneh, Y., Alamirew, T., Zeleke, G., and Kassawmar, T. (2023). Modeling runoff-sediment influx responses to alternative BMP interventions in the Gojeb watershed, Ethiopia, using the SWAT hydrological model. *Environ. Sci. Pollut. Res.* 30 (9), 22816–22834. doi:10.1007/s11356-022-23711-4

Aredo, M. R., Lohani, T. K., and Mohammed, A. K. (2023). Assessment of river response to water abstractions in the Weyib Watershed, Ethiopia. *Int. J. River Basin Manag.* 2023, 1–12. doi:10.1080/15715124.2023.2248488

Arnold, J. G., Kiniry, J. R., Srinivasan, R., Williams, J. R., Haney, E. B., and Neitsch, S. L. (2013). *SWAT 2012 input/output documentation*. Texas Water Resources Institute. Available at: https://swat.tamu.edu/docs/.

Arnold, J. G., Moriasi, D. N., Gassman, P. W., Abbaspour, K. C., White, M. J., Srinivasan, R., et al. (2012). Swat: Model use, calibration, and validation. *Trans. ASABE* 55 (4), 1491–1508. doi:10.13031/2013.42256

Arnold, J. G., Srinivasan, R., Muttiah, R. S., and Williams, J. R. (1998). Large area hydrologic modeling and assessment part I: Model development 1. *JAWRA J. Am. Water Resour. Assoc.* 34 (1), 73–89. doi:10.1111/j.1752-1688.1998.tb05961.x

Asselman, N. E. M. (2000). Fitting and interpretation of sediment rating curves. *J. Hydrology* 234 (3-4), 228–248. doi:10.1016/S0022-1694(00)00253-5

Assfaw, A. T. (2019). Calibration, validation and performance evaluation of SWAT model for sediment yield modelling in Megech reservoir catchment, Ethiopia. *J. Environ. Geogr.* 12 (3-4), 21–31. doi:10.2478/jengeo-2019-0009

Assfaw, A. T. (2020). Modeling impact of land use dynamics on hydrology and sedimentation of megech dam watershed, Ethiopia. *Sci. World J.* 2020, 1–20. doi:10.1155/2020/6530278

Ayalew, L. T., and Bharti, R. (2022). Modeling sediment yield of rib watershed, northwest Ethiopia. *ISH J. Hydraulic Eng.* 28 (1), 491–502. doi:10.1080/09715010.2020.1797544

Ayana, A. B., Edossa, D. C., and Kositsakulchai, E. (2012). Simulation of sediment yield using SWAT model in Fincha Watershed, Ethiopia. *Agric. Nat. Resour.* 46 (2), 283–297.

Ayele, G. T., Kuriqi, A., Jemberrie, M. A., Saia, S. M., Seka, A. M., Teshale, E. Z., et al. (2021). Sediment yield and reservoir sedimentation in highly dynamic watersheds: The case of koga reservoir, Ethiopia. *Water* 13 (23), 3374. doi:10.3390/w13233374

Betrie, G. D., Mohamed, Y. A., van Griensven, A., and Srinivasan, R. (2011). Sediment management modelling in the Blue Nile Basin using SWAT model. *Hydrology Earth Syst. Sci.* 15 (3), 807–818. doi:10.5194/hess-15-807-2011

Boru, G. F., Gonfa, Z. B., and Diga, G. M. (2019). Impacts of climate change on stream flow and water availability in Anger sub-basin, Nile Basin of Ethiopia. *Sustain. Water Resour. Manag.* 5, 1755–1764. doi:10.1007/s40899-019-00327-0

Brhane, G., and Mekonen, K. (2009). Estimating soil loss using Universal Soil Loss Equation (USLE) for soil conservation planning at Medego watershed, Northern Ethiopia. *J. Am. Sci.* 5 (1), 58–69.

Chekol, Y. G. (2019). Hydro-politics and the dynamics of the shifting ethio-Egyptian hydropolitical relations. *Central Eur. J. Int. Secur. Stud.* 13 (3), 88–100. doi:10.51870/cejiss.a130301

Cousino, L. K., Becker, R. H., and Zmijewski, K. A. (2015). Modeling the effects of climate change on water, sediment, and nutrient yields from the Maumee River watershed. *J. Hydrology Regional Stud.* 4, 762–775. doi:10.1016/j.ejrh.2015.06.017

Dakhlalla, A. O., and Parajuli, P. B. (2019). Assessing model parameters sensitivity and uncertainty of streamflow, sediment, and nutrient transport using SWAT. *Inf. Process. Agric.* 6 (1), 61–72. doi:10.1016/j.inpa.2018.08.007

Daramola, J., Ekhwan, T. M., Mokhtar, J., Lam, K. C., and Adeogun, G. A. (2019). Estimating sediment yield at Kaduna watershed, Nigeria using soil and water assessment tool (SWAT) model. *Heliyon* 5 (7), e02106. doi:10.1016/j.heliyon.2019.e02106

Debela, S. K. (2022). Prioritization of sediment yield at sub-watershed level using swat model in Finca'aa watershed, Abay Basin, Ethiopia. *J. Sediment. Environ.* 7 (2), 305–315. doi:10.1007/s43217-022-00099-2

Degife, A., Worku, H., and Gizaw, S. (2021). Environmental implications of soil erosion and sediment yield in Lake Hawassa watershed, south-central Ethiopia. *Environ. Syst. Res.* 10, 28–24. doi:10.1186/s40068-021-00232-6

Deore, S. J. (2005). Prioritization of micro-watersheds of upper Bhama Basin on the basis of soil erosion risk using remote sensing and GIS technology. PhD thesis. Pune, India: University of Pune.

Dibaba, W. T., Demissie, T. A., and Miegel, K. (2020). Drivers and implications of land use/land cover dynamics in Finchaa catchment, northwestern Ethiopia. *Land* 9 (4), 113. doi:10.3390/land9040113

Dibaba, W. T., Demissie, T. A., and Miegel, K. (2021). Prioritization of sub-watersheds to sediment yield and evaluation of best management practices in highland Ethiopia, Finchaa catchment. *Land* 10 (6), 650. doi:10.3390/land10060650

Dissanayake, D. M. S. L. B., Morimoto, T., Ranagalage, M., and Murayama, Y. (2019). Land-use/land-cover changes and their impact on surface urban heat islands: Case study of Kandy City, Sri Lanka. *Climate* 7 (8), 99. doi:10.3390/cli7080099

Djebou, D. C. S. (2018). Assessment of sediment inflow to a reservoir using the SWAT model under undammed conditions: A case study for the somerville reservoir, Texas, USA. *Int. Soil Water Conservation Res.* 6 (3), 222–229. doi:10.1016/j.iswcr.2018.03.003

Duressa, J. N., and Jubir, A. K. (2018). Dam break analysis and inundation mapping, case study of fincha'a dam in horro guduru wollega zone, oromia region, Ethiopia. *Sci. Res.* 6 (2), 29–38. doi:10.11648/j.sr.20180602.11

Duressa, J. N., and Regasa, M. S. (2021). Flood inundation mapping and risk analysis case of finchaa lake. *Am. J. Environ. Sci. Eng.* 5 (3), 53–62. doi:10.11648/j.ajese.20210503.11

Ebabu, K., Tsunekawa, A., Haregeweyn, N., Adgo, E., Meshesha, D. T., Aklog, D., et al. (2019). Effects of land use and sustainable land management practices on runoff and soil loss in the Upper Blue Nile basin, Ethiopia. *Sci. Total Environ.* 648, 1462–1475. doi:10.1016/j.scitotenv.2018.08.273

Franzoia, M., and Nones, M. (2017). Morphological reactions of schematic alluvial rivers: Long simulations with a 0-D model. *Int. J. Sediment Res.* 32 (3), 295–304. doi:10.1016/j.ijsrc.2017.04.002

Gassman, P. W., Reyes, M. R., Green, C. H., and Arnold, J. G. (2007). The soil and water assessment tool: Historical development, applications, and future research directions. *Trans. ASABE* 50 (4), 1211–1250. doi:10.13031/2013.23637

Gebretekle, H., Nigusse, A. G., and Demissie, B. (2022). Stream flow dynamics under current and future land cover conditions in Atsela Watershed, Northern Ethiopia. *Acta Geophys.* 70 (1), 305–318. doi:10.1007/s11600-021-00691-6

Gessese, A., and Yonas, M. (2008). Prediction of sediment inflow to Legedadi reservoir using SWAT watershed and CCHE1D sediment transport models. *Nile Basin Water Eng. Sci. Mag.* 1, 65–74.

Gessesse, B., Bewket, W., and Bräuning, A. (2015). Model-based characterization and monitoring of runoff and soil erosion in response to land use/land cover changes in the Modjo watershed, Ethiopia. *Land Degrad. Dev.* 26 (7), 711–724. doi:10.1002/ldr.2276

Gharibdousti, S. R., Kharel, G., and Stoecker, A. (2019). Modeling the impacts of agricultural best management practices on runoff, sediment, and crop yield in an agriculture-pasture intensive watershed. *PeerJ* 7, e7093. doi:10.7717/peerj.7093

Girmay, G., Moges, A., and Muluneh, A. (2020). Estimation of soil loss rate using the USLE model for Agewmariayam Watershed, northern Ethiopia. *Agric. Food Secur.* 9 (1), 9–12. doi:10.1186/s40066-020-00262-w

Hailu, A. D. (2022). Ethiopia hydropower development and Nile basin hydro politics. *AIMS Energy* 10 (1), 87–101. doi:10.3934/energy.2022006

Horowitz, A. J. (2003). An evaluation of sediment rating curves for estimating suspended sediment concentrations for subsequent flux calculations. *Hydrol. Process.* 17 (17), 3387–3409. doi:10.1002/hyp.1299

Jilo, N. B., Gebremariam, B., Harka, A. E., Woldemariam, G. W., and Behulu, F. (2019). Evaluation of the impacts of climate change on sediment yield from the logiya watershed, lower awash basin, Ethiopia. *Hydrology* 6 (3), 81. doi:10.3390/hydrology6030081

Kenea, U., Adeba, D., Regasa, M. S., and Nones, M. (2021). Hydrological responses to land use land cover changes in the Fincha'a Watershed, Ethiopia. *Land* 10 (9), 916. doi:10.3390/land10090916

Khanchoul, K., Amamra, A., and Saaidia, B. (2020). Assessment of sediment yield using swat model: Case study of kebir watershed, northeast of Algeria. *Big Data Water Resour. Eng. (BDWRE)* 2, 36–42. doi:10.26480/bdwre.02.2020.36.42

Khelifa, W. B., Hermassi, T., Strohmeier, S., Zucca, C., Ziadat, F., Boufaroua, M., et al. (2017). Parameterization of the effect of bench terraces on runoff and sediment yield by SWAT modeling in a small semi-arid watershed in Northern Tunisia. *Land Degrad. Dev.* 28 (5), 1568–1578. doi:10.1002/ldr.2685

Kidane, D., and Alemu, B. (2015). The effect of upstream land use practices on soil erosion and sedimentation in the Upper Blue Nile Basin, Ethiopia. *Res. J. Agric. Environ. Manag.* 4 (2), 55–68.

Kidane, M., Bezie, A., Kesete, N., and Tolessa, T. (2019). The impact of land use and land cover (LULC) dynamics on soil erosion and sediment yield in Ethiopia. *Heliyon* 5 (12), e02981. doi:10.1016/j.heliyon.2019.e02981

Kitila, G., Kabite, G., and Alamirew, T. (2015). Severity classification and characterization of waterlogged irrigation fields in the fincha'a valley sugar estate, Nile Basin of western Ethiopia. *Hydrology Curr. Res.* 6 (2), 1. doi:10.4172/2157-7587.1000209

Krysanova, V., and White, M. (2015). Advances in water resources assessment with SWAT - an overview. *Hydrological Sci. J.* 60 (5), 771–813. doi:10.1080/02626667.2015.1029482

Leta, M. K., Demissie, T. A., and Tränckner, J. (2021b). Hydrological responses of watershed to historical and future land use land cover change dynamics of Nashe watershed, Ethiopia. *Water* 13 (17), 2372. doi:10.3390/w13172372

Leta, M. K., Demissie, T. A., and Tränckner, J. (2021a). Modeling and prediction of land use land cover change dynamics based on land change modeler (LCM) in Nashe watershed, Upper Blue Nile basin, Ethiopia. *Sustainability* 13 (7), 3740. doi:10.3390/su13073740

Leta, M. K., Waseem, M., Rehman, K., and Tränckner, J. (2023). Sediment yield estimation and evaluating the best management practices in Nashe watershed, Blue Nile Basin, Ethiopia. *Environ. Monit. Assess.* 195 (6), 716. doi:10.1007/s10661-023-11337-z

Li, C., Li, Z., Yang, M., Ma, B., and Wang, B. (2021). Grid-scale impact of climate change and human influence on soil erosion within East African highlands (Kagera Basin). *Int. J. Environ. Res. Public Health* 18 (5), 2775. doi:10.3390/ijerph18052775

Lin, F., Chen, X., Yao, H., and Lin, F. (2022). SWAT model-based quantification of the impact of land-use change on forest-regulated water flow. *Catena* 211, 105975. doi:10.1016/j.catena.2021.105975

Mariye, M., Mariyo, M., Changming, Y., Teffera, Z. L., and Weldegebrial, B. (2022). Effects of land use and land cover change on soil erosion potential in berhe district: A case study of legedadi watershed, Ethiopia. *Int. J. River Basin Manag.* 20 (1), 79–91. doi:10.1080/15715124.2020.1767636

Megersa, T., Nedaw, D., and Argaw, M. (2019). Combined effect of land use/cover types and slope gradient in sediment and nutrient losses in Chancho and Sorga sub watersheds, East Wollega Zone, Oromia, Ethiopia. *Environ. Syst. Res.* 8 (1), 24–14. doi:10.1186/s40068-019-0151-3

Mekuriaw, T. (2019). Evaluating impact of land-use/land-cover change on surface runoff using Arc SWAT model in sore and geba watershed. *Ethiop. J. Environ. Earth Sci.* 10, 7–17. doi:10.7176/JEES/9-10-02

Miheretu, B. A., and Yimer, A. A. (2018). Estimating soil loss for sustainable land management planning at the Gelana sub-watershed, northern highlands of Ethiopia. *Int. J. River Basin Manag.* 16 (1), 41–50. doi:10.1080/15715124.2017.1351978

Moriasi, D. N., Wilson, B. N., Douglas-Mankin, K. R., Arnold, J. G., and Gowda, P. H. (2012). Hydrologic and water quality models: Use, calibration, and validation. *Trans. ASABE* 55 (4), 1241–1247. doi:10.13031/2013.42265

Negash, D. A., Moisa, M. B., Merga, B. B., Sedeta, F., and Gemeda, D. O. (2021). Soil erosion risk assessment for prioritization of sub-watershed: The case of Chogo watershed, horo guduru wollega, Ethiopia. *Environ. Earth Sci.* 80 (17), 589–611. doi:10.1007/s12665-021-09901-2

Negewo, T. F., and Sarma, A. K. (2023). Sustainable and cost-effective management of degraded sub-watersheds using ecological management practices (EMPs) for genale basin, Ethiopia. *J. Hydrology* 619, 129289. doi:10.1016/j.jhydrol.2023.129289

Neitsch, S. L., Arnold, J. G., and Kiniry, J. R. (2011). *SWAT user manual, version 2009*. Texas, USA: Texas Water Resources Institute Technical Report, A&M University. Available at: https://swat.tamu.edu/media/99192/swat2009-theory.pdf.

Obengo, J. O. (2016). Hydropolitics of the nile: The case of Ethiopia and Egypt. *Afr. Secur. Rev.* 25 (1), 95–103. doi:10.1080/10246029.2015.1126527

Pandey, A., Bishal, K. C., Kalura, P., Chowdary, V. M., Jha, C. S., and Cerdà, A. (2021). A soil water assessment tool (SWAT) modeling approach to prioritize soil conservation management in river basin critical areas coupled with future climate scenario analysis. *Air, Soil Water Res.* 14, 117862212110213. doi:10.1177/11786221211021395

Pennock, D. (2019). *Soil erosion: The greatest challenge for sustainable soil management*. Food & Agriculture Org, 100. Available at: https://www.fao.org/3/ca4395en/ca4395en.pdf.

Phuong, T. T., Thong, C. V. T., Ngoc, N. B., and Van Chuong, H. (2014). Modeling soil erosion within small mountainous watershed in central Vietnam using GIS and SWAT. *Resour. Environ.* 4 (3), 139–147. doi:10.5923/j.re.20140403.02

Pomázi, F., and Baranya, S. (2022). Acoustic based assessment of cross-sectional concentration inhomogeneity at a suspended sediment monitoring station in a large river. *Acta Geophys.* 70 (5), 2361–2377. doi:10.1007/s11600-022-00805-8

Pulighe, G., Bonati, G., Colangeli, M., Traverso, L., Lupia, F., Altobelli, F., et al. (2019). Predicting streamflow and nutrient loadings in a semi-arid Mediterranean watershed with ephemeral streams using the SWAT model. *Agronomy* 10 (1), 2. doi:10.3390/agronomy10010002

Qiu, Z., and Wang, L. (2014). Hydrological and water quality assessment in a suburban watershed with mixed land uses using the SWAT model. *J. Hydrologic Eng.* 19 (4), 816–827. doi:10.1061/(ASCE)HE.1943-5584.0000858

Rathjens, H., and Oppelt, N. (2012). SWAT model calibration of a grid-based setup. *Adv. Geosciences* 32, 55–61. doi:10.5194/adgeo-32-55-2012

Regasa, M. S., Nones, M., and Adeba, D. (2021). A review on land use and land cover change in Ethiopian basins. *Land* 10 (6), 585. doi:10.3390/land10060585

Regasa, M. S., and Nones, M. (2022). Past and future land use/land cover changes in the Ethiopian Fincha sub-basin. *Land* 11 (8), 1239. doi:10.3390/land11081239

Sadeghi, S. H., and Saeidi, P. (2010). Reliability of sediment rating curves for a deciduous forest watershed in Iran. *Hydrological Sci. J.* 55 (5), 821–831. doi:10.1080/02626667.2010.489797

Sahar, A. A., Hassan, M. A., and Abd Jasim, A. (2021). Estimating the volume of sediments and assessing the water balance of the badra basin, eastern Iraq, using swat model and remote sensing data. *Iraqi Geol. J.* 54, 88–99. doi:10.46717/igj.54.2C.9Ms-2021-09-28

Senti, E. T., Tufa, B. W., and Gebrehiwot, K. A. (2014). Soil erosion, sediment yield and conservation practices assessment on Lake Haramaya Catchment. *World J. Agric. Sci.* 2 (7), 186–193.

Setegn, S. G., Dargahi, B., Srinivasan, R., and Melesse, A. M. (2010). Modeling of sediment yield from anjeni-gauged watershed, Ethiopia using SWAT model 1. *JAWRA J. Am. Water Resour. Assoc.* 46 (3), 514–526. doi:10.1111/j.1752-1688.2010.00431.x

Setegn, S. G., Srinivasan, R., and Dargahi, B. (2008). Hydrological modelling in the lake tana basin, Ethiopia using SWAT model. *Open Hydrology J.* 2 (1), 49–62. doi:10.2174/1874378100802010049

Sharma, A., Patel, P. L., and Sharma, P. J. (2022). Influence of climate and land-use changes on the sensitivity of SWAT model parameters and water availability in a semi-arid river basin. *Catena* 215, 106298. doi:10.1016/j.catena.2022.106298

Swami, V. A., and Kulkarni, S. S. (2016). Simulation of runoff and sediment yield for a kaneri watershed using SWAT model. *J. Geoscience Environ. Prot.* 4 (01), 1–15. doi:10.4236/gep.2016.41001

Tefera, B., and Sterk, G. (2008). Hydropower-induced land use change in Fincha'a watershed, western Ethiopia: Analysis and impacts. *Mt. Res. Dev.* 28 (1), 72–80. doi:10.1659/mrd.0811

Tefera, B., and Sterk, G. (2010). Land management, erosion problems and soil and water conservation in Fincha'a watershed, western Ethiopia. *Land Use Policy* 27 (4), 1027–1037. doi:10.1016/j.landusepol.2010.01.005

Tegegne, G., Park, D. K., and Kim, Y. O. (2017). Comparison of hydrological models for the assessment of water resources in a data-scarce region, the Upper Blue Nile River Basin. *J. Hydrology Regional Stud.* 14, 49–66. doi:10.1016/j.ejrh.2017.10.002

Temiz, T., Sonmez, O., Dogan, E., Oner, A., and Opan, M. (2022). Evaluation of the effects of land-use change and increasing deforestation in the Sapanca Basin on total suspended solids (TSS) movement with predictive models. *Acta Geophys.* 70 (3), 1331–1347. doi:10.1007/s11600-022-00783-x

Tilahun, A. K., Verstraeten, G., Chen, M., Gulie, G., Belayneh, L., and Endale, T. (2023). Temporal and spatial variability of suspended sediment rating curves for rivers draining into the Ethiopian Rift Valley. *Land Degrad. Dev.* 34 (2), 478–492. doi:10.1002/ldr.4473

Tomkins, K. M. (2014). Uncertainty in streamflow rating curves: Methods, controls and consequences. *Hydrol. Process.* 28 (3), 464–481. doi:10.1002/hyp.9567

UNESCO WINS (2023). Sediment yield map. Available at: http://ihp-wins.unesco.org/layers/datastore:geonode:SedYield_calibrated_NC.

Weldu Woldemariam, G., and Edo Harka, A. (2020). Effect of land use and land cover change on soil erosion in Erer sub-basin, Northeast Wabi Shebelle Basin, Ethiopia. *Land* 9 (4), 111. doi:10.3390/land9040111

Winchell, M., Srinivasan, R., Di Luzio, M., and Arnold, J. (2007). ArcSWAT interface for SWAT 2005 user's guide, *blackland research center*, Texas agricultural experiment station, temple. Available at: https://colinmayfield.com/public/PDF_files/ArcSWAT_Documentation.pdf.

Xue, C., Chen, B., and Wu, H. (2014). Parameter uncertainty analysis of surface flow and sediment yield in the Huolin Basin, China. *J. Hydrologic Eng.* 19 (6), 1224–1236. doi:10.1061/(ASCE)HE.1943-5584.0000909

Yasir, M., Hu, T., and Abdul Hakeem, S. (2020). Simulating reservoir induced Lhasa streamflow variability using ArcSWAT. *Water* 12 (5), 1370. doi:10.3390/w12051370

Yesuf, H. M., Assen, M., Alamirew, T., and Melesse, A. M. (2015). Modeling of sediment yield in Maybar gauged watershed using SWAT, northeast Ethiopia. *Catena* 127, 191–205. doi:10.1016/j.catena.2014.12.032

Yuan, L., and Forshay, K. J. (2019). Using SWAT to evaluate streamflow and lake sediment loading in the Xinjiang River Basin with limited data. *Water* 12 (1), 39. doi:10.3390/w12010039

Zeiger, S. J., and Hubbart, J. A. (2016). A SWAT model validation of nested-scale contemporaneous stream flow, suspended sediment and nutrients from a multiple-land-use watershed of the central USA. *Sci. Total Environ.* 572, 232–243. doi:10.1016/j.scitotenv.2016.07.178

frontiers | Frontiers in Earth Science

TYPE Original Research
PUBLISHED 23 October 2023
DOI 10.3389/feart.2023.1188093

OPEN ACCESS

EDITED BY
George Xian,
United States Department of the Interior,
United States

REVIEWED BY
Shi Qiu,
Chinese Academy of Sciences (CAS),
China
Danfeng Hong,
Chinese Academy of Sciences (CAS),
China

*CORRESPONDENCE
Suwit Ongsomwang,
suwit@sut.ac.th

RECEIVED 16 March 2023
ACCEPTED 09 October 2023
PUBLISHED 23 October 2023

CITATION
Sun J and Ongsomwang S (2023), Optimal parameters of random forest for land cover classification with suitable data type and dataset on Google Earth Engine.
Front. Earth Sci. 11:1188093.
doi: 10.3389/feart.2023.1188093

Optimal parameters of random forest for land cover classification with suitable data type and dataset on Google Earth Engine

Jing Sun[1] and Suwit Ongsomwang[2]*

[1]Department of Geographic Information Science, School of Architectural Engineering, Tongling University, Tongling, China, [2]School of Mathematics and Geoinformatics, Institute of Science, Suranaree University of Technology, Nakhon Ratchasima, Thailand

Exact land cover (LC) map is essential information for understanding the development of human societies and studying the impacts of climate and environmental change. To fulfill this requirement, an optimal parameter of Random Forest (RF) for LC classification with suitable data type and dataset on Google Earth Engine (GEE) was investigated. The research objectives were 1) to examine optimum parameters of RF for LC classification at local scale 2) to classify LC data and assess accuracy in model area (Hefei City), 3) to identify a suitable data type and dataset for LC classification and 4) to validate optimum parameters of RF for LC classification with a suitable data type and dataset in test area (Nanjing City). This study suggests that the suitable data types for LC classification were Sentinel-2 data with auxiliary data. Meanwhile, the suitable dataset for LC classification was monthly and seasonal medians of Sentinel-2, elevation, and nighttime light data. The appropriate values of the number of trees, the variable per split, and the bag fraction for RF were 800, 22, and 0.9, respectively. The overall accuracy (OA) and Kappa index of LC in model area (Hefei City) with suitable dataset was 93.17% and 0.9102. In the meantime, the OA and Kappa index of LC in test area (Nanjing City) was 92.38% and 0.8914. Thus, the developed research methodology can be applied to update LC map where LC changes quickly occur.

KEYWORDS

land cover classification, sentinel data, random forest, Google Earth Engine, Hefei City, Nanjing City, China

1 Introduction

Detailed, timely and accurate land cover (LC) can help people understand the relationship between the development of human societies and climate and environmental change (Turner et al., 2007; Song et al., 2018; Liu et al., 2020b). LC classification and mapping are considered to be the key technologies to obtain surface information at various scales (Feddema et al., 2005), which is critical for understanding the impact of LC changes on agricultural production, ecotourism, carbon sequestration, water quality, runoff, and species conservation. In recent years, more and more fields require LC maps with higher temporal and spatial resolution, and more and more government departments and institutions need LC maps as the basis for decision-making, planning, and budgeting. However, due to surface heterogeneity and spectral confusion, accurate LC classification and mapping still face many challenges, especially in utilizing time-series satellite data.

The Landsat images have been shared data source for LC mapping and monitoring in the past 50 years (Hansen and Loveland, 2012; Gómez et al., 2016). The Sentinel-2 (S2) satellite provides higher spatial and spectral resolution data than Landsat and opens up new opportunities for LC classification (Pirotti et al., 2016; Forkuor et al., 2018). Recent studies have demonstrated that S2 data can classify LC from a single date image (Clark, 2017; Mongus and Žalik, 2018). However, a single scene of such data cannot effectively monitor dynamic changes to distinguish spectrally similar LC classes. Time-series images often yield better performance than single-temporal images do (Sothe et al., 2017). S2 is superior to Landsat in terms of spatial resolution, time resolution and spectral bands, and it can provide rich phenological information, spatial information and spectral information, making it an increasingly important data source for LC classification.

Nevertheless, the availability of optical data becomes limited and difficult with the occurrence of frequent cloud cover when more than one cloud-free observation per month in time-series images is required for LC classification (Ju and Roy, 2008). The synthetic aperture radar (SAR) data have been increasingly utilized recently as they do not rely on sunlight and are not influenced by cloud and fog (DeFries, 2008; Freitas et al., 2008; Zeng et al., 2020). By exploiting different physical principles, the optical and radar data deliver complementary information, providing higher accuracy for LC classification than a single data source do (Erasmi and Twele, 2009; Stefanski et al., 2014; Joshi et al., 2016). With the free open-access policy of the ESA Sentinel satellite constellation, both multi-sensor and multi-temporal LC mapping have become even more attractive (Drusch et al., 2012; Torres et al., 2012). Some studies have used the multi-sensor method of Sentinel-1 (S1) and S2 data for LC classification and mapping (Pesaresi et al., 2016; Ban et al., 2017; Chatziantoniou et al., 2017; Clerici et al., 2017).

LC is usually affected by natural conditions and human activities. Elevation data can intuitively reflect the natural conditions of a region, while nighttime light images provide unique footprints of human activities and settlements. More and more scholars have begun to add night light data and elevation data to the classification of LC, and discuss their importance in the classification of LC. For example, Tang et al. (2020) use JL1-3B high-resolution nighttime light imagery and Sentinel-2 time series imagery fusion for impervious surface area mapping. Goldblatt et al. (2018) classify the urban LC with fusion approach utilizing nighttime light data and Landsat imagery. Liu et al. (2020a) classified the Landsat data for the Gannan Prefecture and the results showed that the topographic features contributed the most, followed by the spectral indices and bands. Phan et al. (2020) used Landsat 8 data to classify the LC in Mongolia, and the results showed that elevation was the most important feature.

In recent years, deep learning (DL) and machine learning (ML) have gained increasing attention, and their uses are constantly increasing in LC classification. DL is often confusing with ML, but it should be noted that DL is a subset of ML, and both belong to the category of artificial intelligence (AI) (Chen et al., 2019; Klaiber, 2021). The commonly used ML algorithms include linear regression, logistic regression, naïve bayes (NB), support vector machines (SVM), decision tree, Bayesian learning, K nearest neighbor (KNN), neural networks (NN) and random forest (RF) (Ray, 2019). DL algorithms are the upgraded version of artificial neural networks, and commonly used DL algorithms include deep Boltzmann machine (DBM), deep belief network (DBN), convolutional neural network (CNN), graph convolutional network (GCN), recurrent neural networks (RNN), and recursive neural networks (RvNN) (Shrestha and Mahmood, 2019; Hong et al., 2021a; Hong et al., 2021b; Wu et al., 2022). In the field of LC classification, these state-of-the-art (SOTA) classification methods mentioned above and their improved algorithms have been widely adopted in various research topics. Lin et al. (2018) extract the LC types of Weihai from 1985–2015 using SVM classification method with Landsat MSS/TM/OLI images. Thanh Noi and Kappas (2018) compare RF, KNN, and SVM for LC classification using Sentinel-2 in Red River Delta. Sun et al. (2019) build a long short-term memory (LSTM) RNN model for LC classification in North Dakota with time series Landsat. Hong et al. (2021a) develop a new minibatch GCN for hyperspectral image classification, which allows to train large-scale GCNs in a minibatch fashion.

The RF (Breiman, 2001), which is one of ML classifiers and developed based on decision tree, became one of the favorite and most promising LC classifiers due to its relatively stable and robust classification accuracy and effectiveness in handling large and high-dimensional datasets, and it has been widely used in multi-temporal and multi-sensor images classification (Gislason et al., 2006; Rodriguez-Galiano et al., 2012; Pelletier et al., 2016; Ghorbanian et al., 2020; Phan et al., 2020; Ghorbanian et al., 2021). Bourgoin et al. (Bourgoin et al., 2020) used the RF algorithm for LC classification based on Landsat and S2 data and reported overall accuracy (OA) and Kappa index of 0.81 and 0.87, respectively.

Recently, the explosive growth in data volume, including multi-temporal and multi-sensor datasets that are effective in LC information extraction, has led to problems of time consumption with low efficient processing using personal or workstation computers. The Google Earth Engine (GEE) can easily get access to multi-sensor and multi-temporal images and it provides high-performance operation without downloading these data to a local machine (Gorelick et al., 2017; Kumar and Mutanga, 2018; Mutanga and Kumar, 2019; Amani et al., 2020; Tamiminia et al., 2020). Furthermore, the temporal aggregation method, such as the median, in the GEE significantly reduces cloud interference, resolves the problems of unavailable satellite data for specific periods. In addition, the availability of powerful classification models, such as RF (Shelestov et al., 2017), makes the GEE a widely used remote-sensing tool for LC research. Some studies have used the RF algorithm to classify LC on the GEE platform (Azzari and Lobell, 2017; Ghorbanian et al., 2020; Phan et al., 2020; Zhang et al., 2020; Yang et al., 2021).

Meanwhile, LC datasets at regional and global scales, including FROM-GLC30 (Gong et al., 2013), FROM-GLC10 (Gong et al., 2019), GlobeLand30 (Chen et al., 2015), GLC_FCS30 (Zhang et al., 2021), ESA WorldCover (Zanaga et al., 2021), and ESRI Land Cover (Krishna et al., 2021) are available for public uses. In this study, the LC dataset in 2020 was used as reference data to extract training and validating areas and examine optimal parameters of RF for LC classification at a local scale under the GEE platform with S1 and S2 satellites in the model area. Then, the derived optimal parameters

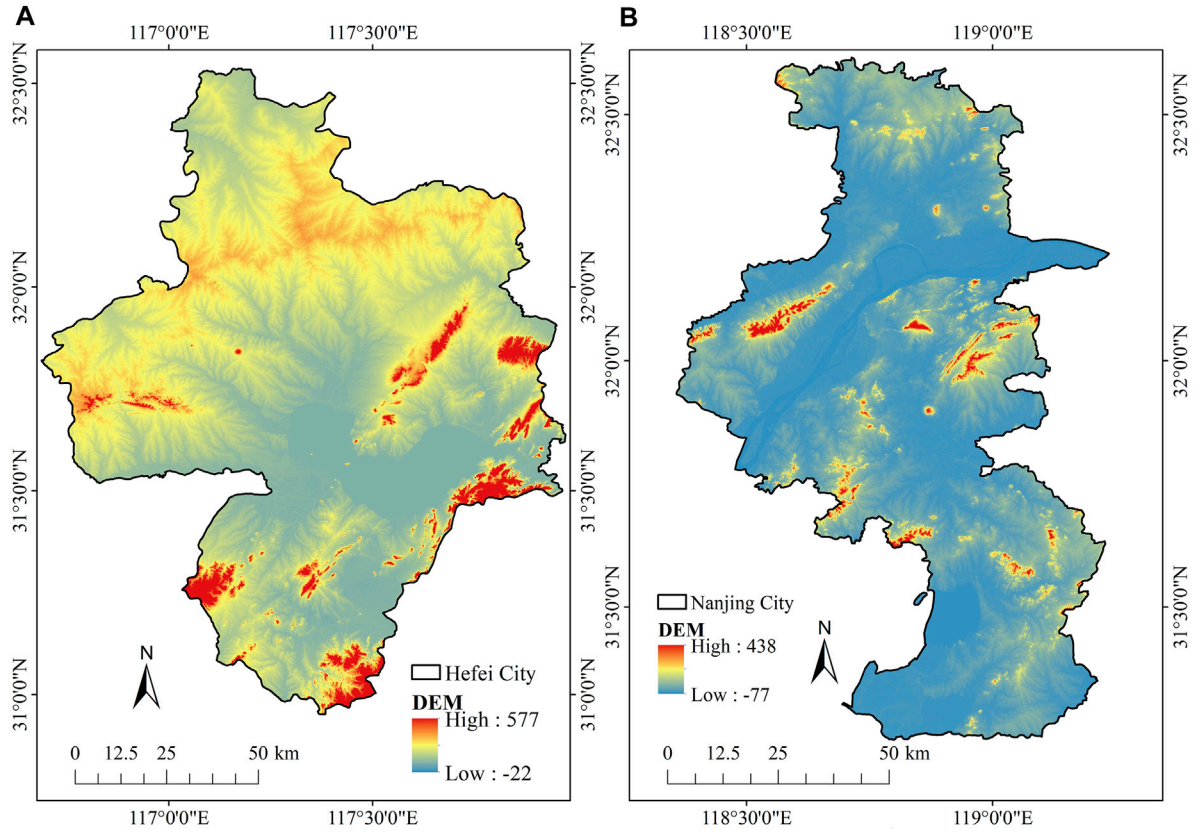

FIGURE 1
Location of the study area: **(A)** model area (Hefei City), and **(B)** test area (Nanjing City).

of RF were applied to classify LC type in the test area with the suitable dataset for validation.

Our specific research objectives were 1) to examine optimum parameters of RF for LC classification at local scale 2) to classify LC data and assess accuracy in model area (Hefei City), 3) to identify a suitable data type and dataset for LC classification and 4) to validate optimum parameters of RF for LC classification with a suitable data type and dataset in test area (Nanjing City). The proposed method can reduce the cost for updating LC map at local scale.

2 Materials and methods

2.1 Study area

Hefei City and Nanjing City were selected as the model and test areas respectively. Hefei City, with a population of more than 8 million, is the capital and the largest city in Anhui Province, China. It was chosen to examine an optimal parameter of RF and to identify a suitable data type and dataset for LC classification (Figure 1A). At the same time, Nanjing City, with a population of more than 8.5 million, is a sub-provincial city and the capital city in Jiangsu Province, China. It was selected to validate the optimal parameters of RF for LC classification under GEE with suitable datatype and dataset (Figure 1B).

2.2 Data

The data used in this study were categorized into three groups: 1) Sentinel satellite data, 2) auxiliary data, and 3) LC data. Brief information on each data group is summarized below.

2.2.1 Sentinel satellite data

Both S1 and S2 satellites were launched by European Space Agency (ESA).

(1) S1 data (ESA, 2023b). The S1 ground range detected (GRD) products were delivered with polarizations of the vertical transmit vertical receive (VV) and the vertical transmit horizontal receive (VH). The S1 can provide continuous all-weather, high spatial (10 m), and improved temporal resolution images at C-band unaffected by clouds, to support land monitoring (Cremer et al., 2020).
(2) S2 data (ESA, 2023c). The S2 multi-spectral instrument (MSI) sensor provides high spatial (10 m) and multi-spectral images over the global surface, with unprecedented potential in LC monitoring and mapping (Drusch et al., 2012; Spoto et al., 2012; Zheng et al., 2017).

In this study, S1 GRD and S2 MSI products acquired in 2020 were the primary data input for LC classification.

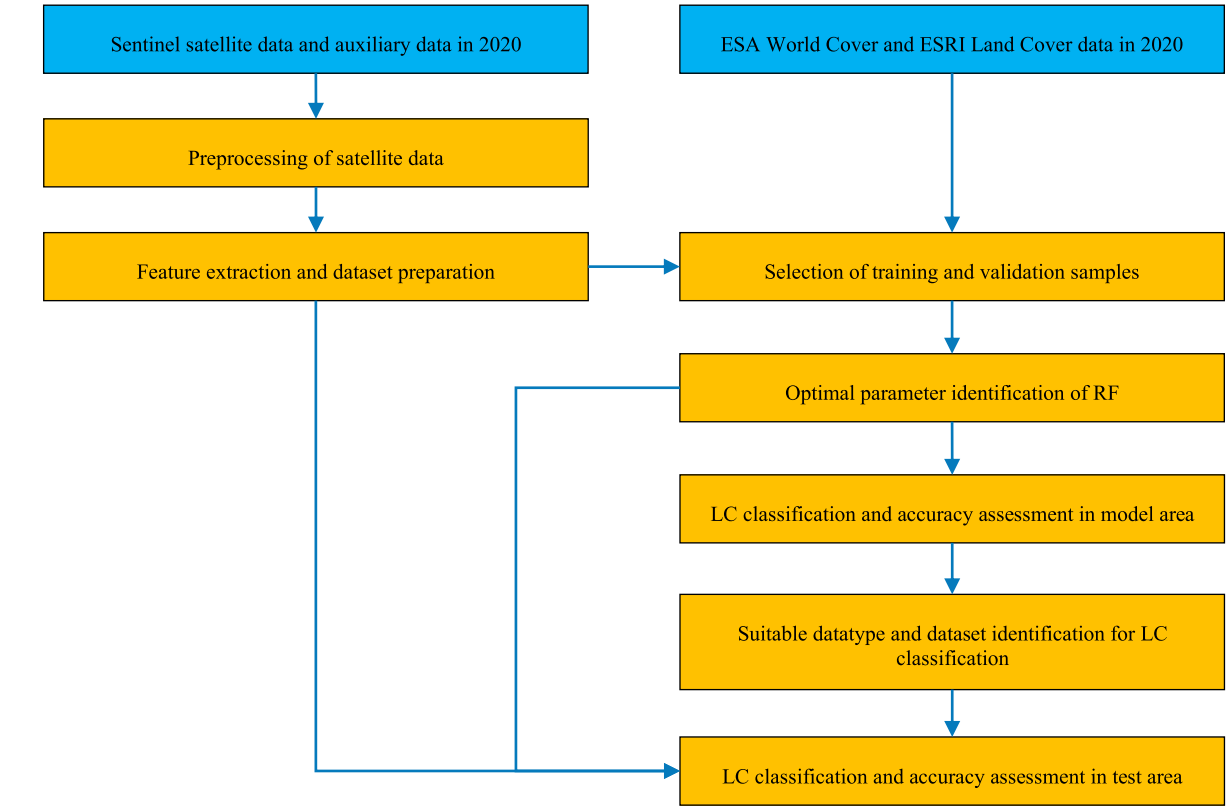

FIGURE 2
Workflow of research methodology.

2.2.2 Auxiliary data

(1) Elevation (NASA, 2023). The 30 m spatial resolution elevations over the study area were extracted from the Shuttle Radar Topography Mission (SRTM) data (Su et al., 2021). It is helpful to distinguish various LC types if we adopt the combination of satellite images and physiography variables (Phan et al., 2020).

(2) Nighttime light products (EOG, 2023). Obtained from the NPP-VIIRS day/night band (DNB), the 464 m spatial resolution nighttime light products were used to distinguish between artificial surfaces and bare ground (Miller et al., 2013).

2.2.3 LC data

(1) ESA WorldCover (ESA, 2023a). It is a global LC product with 10 m spatial resolution published by the ESA WorldCover team based on S1 and S2 data, which consists of 11 LC classes (Zanaga et al., 2021).

(2) ESRI Land Cover (ESRI, 2023). It is also a global LC product with 10 m spatial resolution produced by ESRI Impact Observatory through S2 image, which consists of 10 LC classes (Krishna et al., 2021).

The common areas of LC type of ESA WorldCover and ESRI Land Cover products are used to select training and validation samples in this study.

2.3 Methods

The research methodology consisted of 7 steps: 1) preprocessing of Sentinel satellite data, 2) feature extraction and dataset preparation, 3) selection of training and validation samples, 4) optimal parameters identification of RF, 5) LC classification and accuracy assessment in model area, 6) suitable datatype and dataset identification for LC classification, and 7) LC classification and accuracy assessment in test area. The workflow is displayed in Figure 2. Details are described in the following sections.

2.3.1 Preprocessing of sentinel satellite data

There are two steps for preprocessing of Sentinel satellite data.

(1) Data selection, cloud pixels masking, and topographic correction for S2

Unlike S1 data, which is not affected by the cloud, scenes covered by cloud are typical in S2 data, so S2 data must be pre-processed to minimize the impact of cloud coverage. Only S2 scenes with a cloud coverage percentage of less than 85% were selected and used in subsequent steps according to the mask information of QA60 in the S2 image collection, while the S2 scenes with a cloud coverage percentage of more than 85% were removed. Then, the cloud coverage pixels in the selected S2 scene were identified and masked based on the QA60 band information, and these cloud

TABLE 1 Combination of features in 18 datasets for classifying LC data.

Data type	Dataset code	Feature combination	Number of features
S1	D1	S1 Monthly median (12 months × 3 features: VH, VV, VH/VV)	36
	D2	S1 Season median (4 seasons × 3 features: VH, VV, VH/VV)	12
	D3	S1 Monthly median + Season median (D1 + D2)	48
S1+ Auxiliary	D4	S1 Monthly median + Elevation + Nighttime light	38
	D5	S1 Season median + Elevation + Nighttime light	14
	D6	S1 Monthly median + S1 Season median + Elevation + Nighttime light	50
S2	D7	S2 Monthly median (12 months × 13 features)	156
	D8	S2 Season median (4 seasons × 13 features)	52
	D9	S2 Monthly median + S2 Season median (D7 + D8)	208
S2+ Auxiliary	D10	S2 Monthly median + Elevation + Nighttime light	158
	D11	S2 Season median + Elevation + Nighttime light	54
	D12	S2 Monthly median + S2 Season median + Elevation + Nighttime light	210
S1 and S2	D13	S1 and S2 Monthly median (36 features of S1 + 156 features of S2)	192
	D14	S1 and S2 Season median (12 features of S1 + 52 features of S2)	64
	D15	S1 and S2 Monthly median + S1 and S2 Season median (D13 + D14)	256
S1 and S2+ Auxiliary	D16	S1 and S2 Monthly median + Elevation + Nighttime light	194
	D17	S1 and S2 Season median + Elevation + Nighttime light	66
	D18	S1 and S2 Monthly median + S1 and S2 Season median + Elevation + Nighttime light	258

coverage pixels did not participate in subsequent processing. Moreover, topographic correction was performed (Soenen et al., 2005) to compensate for the solar irradiance, thereby minimizing terrain-induced reflectance changes. This work was implemented by executing open-source code on GEE (https://mygeoblog.com/2018/07/27/sentinel-2-terrain-correction/). Finally, all data used in this study will be clipped to the scope of the study area to improve computational efficiency.

(2) Monthly/Seasonal median calculation for S1 and S2

To minimize the influence of holes in the image caused by the masked cloud cover pixels in the S2 scene in the previous step, and to reduce the amount of data to improve the speed of classification, the median calculation was performed. The monthly median for 12 months and seasonal median for four seasons were calculated by time aggregation for both S1 and S2 data (Luo et al., 2021; Shetty et al., 2021; Masroor et al., 2022).

2.3.2 Feature extraction and dataset preparation

For S1 data, each monthly/seasonal median included VV and VH polarizations, and the ratio between VH and VV were extracted.

For S2 data, spectral bands (Blue, Green, Red, Red Edge 1, Red Edge 2, Red Edge 3, NIR, Red Edge 4, SWIR 1, and SWIR 2) were extracted. Additionally, three significant indices for representative vegetation, urban and built-up and wetness features: normalized difference vegetation index (NDVI) (Tucker, 1979), normalized difference built index (NDBI) (Zha et al., 2003), and normalized difference water index (NDWI) (Gao, 1996) were calculated using the following equations.

$$NDVI = \frac{\rho_{NIR} - \rho_{RED}}{\rho_{NIR} + \rho_{RED}} \quad (1)$$

$$NDBI = \frac{\rho_{SWIR2} - \rho_{NIR}}{\rho_{SWIR2} + \rho_{NIR}} \quad (2)$$

$$NDWI = \frac{\rho_{NIR} - \rho_{SWIR1}}{\rho_{NIR} + \rho_{SWIR1}} \quad (3)$$

Where ρ_{RED}, ρ_{NIR}, ρ_{SWIR2}, and ρ_{SWIR1} are Band 4, Band 8, Band 12, and Band 11 of S2 satellite.

For auxiliary data, nighttime light data from the NPP-VIIRS DNB and elevation data from the SRTM, were added to the S1 and S2 data.

Finally, eighteen datasets were designed to examine an optimal parameter of RF and suitable data type and dataset for LC classification (Table 1). According to the data type, the datasets were categorized into six groups: S1 data (D1–D3), S1 and auxiliary data (D4–D6), S2 data (D7–D9), S2 and auxiliary data (D10–D12), S1 and S2 data (D13–D15), and S1, S2, and auxiliary data (D16–D18).

2.3.3 Selection of training and validation samples

In this study, samples were selected from the area with consistent LC attributes of ESA WorldCover and ESRI Land Cover data in 2020. In practice, the LC map from ESA WorldCover and the LC map from ESRI Land Cover were compared to find pixels with the same LC attributes, which are

potential samples. Then, a stratified proportional random sampling method was used to reselect the samples from the potential samples, which could avoid the final samples from being too concentrated in a certain area or a certain LC type. As a result, a total of 5,000 samples were obtained in the model area (Hefei City), and 70% of the training samples and 30% of the validation samples were divided by using the "randomColumn" function on the GEE platform.

2.3.4 Optimal parameter of RF identification for LC classification

The operation of the RF algorithm on the GEE platform requires providing six parameters. In this study, the number of trees (NT) from 100 to 1,000 at 100-tree intervals, the variables per split (VPS) from 1 to 30 at 1-variable intervals, and the bag fraction (BF) from 0.1 to 1 at 0.1 fraction intervals were examined to identify optimal parameters of RF for LC classification. As a result, a total of 3,000 combinations (NT = 10, VPS = 30, and BF = 10) were generated and evaluated. To find suitable parameter values, the RF classifier was executed 3,000 times for each dataset (D1 to D18). Then, optimal values of three primary parameters: NT, VPS, and BF, were selected based on the small out-of-bag (OOB) error. Meanwhile, the other three parameters, maximum nodes, minimum leaf population, and seed were set up using the default values with values of null, 1, and 0, respectively.

2.3.5 LC classification and accuracy assessment in model area

This study applied the RF algorithm with optimum parameters on the GEE platform to classify six LC types: urban and built-up land, cropland, forest land, grassland, water bodies, and bare land in model area. Urban and built-up land comprises rural and urban areas, commercial and industrial areas, transportation, utilities, and infrastructures. Cropland consists of crops, orchards, tea gardens, and vegetable fields. Forest land includes natural and man-made forests. Grassland encompasses natural grass and artificial grassland. Water bodies consists of rivers, streams, ponds, and lakes. Bare land includes abandoned fields, exposed rock or soil, and open land. The expected LC types in this study were considered on the basis of the regional characteristics of Hefei City and the existing LC products. The LC classification was performed by "ee.smileRandomForest" function in the GEE.

In practices, the OA, Kappa index, producer's accuracy (PA), and user's accuracy (UA) calculated using "confusionMatrix.accuracy," "ConfusionMatrix.kappa," "confusionMatrix.producersAccuracy," and "confusionMatrix.consumersAccuracy" functions through GEE platform, respectively, were used for the accuracy assessment (Huang et al., 2017; Lyons et al., 2018). Then, 18 groups of the OA, Kappa index, PA, and UA corresponding to 18 datasets were obtained after executing RF classifier.

2.3.6 Suitable datatype and dataset identification for LC classification

In this step, the appropriate datasets for LC classification were selected by comparing the OA and Kappa index values. Average values of OA and Kappa index by datatype, as categorized into six groups in Table 1, were applied to identify an appropriate datatype for LC classification using RF under GEE platform. Meanwhile, Kappa index values with a thresholding value of 0.8 were compared among 18 datasets to identify the suitable dataset for LC classification using RF under GEE platform.

Moreover, pairwise Z-test among top three datasets providing the highest Kappa values was applied to identify significant difference value as suggested by (Congalton and Green, 2009) as below.

$$Z = \frac{\left|\widehat{K_1} - \widehat{K_2}\right|}{\sqrt{\widehat{var}\left(\widehat{K_1}\right) + \widehat{var}\left(\widehat{K_2}\right)}} \tag{4}$$

Where Z is standard normal distribution, $\widehat{K_1}$, and $\widehat{K_2}$ are Kappa indices of the first and the second dataset, and $\widehat{var}\left(\widehat{K_1}\right)$ and $\widehat{var}\left(\widehat{K_2}\right)$ are variances of Kappa indices of the first and the second dataset. The variance of Kappa index was calculated through Eq. 5.

$$\widehat{var}\left(\hat{K}\right) = \frac{1}{n}\left\{\frac{\theta_1\left(1-\theta_1\right)}{\left(1-\theta_2\right)^2} + \frac{2\left(1-\theta_1\right)\left(2\theta_1\theta_2-\theta_3\right)}{\left(1-\theta_2\right)^3} + \frac{\left(1-\theta_1\right)^2\left(\theta_4-4\theta_2^2\right)}{\left(1-\theta_2\right)^4}\right\} \tag{5}$$

where $\theta_1 = \frac{1}{n}\sum_{i=1}^{k} n_{ii}$,

$\theta_2 = \frac{1}{n^2}\sum_{i=1}^{k} n_{i+}n_{+i}$,

$\theta_3 = \frac{1}{n^2}\sum_{i=1}^{k} n_{ii}\left(n_{i+} + n_{+i}\right)$, and

$\theta_4 = \frac{1}{n^3}\sum_{i=1}^{k}\sum_{j=1}^{k} n_{ij}\left(n_{j+} + n_{+i}\right)^2$

In principle, given the null hypothesis and the alternative, null hypothesis is rejected if Z ≥ Zα/2 (Congalton and Green, 2009).

2.3.7 LC classification and accuracy assessment in test area

A suitable datatype for LC classification in the model area (Hefei City) was firstly prepared for test area (Nanjing City). Then, the prepared suitable datatype was used to classify LC type with an optimal parameter of RF as identified in the Step 2.3.4. The classified LC map was assessed its thematic accuracy. The thematic accuracy information of Hefei City and Nanjing City was compared to validate LC classification using RF under GEE platform.

3 Results

3.1 Optimal parameters of RF for LC classification

For this study, the three critical parameters, NT, VPS, and BF, of the RF classifier on the GEE platform were analyzed, and the OOB error was used to select the optimal one for 18 datasets. Figure 3 shows the average OOB error values of all 18 datasets at different NT. The OOB error tends to decrease as the NT increases, no matter what kind of datasets are used. When the NT is higher than 600, the OOB error value changes less; however, the execution time of the algorithm becomes longer when the NT increases. To balance the efficiency and accuracy of the RF algorithm, the optimal NT for all 18 datasets was set to 800 because the OOB errors of all datasets did not change much after increasing the NT to 900 and 1,000.

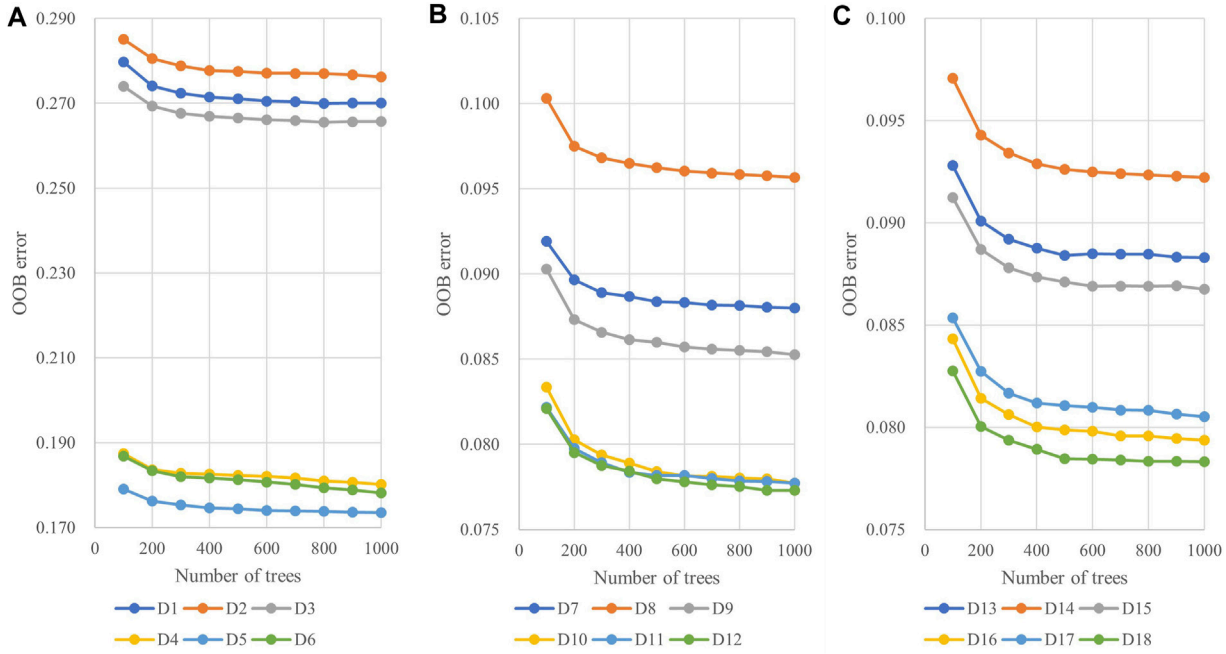

FIGURE 3
The average OOB error values for the number of trees (NT) of 18 datasets: **(A)** D1–D6; **(B)** D7–D12; and **(C)** D13–D18.

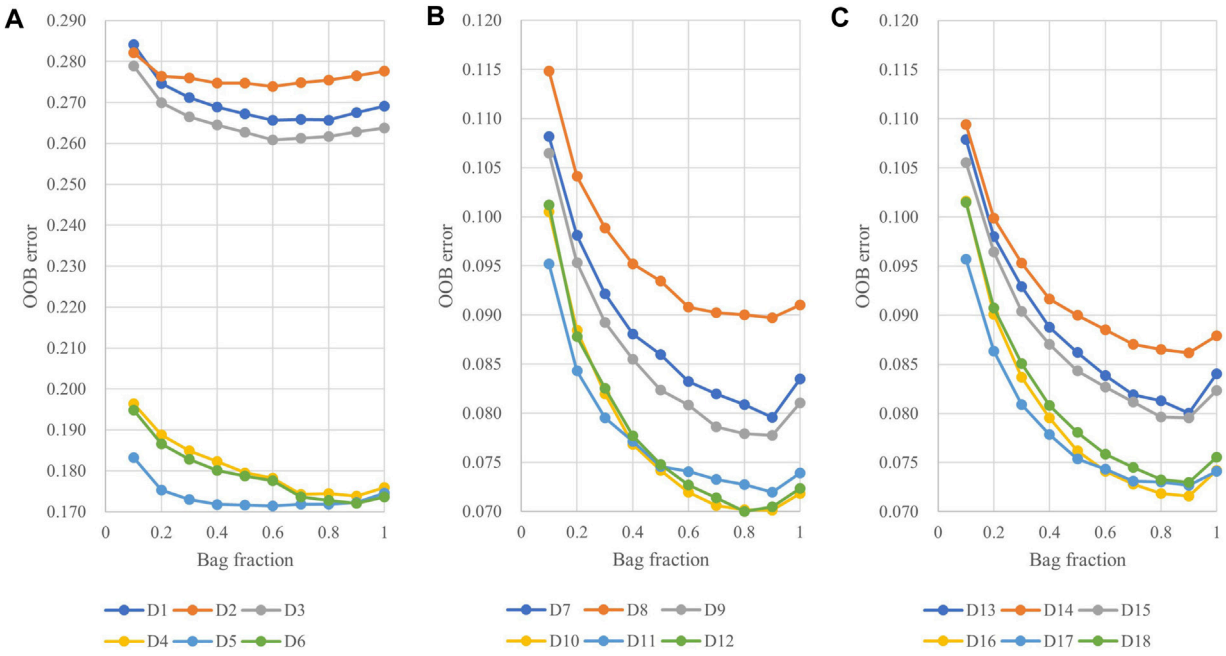

FIGURE 4
The average OOB error values for the bag fraction (BF) of 18 datasets: **(A)** D1–D6; **(B)** D7–D12; and **(C)** D13–D18.

Figure 4 shows the average OOB error values of all 18 datasets at different BF when NT is 800. Regardless of the datasets used, OOB errors first decrease and then increase as the BF increases. For D1, D2, D3, and D5, the value of OOB reaches the minimum when the BF is around 0.6, while for other datasets, the value of OOB is the smallest when the BF is 0.9.

Figure 5 shows the average OOB error values for all 18 datasets at different VPS when NT is 800. For D2, D5, D8,

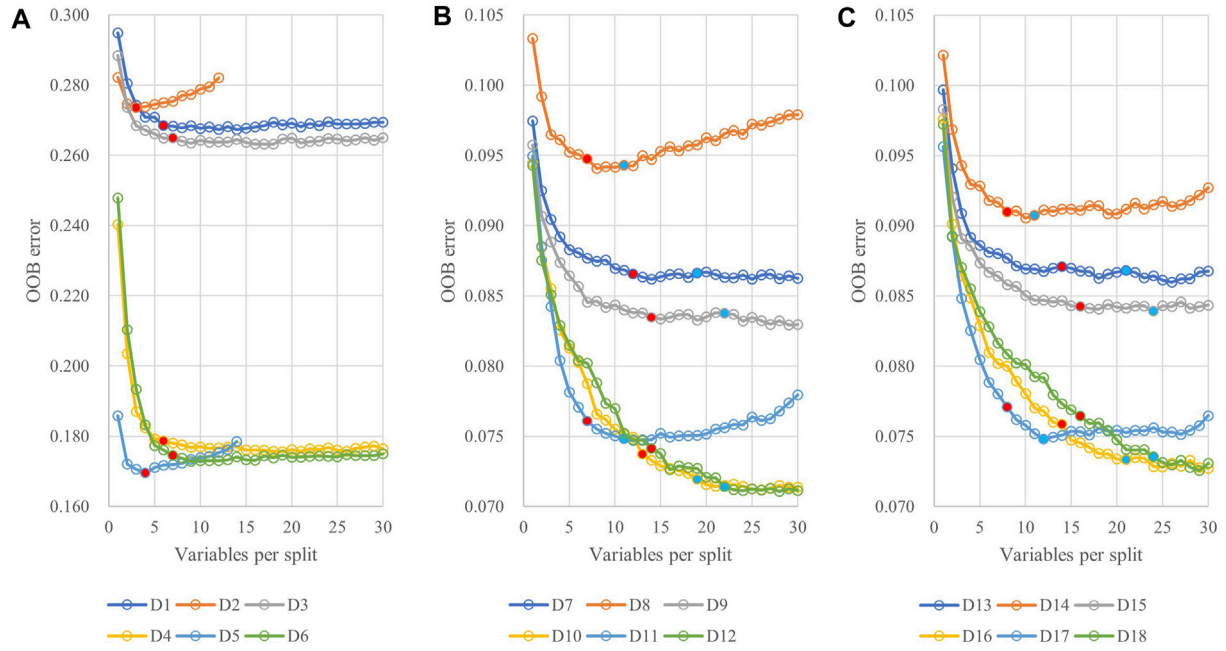

FIGURE 5
The average OOB error values for the variables per split (VPS) of 18 datasets: **(A)** D1–D6; **(B)** D7–D12; and **(C)** D13–D18.

TABLE 2 Optimal combination values of VPS and BF.

Dataset	VPS	BF	Dataset	VPS	BF	Dataset	VPS	BF
D1	6	0.6	D7	19	0.9	D13	21	0.9
D2	3	0.6	D8	11	0.9	D14	12	0.9
D3	7	0.6	D9	22	0.9	D15	24	0.9
D4	6	0.9	D10	19	0.9	D16	21	0.9
D5	4	0.6	D11	11	0.9	D17	12	0.9
D6	7	0.9	D12	22	0.9	D18	24	0.9

D11, D14, and D17, which only use season median or season median + auxiliary data, the OOB error showed a trend of decreasing at first and then increasing. For other data sets, OOB error shows a trend of decreasing and then tending to be stable with the increase of VPS value. The VPS value corresponding to the red solid circle in Figure 5 is the suggested value of GEE (square root of the number of variables). In Figure 5A, we found that when only the S1 data or S1+auxiliary data are used, the VPS value suggested by GEE is appropriate, and the OOB value obtained at this time is smaller. In Figures 5B, C, it is beneficial to use a VPS value larger than the GEE recommendation to reduce the value of OOB, especially for the four data sets D10, D12, D16 and D18. So, without loss of generality, we recommend using 1.5 times the square root of the number of variables as the value of VPS, as marked by the blue solid circle in the figure. At this time, the OBB errors of the 12 data sets D7-D18 are all small.

Table 2 summarizes the optimal combination values for the parameter pair of VPS and BF with the smallest OOB error value when the NT value is set to 800. It was found that the optimal BF value was 0.9 for D7 to D18, see Table 2, which differs from the default value of BF (0.5) suggested by the GEE.

3.2 LC classification in model area

The results of a LC classification in model area (Hefei City) in 2020 of 18 datasets (D1-D18) using the identified optimum parameters of the RF on the GEE are presented in Figure 6 and Table 3.

As a result, in Figure 7, the patterns of LC distribution from 18 datasets are slightly different according to the number of features in the datasets. Likewise, the area of each LC type of 18 datasets in Table 3 is changed according to the number of features in the datasets. These phenomena can be clearly observed in each LC type change from 18 datasets (see Figure 7). Urban and built-up land areas are increased after adding auxiliary data to Sentinel-1 data (D1–D3), and they are relatively stable. Similarly, areas of forest land are stable using D7–D18 datasets. On the contrary, areas of cropland, grassland, water bodies, and bare land fluctuate for all 18 datasets.

3.3 Thematic accuracy assessment of LC map in model area

The results of the OA and Kappa index for the thematic accuracy assessment of LC maps of 18 datasets (D1–D18) in model area (Hefei City) are presented in Figure 8. As a result, the OA values vary from 71.37% for D2 to 93.62% for D18, and the Kappa index values vary from 0.6017 for D2 to 0.9154 for D18.

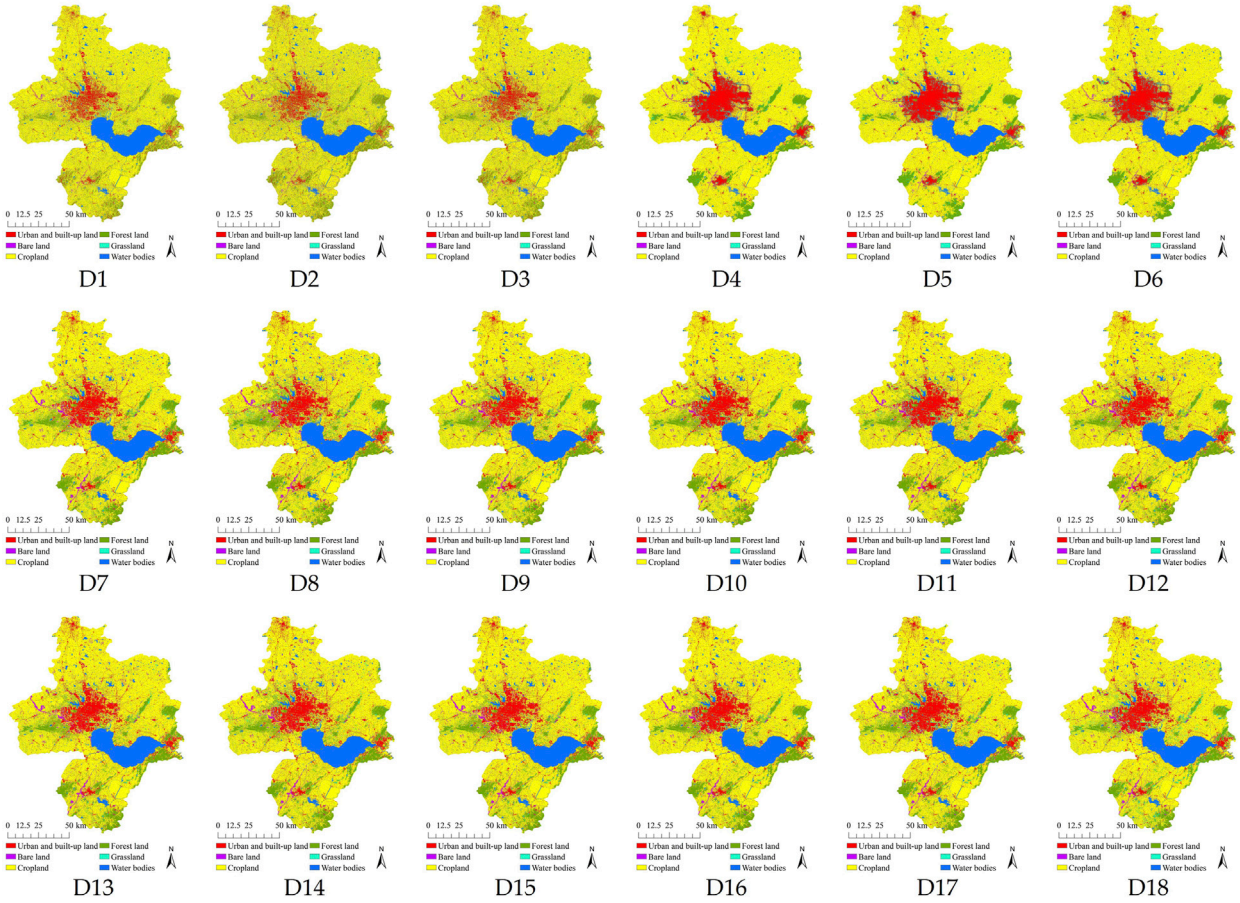

FIGURE 6
LC maps of Hefei City in 2020 of 18 datasets: D1–D18.

Meanwhile, the PA and UA values of each LC type are calculated on GEE. The PA values of urban and built-up land vary from about 51% for D2 to 95% for D18, the PA values of bare land vary from about 26% for D1 to 80% for D10, the PA values of cropland vary from about 89% for D2 to 98% for D10, the PA values of forest land vary from about 58% for D2 to 95% for D16, the PA values of grassland vary from about 12% for D1 to 82% for D12, and the PA values of water bodies vary from about 95% for D5 to 99% for D9. The UA values of urban and built-up land vary from about 67% for D3 to 93% for D12, the UA values of bare land vary from about 46% for D2 to 91% for D10, the UA values for cropland vary from about 69% for D2 to 93% for D18, the UA values of forest land vary from about 64% for D2 to 98% for D16, the UA values of grassland vary from about 45% for D2 to 95% for D18, and the UA values of water bodies vary from about 97% for D3 to 100% for D14 and D16.

In addition, the average PA and UA of three main data types of 18 datasets, S1 (D1–D6), S2 (D7–D12), and S1 and S2 (D13–D18), are summarized in Table 4.

For average PA in Table 4, the six datasets of S1 data (without and with auxiliary data), D1-D6, delivered average PA values from 32.20% for bare land to 96.84% for water bodies. On the contrary, the six datasets of S2 data (without and with auxiliary data), D7–D12, delivered average PA values from 73.00% for grassland to 98.16% for water bodies. Meanwhile, the six datasets of S1 and S2 data (without and with auxiliary data), D13–D18, delivered average PA values from 72.69% for bare land to 97.55% for water bodies.

Like PA, for average UA in Table 4, the six datasets of S1 data (without and with auxiliary data), D1-D6, delivered average UA values from 54.75% for grassland to 97.88% for water bodies. On the contrary, the six datasets of S2 data (without and with auxiliary data), D7-D12, delivered average UA values from 84.19% for grassland to 98.16% for water bodies. Meanwhile, the six datasets of S1 and S2 data (without and with auxiliary data), D13-D18, delivered average UA values from 84.55% for bare land to 99.47% for water bodies.

Furthermore, all six datasets of S1 data (without and with auxiliary data), (D1–D6), delivered a lower average PA and UA than the other two main data types.

3.4 Suitable data type for LC classification in model area

As summarized in Table 5, the OA, Kappa index, and the average value by data type for S2 data without auxiliary data (D7–D9) and with auxiliary data (D10–D12) were higher than that of S1 data without auxiliary data (D1–D3) and with auxiliary data (D4–D6). The

TABLE 3 Area of each LC type of 18 datasets: D1–D18.

Dataset	Area of LC in sq. km					
	Urban and built-up land	Cropland	Forest land	Grassland	Water bodies	Bare land
D1	912.28	7,723.11	1,292.85	204.08	1,133.52	199.16
D2	976.52	7,089.43	1,673.17	254.00	1,149.27	322.60
D3	925.18	7,429.65	1,560.45	152.01	1,129.74	267.97
D4	1,292.31	7,727.18	915.58	226.49	1,120.10	183.35
D5	1,215.92	7,644.06	1,009.02	258.60	1,130.44	206.96
D6	1,311.72	7,580.82	1,015.55	236.41	1,112.64	207.84
D7	1,271.13	7,453.79	1,167.42	142.97	1,175.13	254.56
D8	1,297.08	7,267.89	1,232.78	212.85	1,159.61	294.80
D9	1,251.57	7,443.08	1,200.51	157.28	1,138.10	274.46
D10	1,292.30	7,473.24	1,163.31	146.34	1,155.14	234.66
D11	1,288.11	7,345.78	1,215.92	192.19	1,127.70	295.30
D12	1,285.03	7,451.36	1,175.13	118.64	1,140.14	294.70
D13	1,280.82	7,452.87	1,167.64	125.29	1,157.41	280.97
D14	1,332.17	7,308.81	1,247.75	182.95	1,118.00	275.33
D15	1,258.65	7,452.53	1,204.60	124.23	1,144.16	280.82
D16	1,245.59	7,525.48	1,174.92	126.00	1,126.82	266.19
D17	1,275.14	7,419.25	1,209.28	151.27	1,126.90	283.15
D18	1,310.45	7,363.97	1,156.82	238.47	1,141.91	253.38

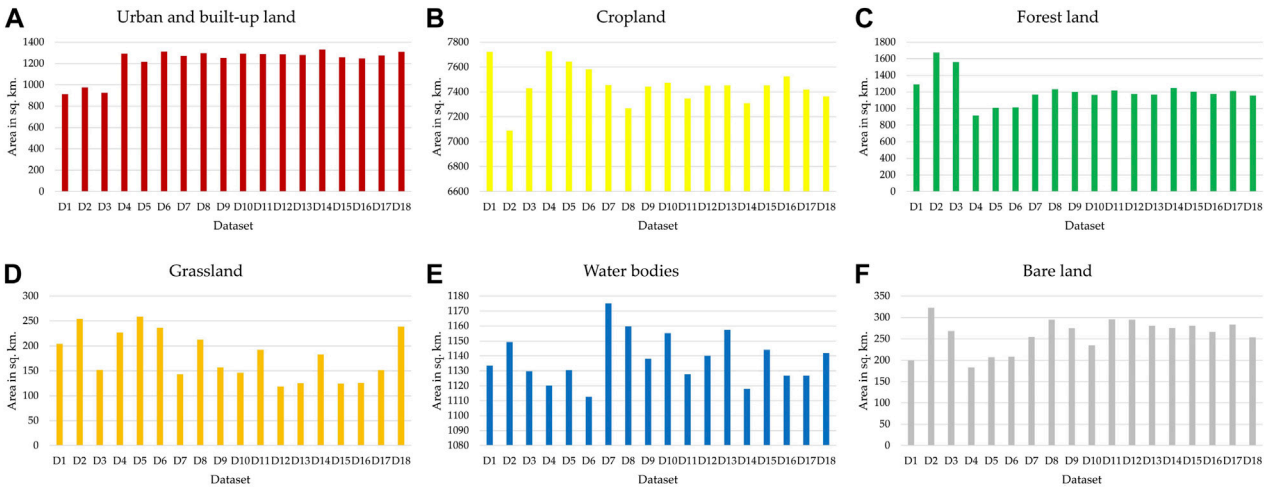

FIGURE 7
Change of each LC area from 18 datasets: **(A)** urban and built-up land, **(B)** cropland, **(C)** forest land, **(D)** grassland, **(E)** water bodies, and **(F)** bare land.

average values of OA for the datasets of S2 data without and with auxiliary data were 90.94% and 92.64%, respectively, but the average values of OA for the datasets of S1 data without and with auxiliary data were only 72.61% and 82.66%, respectively. Likewise, the average values of the Kappa index for datasets of S2 data without and with auxiliary data were 0.8796 and 0.9004, respectively, but the average values of the Kappa index for datasets of S1 data without and with auxiliary data were only 0.6216 and 0.7667, respectively. Therefore, S2 data with and without auxiliary data were suitable for LC classification in terms of data type.

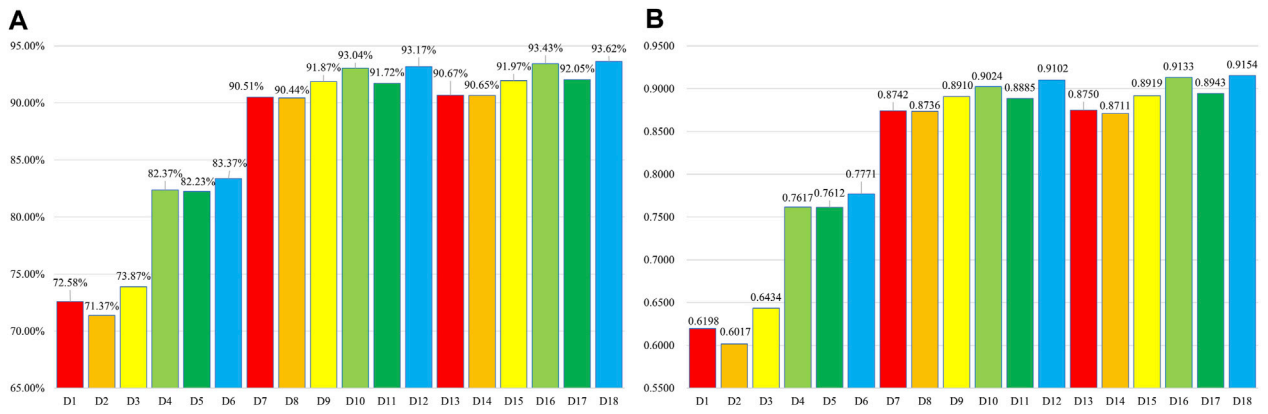

FIGURE 8
OA and Kappa index results for the 18 datasets: **(A)** OA and **(B)** Kappa index.

TABLE 4 Average PA and UA of three primary data types of 18 datasets (D1–D18).

Land cover type	Average PA value			Average UA value		
	D1–D6 (%)	D7–D12 (%)	D13–D18 (%)	D1–D6 (%)	D7–D12 (%)	D13–D18 (%)
Urban and Built-up land	66.44	92.06	92.34	73.26	88.41	89.97
Cropland	92.45	95.97	96.76	76.41	91.14	90.57
Forest land	69.79	90.40	92.23	74.36	94.79	95.09
Grassland	36.37	73.00	73.84	54.75	84.19	89.69
Water bodies	96.84	98.16	97.55	97.88	98.37	99.47
Bare land	32.20	73.96	72.69	60.19	85.82	84.55

3.5 Suitable dataset for LC classification in model area

To identify a suitable dataset for LC classification, Kappa index values were compared among 18 datasets (see Table 5); the top three datasets, D18, D16, and D12, provided the highest Kappa index, with values of 0.9154, 0.9133, and 0.9102, respectively. On the contrary, three datasets, D3, D1, and D2, displayed the lowest Kappa index, with values of 0.6434, 0.6198, and 0.6017, respectively.

The z-statistic value for D12 and D16, D12 and D18, and D16 and D18 are 0.130737, 0.341274, and 0.208664, respectively, which are less than 1.28 (80% confidential level), 1.65 (90% confidential level), and 2.58 (100% confidential level). It means that when we consider the change of Kappa index value of top three datasets (D12, D16, and D18), the increasing of Kappa index of D16 and D18 is insignificant. So, D12 was selected as the suitable dataset for LC classification since we can reduce the time for preparing S1 data.

3.6 LC classification in test area

The results of LC classification in test area (Nanjing City) in 2020 from suitable data type (D7–D12) using RF on the GEE platform are presented in Figure 9 and Table 6.

As a result, in Figure 9, the patterns of LC distribution from 6 datasets are different according to the number of features in the datasets. Meanwhile, using the D7-D12 datasets, the areas of forest land are stable, while the areas of urban and built-up land, cropland, grassland, and water bodies fluctuate slightly (see Table 6).

Furthermore, thematic accuracy assessment of LC maps of 6 datasets (D7-D12) are presented in Table 6. The OA values vary from 88.10% for D8 to 92.38% for D12, and the Kappa index values vary from 0.8361 for D8 to 0.8914 for D12. As a result, the classified LC map in test area (Nanjing City) using the identified optimal parameters of RF from model area (Hefei city) with the suitable dataset can be accepted.

4 Discussion

4.1 Optimal parameters for RFs

Based on OOB error measurement, an optimal number of trees (NT) was 800 for balancing the efficiency and accuracy of the RF (see Figure 3). Meanwhile, the optimal combination values of VPS and BF of the RF algorithm for each dataset (D1–D18) were identified by trial and error with the smaller OOB error value, summarized in Table 2. The selection of a suitable NT and appropriate VPS and BF

TABLE 5 OA, Kappa index, and average value by data type.

Data type	Dataset	OA (%)	Average by data type (%)	Kappa index	Average by data type
S1	D1	72.58	72.61	0.6198	0.6216
	D2	71.37		0.6017	
	D3	73.87		0.6434	
S1 + Auxiliary	D4	82.37	82.66	0.7617	0.7667
	D5	82.23		0.7612	
	D6	83.37		0.7771	
S2	D7	90.51	90.94	0.8742	0.8796
	D8	90.44		0.8736	
	D9	91.87		0.8910	
S2 + Auxiliary	D10	93.04	92.64	0.9024	0.9004
	D11	91.72		0.8885	
	D12	93.17		0.9102	
S1 + S2	D13	90.67	91.10	0.8750	0.8793
	D14	90.65		0.8711	
	D15	91.97		0.8919	
S1 + S2 + Auxiliary	D16	93.43	93.03	0.9133	0.9077
	D17	92.05		0.8943	
	D18	93.62		0.9154	

values can increase the classification accuracy of the RF classifier. This finding was consistent with the Svoboda's (Svoboda et al., 2022) study that used the appropriate values of NT, VPS and BF of the RF for land use change and forestry in the Czech Republic.

4.2 Suitable data type and dataset for LC classification in model area

According to OA, the Kappa index, and the average value by data type in Table 5, S2 data without and with auxiliary data, D7–D9 and D10–D12, respectively, were suitable data types compared with S1 data without and with auxiliary data, D1–D3 and D4–D6, respectively. In this study, S2 data could distinguish between forest land and grassland better than S1 data since broad vegetation classes are discriminated more easily by their physiology using the optical sensor than their physical structure from the radar sensor. This finding is consistent with LC studies combining optical and radar data in other geographic regions (Vaglio Laurin et al., 2013; Stefanski et al., 2014).

For suitable dataset identification, when comparing the OA and Kappa index of 18 datasets, the top three datasets, D18, D16, and D12, provided the highest OA and Kappa index, as reported in Table 5. However, the derived Kappa index of three datasets were not significantly different according to pairwise Z test. This study selected D12 (S2 Monthly median + S2 Season median + DNB + Elevation), as the suitable dataset for LC classification. The combining S2 and auxiliary data could provide an OA and a Kappa index of 93.17% and 0.9102, respectively. This dataset was sufficient and acceptable to classify LC with high accuracy, as suggested by Anderson et al. (1976). and Rosenfield and Fitzpatrick-Lins, (1986).

4.3 LC classification and its accuracy in model area

As a result of LC classification in model area (Hefei City) shown in Figure 6 and Table 3, patterns of LC distribution and the area of each LC type were dependent on the selected features of each dataset (D1–D18). Meanwhile, the OA values of the 18 datasets varied from 71.37% to about 94%, and their Kappa index values varied from 0.6017 (or about 60%) to 0.9154 (or about 92%) (see Figure 8). The OA and Kappa index of LC maps from the D7–D18 dataset was higher than 85% and 0.8, respectively, indicating that the classification results are acceptable (Anderson et al., 1976; Rosenfield and Fitzpatrick-Lins, 1986). The results suggested that a dataset of S2 data without and with auxiliary data, D7–D12, could classify LC better than a dataset of S1 data without and with auxiliary data, D1–D6. The results are consistent with other studies (Gislason et al., 2006; Rodriguez-Galiano et al., 2012; Pelletier et al., 2016; Ghorbanian et al., 2020; Phan et al., 2020; Ghorbanian et al., 2021), that is, when classifying LC, the classification accuracy of S2 data is better than that of S1 data.

According to the results of PA and UA of each LC type (Supplementary Appendix S1, S2) and the average PA and UA of

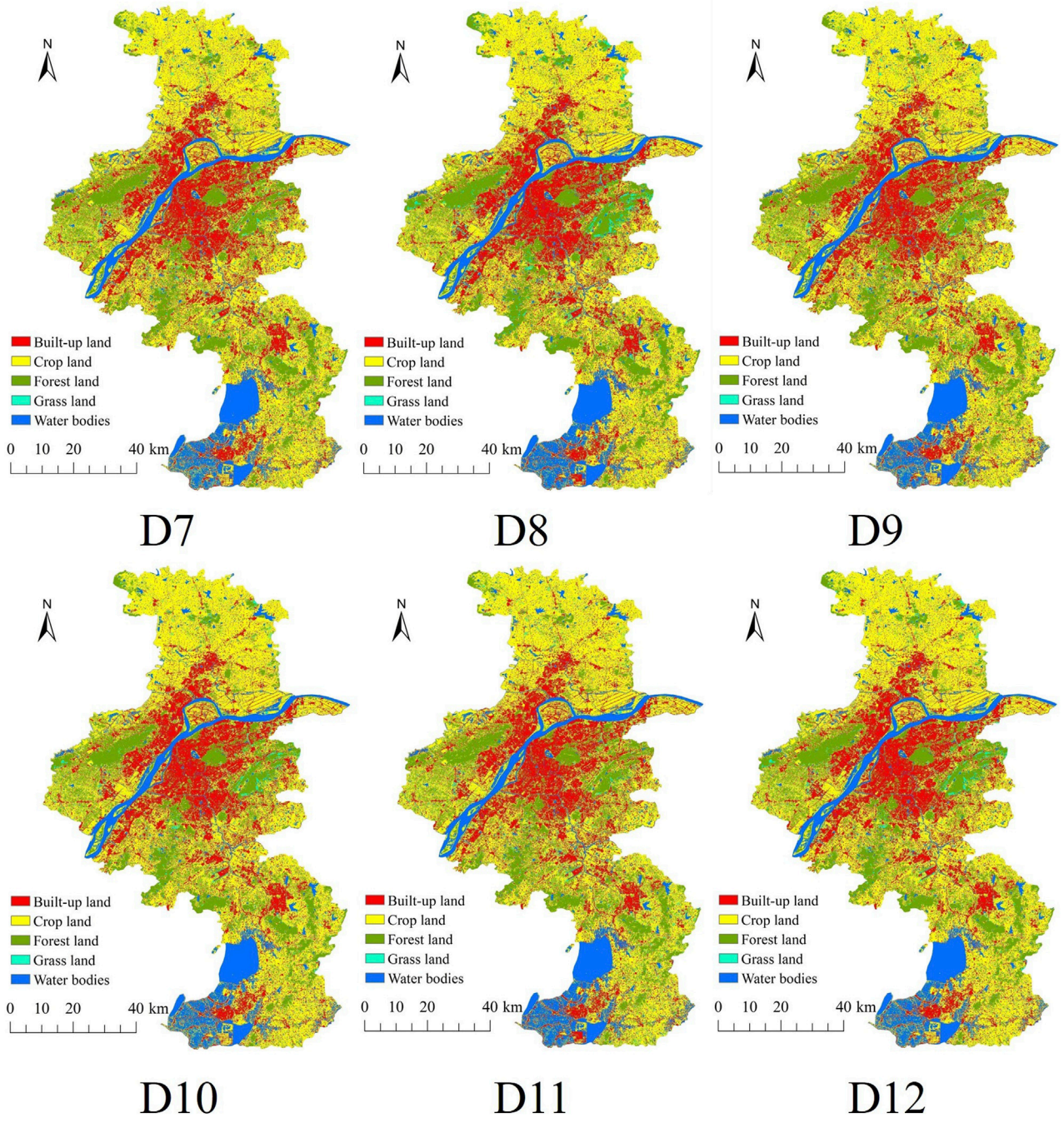

FIGURE 9
LC maps of Nanjing City in 2020 from datasets: D7–D12.

three primary data types of 18 datasets (Table 4), the derived values of PA and UA of each LC depend on the data type and its feature for LC classification using RF. In this study, water bodies can be classified with a highly accurate value of PA and UA in 18 datasets. Similarly, cropland can be classified with a highly accurate PA value in 18 datasets, while cropland can be classified with high accurate UA value in 15 datasets, but not in D1–D3. On the contrary, urban and built-up land, bare land, forest land, and grassland can be classified with highly accurate PA and UA values in 12 datasets, but not in D1–D6.

4.4 LC classification and its accuracy in test area

For the result of LC classification in the model area (Nanjing City) displayed in Figure 9 and Table 6, patterns of LC distribution and the area of each LC type also rely on the selected features of each dataset (D7-D12). In the meantime, the overall accuracy values of the six datasets fluctuated between 88.10% and 92.38%, and their Kappa index values varied from 0.8361 (or about 84%) to 0.8914 (or about 89%) (see Table 6). The OA and Kappa indexes of each LC maps from

TABLE 6 Area of each LC type and OA and Kappa index results in Nanjing City in 2020.

Dataset	Urban and built-up land	Cropland	Forest land	Grassland	Water bodies	OA (%)	Kappa index
D7	1374.76	2853.74	1112.78	161.74	783.14	90.58	0.8712
D8	1406.47	2778.26	1091.14	191.14	815.56	88.10	0.8361
D9	1360.64	2833.79	1118.59	170.78	798.72	90.80	0.8720
D10	1380.76	2835.37	1094.61	175.27	796.51	91.76	0.8861
D11	1393.85	2778.99	1103.09	186.87	819.76	91.33	0.8818
D12	1368.58	2837.40	1115.56	170.79	790.19	92.38	0.8914

D7–D12 datasets were higher than 85% and 80% respectively, indicating that they can provide acceptable results (Anderson et al., 1976).

As a result, whether it is OA or Kappa index, the dataset of S2 data with auxiliary data (D10–D12) is higher than the dataset of S2 data without auxiliary data (D7–D9). In addition, datasets that adopt a combination of monthly median and season median (D9 and D12) have the highest OA and Kappa index, followed by the datasets using the monthly median (D7 and D10). Although datasets utilizing season median (D8 and D11) yield the lowest OA and Kappa, their values are still higher than 85% and 0.8, respectively, which are still acceptable results (Anderson et al., 1976).

4.5 Validation of optimal parameter of RF for LC classification

As far as the NT is concerned, there is a decreasing relationship between the value of OOB and the NT, which means that the more the NT, the more conducive to improving the classification accuracy, but the larger the value, the more memory and calculation time required, which affects the classification efficiency. In addition, the classification benefit brought by the increase in the NT also decreases as the NT increases. Therefore, it is vital to choose an appropriate NT. In this study, we choose 800 as a suitable value of NT, which is similar to the previous studies that set 300 or 500 (Nguyen et al., 2020; Fekri et al., 2021; Piao et al., 2021; Xiao et al., 2021; Yang et al., 2021).

As far as BF is concerned, the value of OOB and the value of BF show a relationship of decreasing at first and then increasing. For the D1, D2, D3, and D5 datasets, the most suitable BF value is about 0.6, while for other datasets (D6, D6, and D7–D18), the most suitable BF value is about 0.9, both of which are higher than the value suggested by GEE (0.5). This finding is consistent with Patrick's (Kacic et al., 2021) work concluding that the classification accuracy is higher when the BF is equal to 0.9. But the finding is more different from the research (Svoboda et al., 2022), who set the value of bag fraction to 0.1 when using S2 for land use change and forestry.

For the value of VPS, the datasets using season median data or using season median data with auxiliary data (D2, D5, D8, D11, D14, and D17), there is a relationship of decrease at beginning and then increase between the value of VPS and the value of OOB. And the other 12 datasets show a decreasing relationship between the value of VPS and the value of OOB. In addition, the suitable values of VPS for these 18 different datasets are related to the number of features in the dataset. In this study, we choose 1.5 times square root of the number of features as the appropriate value, which is higher than GEE suggests 1 times square root of the number of features. This choice is consistent with the result of Patrick's (Kacic et al., 2021) research proposing that the number of VPS holds positive correlations with classification accuracy. But the finding is slightly different from the research (Ghorbanian et al., 2021; Venter and Sydenham, 2021) using the value of VPS suggested by GEE.

As shown in Figure 8, the OA and Kappa index of the LC map in Hefei City using D12 as the dataset through RF under GEE are 93.17% and 0.9102, respectively. Meanwhile, in Table 6, the OA and Kappa index of the LC map in Nanjing City of D12 are 92.83% and 0.8914, respectively. The OA and Kappa index of the LC of the two cities are higher than 90% and 0.8, respectively, indicating that the appropriate data types, datasets and RF parameters obtained in this study have certain generalizability and can be applied to other cities.

4.6 Impact of Sentinel-2 data missing on LC classification

Since S2 data is susceptible to atmospheric influences, it is likely that some regions or some years do not have S2 median data during the rainy season. To study the effect of S2 median data missing on LC classification, taking the D7 dataset (OA = 90.51%) as a reference, the S2 median data of a certain month were artificially removed. We found that when the median data of S2 in any month are missing, the OA does not change much, and the change of OA is within ±1%. OA decreased the most (−0.83%) when the median data for June were missing, and OA improved the most (+0.94%) when the median data for July were missing. The possible reason is that there were more cloudy and rainy days in July, and some cloud coverage pixels were not identified by the QA band, which cause the data in July to play a negative role in the LU classification. Taking the D8 dataset (OA = 90.44%) as a reference, the S2 median data of a certain season were artificially removed. We found that when the median data of Spring, Summer, Autumn, and Winter were missing, the OA changed to 90.62%, 88.71%, 89.98%, and 90.22%. It shows that the median data of Spring have a slight negative impact on the classification of LC. The median data of Summer are more important than other seasons, and when the data are missing, the classification accuracy of LC is reduced by about 1.7%. This shows that median data of Summer are more important for LC classification, but at the same time, it should be noted that the quality of data in some months of Summer may be low. So, accurate identification of cloud contamination pixels is conducive to improving the OA of LC classification.

4.7 Strength and limitation of google earth engine

GEE's data archive contains more than 40 years of historical datasets that are updated and expanded daily, including the Landsat, Sentinel, MODIS, land cover data, and so on. GEE also provides a variety of ML classification algorithms, such as CART, RF, SVM, naive Bayes, and decision tree. Since it is cloud-based, there is no need to download a large number of image files, and when the relevant parameters are set, the classification results of city-scale LC can be obtained within a few minutes. When running analytics on platforms like ERDAS and ENVI, it can take hours or even days to download the data and process the analytics. Therefore, the research method developed based on GEE can be applied to the update of LC maps where LC changes quickly occur. However, GEE is also limited in some cases, such as memory overflow, and other cloud platforms such as Amazon Web Services and Pixel Information Expert (PIE) Engine can be tried in the future.

5 Conclusion

In recent years, the advantages of GEE's abundance of available data and fast processing of remote sensing data have facilitated the remarkable development of RF algorithm for LC classification. To this end, it is crucial to investigate suitable data types, datasets, and input parameters of RF for LC classification.

This study classifies the LC of the model area (Hefei City) and evaluates the accuracy to determine the suitable data types, datasets and RF input parameters. The results show that the OA, Kappa index, PA and UA of all six datasets of S2 data (D7–D12) are higher than that of S1 data (D1–D6).

Meanwhile, the most suitable dataset for LC classification is D12, which combines S2 and auxiliary data. The OA and Kappa index of Hefei City reach 93.17% and 0.9102, respectively, when the values of the three primary parameters NT, VPS and BF of RF are 800, 22 and 0.9, respectively. Then, the suitable dataset and parameters of the RF obtained in the model area (Hefei City) were verified in a test area (Nanjing City). The results show that the OA and Kappa index of Nanjing City are 92.38% and 0.8914 respectively. The OA and Kappa index of LC in Nanjing City and Hefei City are higher than 90% and 0.85 respectively, and the OAs are also higher than the accuracies reported by the LC products data providers themselves: ESA WorldCover reported 74%; ESRI Land Cover reported 85% (Venter et al., 2022). It turns out that based on the suitable data type obtained from the model area (Hefei City), the dataset and the input parameters of the RF can be generalized to test area (Nanjing City). In conclusion, the proposed method and the appropriate data types, datasets and RF parameters obtained in this study have certain universality and reference, and can be used to update the local LC information in other cities at low cost and high speed in the future. However, LC classification usually depends heavily on samples, data and algorithms. In future work, we will study sample generation strategies based on data distribution characteristics, open source databases, and existing land cover products; data integration techniques on the basis of multi-scale, multi-platform, and multi-modal; and algorithm integration of various ML and DL algorithms.

Data availability statement

Publicly available datasets were analyzed in this study. This data can be found here: https://developers.google.com/earth-engine/datasets/catalog/NOAA_VIIRS_DNB_MONTHLY_V1_VCMCFG?hl=en, https://developers.google.com/earth-engine/datasets/catalog/ESA_WorldCover_v100, https://developers.google.com/earth-engine/datasets/catalog/COPERNICUS_S1_GRD, https://developers.google.com/earth-engine/datasets/catalog/COPERNICUS_S2_SR, https://livingatlas.arcgis.com/landcover/, https://developers.google.com/earth-engine/datasets/catalog/USGS_SRTMGL1_003?hl=en.

Author contributions

JS: Conceptualization, methodology, software, validation, formal analysis, investigation, resources, data curation, original draft preparation, visualization, project administration, funding acquisition. SO: Conceptualization, methodology, validation, review and editing, supervision. All authors contributed to the article and approved the submitted version.

Funding

This research was funded by the Natural Science Research Project of the Anhui Education Department, grant number KJ2019A0707.

Acknowledgments

The facility support from Tongling University is gratefully acknowledged by the authors. Special thanks from the authors go to the reviewers for their valuable comments and suggestions that improved our manuscript from various perspectives.

Conflict of interest

The authors declare that the research was conducted in the absence of any commercial or financial relationships that could be construed as a potential conflict of interest.

Publisher's note

Supplementary material

The Supplementary Material for this article can be found online at: https://www.frontiersin.org/articles/10.3389/feart.2023.1188093/full#supplementary-material

References

Amani, M., Ghorbanian, A., Ahmadi, S. A., Kakooei, M., Moghimi, A., Mirmazloumi, S. M., et al. (2020). Google Earth engine cloud computing platform for remote sensing big data applications: a comprehensive review. *IEEE J. Sel. Top. Appl. Earth Observations Remote Sens.* 13, 5326–5350. doi:10.1109/jstars.2020.3021052

Anderson, J. R., Hardy, E. E., Roach, J. T., and Witmer, R. E. (1976). A land use and land cover classification system for use with remote sensor data. *Professional Paper*. -.

Azzari, G., and Lobell, D. B. (2017). Landsat-based classification in the cloud: an opportunity for a paradigm shift in land cover monitoring. *Remote Sens. Environ.* 202, 64–74. doi:10.1016/j.rse.2017.05.025

Ban, Y., Webber, L., Gamba, P., and Paganini, M. (2017). *Joint urban remote sensing event (JURSE), 6-8 march 2017 2017*, 1–4.EO4Urban: sentinel-1A SAR and Sentinel-2A MSI data for global urban services

Bourgoin, C., Oszwald, J., Bourgoin, J., Gond, V., Blanc, L., Dessard, H., et al. (2020). Assessing the ecological vulnerability of forest landscape to agricultural frontier expansion in the Central Highlands of Vietnam. *Int. J. Appl. Earth Observation Geoinformation* 84, 101958. doi:10.1016/j.jag.2019.101958

Breiman, L. (2001). Random forests. *Mach. Learn.* 45, 5–32. doi:10.1023/a:1010933404324

Chatziantoniou, A., Psomiadis, E., and Petropoulos, G. P. (2017). Co-orbital sentinel 1 and 2 for LULC mapping with emphasis on wetlands in a mediterranean setting based on machine learning. *Remote Sens.* 9, 1259. doi:10.3390/rs9121259

Chen, J., Chen, J., Liao, A., Cao, X., Chen, L., Chen, X., et al. (2015). Global land cover mapping at 30m resolution: a POK-based operational approach. *ISPRS J. Photogrammetry Remote Sens.* 103, 7–27. doi:10.1016/j.isprsjprs.2014.09.002

Chen, Y., Wang, Y., Gu, Y., He, X., Ghamisi, P., and Jia, X. (2019). Deep learning ensemble for hyperspectral image classification. *IEEE J. Sel. Top. Appl. Earth Observations Remote Sens.* 12, 1882–1897. doi:10.1109/jstars.2019.2915259

Clark, M. L. (2017). Comparison of simulated hyperspectral HyspIRI and multispectral Landsat 8 and Sentinel-2 imagery for multi-seasonal, regional land-cover mapping. *Remote Sens. Environ.* 200, 311–325. doi:10.1016/j.rse.2017.08.028

Clerici, N., Valbuena CalderóN, C. A., and Posada, J. M. (2017). Fusion of Sentinel-1A and Sentinel-2A data for land cover mapping: a case study in the lower Magdalena region, Colombia. *J. Maps* 13, 718–726. doi:10.1080/17445647.2017.1372316

Congalton, R. G., and Green, K. (2009). *Assessing the accuracy of remotely sensed data - principles and practices*. Second edition. Boca Raton, NW, USA: CRC Press, Taylor & Francis Group.

Cremer, F., Urbazaev, M., CortéS, J., Truckenbrodt, J., Schmullius, C., and Thiel, C. (2020). "Potential of recurrence metrics from sentinel-1 time series for deforestation mapping," in IEEE Journal of Selected Topics in Applied Earth Observations and Remote Sensing, 13, 5233–5240. doi:10.1109/jstars.2020.3019333

Defries, R. (2008). Terrestrial vegetation in the coupled human-earth system: contributions of remote sensing. *Annu. Rev. Environ. Resour.* 33, 369–390. doi:10.1146/annurev.environ.33.020107.113339

Drusch, M., Del Bello, U., Carlier, S., Colin, O., Fernandez, V., Gascon, F., et al. (2012). Sentinel-2: ESA's optical high-resolution mission for GMES operational services. *Remote Sens. Environ.* 120, 25–36. doi:10.1016/j.rse.2011.11.026

EOG (2023). *Earth observation group*. Payne Institute for Public Policy, Colorado School of Mines. Available: https://developers.google.com/earth-engine/datasets/catalog/NOAA_VIIRS_DNB_MONTHLY_V1_VCMCFG?hl=en (Accessed February 16, 2023).*VIIRS nighttime day/night band composites version 1*.

Erasmi, S., and Twele, A. (2009). Regional land cover mapping in the humid tropics using combined optical and SAR satellite data—a case study from Central Sulawesi, Indonesia. *Int. J. Remote Sens.* 30, 2465–2478. doi:10.1080/01431160802552728

ESA (2023a). ESA WorldCover 10m v100. Available: https://developers.google.com/earth-engine/datasets/catalog/ESA_WorldCover_v100 (Accessed February 16, 2023).

ESA (2023b). Sentinel-1 SAR GRD. Available: https://developers.google.com/earth-engine/datasets/catalog/COPERNICUS_S1_GRD (Accessed February 16, 2023).

ESA (2023c). Sentinel-2 MSI. Available: https://developers.google.com/earth-engine/datasets/catalog/COPERNICUS_S2_SR (Accessed February, 2023).

ESRI (2023). Esri land cover. Available: https://livingatlas.arcgis.com/landcover/ (Accessed February 16, 2023).

Feddema, J. J., Oleson, K. W., Bonan, G. B., Mearns, L. O., Buja, L. E., Meehl, G. A., et al. (2005). The importance of land-cover change in simulating future climates. *Science* 310, 1674–1678. doi:10.1126/science.1118160

Fekri, E., Latifi, H., Amani, M., and Zobeidinezhad, A. (2021). A training sample migration method for wetland mapping and monitoring using sentinel data in Google Earth engine. *Remote Sens.* 13, 4169. doi:10.3390/rs13204169

Forkuor, G., Dimobe, K., Serme, I., and Tondoh, J. E. (2018). Landsat-8 vs. Sentinel-2: examining the added value of sentinel-2's red-edge bands to land-use and land-cover mapping in Burkina Faso. *GIScience Remote Sens.* 55, 331–354. doi:10.1080/15481603.2017.1370169

Freitas, C. D. C., Soler, L. D. S., San" Anna, S. J. S., Dutra, L. V., Santos, J. R. D., Mura, J. C., et al. (2008). Land use and land cover mapping in the Brazilian Amazon using polarimetric airborne P-band SAR data. *IEEE Trans. Geoscience Remote Sens.* 46, 2956–2970. doi:10.1109/tgrs.2008.2000630

Gao, B.-C. (1996). NDWI—a normalized difference water index for remote sensing of vegetation liquid water from space. *Remote Sens. Environ.* 58, 257–266. doi:10.1016/s0034-4257(96)00067-3

Ghorbanian, A., Kakooei, M., Amani, M., Mahdavi, S., Mohammadzadeh, A., and Hasanlou, M. (2020). Improved land cover map of Iran using Sentinel imagery within Google Earth Engine and a novel automatic workflow for land cover classification using migrated training samples. *ISPRS J. Photogrammetry Remote Sens.* 167, 276–288. doi:10.1016/j.isprsjprs.2020.07.013

Ghorbanian, A., Zaghian, S., Asiyabi, R. M., Amani, M., Mohammadzadeh, A., and Jamali, S. (2021). Mangrove ecosystem mapping using sentinel-1 and sentinel-2 satellite images and random forest algorithm in Google Earth engine. *Remote Sens.* 13, 2565. doi:10.3390/rs13132565

Gislason, P. O., Benediktsson, J. A., and Sveinsson, J. R. (2006). Random Forests for land cover classification. *Pattern Recognit. Lett.* 27, 294–300. doi:10.1016/j.patrec.2005.08.011

Goldblatt, R., Stuhlmacher, M. F., Tellman, B., Clinton, N., Hanson, G., Georgescu, M., et al. (2018). Using Landsat and nighttime lights for supervised pixel-based image classification of urban land cover. *Remote Sens. Environ.* 205, 253–275. doi:10.1016/j.rse.2017.11.026

GóMEZ, C., White, J. C., and Wulder, M. A. (2016). Optical remotely sensed time series data for land cover classification: a review. *ISPRS J. Photogrammetry Remote Sens.* 116, 55–72. doi:10.1016/j.isprsjprs.2016.03.008

Gong, P., Liu, H., Zhang, M., Li, C., Wang, J., Huang, H., et al. (2019). Stable classification with limited sample: transferring a 30-m resolution sample set collected in 2015 to mapping 10-m resolution global land cover in 2017. *Sci. Bull.* 64, 370–373. doi:10.1016/j.scib.2019.03.002

Gong, P., Wang, J., Yu, L., Zhao, Y., Zhao, Y., Liang, L., et al. (2013). Finer resolution observation and monitoring of global land cover: first mapping results with Landsat TM and ETM+ data. *Int. J. Remote Sens.* 34, 2607–2654. doi:10.1080/01431161.2012.748992

Gorelick, N., Hancher, M., Dixon, M., Ilyushchenko, S., Thau, D., and Moore, R. (2017). Google Earth Engine: planetary-scale geospatial analysis for everyone. *Remote Sens. Environ.* 202, 18–27. doi:10.1016/j.rse.2017.06.031

Hansen, M. C., and Loveland, T. R. (2012). A review of large area monitoring of land cover change using Landsat data. *Remote Sens. Environ.* 122, 66–74. doi:10.1016/j.rse.2011.08.024

Hong, D., Gao, L., Yao, J., Zhang, B., Plaza, A., and Chanussot, J. (2021a). Graph convolutional networks for hyperspectral image classification. *IEEE Trans. Geoscience Remote Sens.* 59, 5966–5978. doi:10.1109/tgrs.2020.3015157

Hong, D., Gao, L., Yokoya, N., Yao, J., Chanussot, J., Du, Q., et al. (2021b). More diverse means better: multimodal deep learning meets remote-sensing imagery classification. *IEEE Trans. Geoscience Remote Sens.* 59, 4340–4354. doi:10.1109/tgrs.2020.3016820

Huang, D., Xu, S., Sun, J., Liang, S., Song, W., and Wang, Z. (2017). Accuracy assessment model for classification result of remote sensing image based on spatial sampling. *J. Appl. Remote Sens.* 11, 1. doi:10.1117/1.jrs.11.046023

Joshi, N., Baumann, M., Ehammer, A., Fensholt, R., Grogan, K., Hostert, P., et al. (2016). A review of the application of optical and radar remote sensing data fusion to land use mapping and monitoring. *Remote Sens.* 8, 70. doi:10.3390/rs8010070

Ju, J., and Roy, D. P. (2008). The availability of cloud-free Landsat ETM+ data over the conterminous United States and globally. *Remote Sens. Environ.* 112, 1196–1211. doi:10.1016/j.rse.2007.08.011

Kacic, P., Hirner, A., and Da Ponte, E. (2021). Fusing sentinel-1 and -2 to model GEDI-derived vegetation structure characteristics in GEE for the Paraguayan chaco. *Remote Sens.* 13, 5105. doi:10.3390/rs13245105

Klaiber, M. (2021). A fundamental overview of SOTA-ensemble learning methods for deep learning. *A Syst. Lit. Rev.* 2, 14. doi:10.31763/sitech.v2i2.549

Krishna, K., Caitlin, K., Zoe, S.-W., Joseph, M., Mark, M., Steven, B., and IMPACT OBSERVATORY, UNITED STATES (2021). "Global land use/land cover with Sentinel-2 and deep learning," in IGARSS 2021-2021 IEEE International Geoscience and Remote Sensing Symposium.

Kumar, L., and Mutanga, O. (2018). Google Earth engine applications since inception: usage, trends, and potential. *Remote Sens.* 10, 1509. doi:10.3390/rs10101509

Lin, Q., Guo, J., Yan, J., and Heng, W. (2018). Land use and landscape pattern changes of Weihai, China based on object-oriented SVM classification from Landsat MSS/TM/OLI images. *Eur. J. Remote Sens.* 51, 1036–1048. doi:10.1080/22797254.2018.1534532

Liu, C., Li, W., Zhu, G., Zhou, H., Yan, H., and Xue, P. (2020a). Land use/land cover changes and their driving factors in the northeastern Tibetan plateau based on geographical detectors and Google Earth engine: a case study in gannan prefecture. *Remote Sens.* 12, 3139. doi:10.3390/rs12193139

Liu, H., Gong, P., Wang, J., Clinton, N., Bai, Y., and Liang, S. (2020b). Annual dynamics of global land cover and its long-term changes from 1982 to 2015. *Earth Syst. Sci. Data* 12, 1217–1243. doi:10.5194/essd-12-1217-2020

Luo, J., Ma, X., Chu, Q., Xie, M., and Cao, Y. (2021). Characterizing the up-to-date land-use and land-cover change in xiong'an new area from 2017 to 2020 using the multi-temporal sentinel-2 images on Google Earth engine. *ISPRS Int. J. Geo-Information* 10, 464. doi:10.3390/ijgi10070464

Lyons, M. B., Keith, D. A., Phinn, S. R., Mason, T. J., and Elith, J. (2018). A comparison of resampling methods for remote sensing classification and accuracy assessment. *Remote Sens. Environ.* 208, 145–153. doi:10.1016/j.rse.2018.02.026

Masroor, M., Avtar, R., Sajjad, H., Choudhari, P., Kulimushi, L. C., Khedher, K. M., et al. (2022). Assessing the influence of land use/land cover alteration on climate variability: an analysis in the aurangabad district of Maharashtra state, India. *Sustainability* 14, 642. doi:10.3390/su14020642

Miller, S. D., Straka, W., Mills, S. P., Elvidge, C. D., Lee, T. F., Solbrig, J., et al. (2013). Illuminating the capabilities of the suomi national polar-orbiting partnership (NPP) visible infrared imaging radiometer suite (VIIRS) day/night band. *Remote Sens.* 5, 6717–6766. doi:10.3390/rs5126717

Mongus, D., and Žalik, B. (2018). Segmentation schema for enhancing land cover identification: a case study using Sentinel 2 data. *Int. J. Appl. Earth Observation Geoinformation* 66, 56–68. doi:10.1016/j.jag.2017.11.004

Mutanga, O., and Kumar, L. (2019). Google Earth engine applications. *Remote Sens.* 11, 591. doi:10.3390/rs11050591

NASA (2023). NASA SRTM Digital Elevation 30m. Available: https://developers.google.com/earth-engine/datasets/catalog/USGS_SRTMGL1_003?hl=en (Accessed February 16, 2023).

Nguyen, H. T. T., Doan, T. M., Tomppo, E., and Mcroberts, R. E. (2020). Land use/land cover mapping using multitemporal sentinel-2 imagery and four classification methods—a case study from dak nong, vietnam. *Remote Sens.* 12, 1367. doi:10.3390/rs12091367

Pelletier, C., Valero, S., Inglada, J., Champion, N., and Dedieu, G. (2016). Assessing the robustness of Random Forests to map land cover with high resolution satellite image time series over large areas. *Remote Sens. Environ.* 187, 156–168. doi:10.1016/j.rse.2016.10.010

Pesaresi, M., Corbane, C., Julea, A., Florczyk, A. J., Syrris, V., and Soille, P. (2016). Assessment of the added-value of sentinel-2 for detecting built-up areas. *Remote Sens.* 8, 299. doi:10.3390/rs8040299

Phan, T. N., Kuch, V., and Lehnert, L. W. (2020). Land cover classification using Google Earth engine and random forest classifier—the role of image composition. *Remote Sens.* 12, 2411. doi:10.3390/rs12152411

Piao, Y., Jeong, S., Park, S., and Lee, D. (2021). Analysis of land use and land cover change using time-series data and random forest in North Korea. *Remote Sens.* 13, 3501. doi:10.3390/rs13173501

Pirotti, F., Sunar, F., and Piragnolo, M. (2016). Benchmark of machine learning methods for classification of a Sentinel-2 image. *Int. Arch. Photogramm. Remote Sens. Spat. Inf. Sci.*, 335–340. doi:10.5194/isprsarchives-xli-b7-335-2016

Ray, S. (2019). "A quick review of machine learning algorithms," in International Conference on Machine Learning, Big Data, Cloud and Parallel Computing (COMITCon), 14-16 Feb. 2019, 35–39.

Rodriguez-Galiano, V. F., Ghimire, B., Rogan, J., Chica-Olmo, M., and Rigol-Sanchez, J. P. (2012). An assessment of the effectiveness of a random forest classifier for land-cover classification. *ISPRS J. Photogrammetry Remote Sens.* 67, 93–104. doi:10.1016/j.isprsjprs.2011.11.002

Rosenfield, G. H., and Fitzpatrick-Lins, K. (1986). A coefficient of agreement as a measure of thematic classification accuracy. *Photogramm. Eng. remote Sens.* 52, 223–227.

Shelestov, A., Lavreniuk, M., Kussul, N., Novikov, A., and Skakun, S. (2017). Exploring Google Earth engine platform for big data processing: classification of multi-temporal satellite imagery for crop mapping. *Front. Earth Sci.* 5. doi:10.3389/feart.2017.00017

Shetty, S., Gupta, P. K., Belgiu, M., and Srivastav, S. K. (2021). Assessing the effect of training sampling design on the performance of machine learning classifiers for land cover mapping using multi-temporal remote sensing data and Google Earth engine. *Remote Sens.* 13, 1433. doi:10.3390/rs13081433

Shrestha, A., and Mahmood, A. (2019). Review of deep learning algorithms and architectures. *IEEE Access* 7, 53040–53065. doi:10.1109/access.2019.2912200

Soenen, S. A., Peddle, D. R., and Coburn, C. A. (2005). SCS+C: a modified Sun-canopy-sensor topographic correction in forested terrain. *IEEE Trans. Geoscience Remote Sens.* 43, 2148–2159. doi:10.1109/tgrs.2005.852480

Song, X.-P., Hansen, M. C., Stehman, S. V., Potapov, P. V., Tyukavina, A., Vermote, E. F., et al. (2018). Global land change from 1982 to 2016. *Nature* 560, 639–643. doi:10.1038/s41586-018-0411-9

Sothe, C., Almeida, C. M. D., Liesenberg, V., and Schimalski, M. B. (2017). Evaluating sentinel-2 and landsat-8 data to map sucessional forest stages in a subtropical forest in southern Brazil. *Remote Sens.* 9, 838. doi:10.3390/rs9080838

Spoto, F., Sy, O., Laberinti, P., Martimort, P., Fernandez, V., Colin, O., et al. (2012). "Overview of sentinel-2," in 2012 IEEE International Geoscience and Remote Sensing Symposium, 22-27 July 2012, 1707–1710.

Stefanski, J., Kuemmerle, T., Chaskovskyy, O., Griffiths, P., Havryluk, V., Knorn, J., et al. (2014). Mapping land management regimes in western Ukraine using optical and SAR data. *Remote Sens.* 6, 5279–5305. doi:10.3390/rs6065279

Su, Y., Li, X., Feng, M., Nian, Y., Huang, L., Xie, T., et al. (2021). High agricultural water consumption led to the continued shrinkage of the Aral Sea during 1992–2015. *Sci. Total Environ.* 777, 145993. doi:10.1016/j.scitotenv.2021.145993

Sun, Z., Di, L., and Fang, H. (2019). Using long short-term memory recurrent neural network in land cover classification on Landsat and Cropland data layer time series. *Int. J. Remote Sens.* 40, 593–614. doi:10.1080/01431161.2018.1516313

Svoboda, J., Štych, P., Laštovička, J., Paluba, D., and Kobliuk, N. (2022). Random forest classification of land use, land-use change and forestry (LULUCF) using sentinel-2 data—a case study of Czechia. *Remote Sens.* 14, 1189. doi:10.3390/rs14051189

Tamiminia, H., Salehi, B., Mahdianpari, M., Quackenbush, L., Adeli, S., and Brisco, B. (2020). Google Earth Engine for geo-big data applications: a meta-analysis and systematic review. *ISPRS J. Photogrammetry Remote Sens.* 164, 152–170. doi:10.1016/j.isprsjprs.2020.04.001

Tang, P., Du, P., Lin, C., Guo, S., and Qie, L. (2020). A novel sample selection method for impervious surface area mapping using JL1-3B nighttime light and sentinel-2 imagery. *IEEE J. Sel. Top. Appl. Earth Observations Remote Sens.* 13, 3931–3941. doi:10.1109/jstars.2020.3004654

Thanh Noi, P., and Kappas, M. (2018). Comparison of random forest, k-nearest neighbor, and support vector machine classifiers for land cover classification using sentinel-2 imagery. *Sensors* 18, 18. doi:10.3390/s18010018

Torres, R., Snoeij, P., Geudtner, D., Bibby, D., Davidson, M., Attema, E., et al. (2012). GMES Sentinel-1 mission. *Remote Sens. Environ.* 120, 9–24. doi:10.1016/j.rse.2011.05.028

Tucker, C. J. (1979). Red and photographic infrared linear combinations for monitoring vegetation. *Remote Sens. Environ.* 8, 127–150. doi:10.1016/0034-4257(79)90013-0

Turner, B. L., Lambin, E. F., and Reenberg, A. (2007). The emergence of land change science for global environmental change and sustainability. *Proc. Natl. Acad. Sci.* 104, 20666–20671. doi:10.1073/pnas.0704119104

Vaglio Laurin, G., Liesenberg, V., Chen, Q., Guerriero, L., Del Frate, F., Bartolini, A., et al. (2013). Optical and SAR sensor synergies for forest and land cover mapping in a tropical site in West Africa. *Int. J. Appl. Earth Observation Geoinformation* 21, 7–16. doi:10.1016/j.jag.2012.08.002

Venter, Z. S., Barton, D. N., Chakraborty, T., Simensen, T., and Singh, G. (2022). Global 10 m land use land cover datasets: a comparison of dynamic World, World cover and esri land cover. *Remote Sens.* 14, 4101. doi:10.3390/rs14164101

Venter, Z. S., and Sydenham, M. A. K. (2021). Continental-scale land cover mapping at 10 m resolution over europe (ELC10). *Remote Sens.* 13, 2301. doi:10.3390/rs13122301

Wu, X., Hong, D., and Chanussot, J. (2022). Convolutional neural networks for multimodal remote sensing data classification. *IEEE Trans. Geoscience Remote Sens.* 60, 1–10. doi:10.1109/tgrs.2021.3124913

Xiao, W., Xu, S., and He, T. (2021). Mapping paddy rice with sentinel-1/2 and phenology-object-based algorithm—a implementation in hangjiahu plain in China using GEE platform. *Remote Sens.* 13, 990. doi:10.3390/rs13050990

Yang, Y., Yang, D., Wang, X., Zhang, Z., and Nawaz, Z. (2021). Testing accuracy of land cover classification algorithms in the qilian mountains based on GEE cloud platform. *Remote Sens.* 13, 5064. doi:10.3390/rs13245064

Zanaga, D., Van De Kerchove, R., De Keersmaecker, W., Souverijns, N., Brockmann, C., Quast, R., et al. (2021). *ESA WorldCover 10 m 2020 v100.*

Zeng, H., Wu, B., Wang, S., Musakwa, W., Tian, F., Mashimbye, Z. E., et al. (2020). A synthesizing land-cover classification method based on Google Earth engine: a case study in nzhelele and levhuvu catchments, South Africa. *Chin. Geogr. Sci.* 30, 397–409. doi:10.1007/s11769-020-1119-y

Zha, Y., Gao, J., and Ni, S. (2003). Use of normalized difference built-up index in automatically mapping urban areas from TM imagery. *Int. J. Remote Sens.* 24, 583–594. doi:10.1080/01431160304987

Zhang, M., Huang, H., Li, Z., Hackman, K. O., Liu, C., Andriamiarisoa, R. L., et al. (2020). Automatic high-resolution land cover production in Madagascar using sentinel-2 time series, tile-based image classification and Google Earth engine. *Remote Sens.* 12, 3663. doi:10.3390/rs12213663

Zhang, X., Liu, L., Chen, X., Gao, Y., Xie, S., and Mi, J. (2021). GLC_FCS30: global land-cover product with fine classification system at 30 m using time-series Landsat imagery. *Earth Syst. Sci. Data,* 13, 2753–2776. doi:10.5194/essd-13-2753-2021

Zheng, H., Du, P., Chen, J., Xia, J., Li, E., Xu, Z., et al. (2017). Performance evaluation of downscaling sentinel-2 imagery for land use and land cover classification by spectral-spatial features. *Remote Sens.* 9, 1274. doi:10.3390/rs9121274

Frontiers in
Environmental Science

Explores the anthropogenic impact on our natural world

An innovative journal that advances knowledge of the natural world and its intersections with human society. It supports the formulation of policies that lead to a more inhabitable and sustainable world.

Discover the latest Research Topics

See more →

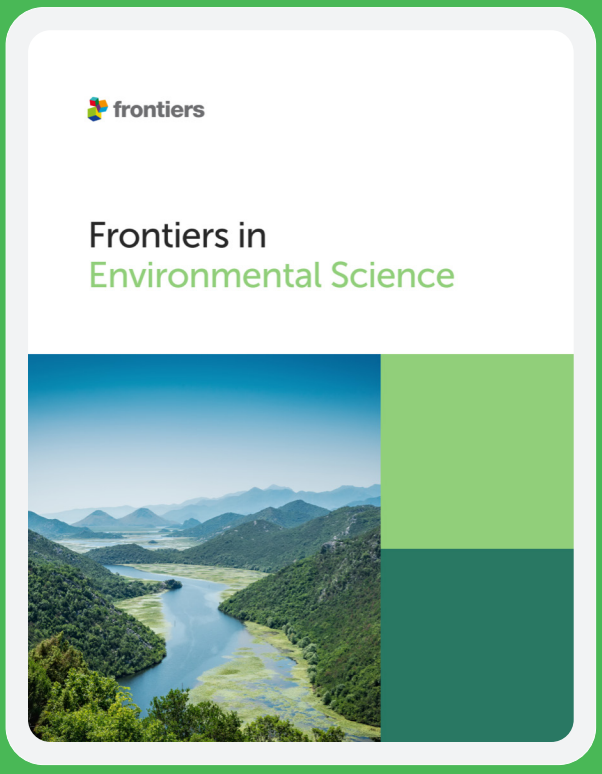

Frontiers

Avenue du Tribunal-Fédéral 34
1005 Lausanne, Switzerland
frontiersin.org

Contact us

+41 (0)21 510 17 00
frontiersin.org/about/contact